frontiers | Research Topics

# Functional biomaterials design, synthesis and applications

**Edited by**
Manjie Zhang, Wenliang Wang, Xiangjun Chen, Oommen Podiyan Oommen and Yun Chang

**Coordinated by**
Yakun Luo

**Published in**
Frontiers in Bioengineering and Biotechnology

ISSN 1664-8714
ISBN 978-2-8325-5219-3
DOI 10.3389/978-2-8325-5219-3

## About Frontiers

Frontiers is more than just an open access publisher of scholarly articles: it is a pioneering approach to the world of academia, radically improving the way scholarly research is managed. The grand vision of Frontiers is a world where all people have an equal opportunity to seek, share and generate knowledge. Frontiers provides immediate and permanent online open access to all its publications, but this alone is not enough to realize our grand goals.

## Frontiers journal series

The Frontiers journal series is a multi-tier and interdisciplinary set of open-access, online journals, promising a paradigm shift from the current review, selection and dissemination processes in academic publishing. All Frontiers journals are driven by researchers for researchers; therefore, they constitute a service to the scholarly community. At the same time, the *Frontiers journal series* operates on a revolutionary invention, the tiered publishing system, initially addressing specific communities of scholars, and gradually climbing up to broader public understanding, thus serving the interests of the lay society, too.

## Dedication to quality

Each Frontiers article is a landmark of the highest quality, thanks to genuinely collaborative interactions between authors and review editors, who include some of the world's best academicians. Research must be certified by peers before entering a stream of knowledge that may eventually reach the public - and shape society; therefore, Frontiers only applies the most rigorous and unbiased reviews. Frontiers revolutionizes research publishing by freely delivering the most outstanding research, evaluated with no bias from both the academic and social point of view. By applying the most advanced information technologies, Frontiers is catapulting scholarly publishing into a new generation.

## What are Frontiers Research Topics?

Frontiers Research Topics are very popular trademarks of the *Frontiers journals series*: they are collections of at least ten articles, all centered on a particular subject. With their unique mix of varied contributions from Original Research to Review Articles, Frontiers Research Topics unify the most influential researchers, the latest key findings and historical advances in a hot research area.

Find out more on how to host your own Frontiers Research Topic or contribute to one as an author by contacting the Frontiers editorial office: frontiersin.org/about/contact

# Functional biomaterials design, synthesis and applications

**Topic editors**
Manjie Zhang — Harbin Medical University, China
Wenliang Wang — The University of Texas at Austin, United States
Xiangjun Chen — Northeast Normal University in Changchun, China
Oommen Podiyan Oommen — Tampere University, Finland
Yun Chang — Purdue University, United States

**Topic coordinator**
Yakun Luo — Harbin Medical University, China

**Citation**
Zhang, M., Wang, W., Chen, X., Oommen, O. P., Chang, Y., Luo, Y., eds. (2024). *Functional biomaterials design, synthesis and applications*.
Lausanne: Frontiers Media SA. doi: 10.3389/978-2-8325-5219-3

# Table of contents

frontiers | Frontiers in Bioengineering and Biotechnology

TYPE Original Research
PUBLISHED 03 July 2023
DOI 10.3389/fbioe.2023.1209752



OPEN ACCESS

EDITED BY
Oommen Podiyan Oommen,
Tampere University, Finland

REVIEWED BY
Jianxun Ding,
Chinese Academy of Sciences (CAS), China
Zhihao Chen,
Northwestern Polytechnical University, China

*CORRESPONDENCE
Yuan Qu,
quyuan0127@jlu.edu.cn

RECEIVED 25 April 2023
ACCEPTED 20 June 2023
PUBLISHED 03 July 2023

CITATION
Zhang S, Ding L, Chen G, Zhang J, Ge W and Qu Y (2023), Enhanced bone regeneration via local low-dose delivery of $PTH_{1-34}$ in a composite hydrogel. *Front. Bioeng. Biotechnol.* 11:1209752. doi: 10.3389/fbioe.2023.1209752



# Enhanced bone regeneration via local low-dose delivery of $PTH_{1-34}$ in a composite hydrogel

Shanyong Zhang[1], Lei Ding[2], Gaoyang Chen[3], Jiayin Zhang[1], Wanbao Ge[1] and Yuan Qu[1]*

[1]Department of Spine Surgery, The Second Hospital of Jilin University, Changchun, China, [2]Department of Rehabilitation, The Second Hospital of Jilin University, Changchun, China, [3]Shenzhen Key Laboratory of Musculoskeletal Tissue Reconstruction and Function Restoration, Department of Hand Surgery, Shenzhen People's Hospital, The First Affiliated Hospital of Southern University of Science and Technology, Jinan University Second College of Medicine, Shenzhen, China

Introducing bone regeneration–promoting factors into scaffold materials to improve the bone induction property is crucial in the fields of bone tissue engineering and regenerative medicine. This study aimed to develop a Sr-HA/$PTH_{1-34}$-loaded composite hydrogel system with high biocompatibility. Teriparatide ($PTH_{1-34}$) capable of promoting bone regeneration was selected as the bioactive factor. Strontium-substituted hydroxyapatite (Sr-HA) was introduced into the system to absorb $PTH_{1-34}$ to promote the bioactivity and delay the release cycle. $PTH_{1-34}$-loaded Sr-HA was then mixed with the precursor solution of the hydrogel to prepare the composite hydrogel as bone-repairing material with good biocompatibility and high mechanical strength. The experiments showed that Sr-HA absorbed $PTH_{1-34}$ and achieved the slow and effective release of $PTH_{1-34}$. *In vitro* biological experiments showed that the Sr-HA/$PTH_{1-34}$-loaded hydrogel system had high biocompatibility, allowing the good growth of cells on the surface. The measurement of alkaline phosphatase activity and osteogenesis gene expression demonstrated that this composite system could promote the differentiation of MC3T3-E1 cells into osteoblasts. In addition, the *in vivo* cranial bone defect repair experiment confirmed that this composite hydrogel could promote the regeneration of new bones. In summary, Sr-HA/$PTH_{1-34}$ composite hydrogel is a highly promising bone repair material.

KEYWORDS

**PTH, bone regeneration, hydrogel, strontium, hydroxyapatite**

## 1 Introduction

Bone tissue engineering has emerged as a promising strategy for addressing the limitations associated with traditional methods of bone repair and reconstruction. Current procedures often involve graft transplantation, which faces challenges such as donor site morbidity, limited graft availability, and potential immunogenic responses. As a result, there is a growing interest in developing alternative strategies that can stimulate the body's innate regenerative capacity. Among these, *in-situ* bone tissue engineering stands out as it combines the principles of biology and engineering to create functional bone tissue directly at the site of injury or disease (Kim et al., 2011; Hou et al., 2018; Chen et al., 2021a; Chen et al., 2021b). The use of scaffolds that either have inherent bone-inducing properties or are functionalized with osteoinductive growth factors is increasingly being recognized as a key factor in successful *in-situ* bone regeneration (Hasani-Sadrabadi et al., 2020a; Wan et al., 2022; Zhang et al., 2023). Novel scaffold materials, including bioactive ceramics,

synthetic polymers, and composite materials, have been engineered to not only provide structural support but also to facilitate bone cell adhesion, proliferation, differentiation, and ultimately, new bone formation (Annamalai et al., 2018; Johnson et al., 2019; Olov et al., 2022; Liu et al., 2023).

An injectable hydrogel has the advantages of high-water content, injectability, *in situ* formation, controllable physical and chemical properties, and high biocompatibility (Cui et al., 2019; Zhao et al., 2019; Hasani-Sadrabadi et al., 2020b; Wu et al., 2021). It has been considered one of the most promising biological materials and is used in the field of bone tissue engineering. Furthermore, the injectable hydrogel can mini-invasively load cells, drugs, and various biological factors and thus has several advantages in bone tissue engineering (Olov et al., 2022; Zhao et al., 2022). Therefore, using mini-invasive techniques for administering the injectable hydrogel loaded with bone regeneration–promoting factors into the high-risk regions of osteoporotic fractures in elderly people with initial fractures, followed by *in situ* solidification, can rapidly enhance the mechanical strength of local bone tissues and exert short-term protective effects (Zhang et al., 2020; Oprita et al., 2022). In addition, the controlled local release of biological factors and the degradation of the hydrogel can persistently enhance the bone density and bone mass of patients and thus exert long-term protective effects (Cheng et al., 2020). This treatment can be used to treat OP and prevent the occurrence of fractures in key regions.

In recent years, various types of gelatin hydrogels have been widely investigated and used for bone defect repair. Gelatin has several advantages, including high biocompatibility, biodegradability, low production cost, and capability of being chemically modified. For instance, gelatin methacryloyl (GelMA) hydrogel is a relatively ideal bone-substitute material. The methacrylic acid groups of GelMA are linked to the amino group on the side chain of gelatin, which can well mimic the extracellular matrix (ECM) (Chai et al., 2022; Wang et al., 2022). The chemical cross-linking of GelMA can effectively maintain cell viability, combine bioactive factors that promote cell or bone regeneration, and thus produce more excellent biological materials for bone tissue engineering (Yue et al., 2015). Heparin hydrogel is also a material widely used as a bone tissue engineering material, which has not only high histocompatibility but also high bioactivity (Sakiyama-Elbert, 2014; Nilasaroya et al., 2021). Combining chemically modified heparin with other high-molecular-weight materials can produce bone-substitute materials for bone defect repair. Strontium (Sr) is an extremely important element in the human skeleton (Place et al., 2011; Malinovsky et al., 2013). Various previous studies demonstrated that Sr could inhibit bone resorption to increase bone strength and improve the rate of the bone union. Sr ranelate is an effective drug for treating OP in clinical practice (Tournis et al., 2006). Recent studies have also demonstrated the osteogenic capability of Sr The supplementation of Sr ions to bone-substitute materials, such as bioactive glass and calcium phosphate, improves not only the mechanical properties of the materials but also the bone induction capability of the system, thus inducing the differentiation of osteoblasts *in vitro* and accelerating bone regeneration in the area of osteoporotic bone defect *in vivo* (Kargozar et al., 2019; Demirel and Kaya, 2020). Hydroxyapatite (HAP) is the major component of bones and teeth in vertebrates, which has high bioactivity and biocompatibility. Compared with conventional bone-substitute materials such as metals (e.g., stainless steel and titanium alloy) and ceramics (e.g., aluminum oxide and silicon nitride), HAP has the advantages of high resistance to corrosion and high capability of inducing bone generation (Shi et al., 2021). In addition, the degradation of HAP also eliminates the safety concerns associated with the use of conventional materials. Previous studies on the application of HAP as bone-substitute materials mainly focused on two aspects: HAP coating and human bone biomimetic regenerative material. Compared with HAP, strontium-substituted hydroxyapatite (Sr-HA) could more significantly accelerate bone union and enhance bone-forming capability (Vestermark, 2011). Small amounts of Sr-HA with the hydrogel also have such effects.

Achieving the balance between osteoblasts and osteoclasts is critical for effectively promoting bone regeneration. Currently, teriparatide ($PTH_{1-34}$) is the only bone regeneration–promoting drug approved by the Food and Drug Administration (Gomes-Ferreira et al., 2022). The unique capability of $PTH_{1-34}$ in activating osteoclasts and osteoblasts can help achieve the balance between bone resorption and bone regeneration and thus maintain the good state of bone. Various previous studies demonstrated that the local intermittent injection of PTH could effectively repair bone defects (Yoshida et al., 2019). However, the development of a local drug delivery system is generally limited, restricting the precise release of drugs. On the contrary, the local high-dose injection of $PTH_{1-34}$ may induce net bone resorption (Chandra et al., 2014; Orbeanu et al., 2022). Therefore, we hypothesized that the local low-dose $PTH_{1-34}$ intervention could provide a microenvironment to promote bone regeneration.

In this study, Sr-HA was used to absorb $PTH_{1-34}$ polypeptide and obtain Sr-HA/$PTH_{1-34}$. Then, double-bonded heparin (HepMA) and methacrylate gelatin (GelMA) were used as the main body of the hydrogel to produce the precursor solution of the hydrogel with high biocompatibility. Further, Sr-HA/$PTH_{1-34}$ was combined with the precursor solution of the hydrogel to prepare the Sr-HA/$PTH_{1-34}$composite hydrogel, which could allow the local controlled release of low-dose PTH to achieve the repair of defected bone tissues. *In vitro* cellular experiments showed that Sr-HA/$PTH_{1-34}$-loaded hydrogel system had high biocompatibility (Figure 1). This composite hydrogel could promote the differentiation of MC3T3-E1 cells into osteoblasts. *In vitro* cranial bone defect repair experiments confirmed that this composite hydrogel could effectively promote the regeneration of new bones. The composite hydrogel was mini-invasively injected into the site of osteoporotic fractures, followed by *in situ* solidification, which could rapidly enhance the mechanical strength of the local bone tissues and thus exert supporting effects. In addition, with the swelling and degradation of the composite hydrogel, the released $PTH_{1-34}$ could induce bone marrow mesenchymal stem cells (BMSCs) to promote osteoblastic differentiation, persistently increase the bone density and bond mass at specific sites, and thus exert long-term protective effects.

# 2 Experimental

## 2.1 Preparation of the composite hydrogel

GelMA and HepMA were prepared as described in previous studies (Yue et al., 2015; Brown et al., 2017; Kurian et al., 2022). In brief, gelatin or heparin was dissolved in phosphate-buffered saline (PBS) to prepare a 10% gelatin solution or 2% heparin solution. Then, a certain amount of

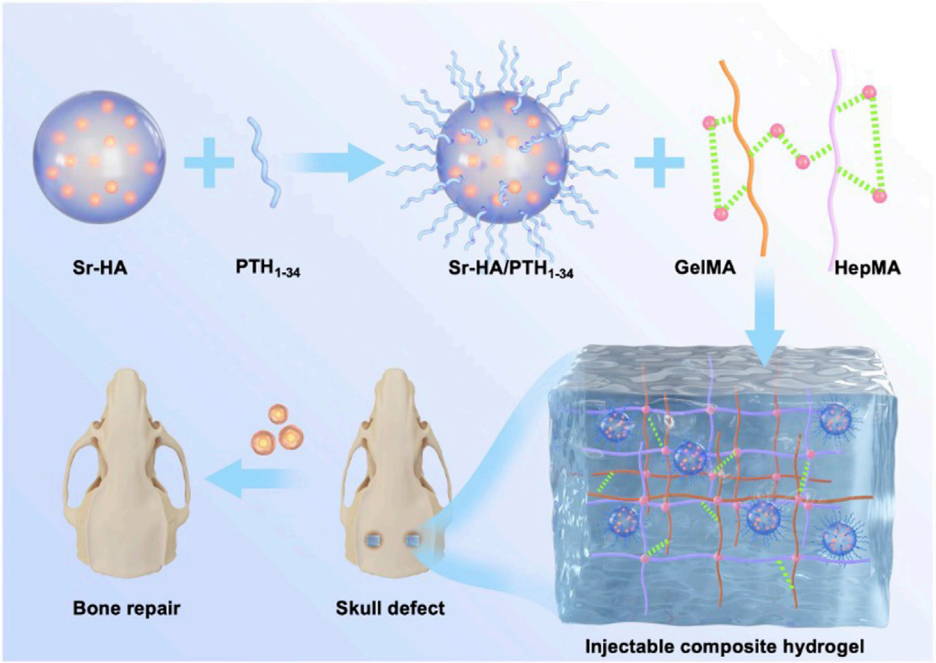


FIGURE 1
Schematic illustration of a composite hydrogel for local low dose delivery of $PTH_{1-34}$ for bone repair.

methacrylic anhydride was added to react for 3–4 h. A high amount of deionized water was added for dialysis for 5 days, which was then freeze-dried to obtain the GelMA and HepMA monomers. The prepared HepMA and GelMA were dissolved in PBS and mixed evenly. Sr-HAwas dissolved in a weak acid to prepare a homogeneous emulsion. The aforementioned solutions were mixed evenly, and then $PTH_{1-34}$ was added. Blue ray photoinitiator Lithium phenyl-2,4,6-trimethylbenzoylphosphinate (LAP) was added to induce rapid cross-linking and solidification, forming the injectable composite hydrogel. LAP has high biocompatibility and can be used to induce the solidification of the hydrogel that wraps the cells (Wang et al., 2012; Magalhães et al., 2020).

## 2.2 Physical and chemical properties of the composite hydrogel

### 2.2.1 Gel formation time of the hydrogel

The tube inversion method was used to measure the gel formation time of the hydrogel. Different concentrations of the hydrogel were prepared at 37°C. The gel formation time was the time during which the inverted tube showed no flow. All samples were prepared in triplicate for the measurement.

### 2.2.2 Analysis of the microstructure of the hydrogel

Cylinders with a diameter of 6 mm and thickness of 1 mm were prepared, which were then freeze-dried. Then, the samples were placed on the platform of a scanning electron microscope. The sizes and numbers of pores, as well as the pokiness rate, were analyzed using scanning electron microscopy.

### 2.2.3 Analysis of mechanical properties

The Shimadzu mechanical system (AG-IS, Shimadzu, Japan) was used to assess the mechanical properties of the hydrogel. The cylindrical hydrogel with a diameter of 8 mm and thickness of 6 mm was compressed at the strain rate of 5 mm/min, and the modulus of compression was calculated using the slope of the stress–strain curve in the range of linearity corresponding to 5%–10% of strain. The limiting stress was the highest stress before the rupture of the hydrogel.

### 2.2.4 Analysis of the swelling behavior of the hydrogel

The hydrogel was freeze-dried, and the dry weight ($W_d$) was measured. The dry hydrogel was placed in deionized water and retrieved at predefined time points (i.e., 0.5, 1, 3, 6, 12, 24, and 36 h). The wet weight ($W_w$) of the hydrogel at each time point was measured. The swelling ratio was calculated using the equation: swelling ratio = $(W_w - W_d)/W_d \times 100\%$, where $W_w$ is the wet weight at predefined time points and $W_d$ is the dry weight of the initial material.

### 2.2.5 Analysis of the degradation of the hydrogel

The hydrogel was freeze-dried, and the dry weight ($W_d$) was measured. The hydrogel was placed in 1× PBS, and the PBS was changed every other day. The hydrogel was retrieved on a predefined day 7 and freeze-dried, and the dry weight ($W_t$) was measured. The hydrogel was then placed in 1× PBS again and retrieved seven more days later (a total of 14 days) and freeze-dried, and the dry weight was measured. The experiment was continued for 28 days. The remaining mass of the hydrogel was calculated using the equation: Remaining mass = $W_t/W_d \times 100\%$, where $W_t$ is the dry weight at the predefined time points and $W_d$ is the initial dry weight.

## 2.3 *In vitro* drug release test of the composite hydrogel

The drug release test of the hydrogel was performed. In brief, 1 mL of the hydrogel sample loaded with $PTH_{1-34}$ (1 mg/mL) was dispersed in 5 mL of 1× PBS and vortexed in a water bath at 37°C. The samples were retrieved at different time points (i.e., 0, 5, 10, 20, 30, 50, 70, 90, 120, 140, and 180 h) and centrifuged to obtain the supernatant. Then, high-performance liquid chromatography was used to measure the $PTH_{1-34}$ level in the solution. The cumulative drug release level was assessed, and the cumulative drug release curve was plotted. The chromatographic column used in this study was the X-Bridge-Shield-RP-C18 column (Waters, United States) (50 × 4.6 $mm^2$, 3.5 μm), the flow rate was 2.5 mL/min, and the column temperature was 40°C. The volume of the sample load was 100 μL, and the wavelength of measurement was 245 nm. The mobile phase A was 0.05% Trifluoroacetic acid (TFA)–water solution and the mobile phase B was 0.05% TFA–acetonitrile, which were used for gradient elution.

## 2.4 *In vitro* assay of the composite hydrogel

### 2.4.1 Biocompatibility of the composite hydrogel

MC3T3-E1 (ATCC, United States) were cultured in α-minimum essential medium (α-MEM, Gibco, United States) supplemented with 10% fetal bovine serum (Gibco), 1% penicillin, and streptomycin (Gibco). The cells were cultured under standard conditions in the presence of 5% $CO_2$ and at 95% humidity. The merged cells were collected after digestion with EDTA containing 0.25% trypsin (Gibco) for the subsequent experiments.

The live/dead detection reagent Calcein AM and propidium (PI) were prepared, added to cells co-cultured with the hydrogel, and incubated at 37°C for 15 min. The samples were washed with PBS twice, and then an inverted fluorescence microscope was used for imaging. The CellTiter 96 aqueous solution cell proliferation assay (MTS, Promega, United States) was used to measure the viability of hBMSCs. The culture medium was discarded after the cells were cultured for 1, 3, and 7 days, and then 200 μL of the fresh culture medium with 10% MTS was added to incubate the cells for 4 h. A microplate reader (ELX808, BioTek, United States) was used to measure the optical density at 490 nm.

### 2.4.2 Induction of osteoblast differentiation by the hydrogel

The alkaline phosphatase (ALP) activity was measured to assess osteoblast differentiation. The BCIP/NBT ALP detection kit (Beyotime, China) was used to measure the ALP activity following the manufacturer's protocols. In brief, the 48-well plate was fixed with formalin solution, washed with PBS, and stained with 300 μL of the dye. Then, the cells were rinsed with running water and blotted dry, and the Olympus CKX53 microscope was used for imaging.

### 2.4.3 Expression of osteogenesis-related genes induced by the composite hydrogel

Quantitative real-time polymerase chain reaction (qRT-PCR) was performed to assess the expression of osteogenesis-related genes. The AG RNAex Pro reagent (AG21102, Accurate Biotechnology, China) was used to extract the total RNA from cells following the manufacturer's protocols. The Nanodrop 2000 spectrophotometer (Thermo Scientific, United States) was used to quantitatively assess the RNA level, and the OD260/OD280 was between 1.9 and 2.1. Total RNA (1 μg) was obtained and reverse transcribed to obtain cDNA using the PrimeScript RT kit (RR037A, TaKaRa, Japan). The StepOnePlus quantitative PCR system (Applied Biosystems, United States) with TB Green pre-mixed Ex Taq (RR420A, Takara, Japan) was used for the qRT-PCR. When assessing osteogenesis-related genes (*ALP*, osteocalcin (*OCN*), osteopontin (*OPN*), and runt-related transcription factor 2 (*RUNX2*)), GAPDH was used as the internal reference, and the $2^{-\Delta\Delta CT}$ method was used to estimate the relative expression of mRNA. All the primers were synthesized by Sangon Biotech, China.

## 2.5 Induction of the cranial bone defect model

All the animal procedures were approved by the Animal Research Committee of Shenzhen People's Hospital, Jinan University. Forty-eight male rats (10 weeks old, body weight of 280–300 g) were obtained from the Guangzhou Animal Experiment Center. After the rats were anesthetized with an intraperitoneal injection of pentobarbital sodium (45 mg/kg), a manual electric trephine was used to make two symmetric full-thickness round defects of 4.5-mm diameter on the bilateral sides of the skull in the rats. GelMA, GelMA + HepMA + Sr-HA, and GelMA + HepMA + Sr-HA + $PTH_{1-34}$ were injected into the skull defects (each group consisting of six rats), and normal saline was injected into the rats in the control group (sham surgery group). The antibiotics were injected into all the rats after the surgery once every 3 days. All the rats were sacrificed by cervical dislocation after 4 weeks. The skull was obtained and stored in 4% formalin, which was consequently used for imaging and histological analyses.

## 2.6 Micro-CT assay

The rats were sacrificed 4 weeks after the surgery, the root skull was collected and fixed in 4% paraformaldehyde (PFA), and then the skull was scanned using the high-resolution images were acquired using the 3D creator software, and then the parameters including bone mass density (BMD), bone volume (BV/TV), bone trabecular number (Tb.N), and trabecular separation (Tb. sp) were calculated.

## 2.7 Histological analysis and immunohistochemistry

After micro-CT assay, the skull was immersed in 10% EDTA for decalcification, followed by dehydration and paraffin embedding. Then, 5-μm-thick slices were prepared, stained using hematoxylin and eosin (H&E) (Sigma, United States) and Masson trichrome staining (Solarbio, China) for assessing

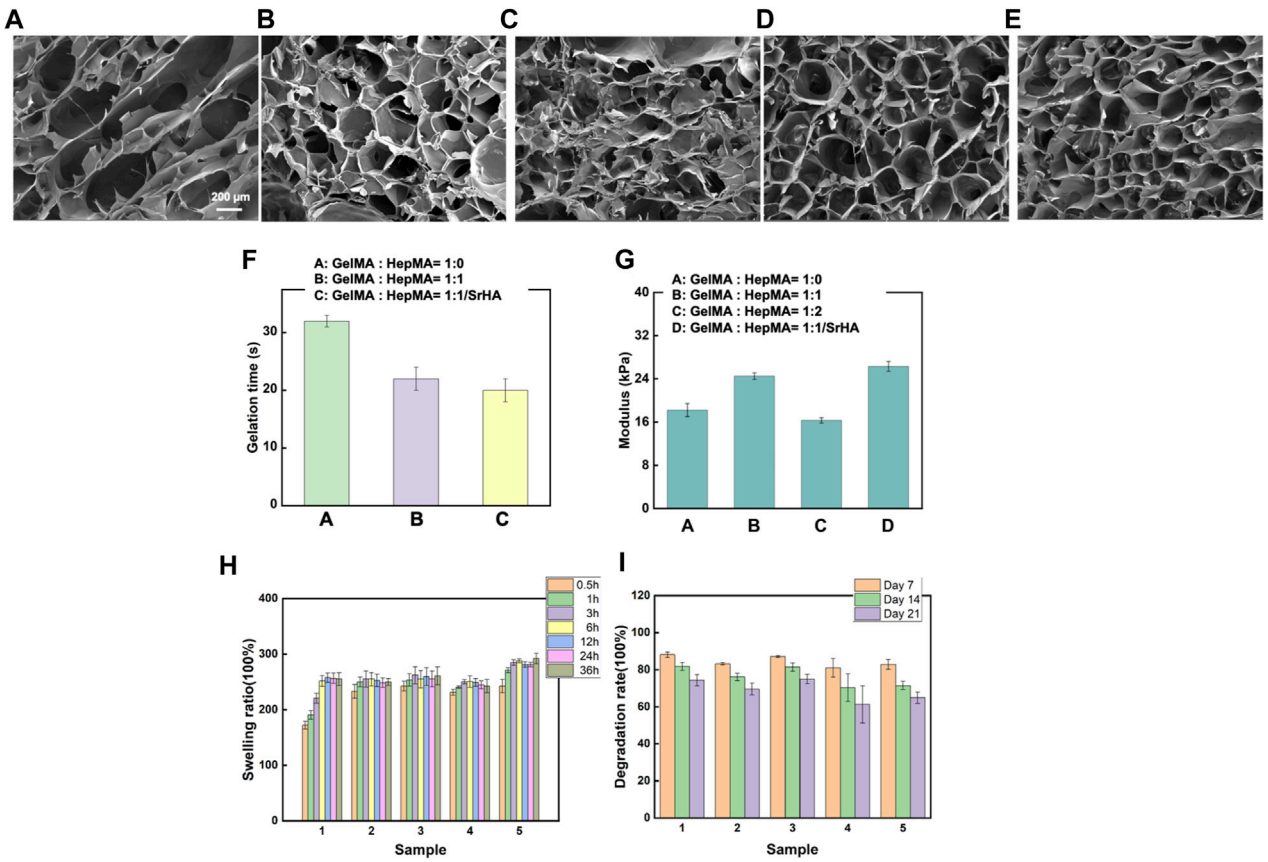


FIGURE 2
Physical and chemical properties of different hydrogels. **(A–E)** Microstructural properties of the hydrogels **(A)**: GelMA hydrogel; **(B)** SrHA; **(C)** GelMA + HepMA hydrogel; **(D)** GelMA + HepMA + SrHA hydrogel; **(E)** GelMA + HepMA + SrHA/$PTH_{1-34}$ hydrogel). **(F)** Time of gel formation of the hydrogel. **(G)** Comparison of modulus of compression of different hydrogel preparations. **(H, I)** Swelling and degradation behaviors of different hydrogel systems.

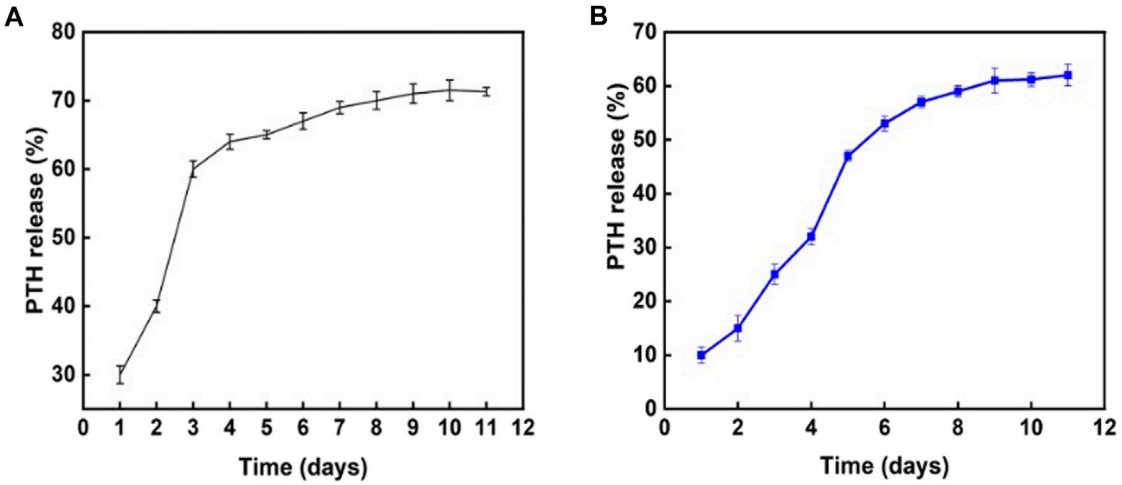


FIGURE 3
Influence of different hydrogel systems on $PTH_{1-34}$ release behaviors. **(A)** $PTH_{1-34}$ mixed with the hydrogel system of GelMA:HepMA = 1:1. **(B)** $PTH_{1-34}$ mixed with the hydrogel system of GelMA:HepMA = 1:1 (with SrHA).

the histological morphology of the defect region of the skull. For the immunohistochemistry (IHC), the skull was fixed in 4% PFA, dehydrated, and paraffin embedded. The slices (5 μm) were prepared and dewaxed with xylene, rehydrated with ethanol, processed using 3% $H_2O_2$ in absolute methanol for 30 min, immersed and boiled in citrate buffer (pH = 6.0) for 10 min, and then cooled to room temperature. The slices were blocked with normal goat serum for 30 min and then incubated with rat anti-RUNX2 and anti-OCN monoclonal antibodies at 4°C overnight. Afterward, the samples were subjected to processing using an Avidin-Biotin Complex (ABC) kit (Zhongshanjinqiao Biotechnology Co., Ltd, China) (biotin: 1 h; streptavidin: 30 min, 37°C) and then incubated using the 3,3′Diaminobenzidine (DAB) kit (Zhongshanjinqiao Biotechnology Co., Ltd.) for 1 min. The Mayer hematoxylin was used for counterstaining. The omission of the primary antibody was used as the negative control.

## 2.8 Statistical analysis

All the data were described as means and standard deviations (≥3 samples). One-way analysis of variance and paired-sample *t*-test were used for the statistical analysis. A $p$-value < 0.05 indicated a statistically significant difference. All the statistical analysis and figure plotting were performed using the Origin 8.5 software.

# 3 Results and discussion

## 3.1 Preparation of the composite hydrogel and analysis of physical and chemical properties

The composite hydrogel system was prepared by rapid solidification of HepMA (10 wt%) and GelMA (2 wt%)

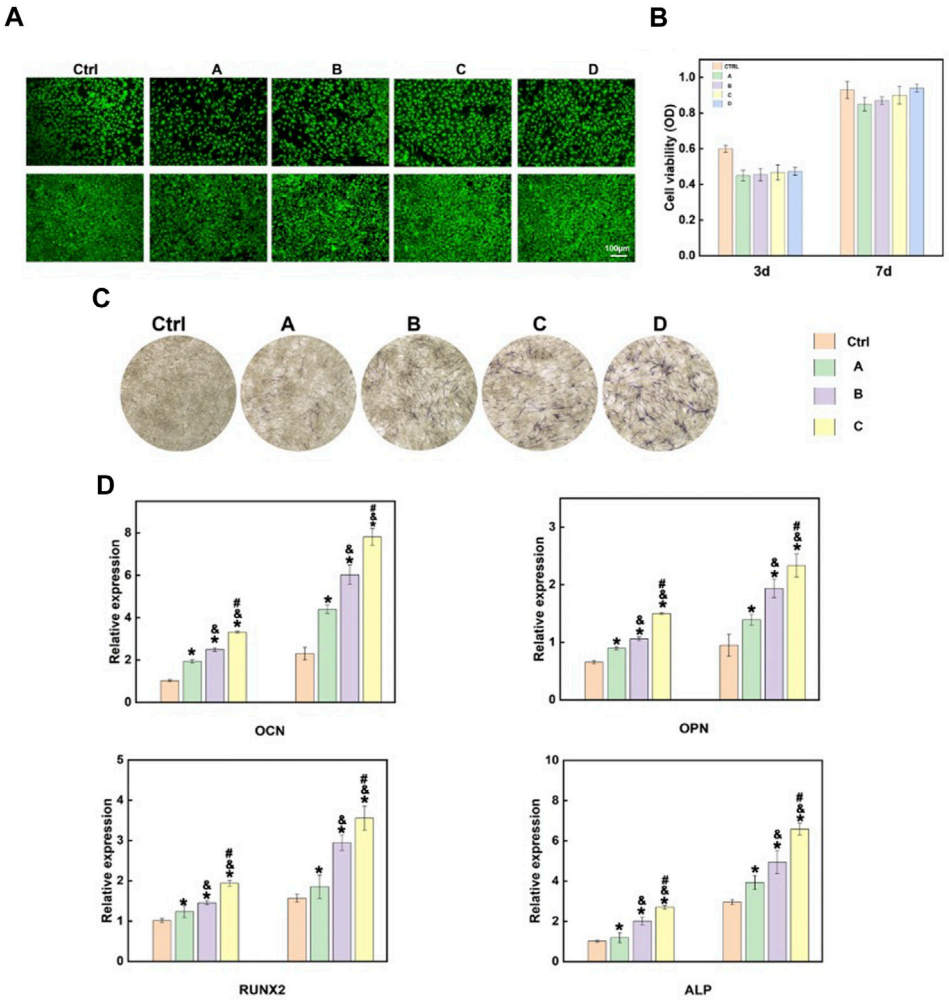


FIGURE 4
*In vitro* cellular experiments of the composite hydrogel. **(A)** Live-dead cell staining findings after MC3T3-E1 cells were co-cultured with different hydrogel systems for 3 and 7 days **(B)** Quantitative analysis of the cell proliferation of MC3T3-E1 cells co-cultured with different hydrogel systems for 3 and 7 days using MTS. **(C)** The ALP activity of MC3T3-E1 cells after 7-day growth on various hydrogels-conditioned medium **(A)**: GelMA hydrogel; **(B)** GelMA + HepMA hydrogel; **(C)** GelMA + HepMA + SrHA hydrogel; **(D)** GelMA + HepMA + SrHA/$PTH_{1-34}$ hydrogel); **(D)** Measurement of the expression of different osteogenesis-related genes **(A)**:GelMA + HepMA hydrogel; **(B)** GelMA + HepMA + SrHA hydrogel; **(C)** GelMA + HepMA + SrHA/$PTH_{1-34}$ hydrogel).

induced by a blue ray photoinitiator LAP. The gel formation time of the different systems is shown in Supplementary Table S1. The Sr-HA showed no significant influence on the gel formation time of the ultimate systems (Figure 2F). The porosity and sizes of pores were critical for some cellular functions, such as influencing cell growth and nutrient transportation. The freeze-dried samples were scanned using electron microscopy. The findings are shown in Figures 2A–E. Adding HepMA to GelMA could increase the cross-linking of the hydrogel and the number of pores in the hydrogel, making the network more dense and even. In addition, when the ratio of GelMA to HepMA was 1:1, the best modulus of compression was obtained. The introduction of HAP could reduce the modulus of compression of the hydrogel (Figure 2G). The swelling equilibrium of the hydrogel was achieved in approximately 12 h. Compared with pure GelMA hydrogel, adding HepMA reduced the swelling ratio of the system, and adding SrHA also slightly but not significantly reduced the swelling ratio (Figure 2H). After the different hydrogel preparations were freeze-dried, the degradation assay was performed by immersing the samples in PBS, followed by degradation after 7, 14, and 21 days. The findings are shown in Figure 2I, which indicated that the introduction of Sr-HA could delay the degradation of the system.

## 3.2 *In vitro* drug release assay of the composite hydrogel

The *in vitro* effects of the composite hydrogel on $PTH_{1-34}$ release were assessed. As shown in Figure 3A, the direct combination of $PTH_{1-34}$ with the hydrogel resulted in a relatively fast release in the first 3 days. On the contrary, introducing Sr-HA into loaded $PTH_{1-34}$ reduced the

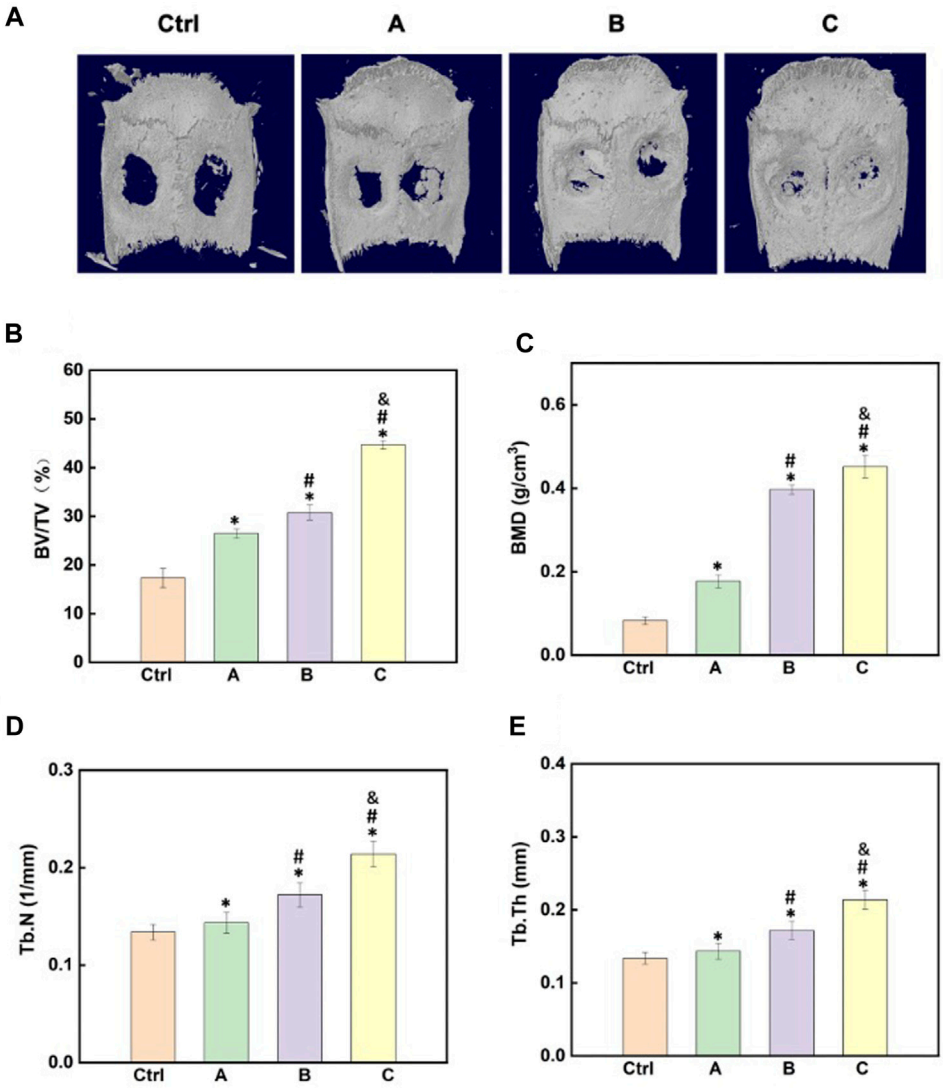


FIGURE 5
Effects of the composite hydrogel systems in promoting bone regeneration *in vivo*. **(A)** 3D reconstruction images of the skull after different hydrogel materials were implanted to the site of skull bone defects for 4 weeks. **(B–E)** Quantitative analysis of the micro-CT images for the assessment of BV/TV, BMD, Tb.N, and Tb.Th. **(A)**: GelMA + HepMA hydrogel; **(B)** GelMA + HepMA + SrHA hydrogel; **(C)** GelMA + HepMA + SrHA/$PTH_{1-34}$ hydrogel).

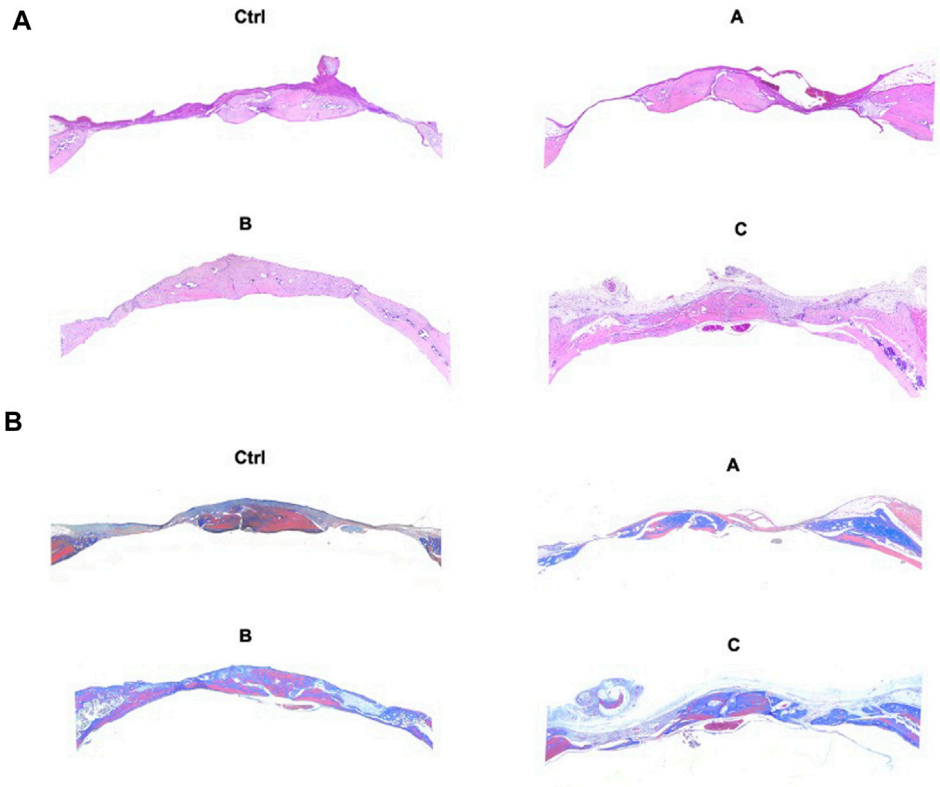


FIGURE 6
H&E staining **(A)** and Masson trichrome staining **(B)** after the bone defects were treated with different hydrogel systems for 4 weeks (4×).

release rate in the initial stage and allowed the slow, low-dose release of $PTH_{1-34}$ in the following week (Figure 3B).

## 3.3 *In vitro* cellular experiments of the hydrogel

MC3T3-E1 cells were co-cultured with the hydrogel, and MTS and live-dead cell staining were performed after the cells were cultured for 3 and 7 days, respectively, to assess the influences of different hydrogel systems on cell viability. As shown in Figures 4A, B, the co-culture of cells with different hydrogel systems-maintained cell viability. In addition, the introduction of Sr-HA and $PTH_{1-34}$promoted the proliferation of cells. Scanning electron microscope (SEM) was used to visualize the state of cells co-cultured with the hydrogel (Supplementary Figure S1), showing that the cells could attach to the surface of hydrogel materials and survive. ALP staining was performed to assess the effects of the hydrogel systems on the osteoblast differentiation of MC3T3-E1 cells. The findings showed that compared with the control group, the hydrogel loaded with Sr-HA and $PTH_{1-34}$ showed the most significant ALP staining signals, which were higher than those for the system loaded with Sr-HA only, indicating that Sr-HA and $PTH_{1-34}$ could jointly promote the differentiation of MC3T3-E1 cells into osteoblasts (Figure 4C). The hydrogel systems loaded with Sr-HA increased the expression of osteogenesis-related genes, including OCN, OPN, RUNX2, and ALP (Figure 4D). More significantly, the simultaneous loading of Sr-HA and PTH in the system resulted in the highest expression levels of the osteogenesis-related genes. These findings demonstrated that the joint effects of Sr-HA and $PTH_{1-34}$ could better promote the differentiation into osteoblasts.

## 3.4 *In vivo* effects of the composite hydrogel in promoting bone regeneration

After the materials were implanted in the body for 4 weeks, micro-CT images clearly displayed the differences in the regeneration of new bone tissues after treatment with different components (Figure 5). The images clearly showed that the *in vivo* osteogenesis effects were in agreement with the *in vitro* findings, and the hydrogel with both Sr-HA and PTH could better promote the repair and regeneration of bone tissues at the bone defects (Figure 5A). The quantitative analysis of BMD, BV/TV, Tb.N, and Tb.Th was performed to further assess the osteogenesis effects. The findings showed that after treatment with the composite hydrogel system for 4 weeks, the hydrogel loaded with both Sr-HA and PTH could induce the regeneration of new bones at the site of bone defects, and the effects were higher than those for the hydrogel system loaded with Sr-HA only (Figures 5B–E).

## 3.5 Histological assessment and IHC of the new bones

H&E staining, Masson trichrome staining, and IHC were used for the assessment of bone regeneration at the site of bone

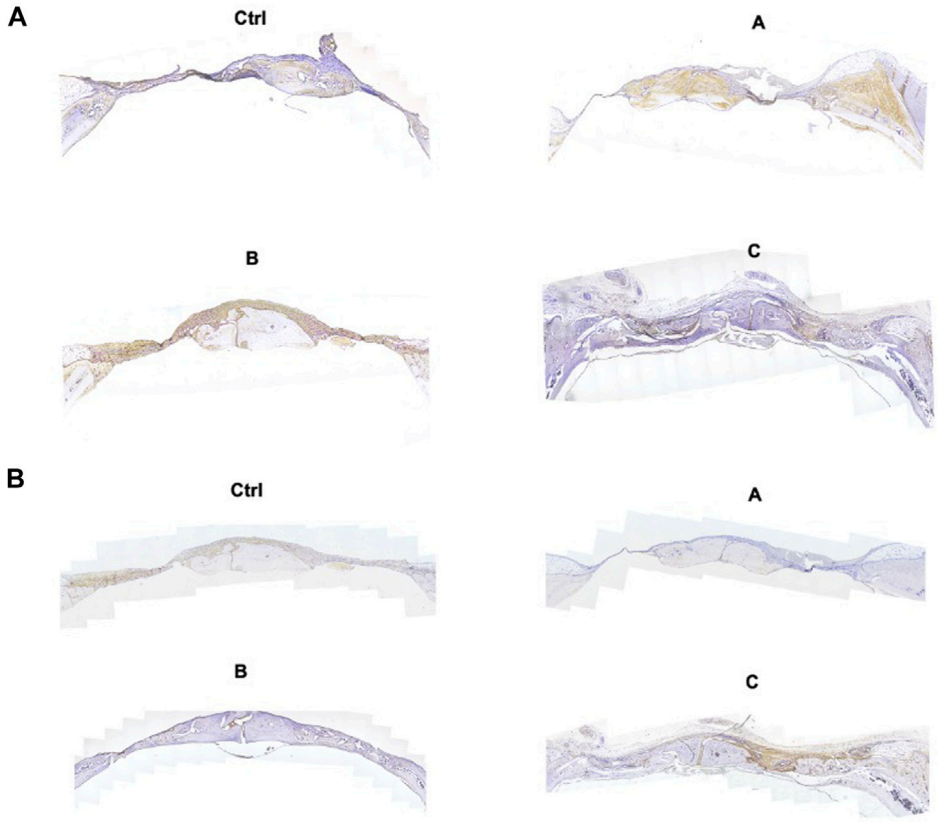


FIGURE 7
IHC images of OCN **(A)** and RUNX2 **(B)** after the bone defects were treated with different hydrogel systems for 4 weeks (4×).

defects to further verify the effects of the composite hydrogel systems on bone regeneration. The Figure 6 shows the H&E staining and Masson trichrome staining results of bone defects in different groups. The findings were in agreement with the micro-CT results. Compared with other treatments, Sr-HA and PTH co-treatment induced the highest amount of new bone tissues, with the new bones filling the whole defect site, and the regenerated collagenous fibers were denser than those in other groups. The Masson trichrome staining further showed that the GelMA/HepMA/SrHA/PTH group had more calcified bone-like tissues connected to each other, indicating the presence of more new bones with higher maturity. The IHC assay showed slightly lower expression in the GelMA/HepMA/Sr-HA group, while the expression of OCN and RUNX2 significantly increased in the GelMA/HepMA/SrHA/PTH group (Figures 7A, B).

## 4 Conclusion

In this study, we established a composite hydrogel capable of the controlled release of PTH to achieve the local controlled release of low-dose PTH, providing a good microenvironment for promoting bone regeneration at the site of bone defects. First, Sr-HA was used to absorb the PTH polypeptide, which was then mixed with the precursor solution of GelMA/HepMA hydrogel to prepare the composite hydrogel system with high mechanical strength and high biocompatibility and capable of the local controlled release of low-dose PTH by light cross-linking. The treatment of bone defects using the composite hydrogel could effectively promote the cells to differentiate into osteoblasts and promote tissue regeneration via the local controlled release of low-dose PTH. In addition, the mini-invasive injection of the composite hydrogel into the site of osteoporotic fracture, followed by *in situ* solidification, could rapidly enhance the mechanical strength of local bone tissues, thus exerting the supporting effects. Furthermore, with the swelling and degradation of the hydrogel, the PTH released by the composite hydrogel could induce the BMSCs to promote bone differentiation, persistently improve the local bone density and bone mass, and thus exert long-term protective effects.

Despite the promising results demonstrated in our research, several limitations must be acknowledged. Firstly, the results indicated that the local low dose PTH treatment could better activate the signaling pathways associated with osteoblasts and thus promote bone regeneration. However, the exact mechanisms involved in the effects on osteoblasts and osteoclasts were not investigated, which should be explored in future. Secondly, the current study only examined the short-term effects of the developed hydrogel in bone repair. Long-term studies are necessary to assess the persistence of the newly formed bone and

the possible long-term effects or complications related to the hydrogel or its degradation products. In addition, the use of strontium and PTH was based on their proven benefits in osteoporosis treatment and bone regeneration. However, the specific doses and ratios used in this study were determined empirically. Further dose-response studies may be necessary to optimize the concentrations of strontium and PTH for maximal therapeutic effects and minimal side effects. Nevertheless, future work will need to explore the long-term safety, efficacy, and practicality of these hydrogel systems.

## Data availability statement

The original contributions presented in the study are included in the article/Supplementary Material, further inquiries can be directed to the corresponding author.

## Ethics statement

The studies involving animals were reviewed and approved by the Animal Research Committee of Shenzhen People's Hospital, Jinan University.

## Author contributions

YQ and SZ conceived the concept and designed the project. SZ and LD performed the experiments and analyzed the results. GC, JZ, and WG assisted with the figure production and experiment design. YQ and SZ wrote and revised the original draft of the manuscript. All authors contributed to the article and approved the submitted version.

## Funding

This work was supported by the National Natural Science Foundation of China (82001448) and Natural Science Foundation of Jilin Province (YDZJ202201ZYTS066), Sanming Project of Medicine in Shenzhen (No.SZSM202111015), and Shenzhen Key Laboratory of Musculoskeletal Tissue Reconstruction and Function Restoration (ZDSYS20200811143752005).

## Conflict of interest

The authors declare that the research was conducted in the absence of any commercial or financial relationships that could be construed as a potential conflict of interest.

## Publisher's note

All claims expressed in this article are solely those of the authors and do not necessarily represent those of their affiliated organizations, or those of the publisher, the editors and the reviewers. Any product that may be evaluated in this article, or claim that may be made by its manufacturer, is not guaranteed or endorsed by the publisher.

## Supplementary material

The Supplementary Material for this article can be found online at: https://www.frontiersin.org/articles/10.3389/fbioe.2023.1209752/full#supplementary-material

## References

Annamalai, R. T., Turner, P. A., Carson IV, W. F., Levi, B., Kunkel, S., and Stegemann, J. P. (2018). Harnessing macrophage-mediated degradation of gelatin microspheres for spatiotemporal control of BMP2 release. *Biomaterials* 161, 216–227. doi:10.1016/j.biomaterials.2018.01.040

Brown, G. C., Lim, K. S., Farrugia, B. L., Hooper, G. J., and Woodfield, T. B. (2017). Covalent incorporation of heparin improves chondrogenesis in photocurable gelatin-methacryloyl hydrogels. *Macromol. Biosci.* 17 (12), 1700158. doi:10.1002/mabi.201700158

Chai, S., Huang, J., Mahmut, A., Wang, B., Yao, Y., Zhang, X., et al. (2022). Injectable photo-crosslinked bioactive BMSCs-BMP2-GelMA scaffolds for bone defect repair. *Front. Bioeng. Biotechnol.* 10, 875363. doi:10.3389/fbioe.2022.875363

Chandra, A., Lin, T., Tribble, M. B., Zhu, J., Altman, A. R., Tseng, W.-J., et al. (2014). PTH1–34 alleviates radiotherapy-induced local bone loss by improving osteoblast and osteocyte survival. *Bone* 67, 33–40. doi:10.1016/j.bone.2014.06.030

Chen, X., Tan, B., Bao, Z., Wang, S., Tang, R., Wang, Z., et al. (2021a). Enhanced bone regeneration via spatiotemporal and controlled delivery of a genetically engineered BMP-2 in a composite Hydrogel. *Biomaterials* 277, 121117. doi:10.1016/j.biomaterials.2021.121117

Chen, X., Tan, B., Wang, S., Tang, R., Bao, Z., Chen, G., et al. (2021b). Rationally designed protein cross-linked hydrogel for bone regeneration via synergistic release of magnesium and zinc ions. *Biomaterials* 274, 120895. doi:10.1016/j.biomaterials.2021.120895

Cheng, W., Ding, Z., Zheng, X., Lu, Q., Kong, X., Zhou, X., et al. (2020). Injectable hydrogel systems with multiple biophysical and biochemical cues for bone regeneration. *Biomater. Sci.* 8 (9), 2537–2548. doi:10.1039/d0bm00104j

Cui, Z.-K., Kim, S., Baljon, J. J., Wu, B. M., Aghaloo, T., and Lee, M. (2019). Microporous methacrylated glycol chitosan-montmorillonite nanocomposite hydrogel for bone tissue engineering. *Nat. Commun.* 10 (1), 3523–3533. doi:10.1038/s41467-019-11511-3

Demirel, M., and Kaya, A. I. (2020). Effect of strontium-containing compounds on bone grafts. *J. Mater Sci.* 55 (15), 6305–6329. doi:10.1007/s10853-020-04451-7

Gomes-Ferreira, P. H. S., Micheletti, C., Frigério, P. B., de Souza Batista, F. R., Monteiro, N. G., Bim-Júnior, O., et al. (2022). PTH 1-34-functionalized bioactive glass improves peri-implant bone repair in orchiectomies rats: Microscale and ultrastructural evaluation. *Mat. Sci. Eng. C* 134, 112688. doi:10.1016/j.msec.2022.112688

Hasani-Sadrabadi, M. M., Sarrion, P., Pouraghaei, S., Chau, Y., Ansari, S., Li, S., et al. (2020a). An engineered cell-laden adhesive hydrogel promotes craniofacial bone tissue regeneration in rats. *Sci. Transl. Med.* 12 (534), eaay6853. doi:10.1126/scitranslmed.aay6853

Hasani-Sadrabadi, M. M., Sarrion, P., Pouraghaei, S., Chau, Y., Ansari, S., Li, S., et al. (2020b). An engineered cell-laden adhesive hydrogel promotes craniofacial bone tissue regeneration in rats. *Sci. Transl. Med.* 12 (534), eaay6853. doi:10.1126/scitranslmed.aay6853

Hou, S., Lake, R., Park, S., Edwards, S., Jones, C., and Jeong, K. J. (2018). Injectable macroporous hydrogel formed by enzymatic cross-linking of gelatin microgels. *ACS Appl. bio Mater.* 1 (5), 1430–1439. doi:10.1021/acsabm.8b00380

Johnson, C. T., Sok, M. C. P., Martin, K. E., Kalelkar, P. P., Caplin, J. D., Botchwey, E. A., et al. (2019). Lysostaphin and BMP-2 co-delivery reduces *S. aureus* infection and regenerates critical-sized segmental bone defects. *Sci. Adv.* 5 (5), eaaw1228. doi:10.1126/sciadv.aaw1228

Kargozar, S., Montazerian, M., Fiume, E., and Baino, F. (2019). Multiple and promising applications of strontium (Sr)-containing bioactive glasses in bone tissue engineering. *Front. Bioeng. Biotechnol.* 7, 161. doi:10.3389/fbioe.2019.00161

Kim, S., Tsao, H., Kang, Y., Young, D. A., Sen, M., Wenke, J. C., et al. (2011). *In vitro* evaluation of an injectable chitosan gel for sustained local delivery of BMP-2 for osteoblastic differentiation. *J. Biomed. Mater. Res. Part B Appl. Biomaterials* 99 (2), 380–390. doi:10.1002/jbm.b.31909

Kurian, A. G., Singh, R. K., Patel, K. D., Lee, J.-H., and Kim, H.-W. (2022). Multifunctional GelMA platforms with nanomaterials for advanced tissue therapeutics. *Bioact. Mat.* 8, 267–295. doi:10.1016/j.bioactmat.2021.06.027

Liu, Z., Zhang, J., Fu, C., and Ding, J. (2023). Osteoimmunity-regulating biomaterials promote bone regeneration. *AJPS* 18 (1), 100774. doi:10.1016/j.ajps.2023.100774

Magalhães, L. S. S., Santos, F. E. P., Elias, C. d. M. V., Afewerki, S., Sousa, G. F., Furtado, A. S., et al. (2020). Printing 3D hydrogel structures employing low-cost stereolithography technology. *J. Funct. Biomater.* 11 (1), 12. doi:10.3390/jfb11010012

Malinovsky, G., Yarmoshenko, I., Zhukovsky, M., Starichenko, V., and Modorov, M. (2013). Strontium biokinetic model for mouse-like rodent. *J. Environ. Radioact.* 118, 57–63. doi:10.1016/j.jenvrad.2012.11.003

Nilasaroya, A., Kop, A. M., and Morrison, D. A. (2021). Heparin-functionalized hydrogels as growth factor-signaling substrates. *J. Biomed. Mater Res. A* 109 (3), 374–384. doi:10.1002/jbm.a.37030

Olov, N., Bagheri-Khoulenjani, S., and Mirzadeh, H. (2022). Injectable hydrogels for bone and cartilage tissue engineering: A review. *Prog. Biomater.* 11, 113–135. doi:10.1007/s40204-022-00185-8

Oprita, E. I., Iosageanu, A., and Craciunescu, O. (2022). Progress in composite hydrogels and scaffolds enriched with icariin for osteochondral defect healing. *Gels* 8 (10), 648. doi:10.3390/gels8100648

Orbeanu, V., Haragus, H., Crisan, D., Cirstoiu, C., Ristic, B., and Jamieson, V. (2022). Novel parathyroid hormone-based bone graft, KUR-113, in treatment of acute open tibial shaft fracture: A phase-2 randomized controlled trial. *J. Bone Jt. Surg. Am.* 104 (5), 441–450. doi:10.2106/jbjs.20.02109

Place, E. S., Rojo, L., Gentleman, E., Sardinha, J. P., and Stevens, M. M. (2011). Strontium-and zinc-alginate hydrogels for bone tissue engineering. *Tissue Eng. Part A* 17 (21-22), 2713–2722. doi:10.1089/ten.tea.2011.0059

Sakiyama-Elbert, S. E. (2014). Incorporation of heparin into biomaterials. *Acta Biomater.* 10 (4), 1581–1587. doi:10.1016/j.actbio.2013.08.045

Shi, H., Zhou, Z., Li, W., Fan, Y., Li, Z., and Wei, J. (2021). Hydroxyapatite based materials for bone tissue engineering: A brief and comprehensive introduction. *Crystals* 11 (2), 149. doi:10.3390/cryst11020149

Tournis, S., Economopoulos, D., and Lyritis, G. (2006). Strontium ranelate: A novel treatment in postmenopausal osteoporosis. *Ann. N. Y. Acad. Sci.* 1092 (1), 403–407. doi:10.1196/annals.1365.037

Vestermark, M. T. (2011). Strontium in the bone-implant interface. *Dan. Med. Bull.* 58 (5), B4286. doi:10.1016/j.jpainsymman.2010.07.016

Wan, X., Zhao, Y., Li, Z., and Li, L. (2022). Emerging polymeric electrospun fibers: From structural diversity to application in flexible bioelectronics and tissue engineering. *Exploration* 2, 20210029. doi:10.1002/exp.20210029

Wang, T., Nie, J., and Yang, D. (2012). Dextran and gelatin based photocrosslinkable tissue adhesive. *Carbohydr. Polym.* 90 (4), 1428–1436. doi:10.1016/j.carbpol.2012.07.011

Wang, T., Xu, W., Zhao, X., Bai, B., Hua, Y., Tang, J., et al. (2022). Repair of osteochondral defects mediated by double-layer scaffolds with natural osteochondral-biomimetic microenvironment and interface. *Mater. today bio* 14, 100234. doi:10.1016/j.mtbio.2022.100234

Wu, D., Qin, H., Wang, Z., Yu, M., Liu, Z., Peng, H., et al. (2021). Bone mesenchymal stem cell-derived sEV-encapsulated thermosensitive hydrogels accelerate osteogenesis and angiogenesis by release of exosomal miR-21. *Front. Bioeng. Biotechnol.* 9, 829136. doi:10.3389/fbioe.2021.829136

Yoshida, W., Matsugami, D., Murakami, T., Bizenjima, T., Imamura, K., Seshima, F., et al. (2019). Combined effects of systemic parathyroid hormone (1–34) and locally delivered neutral self-assembling peptide hydrogel in the treatment of periodontal defects: An experimental *in vivo* investigation. *J. Clin. Periodontol.* 46 (10), 1030–1040. doi:10.1111/jcpe.13170

Yue, K., Trujillo-de Santiago, G., Alvarez, M. M., Tamayol, A., Annabi, N., and Khademhosseini, A. (2015). Synthesis, properties, and biomedical applications of gelatin methacryloyl (GelMA) hydrogels. *Biomaterials* 73, 254–271. doi:10.1016/j.biomaterials.2015.08.045

Zhang, Y., Xu, Y., Kong, H., Zhang, J., Chan, H. F., Wang, J., et al. (2023). Microneedle system for tissue engineering and regenerative medicine. *Exploration* 3 (2023), 20210170. doi:10.1002/exp.20210170

Zhang, Y., Yu, T., Peng, L., Sun, Q., Wei, Y., and Han, B. (2020). Advancements in hydrogel-based drug sustained release systems for bone tissue engineering. *Front. Pharmacol.* 11, 622. doi:10.3389/fphar.2020.00622

Zhao, Y., Cui, Z., Liu, B., Xiang, J., Qiu, D., Tian, Y., et al. (2019). An injectable strong hydrogel for bone reconstruction. *Adv. Healthc. Mat.* 8 (17), 1900709. doi:10.1002/adhm.201900709

Zhao, Y., Xing, Y., Wang, M., Huang, Y., Xu, H., Su, Y., et al. (2022). Supramolecular hydrogel based on an osteogenic growth peptide promotes bone defect repair. *ACS omega* 7 (13), 11395–11404. doi:10.1021/acsomega.2c00501

frontiers | Frontiers in Bioengineering and Biotechnology

TYPE Original Research
PUBLISHED 20 September 2023
DOI 10.3389/fbioe.2023.1257778



OPEN ACCESS

EDITED BY
Oommen Podiyan Oommen,
Tampere University, Finland

REVIEWED BY
Xuefang Hao,
Inner Mongolia University for Nationalities, China
Cheng Hu,
Sichuan University, China

*CORRESPONDENCE
Juan C. Briceño,
jbriceno@uniandes.edu.co

RECEIVED 12 July 2023
ACCEPTED 05 September 2023
PUBLISHED 20 September 2023

CITATION
Rodríguez-Soto MA, Suárez Vargas N, Ayala-Velásquez M, Aragón-Rivera AM, Ostos C, Cruz JC, Muñoz Camargo C, Kim S, D'Amore A, Wagner WR and Briceño JC (2023), Polyester urethane urea (PEUU) functionalization for enhanced anti-thrombotic performance: advancing regenerative cardiovascular devices through innovative surface modifications.
*Front. Bioeng. Biotechnol.* 11:1257778.
doi: 10.3389/fbioe.2023.1257778



# Polyester urethane urea (PEUU) functionalization for enhanced anti-thrombotic performance: advancing regenerative cardiovascular devices through innovative surface modifications

María A. Rodríguez-Soto[1], Natalia Suárez Vargas[1], María Ayala-Velásquez[1], Andrés M. Aragón-Rivera[1], Carlos Ostos[2], Juan C. Cruz[1], Carolina Muñoz Camargo[1], Seungil Kim[3], Antonio D'Amore[3], William R. Wagner[3] and Juan C. Briceño[1,4]*

[1]Department of Biomedical Engineering, Universidad de los Andes, Bogotá, Colombia, [2]Group CATALAD, Instituto de Química, Universidad de Antioquia, Medellín, Colombia, [3]McGowan Institute for Regenerative Medicine and Department of Bioengineering, University of Pittsburgh, Pittsburgh, PA, United States, [4]Department of Congenital Heart Disease and Cardiovascular Surgery, Fundación CardioInfantil Instituto de Cardiología, Bogotá, Colombia

**Introduction:** Thrombogenesis, a major cause of implantable cardiovascular device failure, can be addressed through the use of biodegradable polymers modified with anticoagulating moieties. This study introduces a novel polyester urethane urea (PEUU) functionalized with various anti-platelet deposition molecules for enhanced antiplatelet performance in regenerative cardiovascular devices.

**Methods:** PEUU, synthesized from poly-caprolactone, 1,4-diisocyanatobutane, and putrescine, was chemically oxidized to introduce carboxyl groups, creating PEUU-COOH. This polymer was functionalized *in situ* with polyethyleneimine, 4-arm polyethylene glycol, seleno-L-cystine, heparin sodium, and fondaparinux. Functionalization was confirmed using Fourier-transformed infrared spectroscopy and X-ray photoelectron spectroscopy. Bio-compatibility and hemocompatibility were validated through metabolic activity and hemolysis assays. The anti-thrombotic activity was assessed using platelet aggregation, lactate dehydrogenase activation assays, and scanning electron microscopy surface imaging. The whole-blood clotting time quantification assay was employed to evaluate anticoagulation properties.

**Results:** Results demonstrated high biocompatibility and hemocompatibility, with the most potent anti-thrombotic activity observed on pegylated surfaces. However, seleno-L-cystine and fondaparinux exhibited no anti-platelet activity.

**Discussion:** The findings highlight the importance of balancing various factors and addressing challenges associated with different approaches when developing innovative surface modifications for cardiovascular devices.

KEYWORDS

**anti-thrombotic performance, polyester urethane urea (PEUU), biocompatibility, surface modifications, regenerative cardiovascular devices**

# 1 Introduction

Various cardiovascular devices, including vascular grafts, stents, valves, and venous catheters, are intended for blood contact. However, thrombogenesis remains a critical factor contributing to the short- and long-term failure of these devices (Rodriguez-Soto et al., 2021; Rodriguez-Soto et al., 2021). For example, recurrent thrombogenesis is the leading cause of patency loss in vascular grafts for hemodialysis access, with primary patency rates of just 41% after 1 year and 28% after 2 years of implantation (Halbert et al., 2020; Halbert et al., 2020). Although secondary patency can be achieved by mechanically removing the thrombus, 29% of cases require a reintervention for replacement (Guidoin et al., 1992; Guidoin et al., 1992).

In healthy blood vessels, a functional endothelium actively serves to prevent thrombogenesis. In contrast, non-endothelialized surfaces facilitate thrombogenesis through protein adsorption, platelet aggregation, complement activation, and thrombin generation. Thrombogenesis not only obstructs the vessel but also is associated with immune system activity, leading to increased foreign body responses and bacterial colonization in specific applications like catheters and vascular grafts for hemodialysis access. In such circumstances, infection rates can reach up to 44% (Ed Rainger et al., 2015; Ed Rainger et al., 2015; Rodriguez-Soto et al., 2021; Rodriguez-Soto et al., 2021).

Historically, efforts to prevent thrombosis on blood-contacting surfaces have centered on systemic anti-thrombotic or anticoagulant drug administration. Furthermore, there is no conclusive evidence on how oral anticoagulation management improves the outcome of patients requiring the use of vascular grafts. Furthermore, there is no clear evidence regarding the benefits of mid-term and long-term anticoagulation in the vascular graft patency outweighing the increased risk of bleeding (Liang et al., 2017; Liang et al., 2017; Schoenrath et al., 2021; Schoenrath et al., 2021). However, developing surfaces with inherent thrombogenesis prevention capabilities can enhance the prognosis of implanted cardiovascular devices. For example, bioprosthetic heart valves that have been modified to exhibit anti-thrombogenic and anti-immunogenic characteristics have demonstrated encouraging outcomes in *in vivo* studies. Such outcomes indicate that inhibiting the formation of thrombi not only enhances hemocompatibility but also bolsters the performance of medical devices. This is achieved by mitigating the risk of extreme immune reactions triggered by hyperactivation, which in turn supports more effective tissue regeneration (Hu et al., 2020; Liang et al., 2023).

Passive and active surface modifications have been proposed to reduce thrombus formation by minimizing protein adsorption (Irvine et al., 2012; Irvine et al., 2012). The interaction between electrostatic and hydrophobic forces influences protein adherence to surfaces, resulting in an increased entropy due to the displacement of water molecules and counter ions from proteins. Specific adsorbed proteins can present binding sites, for platelets and reendothelialization (Tang et al., 2009; Tang et al., 2009; Liu et al., 2013; Liu et al., 2013). Passive surface modifications, such as low-adherent topographies or PEGylation to improve hydrophilicity, can be employed to modify these processes. However, caution is necessary when considering these approaches for cardiovascular devices that require reendothelialization for optimal clinical outcomes (Valencia-Rivero et al., 2019; Valencia-Rivero et al., 2019). Alternatively, active surface modification mainly focuses on surface functionalization with bioactive molecules that target thrombin generation and fibrin formation. For instance, heparin attachment to the surface, as a catalyst for the inactivation of thrombin and factor X, has been proposed (Janairo et al., 2012; Janairo et al., 2012). The PROPATEN® graft, a PTFE vascular graft modified with heparin and approved by the FDA in 2006, has demonstrated a nearly 16% increase in patency compared to its non-coated counterpart. Although direct thrombin inhibitors like hirudin and bivalirudin have been investigated, they have not been widely adopted. Recent research, however, suggests that combining both alternatives can provide a synergistic effect in anti-thrombotic surface modifications (Zhu et al., 2021; Zhu et al., 2021).

In this work, we propose the use of carboxyl group-modified poly (ester urethane) urea (PEUU-COOH) for functionalization with various anti-thrombotic strategies. PEUU exhibits biodegradability and superior mechanical performance, making it a promising biomaterial for cardiovascular tissue engineering applications. It offers the necessary compliance to withstand blood pressure and facilitates mechanotransduction from flow to cells on the surface, which is required for reendothelialization (Fang et al., 2014; Fang et al., 2014). By considering only one bulk material we were able to independently analyze the efficiency of proposed antiaggregating surface treatments.

First, we examined polymer functionalization with a high molecular weight 4-arm PEG (20,000 mW), which could be an outstanding strategy due to its steric inhibition potential and increased hydrophilicity (Pozzi et al., 2014; Pozzi et al., 2014). We then utilized a similar molecule, polyethyleneimine (PEI 400 mW), shown to prolong prothrombin time by blocking thrombin-catalyzed fibrin formation (Chu et al., 2003; Chu et al., 2003). Additionally, considering that heparin is one of the most widely used anti-thrombotic surface modifications, we hypothesized that a synthetic heparin analog, Fondaparinux, might also be suitable for anti-thrombotic functionalization. Fondaparinux selectively inhibits factor Xa and thrombin generation but not its activity, thereby allowing protein C activation for its anticoagulation function. Furthermore, heparin is anti-angiogenic due to the downregulation of endothelial cell migration genes (Shen et al., 2011; Shen et al., 2011). Fondaparinux may offer a selective anticoagulant strategy without interfering with the reendothelialization necessary for regenerative cardiovascular devices (Zhang et al., 2019; Zhang et al., 2019).

Lastly, nitric oxide (NO) released from endothelial cells has been recognized for its antiplatelet function through the inhibition of glycoprotein Ib (GPIb)-V-IX and integrin αIIbβ3 complex in platelets (Yau et al., 2015; Yau et al., 2015). Moreover, NO activates the cGMP (cyclic guanosine monophosphate) dependent protein kinase pathways and reduces cytosolic $Ca^{2+}$, thus inhibiting platelet adhesion, and aggregation, and disrupting platelet aggregates (G.-R. Wang et al., 1998; Wang et al., 1998). Consequently, we hypothesized that surfaces capable of inducing NO production could prevent platelet activation. For this, we selected an organoselenium compound to increase nitric oxide from blood plasma S-nitrosothiols (Yang et al., 2008; Yang et al.,

2008; An et al., 2015; An et al., 2015). Furthermore, increased NO levels have been shown to promote endothelial cell proliferation and reduce the inflammatory response of biomaterials by inhibiting proinflammatory cytokine production (Tousoulis et al., 2012; Tousoulis et al., 2012), all of which are desirable properties for regenerative applications.

Building upon these principles, our study aims to develop and evaluate the effectiveness of these anti-thrombotic strategies on the modified PEUU (PEUU-COOH) surfaces. We investigate the biocompatibility, mechanical properties, and anti-thrombotic performance of the functionalized PEUU, comparing each strategy's efficacy *in vitro* and *in vivo*.

# 2 Materials and methods

## 2.1 Materials

For polymer synthesis, Polycaprolactone diol (PCL, Mn = 2000), dimethylolpropionic acid (DMPA), 1,4-Diisocyanatobutane (BDI), putrescine and stannous octoate (Sn(Oct)2) were purchased from Sigma-Aldrich (St. Louis, MO, USA). 1,1,1,6,6,6-Hexafluoroisopropanol (HFIP) was purchased from Oakwood Products, Inc. (Columbia Hwy, N, Estill, USA). For polymer functionalization, Heparin sodium salt from porcine intestinal mucosa (H3393), Fondaparinux sodium (SML1240), Polyethyleneimine mW 400 (PEI - P3143), 4-arm Polyethylene Glycol with amine terminal groups Mw 20.000 (PEG 4 Arm NH2 - JKA7026), Seleno-L-cystine (545996), N-(3-Dimethylaminopropyl)-N′-ethyl carbodiimide hydrochloride (EDC - E7750), N-Hydroxysuccinimide (NHS - 130672), Chloroform (99.8%) and hydrofluoric acid (48%) were purchased from Sigma-Aldrich (St. Louis, MO, USA). For nanoparticles synthesis used in the functionalization of heparin and fondaporinux surfaces, hydrochloric acid (HCl, 37%, CAS 7647-01-0), glutaraldehyde (GTA, 25%, CAS 111-30-8), acetone (99.5%, CAS 67-64-1), glacial acetic acid (99.7%, CAS 64-19-7), and sodium hydroxide (NaOH, 98%, CAS 1310-73-2) were purchased from PanReac AppliChem (Chica-go, IL, USA). For biological assays, Triton X-100, Phosphate Buffer Saline (PBS), thiazolyl blue tetrazolium bromide (MTT), dimethyl sulfoxide (DMSO, 99%), Dulbecco's modified Eagle's medium (DMEM), Roswell Park Memorial Institute 1640 Medium (RPMI1640), and Fetal Bovine Serum (FBS) were purchased from Sig-ma-Aldrich (St. Louis, MO, USA). VERO cells (CCL-81) and THP-1 cells (ATCC TIB-202) were acquired from ATCC®. Lactate Dehydrogenase (LDH) kit was acquired from Sigma Aldrich (MAK066, St. Louis, MO, USA). The Nitric Oxide Assay kit was acquired from Abnova (KA1641, Taipei, Taiwan). Fetal bovine serum (FBS) was obtained from Biowest (Riverside, MO, USA), and Type B gelatin was purchased from the local store Químicos Campota (Bogotá, Colombia).

## 2.2 Biomaterial synthesis and modification

### 2.2.1 PEUU-COOH (PC) synthesis and modification

To facilitate functionalization with various anti-thrombotic bioactive molecules, carboxyl groups were incorporated into the PEUU backbone (Guan et al., 2002; Guan et al., 2002; Hong et al., 2012; Hong et al., 2012; Zhou et al., 2014; Zhou et al., 2014). Briefly, PCL and DMPA were dried in a vacuum oven at 60°C overnight to remove residual water, and BDI and Putrescine were purified through vacuum distillation before PC synthesis. Sn $(Oct)_2$ was dried using 4 Å molecular sieves.

PCL was used as the soft segment. DMPA and putrescine are chain extenders and BDI is the hard segment. PCL was dissolved in DMSO in a three-necked flask under argon protection stirring at 75°C. BDI was added followed by 3 drops of Sn $(Oct)_2$ as a catalyst. The reaction was allowed for 3 h at 75°C and then the prepolymer solution was cooled at room temperature. DMPA dissolved in DMSO was added dropwise to the pre-polymer solution and the reaction was allowed for 1 h at 25°C. Putrescine diluted in DMSO was slowly added to the reactor then the reactor was kept at 25°C overnight under argon. PCL/DMPA/BDI/putrescine molar ratio was 1:0.5:2:0.5, for a final polymer concentration of 4% on the solution. The polymer was then precipitated with cold deionized water, rinsed with isopropyl alcohol, and dried in a vacuum oven at 60°C for 3 days to obtain fine PC pellets. The reaction yield was over 90%. Figure 1 presents a schematic representation of the PEUU synthesis and carboxylation process. The chemical structure of the synthesized PC was confirmed by proton nuclear magnetic resonance ($^1$H-NMR) spectrum and the ratio of PCL:BDI in the backbone was calculated as 1:2.6 from the spectrum (Supplementary Figure S1).

### 2.2.2 PEUU-COOH (PC) physicochemical characterization

PEUU carboxylation was confirmed through an X-ray photoelectron spectroscopy (XPS), a Fourier-Transform Infrared Spectroscopy (FTIR), and a thermogravimetric analysis.

A photoelectron spectrometer (SPECS Surface Nano Analysis GmbH, Germany) equipped with a PHOIBOS-150 hemispherical electron energy analyzer and a μfocus-600 Al X-ray source was used for XPS measurements. The ultra-high vacuum conditions were kept below $3 \times 10^{-9}$ mbar in the operation procedure. The surface charge compensation of the samples, previously mounted on a non-conductive tape, was achieved by an electron flood gun operated at 3 eV (20 μA) over a tantalum mesh with a nominal aperture of 430 μm. The spot diameter was 200 nm, the energy pass was fixed at 20 eV and the scan number for the high-resolution measurements was 20. The signals were calibrated to a binding energy of 284.6 eV for adventitious carbon and the Ta4f7/2 peak from the tantalum mesh was employed as a reference. The HR spectra were fit by the XPSPeak4.1 software, using a Shirley-type single-peak background with a simultaneous GL peak shape of 30% and full-width at half maximum (FWHM) data from the literature. A deconvolution process was conducted to analyze the surface chemical species after the functionalization of the involved materials.

An Alpha II FTIR Eco-ART (Bruker Optik GmbH, Ettlingen, Germany) was used for the identification of the oxygen-containing functional groups by recording the infrared spectra from 4000 to 600 $cm^{-1}$ with a 2 $cm^{-1}$ spectra resolution. Changes in the characteristic peaks of PEUU were analyzed to identify the backbone structural modifications.

To evaluate alterations in the covalent bonds of the PEUU backbone, a thermal degradation profile was determined using thermogravimetric analysis (TGA) and differential scanning

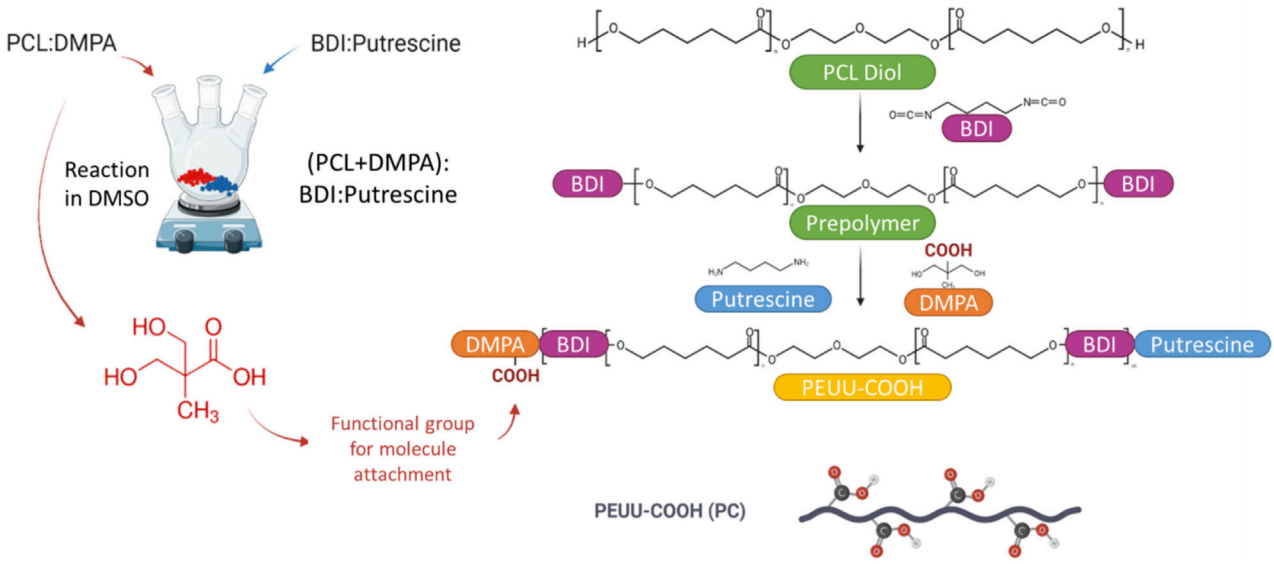


FIGURE 1
Schematic representation of the workflow for the Synthesis of PEUU-COOH (PC), detailed structure can be seen on Supplementary Figure S1.

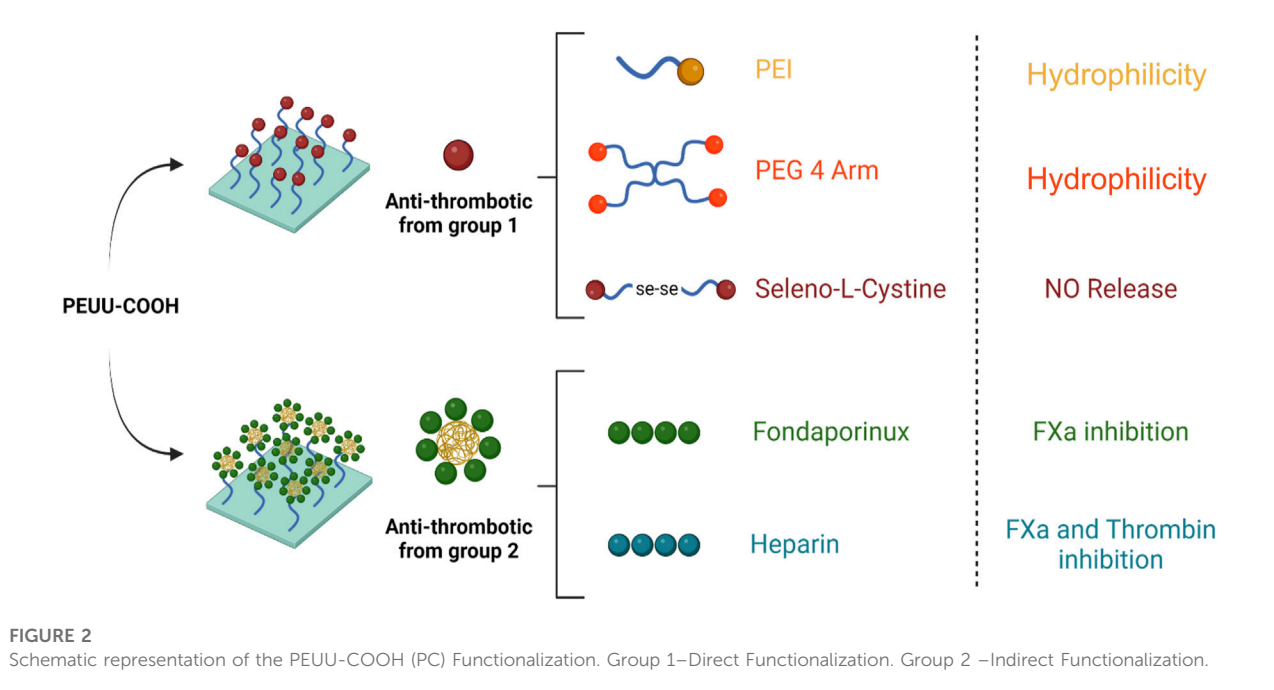


FIGURE 2
Schematic representation of the PEUU-COOH (PC) Functionalization. Group 1–Direct Functionalization. Group 2 –Indirect Functionalization.

calorimetry (DSC) assays. Both experiments were conducted using a TA Instrument Q600 Thermogravimetric Analyzer® (New Castle, DE, USA). The thermogravimetric profile was obtained under a nitrogen atmosphere (100 mL/min) at a heating rate of 10°C/min, reaching up to 600°C, following ASTM E1131. The DSC analysis was carried out under a nitrogen atmosphere (300 mL/min) at a heating rate of 10°C/min, reaching up to 130°C, and maintained at an isothermal condition for 5 min to eliminate prior thermal history. Subsequently, samples were cooled at a rate of 10°C/min and reheated to 130°C for a second time.

For the COOH quantification, a titration of PEUU and PC was performed. A 30 mL solution of 1 mg/mL of the polymer was resuspended in distilled water, and the pH was adjusted to 3 by adding 0.1 N HCl. Then, 20 µL of 0.1 N, NaOH was added to the solution, and the resulting pH was recorded. A titration curve was built to determine the equivalence point. The content of carboxyl groups was calculated through the product of the titrant concentration (N) and volume at the equivalence point (V), divided by the polymer mass (M) (Barbosa et al., 2013; Barbosa et al., 2013).

### 2.2.3 PEUU-COOH (PC) anti-thrombotic modification

PC was subsequently functionalized *in situ* with a series of bioactive molecules possessing anti-thrombotic properties. These molecules were divided into two groups for further functionalization. The first group, referred to as "Direct," encompassed bioactive molecules with $NH_2$ functional groups, enabling the formation of a peptidic-covalent bond with the COOH functional groups of PC. The molecules in this group included Polyethyleneimine Mw 400 (PEI), 4-arm Polyethylene Glycol with amine terminal groups Mw 20,000 (P4A), and Seleno-L-cystine (SLC). The second group, designated "Indirect," involved bioactive molecules containing functional COOH groups, necessitating the use of a linker. Gelatin nanoparticles with $NH_2$ functional groups were employed to establish a bond between PC and the anticoagulant molecule. This group comprised molecules such as heparin sodium salt derived from porcine intestinal mucosa (HEP) and fondaparinux sodium (FPX).

For direct *in-situ* functionalization, PC pellets were dissolved in chloroform (5% w/v) at 30°C under magnetic stirring. Then, according to the number of COOH functional groups quantified in the PC ($3 \times 10^{-4}$ mol/g), a 1:10 ratio of polymer/EDC and NHS were added ($3 \times 10^{-3}$ mol/g), and the activation reaction was allowed for 15 min at 37°C under magnetic stirring. Following this, the anti-thrombotic bioactive molecule with $NH_2$ functional groups was added to the solution and the reaction was allowed for 24 h at 50°C under magnetic stirring. In this regard, a 1:2 ratio was considered for PEI ($2 \times 10^{-4}$ mol/g) and P4A ($2 \times 10^{-4}$ mol/g), while a 1:1 ratio was considered for SLC ($2 \times 10^{-4}$ mol/g). Upon completion of each reaction, solutions underwent solvent casting for 24 h, and the resulting film was washed twice with Type II water.

For indirect *in-situ* functionalization, the gelatin B nanoparticles (GNPs) were synthesized using a previously reported two-step desolvation method (Gonzalez-Melo et al., 2021; Gonzalez-Melo et al., 2021). Briefly, Type B gelatin was dissolved in type II water (5% w/v) and an equal volume of acetone was added dropwise for 5 min to induce coiling. The supernatant was collected and centrifuged at 810 *g* for 3 min to recover the high molecular weight gelatin. The resulting pellet was resuspended in an equal volume mixture of water and acetone, and the pH was adjusted from 10.5 to 11.5 before initiating the second desolvation process. Chemical crosslinking of the $NH_2$ groups to form the GNPs was achieved by gradually adding glutaraldehyde to a final concentration of 0.4% w/v while stirring magnetically and allowing the reaction to proceed for 16 h. Excess acetone was removed by evaporation, with simultaneous water addition to prevent agglomeration, and the GNPs were recovered by freeze-drying.

For indirect functionalization, PC pellets were dissolved in chloroform (2.5% w/v) at 30°C under magnetic stirring. Then, a 1: 10 ratio of polymer/EDC and NHS ($3 \times 10^{-3}$ mol/g) was added, and the activation reaction proceeded for 15 min at 37°C under magnetic stirring. Subsequently, a 1:10 ratio of polymer/GNPs ($3 \times 10^{-3}$ mol/g) and a 1:5 ratio of HEP or FPX ($2 \times 10^{-3}$ mol/g) were added. The mixture was allowed to react for 24 h at 50°C under magnetic stirring. Each solution underwent solvent casting for 24 h and the obtained film was washed twice with Type II water. Figure 2 Shows a schematic representation of the PEUU-COOH (PC) Functionalization. Two different groups were assigned as Group 1–Direct Functionalization and Group 2–Indirect Functionalization.

To confirm surface functionalization, XPS and FTIR spectra were obtained and analyzed following the previously described procedure. The primary peaks of the raw bioactive molecules were compared with the functionalized surfaces on the PC. TGA and DSC assays were also performed as previously described to assess differences in thermal degradation profiles resulting from the chemical modification of the PC films. Films, each measuring 1 $cm^2$ films were sterilized with ethylene oxide at the sterilization center of Fundación CardioInfantil following the NTC 4426-1 and NTC 4426–2 standards, ahead of the subsequent biocompatibility and anti-thrombogenic tests. Surface hydrophilicity was evaluated by measuring the contact angle using a 100 µL droplet of Type II water before and after sterilization.

To elucidate the nitric oxide production capacity of PC functionalized with seleno-L-cystine (PC + SLC) and its relation with anti-thrombotic activity, we quantified the total $NO_2$-/$NO_3$- released by plasma in contact with the functionalized polymer as an indicator of NO production. Briefly, O+ fresh human blood was collected in sodium citrate blood collection tubes after obtaining informed consent (Ethical Committee at the Universidad de Los Andes, minute number 928-2018). The anticoagulated blood was centrifuged at 324 *g* for 15 min to obtain platelet-poor plasma (PPP). Films were then exposed to 400 µL of PPP, followed by incubation for 24 h at 37°C and 5%$CO_2$. The supernatant was collected, deproteinized with $ZnSO_4$ and NaOH according to the manufacturer's instructions (KA1641, Taipei, Taiwan), and centrifuged at 2250 *g* for 10 min to remove the protein pellet. The reaction proceeded via the reduction of nitrates to nitrite using the Griess method, incubating the sample with the required A and B reagents for 10 min at 60°C. Centrifugation was performed at 2250 g for 30 s, and the supernatant was transferred to a brand new 96 well-plate to measure absorbance at 540 nm. Controls included pristine PC and PPP alone. NO concentration was calculated using a linear dependency of $y = 0.003x + 0.07$ from a linear regression model according to nitrite standard curve with a known nitrite concentration (100 uM), and NO release was then normalized based on the surface area.

## 2.3 Biocompatibility analysis

Considering that the films presented in this study are intended to be in contact with live tissues and blood, cytocompatibility, and hemolytic propensity were assessed according to the ISO 10993 standard. For the hemolysis test, O+ fresh human blood was collected in Ethylenediaminetetraacetic acid (EDTA) blood collection tubes after obtaining informed consent (Ethical Committee at the Universidad de Los Andes, min number 928-2018). To isolate erythrocytes and remove the plasma contents, the anticoagulated blood was washed five times with a 0.9% w/v NaCl physiological solution at 324 g for 5 min. The isolated erythrocytes were resuspended in PBS 1x to obtain an initial stock of $4 \times 10^6$ erythrocytes/µL. Sterilized films of 0.3 $cm^2$ were immersed in 150 µL of the erythrocyte solution, while 1x PBS and 1% v/v Triton X-100 served as negative and positive controls, respectively. The samples were incubated at 37°C for 1 h, centrifuged, and the supernatant absorbance was determined at 454 nm. The hemolysis percentage was determined by means of the positive control with Triton X-100

(International Organization for Standardization, 2017; International Organization for Standardization, 2017).

To evaluate cytocompatibility, a metabolic activity assay was performed using MTT on VERO cells and THP-1 cells. For this purpose, $1.0 \times 10^5$ VERO cells/mL were seeded onto 96-well plates containing DMEM supplemented with 10% FBS and allowed to adhere for 24 h at 37°C in a 5% $CO_2$ atmosphere. To assess cytocompatibility, the MTT metabolic activity assay was performed on VERO cells and THP-1 cells. VERO cells (1.0 × 105 cells/mL) were seeded on 96-well plates with DMEM supplemented with 10% FBS and allowed 24 h for adhesion at 37°C in a 5% CO2 atmosphere. In parallel, THP-1 cells (5.0 × 105 cells/mL) were seeded on 96-well plates containing RPMI 1640 supplemented with 10% FBS. Cells were then exposed to previously sterilized 0.4 $cm^2$ films for an additional 24 h and 72 h in serum-free media. DMSO at a concentration of 10% v/v and untreated cells were used as negative and positive controls, respectively. Post incubation, films were carefully removed, and the MTT solution was applied to facilitate formazan crystal formation over a 2-h incubation period. Media was removed after centrifuging the culture plates at 250 g for 5 min, and DMSO was added to dissolve the formazan crystals. Absorbance was then read at 595 nm, with cell viability percentages benchmarked against a live cell control (International Organization for Standardization, 2017; International Organization for Standardization, 2017).

## 2.4 Anti-thrombotic activity analysis

To assess the anti-thrombotic activity of the different bioactive molecules employed, multiple assays were performed to examine protein adsorption, platelet aggregation, activation, and clot formation.

We hypothesized that surface modifications increasing wettability would also reduce platelet aggregation due to potential alterations in the protein adsorption profile. Therefore, the contact angle was determined by directly measuring the tangent angle at the interfacial point when a 100 µL drop of type II water reached the three-phase equilibrium point on a 1 $cm^2$ sample before and after sterilization. To evaluate the protein adsorption capacity, 0.5 $cm^2$ samples were immersed in 10% FBS and incubated for 12 h. The samples were then transferred to a 96-well plate and washed with 50 µL of a 1% SDS solution for 35 min at 37°C under gentle agitation at 100 rpm. Supernatant protein concentrations were quantified using a Bicinchoninic Acid (BCA) Assay Kit (Quanti-Pro, Sigma Aldrich). Solutions with and without FBS in the absence of any treatment served as positive and negative controls, respectively. BCA working solution incubation was allowed for 30 min and absorbances were measured at 565 nm. Protein concentration was calculated using a linear dependency of $y = 0.2633x + 0.1019$ from a linear regression model according to a Bovine serum albumin (BSA) standard curve with a known protein concentration (2 mg/mL), and protein concentration was then normalized based on the surface area.

For platelet aggregation and activation, O+ fresh human blood was collected in sodium citrate blood collection tubes after obtaining informed consent (Ethical Committee at the Universidad de Los Andes, min number 928-2018). The anticoagulated blood was centrifuged at 180 *g* for 10 min to obtain platelet-rich plasma (PRP). Films of 0.5 $cm^2$ films were then exposed to 200 µL of PRP that had been activated with 20 µL 0.1 M CaCl, allowing contact for 20 min. After incubation, films were removed and the supernatant absorbance was determined at 620 nm. Surfaces functionalized with epinephrine, adenosine diphosphate (ADP) and collagen were used as positive controls with high, medium, and low aggregation potential, respectively. Platelet aggregation was expressed as a percentage of the epinephrine control (International Organization for Standardization, 2017; International Organization for Standardization, 2017).

Scanning electron microscopy (SEM) was used to verify platelet presence and activation. Sterilized 0.5 $cm^2$ films were exposed to PRP for 30 min under gentle agitation at 10 rpm. The films were then removed, fixed with glutaraldehyde 4% v/v for 30 min, and washed 3 times with PBS 1x. The samples were dried using a decreasing ethanol curve, affixed onto aluminum plates with carbon tape, and coated with a gold layer using a Vacuum Desk IV apparatus (Denton Vacuum, Moorestown, NJ, USA). An SEM model JSM-6490LV® (JEOL USA Inc., Peabody, MA, USA) with a 10 kV accelerating voltage was used for sample analysis.

An LDH assay was performed to quantify the platelet number adhered to the film surfaces exposed to PRP for 1 h. For quantification, a calibration curve was built using PRP with 10 serial dilutions of $3.56 \times 10^5$ platelets/µL, and absorbance was recorded at 493 nm. The exposed films were transferred to brand new plates, and platelets were lysed with 1% Triton X-100 for 5 min. The films were then removed and the LDH working solution (MAK066, St. Louis, MO, USA) was applied to the supernatant with absorbance recorded at 493 nm. The number of platelets was determined with the aid of a linear dependency of $y = 4 \times 10^{-8} x + 0.1427$ obtained from a linear regression model of a standard curve created with decreasing concentrations of PRP. Data were normalized based on the contact surface area (Braune et al., 2015; Braune et al., 2015).

To assess whole blood clotting on the film surfaces, the O+ whole blood from human donors was collected in sodium citrate tubes with the first tube discarded to avoid contamination with tissue thromboplastin. 5 mL of whole blood was transferred to a centrifuge tube, and 500 µL of 0.1 M CaCl was added immediately before the assay to restore coagulability. Sterilized 1.5 $cm^2$ films were placed in 12-well plates and 200 µL of the activated blood was applied to the film surface. The samples were incubated for 15 min or 1 h at 37°C to facilitate clot formation. After incubation, 3 mL of type II water was carefully added to each sample and incubated for 5 min. 100 µL of the supernatant was transferred to a 96-well plate and absorbance was recorded at 540 nm. Positive control for coagulation was obtained with a glass slide. Absorbance is proportional to free hemoglobin released by the red blood cells that are not protected by the polymerized fibrin mesh and is inversely related to thrombus formation (Sabino and Popat, 2020; Sabino and Popat, 2020).

## 2.5 Statistical analysis

Statistical analysis of the data was conducted using GraphPad Prism® 9.1.1 software (Windows, GraphPad Software, San Diego, CA, USA, www.graphpad.com, accessed on 24 March 2023). A two-way ANOVA test with Tukey's multiple comparisons of means was employed after confirming the normality, independence of

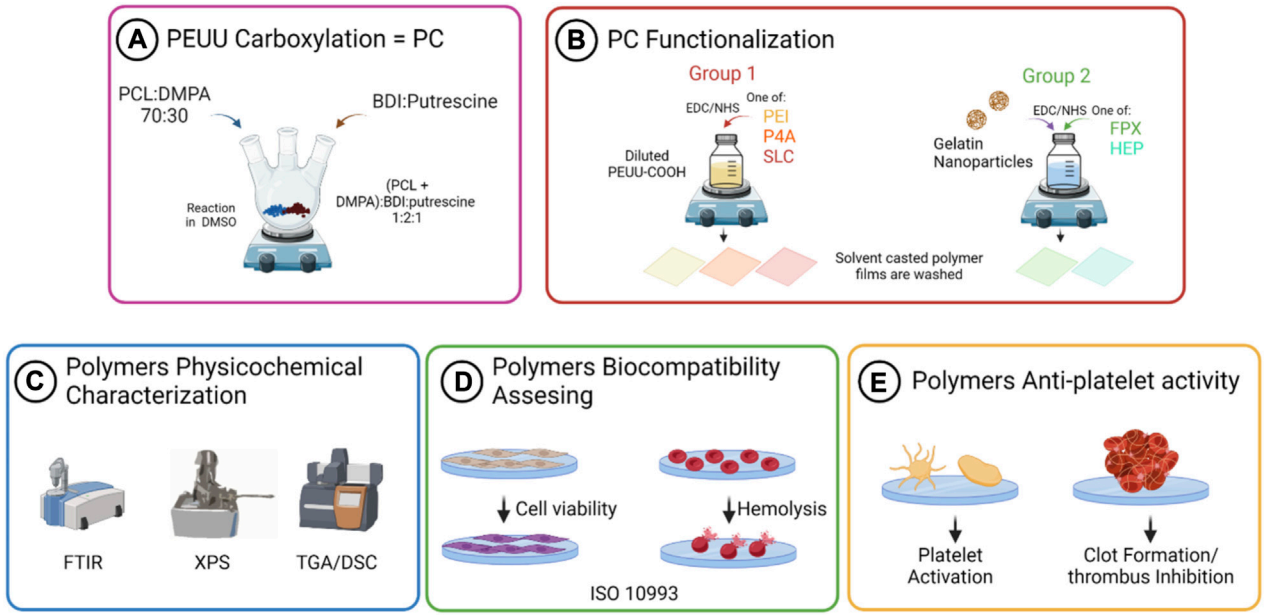


FIGURE 3
Schematic representation of the workflow for the PEUU-COOH (PC) *in-situ* functionalization with anticoagulant molecules and anti-thrombotic activity assessment. **(A)** PEUU carboxylation with DMPA **(B)** Physicochemical characterization of PEUU-COOH. **(C)** *In-situ* functionalization with anti-thrombotic bioactive molecules. **(D)** Biocompatibility assessment. **(E)** Anti-thrombotic activity assessment.

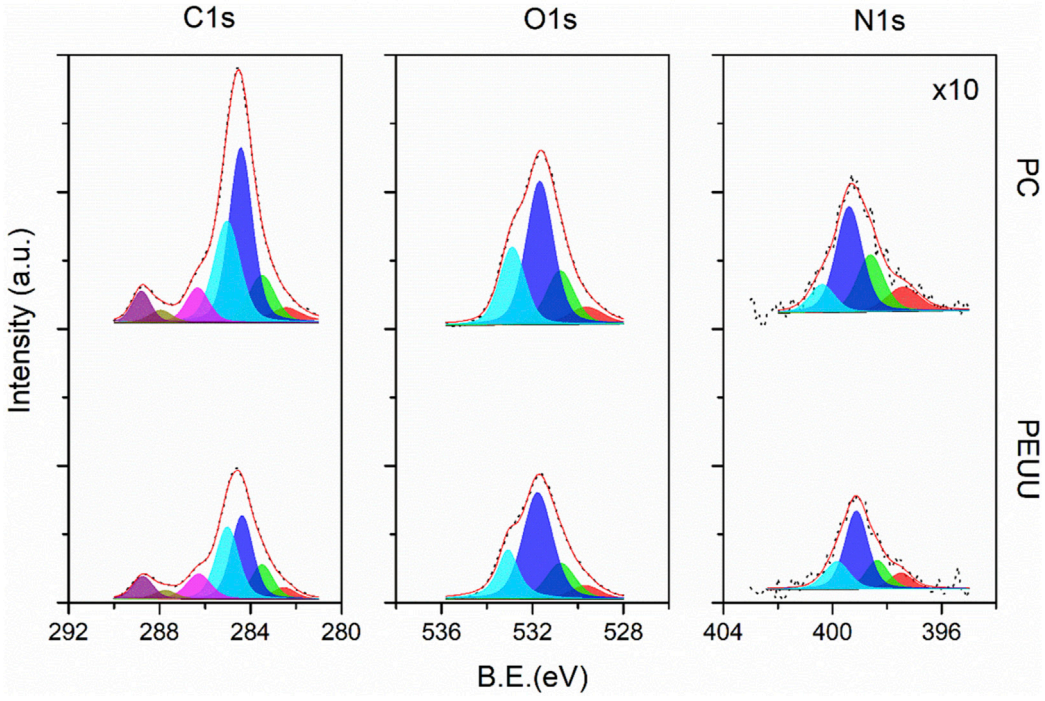


FIGURE 4
High-resolution XPS spectra for the C1s, O1s, and N1s core-level of PEUU (bottom) and PC (top) samples. Colored areas correspond to the sub-peak components referred to in Supplementary Table S1.

observations, and homoscedasticity of the data. Data conforming to normal distribution are presented as mean ± standard deviation, with *p*-values less than 0.05 ($p < 0.05$) deemed significant. Grubbs' test was applied to identify single outliers within the data sets (data not shown). A schematic illustration of the scaffold fabrication process is provided in Figure 3.

# 3 Results and discussion

## 3.1 PEUU carboxylation

### 3.1.1 PEUU-COOH (PC) X-ray photoelectron spectroscopy (XPS) analysis

The chemical surface characterization of PC was conducted by the XPS. A reference sample of PEUU reference was analyzed to determine the incorporation of dimethylolpropionic acid (DMPA) into the PEUU backbone. Figure 4 shows the high-resolution (HR) spectra for the main peaks of C1s, O1s, and N1s, subdivided into component sub-peaks delineated by distinct color zones. The spectra were normalized to the C1s mean signal. The binding energy (BE) values for all components, integral to the overall fitting, are indicated by red lines overlaid on black dots that represent the experimentally recorded data A summary of the BE, full width at half maximum (FWHM), and area under the curve values for all analyzed systems is presented in Supplementary Table S1 (Supplementary Section S1). Charging artifacts, evidenced as asymmetric tails at lower energies, are marked in red.

For the C1s core level, both samples showed sub-peaks corresponding to -O-C=O (C6—magenta-), N-C=O (C5—brown), -C-O (C4 –purple), -C-N (C3 –cyan), C-C (C2 –blue) and C-H (C1 –green) bonds, arranged from high to low binding energies. The peak integration counts, calculated from the area under the peak, demonstrated a noticeable disparity; the PC sample had higher counts than the PEUU, attributed to the presence of DMPA molecules. This variation confirms successful functionalization, as the urea/urethane ratio decreased from 1/1 to 1/3 after substituting DMPA for putrescine on a 1:1 basis. This substitution suggests an increased concentration of pi-bond resonant structures, caused by the interaction between DMPA, BDI, and PCL molecules. Consequently, the chemical potential of the PC sample surface exceeded that of PEUU. This observation correlates with the homogeneous distribution of the electronic density of states along the chain extension. It is noteworthy that XPS analysis was conducted on large polymer compounds, thus the fitting data reflect the aggregate chemical environment, directly linked to the functional groups introduced during the carboxylation process.

For the O1s core level, the spectrum consisted of three sub-peak components corresponding to chemisorbed hydroxyl (O3—cyan), -O-C (O2—blue), and C=O (O2—green) bonds, arranged from high to low binding energies. The results align with those of the carbon species since the O1s intensities for the PC sample exceeded those of the reference sample. Similarly, the N1s core-level exhibited weak signals for -N-C=O (N3—cyan), -N-H2 (N2—blue), and --N-H (N1– green) bonds, which are congruent with the organic matrix. Despite the general increase in count observed with the introduction of DMPA molecules, the -N-C=O bond component remained relatively consistent due to the expected reduction of amides with putrescine substitution.

### 3.1.2 PEUU-COOH (PC) FTIR analysis

The physicochemical evaluation of PEUU was conducted by Fourier Transform analysis, which confirmed the presence of functional groups in the polymer and the successful introduction of carboxyl groups of the PEUU (PC). The characteristic peaks of PEUU were identified at 3320 $cm^{-1}$ (urethane and urea N-H stretching vibration), 2933 and 2855 $cm^{-1}$ (carboxyl C-H stretching vibration), 1724 $cm^{-1}$ (ester carbonyl stretching vibration of the urethane group C=O) and 1160 $cm^{-1}$ (stretching vibration of the ester group C-O-C) (Nair and Ramesh, 2013; Nair and Ramesh, 2013; Włoch et al., 2018; Włoch et al., 2018). As shown above (Figures 5A, B) the carbonyl group peak of the PC (1724 $cm^{-1}$) exhibited elongation and broadening, indicating the oxidation of the PEUU and the presence of the COOH free radicals, which confirmed the successful functionalization of the polymer.

Additionally, the titration curve was used to confirm the carboxylation process. The presence of a higher number of carboxyl groups in the polymer results in increased acidity, requiring a greater quantity of NaOH solution to raise the pH level, as shown in Figure 5C. This technique has been widely used to determine the quantification of carboxyl groups in materials, considering the material's acidity (El Jundi et al., 2020; El Jundi et al., 2020; Babaev et al., 2022; Babaev et al., 2022). Therefore, the results of the titration curve provide additional evidence of the successful carboxylation of PEUU.

### 3.1.3 PEUU-COOH (PC) thermogravimetric analysis

The weight degradation profile of both PEUU and PC was analyzed via TGA, and the results are presented in Figures 5D, E. The two polymers exhibit similar behavior, but PC displays a distinct degradation temperature compared to PEUU, with temperature peaks dropping from 365°C to 305°C. This variation may be due to structural modifications in the PEUU, leading to weaker bonds or less stability in the carboxylated polymer itself. Alternatively, the decrease in temperature could be due to the reduction in molecular weight when compared to the unmodified polymer (Hong et al., 2012; Hong et al., 2012). Nevertheless, this difference in degradation temperature does not represent a significant inconvenience, as the melting temperature does not differ greatly from that of PEUU. Furthermore, a second weight loss can be observed at 350°C which may be related to the decomposition of urethane and urea bonds, and a total and remaining decomposition at 442 °C related to the decomposition of ester bonds (El-Raheem et al., 2021; El-Raheem et al., 2021).

The DSC thermogram confirmed the TGA results, showing a melting temperature of 363°C for PEUU and 305°C for PC (Figure 5F). The differences in both degradation temperatures can be attributed to the loss of bonds resulting from COOH generation on the backbone of the PC, leading to a slightly less stable polymer. However, these structural changes do not represent critical modifications in the material but are made to facilitate the formation of peptide bonds with the available amine (-NH) terminals of anti-thrombotic molecules studied (Fang et al., 2014; Fang et al., 2014).

## 3.2 PEUU-COOH (PC) biocompatibility and hemocompatibility

As the proposed biomaterial is intended for implantation and will come into contact with blood, its biocompatibility was assessed by evaluating cell viability, hemolysis percentage, and platelet activity.

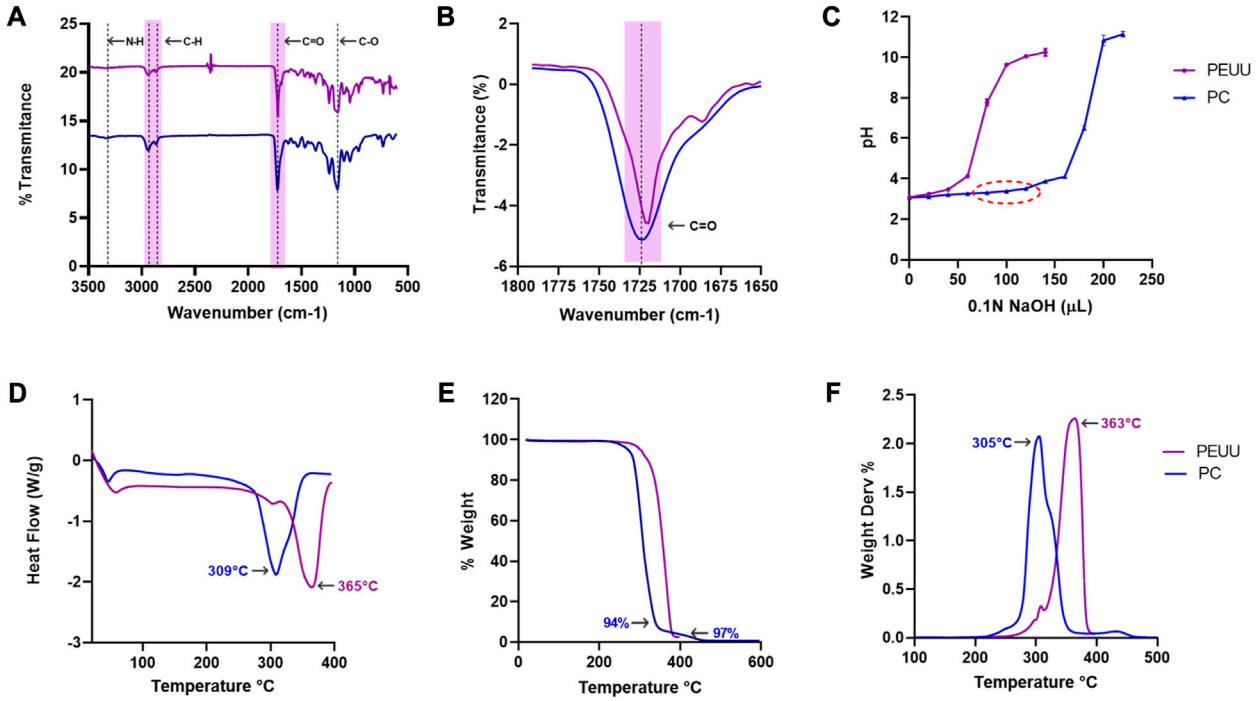


FIGURE 5
Physicochemical evaluation of the carboxylation of PEUU. **(A)** FTIR spectra of PEUU and PC measured in the range between 3500 and 500 $cm^{-1}$. Magnification of the **(B)** carbonyl (C=O) stretching. **(C)** Titration curve for COOH quantification (Mean ± SD). **(D)** DSC thermograms of PEUU and PC **(E)** Thermogravimetric (TGA) analysis and **(F)** DTGA curves of PEUU and PC.

Cell viability of VERO cells exposed to the PC film was analyzed at 24 and 72 h (Figure 6A). Results indicated no significant decrease in viability for both polymers, with PC showing cell viability percentages of 93% ± 11 at 24 h and 95% ± 11 at 72 h, compared to PEUU at 96% ± 4% and 90% ± 4, respectively. No apparent cell morphological changes were observed, and both maintained a viability percentage above the minimum allowed by the 10993 ISO standard (80%). Similar results are found when the viability of exposed THP-1 cells was evaluated (Figure 6B). PEUU-COOH showed 87% ± 4 and 111 ± 4 after 24 h and 72 h, while PEUU maintained the viability at 96% ± 5% and 91% ± 5 after 24 h and 72 h. No statistically significant differences were found.

The hemolysis percentage (Figure 6C) of the PC remained below 1% (0.6% ± 0.6) similar to PEUU (0.2% ± 0.4), with no statistically significant differences, and well below the maximum percentage allowed by the 10993 standards (5%), indicating hemocompatibility for both polymers.

To further analyze anti-thrombotic activity, contact angle (Figure 6D) and protein adsorption (Figure 6E) profiles were examined. Findings revealed that polymer functionalization led to a decrease in contact angle and an increase in hydrophilicity, this behavior did not present any significant difference after ethylene oxide sterilization. Post-sterilization contact angle measurements yielded 64 ± 6 for PEUU-COOH *versus* 78 ± 5 for PEUU ($p \leq 0.01$), with a PTFE graft serving as a hydrophobic control (96 ± 2). No discernible differences were observed post-sterilization in either film's manipulability or flexibility. Previous reports have shown that ethylene oxide sterilization might cause an increase on the rigidity of the biomaterial, thus mechanical property assessment is crucial for each specific application (Bednarz et al., 2018).

PC had lower mean protein adsorption than PEUU ($3 \times 10^{-2}$ mg/mm$^2$ ± $8 \times 10^{-3}$ vs. $2 \times 10^{-2}$ mg/mm$^2$ ± $6 \times 10^{-3}$), though these surfaces were not statistically different. According to Ramachandran, B. et al., PEUU's wettability can be influenced by both the density of carboxyl groups present on its surface and its surface roughness. Consequently, PC exhibits more pronounced hydrophilic behavior in comparison to the unmodified polymer. As the carboxyl group density on the polymer surface increased, protein adsorption decreased (Ramachandran et al., 2018; Ramachandran et al., 2018).

Upon 20 min of exposure to PRP, the platelet aggregation rate elicited by the PEUU-COOH was comparable to that of PEUU, registering 37% ± 1 *versus* 36% ± 2 ($p \leq 0.05$) (Figure 6E). Films functionalized with epinephrine, collagen, and ADP served as platelet aggregator inducers, categorizing them as high (100% ± 5), medium (47% ± 5), and mild (32% ± 1) aggregators, respectively. To determine if this result was related to platelet activation, an LDH test was performed, and the total count of adhered platelets/mm$^2$ was calculated through a linear regression from a calibration curve (Figure 6). Findings showed that the number of platelets adhered to the film surface increased proportionally with time, with a statistically significant increase from 15 min to 1 h for both groups. The increase in platelets adhered to surfaces was from $4 \times 10^5 \pm 2 \times 10^4$/mm$^2$ at 15 min to $6 \times 10^5 \pm 1 \times 10^5$/mm$^2$ at 1 h for PEUU ($p \leq 0.05$), and from $3 \times 10^5 \pm 2 \times 10^5$/mm$^2$ at 15 min to $8 \times 10^5 \pm 1 \times 10^5$/mm$^2$ at 1 h for PC ($p \leq 0.01$). Although platelet aggregation was lower for PC than for PEUU, platelet adhesion to the modified surface was twice as high, and the platelet density increased at a faster rate over time. This may be attributed to the presence of -COOH free radicals, which facilitate platelet adhesion, a

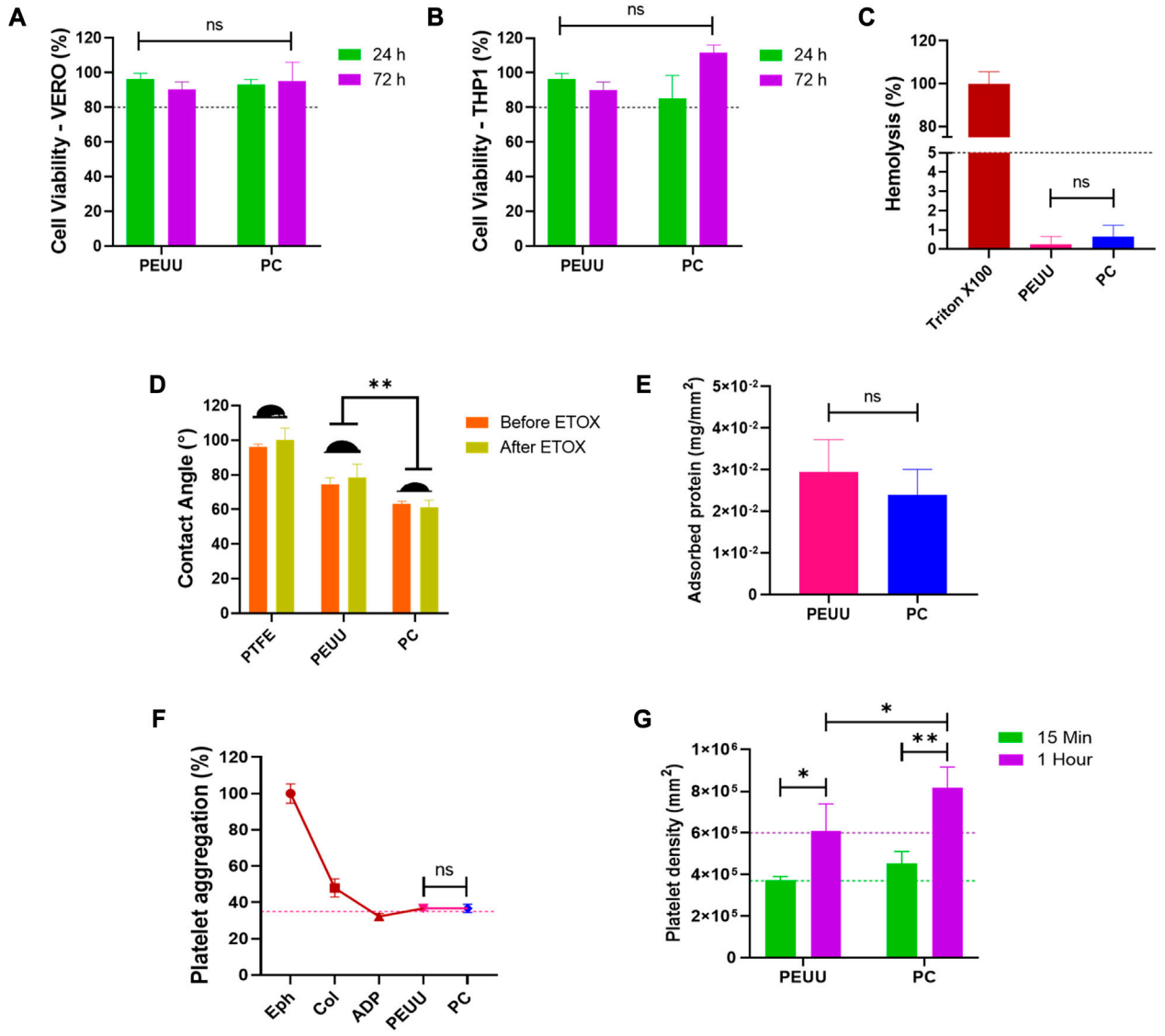


FIGURE 6
Biocompatibility testing of PC. Viability percentage extracted from MTT data of tests performed by directly exposing **(A)** VERO cell cultures (ATCC CCL81.4) and **(B)** THP-1 Cell cultures (ATCC TIB-202) to film's fragments for 24 h and 72 h. **(C)** Hemolysis percentage of films exposed to only erythrocytes. **(D)** Contact Angle of type II H2O on the surface of the polymers before and after sterilization with ethylene oxide. **(E)** Adsorbed serum protein on the film surface. **(F)** Platelet aggregation percentage of PRP exposed to films. **(G)**) Number of platelets adhered to the surface of the film by LDH activation analysis. Data compared to PEUU. Mean ± SD) where, ns = no significant *$p \leq 0.05$ **$p \leq 0.01$ ***$p \leq 0.001$ ****$p \leq 0.0001$.

property that PEUU does not possess. Platelet aggregation is primarily driven by platelet-to-platelet adhesion, a process initiated by an elevation in the intracellular calcium levels. This increase subsequently boosts the activity of the GPIIb/IIIa complex, which serves as an adhesive molecule. Given this mechanism, the carboxyl groups present on PC could potentially serve as anchoring sites for platelet adhesion (Poussard et al., 2004). Furthermore, previous research has highlighted that the negative charge provided by the terminal carboxyl groups has the capacity to activate the FXII coagulation factor, further promoting platelet adhesion (Stavrou and Schmaier, 2010; Shiu et al., 2014). Importantly, cell viability can be influenced by a myriad of factors, among which surface charge and the types of functional groups on the surface stand out as particularly significant.

## 3.3 PEUU anti-thrombogenic functionalization

Surface functionalization was classified into two distinct groups based on the strategy employed for incorporating anti-thrombotic molecules. Group 1 involved direct functionalization, while Group 2 necessitated indirect functionalization using gelatin nanoparticles as intermediaries between the polymer and the bioactive molecules.

In Group 1, anti-thrombotic molecules were directly grafted onto the polymer surface, facilitating a straightforward interaction between the polymer and the molecules. This approach aimed to enhance the inherent anti-thrombotic properties of the modified polyester urethane urea (PEUU) surface, potentially improving the

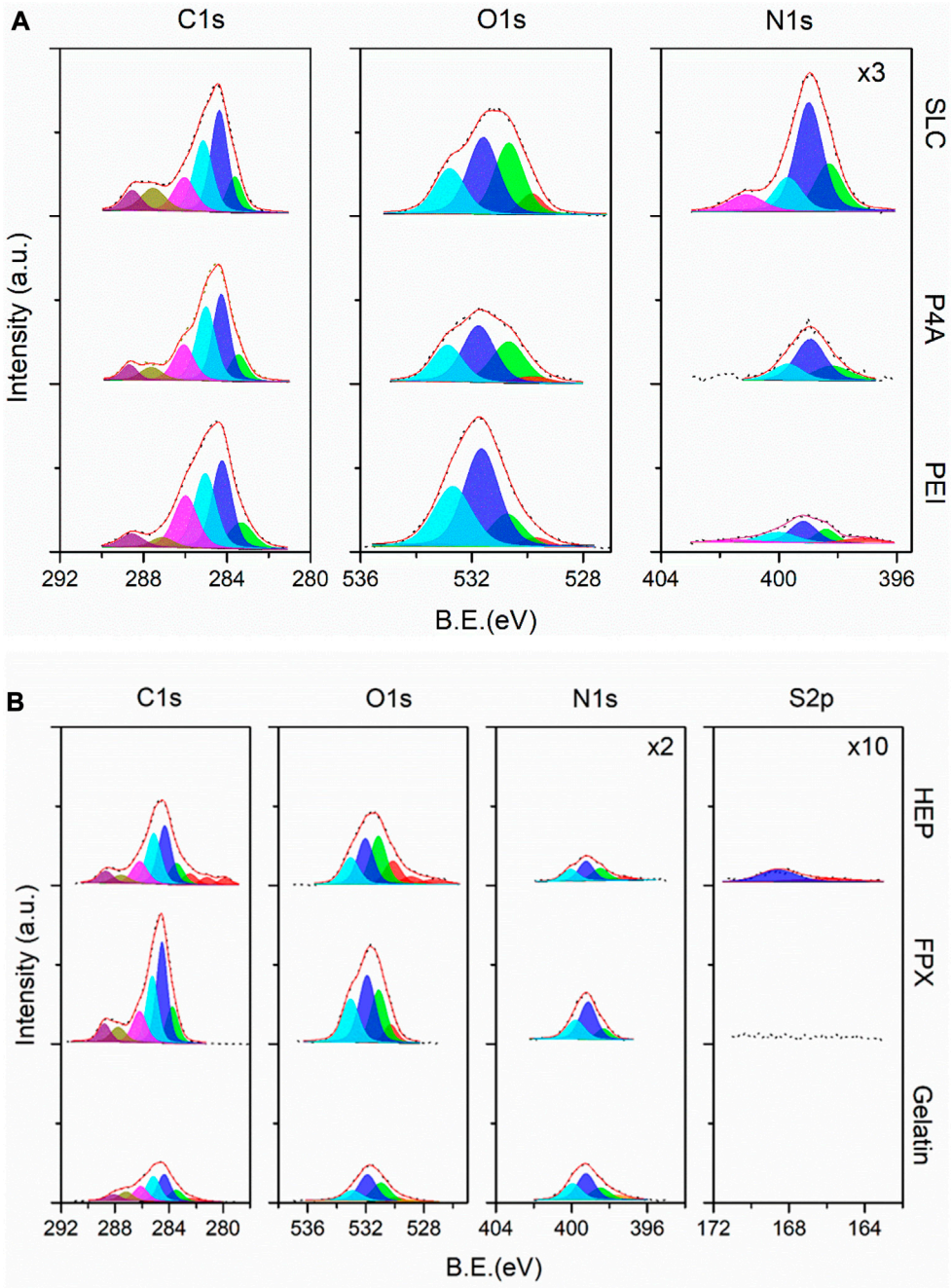


FIGURE 7
**(A)** High-resolution XPS spectra for SLC, P4A, and PEI samples (top-down) corresponding to the Group 1 of the PEUU-COOH (PC)/Anti-thrombotic functionalization system. **(B)** High-resolution XPS spectra for HEP, FPX, and gelatin (reference) samples (top-down) corresponding to the Group 2 of the PEUU-COOH (PC)/Anti-thrombotic functionalization system.

performance of regenerative cardiovascular devices. Conversely, Group 2 employed gelatin nanoparticles as a bridge between the polymer and the bioactive molecules. This indirect functionalization strategy allowed for the controlled release of anti-thrombotic agents and facilitated a more stable interaction between the polymer and the bioactive molecules. The utilization of gelatin nanoparticles as a delivery system may offer additional benefits, such as improved biocompatibility and the ability to incorporate multiple bioactive agents for synergistic effects.

### 3.3.1 PEUU-COOH (PC)/anti-thrombogenic functionalization XPS analysis

The surface chemistry evaluation of the functionalized samples was organized into two categories. The first involved a direct reaction of Seleno-L-Cystine (PC + SLC), PEG 4 ARM (PC + P4A), and polyethyleneimine (PC + PEI). The high-resolution XPS spectra for these reactions are displayed in Figure 7A (top-down). The results and discussion are drawn from Section 3.3.1, and henceforth, all three systems will be discussed concurrently for each

core level. Beginning with the C1s peak, atomic percentages linked to carboxyl and amide functional groups escalated in a sequence from PEI, P4A, to SLC samples. Contrarily, the C-O interaction was more pronounced in the PEI sample, while hydroxyl species peaked as anticipated. These observations correlate well with the N1s core level, where the peak intensity also ascended in the same sequence. Protonated species were readily discernible at a binding energy of 401.1 eV (N4—blue). In addition, carbonyl species were scrutinized. The O1s subpeak suggested a superior functionalization yield for the SLC sample, trailed by P4A and PEI, in that order.

The second part of the evaluation involved an indirect, *in-situ* functionalization, as depicted in the high-resolution XPS spectra presented in Figure 7B. This section includes gelatin nanoparticles (GNPs) as a reference, with Fondaparinux (PC + FPX) and Heparin (PC + HEP) serving as anti-thrombogenic agents. Significant changes were observed in the overall intensity of the anti-thrombogenic agents relative to the GNPs. Moreover, charge artifacts were more prominent for the PC + HEP sample. This finding suggests a successful surface modification, given the constant electron bombardment maintained throughout the experimental setup across different sample types. To delve further, the S2p core level was analyzed, confirming the presence of sulfate species at 168 eV for PC + HEP. This was not observed for PC + FPX. However, both samples demonstrated an increased count of -C=O bond types and a considerably higher atomic percentage of oxygen species compared to GNPs. The analysis of the N1s core level revealed that GNPs were fully covered by N-H bonds. Its intensity diminished following anti-thrombotic functionalization, which could be attributed to the presence of larger molecules on the outer layers. It is worth noting that atomic ratios should be compared between sub-peak components. Accordingly, the presence of nitrogenated species significantly decreased for both PC + HEP and PC + FPX. The findings substantiate the successful anti-thrombotic functionalization achieved via an indirect, *in-situ* reaction using GNPs as an intermediary.

### 3.3.2 PEUU-COOH (PC)/anti-thrombotic functionalization FTIR spectroscopy analysis

Physicochemical evaluation by Fourier Transform analysis confirmed the presence of functional groups related to the functionalization of PC with polyethyleneimine (PC + PEI), PEG 4 ARM (PC + P4A), Seleno-L-Cystine (PC + SLC), Fondaparinux (PC + FPX) and Heparin (PC + HEP).

For group 1 molecules, the carbonyl group peak of the PC (1720 $cm^{-1}$) exhibited attenuation, which is evident in PC + PEI, indicating functionalization, moreover, a decrease in absorption at 1720 $cm^{-1}$ is also evident, a characteristic peak for imide carbonyl groups in PEI (Chen et al., 2006; Chen et al., 2006). Other identified peaks were located between 2950 and 2865 $cm^{-1}$ (C-H stretching vibration) and decreased following PEI functionalization. Furthermore, the peak at 1100 $cm^{-1}$ (stretching vibration of the ester group C-O-C) exhibited an increase. For PC + P4A, the C-H stretching vibration (2933 $cm^{-1}$ to 2852 $cm^{-1}$) and the amine group (1625 $cm^{-1}$) stretching appeared more pronounced than in PC, suggesting that functionalization was successful. Conversely, the N-O group peak at 1498 $cm^{-1}$ has decreased. Finally, the ether group at the 1100 $cm^{-1}$ peak increased because of the formation of bonds during the functionalization process. Furthermore, a slight attenuation of the carbonyl group at 1720 $cm^{-1}$ is observed at the time of functionalization, which indicates the bonding of the NH2 groups of P4A to PC. The characteristic peaks of PC + SLC include the carbonyl group peak of 1720 $cm^{-1}$, where the PC + SLC polymer shows a decrease compared to PC. Similarly, the peak at 1600 $cm^{-1}$, corresponding to the amine group, increased, and the peak of the ether group at 1170 $cm^{-1}$ decreased (Figures 8A–C).

On the other hand, the analysis of group 2 molecules revealed notable peak changes, suggesting that Heparin (PC + HEP), and Fondaparinux (PC + FPX) functionalization led to a decrease (Figures 8D, E). For HEP functionalization, the characteristic peaks show a decrease in the peaks in 1720 $cm^{-1}$ (corresponding to the vibration of the carbonyl stretching, C=O), 1640 $cm^{-1}$ (corresponding to the vibration of amine stretching, N-H), and 1100 $cm^{-1}$ (corresponding to the vibration of ester stretching, C-O-C) in comparison to the PC. This observation is consistent with the HEP control displaying higher inverse peaks. Additionally, a new peak emerged at 1780 $cm^{-1}$ (corresponding to the vibration of carbonyl C=O) that was not present in the PC control but appeared in the PC + HEP functionalization. Similarly, FPX functionalization demonstrated peak reductions at 2941 $cm^{-1}$ (corresponding to the C-H stretching), 1592 $cm^{-1}$ (corresponding to nitro-compounds), 1240 $cm^{-1}$, and 1154 $cm^{-1}$ (corresponding to the ester group) when compared to the PC control. In contrast, the carbonyl stretching (C=O) peak (1720 $cm^{-1}$) increased. The FTIR analysis substantial peak changes after each functionalization, which collectively suggest successful functionalization of the polymer surface with the anti-thrombotic molecules.

### 3.3.3 PEUU-COOH (PC)/anti-thrombotic functionalization thermogravimetric analysis

DCS analysis of the different functionalization was performed to confirm the presence of active components. The DSC curves revealed that the melting temperatures (Tm) of functionalized polymers deviated from the PC control. In group 1, Tm for PC + PEI peaked at 309°C, for PC + P4A at 334°C, and for PC + SLC at 388°C. Similarly, in group 2, for PC + HEP the Tm peaked at 324°C while for PC + FPX at 328°C (Figure 9A).

TGA of functionalized polymers exhibited an initial weight loss at low temperatures due to the evaporation of water present in the sample. For group 1, varying percentages of weight loss were observed (Figure 9B). For PC + PEI and PC + P4A, two distinct percentages of weight loss were noted at 269°C and 322°C, which approached 22% and 87% for PC + PEI, since it has been found that pure PEI decomposition can occur at temperatures between 250°C and 350 °C (Zhu et al., 2007; Zhu et al., 2007), and weight loss at 305°C and 361°C which approached 30% and 93% for PC + P4A, in which the first weight loss is related to the decomposition temperature of P4A molecule, reported to be between 200°C and 300°C, and, the remaining percentage is associated with PC decomposition (Zarour et al., 2021; Zarour et al., 2021). A single weight loss of 35% at 317°C was observed for PC + SLC, which could be attributed to the rapid and spontaneous release of functionalizing molecules. This behavior might be explained by the detachment of each active molecule as the temperature increases, most likely reflecting the strength and the number of functionalized molecules on the surface.

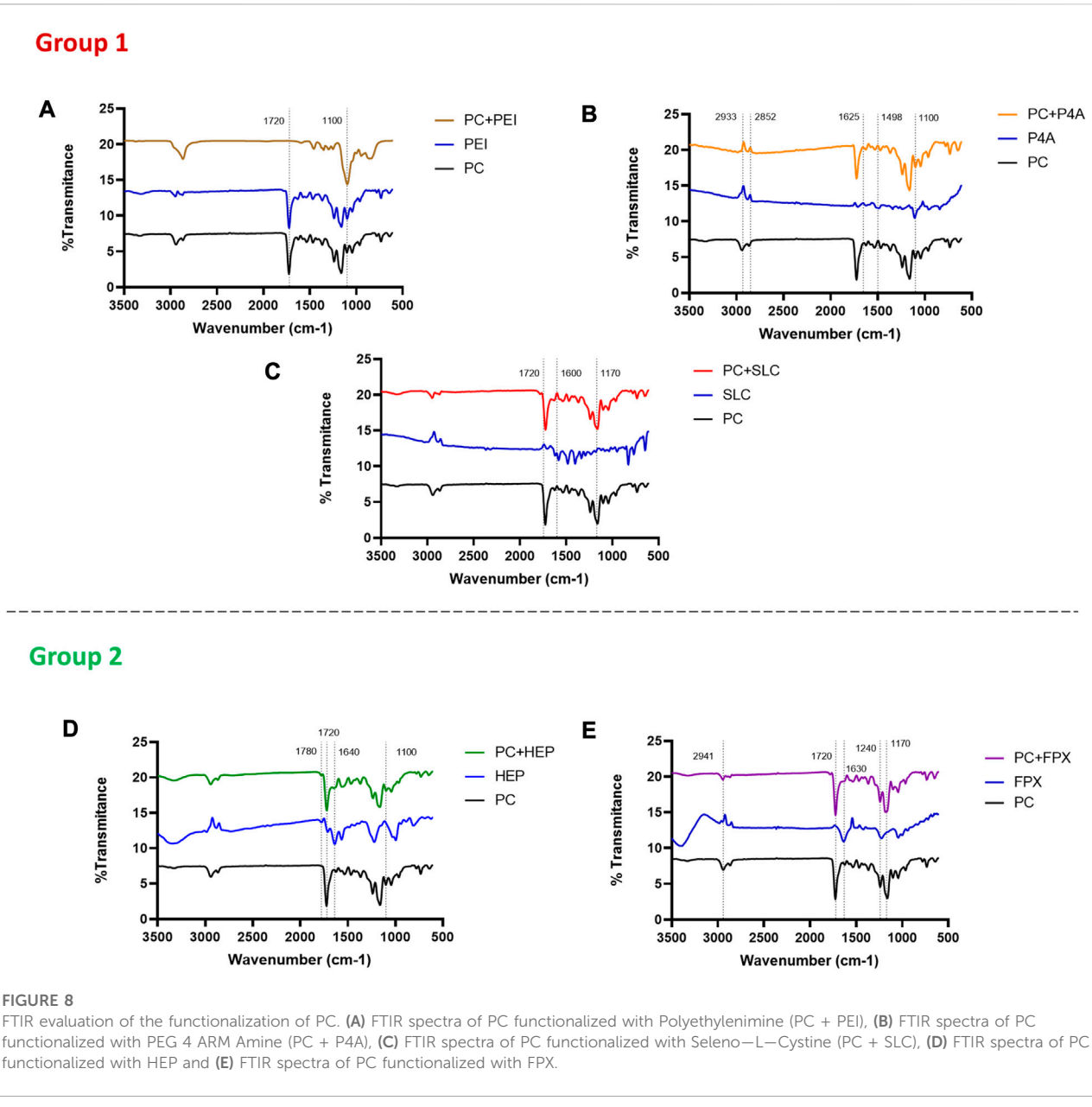


FIGURE 8
FTIR evaluation of the functionalization of PC. **(A)** FTIR spectra of PC functionalized with Polyethylenimine (PC + PEI), **(B)** FTIR spectra of PC functionalized with PEG 4 ARM Amine (PC + P4A), **(C)** FTIR spectra of PC functionalized with Seleno—L—Cystine (PC + SLC), **(D)** FTIR spectra of PC functionalized with HEP and **(E)** FTIR spectra of PC functionalized with FPX.

In contrast, the degradation percentages for group 2 were higher than those of group 1 (Figure 9B), which might indicate the weight loss produced by the gelatin nanoparticles serving as bridges between the active molecule and the polymer. For PC + HEP, weight losses of 10% (180°C) and 36% (290°C) were observed, resulting from the degradation of the functionalization molecule and the gelatin nanoparticle. In the case of PC + FPX, a single weight loss of 23% (285°C) was observed, most likely due to the rapid degradation of both the gelatin nanoparticle and the FPX molecule. These results can be compared with the temperatures shown by the DTGA, where the points of inflection indicate the regimes of highest degradation of mass loss (Figure 9C). For PC + PEI and PC + P4A, the inflection points were 305°C and 334°C, respectively. On the other hand, the PC + SLC shows two important inflection points, 350°C and 388°C, which can be correlated to degradation events, leading to the release of material. This behavior is more evident in group 2, where bonding with gelatin likely causes a double inflection peak at 205°C and 322°C for PC + FPX. This is also the case of PC + HEP where the peaks appeared at 217°C and 322°C. This behavior can be similar to other articles that show similar temperature degradation against molecules such as HEP, PEG, and PEI (Kim et al., 2017; Kim et al., 2017; Zhu et al., 2021; Zhu et al., 2021).

## 3.4 PEUU-COOH (PC)/anti-thrombotic functionalization biocompatibility

The PC functionalization success with the anti-thrombotic molecules is contingent upon the biocompatibility of these biomaterials. The viability of VERO cells exposed directly to PC functionalized with the bioactive molecules was assessed at 24 and 72 h (Figure 10A). Results indicated that cell viability was maintained for all functionalized films. The highest viability percentages were observed for PC + PEI with 98% ± 28 at 24 h

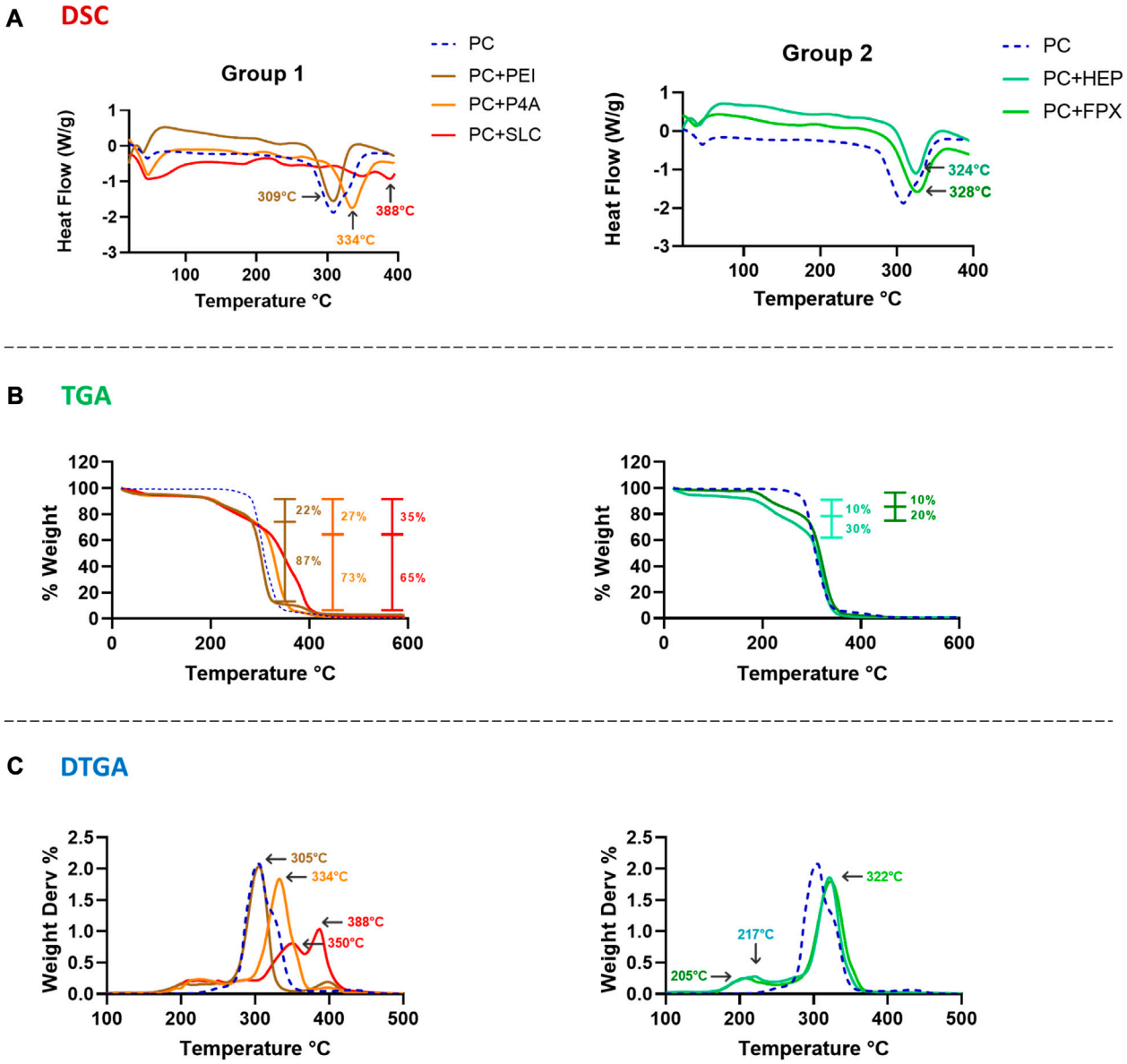


FIGURE 9
**(A)** DSC. **(B)** TGA. **(C)** DTGA results for PC *in-situ* functionalization (Blue dotted line) according to two different groups of bioactive molecules. Right column of data from Group 1–Direct Functionalization of PC + PEI (Brown), PC + P4A (Orange) and PC + SLC (Red). Left column of data from Group 2–Indirect Functionalization of PC + HEP (Aqua) and PC + FPX (Green).

and 91% ± 28 at 72 h, followed by PC + P4A with 98% ± 12 at 24 h and 93% ± 12 at 72 h, and PC + HEP with 97% ± 9 at 24 h and 80% ± 9 at 72 h. Lower viability percentages were found for PC + FPX with 90% ± 16 at 24 h and 88% ± 15 at 72 h and PC + SLC with 89% ± 30 at 24 h and 80% ± 30 at 72 h. However, all groups exhibited a viability percentage above the minimum threshold specified by the 10993 ISO standard (80%), and no discernible cell morphological changes were observable. Similar behavior was found for THP-1 cells directly exposed to the films (Figure 10B). Higher viability rates were found for PC + PEI with 105% ± 27% and 109% ± 4 after 24 h and 72 h, followed by PC + P4A with 99% ± 23 and 104 ± 5 after 24 h and 72 h. Neither did the evaluated groups decrease the cell viability below 85%, nor did they show any statistically significant difference. Concurrently, the hemolysis percentage (Figure 10C) for all functionalized films remained below 1% without any statistically significant differences, considerably lower than the maximum percentage permitted by the 10993 ISO standard (5%).

## 3.5 PEUU-COOH (PC)/anti-thrombotic functionalization and anti-thrombogenic activity

An assessment of platelet aggregation percentages was conducted in light of the anticoagulant functionalization (Figure 11A). Films functionalized with epinephrine, collagen,

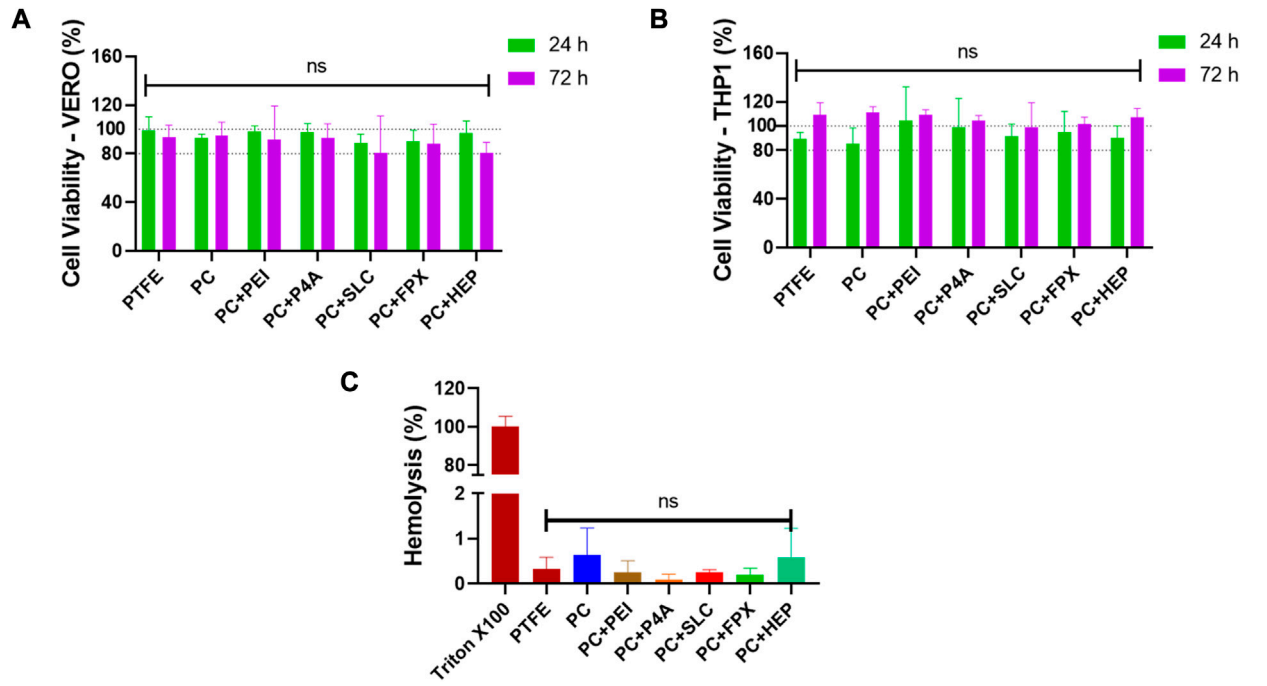


FIGURE 10
Viability percentage extracted from MTT data of tests performed by directly exposing **(A)** VERO cell cultures (ATCC CCL81.4) and **(B)** THP-1 Cell cultures (ATCC TIB-202) to film's fragments for 24 h and 72 h. **(C)** Hemolytic behavior after an incubation time of 1 h. Triton X-100 and PBS were used as positive and negative controls respectively. Data compared to PC (PC) (Mean ± SD) where, ns = no significant *$p \leq 0.05$ **$p \leq 0.01$ ***$p \leq 0.001$ ****$p \leq 0.0001$.

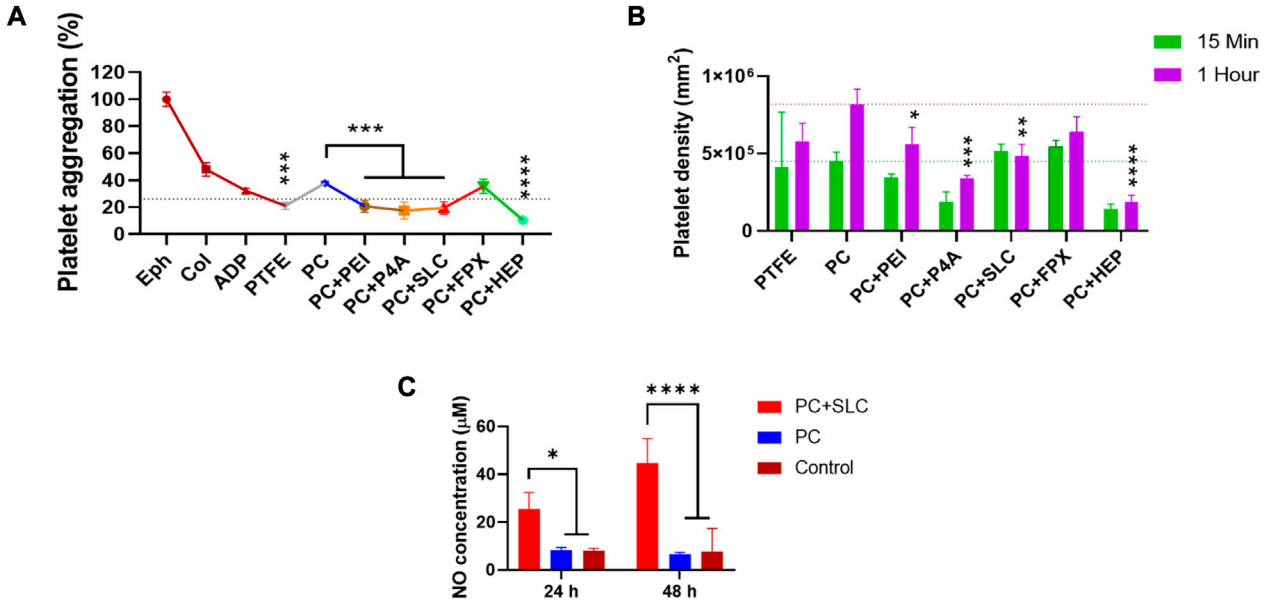


FIGURE 11
Platelet activation evaluation. **(A)** Platelet aggregation percentage, Epinephrine, Collagen, and ADP solutions were used as positive controls of high, medium, and low platelet aggregants. **(B)** Platelet density calculated as means of LDH release content of films exposed to platelets and treated with Triton X-100. **(C)** Concentration of nitric oxide species at 24 h and 48 h. Data compared to PC (Mean ± SD) where, ns = no significant *$p \leq 0.05$ **$p \leq 0.01$ ***$p \leq 0.001$ ****$p \leq 0.0001$.

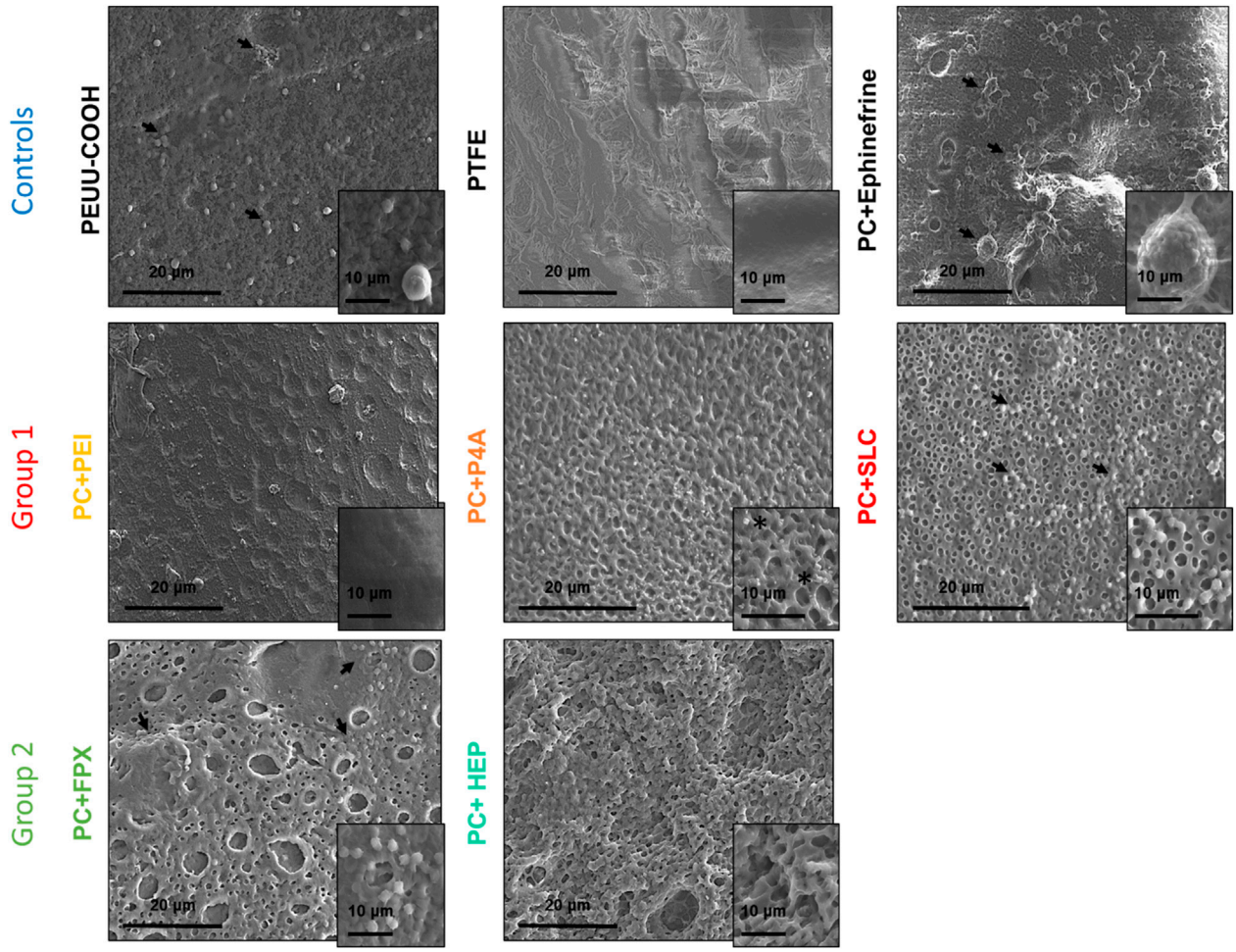


FIGURE 12
SEM microscopy images of the film's surfaces exposed to PRP, the changes in topography and platelet adhesion and activation can be observed. Arrows show platelets, asterisks indicate salt crystals.

and ADP were used as high, medium, and mild platelet aggregation inducers, respectively. In general, the anti-thrombotic functionalization led to a decreased platelet aggregation percentage compared to PEUU-COOH alone (37% ± 1). The lowest aggregation percentage was observed for PC + HEP, which registered 10% ± 2 ($p \leq 0.0001$), followed by PC + P4A at 17% ± 6 ($p \leq 0.001$), PC + SLC at 19% ± 5 ($p \leq 0.001$) and PC + PEI at 20% ± 4 ($p \leq 0.001$). Unexpectedly, PC + FPX presented a higher platelet aggregation percentage of 35% ± 5%, which was higher than that of PEUU-COOH.

To correlate these findings with the platelet adhesion and activation on the polymer surfaces, an LDH activation test was performed, and the total count of adhered platelets was calculated through a linear regression from a calibration curve (Figure 11B). The results indicated that the number of platelets adhering to the film surface was directly proportional to time. Platelet density increased after 1 h of exposure to PRP for all groups, except for SLC. According to the platelet aggregation test at 1 h, PC + HEP presented the lowest platelet count of 18022 2 ± 41460/mm$^2$ ($p \leq 0.0001$) followed by PC + P4A with $3 \times 10^5 \pm 2 \times 10^4$/mm$^2$ ($p \leq 0.001$), PC + SLC with $4 \times 10^5 \pm 7 \times 10^4$/mm$^2$ ($p \leq 0.01$) and PC + PEI with $5 \times 10^5 \pm 1 \times 10^5$/mm$^2$ ($p \leq 0.05$). Higher platelet counts were found for PC + FPX with $6 \times 10^5 \pm 9 \times 10^4$/mm$^2$, with no significant difference from PC.

Platelet activation might be observed by SEM images (Figure 12). The surface functionalized with epinephrine showed a high platelet density, and platelets displayed filopodia, indicating attachment and activation. Similarly, PC showed high platelet density, albeit without filopodia. In contrast, a fragment of a PTFE vascular graft was presented without platelets. Regarding the anti-thrombotic activity functionalization, the surfaces of the functionalized polymers appeared markedly different from the PC alone. A highly porous surface was observed for PC + FPX, less porous surfaces for PC + HEP and PC + P4A, and smoother surfaces for PC + SLC and PC + PEI. Platelets were found to attach on PC + FPX and PC + SLC, whereas PC + HEP, PC + P4A, and PC + PEI showed no adhered platelets. On the other hand, given that the SLC action process is attributed to the production of reactive nitric oxide species, its efficacy was verified by quantifying the NO2-/NO3- species ratio. Nitric oxide at 24 and 48 h was evaluated for PC + SLC to confirm its activity (Figure 11C), and results indicated an increase from 25 uM to 45 uM, almost doubling the amount at 24 h. This is

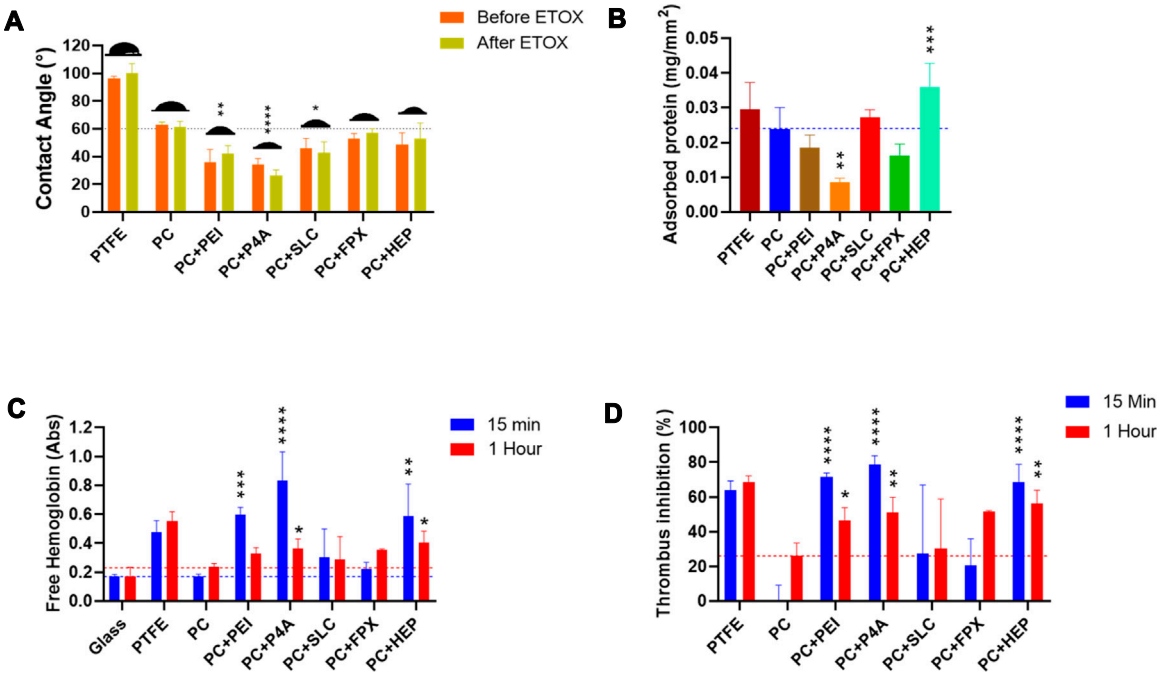


FIGURE 13
Antithrombogenic activity evaluation. **(A)** Contact angle of the surface of the functionalized films. **(B)** Adsorbed protein over the surface of the functionalized films. **(C)** Free hemoglobin released of clots formed on the surfaces of the films and exposed to water at 15 and 1 h, glass and PTFE were used as negative and positive controls. **(D)** Thrombus Inhibition percentage extracted from free hemoglobin and considering the PC value as the initial condition.

most likely a result of the enhanced production of nitric oxide species due to PC-SLC activity as an organoselenium compound, this might lead to elevated cyclic guanosine monophosphate levels and decreasing $Ca^{2+}$ levels, which are required for platelet activation in the coagulation process (Suchyta et al., 2014; Suchyta et al., 2014).

As shown above, the most potent anticoagulant activity was achieved for heparin-functionalized materials followed by PEG-4-Arm-NH2 and PEI. Surprisingly, Seleno-L-cystine and Fondaparinux showed no anti-platelet activity. These results align with the literature, in which the two molecules showing the most significant anti-platelet effects are Heparin and various PEG polymers such as the PEG-4-Arm (Ashcraft et al., 2021; Ashcraft et al., 2021). These compounds shown to be effective because they neutralize the prostaglandin prostacyclin, a potent inhibitor of platelet aggregation that can also inhibit integrin exposure. Additionally, the PEG-4-arm used here is of a longer chain. As previously mentioned, increased PEG length reduces protein adsorption and cell adhesion capabilities, which is beneficial for controlling cell adhesion and inflammation (J.-L. Wang et al., 2018). This technique has also been previously reported as a passivation strategy to inhibit unspecific surface interaction (Sauter et al., 2013).

For a more detailed analysis of the anti-thrombotic properties of the surface-functionalized films, we measured the contact angle and protein adsorption. Furthermore, free hemoglobin and thrombus inhibition tests were performed. As anticipated, Surface functionalization with P4A and PEI, given their inherent hydrophilicity, reduced the contact angle on PEUU-COOH (Figure 13A) with 34° ± 6 for PC + P4A ($p \leq 0.001$) and 36 ± 9 for PC + PEI ($p \leq 0.001$). However, post-ethylene oxide sterilization, a slight decrease for PC + P4A and an increase for PC + PEI were noted, with both changes lacking statistical significance, i.e., 26° ± 4 and 42° ± 5, respectively. Functionalization with SLC and HEP also resulted in minor contact angle reductions with 46° ± 7 and 42° ± 8 ($p \leq 0.05$) and 49° ± 8 and 52 ± 8 ($p \leq 0.05$) pre- and post-sterilization for PC + SLC and PC + HEP, respectively. In contrast, PC + FPX contact angle remained relatively stable (53° ± 4 and 57° ± 3 pre- and post-sterilization). Accordingly, adsorbed protein for PC was determined to be $2 \times 10^{-2} \pm 6 \times 10^{-3}$ mg/mm$^2$ (Figure 13B) and the protein adsorbed on the PC + P4A film was $8 \times 10^{-3} \pm 1 \times 10^{-3}$ mg/mm$^2$ ($p \leq 0.01$). Contrary to expectations, PC + HEP exhibited even higher adsorbed protein levels than PC, with $3 \times 10^{-2} \pm 6 \times 10^{-3}$ mg/mm$^2$ ($p \leq 0.001$). No other statistically significant differences were found among the groups. Furthermore, it is noteworthy that both PC + PEI and PC + P4A formulations exhibited a marginal decline in protein adsorption, aligning with reduced hemolysis percentages. Conventionally, the positive charge of PEI and P4A surfaces, due to their terminal amine groups, would suggest enhanced protein adsorption. However, the observed attenuation in protein adsorption could conceivably hint at potential amide bond formation between the carboxyl groups of PC and the amine groups of PEI and P4A, possibly leading to a muted positive charge on these surfaces. Concurrently, this diminished positive charge is postulated to boost hemocompatibility, a phenomenon attributable to the reduced interaction between the polymer and negatively charged erythrocytes (Monfared et al., 2022; S; Zhu et al., 2007).

The free hemoglobin tests were performed to measure the amount of free hemoglobin released due to reduced coagulation processes. Higher absorbance values correlate with lower coagulation potential and increased hemocompatibility. After exposing the films to whole and activated blood for 15 min, free hemoglobin levels were recorded. In agreement with previous experiments, PC + P4A showed the highest absorbance for free hemoglobin with $0.8 \pm 0.2$ ($p \leq 0.0001$), compared to PC alone with $0.2 \pm 3 \times 10^{-3}$, followed by PC + PEI with $0.6 \pm 5 \times 10^{-2}$ ($p \leq 0.001$) and PC + HEP with $0.58 \pm 0.2$ ($p \leq 0.01$). The behavior persisted for 1 h, during which the PC + P4A and PC + HEP maintained their anticoagulant effects. No other statistically significant differences were found among the groups (Figure 13C).

To further analyze data, thrombus generation was induced on a glass surface, which was considered the maximum value for coagulation. Accordingly, thrombus inhibition percentages were derived from the free hemoglobin test. Consistent data showed the highest thrombus inhibition percentage achieved by PC + P4A with 79% ± 5 ($p \leq 0.0001$) followed by PC + PEI with 71% ± 2 ($p \leq 0.0001$) and PC + HEP with 69% ± 10 ($p \leq 0.0001$). This behavior persisted for up to 1 h for these groups. Nevertheless, PC + FPX did not exhibit a significant increase in the thrombus inhibition percentage, and PC + SLC displayed a highly variable behavior (Figure 13D).

## 4 Conclusion

The development of innovative surface modifications to enhance the anti-thrombotic performance of Polyester Urethane Urea (PEUU) is critical for advancing regenerative cardiovascular devices. In this study, a biodegradable PEUU elastomer with carboxyl groups was synthesized to facilitate functionalization with anti-thrombotic molecules. The carboxylation of PEUU proved successful, maintaining excellent biocompatibility with cellular viability above 85% and hemolysis percentage below 2%, in accordance with international ISO10993 standards. Various strategies were employed to functionalize the carboxylated PEUU, targeting different biochemical routes to inhibit platelet adhesion, activation, or activity. These included the use of PEI (400 MW) and PEG-4-arm (20000 MW) to induce steric inhibition, Seleno-L-Cystine as a Nitric Oxide producer, Fondaporinux as a selective factor Xa inhibitor, and Heparin as an inhibitor of both factor Xa and thrombin. Physicochemical characterization confirmed successful functionalization and excellent biocompatibility for all bioactive molecules.

The most effective anti-thrombotic results were achieved with PC functionalized with Heparin and PEG-4-arm, significantly reducing platelet adhesion, and demonstrating high thrombus inhibition. While PEI and Seleno-L-Cystine functionalization exhibited anti-thrombotic effects, they were not as potent. Surprisingly, Fondaporinux functionalization did not yield any significant improvement in thrombogenesis. Future applications of synthesized PEUU functionalized with anti-thrombotic molecules could include anti-thrombogenic biomaterials for cardiovascular devices such as tissue-engineered vascular grafts, synthetic vascular graft coatings, stents, valves, or catheters. Additionally, PC functionalization with other bioactive molecules could broaden its potential biomedical applications.

All in all, the development of anti-thrombotic-functionalized PEUU offers promising advancements for regenerative cardiovascular devices by improving hemocompatibility and reducing thrombogenesis. However, it is essential to consider the tradeoffs between various functionalization strategies and the challenges associated with different approaches to optimize outcomes.

## 5 Patents

Biodegradable, Non-Thrombogenic Elastomeric Polyurethanes. Patent Application Publication, United States. Pub. No: US 2014/0248232 A[1]. Pub. Date: Sep. 4, 20164.

## Data availability statement

The original contributions presented in the study are included in the article/Supplementary Material, further inquiries can be directed to the corresponding author.

## Ethics statement

The studies involving humans were approved by Ethical Committee at the Universidad de Los Andes, minute number 928-2018. The studies were conducted in accordance with the local legislation and institutional requirements. The participants provided their written informed consent to participate in this study.

## Author contributions

MR-S: Conceptualization, Data curation, Formal Analysis, Investigation, Methodology, Software, Visualization, Writing–original draft. NS: Conceptualization, Formal Analysis, Investigation, Methodology, Validation, Writing–review and editing. MA-V: Data curation, Formal Analysis, Investigation, Software, Visualization, Writing–original draft. AA-R: Data curation, Formal Analysis, Investigation, Methodology, Visualization, Writing–original draft. CO: Formal Analysis, Investigation, Methodology, Visualization, Writing–original draft, Writing–review and editing. JC: Conceptualization, Project administration, Resources, Supervision, Validation, Writing–review and editing. CM: Project administration, Resources, Supervision, Validation, Writing–review and editing. SK: Data curation, Investigation, Methodology, Software, Validation, Writing–review and editing. AD'A: Methodology, Project administration, Resources, Supervision, Validation, Writing–review and editing. WW: Funding acquisition, Project administration, Resources, Supervision, Validation, Writing–review and editing. JB: Conceptualization, Funding acquisition, Project administration, Resources, Supervision, Validation, Writing–review and editing.

## Funding

The authors declare financial support was received for the research, authorship, and/or publication of this article. This research was funded by MINCIENCIAS, grant number RC # 635-2021 Code 1544101252100 with the project "Multigraft-Bac: Injerto vascular bacteriostático/bactericida y regenerativo para la reconstrucción de extremidades y el tratamiento de infección de aneurismas micóticos".

## Acknowledgments

The authors would like to thank the departments of Biomedical Engineering, and Chemical and Food Engineering at Universidad de los Andes. Furthermore, the authors acknowledge Fundación Cardioinfantil Instituto de Cardiología for providing financial and technical support as well as the μ-Core Facility at Universidad de los Andes for technical assistance with the SEM microscopy imaging. Special acknowledgments to Andres Brand, Cristina Gonzales, and Gabriela Peralta-Peluffo from the departments of Biomedical Engineering and Chemical Engineering at Universidad de los Andes for providing the gelatin nanoparticles and assisting with the *in vitro* testing.

## Conflict of interest

The authors declare that the research was conducted in the absence of any commercial or financial relationships that could be construed as a potential conflict of interest.

The authors declared that they were an editorial board member of Frontiers, at the time of submission. This had no impact on the peer review process and the final decision.

## Publisher's note



## Supplementary material

The Supplementary Material for this article can be found online at: https://www.frontiersin.org/articles/10.3389/fbioe.2023.1257778/full#supplementary-material

## References

An, J., Chen, S., Gao, J., Zhang, X., Wang, Y., Li, Y., et al. (2015). Construction and evaluation of nitric oxide generating vascular graft material loaded with organoselenium catalyst via layer-by-layer self-assembly. *Sci. China Life Sci.* 58 (8), 765–772. doi:10.1007/s11427-015-4870-z

Ashcraft, M., Douglass, M., Chen, Y., and Handa, H. (2021). Combination strategies for antithrombotic biomaterials: an emerging trend towards hemocompatibility. *Biomaterials Sci.* 9 (7), 2413–2423. doi:10.1039/D0BM02154G

Babaev, M. S., Lobov, A. N., Shishlov, N. M., and Kolesov, S. V. (2022). pH-sensitive particles of polymer-surfactant complexes based on a copolymer of N,N′-diallyl-N,N′-dimethylammonium chloride with maleic acid and sodium dodecyl sulfate. *React. Funct. Polym.* 178, 105359. doi:10.1016/j.reactfunctpolym.2022.105359

Barbosa, L. C. A., Maltha, C. R. A., Demuner, A. J., Cazal, C. M., Reis, E. L., and Colodette, J. L. (2013). A rapid method for quantification of carboxyl groups in cellulose pulp. *BioResources* 8 (1). doi:10.15376/biores.8.1.1043-1054

Bednarz, P., Bernasik, A., and Laska, J. (2018). The influence of sterilization on properties of polyurethane/polylactide blend. *Sci. Technol. Innovation* 2 (1), 13–18. doi:10.5604/01.3001.0012.1264

Braune, S., Zhou, S., Groth, B., and Jung, F. (2015). Quantification of adherent platelets on polymer-based biomaterials. Comparison of colorimetric and microscopic assessment. *Clin. Hemorheol. Microcirc.* 61 (2), 225–236. doi:10.3233/CH-151995

Chen, B.-K., Su, C.-T., Tseng, M.-C., and Tsay, S.-Y. (2006). Preparation of polyetherimide nanocomposites with improved thermal, mechanical and dielectric properties. *Polym. Bull.* 57 (5), 671–681. doi:10.1007/s00289-006-0630-3

Chu, A. J., Beydoun, S., Mathews, S. T., and Hoang, J. (2003). Novel anticoagulant polyethylenimine: inhibition of thrombin-catalyzed fibrin formation. *Archives Biochem. Biophysics* 415 (1), 101–108. doi:10.1016/S0003-9861(03)00216-9

Ed Rainger, G., Chimen, M., Harrison, M. J., Yates, C. M., Harrison, P., Watson, S. P., et al. (2015). The role of platelets in the recruitment of leukocytes during vascular disease. *Platelets* 26 (6), 507–520. doi:10.3109/09537104.2015.1064881

El Jundi, A., Buwalda, S., Bethry, A., Hunger, S., Coudane, J., Bakkour, Y., et al. (2020). Double-hydrophilic block copolymers based on functional poly(ε-caprolactone)s for pH-dependent controlled drug delivery. *Biomacromolecules* 21 (2), 397–407. doi:10.1021/acs.biomac.9b01006

El-Raheem, H. A., Hassan, R. Y. A., Khaled, R., Farghali, A., and El-Sherbiny, I. M. (2021). New sensing platform of poly(ester-urethane)urea doped with gold nanoparticles for rapid detection of mercury ions in fish tissue. *RSC Adv.* 11 (50), 31845–31854. doi:10.1039/D1RA03693A

Fang, J., Ye, S.-H., Shankarraman, V., Huang, Y., Mo, X., and Wagner, W. R. (2014). Biodegradable poly(ester urethane)urea elastomers with variable amino content for subsequent functionalization with phosphorylcholine. *Acta Biomater.* 10 (11), 4639–4649. doi:10.1016/j.actbio.2014.08.008

Gonzalez-Melo, C., Garcia-Brand, A. J., Quezada, V., Reyes, L. H., Muñoz-Camargo, C., and Cruz, J. C. (2021). Highly efficient synthesis of type B gelatin and low molecular weight chitosan nanoparticles: potential applications as bioactive molecule carriers and cell-penetrating agents. *Polymers* 13 (23), 4078. doi:10.3390/polym13234078

Guan, J., Sacks, M. S., Beckman, E. J., and Wagner, W. R. (2002). Synthesis, characterization, and cytocompatibility of elastomeric, biodegradable poly(ester-urethane)ureas based on poly(caprolactone) and putrescine. *J. Biomed. Mater. Res.* 61 (3), 493–503. doi:10.1002/jbm.10204

Guidoin, R., Canizales, S., Charara, J., How, T., Marois, Y., Batt, M., et al. (1992). Vascular access for hemodialysis: pathologic features of surgically excised ePTFE grafts. *Ann. Vasc. Surg.* 6 (6), 517–524. doi:10.1007/BF02000823

Halbert, R. J., Nicholson, G., Nordyke, R. J., Pilgrim, A., and Niklason, L. (2020). Patency of ePTFE arteriovenous graft placements in hemodialysis patients: systematic literature review and meta-analysis. *Kidney360* 1 (12), 1437–1446. doi:10.34067/KID.0003502020

Hong, Y., Ye, S.-H., Pelinescu, A. L., and Wagner, W. R. (2012). Synthesis, characterization, and paclitaxel release from a biodegradable, elastomeric, poly(ester urethane)urea bearing phosphorylcholine groups for reduced thrombogenicity. *Biomacromolecules* 13 (11), 3686–3694. doi:10.1021/bm301158j

Hu, C., Luo, R., and Wang, Y. (2020). Heart valves cross-linked with erythrocyte membrane drug-loaded nanoparticles as a biomimetic strategy for anti-coagulation, anti-inflammation, anti-calcification, and endothelialization. *ACS Appl. Mater. Interfaces* 12 (37), 41113–41126. doi:10.1021/acsami.0c12688

International Organization for Standardization (2017). *ISO 10993-4:2017 - biological evaluation of medical devices — Part 4: Selection of tests for interactions with blood*. Geneva, Switzerland: The ISO Centra Secretariat.

Irvine, S. A., Yun, X., and Venkatraman, S. (2012). Anti-platelet and tissue engineering approaches to biomaterial blood compatibilization: how well have these been translated into the clinic? *Drug Deliv. Transl. Res.* 2 (5), 384–397. doi:10.1007/s13346-012-0077-z

Janairo, R. R. R., Henry, J. J. D., Lee, B. L.-P., Hashi, C. K., Derugin, N., Lee, R., et al. (2012). Heparin-modified small-diameter nanofibrous vascular grafts. *IEEE Trans. NanoBioscience* 11 (1), 22–27. doi:10.1109/TNB.2012.2188926

Kim, M., Lin, M. M., Sohn, Y., Kim, J., Kang, B. S., and Kim, D. K. (2017). Polyethyleneimine-associated polycaprolactone—superparamagnetic iron oxide nanoparticles as a gene delivery vector. *J. Biomed. Mater. Res. Part B Appl. Biomaterials* 105 (1), 145–154. doi:10.1002/jbm.b.33519

Liang, N. L., Baril, D. T., Avgerinos, E. D., Leers, S. A., Makaroun, M. S., and Chaer, R. A. (2017). Comparative effectiveness of anticoagulation on midterm infrainguinal bypass graft patency. *J. Vasc. Surg.* 66 (2), 499–505.e2. doi:10.1016/j.jvs.2016.12.141

Liang, X., Hu, C., and Wang, Y. (2023). Biomimetic-modified bioprosthetic heart valves with controlled release of glycyrrhizin acid mediated by the inflammatory microenvironment for anti-thrombotic, anti-inflammatory, and anti-calcification. *Chem. Eng. J.* 472, 145044. doi:10.1016/j.cej.2023.145044

Liu, R., Qin, Y., Wang, H., Zhao, Y., Hu, Z., and Wang, S. (2013). The *in vivo* blood compatibility of bio-inspired small diameter vascular graft: effect of submicron longitudinally aligned topography. *BMC Cardiovasc. Disord.* 13 (1), 79. doi:10.1186/1471-2261-13-79

Monfared, Y. K., Mahmoudian, M., Cecone, C., Caldera, F., Haiaty, S., Heidari, H. R., et al. (2022). Hyper-branched cationic cyclodextrin polymers for improving plasmid transfection in 2D and 3D spheroid cells. *Pharmaceutics* 14 (12), 2690. doi:10.3390/pharmaceutics14122690

Nair, P. A., and Ramesh, P. (2013). Electrospun biodegradable calcium containing poly(ester-urethane)urea: synthesis, fabrication, *in vitro* degradation, and biocompatibility evaluation. *J. Biomed. Mater. Res. Part A* 101A (7), 1876–1887. doi:10.1002/jbm.a.34490

Poussard, L., Burel, F., Couvercelle, J.-P., Merhi, Y., Tabrizian, M., and Bunel, C. (2004). Hemocompatibilty of new ionic polyurethanes: influence of carboxylic group insertion modes. *Biomaterials* 25 (17), 3473–3483. doi:10.1016/j.biomaterials.2003.10.069

Pozzi, D., Colapicchioni, V., Caracciolo, G., Piovesana, S., Capriotti, A. L., Palchetti, S., et al. (2014). Effect of polyethyleneglycol (PEG) chain length on the bio–nano-interactions between PEGylated lipid nanoparticles and biological fluids: from nanostructure to uptake in cancer cells. *Nanoscale* 6 (5), 2782. doi:10.1039/c3nr05559k

Ramachandran, B., Chakraborty, S., Dixit, M., and Muthuvijayan, V. (2018). A comparative study of polyethylene terephthalate surface carboxylation techniques: characterization, *in vitro* haemocompatibility and endothelialization. *React. Funct. Polym.* 122, 22–32. doi:10.1016/j.reactfunctpolym.2017.11.001

Rodriguez-Soto, M. A., Suarez Vargas, N., Riveros, A., Camargo, C. M., Cruz, J. C., Sandoval, N., et al. (2021). Failure analysis of TEVG's I: overcoming the initial stages of blood material interaction and stabilization of the immune response. *Cells* 10 (11), 3140. doi:10.3390/cells10113140

Sabino, R., and Popat, K. (2020). Evaluating whole blood clotting *in vitro* on biomaterial surfaces. *BIO-PROTOCOL* 10 (3), e3505. doi:10.21769/BioProtoc.3505

Sauter, A., Richter, G., Micoulet, A., Martinez, A., Spatz, J. P., and Appel, S. (2013). Effective polyethylene glycol passivation for the inhibition of surface interactions of peripheral blood mononuclear cells and platelets. *Biointerphases* 8 (1), 14. doi:10.1186/1559-4106-8-14

Schoenrath, F., Just, I. A., Falk, V., and Emmert, M. Y. (2021). Antiplatelet and direct oral anticoagulation management after coronary artery bypass graft surgery: the cinderella of current cardiovascular trials, please show me (some) evidence. *Eur. Heart J.* 42 (22), 2145–2148. doi:10.1093/eurheartj/ehab033

Shen, X., Fang, J., Lv, X., Pei, Z., Wang, Y., Jiang, S., et al. (2011). Heparin impairs angiogenesis through inhibition of MicroRNA-10b. *J. Biol. Chem.* 286 (30), 26616–26627. doi:10.1074/jbc.M111.224212

Shiu, H. T., Goss, B., Lutton, C., Crawford, R., and Xiao, Y. (2014). Controlling whole blood activation and resultant clot properties by carboxyl and alkyl functional groups on material surfaces: a possible therapeutic approach for enhancing bone healing. *J. Mater. Chem. B* 2 (20), 3009–3021. doi:10.1039/C4TB00009A

Stavrou, E., and Schmaier, A. H. (2010). Factor XII: what does it contribute to our understanding of the physiology and pathophysiology of hemostasis and thrombosis. *Thrombosis Res.* 125 (3), 210–215. doi:10.1016/j.thromres.2009.11.028

Suchyta, D. J., Handa, H., and Meyerhoff, M. E. (2014). A nitric oxide-releasing heparin conjugate for delivery of a combined antiplatelet/anticoagulant agent. *Mol. Pharm.* 11 (2), 645–650. doi:10.1021/mp400501c

Tang, C., Kligman, F., Larsen, C. C., Kottke-Marchant, K., and Marchant, R. E. (2009). Platelet and endothelial adhesion on fluorosurfactant polymers designed for vascular graft modification. *J. Biomed. Mater. Res. Part A* 88A (2), 348–358. doi:10.1002/jbm.a.31888

Tousoulis, D., Kampoli, A.-M., Tentolouris Nikolaos Papageorgiou, C., and Stefanadis, C. (2012). The role of nitric oxide on endothelial function. *Curr. Vasc. Pharmacol.* 10 (1), 4–18. doi:10.2174/157016112798829760

Valencia-Rivero, K. T., Cruz, J. C., Wagner-Gutierrez, N., D'Amore, A., Miranda, M. C., López, R., et al. (2019). Evaluation of microscopic Structure–Function relationships of PEGylated small intestinal submucosa vascular grafts for arteriovenous connection. *ACS Appl. Bio Mater.* 2 (9), 3706–3721. doi:10.1021/acsabm.9b00158

Wang, G.-R., Zhu, Y., Halushka, P. V., Lincoln, T. M., and Mendelsohn, M. E. (1998). Mechanism of platelet inhibition by nitric oxide: *in vivo* phosphorylation of thromboxane receptor by cyclic GMP-dependent protein kinase. *Proc. Natl. Acad. Sci.* 95 (9), 4888–4893. doi:10.1073/pnas.95.9.4888

Wang, J.-L., Du, X.-J., Yang, J.-X., Shen, S., Li, H.-J., Luo, Y.-L., et al. (2018). The effect of surface poly(ethylene glycol) length on *in vivo* drug delivery behaviors of polymeric nanoparticles. *Biomaterials* 182, 104–113. doi:10.1016/j.biomaterials.2018.08.022

Włoch, M., Datta, J., and Błażek, K. (2018). The effect of high molecular weight bio-based diamine derivative of dimerized fatty acids obtained from vegetable oils on the structure, morphology and selected properties of poly(ether-urethane-urea)s. *J. Polym. Environ.* 26 (4), 1592–1604. doi:10.1007/s10924-017-1059-5

Yang, J., Welby, J. L., and Meyerhoff, M. E. (2008). Generic nitric oxide (NO) generating surface by immobilizing organoselenium species via layer-by-layer assembly. *Langmuir* 24 (18), 10265–10272. doi:10.1021/la801466e

Yau, J. W., Teoh, H., and Verma, S. (2015). Endothelial cell control of thrombosis. *BMC Cardiovasc. Disord.* 15 (1), 130. doi:10.1186/s12872-015-0124-z

Zarour, A., Omar, S., and Abu-Reziq, R. (2021). Preparation of poly(ethylene glycol) @Polyurea microcapsules using oil/oil emulsions and their application as microreactors. *Polymers* 13 (15), 2566. doi:10.3390/polym13152566

Zhang, Y., Zhang, M., Tan, L., Pan, N., and Zhang, L. (2019). The clinical use of fondaparinux: A synthetic heparin pentasaccharide. *Prog. Mol. Biol. Transl. Sci.* 163, 41–53. doi:10.1016/bs.pmbts.2019.02.004

Zhou, H., Xun, R., Liu, Q., Fan, H., and Liu, Y. (2014). Preparation of thermal and pH dually sensitive polyurethane membranes and their properties. *J. Macromol. Sci. Part B* 53 (3), 398–411. doi:10.1080/00222348.2013.845059

Zhu, S., Qian, F., Zhang, Y., Tang, C., and Yin, C. (2007). Synthesis and characterization of PEG modified N-trimethylaminoethylmethacrylate chitosan nanoparticles. *Eur. Polym. J.* 43 (6), 2244–2253. doi:10.1016/j.eurpolymj.2007.03.042

Zhu, T., Gu, H., Zhang, H., Wang, H., Xia, H., Mo, X., et al. (2021). Covalent grafting of PEG and heparin improves biological performance of electrospun vascular grafts for carotid artery replacement. *Acta Biomater.* 119, 211–224. doi:10.1016/j.actbio.2020.11.013

Zhu, X., Uchikoshi, T., Suzuki, T. S., and Sakka, Y. (2007). Effect of polyethylenimine on hydrolysis and dispersion properties of aqueous Si 3 N4 suspensions. *J. Am. Ceram. Soc.* 90 (3), 797–804. doi:10.1111/j.1551-2916.2007.01491.x

frontiers | Frontiers in Bioengineering and Biotechnology

TYPE Original Research
PUBLISHED 03 October 2023
DOI 10.3389/fbioe.2023.1270618



OPEN ACCESS

EDITED BY
Oommen Podiyan Oommen,
Tampere University, Finland

REVIEWED BY
Timo Ylikomi,
Tampere University, Finland
Juan C. Cruz,
University of Los Andes, Colombia

*CORRESPONDENCE
Yunfan He,
doctorheyunfan@hotmail.com
Feng Lu,
doctorlufeng@hotmail.com

†These authors have contributed equally to this work

‡These authors have contributed equally to this work and share first authorship

RECEIVED 01 August 2023
ACCEPTED 18 September 2023
PUBLISHED 03 October 2023

CITATION
Ru J, Zhang Q, Zhu S, Cai J, He Y and Lu F (2023), Delivery of adipose-derived growth factors from heparinized adipose acellular matrix accelerates wound healing.
*Front. Bioeng. Biotechnol.* 11:1270618.
doi: 10.3389/fbioe.2023.1270618



# Delivery of adipose-derived growth factors from heparinized adipose acellular matrix accelerates wound healing

Jiangjiang Ru‡, Qian Zhang‡, Shaowei Zhu, Junrong Cai, Yunfan He*† and Feng Lu*†

Department of Plastic Surgery, Nanfang Hospital, Southern Medical University, Guangzhou, Guangdong, China

Dermal white adipocytes are closely associated with skin homeostasis and wound healing. However, it has not been fully investigated whether adipose-derived products improve wound healing. Here, we obtained adipose acellular matrix (AAM) and adipose-derived growth factors (ADGFs) from human adipose tissue and fabricated an ADGF-loaded AAM via surface modification with heparin. The product, HEP-ADGF-AAM, contained an adipose-derived scaffold and released ADGFs in a controlled fashion. To test its efficacy in promoting wound healing, mice with full thickness wound received three different treatments: HEP-ADGF-AAM, AAM and ADM. Control mice received no further treatments. Among these treatments, HEP-ADGF-AAM best improved wound healing. It induced adipogenesis *in situ* after *in vivo* implantation and provided an adipogenic microenvironment for wounds by releasing ADGFs. HEP-ADGF-AAM not only induced adipocyte regeneration, but also enhanced fibroblast migration, promoted vessel formation, accelerated wound closure, and enhanced wound epithelialization. Moreover, there was a close interaction between HEP-ADGF-AAM and the wound bed, and collagen was turned over in HEP-ADGF-AAM. These results show that HEP-ADGF-AAM might substantially improve re-epithelialization, angiogenesis, and skin appendage regeneration, and is thus a promising therapeutic biomaterial for skin wound healing.

KEYWORDS

**acellular dermal matrix, adipocyte, decellularized adipose tissue, growth factor, wound healing**

## 1 Introduction

Impaired wound healing is challenging to treat and places patients at increased risk of wound complications that negatively impact their quality of life and increase healthcare expenditure (Wang et al., 2018; Davis et al., 2018; Okur et al., 2020). Wound dressings that are functionally and structurally similar to normal skin tissue play important roles in the treatment of deep and full-thickness wounds (Landriscina et al., 2015; Obagi et al., 2019). Recent advances in tissue engineering approaches in the field of extracellular matrix (ECM) research have led to the generation of promising scaffold dressings for the treatment of impaired wound healing (Maquart and Monboisse, 2014). Various market products have been developed from the naturally occurring ECM scaffold and approved as skin substitutes for skin wounds and burns (Tavelli et al., 2020).

Adipose tissue is abundant, easily harvested and manipulated, and can be decellularized and converted into a biological scaffold termed acellular adipose matrix (AAM) (Brown et al., 2011). With its unique biological and mechanical properties, AAM has previously become a promising biomaterial scaffold for soft tissue reconstruction (Wu et al., 2012). Furthermore, it is also demonstrated that high efficiency of heparinized AAM loaded with growth factors will promote adipose regeneration and neovascularization with in the long-term (Zhang et al., 2016; Zhang et al., 2016). In recent years, AAM has gradually become a promising approach for tissue repair and regeneration. In the full-thickness skin wound model, AAM-hydrogel accelerated wound closure and increased neovascularization (Chen et al., 2020). During the treatment of bone defects, AAM is defined as an alternative bone graft material with preserved ECM components (Ahn et al., 2022). AAM can be converted into a powder, solution, foam, or sheet for convenient implantation to repair various injuries (Chun et al., 2019; Gentile et al., 2020).

In order to obtain adipose-derived growth factors (ADGFs), the decellularized adipose ECM was collected and undergo a series of centrifugation and dialysis, collecting the supernatant and lyophilize finally (Chun et al., 2019). The type and composition of ADGFs can vary depending on different extract conditions (Choi et al., 2012). Furthermore, numerous growth factors in ADGFs may assist angiogenesis, including vascular endothelial growth factor (VEGF), hepatocyte growth factor (HGF) and stromal cell-derived factor-1 (SDF-1) (Murohara et al., 2009). ADGFs can also stimulate both collagen synthesis and cell viability of dermal fibroblasts, which improved the wrinkling and accelerated wound healing in animal models (Kim et al., 2009).

*In vivo* study of nude mice with full-thickness wounds showed that AAM promotes wound healing and that AAM combined with adipose stem cells (ASCs) elicits the best effects (Xia et al., 2020). Similarly, delivery of ASCs using a hydrogel biological scaffold derived from human decellularized adipose matrix accelerates chronic wound healing and increases neovascularization (Chen et al., 2020). These studies revealed the therapeutic potential of AAM to promote wound healing. However, these strategies require the use of AAM in combination with viable cells, which limits their wider application.

Our previous study showed that a growth factor-rich liquid extract prepared from human subcutaneous adipose tissue contains a wide variety of proangiogenic and proadipogenic factors, which efficiently induce angiogenesis and adipogenesis *in vitro* and *in vivo* (He et al., 2019). Reconstitution of a bioactive AAM by coating it with native ADGFs is a potential strategy for regenerative purposes. Heparin reversibly binds to proteins including growth factors and soluble ECM proteins. Researches demonstrated that heparin-binding domain II in fibrin (the provisional ECM during tissue repair) plays an important role in promiscuous high-affinity GF-binding domain, which may be one of fibrin's main physiological functions, assisting in tissue repair (Martino et al., 2013). Enhancement of the protein-binding ability of a biomaterial using heparin is important for drug delivery systems (Wissink et al., 2000a; Wissink et al., 2000b; Wissink et al., 2001; Pieper et al., 2002).

Acellular dermal matrices (ADMs) are commonly used acellular products, which can capitalize on the properties of native ECM in case of inadequately healing in traumatic or chronic wounds in clinical contexts (Kirsner et al., 2015). After the application of ADMs, recipient cells were tightly preserved in the matrix structure by growth factors and gradually incorporated into the matrix (Kirsner et al., 2015; Boháč et al., 2018). Furthermore, a variety of cells invade into the ADMs and matrix begin to remodel, numbers of collagen and elastin increase, and angiogenesis is initiated (Boháč et al., 2018; Lee et al., 2015; Mirzaei-Parsa et al., 2019; Ye et al., 2016). In recent years, various ADMs have been developed from human cadaver (HADM), bovine (BADM) and porcine (PADM) tissues, which would be used in a variety of different clinical contexts with regard to different applications (Petrie et al., 2022).

In the present study, we aimed to functionalize AAM with heparin in order to enhance its ability to bind ADGFs. The capacity of heparinized ADGF-bound AAM (HEP-ADGF-AAM) to release growth factors and its effects on cellular functions were assessed. The efficiencies with which HEP-ADGF-AAM and AAM repaired full-layer wounds in comparison with acellular dermal matrix (ADM) were assessed, and particular attention was paid to dermal adipogenesis and wound healing.

# 2 Materials and methods

## 2.1 Fat harvesting and AAM preparation

To prepare AAM, adipose tissue was obtained through liposuction in human patients at the department of Plastic and Cosmetic Surgery, Nanfang Hospital. The study protocol was approved by the Institutional Review Board of the Nanfang hospital. After obtaining informed consent, human adipose tissue was harvested from four healthy female patients (aged 22–34 years) undergoing abdominal liposuction. Fat was obtained by manual liposuction using a combination of intravenous general anesthesia and local anesthesia. Two-hole blunt-tipped liposuction needles with diameters of 2.5 and 3.0 mm and a lateral hole (2 mm diameter) were used for suction with a 10 mL screw-tipped syringe under low negative pressure. The detailed procedure of AAM preparation is shown in Figure 1A. Briefly, the tissue was subjected to three cycles (1 h each) of freezing and thawing (−80°C to 37°C) in balanced salt solution. Following centrifugation (2,000 × g, 3 min), the fat samples were homogenized using a specially made blender (Shanghai Tiangong Instruments Co., Ltd., Shanghai, People's Republic of China) at 3,000 rpm for 1 min. After homogenization, the adipose suspension was collected and centrifuged again at 3,000 × g for 3 min to remove the free lipid content. After washing with PBS, the samples underwent 6 h of polar solvent extraction in 99.9% isopropanol to remove the lipid content. After three rinses with phosphate-buffered saline (PBS), the samples were decellularized with aqueous sodium deoxycholate (2%) for 12 h. After three rinses with PBS, the samples were disinfected with 4% ethanol containing 0.1% peracetic acid for 4 h and then rinsed three more times with PBS. The remaining ECM component (i.e., AAM) was soaked in PBS containing 1% penicillin and stored at −20°C.

## 2.2 Preparation of ADGFs and HEP-ADGF-AAM

Human ADGFs were prepared as previously described (He et al., 2019). The obtained adipose tissue was washed with PBS and centrifuged at 1,200 × g for 3 min to remove blood constituents. Then, the adipose tissue was mixed with an equal volume of PBS

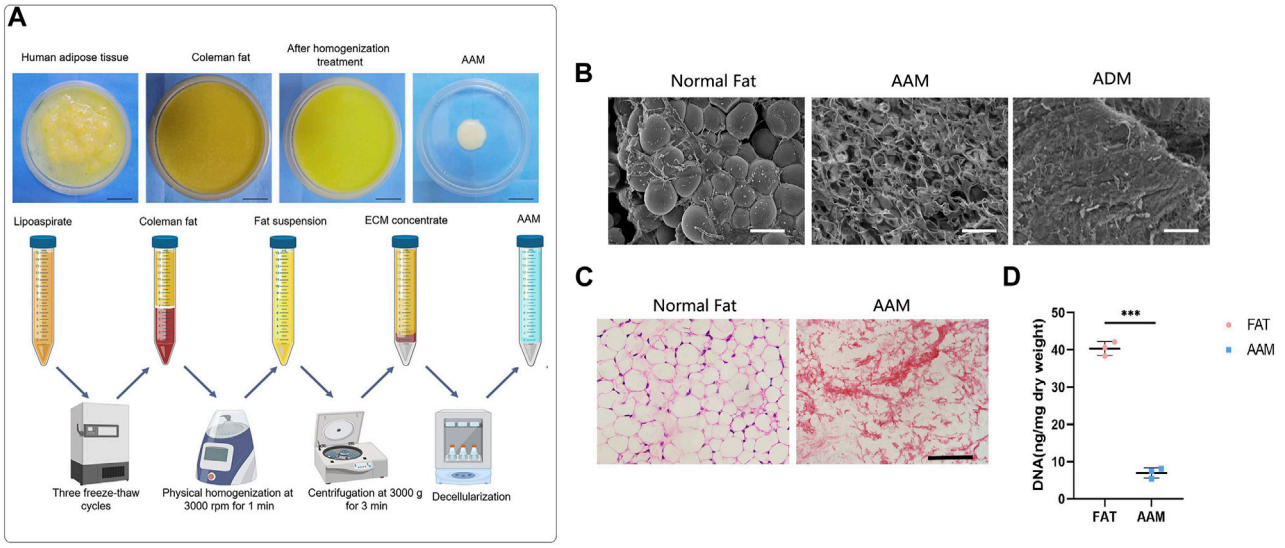


FIGURE 1
Preparation and characterization of AAM **(A)** Scheme of AAM preparation. **(B)** Scanning electron micrographs of AAM, ADM and normal fat tissue. Scale bar = 100 μm. **(C)** H&E staining of AAM and normal adipose tissue. Scale bar = 100 μm. **(D)** Quantification of the residual DNA content of AAM and normal adipose tissue. ***$p < 0.001$.

and physically emulsified by repeated transfer between two 10 mL syringes connected by a female-to-female Luer-Lock connector (1.4 mm internal diameter). Adipose tissue was transferred for 1 min at a constant rate (10 mL/s). After centrifugation at 1,200 × g for 2 min, the liquid portion from emulsified adipose tissue was passed through a 0.20 μm syringe filter (Xiboshi; DIONEX, USA) to remove cell and tissue debris, and was collected as ADGFs.

For loading of ADGFs, heparin and AAM were crosslinked as described previously (Wissink et al., 2001). Briefly, the carboxylic acid groups of heparin were activated with 1-ethyl-3 (3-dimethylaminopropyl) carbodiimide (EDC)/N-hydroxysuccinimide (NHS). One milligram of heparin (H-4784; Sigma, Steinheim, Germany) was activated with 1 mg EDC and 0.6 mg NHS in 500 mL of 0.05 M MES buffer (pH 5.6) for 10 min. The AAM specimen was immersed in this solution, which was then evacuated at 20 mmHg for ~2 min to remove air from AAM. The reaction was allowed to proceed for 4 h at 37°C, after which AAM was extensively washed with 0.1 M $Na_2HPO_4$ (2 h), 4 M NaCl (four times in 24 h), and distilled water (five times in 24 h). After the modification procedure, AAM was frozen at −80°C overnight and lyophilized. Native and heparinized AAM was cut into discs (1 × 1 × 0.5 $cm^3$) for experiments. The native and heparinized AAM samples were incubated with 5 mL ADGF solution for 90 min at room temperature and then washed with 5 mL PBS (two times for 5 min) to remove all non-bound ADGFs. Finally, HEP-ADGF-AAM and ADGF-AAM were frozen at −80°C overnight.

## 2.3 Evaluation of decellularized matrix

Both fat tissue and AAM samples were fixed in 4% paraformaldehyde and embedded in paraffin. Five-micrometer sections were then cut for hematoxylin and eosin (H&E) staining. In addition, residual DNA was extracted using a DNeasy kit (Qiagen, Valencia, CA, USA). DNA content (μg/mg wet weight) was then quantified with a microplate reader (Model 680; Bio-Rad, Hercules, CA, USA) at 260 nm and normalized to the initial wet weight of each sample.

## 2.4 Scanning electron microscopy (SEM)

Scanning electron microscopy (SEM) SEM was used to examine decellulized products and normal fats. Samples were fixed in 2% glutaraldehyde for 2 h, dehydrated using an ethanol series (30%–100%), critical point-dried, coated with gold, and examined under a scanning electron microscope (S-3000N; Hitachi Ltd., Tokyo, Japan). SEM images were captured using a digital camera (Canon Inc., Tokyo, Japan).

## 2.5 Collagen labeling of acellular products

To visualize the collagen turnover in the acellular products, the collagen components of ADM, AAM, and HEP-ADGF-AAM were labeled immediately after preparation according to a previously described protocol (Correa-Gallegos et al., 2019). Before being applied to wounds, ADM, AAM, and HEP-ADGF-AAM (500 mg) were incubated with 100 μM Alexa Fluor 647 NHS Ester (A20006; Thermo Fisher Scientific, Foster City, CA, USA) for 1 h at 25°C, and then washed three times with PBS.

## 2.6 Full-thickness skin wound model

The wound healing efficacy was evaluated using a full-thickness wound mouse model. Male nude mice aged 8–10 weeks and

weighing 20–25 g were purchased from the Laboratory Animal Center of Southern Medical University. For wound healing experiments, mice were anesthetized and two circular full-thickness excisional skin wounds of 8-mm radius were made on the dorsum of mice. A prefabricated 12 mm silicone ring (inner ring radius of 8 mm) was placed around the wound and fixed using 4-0 silk sutures to prevent wound contraction (Lin et al., 2021). To compare *in vivo* wound healing efficacies, 48 nude mice were randomly divided into the HEP-ADGF-AAM, AAM, ADM (Beijing Jayyalife Biological Technology Co.,Ltd.), and control groups ($n$ = 12 per group). Wounds were untreated in the control group, while covered with ADM, AAM, and HEP-ADGF-AAM dressings in other groups, respectively. All dressings had a diameter of 8 mm, and a thickness of 1 mm. Wounds are treated every 2 days and sterile dressings are changed daily. Photographs of the skin around the wound and healthy skin were taken at 5 and 14 days postoperatively ($n$ = 6 per time point) and samples were taken for further histological analysis. At the end of the study, all mice were anesthetized by intraperitoneal injection of pentobarbital sodium (0.3%, 50 mg/kg). Cervical vertebra dislocation was used for euthanasia and death was confirmed by cessation of the heartbeat. Using the ImageJ software to quantify the wound area, wound healing is represented as follows: residual wound area/original wound area 100%. Researchers were blinded to the analysis of data from different groups.

## 2.7 Subcutaneous implantation of acellular products

To assess the adipogenic capacity of these acellular products *in vivo*, ADM, AAM, and HEP-ADGF-AAM (diameter of 8 mm and thickness of 3 mm) were subcutaneously inserted into the backs of nude mice, and then the skin was closed with 7-0 nylon sutures. Twelve weeks later, the implanted material was harvested and analyzed ($n$ = 6 per group).

## 2.8 Histological assessment and immunohistochemical staining

Fresh samples of wound skin and subcutaneous tissue were fixed in formalin for histological assessment and immunohistochemical staining. Briefly, formalin-fixed samples were embedded and sliced into 5-μm sections. For histological assessment, tissue sections were deparaffinized in xylene, rehydrated through graded alcohol in phosphate-buffered saline (PBS), and then stained with a hematoxylin-eosin (HE) working solution. For immunohistochemical analysis, sections were dewaxed and rehydrated, then incubated in 3% $H_2O_2$ to block endogenous peroxidase. Immunohistochemical staining was performed using antibodies against vimentin (1:25, ab92547, Abcam, Cambridge, UK) and perilipin (1:500, GP29; Progen, Heidelberg, Germany). The vimentin + cells and perilipin + adipocytes were evaluated by counting the number of brown-labeled cells from six fields of each slide. For immunofluorescence staining, the sections were incubated with the following primary antibodies: guinea pig anti-mouse Perilipin (Progen, GP29, Germany) and rat anti-CD31 (1:200; Abcam, Cambridge, MA, USA), followed by the corresponding secondary antibodies. After DAPI staining (Sigma, D9542, USA), the sections were observed and photographed using a FV10i-W confocal laser scanning microscope (Olympus, Japan). Angiogenesis was evaluated by counting the number of fluorescent vessel-like structures from six fields of each slide.

## 2.9 *In vitro* growth factor release study

Upon immobilization of ADGFs onto native and heparinized AAM, the scaffolds were immersed in 2 mL PBS. Release of VEGF, HGF, bFGF, and EGF from HEP-ADGF-AAM and ADGF-AAM was assessed at 1, 3, 5 and 7 days. Supernatants were collected at designated time points and was analyzed using VEGF, HGF, bFGF, and EGF enzyme-linked immunosorbent assay (ELISA) kits (R&D Systems, Minneapolis, MN, USA) following the manufacturer's instructions. The experiment was repeated three times.

## 2.10 Scratch-wound assay

Fibroblasts were cultured in six-well plates until reaching 100% confluence and a linear gap was generated using a sterile 200-μL pipette tip. Complete medium was then replaced with a serum-free medium supplemented with 2 mL of soak solution obtained by soaking ADM, AAM or HEP-ADGF-AAM within PBS for 24 h or serum-free medium (control group); the cells were then cultured for 0, 12 and 24 h. Three representative images of each scratched area were obtained using a light microscope (Nikon, Japan). Cell migration rate was analyzed using ImageJ software (NIH, MD, USA). All scratch-wound assays were carried out in triplicate.

## 2.11 Tube formation assay

The Matrigel (diluted 1:1 in PBS) was transferred to a 24-well plate and solidified by incubation at 37°C and 5% $CO_2$ for 30 min. HUVECs ($5 \times 10^5$ per well) were then seeded on the Matrigel and treated with 2 mL medium (1:1, soak solution obtained by soaking ADM, AAM or HEP-ADGF-AAM within PBS for 24 h to endothelial cell basal medium). HUVECs treated with angiogenic factors [20 ng/mL vascular endothelial growth factor (VEGF) and 5 ng/mL basic fibroblast growth factor (bFGF)] served as a positive control, while cells treated with 2 mL medium (1:1, PBS to endothelial cell medium) were used as a negative control. Angiogenesis is evaluated by counting the number of tubular structures from six fields of each well. Tube formation assays were repeated three times.

## 2.12 Induction of adipogenic differentiation of ADSCs

ADSCs ($1 \times 10^5$ per well) were plated on 6-well plates and cultured overnight at 37°C and 5% $CO_2$. The next day, cells in each well were rinsed and treated with 2 mL medium (1:1, supernatants from ADM, AAM or HEP-ADGF-AAM soak solution to human

ADSC complete growth medium). ADSCs treated with 2 mL medium (1:1, PBS to human ADSC complete growth medium) were used as the negative control. The medium in all the groups was changed every 3 days. Adipogenic differentiation of ADSCs was examined for lipid accumulation by Oil Red O (ORO; Sigma-Aldrich, USA) staining. Cells were photographed using a Nikon E200 microscope and collected for gene expression analysis at days 21. Adipogenic induction assays were repeated three times.

## 2.13 qRT-PCR

Samples of wound beds and subcutaneous implants were quickly excised, immediately frozen in liquid nitrogen, and stored at −80°C. Total RNA was extracted from 50 mg frozen tissue using a RNeasy Lipid Tissue Mini Kit (Qiagen, Hilden, Germany), according to the manufacturer's instructions. cDNA was amplified in 40 cycles using the QuantiTect Reverse Transcription Kit (Qiagen, Germany) and Rotor-Gene 3,000 Real-Time PCR Detection System (Corbett Research, Sydney, Australia). GAPDH was used as the reference gene. The primer sequences were as follows: peroxisome proliferator-activated receptor gamma (PPARG), forward 5′-TCG CTGATGCACTGCCTATG-3′ and reverse 5′-GAG AGGTCCACA GAGCTGATT-3′; CCAAT-enhancer-binding protein alpha (CEBPA), forward, 5′-CTTGATGCAATCCGGATCAAAC-3′ and reverse, 5′-CCCGCAGGAACATCTTTAAGT-3′; vascular endothelial growth factor A (VEGFA), forward 5′-TTACTGCTG TACCTCCACC-3′ and reverse 5′-ACAGGACGGCTTGAAGAT G-3′; basic fibroblast growth factor (bFGF), forward 5′- AGC GGCTGTACTGCAAAAACGG-3′ and reverse 5′-CCTTTGATA GACACAACTCCTCTC-3'. Expression levels were calculated using the $2^{-\Delta\Delta CT}$ method.

## 2.14 Statistical analysis

Data were analysed using IBM SPSS (V22.0; IBM Corp., Armonk, NY, USA). An independent variable *t*-test was performed to compare the two mean values. For comparison of three or more means, one-way ANOVA was conducted, followed by the *post hoc* Tukey test. All results were expressed as mean standard deviation. The level of significance was set as $p < 0.05$.

# 3 Results

## 3.1 Physical characteristics of AAM

AAM was prepared as shown in Figure 1A. Scanning electronic microscopy (SEM) showed that AAM had a porous structure, whereas normal fat contained a large volume of connected adipocytes and ADM presented condensed collagen fibers (Figure 1B). Hematoxylin and eosin (H&E) staining showed that AAM only contained ECM and lacked any cellular components (Figure 1C). The residual DNA content of AAM (7.42 ± 2.25 ng/mg) was significantly lower than that of normal adipose tissue (40.65 ± 3.12 ng/mg) ($p < 0.001$) (Figure 1D), indicating that cellular components were effectively removed from AAM.

## 3.2 Controlled release of ADGFs from HEP-ADGF-AAM

HEP-ADGF-AAM was prepared as shown in Figure 2A. To assess the efficiency with which HEP-ADGF-AAM released ADGFs, growth factors released from HEP-ADGF-AAM were quantified using ELISA and compared with those released by ADGF-bound AAM (ADGF-AAM). ELISA of VEGF (Figure 2B), hepatocyte growth factor (HGF) (Figure 2C), bFGF (Figure 2D), and endothelial growth factor (EGF) (Figure 2E) showed that release of these growth factors was sustained after a peak in the HEP-ADGF-AAM group, with relatively high concentrations maintained for up to 7 days, while the concentrations of these growth factors remained low after Day 2 in the ADGF-AAM group.

## 3.3 Comparison of the *in vivo* wound healing efficacies of different acellular wound dressings

Acellular wound dressing was applied to a full-layer wound model of mice. Wound healing was monitored on day 5 and day 14, respectively, and measured by the percentage of lesion area closed. Figure 3A shows representative images of full-layer wound beds of mice in different treatment groups. Histological observations (Figure 3A) showed that on day 5, the wounds treated with HEP-ADGF-AAM showed significant re-epithelialization, while virtually no re-epithelialization was observed in the blank control group. On the 14th day, the blank control group still had unhealed wounds. Compared with a blank control group, AAM, ADM, and HEP-ADGF-AAM all promoted wound healing to varying degrees (Figure 3B, $p < 0.05$). However, there was no significant difference in wound area between the AAM group and the ADM group. Surprisingly, the HEP-ADGF-AAM treatment group achieved almost complete wound healing on day 14, showing the best pro-healing properties. In addition, the level of re-epithelialization induced by HEP-ADGF-AAM at 14 days after injury was significantly higher than that in the control and AAM groups (Figure 3D). HE staining showed (Figure 3C) that granulation tissue, adipose cells, and regenerated skin attachment levels were higher in the HEP-ADGF-AAM group than in the other three groups at day 5 and 14 post-injury. We can see that on day 5, significant subcutaneous fat regeneration can be observed in both ADM and HEP-ADGF-AAM treatment groups. And, unlike the other groups, wound skin in the HEP-ADGF-AAM treated group had more regenerated hair follicles and sebaceous glands at day 14.

## 3.4 HEP-ADGF-AAM enhances fibroblast migration

After the skin defect is formed, the repair process begins with the coordination of a variety of cells. The directional migration and proliferation of activated fibroblasts from the dermis to the wound is important for the remodeling of the extracellular matrix in the defective skin. For this purpose, we used Vimentin to track fibroblasts in the dermis. Immunohistochemical staining suggested (Figure 4A) that AAM, ADM, and HEP-ADGF-AAM

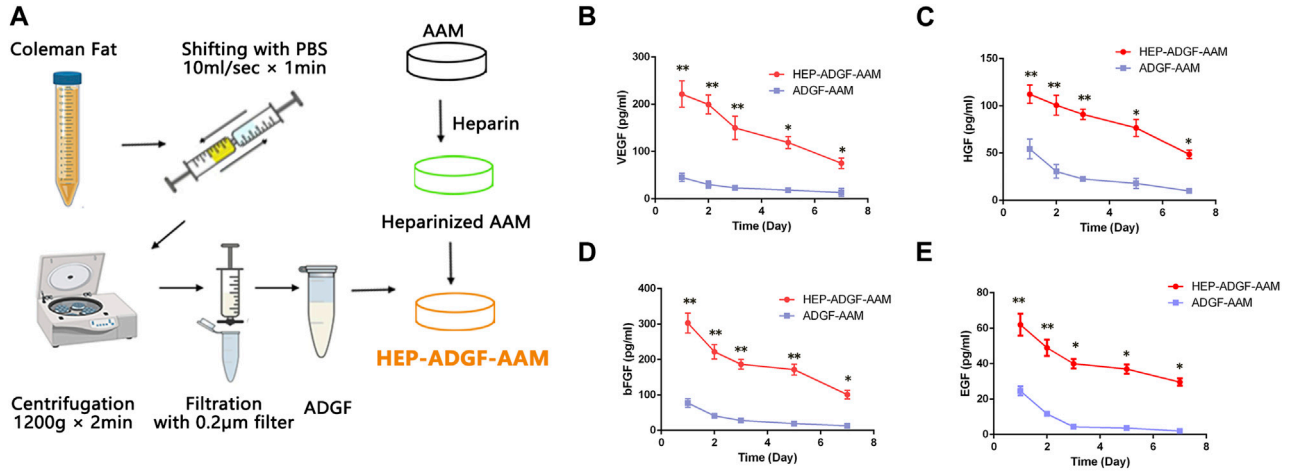


FIGURE 2
Preparation and characterization of ADGFs and HEP-ADGF-AAM **(A)** Scheme of ADGFs and HEP-ADGF-AAM preparation. ELISAs of **(B)** VEGF, **(C)** HGF, **(D)** bFGF, and **(E)** EGF in soak solution obtained by soaking ADGF-AAM or HEP-ADGF-AAM within PBS at 1, 3, 5 and 7 days. *$p < 0.05$, **$p < 0.01$.

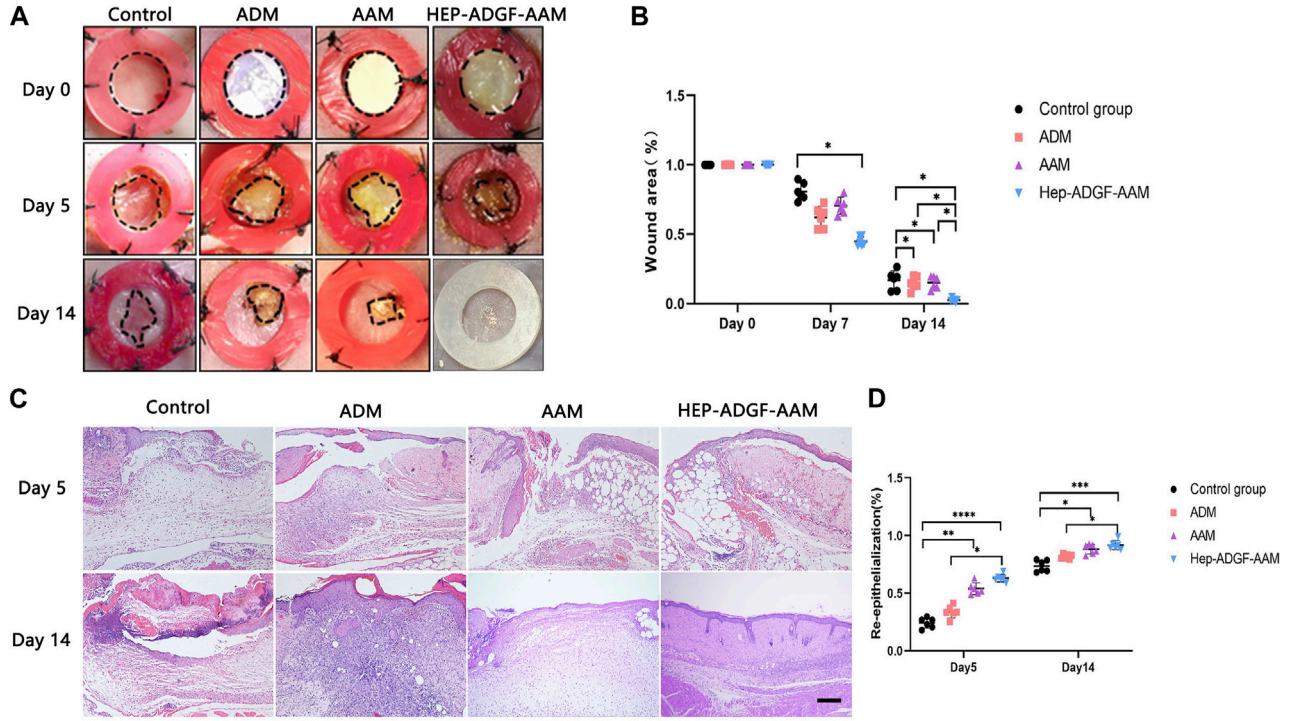


FIGURE 3
Wound healing efficacies of different acellular biomaterials **(A)** Wounds treated with AAM, ADM, and HEP-ADGF-AAM at different time points. **(B)** Wound healing rate in different treatment groups ($p < 0.05$). **(C)** H&E staining of wounds in different treatment groups. Scale bar = 500 μm. **(D)** Re-epithelialization level of the wounds in different groups, *$p < 0.05$, **$p < 0.01$, ***$p < 0.001$.

could effectively promote the migration of fibroblasts to the wound bed on the 5th day after injury. Among them, the number of vimentin-positive fibroblasts in the wound bed of the HEP-ADGF-AAM group was significantly higher than that in AAM, ADM, and control groups ($p < 0.05$) (Figure 4B). In addition, fibroblasts cultured in immersion solution with different acellular products were used for *in vitro* scratch experiments (Figure 4C). The results showed that after 12 and 24 h, the fibroblast migration rate of the HEP-ADGF-AAM group was significantly faster than that of the other three groups. However, fibroblast migration did not differ significantly between ADM, AAM, and negative controls (Figure 4D).

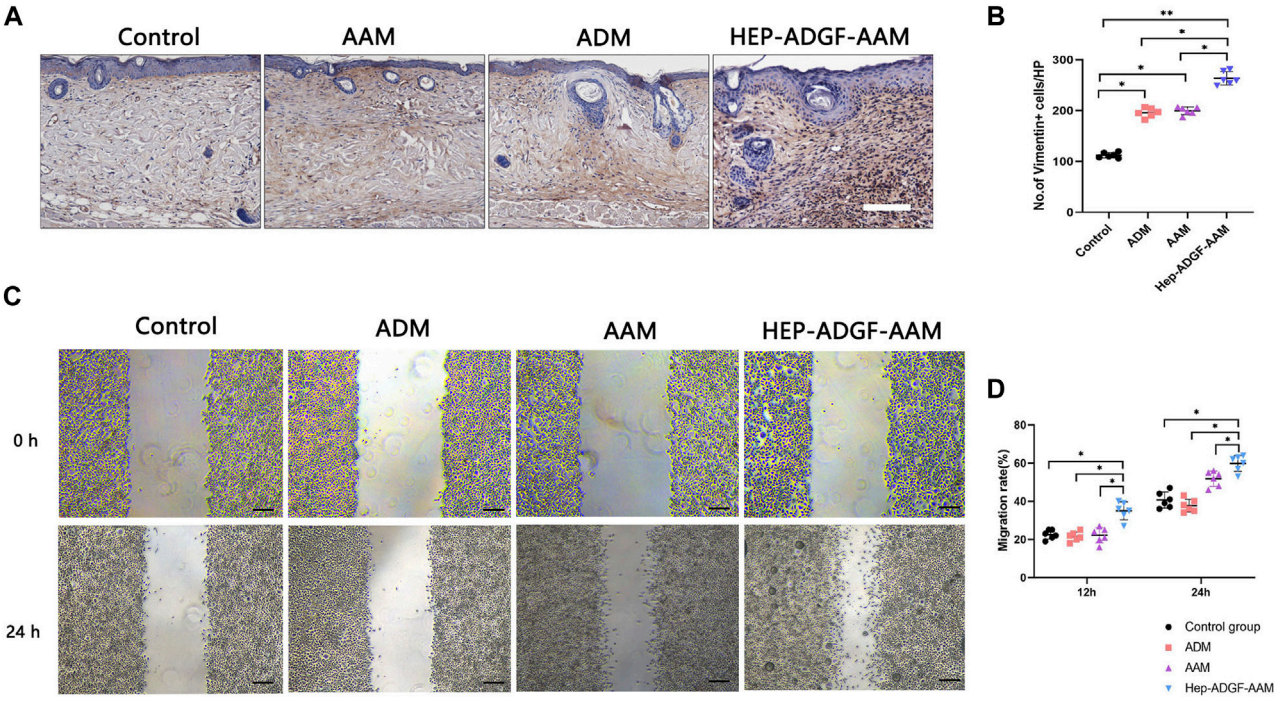


FIGURE 4
HEP-ADGF-AAM promotes fibroblast migration into the wound bed **(A)** Representative immunohistological staining (vimentin) of the wound bed in the four groups. Scale bar = 500 μm. **(B)** Quantification of vimentin + cells of the wound bed in the four groups. *$p < 0.05$, **$p < 0.01$. **(C)** An *in vitro* scratch assay was performed by culturing fibroblasts with soak solution with different acellular products. Scale bar = 100 μm. **(D)** Migration rate of the fibroblasts in the *in vitro* scratch assay. *$p < 0.05$.

## 3.5 HEP-ADGF-AAM promotes angiogenesis

To explore whether treatment with HEP-ADGF-AAM has the effect of stimulating angiogenesis, we used CD31 immunofluorescence staining to characterize and quantify the number of CD31-positive capillary cells in wounds of different treatment groups. Only a small amount of neovascularization was observed in the blank control group, and treatment with AAM, ADM, and HEP-ADGF-AAM significantly promoted wound angiogenesis (Figure 5A). Quantitative angiogenesis showed that the amount of CD31 in AAM group, ADM group, and HEP-ADGF-AAM group was significantly higher than that in the control group ($p < 0.05$) (Figure 5B). To further confirm their ability to promote vascular regeneration, mRNA levels of angiogenic genes (VEGF and bFGF) in the wound bed were detected by qRT-PCR. The results showed that these levels in the HEP-ADGF-AAM, AAM, and ADM groups were significantly higher than those in the control group ($p < 0.05$) (Figure 5C). In addition, we used *in vitro* tube formation experiments to directly observe the angiogenesis induction ability of HEP-ADGF-AAM on human umbilical vein endothelial cells (HUVECs). In the presence of HEP-ADGF-AAM, the typical tubular structure could be observed after 18h, which was similar to the positive control group and significantly higher than the negative group. However, almost no typical tubular structure was observed when HUVECs were cultured with AAM or ADM throughout the assay process (Figure 5D). Quantitative analysis of capillary tubular structures showed (Figure 5E) that the number of tubular structures in the HUVECsHEP-ADGF-AAM group and positive control group cultured with HEP-ADGF-AAM was significantly higher than that in other groups ($p < 0.05$).

## 3.6 HEP-ADGF-AAM induces adipogenesis and promotes adipogenic differentiation of adipose-derived stem cells (ADSCs) in a paracrine manner

At Day 5, perilipin + adipocytes were found in the wound bed in all four groups (Figure 6A). The number of perilipin + adipocytes in the wound bed was significantly higher in the HEP-ADGF-AAM group than in the other three groups ($p < 0.05$) (Figure 6B). Expression of adipogenic genes was tested by qRT-PCR. Expression of PPARγ and CEBP/α in wounds was significantly higher in the HEP-ADGF-AAM group than in the other three groups ($p < 0.05$) (Figure 6C). To evaluate the adipogenic capacities of the acellular products, they were subcutaneously transplanted into nude mice. After 12 weeks, H&E staining showed that grafts in the ADM group did not contain adipocytes, and this was confirmed by immunofluorescence staining of perilipin. Viable adipocytes (perilipin+) were found in the AAM and HEP-ADGF-AAM groups (Figure 6D). mRNA levels of adipogenic genes (PPARγ and CEBP/α) in the grafts were tested by qRT-PCR. Adipogenic gene expression was significantly higher in the HEP-ADGF-AAM and AAM groups than in the ADM group ($p < 0.05$) (Figure 6E). Oil Red O staining was performed following culture of ADSCs with the acellular products under adipogenic

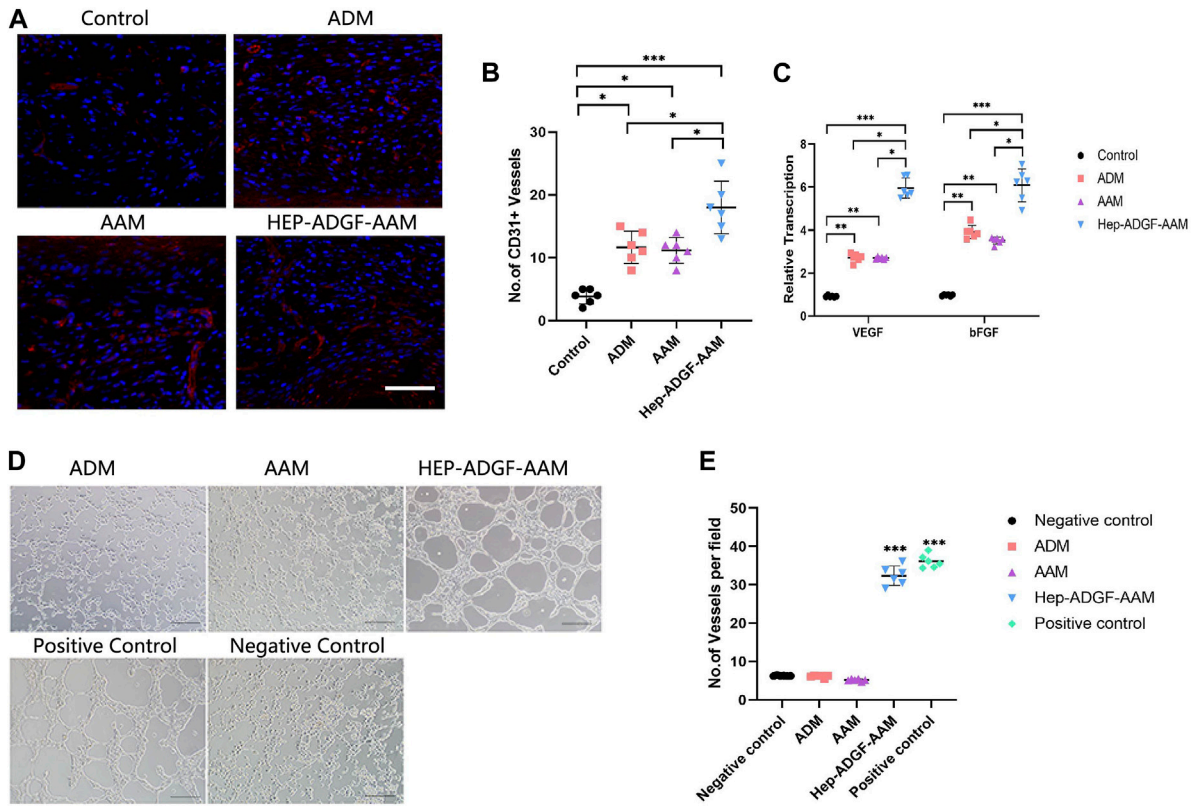


FIGURE 5
Effects of different acellular products on angiogenesis in the wound bed and tube formation *in vitro*. **(A)** Representative immunofluorescence staining(CD31) of the wound bed in the four groups. Scale bar = 100 μm. **(B)** Quantification of CD31⁺ cells of the wound bed in the four groups. **(C)** Real-time PCR measurements of angiogenic genes (VEGF and bFGF) in the four groups. **(D)** Tubule formation assay by HUVECs with different treatment. Scale bar = 100 μm **(E)** The number of tubular structures in the tubule formation assay. *$p < 0.05$, **$p < 0.01$,***$p < 0.001$.

induction conditions (Figure 6F). Measurement of absorbance at 530 nm showed that HEP-ADGF-AAM improved adipogenic differentiation, while AAM and ADM did not (Figure 6G). In addition, the mRNA level of PPARγ was significantly higher in the HEP-ADGF-AAM group than in the other three groups ($p < 0.05$) (Figure 6H).

## 4 Discussion

Large and deep wounds including surgical wounds and burns of both partial and full thickness require bio-functional dressings or dermal substitutes to replace lost tissue and support intrinsic self-regeneration mechanisms (Zhong et al., 2010; Goodarzi et al., 2018). New developments in ECM-derived tissue-engineered scaffolds may achieve the ultimate goal of tissue regeneration rather than tissue replacement (Yi et al., 2017; Varshosaz et al., 2019). Considering that recent studies have provided evidence that adipocytes and an adipogenic microenvironment provide essential support for skin repair and regeneration (Schmidt and Horsley, 2013; Franz et al., 2018; Shook et al., 2020), we fabricated a biomaterial called HEP-ADGF-AAM from adipose tissue to support wound healing. In this study, we obtained AAM and ADGFs from human adipose tissue. These two products were then assembled into a bio-functional wound dressing using heparin. The final product, HEP-ADGF-AAM, contained adipose ECM and stably released ADGFs. In a full-thickness wound mouse model, HEP-ADGF-AAM significantly improved wound closure and angiogenesis. Furthermore, HEP-ADGF-AAM potently induced adipogenesis in the wound bed (Figure 7).

The manufacturing process of AAM varies widely due to the lack of a standardized preparation scheme. Several studies have reported alternative methods to efficiently decellularize adipose tissue (Brown et al., 2011; Choi et al., 2011; Song et al., 2018). Methods for tissue decellularization differ depending on the intended application of AAM. In the present study, AAM was prepared by repeated freeze–thaw cycles followed by high-speed physical homogenization. Mechanical homogenization is a rapid and efficient method to remove lipids from adipose tissue, reduces the use of harsh chemical agents, and may improve the retention of ECM components.

Decellularization of adipose tissue reduces the diversity and levels of proteins in AAM. Surface modification with heparin improves the capacity of collagen scaffolds to bind growth factors (Wissink et al., 2000b; Wissink et al., 2001; Pieper et al., 2002). Our previous study showed that ADGFs effectively promote wound healing by enhancing fibroblast migration, vessel formation, and intradermal adipogenesis (He et al., 2019). In this study, we used heparinized AAM to physically immobilize ADGFs, which were removed from AAM during the decellularization process. ADGFs

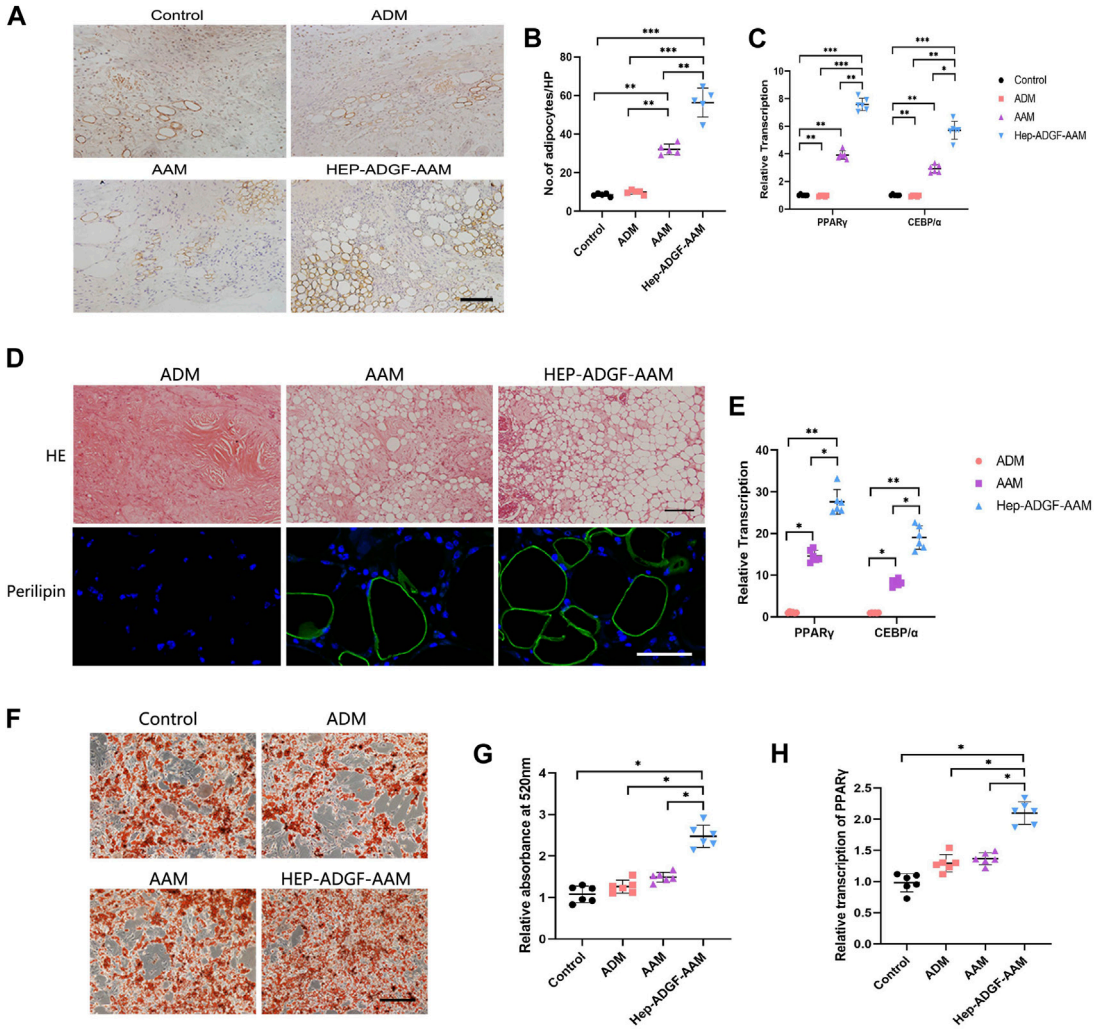


FIGURE 6
HEP-ADGF-AAM induces adipogenesis and promotes adipogenic differentiation of ADSCs **(A)** Representative immunohistological staining (perilipin) of the wound bed in the four groups. Scale bar = 100 μm. **(B)** TQuantification of perilipin + cells of the wound bed in the four groups. **(C)** Real-time PCR measurements of adipogenic genes (PPARγ and CEBP/α) in the four groups. **(D)** H&E staining and immunofluorescence staining (perilipin) of transplanted tissue in different treatment groups. Scale bar = 50 μm. **(E)** Real-time PCR measurements of adipogenic genes (PPARγ and CEBP/α) in the transplanted tissue. **(F)** Oil Red O staining of ADSCs cultured with acellular products under adipogenic induction conditions. Scale bar = 100 μm. **(G)** Measurement of absorbance at 530 nm of ADSCs cultured with acellular products under adipogenic induction conditions. **(H)** Real-time PCR measurements of adipogenic gene (PPARγ) of ADSCs cultured with acellular products under adipogenic induction conditions. Results with $*p < 0.05$, $**p < 0.01$,$***p < 0.001$ were considered statistically significant.

were released from HEP-ADGF-AAM in a controlled fashion. Our results confirmed that relatively high local concentrations of VEGF, bFGF, and HGF released from HEP-ADGF-AAM, but not ADGF-AAM, were stably maintained. The *in vitro* scratch assay and angiogenesis induction test showed that HEP-ADGF-AAM stimulated fibroblast migration and tube formation by endothelial cells in a paracrine manner, while ADM and AAM did not. These results suggest that HEP-ADGF-AAM stably releases ADGFs and improves cellular functions in a paracrine manner.

Heparin was reported to improve the porous structure and maintain good mechanical properties of the scaffolds. Furthermore, the combination of heparin and growth factors into the scaffold can significantly improve the microenvironments of cell growth and increase the secretion function of cells (Fan and Yang, 2017). It is also reported that the use of heparin can increase the biocompatibility of implanted materials and growth factors with a high affinity, which will protect the protein from degradation or denaturation and augmented the biological activity of growth factors (Park et al., 2018). What's more, cells on the heparin-conjugated scaffold exhibit high bioconpatibility and could maintain an effective local concentration of growth factors on the scaffold surface, which also verify the effectiveness of heparin and hopeful prospects (Ikegami and Ijima, 2020).

Adipocytes are traditionally considered to be important energy storage cells and were recently found to have essential functions for skin homeostasis and wound healing (Schmidt and Horsley, 2013; Wang et al., 2018; Franz et al., 2018; Shook et al., 2020). Migration and repopulation of adipocytes may be essential for wound healing. Adipocyte precursor cells proliferate, and mature adipocytes repopulate skin wounds following inflammation and in parallel

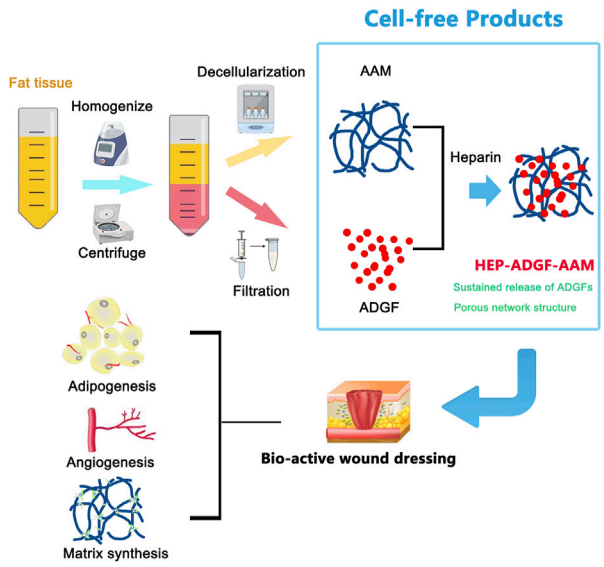


FIGURE 7
Graphical conclusion of the construction and application of HEP-ADGF-AAM. Both AAM and ADGFs were obtained from human adipose tissue via different procedures. The obtained adipose tissue was first processed through homogenization and centrifugation. The adipose layer underwent repeated freeze-thawing and high-speed physical homogenization to obtain AAM. The liquid layer underwent filtration to obtain ADGFs. These two adipose tissue-derived products were then assembled into a biofunctional wound dressing with the assistance of heparin. The HEP-ADGF-AAM is a cell-free product that could be a promising therapeutic biomaterial for skin wound healing. (AAM, adipose acellular matrix; ADGFs, adipose-derived growth factors; HEP-ADGF-AAM, heparinized ADGF-bound AAM).

with fibroblast migration (Schmidt and Horsley, 2013; Franz et al., 2018; Guerrero-Juarez et al., 2019; Shook et al., 2020). In this study, mature adipocytes were observed in the wound bed in the control group, indicative of adipocyte recruitment or spontaneous regeneration during wound healing. Moreover, AAM and HEP-ADGF-AAM increased the number of adipocytes in the wound bed. We compared the adipogenic capacities of these acellular products after transplantation. ADM did not induce adipocyte regeneration *in situ*, while AAM and HEP-ADGF-AAM stimulated adipogenesis, and HEP-ADGF-AAM had the best adipogenic capacity after transplantation. The interaction between biological dressings and wounds may be dependent on direct contact or paracrine mechanisms. ADSCs were cultured with these acellular products during adipogenic induction to verify the effects of growth factors released by these products. The results suggested that only HEP-ADGF-AAM was able to enhance adipogenesis of ADSCs, suggesting that only HEP-ADGF-AAM can release ADGFs to create an adipogenic niche. In summary, ADM is unable to induce adipocyte regeneration, while AAM provides an adipogenic scaffold that induces adipogenesis, and HEP-ADGF-AAM not only functions as an adipogenic scaffold, but also provides an adipogenic niche in a paracrine manner.

The study has some limitations to consider. First, HEP-ADGF-AAM is derived from human adipose tissue, so the differences in tissue activity between different donors and the potential risk of infectious disease transmission cannot be ignored. However, this problem can be solved by rigorous screening for infectious diseases and careful evaluation and selection of donors. Secondly, in this experiment, we used a mouse wound model to demonstrate the excellent efficacy of the lipogenic biomaterials HEP-ADGF-AAM in promoting wound healing. However, major structural and functional differences between mouse skin and human epidermis limit the inference of the results of this therapeutic model. To this end, we tested human cells directly instead of animal cells *in vitro* to minimize this limitation. However, their wound-healing mechanisms are different. At present, the biggest limitation of the mouse wound healing model is that the wound closure in mice is mainly through contraction, while the wound closure in normal people is mainly through re-epithelialization. To this end, attempts can be made to avoid contraction-mediated wound healing by removing the thin striated muscle located between the subcutaneous fat and the dermis during wound modeling, thus mimicking the wound healing process in human skin. In addition, the development of reliable humanized skin wound models in recent years has also provided a more reliable platform for testing skin repair strategies. All in all, more robust preclinical studies are still needed to further confirm the benefits observed in mouse models. In addition, nude mice were used as experimental objects in this study, which could not effectively evaluate the effect of allograft products due to immune deficiency.

## 5 Conclusion

In this study, we showed that HEP-ADGF-AAM accelerates wound epithelialization and angiogenesis, and provides an adipogenic microenvironment for fibroblast activation and vessel formation. This study demonstrated that HEP-ADGF-AAM has a better therapeutic effect than ADM, which has been clinically used for many years. Overall, the results of this study indicate that the adipogenic biomaterial HEP-ADGF-AAM accelerates wound healing by inducing adipocyte regeneration and enhancing angiogenesis and re-epithelialization. Further studies are needed to confirm the role of the adipogenic microenvironment in skin wound healing.

## Data availability statement

The original contributions presented in the study are included in the article/Supplementary Material, further inquiries can be directed to the corresponding authors.

## Ethics statement

This study was reviewed and approved by the Ethics Committee of Nanfang Hospital of Southern Medical University and the National Health and Medical Research Council. All procedures involving animals were approved by the Southern Medical University Institutional Review Board and Nanfang Hospital Institutional Animal Care and Use Committee, and were conducted in accordance with the ethical standards of the National Health and Medical Research Council (China).

## Author contributions

JR: Writing–original draft. QZ: Writing–original draft. SZ: Writing–original draft. JC: Writing–review and editing, Conceptualization. YH: Writing–review and editing. FL: Writing–review and editing.

## Funding

The authors declare financial support was received for the research, authorship, and/or publication of this article. This work was supported by the National Nature Science Foundation of China (81971852, 81801932, and 81901976), the Natural Science Foundation of Guangdong Province of China (2019A1515010641 and 2021A1515011721).

## Conflict of interest

The authors declare that the research was conducted in the absence of any commercial or financial relationships that could be construed as a potential conflict of interest.

## Publisher's note



## References

Ahn, W. B., Lee, Y. B., Ji, Y. H., Moon, K. S., Jang, H. S., and Kang, S. W. (2022). Decellularized human adipose tissue as an alternative graft material for bone regeneration. *Tissue Eng. Regen. Med.* 19 (5), 1089–1098. doi:10.1007/s13770-022-00451-7

Boháč, M., Danišovič, J., Koller, J., Dragúňová, J., and Varga, I. (2018). What happens to an acellular dermal matrix after implantation in the human body? A histological and electron microscopic study. *Eur. J. Histochem.* 62 (1), 2873. doi:10.4081/ejh.2018.2873

Brown, B. N., Freund, J. M., Han, L., Rubin, J. P., Reing, J. E., Jeffries, E. M., et al. (2011). Comparison of three methods for the derivation of a biologic scaffold composed of adipose tissue extracellular matrix. *Tissue Eng. Part C Methods* 17 (4), 411–421. doi:10.1089/ten.TEC.2010.0342

Chen, Z., Zhang, B., Shu, J., Wang, H., Han, Y., Zeng, Q., et al. (2020). Human decellularized adipose matrix derived hydrogel assists mesenchymal stem cells delivery and accelerates chronic wound healing. *J. Biomed. Mater Res. A* 109, 1418–1428. doi:10.1002/jbm.a.37133

Choi, J. S., Kim, B. S., Kim, J. D., Choi, Y. C., Lee, H. Y., and Cho, Y. W. (2012). *In vitro* cartilage tissue engineering using adipose-derived extracellular matrix scaffolds seeded with adipose-derived stem cells. *Tissue Eng. Part A* 18 (1-2), 80–92. doi:10.1089/ten.tea.2011.0103

Choi, J. S., Kim, B. S., Kim, J. Y., Kim, J. D., Choi, Y. C., Yang, H. J., et al. (2011). Decellularized extracellular matrix derived from human adipose tissue as a potential scaffold for allograft tissue engineering. *J. Biomed. Mater Res. A* 97 (3), 292–299. doi:10.1002/jbm.a.33056

Chun, S. Y., Lim, J. O., Lee, E. H., Han, M. H., Ha, Y. S., Lee, J. N., et al. (2019). Preparation and characterization of human adipose tissue-derived extracellular matrix, growth factors, and stem cells: A concise review. *Tissue Eng. Regen. Med.* 16 (4), 385–393. doi:10.1007/s13770-019-00199-7

Correa-Gallegos, D., Jiang, D., Christ, S., Ramesh, P., Ye, H., Wannemacher, J., et al. (2019). Patch repair of deep wounds by mobilized fascia. *Nature* 576 (7786), 287–292. doi:10.1038/s41586-019-1794-y

Davis, F. M., Kimball, A., Boniakowski, A., and Gallagher, K. (2018). Dysfunctional wound healing in diabetic foot ulcers: new crossroads. *Curr. Diab Rep.* 18 (1), 2. doi:10.1007/s11892-018-0970-z

Fan, J., and Yang, J. (2017). Preparation and characterization of a chitosan/galactosylated hyaluronic acid/heparin scaffold for hepatic tissue engineering. *J. Biomater. Sci. Polym. Ed.* 28 (6), 569–581. doi:10.1080/09205063.2017.1288076

Franz, A., Wood, W., and Martin, P. (2018). Fat body cells are motile and actively migrate to wounds to drive repair and prevent infection. *Dev. Cell.* 44 (4), 460–470.e3. doi:10.1016/j.devcel.2018.01.026

Gentile, P., Sterodimas, A., Pizzicannella, J., Dionisi, L., De Fazio, D., Calabrese, C., et al. (2020). Systematic review: allogenic use of stromal vascular fraction (SVF) and decellularized extracellular matrices (ECM) as advanced therapy medicinal products (ATMP) in tissue regeneration. *Int. J. Mol. Sci.* 21 (14), 4982. doi:10.3390/ijms21144982

Goodarzi, P., Falahzadeh, K., Nematizadeh, M., Farazandeh, P., Payab, M., Larijani, B., et al. (2018). Tissue engineered skin substitutes. *Adv. Exp. Med. Biol.* 1107, 143–188. doi:10.1007/5584_2018_226

Guerrero-Juarez, C. F., Dedhia, P. H., Jin, S., Ruiz-Vega, R., Ma, D., Liu, Y., et al. (2019). Single-cell analysis reveals fibroblast heterogeneity and myeloid-derived adipocyte progenitors in murine skin wounds. *Nat. Commun.* 10 (1), 650. doi:10.1038/s41467-018-08247-x

He, Y., Xia, J., Chen, H., Wang, L., Deng, C., and Lu, F. (2019). Human adipose liquid extract induces angiogenesis and adipogenesis: A novel cell-free therapeutic agent. *Stem Cell. Res. Ther.* 10 (1), 252. doi:10.1186/s13287-019-1356-0

Ikegami, Y., and Ijima, H. (2020). Development of heparin-conjugated nanofibers and a novel biological signal by immobilized growth factors for peripheral nerve regeneration. *J. Biosci. Bioeng.* 129 (3), 354–362. doi:10.1016/j.jbiosc.2019.09.004

Kim, W. S., Park, B. S., and Sung, J. H. (2009). Protective role of adipose-derived stem cells and their soluble factors in photoaging. *Arch. Dermatol. Res.* 301 (5), 329–336. doi:10.1007/s00403-009-0951-9

Kirsner, R. S., Bohn, G., Driver, V. R., Mills, J. L., Sr., Nanney, L. B., et al. (2015). Human acellular dermal wound matrix: evidence and experience. *Int. Wound J.* 12 (6), 646–654. doi:10.1111/iwj.12185

Landriscina, A., Rosen, J., and Friedman, A. J. (2015). Systematic approach to wound dressings. *J. Drugs Dermatol* 14 (7), 740–744.

Lee, J. H., Kim, H. G., and Lee, W. J. (2015). Characterization and tissue incorporation of cross-linked human acellular dermal matrix. *Biomaterials* 44, 195–205. doi:10.1016/j.biomaterials.2014.12.004

Lin, Y. A., Chu, P. Y., Ma, W. L., Cheng, W. C., Chan, S. T., Yang, J. C., et al. (2021). Enzyme-digested peptides derived from *Lates calcarifer* enhance wound healing after surgical incision in a murine model. *Mar. Drugs.* 19 (3), 154. doi:10.3390/md19030154

Maquart, F. X., and Monboisse, J. C. (2014). Extracellular matrix and wound healing. *Pathol. Biol. Paris.* 62 (2), 91–95. doi:10.1016/j.patbio.2014.02.007

Martino, M. M., Briquez, P. S., Ranga, A., Lutolf, M. P., and Hubbell, J. A. (2013). Heparin-binding domain of fibrin(ogen) binds growth factors and promotes tissue repair when incorporated within a synthetic matrix. *Proc. Natl. Acad. Sci. U. S. A.* 110 (12), 4563–4568. doi:10.1073/pnas.1221602110

Mirzaei-Parsa, M. J., Ghanbari, H., Alipoor, B., Tavakoli, A., Najafabadi, M., and Faridi-Majidi, R. (2019). Nanofiber-acellular dermal matrix as a bilayer scaffold containing mesenchymal stem cell for healing of full-thickness skin wounds. *Cell. Tissue Res.* 375 (3), 709–721. doi:10.1007/s00441-018-2927-6

Murohara, T., Shintani, S., and Kondo, K. (2009). Autologous adipose-derived regenerative cells for therapeutic angiogenesis. *Curr. Pharm. Des.* 15 (24), 2784–2790. doi:10.2174/138161209788923796

Obagi, Z., Damiani, G., Grada, A., and Falanga, V. (2019). Principles of wound dressings: A review. *Surg. Technol. Int.* 35, 50–57.

Okur, M. E., Karantas, I. D., Şenyiğit, Z., Üstündağ Okur, N., and Siafaka, P. I. (2020). Recent trends on wound management: new therapeutic choices based on polymeric carriers. *Asian J. Pharm. Sci.* 15 (6), 661–684. doi:10.1016/j.ajps.2019.11.008

Park, D., Mewhort, H., Teng, G., Belke, D., Turnbull, J., Svystonyuk, D., et al. (2018). Heparin augmentation enhances bioactive properties of acellular extracellular matrix scaffold. *Tissue Eng. Part A* 24 (1-2), 128–134. doi:10.1089/ten.TEA.2017.0004

Petrie, K., Cox, C. T., Becker, B. C., and MacKay, B. J. (2022). Clinical applications of acellular dermal matrices: A review. *Scars Burn Heal* 8, 205951312110383. doi:10.1177/20595131211038313

Pieper, J. S., Hafmans, T., van Wachem, P. B., van Luyn, M. J., Brouwer, L. A., Veerkamp, J. H., et al. (2002). Loading of collagen-heparan sulfate matrices with bFGF promotes angiogenesis and tissue generation in rats. *J. Biomed. Mater Res.* 62 (2), 185–194. doi:10.1002/jbm.10267

Schmidt, B. A., and Horsley, V. (2013). Intradermal adipocytes mediate fibroblast recruitment during skin wound healing. *Development* 140 (7), 1517–1527. doi:10.1242/dev.087593

Shook, B. A., Wasko, R. R., Mano, O., Rutenberg-Schoenberg, M., Rudolph, M. C., Zirak, B., et al. (2020). Dermal adipocyte lipolysis and myofibroblast conversion are required for efficient skin repair. *Cell. Stem Cell.* 26 (6), 880–895.e6. doi:10.1016/j.stem.2020.03.013

Song, M., Liu, Y., and Hui, L. (2018). Preparation and characterization of acellular adipose tissue matrix using a combination of physical and chemical treatments. *Mol. Med. Rep.* 17 (1), 138–146. doi:10.3892/mmr.2017.7857

Tavelli, L., McGuire, M. K., Zucchelli, G., Rasperini, G., Feinberg, S. E., Wang, H. L., et al. (2020). Extracellular matrix-based scaffolding technologies for periodontal and peri-implant soft tissue regeneration. *J. Periodontol.* 91 (1), 17–25. doi:10.1002/jper.19-0351

Varshosaz, J., Masoudi, S., Mehdikhani, M., Hashemi Beni, B., and Farsaei, S. (2019). Atorvastatin lipid nanocapsules and gold nanoparticles embedded in injectable thermogelling hydrogel scaffold containing adipose tissue extracellular matrix for myocardial tissue regeneration. *IET Nanobiotechnol* 13 (9), 933–941. doi:10.1049/iet-nbt.2019.0035

Wang, P. H., Huang, B. S., Horng, H. C., Yeh, C. C., and Chen, Y. J. (2018a). Wound healing. *J. Chin. Med. Assoc.* 81 (2), 94–101. doi:10.1016/j.jcma.2017.11.002

Wang, Q. A., Song, A., Chen, W., Schwalie, P. C., Zhang, F., Vishvanath, L., et al. (2018b). Reversible de-differentiation of mature white adipocytes into preadipocyte-like precursors during lactation. *Cell. Metab.* 28 (2), 282–288.e3. doi:10.1016/j.cmet.2018.05.022

Wissink, M. J., Beernink, R., Pieper, J. S., Poot, A. A., Engbers, G. H., Beugeling, T., et al. (2001). Binding and release of basic fibroblast growth factor from heparinized collagen matrices. *Biomaterials* 22 (16), 2291–2299. doi:10.1016/s0142-9612(00)00418-x

Wissink, M. J., Beernink, R., Poot, A. A., Engbers, G. H., Beugeling, T., van Aken, W. G., et al. (2000a). Improved endothelialization of vascular grafts by local release of growth factor from heparinized collagen matrices. *J. Control Release* 64 (1-3), 103–114. doi:10.1016/s0168-3659(99)00145-5

Wissink, M. J., Beernink, R., Scharenborg, N. M., Poot, A. A., Engbers, G. H., Beugeling, T., et al. (2000b). Endothelial cell seeding of (heparinized) collagen matrices: effects of bFGF pre-loading on proliferation (after low density seeding) and pro-coagulant factors. *J. Control Release* 67 (2-3), 141–155. doi:10.1016/s0168-3659(00)00202-9

Wu, I., Nahas, Z., Kimmerling, K. A., Rosson, G. D., and Elisseeff, J. H. (2012). An injectable adipose matrix for soft-tissue reconstruction. *Plast. Reconstr. Surg.* 129 (6), 1247–1257. doi:10.1097/PRS.0b013e31824ec3dc

Xia, Z., Guo, X., Yu, N., Zeng, A., Si, L., Long, F., et al. (2020). The application of decellularized adipose tissue promotes wound healing. *Tissue Eng. Regen. Med.* 17 (6), 863–874. doi:10.1007/s13770-020-00286-0

Ye, K., Traianedes, K., Choong, P. F., and Myers, D. E. (2016). Chondrogenesis of human infrapatellar fat pad stem cells on acellular dermal matrix. *Front. Surg.* 3, 3. doi:10.3389/fsurg.2016.00003

Yi, S., Ding, F., Gong, L., and Gu, X. (2017). Extracellular matrix scaffolds for tissue engineering and regenerative medicine. *Curr. Stem Cell. Res. Ther.* 12 (3), 233–246. doi:10.2174/1574888x11666160905092513

Zhang, Q., Johnson, J. A., Dunne, L. W., Chen, Y., Iyyanki, T., Wu, Y., et al. (2016a). Decellularized skin/adipose tissue flap matrix for engineering vascularized composite soft tissue flaps. *Acta Biomater.* 35, 166–184. doi:10.1016/j.actbio.2016.02.017

Zhang, S., Lu, Q., Cao, T., and Toh, W. S. (2016b). Adipose tissue and extracellular matrix development by injectable decellularized adipose matrix loaded with basic fibroblast growth factor. *Plast. Reconstr. Surg.* 137 (4), 1171–1180. doi:10.1097/PRS.0000000000002019

Zhong, S. P., Zhang, Y. Z., and Lim, C. T. (2010). Tissue scaffolds for skin wound healing and dermal reconstruction. *Wiley Interdiscip. Rev. Nanomed Nanobiotechnol* 2 (5), 510–525. doi:10.1002/wnan.100

frontiers | Frontiers in Bioengineering and Biotechnology

TYPE Review
PUBLISHED 07 November 2023
DOI 10.3389/fbioe.2023.1282590



OPEN ACCESS

EDITED BY
Manjie Zhang,
Harbin Medical University, China

REVIEWED BY
Shokouh Attarilar,
Shanghai Jiao Tong University, China
Alina Vladescu (Dragomir),
National Institute for Research and Development in Optoelectronics, Romania

*CORRESPONDENCE
Yuanyuan Kang,
20082068@cmu.edu.cn

RECEIVED 24 August 2023
ACCEPTED 18 October 2023
PUBLISHED 07 November 2023

CITATION
Wen X, Liu Y, Xi F, Zhang X and Kang Y (2023), Micro-arc oxidation (MAO) and its potential for improving the performance of titanium implants in biomedical applications.
*Front. Bioeng. Biotechnol.* 11:1282590.
doi: 10.3389/fbioe.2023.1282590



# Micro-arc oxidation (MAO) and its potential for improving the performance of titanium implants in biomedical applications

Xueying Wen[1], Yan Liu[1], Fangquan Xi[2], Xingwan Zhang[2] and Yuanyuan Kang[1]*

[1]School and Hospital of Stomatology, China Medical University, Liaoning Provincial Key Laboratory of Oral Diseases, Shenyang, China, [2]School of Mechanical Engineering and Automation, Northeastern University, Shenyang, China

Titanium (Ti) and its alloys have good biocompatibility, mechanical properties and corrosion resistance, making them attractive for biomedical applications. However, their biological inertness and lack of antimicrobial properties may compromise the success of implants. In this review, the potential of micro-arc oxidation (MAO) technology to create bioactive coatings on Ti implants is discussed. The review covers the following aspects: 1) different factors, such as electrolyte, voltage and current, affect the properties of MAO coatings; 2) MAO coatings affect biocompatibility, including cytocompatibility, hemocompatibility, angiogenic activity, corrosion resistance, osteogenic activity and osseointegration; 3) antibacterial properties can be achieved by adding copper (Cu), silver (Ag), zinc (Zn) and other elements to achieve antimicrobial properties; and 4) MAO can be combined with other physical and chemical techniques to enhance the performance of MAO coatings. It is concluded that MAO coatings offer new opportunities for improving the use of Ti and its alloys in biomedical applications, and some suggestions for future research are provided.

KEYWORDS

**Ti and its alloys, micro-arc oxidation, biological properties, antibacterial properties, coating**

## 1 Introduction

Metal implants have been a staple in biomedical applications since the onset of the 19th century, with Ti and its alloys becoming the prime choice for medical implant materials with high biocompatibility, excellent corrosion resistance, high specific strength and the best osteogenic potential (Kaur and Singh, 2019). Since the mid-twentieth century, due to their mechanical and chemical properties, titanium and its alloys have been widely used in industrial and biomedical applications, particularly in dentistry and orthopaedics such as dental implants, bone fusion, bone fixation and arthroplasty (joint replacement surgery) (Anderson et al., 2021; Hoque et al., 2022; Lim et al., 2022).

Although titanium and its alloys have been extensively used, they are inert metals that do not effectively promote the proliferation of osteoblasts and osteocytes, which can lead to implant failure. In addition, titanium-based implants still face some clinical problems, such as slow biological reactions to the material surface, slow early bone integration, and implantable diseases caused by bacterial colonization, leading to implant loosening and survival ability loss (Zhang et al., 2020b). Surface morphology, composition, hydrophilicity and roughness are key factors of

**TABLE 1 Surface treatment methods with their advantages, disadvantages, and applications**

| Method | Advantages | Disadvantages | Ref. |
|---|---|---|---|
| Sandblasting | Enhancing implant surface roughness and biocompatibility | Sandblasting particles and etchants may not be completely removed, leading to surface residues | Szmukler-Moncler et al. (2004); Wennerberg and Albrektsson (2009); Shemtov-Yona et al. (2014); Velasco et al. (2016) |
| | Increased cell attachment, promoted osseointegration and bone bonding | Enhancing bacterial adhesion and accumulation | |
| | Improving initial stability of the implant | Uncontrolled sandblasting may result in surface cracking of the implant | |
| | Increased the fatigue test lifespan of the implant | Improper sandblasting speed or particle size may reduce the implant's lifespan | |
| PVD | Improved the hardness and wear resistance of the coating | Not suitable for materials with high melting points and relatively low melting points, such as Al and Mg | Kaseem et al. (2021) |
| | Improved biological activity | Coatings usually have low thickness and poor adhesion | |
| | Improve bonding strength | The process is complex, takes a long time uneconomical | |
| Thermal spraying | Dense and high-temperature oxidation-resistant coating | High cost | Liu et al. (2020); Xue et al. (2020) |
| | High bonding strength convenient | Difficult to coat the inner surface of small holes | |
| | Enhanced wear-resistant, corrosion-resistant, and oxidation-resistant | | |
| | Coating can accelerate bone regeneration and has good biocompatibility | | |
| Ion implantation | Improve the tribological properties and corrosion resistance of metals | May release metal ions, causing cytotoxicity | Rautray et al. (2010); Wang et al. (2014); Xue et al. (2020) |
| | Selectively modify the surface without adversely affecting the overall performance | | |
| | Extremely high controllability and repeatability | | |
| | High accuracy in controlling the concentration and depth distribution of impurities | | |
| Chemical vapour deposition | Improved corrosion resistance | Poor coverage over large areas and complex surfaces | Antunes and de Oliveira (2009) |
| | Wear resistance and fatigue resistance | The thickness of the coating may be uneven | |
| | High purity, easy to control and monitor | High radiant heat may change the properties of the substrate material | |
| | High vaporization rate | | |
| | Relatively low cost | | |
| Anodic oxidation | Enhance coating hardness and thickness | Not environmentally friendly | Hu et al. (2021); Seyidaliyeva et al. (2022); Wang et al. (2022) |
| | Alter coating colour | Slow deposition rate | |
| | Improve the adhesion and abrasion resistance of coating | Strict pre-treatment requirements | |
| | Inexpensive | | |
| Sol-gel method | Simple manufacturing environment and reliable equipment | High Cost | Hsieh et al. (2002); Gan and Pilliar (2004); Ishikawa et al. (2020); Azzouz et al. (2022) |
| | High uniformity of the coatings | Long process time | |
| | Applicability to substrates of different sizes | Poor adhesion to a substrate | |
| | Significant enhancement of corrosion protection and biocompatibility of the metal substrate, reducing the risk of implant rejection | Require postprocessing to obtain more desirable coating properties | |
| | Ease of controlling chemical composition and microstructure | | |

(Continued on following page)

**TABLE 1 (*Continued*) Surface treatment methods with their advantages, disadvantages, and applications**

| Method | Advantages | Disadvantages | Ref. |
|---|---|---|---|
| | Suitable for coating complex-shaped substrates | | |
| | High preparation efficiency | | |
| Micro-arc oxidation | The coating has excellent corrosion resistance, high hardness, good adhesion, and is evenly distributed | Exhibit minor defects such as micro-cracks, micro-pores, and discharge channels | Pesode and Barve (2021); Li et al. (2023) |
| | Suitable for complex surfaces, | Rapid increases in the electrolyte temperature can make it challenging to maintain stable control over the micro-arc oxidation process | |
| | Easy to process and control | Excessively high electrolyte temperatures may result in over-discharge, leading to uneven surface topography of the coating | |
| | Low-cost and cost-effective | Relatively high energy consumption | |

implant tissue interaction and osseointegration (Le Guéhennec et al., 2007). The bioactive calcium phosphate (Ca-P)-containing coatings on titanium are similar to biomimetic implant materials used for bone tissue. Therefore, we can focus on the development of Ca-P-based surface coatings on titanium-based materials for load-bearing implant applications. Hence, typical coating methodologies have emerged in recent years. The methodologies can be divided into three categories: mechanical methods (fine machining, grinding, tumbling, and sandblasting), physical methods [physical vapour deposition (PVD), thermal spraying, and ion implantation] and chemical methods [pickling, chemical vapour deposition (CVD), anodic oxidation, sol-gel, and micro-arc oxidation (MAO)] (Shen et al., 2019; Gabor et al., 2020). These methods can improve the properties of titanium and its alloys, such as their better wear and corrosion resistance, providing strong mechanical adhesion between bone and implant, enhancing osteo-induction and osteo-conduction, improving bioactivity and biocompatibility, and accelerating healing time at the implant site (Sasikumar et al., 2019; Xue et al., 2020). At the same time, they have different advantages and disadvantages (as shown in Table 1).

MAO [plasma electrolytic oxidation (PEO), or anodic spark deposition (ASD)] has attracted substantial attention as an emerging surface coating methodology. MAO uses an arc discharge to enhance and activate the reactions occurring on an anode to form a ceramic film on the surface of a metal through the interaction of the workpiece and electrolyte (Wang Y. et al., 2015; Kaseem and Ko, 2019b; Kaseem and Ko, 2019a; Zhang R. et al., 2021; Xia et al., 2021). This approach can incorporate bioactive electrolyte components such as Ca and P into the coating. Ca-P coatings, particularly HA coatings, can facilitate the process of early and rapid osseointegration. The bioactivity of the coating is determined by its physicochemical characteristics, including roughness, porosity, phase, elemental composition, and adhesive strength (Wang et al., 2022).

In addition, the process of MAO can be regulated by multiple factors. On the one hand, a porous bioactive Ca-P-based composite layer can be deposited on Ti-based implant surfaces according to the selected electrolyte, which would enhance the biocompatibility and bonding strength of the coated layer (Zhao et al., 2007; Sun et al., 2008). On the other hand, antibacterial metal elements can be incorporated into implant surfaces to inhibit the initial adhesion of bacteria and prevent postsurgical complications, thus enhancing the antibacterial properties (Ferraris and Spriano, 2016). Furthermore, the contents of bioactive elements and antibacterial metal elements on the MAO coating surface can be tuned by controlling the voltage, electrolyte components and MAO time.

This review aims to collect and compare recent scientific papers concerning Ti and its alloys modified by MAO technology in the biomedical field. This review is focused on several aspects, including the influences of different factors on the performance of MAO coatings, the biocompatibility of MAO coatings and the combination of MAO with other physical or chemical techniques. In addition, implant-associated infection remains one of the most devastating postoperative complications (Oh-Hyun et al., 2018). It is highly desirable to introduce antimicrobial agents into implant surfaces to provide antibacterial activities and prevent peri-implant infections. Due to their perfect stabilities, superior broad-spectrum antibacterial properties and relatively low toxicity levels, inorganic antibacterial metal elements [e.g., silver (Ag), copper (Cu) and zinc (Zn)] have attracted great attention, which was elaborated in detail in our review. Finally, we highlight the potential challenges and future applications of MAO-modified titanium and its alloys in the biomedical field.

## 2 MAO process parameters for Ti and its alloys

Although more research is needed to fully understand the mechanisms at play, experts have identified three key components of the MAO process: electrochemical oxidation, plasma chemistry, and thermal diffusion in the electrolyte (Hussein et al., 2013). During this process, Ti and its alloys are submerged in an electrolyte containing modified species in the form of dissolved salts, such as silicates (Si), phosphates(P) and Ca salts (Sarbishei et al., 2014). The Ti and its alloys are used as the anode, while stainless steel plates serve as the cathode in the electrolytic bath (as depicted in Figure 1) Typically, MAO treatments last between 5 and 180 min, with current densities ranging from 500 to 2,000 A-m-2 and voltages reaching up to 1,000 V (Snizhko et al., 2004).

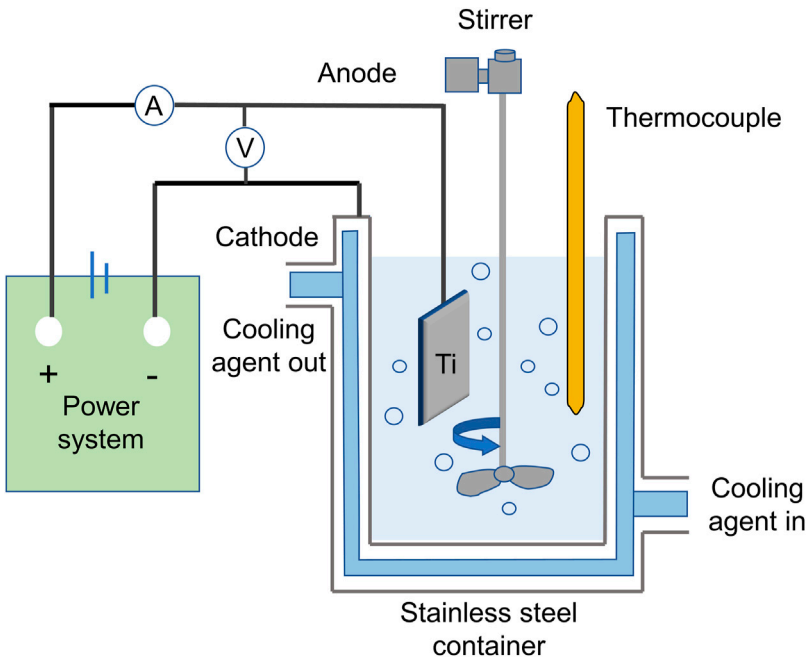


FIGURE 1
Schematic representation of the MAO coating system.

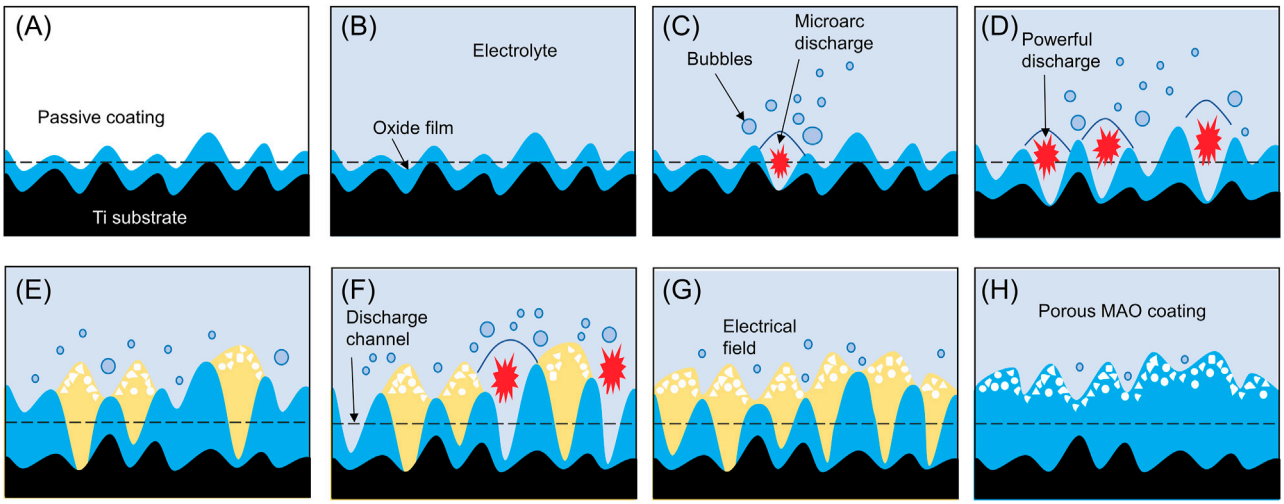


FIGURE 2
Schematic of the formation process of MAO porous coating. When exposed to air, there will be a layer of passive coating **(A)** on the surface of titanium metal. When the metal is exposed to the electrolyte, a protective film **(B)** will be formed. As the voltage increases, a porous oxide coating **(C,D)** is formed under dielectric breakdown conditions. When the voltage exceeds the dielectric breakdown of the oxide coating, spark discharge will occur, forming larger pores and interconnected microstructure **(E,F)**. The cyclic formation and decomposition of oxide coatings cause potential fluctuations **(G)**, thereby allowing the formation of ceramic oxide coatings by material dissolution and electrolyte gasification **(H)**.

As the metal comes into contact with the electrolyte, a protective film gradually forms. As voltage increases, a porous oxide coating emerges under conditions of dielectric breakdown. When voltage surpasses the dielectric breakdown of the oxide coating, spark discharges occur, forming larger pores and an interconnected microstructure. The cyclic formation and breakdown of the oxide coating cause potential fluctuations, allowing for the formation of a ceramic oxide coating through material dissolution and electrolyte gasification. (Figure 2).

In the case of Ti and its alloys, the formation of the coating during MAO is influenced by various factors, including electrolyte composition, voltage, current density, frequency, reaction time and

duty cycle (Chen et al., 2019; Li Z. et al., 2020; Zuo et al., 2020; Huang C. et al., 2021; Yong et al., 2021; Wu and Jiang, 2023). The coating properties obtained after MAO may vary depending on the influence of different parameters. Parameter control aims to obtain a homogeneous, stable, viscous and biologically active surface.

## 2.1 Electrolyte composition

In the MAO process, the choice of electrolyte is of critical significance. The electrolyte not only determines the environment in which MAO occurs but also determines the elemental composition of the final ceramic coating. The electrolyte is important because during the MAO process, the anions in the electrolyte are driven by high voltages, and they strongly bombard the titanium surface, causing them to melt and be deposited in the ceramic coating. Therefore, the chemical composition of the MAO coating depends on the anionic species in the chosen electrolyte. Changing the chemical composition of the electrolyte changes the chemical bonds between the ceramic and titanium, forming the primary bonding force in titanium-ceramic restorations. The electrolyte composition used is established by mixing silicon, calcium, Zn, manganese(Mg) and magnesium particles into the following electrolytes: KOH, $Na_2SiO_3$, NaF, $Na_2P_4O_7$, and $NaAlO_2$ (Pesode and Barve, 2021). To date, the most commonly used electrolytes in MAO technology are Si, P and aluminate-based electrolytes (Walsh et al., 2009; Khorasanian et al., 2011; Shokouhfar et al., 2012). An important factor in the composition of the electrolyte that affects the structure, morphology, and corrosion resistance of MAO coatings on Ti and its alloys is the composition of the electrolyte used (Venkateswarlu et al., 2012; Venkateswarlu et al., 2013; Jiang et al., 2016; Fattah-Alhosseini et al., 2018; Sousa et al., 2021).

Generally, adding silicates to the electrolyte results in thick coatings, rough surfaces and low adhesion. MAO oxide films formed on commercially pure Ti with electrolyte solutions containing silicates have round holes of multiple sizes, whereas P solutions produce mainly round and crater-shaped holes (Shokouhfar et al., 2011; Shokouhfar et al., 2012). In addition, various sodium-based additives in the working electrolyte can significantly affect the corrosion resistance of MAO-modified pure Ti, in terms of microstructure and phase composition (Molaei et al., 2019). Additives such as K2ZrF6 and K2TiF6 in silicate electrolytes can improve the sealed microstructure, increase the hardness and improve the corrosion resistance (Yang et al., 2018). Additionally, wear-resistant ceramic coatings have been generated on novel commercially pure titanium grade 4+ alloys by MAO in an aluminate- and zirconia-containing electrolyte, increasing the hardness and wear resistance of the MAO coatings (Lederer et al., 2021). The research conducted by Xiaohui Yuan et al. shows that using Na2SiO3 or MgSiF6 electrolytes in MAO treatment significantly enhances the bonding strength of titanium-ceramic interfaces. $Na_2SiO_3$ and MgSiF6 groups exhibited uniformly porous MAO coatings, reducing oxygen diffusion and cracks at the titanium-ceramic interface (Yuan et al., 2017).

Phosphate-based electrolytes have low roughness and coating thickness but excellent adhesion. It has been shown that coatings obtained from Ca-P electrolytes exhibit higher surface thickness and corrosion resistance values than coatings obtained from silicate electrolytes (Venkateshwarlu et al., 2012). MAO coatings on valve metals are normally white in appearance, however, colourants, which are normally the salts of transition metal ions, can be used to prepare coloured coatings. Research has shown that MAO treatment can be performed on Ti-6Al-4V alloy in concentrated sodium silicate electrolyte. By controlling the oxidation time, black and white $TiO_2$ coatings with silicon dioxide bases are obtained. The short treatment time results in a black coating with excellent corrosion resistance, which is attributed to the presence of $Ti^{2+}$ and $Ti^{3+}$ in the coating. The white coating exhibits good surface roughness and super hydrophilicity. The bond strengths of the black and white coatings on Ti-6Al-4V alloy are approximately 14.4 and 4.3 MPa, respectively (Han et al., 2018). It has been found that MAO treatment of Ti-6Al-4V in a phosphate electrolyte may produce a yellowish colour, while when vanadate is added to the coating, the colour of the coating may change from yellow to brown (Jiang et al., 2016).

A.L. Yerokhin compared the processing and performance of oxide films formed on a Ti-6Al-4V alloy by MAO in aqueous solutions containing aluminate, phosphate, silicate and sulphate anions and certain combinations of these materials. The film produced by the aluminate-phosphate electrolyte is dense and uniform, which was thicker than that produced by the phosphate electrolyte, but both showed good corrosion behaviour. Thicker $SiO_2/TiO_2$-based films with high bulk porosity produced from silicate and silicate-aluminate electrolytes exhibit good corrosion behaviour in $H_2SO_4$ solutions with high chemical stability (Yerokhin et al., 2000).

Hardness is a basic mechanical property of materials. In Gaoqiang Xu's research, it was found that the hardness of native titanium is low, 265 HV, but the MAO coating on titanium causes a significant increase in the hardness of titanium. It can make the hardness of natural titanium reach 342 HV. After incorporating $SiO_2$ nanoparticles, the hardness of MAO-Si increases to 467 HV. The authors concluded that the highest hardness value of MAO-Si can be attributed to the presence of hard $SiO_2$ nanoparticles and fewer micropores on the surface of MAO-Si (Xu and Shen, 2019).

## 2.2 Voltage

Voltage variation is another key factor affecting the performance parameters of MAO coatings on Ti and its alloys. Studies have shown that different choices of voltage affect the porosity, pore size, elemental content of the coating, high-temperature resistance, surface morphology, contact angle and surface free energy of the coating (Sedelnikova et al., 2017; Du et al., 2018; Komarova et al., 2020b; Yu et al., 2020). Qing Du's experimental results show SEM (scanning electron microscopy) images of pure Ti and MAO coatings formed at 300, 350, 400, 450 and 500 V. It was confirmed that a rough and porous surface structure was observed on the MAO-treated Ti plate. A large number of micropores with a size of approximately 1~3 μm were observed on the MAO coating formed at 300 V. However, as the applied voltage (350~500 V) increases, the average micropore size on the MAO coating surface increases, while the micropore density decreases. In addition, when the applied voltage is 350–500 V,

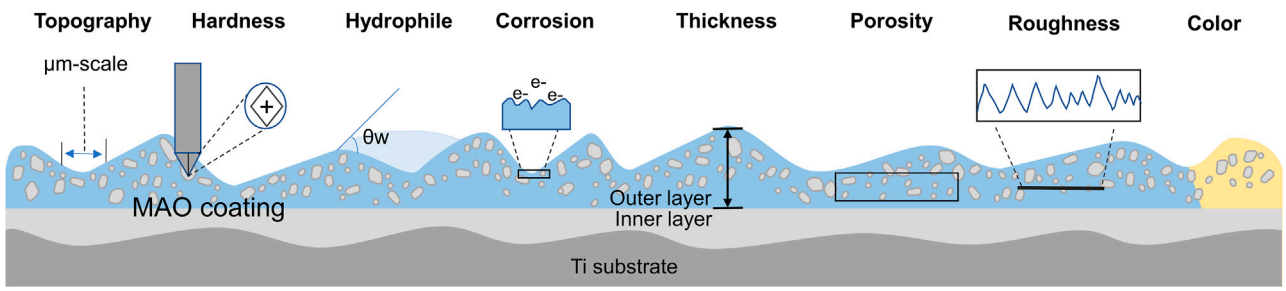


FIGURE 3
Schematic representation of surface properties modification after MAO deposition.

the uniformity of micropore size decreases. The results show that the applied voltage has an important influence on the surface morphology of MAO coating (Du et al., 2018). Increasing voltage during MAO results in a linear increase in thickness, roughness and porosity of the MAO coatings on Ti and Ti-40Nb substrates, as well as a decrease in adhesion strength values (Komarova et al., 2020a). In addition, Zhao Wang et al. used the MAO technique to fabricate ceramic coatings on AlTiCrVZr alloys and adjusted the voltage to 360, 390, 420 and 450 V during the process (Wang et al., 2023). The resulting coating composition was dominated by $Al_2O_3$, $TiO_2$, $Cr_2O_3$, $V_2O_5$, $ZrO_2$, and $SiO_2$. Additionally, the results showed that the MAO coating gradually became smooth and dense with increasing voltage, the surface roughness decreased the coating thickness increased, and the coating prepared at 420 V showed the best high-temperature oxidation resistance after oxidation for 20 h.

## 2.3 Current

The density, frequency, duty cycle and type of current also have a significant effect on the thickness, surface roughness, corrosion resistance and porosity of MAO coatings on Ti and its alloys (Sobolev et al., 2019; Lederer et al., 2021; Grigoriev et al., 2022; Muntean et al., 2023). For example, Grigoriev et al. discovered that higher current densities increased the coating thickness and surface roughness of Ti-6Al-4V alloys (Grigoriev et al., 2022). Meanwhile, increasing the current density, frequency and duty cycle results in thicker and denser coatings with better tribological properties on pure Ti surfaces (Lederer et al., 2021). Higher current pulse frequencies will produce denser and less porous coatings, resulting in improved corrosion resistance (Sobolev et al., 2019). Finally, for smoother MAO coatings with lower porosity and denser structures on Ti and its alloys, pulsed currents can be used in place of direct currents (Muntean et al., 2023).

Research by Mónica Echeverry-Rendón et al. tested different electrolytes, voltages, current densities and anodization times to obtain surfaces with different properties. The obtained materials were characterized by different techniques such as X-ray diffraction (XRD), SEM and glow discharge emission spectroscopy (GDOES). The results show that compared with the untreated surface, MAO treatment can obtain a super-hydrophilic surface with a contact angle of about 0°, which is hydrophilic, and this situation remains stable after several weeks of MAO in some cases (Echeverry-Rendón et al., 2017).

In summary, the MAO process is a complex technique that requires careful parameter control to achieve desired coating properties. Electrolyte composition, voltage variations and current parameters influence the topography, thickness, roughness, colour, porosity, corrosion resistance, hardness, hydrophilicity, etc., of MAO coatings on Ti and its alloys (Figure 3).

# 3 The biocompatibility of the MAO coating

Biocompatibility is the ability of a material to come into contact with a living organism without causing any adverse or rejection reaction. It is mainly determined by how an organism's cells, tissues and immune system respond to the material. In the fields of medicine and biology, it is essential to ensure good biocompatibility of materials. MAO technology facilitates the formation of highly biocompatible oxide coatings on Ti and its alloys. Studies on the biocompatibility of MAO coatings on Ti and its alloys focus on cytocompatibility, hemocompatibility, corrosion resistance, angiogenic activity, osteogenic activity and osseointegration (as shown in Figure 4).

## 3.1 Cytocompatibility

Cytocompatibility is the ability of a material to interact with biological cells without causing a toxic or immune response.

Various cell types have been shown to adhere and proliferate better on MAO-modified Ti and its alloys, including bone marrow stromal stem cells (BMSCs), MC3T3-E1 cells, MG63 cell lines, hMSCs, NIH-3T3, immortalized skin fibroblasts, rabbit mesenchymal stem cells and endothelial cells (Xiu et al., 2016; Zhang X. et al., 2018; Zhou W. et al., 2019; Zhou et al., 2019 J.; Liao et al., 2020; Shen Y. et al., 2022; Kostelac et al., 2022; Molaei et al., 2022). MAO-treated specimens have highly porous layers that can be observed under SEM. Cells on MAO exhibit polygonal shapes with filamentous and lamellar extensions of pseudopods, improved spreading, increased cell density and pseudopods anchored in micropores (Zhou J. et al., 2019; Pan et al., 2019; Zhang et al., 2019; Li Y. et al., 2020; Kostelac et al., 2022; Wang et al., 2022). The

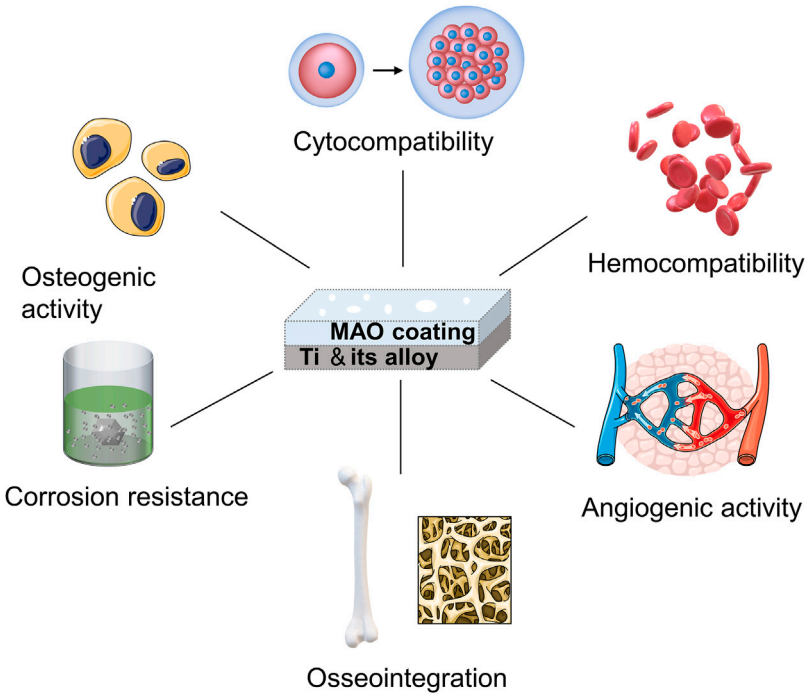


FIGURE 4
The biocompatibility of the MAO coating.

degrees of cell adhesion and proliferation on Ti and its alloy MAO coatings can be influenced by adding different elements or by adjusting the ion concentration in the electrolyte (Wang L. J. et al., 2021; Shen Y. et al., 2022). The longer the MAO process is, the larger the pore size on the coating and the more cells are attached (Zhou W. et al., 2019). Cell adhesion and extension assay on MAO coating on Ti and its alloy as shown in (Figure 5) (Zhou J. et al., 2019; Zhou W. et al., 2019; Zhang et al., 2019; Shen Y. et al., 2022). In addition, under an SEM electron microscope, the smooth titanium surface has parallel scratches arranged along the grinding direction. The surface of the coating treated by micro-arc oxidation shows a typical nano-porous structure. As the duty cycle increases, the surface of the coating shows micron-sized grooves and nano-sized pores that are evenly distributed and connected. Cell proliferation is increasingly obvious in structures with nanoscale porous and micron-scale grooves. (Pan et al., 2019).

Scholars have shown that the MAO-treated Ti surface creates a safe coating that reduces the cytotoxicity of the metal. For example, Ti and its alloys covered with MAO coatings containing Mg, Ca, P, Sr, Co and F show no cellular toxicity, differing from untreated Ti (Zhou J. et al., 2019; Li X. et al., 2020). Additionally, Lorena Kostelac conducted cell adhesion tests to confirm the cytocompatibility of the hydroxyapatite (HAP) coating obtained on the surface of titanium alloys by MAO. Human skin fibroblasts are first incubated with the samples for 48 h and then stained with calcein-AM to visualize viable cells on titanium substrates. The results showed that after 2 days of cell culture, no cytotoxic effects were observed, and fibroblasts spread and colonized all available areas on the sample surface. Furthermore, higher cell densities are observed in all MAO-treated substrates relative to untreated substrates. (Kostelac et al., 2022). However, it is important to note that the presence of excess Cu ions in the coating inhibits cellular activity (Zhang X. et al., 2018). There are also high and low levels of cytotoxicity for each coating, with one study finding that Ti-Ag2O coatings are less cytotoxic than Ti-Ag coatings (Zhang et al., 2021c).

In the design of multifunctional surface coatings for titanium and its alloys, the nanoscale is sometimes involved. Nanoparticles (NPs) can bind to antibodies, ligands, and drugs, thereby enhancing their potential applicability in biotechnology, drug and gene delivery, magnetic separation, and imaging; in addition to their favour properties, they can cause harmful effects if they enter living biological systems and tissues (Attarilar et al., 2020). The formation of MAO coatings on Ti-6Al-4V alloy surfaces with $ZrO_2$ and ZnO nanoparticles significantly improves the corrosion resistance of MAO-treated Ti and its alloys, with corrosion rates that are approximately 14 times lower than those of the substrate (Nadimi and Dehghanian, 2021). These results suggest that MAO treatment is beneficial in reducing cytotoxicity.

Therefore, MAO treatment can create a safe coating on the surface of Ti and its alloys to enhance the cytocompatibility of Ti and its alloys to promote cell adhesion, proliferation and differentiation.

## 3.2 Hemocompatibility

Hemocompatibility refers to the biological reactions and effects that occur when a material comes into contact with blood. One of the important indicators to examine the hemocompatibility of blood contact materials is the hemolysis

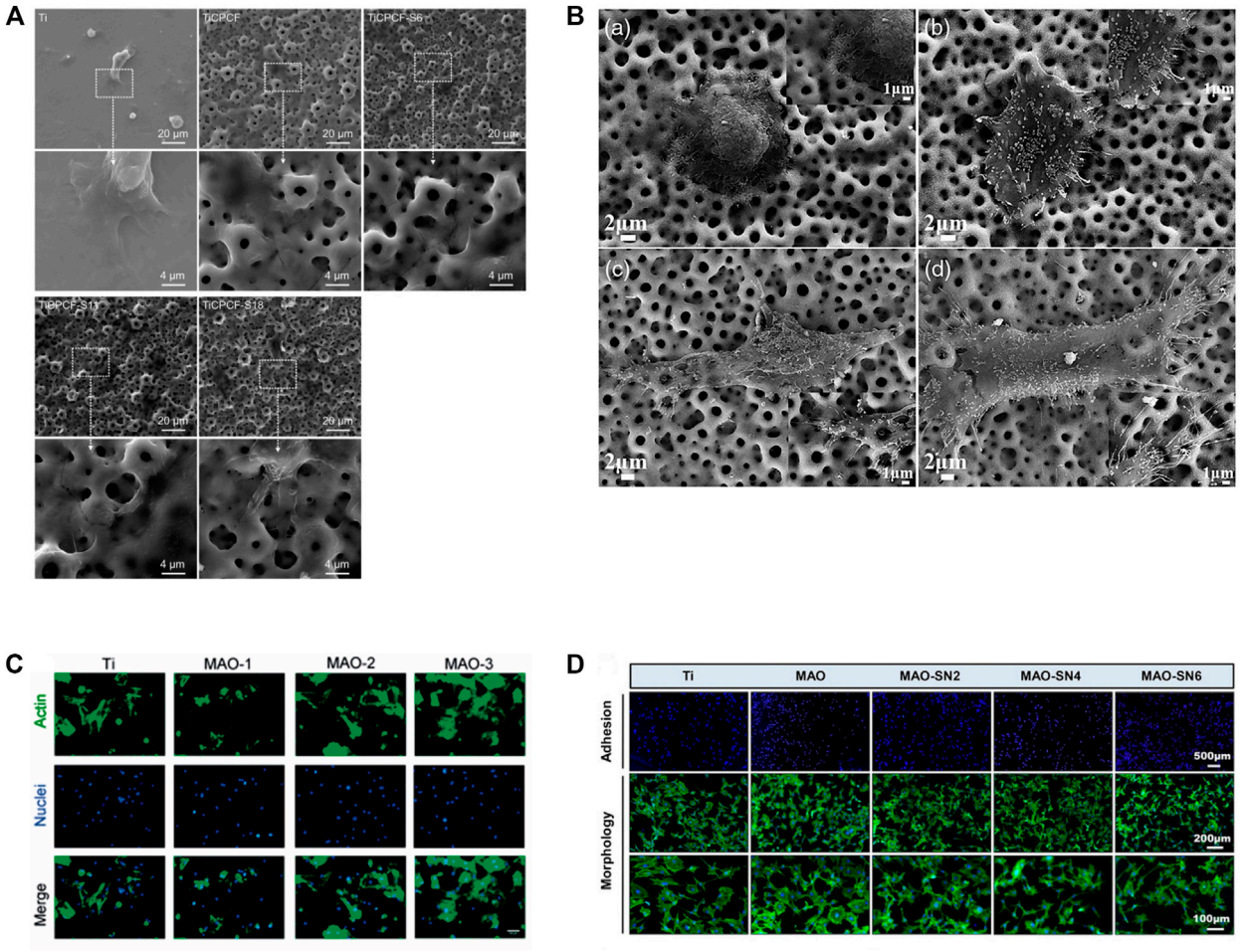


FIGURE 5
Cell adhesion and extension assay. **(A)** SEM micrographs of MSCs cultured for 3 days. Reprinted from Ref. (Zhou J. et al., 2019). Copyright (2019) Springer Nature. **(B)** SEM images of morphologies of SaOS-2 cells adhered to the MAO: A 4 h and C 24 h; MHTZn: B 4 h and D 24 h. Adapted from Ref. (Zhang et al., 2019). © 2019 The Author(s). Published by Informa UK Limited, trading as Taylor & Francis Group. **(C)** BMSCs were stained by FITC-phalloidin and DAPI after incubation for 4 h on four samples. Scale bar = 50 mm. Reprinted from Ref. (Zhou W. et al., 2019). Copyright (2019) Taylor & Francis. **(D)** Representative staining images of the early adhesion and morphology of MC3T3-E1 cells. Reprinted from Ref. (Shen Y. et al., 2022). Copyright (2022) Frontiers.

rate. Studies have shown that the hemolysis rates of MAO-treated Ti-6Al-4V alloy and untreated Ti-6Al-4V alloy are 0.85% and 1.51% respectively, indicating that the former has better hemocompatibility. Furthermore, MAO treatment reduces platelet adhesion and activation to the surface of Ti and its alloys which exhibit a uniform but rough porous microstructure (crater-like), inhibits thrombosis and inflammatory responses, and ultimately reduces the risk of vascular endothelial cell damage (Jiang et al., 2015). However, it should be noted that not all MAO treatments improve hemocompatibility and, in some cases, may even reduce haemotolerance. For example, it has been shown that platelet coverage on MAO-treated Ti surfaces can be higher than that without MAO treatment (Klein et al., 2020). Wang Maosheng et al. also found that platelets spread on MAO-treated surfaces and exhibited extensive pseudopods. The interaction between platelets and the MAO-treated surface resulted in the formation of an almost connected platelet layer (Wang M.-S. et al., 2015).

## 3.3 Corrosion resistance

To be able to evaluate the quality of the coatings produced by MAO on Ti and its alloys, it is necessary to test their corrosion resistance, particularly regarding evaluating their biocompatibility (Molaeipour et al., 2022). For biomedical applications, simulated body fluids (SBF) are often used as electrolytes because of their ionic composition, which is similar to that of human blood plasma. Studies have shown that pure Ti with MAO coating immersed in SBF exhibited no significant damage or cracking, while untreated CP-Ti showed ulcerative corrosion (Molaei et al., 2022). In addition, the corrosion current density of the Ti alloy samples with MAO coating decreased by more than 15 times in SBF. A comparative analysis of the corrosion behaviour of samples with and without protective coating in SBF was performed. Potentiodynamic polarization data reveals an improvement in corrosion properties after surface coating with an MAO layer (Mashtalyar et al., 2020).

Likewise, a study by Gaoqiang Xu showed that the MAO technique can form wear and corrosion-resistant coatings on Ti and its alloys (Xu and Shen, 2019). These results suggest that in the human body, MAO-treated Ti and its alloy implants may possess good corrosion resistance.

## 3.4 Angiogenic activity

Studies have demonstrated that the application of MAO coatings onto the surface of Ti and its alloys can augment the attachment, multiplication, differentiation, and transmigration of vascular endothelial cells and fibroblasts. This ultimately results in invigorating tissue repair and regeneration by inspiring vascular rejuvenation. For instance, research by Yiding Shen et al. revealed that MAO-modified titanium evinced noteworthy enhancement in the viability and translocation of human umbilical vein endothelial cells when compared to untreated titanium. Cells on the surface of MAO-treated titanium and its alloys exhibited intricate vascular networks and significantly high levels of vascular genes, indicating the potential for rapid angiogenesis *in vitro* (Shen Y. et al., 2022). Additionally, mesenchymal stem cells co-cultured with MAO coatings witnessed an elevation in angiogenic factors like HIF-1a and VEGF (Zhou J. et al., 2019). Adding Cu NPs to $TiO_2$ coatings was also found to amplify endothelial cell proliferation and VEGF secretion (Zhang X. et al., 2018). In conclusion, these findings suggest that MAO-treated Ti and its alloys have immense potential for enhancing tissue repair and regeneration by stimulating angiogenesis.

## 3.5 Osteogenic activity

Osteogenic activity refers to the ability of a material to promote the proliferation and differentiation of bone cells, thereby accelerating the repair and regeneration of bone tissue. The MAO coating on the surface of Ti and its alloys, with its porous structure, have been found to improve the adhesion and bioactivity of osteoblasts while releasing beneficial ions and molecules that stimulate the proliferation and differentiation of osteoblasts and the formation of new bone tissue. Various studies have shown that MAO coatings can increase extracellular matrix mineralization and bone-like apatite deposition by osteoblasts, indicating desirable osteogenic activity (Zhang X. et al., 2018; Zhang. et al., 2021c; Shen Y. et al., 2022). In addition, MAO treatment has been found to increase alkaline phosphatase (ALP) activity, along with a wider positive area for ALP staining than the untreated group (Zhou W. et al., 2019; Zhao et al., 2020). The expression of genes related to osteogenesis is also critical in determining osteoblast activity. qRT-PCR studies have shown that MAO treatment significantly increased the expression levels of osteogenic genes such as Runx2, ALP and osteocalcin (OCN) in Ti and its alloys compared to the untreated group (Wang et al., 2022).

Furthermore, the effect of MAO coating on osteoblasts plays an important role in determining osteoblast activity. Studies have shown that MAO-coated Ti and its alloys promote the spread and growth of osteoclasts on their surface and increase osteoclasts (Santos-Coquillat et al., 2019).

Inappropriate use of antibiotics leads to the proliferation of drug-resistant bacteria and the emergence of "superbugs," such as methicillin-resistant *Staphylococcus aureus* (*MRSA*), Multidrug-resistant (MDR) *E. coli* (*Escherichia coli*), Multidrug-resistant Pneumonia *Klebsiella*, and vancomycin-resistant *Enterococcus* (VRE). (Xia et al., 2023). The misuse of antibiotics has increased in cases of osteomyelitis. In the study conducted by Teng Zhang and others, they developed a novel multilevel structured MAO 3D-printed porous Ti6Al4V scaffold for the sustained release of vancomycin. The scholars designed polydopamine (PDA) as an adhesive anchor for heparin; the adhesive was affixed to the underlying microporous MAO-$TiO_2$/CaP layers. As confirmed by high-performance liquid chromatography, this system demonstrates high loading capacity and sustained vancomycin release kinetics. *In vivo* experiments, they injected 0.1 mL of 108 colony-forming units (CFU) of MRSA into the tibiae of rabbits to induce severe osteomyelitis. Physical, haematological, radiological, microbiological, and histopathological analyses were conducted to assess the therapeutic effects. It has been found that rabbits treated with vancomycin-loaded MAO scaffolds inhibit bone infection and enhance bone formation. (Zhang et al., 2020).

## 3.6 Osseointegration

Osseointegration is an important aspect of ensuring the long-term stability and function of artificial implants in the host bone tissue. It shows that the MAO coating process promotes osseointegration by creating a highly porous and rough surface that improves interfacial bonding between bone tissue and Ti and its alloy implants (Huang L. et al., 2021).

MAO-treated Ti-6Al-4V alloys can promote bone growth and implantation in healthy adult male New Zealand rabbits, with early osteogenesis occurring primarily on the implant surface, followed by external expansion (Xiu et al., 2016). Histological examination showed that the microporous clocks of MAO-treated Ti had more bone tissue surrounded by a thicker and continuous bone matrix than untreated Ti, demonstrating the effectiveness of the MAO coating process in promoting osseointegration (Xiu et al., 2016). Similar experiments have shown that 8 weeks after the placement of Ti implants in adult rabbits, the pure Ti surface was still covered with fibrous tissue, while new bone formed on the surface of the titanium implants with MAO coating (Zhao et al., 2020). Other experiments have shown that MAO-coated implants have better bone-to-implant contact and coverage area attached to the implant, the highest density of newly grown paragenetic bone tissue, and can withstand greater shear (Chen et al., 2021; Ding et al., 2022; Ni et al., 2022). Wang et al.'s study demonstrated good osseointegration of the MAO coating was found by observing gross observation and micro-CT reconstruction of the femoral condyle after implant implantation and new bone formation was observed by toluidine blue and fuchsia-methylene blue staining. (Figure 6); (Wang L. J. et al., 2021). Compared to smooth surfaces, the MAO-treated group had more aggressive contact and much distant osteogenesis (Li et al., 2018).

Strontium (Sr), as an essential microelement that acts similarly to calcium with potent bone-seeking properties, has been proven to be an integral feature in the development of bone and/or teeth. Sr-

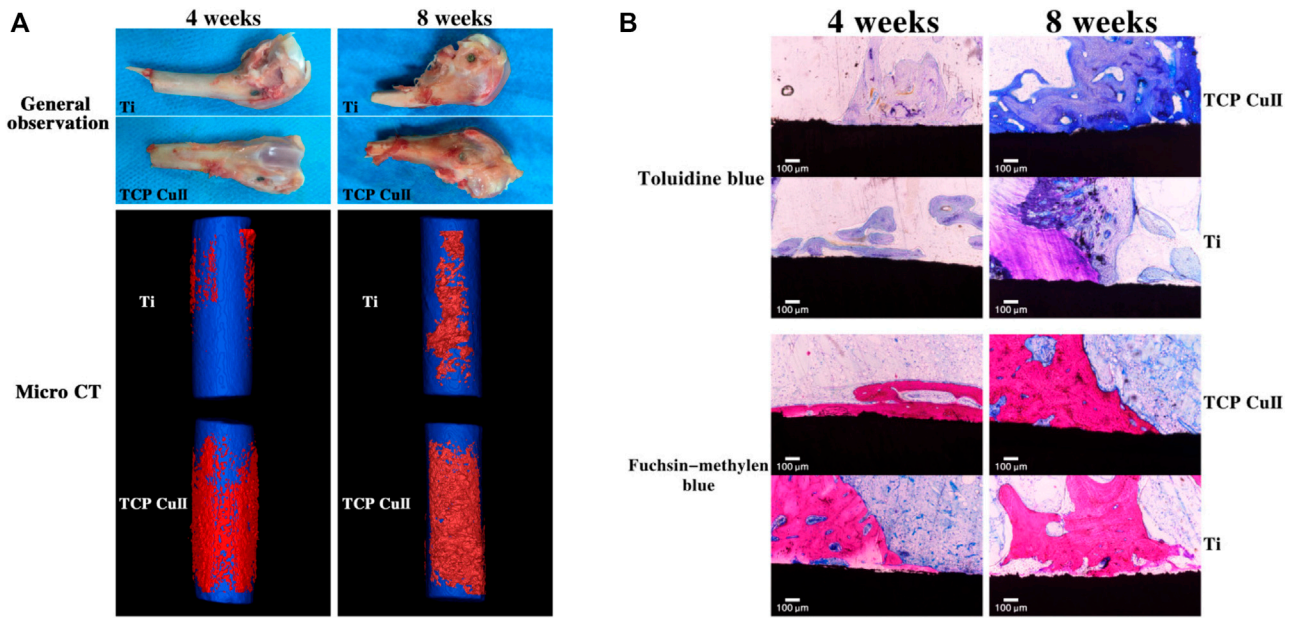


FIGURE 6
Osseointegration assay. **(A)** Gross observation and micro-CT reconstruction of the femoral condyle were observed at 4 and 8 weeks after implantation. **(B)** Toluidine blue and fuchsin-methylene blue staining of new bone formation at 4 and 8 weeks after implantation. Reprinted from Ref. (Wang L. J. et al., 2021). Copyright (2021) Springer Nature.

doped implants have been proven to significantly promote early osseointegration under normal and osteoporotic conditions. (Lu W. et al., 2022). It has been reported that Sr prevents osteoporosis via two mechanisms, simultaneously stimulating osteogenesis and restraining osteoclastogenesis via diverse cellular signalling pathways. Recently, Zhou et al. discovered that Sr-doped titanium samples can significantly promote osteogenesis by decreasing ROS expression and inhibiting adipogenic differentiation of mesenchymal stem cells in ageing rats. (Zhou C. et al., 2019). In addition, scientists have implanted MAO coatings into osteoporotic rats and found that high concentrations of $Sr^{2+}$ significantly reduce the expression of ROS in osteoporosis, showing good results (Shen X. et al., 2022). Overall, MAO significantly improves fixation strength, bone formation, and osseointegration with the Ti and its alloy implant surface.

HA is a biologically active material widely used to enhance the osseointegration of titanium dental implants. During the MAO process, an electrolyte solution containing calcium and phosphate ions is utilized, which can result in the formation of HA within the oxide layer. Subsequent hydrothermal treatment can be employed to increase the HA content. This phenomenon in a titanium oxide surface with high porosity, controlled thickness, and a considerable density of HA. (Lugovskoy and Lugovskoy, 2014).

According to research in the literature, the utilization of HA coatings with a nanoparticle structure can facilitate the adhesion, spreading, and differentiation of bone cells (MC3T3-E1), leading to an improvement in their overall activity. It should be noted, however, that excessive deposition of a large quantity of nano-HA particles on the surface may have adverse effects on cell proliferation (Wang X. et al., 2021).

Additionally, by applying MAO treatment and microwave hydrothermal treatment, a coating containing HA crystals can be rapidly formed on the titanium surface. Research results show that HA can dissolve in SBF, thus increasing the local supersaturation of Ca and phosphorus(P) elements near the coating surface. Furthermore, the material exhibits a good crystallographic match with the deposited apatite, accelerating the formation of the deposited apatite layer. Therefore, this surface demonstrates good cell activity and osseointegration capabilities due to its favourable wettability, high surface energy, and aptitude for apatite formation. (Du et al., 2019).

In summary, the MAO technique can form a layer of biocompatible coating on the surface of Ti and its alloys. This coating promotes the proliferation, adhesion and differentiation of many cell types on the surface and has high cytocompatibility and haem compatibility. In addition, this coating has excellent corrosion resistance and remains stable during long-term use. Importantly, this coating can promote bone formation and therefore has broad application prospects in the medical field.

## 4 The antibacterial properties of the MAO coating

Bacterial infection remains a significant global threat worldwide owing to its potential to cause multiple organ damage and increase the risk of other diseases. (Tang et al., 2021; Huang et al., 2023; Ji et al., 2023; Lin et al., 2023). Similarly, the use of MAO-treated materials for medical applications is also often hampered by the potential risk of bacterial infection. To address this issue, researchers have explored the use of metallic elements such as Cu, Ag, Zn, Mg, etc., as well as biological antimicrobial agents to enhance the antimicrobial properties of MAO coatings on Ti and its alloys. (Figure 7).

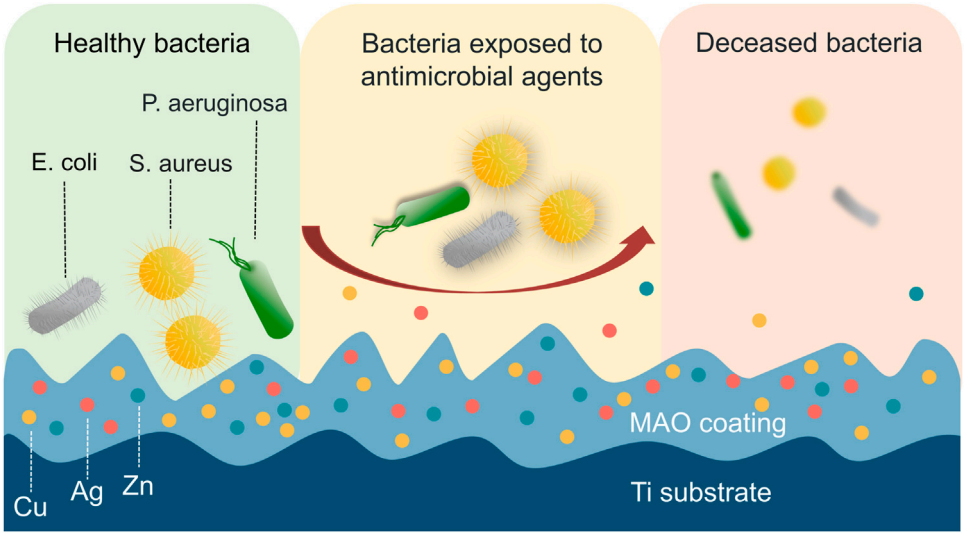


FIGURE 7
Direct contact with antimicrobial elements causes physical damage and cell death in bacteria. The bacteria can experience physical damage to their membrane upon direct contact with antimicrobial elements, including Cu, Ag, and Zn, which ultimately leads to cell death.

Incorporating these elements into the coating can help reduce the risk of bacterial infection, making MAO-treated materials more suitable for medical applications (Supplementary Table S1).

## 4.1 Cu-containing MAO coating

Cu is a vital trace element in the human body with excellent antibacterial properties (Gross et al., 2019). Studies have shown that Cu can enhance lipid peroxidation, inhibit bacterial active DNA and related enzymes, interfere with bacterial energy metabolism, and exhibit a low potential for drug resistance (Shimabukuro, 2020). In addition, Cu ions can kill bacteria or disrupt their replication using direct contact and ion release (Huang et al., 2018; Wang et al., 2019a; He et al., 2020).

The MAO process can be used to successfully produce Cu-containing coatings on Ti and its alloy, resulting in substantially antimicrobial properties (Lu X. et al., 2022). In a related study by Binbin Kang, Cu doping has been found to effectively promote the proliferation of BMSCs and enhance osteogenic differentiation when compared to $TiO_2$ coating. Furthermore, the antibacterial experiments conducted revealed that Cu-doped $TiO_2$ coating had a significant impact on *Streptococcus mutans* (*S. aureus*) and *Porphyromonas gingivalis* (*P. gingivalis*), demonstrating exceptional antibacterial properties (Figure 8) (Kang et al., 2022).

Furthermore, studies have shown that Cu ions exhibit high bioactivity and excellent antibacterial properties over a range of concentrations and that higher concentrations of Cu lead to better antibacterial effects. The research findings indicate that all samples exhibit morphological features indicative of sedimentation phenomena, with porosity following descending order: Ti–10Cu (~1.87%) > Ti–5Cu (~1.55%) > Ti–2Cu (~0.82%). In addition to the presence of flocculent deposits, the Ti–2Cu coating also exhibits spherical, rod-like, and lamellar deposits. Similarly, typical micron-scale clusters containing sediment of various morphologies are observed in the Ti–5Cu coating. Conversely, the Ti–10Cu coating exclusively features lamellar deposits. The antimicrobial capability of the Ti–2Cu, Ti–5Cu, and Ti–10Cu coatings was assessed by measuring the OD600 value of the medium after 24 h of incubation. The results showed that the OD600 value of the copper-doped TiO2 coating was significantly reduced compared with the titanium substrate, indicating that the copper-doped was beneficial to its antibacterial effect. However, the antibacterial efficacy is inconsistent with its Cu content, because the Ti–2Cu coating shows higher antibacterial efficacy than the Ti–5Cu coating, and the Ti–5Cu coating is similar to the Ti–10Cu coating (Zhang X. et al., 2018).

The studies show that the antimicrobial concentrations of Cu ranging from 0.54% to 0.72% on the surface of MAO coatings showed antibacterial and fungicidal properties (Zheng et al., 2018; Rokosz et al., 2020). However, Zhang Xinxin et al. found that the antibacterial rate (AR) of the TiO2 coating formed by adding 2 g/L $Na_2Cu$ EDTA was similar to that of adding 10 g/L; both were superior to the 5 g/L coating (Zhang et al., 2021b). Therefore, the modulation of Cu concentration needs to be further investigated.

Additionally, aside from Cu concentration, the antimicrobial properties of MAO coatings on Ti and its alloys are influenced by the price of Cu ions. It has been shown that Cu-doped $TiO_2$ coatings in the $Cu^{2+}$ enriched region have better antimicrobial activity compared to those with high Cu + content (Zhang et al., 2020e). Furthermore, t increasing the Cu+/Cu2+ content of the coating leads to better antibacterial and antifungal effects (Rokosz et al., 2020).

MAO coatings with Cu ions have been found to possess powerful long-term antibacterial properties. For example, a porous three-dimensional (3D) MAO coating containing 1.92 wt% Cu (Cu-1.92 wt%) developed on a Ti-6Al-4V alloy maintained 100% antimicrobial activity against *S. aureus* (*S. aureus*) even after being immersed in a Hanks solution for 14 days (Liang et al., 2020). In addition, studies have shown Cu-based MAO coatings on Ti alloys exhibit exceptional antibacterial activity against Gram-positive and Gram-negative bacteria even after being submerged in normal brine for 28 days (Shimabukuro et al., 2020b).

**TABLE 2 Combined application of MAO with other treatment methods.**

| Treatments | Substrate | Surface morphology | Cell models | Animal models | Bacteria | Outcome | Reference |
|---|---|---|---|---|---|---|---|
| MAO and hydrothermal treatment | Ti6Al4V | Micro-nano hybrid coating with moderate roughness | MC3T3-E1 cells | rat | - | Enhance biocompatibility, osteogenesis, and osseointegration | Huang et al. (2021) |
| MAO and microwave hydrothermal treatment | Ti | Slightly higher sub-micron roughness | BMMSC | | | Enhancing the differentiation of osteoprogenitor stem cell | Lin et al. (2020) |
| MAO and Steam-Hydrothermal treatment | Ti | Volcanic porous structure and nano-structures | MC3T3-E1 cells, human umbilical vein fusion cells | rabbits | - | Promote Osteogenesis, and angiogenesis and accelerate the process of osseointegration | Wang et al. (2021) |
| MAO and large-grit sandblasting | Ti | Micron-sized craters accompanied by sub-micron-scale pits, more porous architectures | BMMSC | dog | - | Enhance cell adhesion, proliferation, osteogenic and peri-implant new bone Formation and osseointegration | He et al. (2019) |
| MAO and SLA | Cp-Ti | A typical crater-like porous structure was formed on the surface | MC3T3-E1 cells | | | Enhance cellular attachment and proliferation | Kim et al. (2021) |
| MAO and HESP | Cp-Ti | Many non-uniform nanoparticles, some elliptical or circular micro-pores and some obvious cracks on MAO substrates | MC3T3-E1 cells | - | - | MC3T3-E1 cells on S-MAO substrate had better spreading, proliferation, and osteogenic differentiation capacities | Shen et al. (2020b) |
| MAO and HESP | Ti | Some porous structures and no obvious cracks | MC3T3-E1 cells | - | *S. aureus* *S. mutans* | Promoting the spreading, proliferation and differentiation of cells and having bactericidal effects on both bacterial | Shen et al. (2020a) |
| MAO and SFT | Ti3Zr2Sn3Mo25Nb alloy | Evenly distributed with sub-circular or elliptical crater-like and much fewer submicron pores | MC3T3-E1 cells | | | Nanocrystalline micro-arc oxidation coating is conducive to cell adhesion and growth and has good biocompatibility | Yu et al. (2022) |
| MAO and SLM | Ti-6AL-4V | The homogenous micro-/nano-porous oxide layer | Pre-osteoblast MC3T3-E1 cells | - | MRSA USA300 | Highly porous SLM titanium bone implants that were biofunctionalized using PEO with Ag and Zn NPs in ratios of up to 75% Ag and 25% Zn fully eradicated bacterial inocula within 24 h in both *in vitro* and *ex vivo* experiments | Iaj et al. (2020) |
| MAO and SLM | Ti-10Ta-2Nb-2Zr alloy | Covered homogeneously with "volcano-like holes" that were micro/nano-diameter in scale. Large holes were encased in tiny holes and interconnected | MG-63 cells | rabbits | - | MAO coating and porous structure improved cell viability *in vitro* and increased new bone formation *in vivo* | Luo et al. (2021) |
| MAO and SG | Ti | Flower-like and spherical dense micro nanostructured deposits completely cover the surface | - | - | *E. coli* | The coating produced with MAO and sol-gel combined methods is doubly effective for both bioactive and antibacterial properties | Yılmaz (2021) |

(Continued on following page)

**TABLE 2 (*Continued*) Combined application of MAO with other treatment methods.**

| Treatments | Substrate | Surface morphology | Cell models | Animal models | Bacteria | Outcome | Reference |
|---|---|---|---|---|---|---|---|
| MAO and SG | Ti6Al4V alloy | A hierarchically rough structured topography with a large number of crater-like micropores | MC3T3-E1 cells | - | - | Good biocompatibility and enhancing cell proliferation | Li et al. (2020) |
| MAO and SG | Cp-Ti | The thickness and area of the coating increase, and the particle structure on the surface is covered, resulting in the disappearance of cracks | MC3T3-E1 cells | - | - | The composite coating has excellent anti-inflammatory and bone-promoting properties | Zhu et al. (2022) |
| MAO and UA | Cp-Ti | A relatively uniform brownish appearance, porous morphology and presence of depositions were observed | MC3T3-E1 cells | - | *S. aureus* | The introduction of ultrasonic vibration enhances the corrosion resistance, antibacterial capability and cellular response of the Cu-incorporated TiO2 coating | Zhang et al. (2021) |
| MAO and UA | Ti | Formation of an intact substrate/coating interface with the absence of large cracks | MC3T3-E1 cells | - | *S. aureus* | Both *in vitro* and *in vivo* biological examinations indicate the desirable biological response including biocompatibility and antibacterial property | Lv et al. (2021) |
| MAO and UA | Ti-Cu alloy | Increased the roughness | MC3T3-E1 cells | - | *S. aureus* | Improved the antibacterial activity and non-cytotoxicity but improved the early adhesion of MC3T3 cells | Hu et al. (2020) |
| MAO and bioactive factors | Ti6Al4V alloy | More pores on the metallic surface are covered by Ca, P coatings and HA-precipitated | murine bone marrow mesenchymal stem cell line D1 (mBMSCs) | rabbit | - | Ti-alloy implant modified by MAO with CaP-BMP2 is osteo-inductive and osteoconductive which can create better osteogenesis and angiogenesis | Teng et al. (2019) |
| MAO and bioactive factors | Cp-Ti | Petal sheets and roughness decreased | MC3T3-E1 cell | | *E. coli* | The coating with BMP-2/chitosan/hydroxyapatite can significantly improve cell adhesion, spreading and proliferation with excellent antibacterial properties | Wang et al. (2019) |

The Cu-containing MAO coating achieved 98.7 antibacterial activity against *S. mutans*, effectively killing *S. mutans* on almost all surfaces, and also demonstrated potent antibacterial effects against *S. aureus* and *E. coli* (Shen et al., 2020a). These results indicate that Cu-based MAO coatings on Ti and its alloys have strong antibacterial properties.

## 4.2 Ag-containing MAO coating

Ag is a prevalent metal known for its antibacterial properties. The presence of Ag ions can disrupt the membrane integrity of bacterial cells, leading to their death. Many studies have demonstrated that Ag-containing TiO2 coatings can impede the proliferation and adhesion of bacteria such as *S. aureus* while showing extremely high bactericidal activity against multiple antibacterial strains of *S. aureus* (e.g., USA300), *E. coli* and *Pseudomonas aeruginosa* (*P. aeruginosa*), which can destroy planktonic and adherent bacteria (Sedelnikova et al., 2019; Zhang L. et al., 2020; Zhang et al., 2021c; van Hengel et al., 2020; Zhao et al., 2022).

Through SEM analysis, it was observed the Ag-MAO coating was uniformly covered with micro/nanoporous oxide layers. Furthermore, the surface morphology of the biofunctionalized implants remained unaltered by the addition of AgNPs when compared to pure titanium and pure titanium combined with strontium implants. Results indicated that after 24 h, Ag-MAO coating completely prevented bacteria from adhering to the surface. After 48 h, little to no bacteria was observed on the surface of the Ag-MAO samples, whereas the control group had significant bacterial adhesion. *In vivo* experiments on murine femurs showed that the Ag-MAO samples were effective in eliminating bacterial inoculum

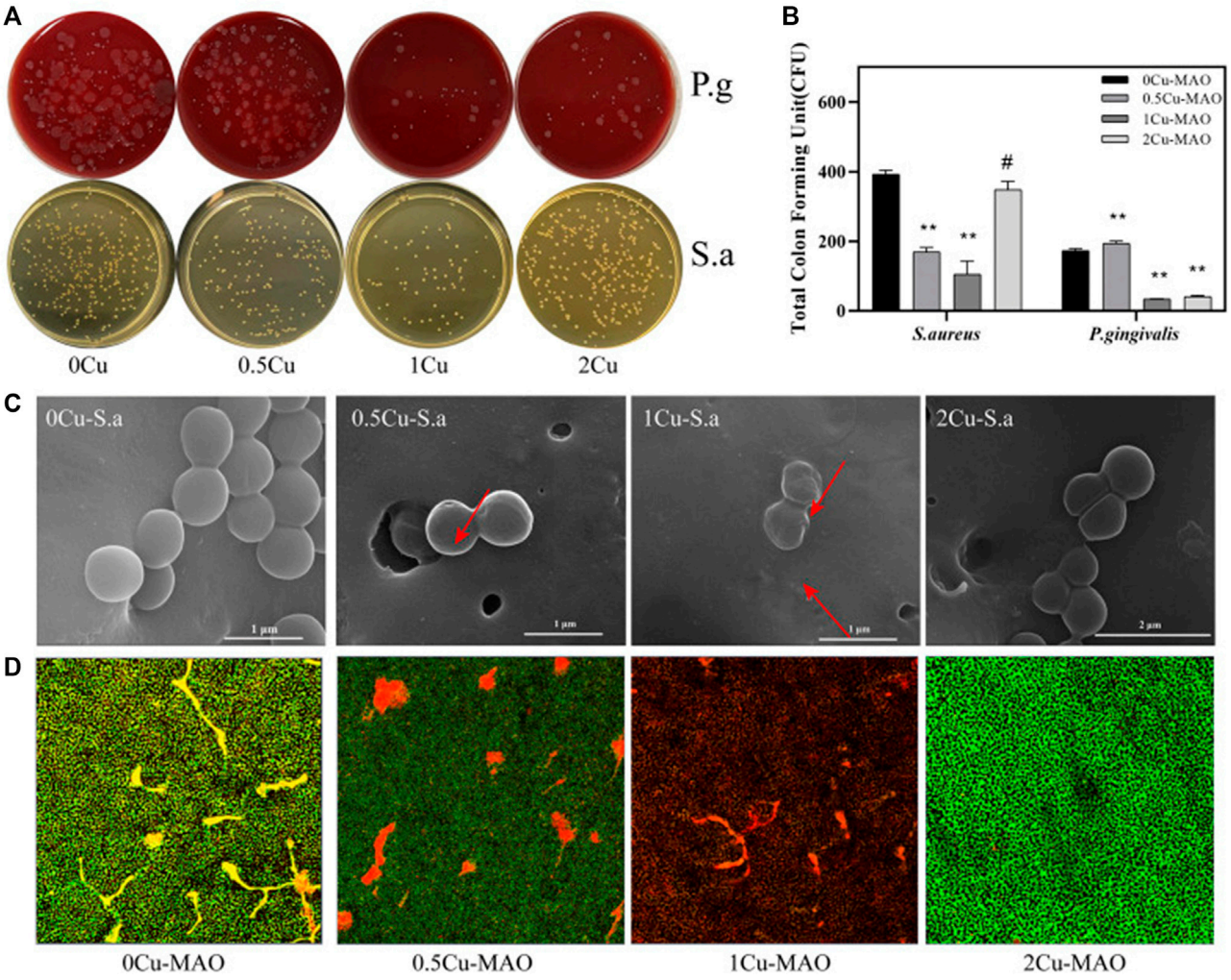


FIGURE 8
Antibacterial activities of Cu-doped coatings against *S. aureus* and P. gingivalis **(A)**; CFU results after *S. aureus* and P. gingivalis were cocultured with the Cu-MAO coating for 24 h. Data are presented as mean ± SD; (**$p < 0.01$, vs. 0Cu-MAO group); **(B)**; Live/Dead assay **(D)** and the corresponding SEM images **(C)** of *S. aureus* cultured on different surface after 24 h of incubation. Source: Reprinted from Ref. (Kang et al., 2022). Copyright © 2022 kang, Lan, Yao, Liu, Chen and Qi, with permission from Frontiers in Bioengineering and Biotechnology.

(Thukkaram et al., 2020). Besides, it has been found that higher concentrations of AgNPs or Ag2O nanoparticles in the electrolyte yield better antibacterial effects for Ag-doped TiO2 coatings. (Lv et al., 2019; Thukkaram et al., 2020). Moreover, TiO2 coatings containing 18.5 wt% Sr and 0.58 wt% Ag showed good osteogenic activity on MC3T3-E1 cells and strong short- and long-term antibacterial effects (Zhang Y.-Y. et al., 2021).

While Ag-rich MAO coatings are highly biocompatible with U2OS cell lines in some studies (Oleshko et al., 2020b), it is important to note that excessive amounts of Ag content can reduce the cytocompatibility of the coating. For instance, coatings synthesised with a concentration of ≥0.001 mol $L^{-1}$ $AgC_2H_3O_2$ to the electrolyte have been shown to harm the proliferation of Saos-2 cells (Teker Aydogan et al., 2018). In their research, Masaya Shimabukuro et al. found that MAO coatings of Ti prepared with an electrolyte containing Ag nitrate at a concentration of 0.04 mm or higher exhibited good antibacterial effects, but when Ag concentration exceeded 2.5 mm, the resulting samples inhibited the activity of MC3T3-E1 cells (Shimabukuro et al., 2019). Therefore, it is crucial to pay attention to the concentration of Ag when using it in the MAO treatment of Ti and its alloys, selecting concentrations that are highly effective against bacteria while still exhibiting biocompatibility.

## 4.3 Zn-containing MAO coating

Zn is an essential trace element for the human body and an important component of superoxide dismutase (Siddiqi et al., 2018). Studies have shown that the incorporation of Zn onto the surface of Ti and its alloys has been shown to not only act as an effective antimicrobial agent but also improve cytocompatibility (Hu et al., 2022; Qin et al., 2022). It was reported that TiO2 coatings significantly inhibited bacterial growth without causing cytotoxicity at concentrations of Zn ions between $10^{-5}$ and $10^{-4}$ M (Zhang et al., 2016).

In addition, Zn was doped on the surface of Ti-15Mo MAO coating, which was found to be effective in reducing the number of attached

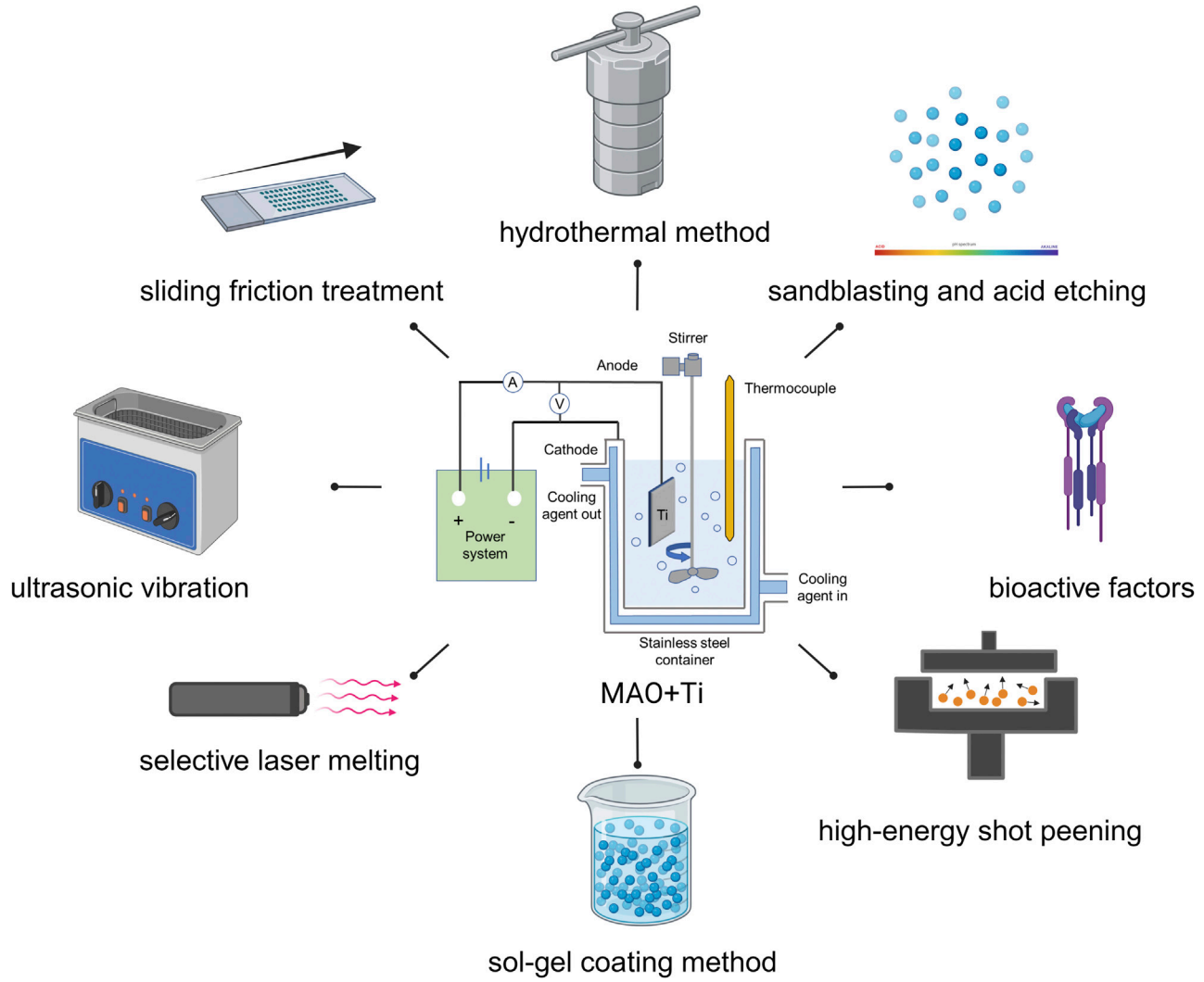


FIGURE 9
Combined application of MAO and other treatment methods. Created with BioRender.com.

*Staphylococcus* epidermidis (ATCC 700296), indicating that Zn can prevent the formation of bacterial biofilm on the implant surface (Leśniak-Ziółkowska et al., 2020). Oleksandr Oleshko et al. used MAO technology to combine ZnO nanoparticles (NPS) with TiZrNb alloys to form high-contact angle ceramic coatings on TiZrNb alloys. Observe the sample with SEM, the surface is covered with an oxide layer, containing small circular holes and craters of various sizes. This coating containing ZnO NP prevents the adhesion of *S. aureus* and significantly improves the antimicrobial properties of TiZrNb alloys (Oleshko et al., 2020a).

## 4.4 Multiple elements-containing MAO coating

Recent research has shown that incorporating multiple elements into MAO coatings can lead to a stronger antibacterial effect than using a single metal element. For instance, $TiO_2$ coatings mixed with both Ag and Zn showed higher antibacterial activity against *S. aureus* than Ti substrates containing only Ag or Zn alone (Lv et al., 2020; Lv et al., 2021b). Cu, Zn, and P were doped into Ti-6Al-4V Ti alloy coatings via MAO, which showed good antibacterial properties against *E. coli*, *S. aureus*, and MRSA (Wang et al., 2020). Meanwhile, $TiO_2$ coatings doped with Mg, Cu, and fluoride (F) elements on the Ti surface were more effective in inhibiting *S. aureus* than pure Ti and oxide coatings containing Mg, Cu, or F alone (Zhao et al., 2019). In addition, doping multiple metal elements into the coatings not only improved the antibacterial properties of Ti and its alloys but also enhanced biocompatibility. For example, co-doping 0.55 wt% Cu and 2.53 wt% Zn further boosted the proliferation of L-929 cells compared to $TiO_2$ doped with 0.77 wt% Cu alone (Zhang et al., 2018a).

Recent studies have revealed that additional elements beyond the usual Cu, Ag, and Zn elements can be added to MAO coatings to confer antibacterial effects on Ti and its alloys. Elements like Zirconium (Zr), Boron (B), Manganese (Mn), Tungsten (W), Yttrium (Y), and Fluorine (F), have demonstrated bactericidal effects against *S. aureus*, *P. aeruginosa*, and *E. coli* (Sopchenski

et al., 2018; Zhou J. et al., 2019; Zhou et al., 2019 T.; Zhang et al., 2020d; Zhang et al., 2020a; Nikoomanzari et al., 2020; Molaei et al., 2022).

In studies evaluating MAO coatings on Ti and its alloys for antibacterial, scholars have also utilized electrolytes containing bioactive elements like $Na_2SiO_3$-$5H_2O$, $C_4H_6O_4Ca$, $NaNO_3$, and $C_3H_7Na_2O_6P$ to form bioactive glass-based coatings (MAO-BG). MAO-BG coatings were found to reduce pathogenic bacteria associated with biofilms and have positive effects on various microbial biofilms. This suggests that incorporating bioactive elements into Ti materials could be a useful way to impart antimicrobial properties (Costa et al., 2020).

To summarize, the incorporation of multiple elements into MAO coatings has the potential to enhance the antimicrobial properties and biocompatibility of Ti and its alloys. In addition to commonly used elements like Cu, Ag, and Zn, alternative elements like Zr, B, Mn, W, Y, and F have shown notable bactericidal effects in MAO coatings. Moreover, MAO-BG coatings formed by electrolytes containing bioactive elements can effectively impart antimicrobial properties to Ti materials and positively impact different microbial biofilms. These discoveries offer novel approaches and concepts for developing more powerful antimicrobial coatings.

# 5 Combined application of MAO and other treatment methods

In modern times, it has been discovered that relying solely on MAO technology may not always suffice for certain biomedical surface modification needs. As a result, researchers have delved into exploring the use of MAO combination with other surface treatment methods, including but not limited to hydrothermal method, sandblasting and acid etching (SLA), selective laser melting (SLM), high-energy shot peening (HESP), sliding friction treatment (SFT), sol-gel coating method (SG), ultrasonic vibration (UV), and bioactive factors (Figure 9). By utilizing a combination of these methods, researchers aim to achieve the desired level of effect (as outlined in Table 2).

## 5.1 The combined application of MAO and hydrothermal method

By subjecting a material to high temperature and pressure, the hydrothermal method activates water molecules to dissolve or react with surface substances. This promotes crystal growth and alters the structure, morphology, and porosity of the material. Recent studies have shown that combining the hydrothermal method with MAO can result in the formation of micro/nano coatings on Ti and its alloys, which possess excellent biocompatibility and bone integration ability (Huang L. et al., 2021). Some studies also indicate that microwave-assisted hydrothermal technology combined with MAO, can regulate stem cell differentiation (Lin et al., 2020). Furthermore, applying HA coating on the Ti surfaces using MAO and hydrothermal steam treatment (SHT) not only shows good biocompatibility but also stimulates endothelial cells to secrete vascular endothelial growth factor, promoting the formation of capillary-like networks and inhibiting inflammation (Wang X. et al., 2021).

## 5.2 The combined application of MAO and SLA

SLA are commonly used method to improve the surface roughness of implants. However, using sharp alumina sand and caustic soda may not completely remove these materials, which may negatively affect bone formation around the implant and interfere with bone bonding. To solve this problem, some researchers have combined large particle sandblasting with MAO to create micro- and submicron-level 3D porous structures on Ti implants. This optimizes surface properties and improves new bone formation and bonding (He et al., 2019). Jinyoung Kim's research on enhancing the surface roughness of Ti by combining sandblasting, acid etching and MAO. The typical crater-like porous structure can be observed under an SEM, which can help enhance the adhesion and differentiation of pre-osteoblasts, ultimately improving the overall biocompatibility (Kim et al., 2021).

## 5.3 The combined application of MAO and HESP

Different from sandblasting technology, shot peening (SP) technology surface cleaning can also enhance residual compressive stress and improve fatigue resistance. In a study conducted by Xinkun Shen et al., Ti substrates were treated with HESP and MAO to create porous $TiO_2$ films containing Ca and P. The results showed that HESP pretreatment improved the stability of $TiO_2$ coating and the bioactivity of MAO-treated samples (Shen et al., 2020c) Furthermore, the research revealed that using HESP-assisted MAO to produce Si/Cu-MAO coatings resulted in osteogenic properties and bactericidal activity against *S. aureus* and *S. mutans* (Shen et al., 2020b).

## 5.4 The combined application of MAO and SFT

SFT technology is widely used to refine the surface grain structure and improve the mechanical properties, as well as to improve the performance and life of biomaterials through severe surface plastic deformation. Yu Sen and other researchers combined SFT with MAO to form a uniform coating with nearly circular or oval crater-like pores of less than one micron on the surface of Ti3Zr2Sn3Mo25Nb alloy. This coating has demonstrated excellent biocompatibility and can promote the attachment and growth of cells (Yu et al., 2022).

## 5.5 The combined application of MAO and SLM

To achieve optimal new bone growth in porous scaffolds, it is crucial to maintain precise control and optimization of pore size, porosity, and connectivity throughout the fabrication process. Recently, SLM has garnered significant attention as an additive manufacturing technique for personalized orthopaedic implant production. Junsi Luo's research team leveraged SLM technology to precisely manufacture Ti alloy implants, using MAO technology to modify their surface for micro/nano-level roughness before

coating them with HA. These novel HA coatings possess appropriate mechanical properties, excellent biocompatibility and bioactivity, and enhanced cell viability *in vitro*, as well as new bone formation *in vivo*. They may be a promising alternative treatment option for high-risk or younger patients in need of more durable implants (Luo et al., 2021). In another study, researchers synthesized porous Ti implants using SLM and functionalized them with Zn and Ag nanoparticles embedded through MAO with Ti oxide layers, effectively preventing implant-associated infections (IAI) caused by antibiotic-resistant bacteria (Iaj et al., 2020).

## 5.6 The combined application of MAO and Sol-gel coating method

Researchers have utilized a sol-gel coating method capable of forming uniform nanofilms on the material surface, resulting in bioactive antimicrobial polymer/Ca-P bio-composites on MAO-modified titanium for dental and orthopaedic implant coatings (Yılmaz, 2021). The findings suggest that the coating promotes cell recruitment and improves cell proliferation during the initial stages of culture, potentially extending the lifespan of the implant (Li R. et al., 2020). To improve the performance of oral implants, researchers used MAO and sol-gel techniques to fabricate a multifunctional composite coating consisting of silica particles and zirconium hydrogen phosphate on the Ti surface, which exhibits higher friction and corrosion resistance, as well as better anti-inflammatory and osteogenic properties (Zhu et al., 2022).

## 5.7 The combined application of MAO and UV

UV is a commonly used auxiliary technique to tune the morphological and structural properties of MAO coatings to enhance their performance. Ultrasound-assisted micro-arc oxidation (UMAO) is a promising surface modification method for fabricating high-quality titanium-based orthopaedic implants. Studies have shown that the use of UV in the MAO process can increase the corrosion resistance and bonding strength of $TiO_2$ coatings, improving their biological properties (Lv et al., 2021a). UMAO can also be used to enhance the corrosion resistance, antimicrobial properties, and cytocompatibility of Cu-doped $TiO_2$ coatings, creating functional surfaces with higher uniformity and performance for biomedical materials (Zhang et al., 2021d). Additionally, UMAO can modify the surface of Ti-Cu alloys to improve their antibacterial properties and cell biocompatibility (Hu et al., 2020).

## 5.8 The combined application of MAO and bioactive factors

Recent research has shown that combining MAO with other bioactive elements such as Bone Morphogenetic Proteins (BMPs), can stimulate new bone formation. However, the effectiveness of BMPs in promoting osteogenesis depends on the careful control of carrier type and release rate. In a study conducted by Teng et al., a unique approach was employed involving 3D printing, MAO treatment, and the coprecipitation of calcium and P layers with BMP-2 technology to fabricate porous titanium alloy-based implants featuring interconnected channel structures.

The growth factor BMP-2 exhibited a continuous diffusion pattern from the central region to the periphery of the implant, thereby facilitating the proliferation, differentiation, and mineralization of bone cells. *In vivo* experiments further revealed the infiltration of bone tissue and blood vessels into the central area of the implant. It was observed that MAO-CaP-BMP-2 outperformed both the MAO and MAO-CaP groups in terms of promoting new bone formation, underscoring the potential of MAO-CaP-BMP2 in enhancing bone healing. As a result, MAO-CaP-BMP2 stands as a promising candidate for applications as a growth factor vector. (Teng et al., 2019).

In addition, some studies have found that a petal-like HA/$TiO_2$ composite coating was prepared on the Ti surface through one-step MAO, and then pure chitosan (CS) was used and BMP-2 respectively loaded with CS coatings on the HA/TiO2 surface using a dip coating method, which can give Ti good antibacterial and biological properties, and the thicker the HA layer, the higher the load of BMP-2 and CS. The larger the amount, the better the bonding strength, antibacterial activity and biocompatibility between coatings. (Wang et al., 2019b).

To sum up, the combined MAO technology with other surface treatment methods has demonstrated immense potential in improving surface properties and enhancing the biological performance of biomedical materials. The integration of MAO with diverse techniques such as hydrothermal method, SLA, HESP, SFT, SLM, sol-gel coating method, UV and bioactive factors has resulted in the development of novel coatings that possess superior biocompatibility, antibacterial properties, corrosion resistance, and osteogenic properties, thereby making them well-suited for orthopaedic and dental implant applications. These advancements hold great promise for enhancing the long-term outcomes of implant surgeries while mitigating associated risks. Continued research and development of these hybrid technologies could lead to further improvements in the field of biomedical surface modification, ultimately benefiting patients worldwide.

# 6 Limitations and future scope

MAO coatings have shown tremendous potential for medical applications, particularly in titanium and its alloys. These coatings enhance surface properties such as biocompatibility, corrosion resistance, wear resistance, and hardness, making them attractive for improving the performance and safety of medical devices. Unfortunately, the use of MAO coatings in medical applications is not without limitations. One major issue is that the coating process can be both expensive and complex, thereby limiting its widespread use. Additionally, the uniformity and thickness of the coating may vary depending on the materials used and the process parameters applied, which can affect the overall performance and reliability of the coating material. Furthermore, while the porous morphologies of MAO coatings theoretically can enhance the bonding between implants and bone tissue, promoting bone tissue growth, the porosity may create channels for accelerated

corrosion ion ($Cl^-$) penetration, thus limiting the application of some biodegradable materials. Therefore, researchers exploring the use of magnesium (Mg) in the biomedical field tend to produce MAO coatings with self-sealing pores.

The parameters of MAO are crucial for producing coatings with excellent performance. Process parameters include electrolyte composition, voltage, current density, frequency, response time, and duty cycle. Parameter control aims to obtain a surface that is uniform, stable, adhesive, and bioactive. Although preliminary research has shown promising results, our understanding of the long-term biocompatibility of MAO coatings remains limited. Further research is needed to evaluate their durability and biocompatibility over time. Regarding antibacterial applications, MAO coatings have great potential to reduce bacterial adhesion and growth. However, the efficacy of these coatings depends on several factors, such as coating thickness, roughness, and bacterial strain. Incorporating high concentrations of metal ions into the coating may have adverse effects on cell biocompatibility, and suitable concentrations need to be investigated. Additionally, further research is needed to explore the mechanisms by which these coatings affect cells and bacteria (Zhang et al., 2018b). Furthermore, MAO may need to be combined with other antibacterial agents and treatments to achieve optimal results. Photodynamic antibacterial therapy is receiving increasing attention due to its bactericidal efficiency and safety being higher than those of metal ions. For example, Han et al. found that a MoS2-modified $TiO_2$ coating prepared using a hybrid process exhibits excellent antibacterial activity when exposed to 808 nm near-infrared light (Han et al., 2021). Scholars also indicate that functional $TiO_2$ coatings co-doped with nitrogen and bismuth achieve antibacterial effects under visible light with good biocompatibility and reactivation potential (Nagay et al., 2019).

Additionally, Wenyue Yang et al. reported that $TiO_2$ nanoparticles can be incorporated into the β titanium alloy Ti-35Nb-2Ta-3Zr (TNTZ) matrix using friction stir processing (FSP) as a bioactive reinforcement, which can build an integrated micro-nano composite layer that facilitates the adhesion and proliferation of BMSCs (Yang et al., 2023). Therefore, MAO technology can be considered in the future to build micro-nanostructures on the surface of titanium alloys.

In summary, despite these limitations, researchers continue to explore methods for optimizing coatings, developing new materials and formulations, and combining MAO with other physical and chemical methods to improve its biocompatibility, antibacterial properties, and other properties. This technology has tremendous potential in enhancing the safety and performance of medical biomaterials made from titanium and its alloys.

## 7 Conclusion

In this review, we delve into recent advancements in the biomedical application of MAO coatings for Ti and its alloys. We focus specifically on process parameters, biocompatibility, antibacterial properties and combinations with other technical aspects. Our conclusions are summarized below:

1) We analyse various process parameters such as electrolyte composition, voltage, and current, that can influence the characteristics of MAO coatings, including their surface roughness, porosity, structure, and morphology attributes.
2) We emphasize the importance of studying the biocompatibility of MAO coatings for Ti and its alloys. Our findings suggest that these coatings have significant potential to enhance cell compatibility, blood compatibility, corrosion resistance, angiogenesis activity, osteogenic activity, and bone integration.
3) Another aspect we highlight is the incorporation of metal elements, such as Cu, Ag, and Zn into MAO coatings. This integration is proven to be an effective technique for imparting antibacterial properties to Ti and its alloys.
4) We discuss several pretreatment and posttreatment hybrid technologies developed to improve the biological properties of MAO coatings. The combination of MAO with hydrothermal methods, SLA, HESP, SFT, SLM, the sol-gel coating method, UV, and bioactive factors provide advantages over using individual techniques.
5) Finally, while considerable progress has been made in researching bioactive MAO coatings on Ti and its alloys, several challenges still need to be addressed. Specifically, further understanding of the mechanism of MAO is needed to facilitate its wider adoption in the industry.

In our review, we emphasize the enormous potential of micro-arc oxidation coatings in improving performance and expanding the applications of titanium and its alloys. In addition, it emphasizes the continuous necessity of MAO technology research in the field of biomedicine. To further promote the application of Ti and its alloys in medical applications, we suggest that future researchers focus on real-world application scenarios, delve into the complex mechanisms behind MAO coatings, and strive to advance this field.

Reducing the gap between laboratory findings and actual medicine is the future research direction. Understanding the complex interactions between MAO coatings and biological systems at the molecular level not only helps to develop customized coatings but also promotes the safe and effective integration of titanium-based materials in the human body. In addition, collaborative efforts bringing together materials scientists, biologists, medical practitioners, and engineers will play a crucial role in promoting the transformation of MAO-coated titanium and its alloys into innovative medical devices and implants. These interdisciplinary methods can bring breakthroughs, redefine the prospects of medical technology, provide enhanced treatment for patients, and improve their quality of life.

In summary, our review serves as a catalyst, and it highlights the potential and necessity for research in the field of micro-arc oxidation coatings on titanium and its alloys. It is through joint efforts and a deeper understanding of basic science that we can fully utilize the capabilities of MAO technology, completely transform biomedical applications, and usher in a new era of medical innovation.

## Author contributions

XW: Conceptualization, Investigation, Visualization, Writing–original draft, Writing–review and editing. YL: Investigation, Resources, Writing–review and editing. FX: Investigation, Visualization, Writing–review and editing. XZ: Investigation, Resources, Writing–review and editing. YK: Funding acquisition, Project administration, Supervision, Writing–review and editing.

## Funding

The authors declare financial support was received for the research, authorship, and/or publication of this article. This work was supported by the National Natural Science Foundation of China (82002886), and the Shenyang Science and Technology Plan Project (21-173-9-40).

## Conflict of interest

The authors declare that the research was conducted in the absence of any commercial or financial relationships that could be construed as a potential conflict of interest.

## Publisher's note

All claims expressed in this article are solely those of the authors and do not necessarily represent those of their affiliated organizations, or those of the publisher, the editors and the reviewers. Any product that may be evaluated in this article, or claim that may be made by its manufacturer, is not guaranteed or endorsed by the publisher.

## Supplementary material

The Supplementary Material for this article can be found online at: https://www.frontiersin.org/articles/10.3389/fbioe.2023.1282590/full#supplementary-material

## References

Anderson, L. A., Christie, M., Blackburn, B. E., Mahan, C., Earl, C., Pelt, C. E., et al. (2021). 3D-printed titanium metaphyseal cones in revision total knee arthroplasty with cemented and cementless stems. *Bone Jt. J.* 103-B, 150–157. doi:10.1302/0301-620X.103B6.BJJ-2020-2504.R1

Antunes, R. A., and de Oliveira, M. C. L. (2009). Corrosion processes of physical vapor deposition-coated metallic implants. *Crit. Rev. Biomed. Eng.* 37, 425–460. doi:10.1615/critrevbiomedeng.v37.i6.10

Attarilar, S., Yang, J., Ebrahimi, M., Wang, Q., Liu, J., Tang, Y., et al. (2020). The toxicity phenomenon and the related occurrence in metal and metal oxide nanoparticles: a brief review from the biomedical perspective. *Front. Bioeng. Biotechnol.* 8, 822. doi:10.3389/fbioe.2020.00822

Azzouz, I., Khlifi, K., Faure, J., Dhiflaoui, H., Larbi, A. B. C., and Benhayoune, H. (2022). Mechanical behavior and corrosion resistance of sol-gel derived 45S5 bioactive glass coating on Ti6Al4V synthesized by electrophoretic deposition. *J. Mech. Behav. Biomed. Mater.* 134, 105352. doi:10.1016/j.jmbbm.2022.105352

Chen, H.-T., Lin, H.-I., Chung, C.-J., Tang, C.-H., and He, J.-L. (2021). Osseointegrating and phase-oriented micro-arc-oxidized titanium dioxide bone implants. *J. Appl. Biomaterials Funct. Mater.* 19. doi:10.1177/22808000211006878

Chen, Z., Yan, X., Chang, Y., Xie, S., Ma, W., Zhao, G., et al. (2019). Effect of polarization voltage on the surface componentization and biocompatibility of micro-arc oxidation modified selective laser melted Ti6Al4V. *Mater. Res. Express* 6, 086425. doi:10.1088/2053-1591/ab1abc

Costa, R. C., Souza, J. G. S., Cordeiro, J. M., Bertolini, M., de Avila, E. D., Landers, R., et al. (2020). Synthesis of bioactive glass-based coating by plasma electrolytic oxidation: untangling a new deposition pathway toward titanium implant surfaces. *J. Colloid Interface Sci.* 579, 680–698. doi:10.1016/j.jcis.2020.06.102

Ding, M., Shi, J., Wang, W., Li, D., and Tian, L. (2022). Early osseointegration of micro-arc oxidation coated titanium alloy implants containing Ag: a histomorphometric study. *BMC Oral Health* 22, 628. doi:10.1186/s12903-022-02673-6

Du, Q., Wei, D., Wang, S., Cheng, S., Wang, Y., Li, B., et al. (2019). Rapidly formation of the highly bioactive surface with hydroxyapatite crystals on the titania micro arc oxidation coating by microwave hydrothermal treatment. *Appl. Surf. Sci.* 487, 708–718. doi:10.1016/j.apsusc.2019.05.165

Du, Q., Wei, D., Wang, Y., Cheng, S., Liu, S., Zhou, Y., et al. (2018). The effect of applied voltages on the structure, apatite-inducing ability and antibacterial ability of micro arc oxidation coating formed on titanium surface. *Bioact. Mater* 3, 426–433. doi:10.1016/j.bioactmat.2018.06.001

Echeverry-Rendón, M., Galvis, O., Aguirre, R., Robledo, S., Castaño, J. G., and Echeverría, F. (2017). Modification of titanium alloys surface properties by plasma electrolytic oxidation (PEO) and influence on biological response. *J. Mater Sci. Mater Med.* 28, 169. doi:10.1007/s10856-017-5972-x

Fattah-Alhosseini, A., Keshavarz, M. K., Molaei, M., and Gashti, S. O. (2018). Plasma electrolytic oxidation (PEO) process on commercially pure Ti surface: effects of electrolyte on the microstructure and corrosion behavior of coatings. *Metall. Mater Trans. A* 49, 4966–4979. doi:10.1007/s11661-018-4824-8

Ferraris, S., and Spriano, S. (2016). Antibacterial titanium surfaces for medical implants. *Mater Sci. Eng. C Mater Biol. Appl.* 61, 965–978. doi:10.1016/j.msec.2015.12.062

Gabor, R., Doubkova, M., Gorosova, S., Malanik, K., Vandrovcova, M., Cvrcek, L., et al. (2020). Preparation of highly wettable coatings on Ti–6Al–4V ELI alloy for traumatological implants using micro-arc oxidation in an alkaline electrolyte. *Sci. Rep.* 10. doi:10.1038/s41598-020-76448-w

Gan, L., and Pilliar, R. (2004). Calcium phosphate sol–gel-derived thin films on porous-surfaced implants for enhanced osteoconductivity. Part I: synthesis and characterization. *Biomaterials* 25, 5303–5312. doi:10.1016/j.biomaterials.2003.12.038

Grigoriev, S., Peretyagin, N., Apelfeld, A., Smirnov, A., Yanushevich, O., Krikheli, N., et al. (2022). Investigation of MAO coatings characteristics on titanium products obtained by EBM method using additive manufacturing. *Materials* 15, 4535. doi:10.3390/ma15134535

Gross, T. M., Lahiri, J., Golas, A., Luo, J., Verrier, F., Kurzejewski, J. L., et al. (2019). Copper-containing glass ceramic with high antimicrobial efficacy. *Nat. Commun.* 10, 1979. doi:10.1038/s41467-019-09946-9

Han, J., Cheng, Y., Tu, W., Zhan, T.-Y., and Cheng, Y. (2018). The black and white coatings on Ti-6Al-4V alloy or pure titanium by plasma electrolytic oxidation in concentrated silicate electrolyte. *Appl. Surf. Sci.* 428, 684–697. doi:10.1016/j.apsusc.2017.09.109

Han, X., Zhang, G., Chai, M., and Zhang, X. (2021). Light-assisted therapy for biofilm infected micro-arc oxidation TiO2 coating on bone implants. *Biomed. Mater.* 16, 025018. doi:10.1088/1748-605X/abdb72

He, W., Yin, X., Xie, L., Liu, Z., Li, J., Zou, S., et al. (2019). Enhancing osseointegration of titanium implants through large-grit sandblasting combined with micro-arc oxidation surface modification. *J. Mater Sci. Mater Med.* 30, 73. doi:10.1007/s10856-019-6276-0

He, X., Zhang, G., Zhang, H., Hang, R., Huang, X., Yao, X., et al. (2020). Cu and Si co-doped microporous TiO2 coating for osseointegration by the coordinated stimulus action. *Appl. Surf. Sci.* 503, 144072. doi:10.1016/j.apsusc.2019.144072

Hoque, M. E., Showva, N. N., Ahmed, M., Rashid, A. B., Sadique, S. E., El-Bialy, T., et al. (2022). Titanium and titanium alloys in dentistry: current trends, recent developments, and future prospects. *Heliyon* 8, e11300. doi:10.1016/j.heliyon.2022.e11300

Hsieh, M.-F., Perng, L.-H., and Chin, T.-S. (2002). Hydroxyapatite coating on Ti6Al4V alloy using a sol–gel derived precursor. *Mater. Chem. Phys.* 74, 245–250. doi:10.1016/S0254-0584(01)00474-6

Hu, J., Li, H., Wang, X., Yang, L., Chen, M., Wang, R., et al. (2020). Effect of ultrasonic micro-arc oxidation on the antibacterial properties and cell biocompatibility of Ti-Cu alloy for biomedical application. *Mater Sci. Eng. C Mater Biol. Appl.* 115, 110921. doi:10.1016/j.msec.2020.110921

Hu, Y., Zhou, H., Liu, T., Yang, M., Zhang, Q., Pan, C., et al. (2022). Construction of mussel-inspired dopamine-Zn2+ coating on titanium oxide nanotubes to improve hemocompatibility, cytocompatibility, and antibacterial activity. *Front. Bioeng. Biotechnol.* 10, 884258. doi:10.3389/fbioe.2022.884258

Hu, Z., Cai, J., Song, G., Tian, Y., and Zhou, M. (2021). Anodic oxidation of organic pollutants: anode fabrication, process hybrid and environmental applications. *Curr. Opin. Electrochem.* 26, 100659. doi:10.1016/j.coelec.2020.100659

Huang, C., Li, H., Li, D., and Lin, S. (2021a). The performance of titanium composite coatings obtained through thermal spraying and microarc oxidation. *Compos. Adv. Mater.* 30, 2633366X20974686. doi:10.1177/2633366X20974686

Huang, J., Jiang, Y., Lin, W., Chen, R., Zhou, J., Guo, S., et al. (2023). Virulence and adhesion of the *Treponema pallidum nichols* strain simultaneously decrease in a continuous-infection New Zealand white rabbit model. *ACS Infect. Dis.* 9, 1221–1231. doi:10.1021/acsinfecdis.2c00601

Huang, L., Cai, B., Huang, Y., Wang, J., Zhu, C., Shi, K., et al. (2021b). Comparative study on 3D printed Ti6Al4V scaffolds with surface modifications using hydrothermal treatment and microarc oxidation to enhance osteogenic activity. *ACS Omega* 6, 1465–1476. doi:10.1021/acsomega.0c05191

Huang, Q., Li, X., Elkhooly, T. A., Liu, X., Zhang, R., Wu, H., et al. (2018). The Cu-containing TiO2 coatings with modulatory effects on macrophage

polarization and bactericidal capacity prepared by micro-arc oxidation on titanium substrates. *Colloids Surfaces B Biointerfaces* 170, 242–250. doi:10.1016/j.colsurfb.2018.06.020

Hussein, R. O., Nie, X., and Northwood, D. O. (2013). An investigation of ceramic coating growth mechanisms in plasma electrolytic oxidation (PEO) processing. *Electrochimica Acta* 112, 111–119. doi:10.1016/j.electacta.2013.08.137

Iaj, van H., Ne, P., Mwam, T., Minneboo, M., Ac, F., Le, F.-A., et al. (2020). Biofunctionalization of selective laser melted porous titanium using silver and zinc nanoparticles to prevent infections by antibiotic-resistant bacteria. *Acta biomater.* 107. doi:10.1016/j.actbio.2020.02.044

Ishikawa, K., Garskaite, E., and Kareiva, A. (2020). Sol–gel synthesis of calcium phosphate-based biomaterials—a review of environmentally benign, simple, and effective synthesis routes. *J. Sol-Gel Sci. Technol.* 94, 551–572. doi:10.1007/s10971-020-05245-8

Ji, Z., Zheng, J., Ma, Y., Lei, H., Lin, W., Huang, J., et al. (2023). Emergency treatment and photoacoustic assessment of spinal cord injury using reversible dual-signal transform-based selenium antioxidant. *Small* 19, 2207888. doi:10.1002/smll.202207888

Jiang, J. Y., Xu, J. L., Liu, Z. H., Deng, L., Sun, B., Liu, S. D., et al. (2015). Preparation, corrosion resistance and hemocompatibility of the superhydrophobic TiO2 coatings on biomedical Ti-6Al-4V alloys. *Appl. Surf. Sci.* 347, 591–595. doi:10.1016/j.apsusc.2015.04.075

Jiang, Y., Wang, J., Hu, B., Yao, Z., Xia, Q., and Jiang, Z. (2016). Preparation of a novel yellow ceramic coating on Ti alloys by plasma electrolytic oxidation. *Surf. Coatings Technol.* 307, 1297–1302. doi:10.1016/j.surfcoat.2016.05.027

Kang, B., Lan, D., Yao, C., Liu, P., Chen, X., and Qi, S. (2022). Evaluation of antibacterial property and biocompatibility of Cu doped TiO2 coated implant prepared by micro-arc oxidation. *Front. Bioeng. Biotechnol.* 10, 941109. doi:10.3389/fbioe.2022.941109

Kaseem, M., Fatimah, S., Nashrah, N., and Ko, Y. G. (2021). Recent progress in surface modification of metals coated by plasma electrolytic oxidation: principle, structure, and performance. *Prog. Mater. Sci.* 117, 100735. doi:10.1016/j.pmatsci.2020.100735

Kaseem, M., and Ko, Y. G. (2019a). Effect of starch on the corrosion behavior of Al-Mg-Si alloy processed by micro arc oxidation from an ecofriendly electrolyte system. *Bioelectrochemistry* 128, 133–139. doi:10.1016/j.bioelechem.2019.04.004

Kaseem, M., and Ko, Y. G. (2019b). Morphological modification and corrosion response of MgO and Mg3(PO4)2 composite formed on magnesium alloy. *Compos. Part B Eng.* 176, 107225. doi:10.1016/j.compositesb.2019.107225

Kaur, M., and Singh, K. (2019). Review on titanium and titanium based alloys as biomaterials for orthopaedic applications. *Mater Sci. Eng. C Mater Biol. Appl.* 102, 844–862. doi:10.1016/j.msec.2019.04.064

Khorasanian, M., Dehghan, A., Shariat, M. H., Bahrololoom, M. E., and Javadpour, S. (2011). Microstructure and wear resistance of oxide coatings on Ti–6Al–4V produced by plasma electrolytic oxidation in an inexpensive electrolyte. *Surf. Coatings Technol.* 206, 1495–1502. doi:10.1016/j.surfcoat.2011.09.038

Kim, J., Lee, H., Jang, T.-S., Kim, D., Yoon, C.-B., Han, G., et al. (2021). Characterization of titanium surface modification strategies for osseointegration enhancement. *Metals* 11, 618. doi:10.3390/met11040618

Klein, M., Kuhn, Y., Woelke, E., Linde, T., Ptock, C., Kopp, A., et al. (2020). *In vitro* study on the hemocompatibility of plasma electrolytic oxidation coatings on titanium substrates. *Artif. Organs* 44, 419–427. doi:10.1111/aor.13592

Komarova, E. G., Sharkeev, Y. P., Sedelnikova, M. B., Prosolov, K. A., Khlusov, I. A., Prymak, O., et al. (2020a). Zn- or Cu-containing CaP-based coatings formed by Micro-arc oxidation on titanium and Ti-40Nb alloy: part I—microstructure, composition and properties. *Materials* 13, 4116. doi:10.3390/ma13184116

Komarova, E. G., Sharkeev, Y. P., Sedelnikova, M. B., Prymak, O., Epple, M., Litvinova, L. S., et al. (2020b). Zn- or Cu-containing CaP-based coatings formed by Micro-Arc oxidation on titanium and Ti-40Nb alloy: part II—wettability and biological performance. *Materials* 13. doi:10.3390/ma13194366

Kostelac, L., Pezzato, L., Settimi, A. G., Franceschi, M., Gennari, C., Brunelli, K., et al. (2022). Investigation of hydroxyapatite (HAP) containing coating on grade 2 titanium alloy prepared by plasma electrolytic oxidation (PEO) at low voltage. *Surfaces Interfaces* 30, 101888. doi:10.1016/j.surfin.2022.101888

Lederer, S., Arat, S., and Fuerbeth, W. (2021). Influence of process parameters on the tribological behavior of PEO coatings on CP-titanium 4+ alloys for biomedical applications. *Mater. (Basel, Switz.* 14. doi:10.3390/ma14185364

Le Guéhennec, L., Soueidan, A., Layrolle, P., and Amouriq, Y. (2007). Surface treatments of titanium dental implants for rapid osseointegration. *Dent. Mater* 23, 844–854. doi:10.1016/j.dental.2006.06.025

Leśniak-Ziółkowska, K., Kazek-Kęsik, A., Rokosz, K., Raaen, S., Stolarczyk, A., Krok-Borkowicz, M., et al. (2020). Electrochemical modification of the Ti-15Mo alloy surface in solutions containing ZnO and Zn3(PO4)2 particles. *Mater. Sci. Eng. C* 115, 111098. doi:10.1016/j.msec.2020.111098

Li, G., Ma, F., Liu, P., Qi, S., Li, W., Zhang, K., et al. (2023). Review of micro-arc oxidation of titanium alloys: mechanism, properties and applications. *J. Alloys Compd.* 948, 169773. doi:10.1016/j.jallcom.2023.169773

Li, R., Wei, Y., Gu, L., Qin, Y., and Li, D. (2020a). Sol–gel-assisted micro-arc oxidation synthesis and characterization of a hierarchically rough structured Ta–Sr coating for biomaterials. *RSC Adv.* 10, 20020–20027. doi:10.1039/D0RA01079K

Li, X., Wang, M., Zhang, W., Bai, Y., Liu, Y., Meng, J., et al. (2020b). A magnesium-incorporated nanoporous titanium coating for rapid osseointegration. *Int. J. Nanomedicine* 15, 6593–6603. doi:10.2147/IJN.S255486

Li, X., Xu, H., Zhao, B., and Jiang, S. (2018). Accelerated and enhanced osteointegration of MAO-treated implants: histological and histomorphometric evaluation in a rabbit model. *Int. J. Oral Sci.* 10, 11. doi:10.1038/s41368-018-0008-z

Li, Y., Wang, W., Yu, F., Wang, D., Guan, S., Li, Y., et al. (2020c). Characterization and cytocompatibility of hierarchical porous TiO(2) coatings incorporated with calcium and strontium by one-step micro-arc oxidation. *Mater Sci. Eng. C Mater Biol. Appl.* 109, 110610. doi:10.1016/j.msec.2019.110610

Li, Z., Cai, Z., Ding, Y., Cui, X.-J., Yang, Z., and Zhu, M. (2020d). Characterization of graphene oxide/ZrO2 composite coatings deposited on zirconium alloy by micro-arc oxidation. *Appl. Surf. Sci.* 506, 144928. doi:10.1016/j.apsusc.2019.144928

Liang, T., Wang, Y., Zeng, L., Liu, Y., Qiao, L., Zhang, S., et al. (2020). Copper-doped 3D porous coating developed on Ti-6Al-4V alloys and its *in vitro* long-term antibacterial ability. *Appl. Surf. Sci.* 509, 144717. doi:10.1016/j.apsusc.2019.144717

Liao, S.-C., Chang, C.-T., Chen, C.-Y., Lee, C.-H., and Lin, W.-L. (2020). Functionalization of pure titanium MAO coatings by surface modifications for biomedical applications. *Surf. Coatings Technol.* 394, 125812. doi:10.1016/j.surfcoat.2020.125812

Lim, H. K., Choi, Y. J., Choi, W. C., Song, I. S., and Lee, U. L. (2022). Reconstruction of maxillofacial bone defects using patient-specific long-lasting titanium implants. *Sci. Rep.* 12, 7538. doi:10.1038/s41598-022-11200-0

Lin, D.-J., Fuh, L.-J., and Chen, W.-C. (2020). Nano-morphology, crystallinity and surface potential of anatase on micro-arc oxidized titanium affect its protein adsorption, cell proliferation and cell differentiation. *Mater. Sci. Eng. C* 107, 110204. doi:10.1016/j.msec.2019.110204

Lin, W., Huang, J., Guo, S., Zhao, M., Chen, X., Shang, Q., et al. (2023). A tunable fluorescent probe for superoxide anion detection during inflammation caused by *Treponema pallidum*. *J. Mater. Chem. B* 11, 4523–4528. doi:10.1039/D3TB00747B

Liu, Y.-C., Lin, G.-S., Lee, Y.-T., Huang, T.-C., Chang, T.-W., Chen, Y.-W., et al. (2020). Microstructures and cell reaction of porous hydroxyapatite coatings on titanium discs using a novel vapour-induced pore-forming atmospheric plasma spraying. *Surf. Coatings Technol.* 393, 125837. doi:10.1016/j.surfcoat.2020.125837

Lu, W., Zhou, Y., Yang, H., Cheng, Z., and He, F. (2022a). Efficacy of strontium supplementation on implant osseointegration under osteoporotic conditions: a systematic review. *J. Prosthet. Dent.* 128, 341–349. doi:10.1016/j.prosdent.2020.12.031

Lu, X., Zhang, T., Lv, Y., Zhang, X., and Dong, Z. (2022b). Corrosion behviour of micro-arc oxidized titanium in NaCl solution with H2O2 and albumin. *Mater. Chem. Phys.* 276, 125376. doi:10.1016/j.matchemphys.2021.125376

Lugovskoy, A., and Lugovskoy, S. (2014). Production of hydroxyapatite layers on the plasma electrolytically oxidized surface of titanium alloys. *Mater. Sci. Eng. C* 43, 527–532. doi:10.1016/j.msec.2014.07.030

Luo, J., Wu, Z., Dai, Y., Wang, X., Ye, R., Huang, H., et al. (2021). Biofunctional micro/nanostructured "volcano-like" layer-coated 3D porous Ti-10Ta-2Nb-2Zr scaffolds improve osteogenesis and osseointegration for dental implants *in vitro* and *in vivo*. *Surf. Coatings Technol.* 427, 127852. doi:10.1016/j.surfcoat.2021.127852

Lv, Y., Cai, G., Zhang, X., Fu, S., Zhang, E., Yang, L., et al. (2020). Microstructural characterization and *in vitro* biological performances of Ag, Zn co-incorporated TiO2 coating. *Ceram. Int.* 46, 29160–29172. doi:10.1016/j.ceramint.2020.08.089

Lv, Y., Sun, S., Zhang, X., Lu, X., and Dong, Z. (2021a). Construction of multi-layered Zn-modified TiO2 coating by ultrasound-auxiliary micro-arc oxidation: microstructure and biological property. *Mater. Sci. Eng. C* 131, 112487. doi:10.1016/j.msec.2021.112487

Lv, Y., Wu, Y., Lu, X., Yu, Y., Fu, S., Yang, L., et al. (2019). Microstructure, bio-corrosion and biological property of Ag-incorporated TiO2 coatings: influence of Ag2O contents. *Ceram. Int.* 45, 22357–22367. doi:10.1016/j.ceramint.2019.07.265

Lv, Y., Zhang, T., Zhang, X., Fu, S., Yang, L., Dong, Z., et al. (2021b). The synergistic effect of Ag and ZnO on the microstructure, corrosion resistance and *in vitro* biological performance of titania coating. *Surf. Coatings Technol.* 426, 127798. doi:10.1016/j.surfcoat.2021.127798

Mashtalyar, D. V., Nadaraia, K. V., Gnedenkov, A. S., Imshinetskiy, I. M., Piatkova, M. A., Pleshkova, A. I., et al. (2020). Bioactive coatings formed on titanium by plasma electrolytic oxidation: composition and properties. *Mater. (Basel)* 13, 4121. doi:10.3390/ma13184121

Molaei, M., Fattah-Alhosseini, A., and Keshavarz, M. K. (2019). Influence of different sodium-based additives on corrosion resistance of PEO coatings on pure Ti. *J. Asian Ceram. Soc.* 7, 247–255. doi:10.1080/21870764.2019.1604609

Molaei, M., Fattah-alhosseini, A., Nouri, M., Mahmoodi, P., Navard, S. H., and Nourian, A. (2022). Enhancing cytocompatibility, antibacterial activity and corrosion resistance of PEO coatings on titanium using incorporated ZrO2 nanoparticles. *Surfaces Interfaces* 30, 101967. doi:10.1016/j.surfin.2022.101967

Molaeipour, P., Allahkaram, S. R., and Akbarzadeh, S. (2022). Corrosion inhibition of Ti6Al4V alloy by a protective plasma electrolytic oxidation coating modified with boron carbide nanoparticles. *Surf. Coatings Technol.* 430, 127987. doi:10.1016/j.surfcoat.2021.127987

Muntean, R., Brîndușoiu, M., Buzdugan, D., Nemeș, N. S., Kellenberger, A., and Uțu, I. D. (2023). Characteristics of hydroxyapatite-modified coatings based on TiO2 obtained by plasma electrolytic oxidation and electrophoretic deposition. *Mater. (Basel)* 16, 1410. doi:10.3390/ma16041410

Nadimi, M., and Dehghanian, C. (2021). Incorporation of ZnO–ZrO2 nanoparticles into TiO2 coatings obtained by PEO on Ti–6Al–4V substrate and evaluation of its corrosion behavior, microstructural and antibacterial effects exposed to SBF solution. *Ceram. Int.* 47, 33413–33425. doi:10.1016/j.ceramint.2021.08.248

Nagay, B. E., Dini, C., Cordeiro, J. M., Ricomini-Filho, A. P., de Avila, E. D., Rangel, E. C., et al. (2019). Visible-light-Induced photocatalytic and antibacterial activity of TiO2 codoped with nitrogen and bismuth: new perspectives to control implant-biofilm-related diseases. *ACS Appl. Mater. Interfaces* 11, 18186–18202. doi:10.1021/acsami.9b03311

Ni, R., Jing, Z., Xiong, C., Meng, D., Wei, C., and Cai, H. (2022). Effect of micro-arc oxidation surface modification of 3D-printed porous titanium alloys on biological properties. *Ann. Transl. Med.* 10, 710. doi:10.21037/atm-22-2536

Nikoomanzari, E., Fattah-alhosseini, A., Pajohi Alamoti, M. R., and Keshavarz, M. K. (2020). Effect of ZrO2 nanoparticles addition to PEO coatings on Ti–6Al–4V substrate: microstructural analysis, corrosion behavior and antibacterial effect of coatings in Hank's physiological solution. *Ceram. Int.* 46, 13114–13124. doi:10.1016/j.ceramint.2020.02.084

Oh-Hyun, C., In-Gyu, B., Mi, M., Yeon, P., Gyung, Y., and Nae, Y. (2018). Therapeutic outcome of spinal implant infections caused by *Staphylococcus aureus* A retrospective observational study. *Medicine* 97. doi:10.1097/MD.0000000000012629

Oleshko, O., Husak, Y., Korniienko, V., Pshenychnyi, R., Varava, Y., Kalinkevich, O., et al. (2020a). Biocompatibility and antibacterial properties of ZnO-incorporated anodic oxide coatings on TiZrNb alloy. *Nanomaterials* 10, 2401. doi:10.3390/nano10122401

Oleshko, O., Liubchak, I., Husak, Y., Korniienko, V., Yusupova, A., Oleshko, T., et al. (2020b). *In vitro* biological characterization of silver-doped anodic oxide coating on titanium. *Materials* 13. doi:10.3390/ma13194359

Pan, X., Li, Y., Abdullah, A. O., Wang, W., Qi, M., and Liu, Y. (2019). Micro/nano-hierarchical structured TiO2 coating on titanium by micro-arc oxidation enhances osteoblast adhesion and differentiation. *R. Soc. Open Sci.* 6, 182031. doi:10.1098/rsos.182031

Pesode, P., and Barve, S. (2021). Surface modification of titanium and titanium alloy by plasma electrolytic oxidation process for biomedical applications: a review. *Mater. Today Proc.* 46, 594–602. doi:10.1016/j.matpr.2020.11.294

Qin, Y., Yang, H., Liu, A., Dai, J., Wen, P., Zheng, Y., et al. (2022). Processing optimization, mechanical properties, corrosion behavior and cytocompatibility of additively manufactured Zn-0.7Li biodegradable metals. *Acta Biomater.* 142, 388–401. doi:10.1016/j.actbio.2022.01.049

Rautray, T. R., Narayanan, R., Kwon, T.-Y., and Kim, K.-H. (2010). Surface modification of titanium and titanium alloys by ion implantation. *J. Biomed. Mater. Res. Part B Appl. Biomaterials* 93B, 581–591. doi:10.1002/jbm.b.31596

Rokosz, K., Hryniewicz, T., Kacalak, W., Tandecka, K., Raaen, S., Gaiaschi, S., et al. (2020). Porous coatings containing copper and phosphorus obtained by plasma electrolytic oxidation of titanium. *Mater. (Basel)* 13, 828. doi:10.3390/ma13040828

Santos-Coquillat, A., Mohedano, M., Martinez-Campos, E., Arrabal, R., Pardo, A., and Matykina, E. (2019). Bioactive multi-elemental PEO-coatings on titanium for dental implant applications. *Mater. Sci. Eng. C* 97, 738–752. doi:10.1016/j.msec.2018.12.097

Sarbishei, S., Faghihi Sani, M. A., and Mohammadi, M. R. (2014). Study plasma electrolytic oxidation process and characterization of coatings formed in an alumina nanoparticle suspension. *Vacuum* 108, 12–19. doi:10.1016/j.vacuum.2014.05.008

Sasikumar, Y., Indira, K., and Rajendran, N. (2019). Surface modification methods for titanium and its alloys and their corrosion behavior in biological environment: a review. *J. Bio Tribo Corros.* 5, 36. doi:10.1007/s40735-019-0229-5

Sedelnikova, M. B., Komarova, E. G., Sharkeev, Y. P., Tolkacheva, T. V., Khlusov, I. A., Litvinova, L. S., et al. (2017). Comparative investigations of structure and properties of micro-arc wollastonite-calcium phosphate coatings on titanium and zirconium-niobium alloy. *Bioact. Mater* 2, 177–184. doi:10.1016/j.bioactmat.2017.01.002

Sedelnikova, M. B., Komarova, E. G., Sharkeev, Y. P., Ugodchikova, A. V., Tolkacheva, T. V., Rau, J. V., et al. (2019). Modification of titanium surface via Ag-, Sr- and Si-containing micro-arc calcium phosphate coating. *Bioact. Mater.* 4, 224–235. doi:10.1016/j.bioactmat.2019.07.001

Seyidaliyeva, A., Rues, S., Evagorou, Z., Hassel, A. J., Büsch, C., Rammelsberg, P., et al. (2022). Predictability and outcome of titanium color after different surface modifications and anodic oxidation. *Dent. Mater. J.* 41, 930–936. doi:10.4012/dmj.2022-075

Shemtov-Yona, K., Rittel, D., and Dorogoy, A. (2014). Mechanical assessment of grit blasting surface treatments of dental implants. *J. Mech. Behav. Biomed. Mater* 39, 375–390. doi:10.1016/j.jmbbm.2014.07.027

Shen, X., Al-Baadani, M. A., He, H., Cai, L., Wu, Z., Yao, L., et al. (2019). Antibacterial and osteogenesis performances of LL37-loaded titania nanopores *in vitro* and *in vivo*. *Int. J. Nanomedicine* 14, 3043–3054. doi:10.2147/IJN.S198583

Shen, X., Fang, K., Ru Yie, K. H., Zhou, Z., Shen, Y., Wu, S., et al. (2022a). High proportion strontium-doped micro-arc oxidation coatings enhance early osseointegration of titanium in osteoporosis by anti-oxidative stress pathway. *Bioact. Mater* 10, 405–419. doi:10.1016/j.bioactmat.2021.08.031

Shen, X., Hu, W., Ping, L., Liu, C., Yao, L., Deng, Z., et al. (2020a). Antibacterial and osteogenic functionalization of titanium with silicon/copper-doped high-energy shot peening-assisted Micro-Arc oxidation technique. *Front. Bioeng. Biotechnol.* 8. doi:10.3389/fbioe.2020.573464

Shen, X., Hu, W., Ping, L., Liu, C., Yao, L., Deng, Z., et al. (2020b). Antibacterial and osteogenic functionalization of titanium with silicon/copper-doped high-energy shot peening-assisted Micro-Arc oxidation technique. *Front. Bioeng. Biotechnol.* 8, 573464. doi:10.3389/fbioe.2020.573464

Shen, X., Ping, L., Wang, L., Liu, C., Liu, J., and Deng, Z. (2020c). Improving the stability and bioactivity of micro-arc oxidized calcium phosphate/titania porous coatings by high energy shot peening pretreatment. *Ceram. Int.* 46, 2041–2048. doi:10.1016/j.ceramint.2019.09.183

Shen, Y., Fang, K., Xiang, Y., Xu, K., Yu, L., Chen, J., et al. (2022b). Improvement in osteogenesis, vascularization, and corrosion resistance of titanium with silicon-nitride doped micro-arc oxidation coatings. *Front. Bioeng. Biotechnol.* 10, 1023032. doi:10.3389/fbioe.2022.1023032

Shimabukuro, M. (2020). Antibacterial property and biocompatibility of silver, copper, and zinc in titanium dioxide layers incorporated by one-step Micro-Arc oxidation: a review. *Antibiot. (Basel)* 9, 716. doi:10.3390/antibiotics9100716

Shimabukuro, M., Hiji, A., Manaka, T., Nozaki, K., Chen, P., Ashida, M., et al. (2020a). Time-transient effects of silver and copper in the porous titanium dioxide layer on antibacterial properties. *J. Funct. Biomater.* 11. doi:10.3390/jfb11020044

Shimabukuro, M., Tsutsumi, Y., Nozaki, K., Chen, P., Yamada, R., Ashida, M., et al. (2020b). Investigation of antibacterial effect of copper introduced titanium surface by electrochemical treatment against facultative anaerobic bacteria. *Dent. Mater. J.* 39, 639–647. doi:10.4012/dmj.2019-178

Shimabukuro, M., Tsutsumi, Y., Yamada, R., Ashida, M., Chen, P., Doi, H., et al. (2019). Investigation of realizing both antibacterial property and osteogenic cell compatibility on titanium surface by simple electrochemical treatment. *ACS Biomater. Sci. Eng.* 5, 5623–5630. doi:10.1021/acsbiomaterials.8b01058

Shokouhfar, M., Dehghanian, C., and Baradaran, A. (2011). Preparation of ceramic coating on Ti substrate by Plasma electrolytic oxidation in different electrolytes and evaluation of its corrosion resistance. *Appl. Surf. Sci.* 257, 2617–2624. doi:10.1016/j.apsusc.2010.10.032

Shokouhfar, M., Dehghanian, C., Montazeri, M., and Baradaran, A. (2012). Preparation of ceramic coating on Ti substrate by plasma electrolytic oxidation in different electrolytes and evaluation of its corrosion resistance: part II. *Appl. Surf. Sci.* 258, 2416–2423. doi:10.1016/j.apsusc.2011.10.064

Siddiqi, K. S., ur Rahman, A., Tajuddin, and Husen, A. (2018). Properties of zinc oxide nanoparticles and their activity against microbes. *Nanoscale Res. Lett.* 13, 141. doi:10.1186/s11671-018-2532-3

Snizhko, L. O., Yerokhin, A. L., Pilkington, A., Gurevina, N. L., Misnyankin, D. O., Leyland, A., et al. (2004). Anodic processes in plasma electrolytic oxidation of aluminium in alkaline solutions. *Electrochimica Acta* 49, 2085–2095. doi:10.1016/j.electacta.2003.11.027

Sobolev, A., Kossenko, A., and Borodianskiy, K. (2019). Study of the effect of current pulse frequency on Ti-6Al-4V alloy coating formation by micro arc oxidation. *Mater. (Basel)* 12, 3983. doi:10.3390/ma12233983

Sopchenski, L., Cogo, S., Dias-Ntipanyj, M. F., Elifio-Espósito, S., Popat, K. C., and Soares, P. (2018). Bioactive and antibacterial boron doped TiO2 coating obtained by PEO. *Appl. Surf. Sci.* 458, 49–58. doi:10.1016/j.apsusc.2018.07.049

Sousa, L., Mendes, A. R., Pinto, A. M. P., Toptan, F., and Alves, A. C. (2021). Influence of calcium acetate concentration in electrolyte on tribocorrosion behaviour of MAO treated titanium. *Metals* 11, 1985. doi:10.3390/met11121985

Sun, J., Han, Y., and Cui, K. (2008). Microstructure and apatite-forming ability of the MAO-treated porous titanium. *Surf. Coatings Technol.* 202, 4248–4256. doi:10.1016/j.surfcoat.2008.03.020

Szmukler-Moncler, S., Perrin, D., Ahossi, V., Magnin, G., and Bernard, J. P. (2004). Biological properties of acid etched titanium implants: effect of sandblasting on bone anchorage. *J. Biomed. Mater. Res. Part B Appl. Biomaterials* 68B, 149–159. doi:10.1002/jbm.b.20003

Tang, Y., Liu, S., Deng, Y., Zhang, Y., Yin, L., and Zheng, W. (2021). An improved method for soft tissue modeling. *Biomed. Signal Process. Control* 65, 102367. doi:10.1016/j.bspc.2020.102367

Teker Aydogan, D., Muhaffel, F., Menekse Kilic, M., Karabiyik Acar, O., Cempura, G., Baydogan, M., et al. (2018). Optimisation of micro-arc oxidation electrolyte for fabrication of antibacterial coating on titanium. *Mater. Technol.* 33, 119–126. doi:10.1080/10667857.2017.1391931

Teng, F.-Y., Tai, I.-C., Ho, M.-L., Wang, J.-W., Weng, L. W., Wang, Y. J., et al. (2019). Controlled release of BMP-2 from titanium with electrodeposition modification

enhancing critical size bone formation. *Mater. Sci. Eng. C* 105, 109879. doi:10.1016/j.msec.2019.109879

Thukkaram, M., Cools, P., Nikiforov, A., Rigole, P., Coenye, T., Van Der Voort, P., et al. (2020). Antibacterial activity of a porous silver doped TiO2 coating on titanium substrates synthesized by plasma electrolytic oxidation. *Appl. Surf. Sci.* 500, 144235. doi:10.1016/j.apsusc.2019.144235

van Hengel, I. A. J., Gelderman, F. S. A., Athanasiadis, S., Minneboo, M., Weinans, H., Fluit, A. C., et al. (2020). Functionality-packed additively manufactured porous titanium implants. *Mater. Today Bio* 7, 100060. doi:10.1016/j.mtbio.2020.100060

Velasco, E., Monsalve-Guil, L., Jimenez, A., Ortiz, I., Moreno-Muñoz, J., Nuñez-Marquez, E., et al. (2016). Importance of the roughness and residual stresses of dental implants on fatigue and osseointegration behavior. *in vivo* study in rabbits. *J. Oral Implant.* 42, 469–476. doi:10.1563/aaid-joi-D-16-00088

Venkateswarlu, K., Rameshbabu, N., Sreekanth, D., Bose, A. C., Muthupandi, V., Babu, N. K., et al. (2012). Role of electrolyte additives on *in-vitro* electrochemical behavior of micro arc oxidized titania films on Cp Ti. *Appl. Surf. Sci.* 258, 6853–6863. doi:10.1016/j.apsusc.2012.03.118

Venkateswarlu, K., Rameshbabu, N., Sreekanth, D., Bose, A. C., Muthupandi, V., Babu, N. K., et al. (2013). Role of electrolyte chemistry on electronic and *in vitro* electrochemical properties of micro-arc oxidized titania films on Cp Ti. *Electrochimica Acta* 105, 468–480. doi:10.1016/j.electacta.2013.05.032

Walsh, F. C., Low, C. T. J., Wood, R. J. K., Stevens, K. T., Archer, J., Poeton, A. R., et al. (2009). Plasma electrolytic oxidation (PEO) for production of anodised coatings on lightweight metal (Al, Mg, Ti) alloys. *Trans. IMF* 87, 122–135. doi:10.1179/174591908X372482

Wang, F., Wang, X., Xie, E., Wang, W., Gan, Q., Li, F., et al. (2022a). Simultaneous incorporation of gallium oxide and tantalum microparticles into micro-arc oxidation coating of titanium possessing antibacterial effect and stimulating cellular response. *Biomater. Adv.* 135. doi:10.1016/j.bioadv.2022.212736

Wang, G., Li, J., Zhang, W., Xu, L., Pan, H., Wen, J., et al. (2014). Magnesium ion implantation on a micro/nanostructured titanium surface promotes its bioactivity and osteogenic differentiation function. *Int. J. Nanomedicine* 9, 2387–2398. doi:10.2147/IJN.S58357

Wang, L. J., Ni, X. H., Zhang, F., Peng, Z., Yu, F. X., Zhang, L. B., et al. (2021a). Osteoblast response to copper-doped microporous coatings on titanium for improved bone integration. *Nanoscale Res. Lett.* 16, 146. doi:10.1186/s11671-021-03602-2

Wang, M.-S., Lee, F.-P., Shen, Y.-D., Chen, C.-H., Ou, K.-L., and Ou, S.-F. (2015a). Surface, biocompatible and hemocompatible properties of meta-amorphous titanium oxide film. *Int. J. Appl. Ceram. Technol.* 12, 341–350. doi:10.1111/ijac.12184

Wang, R., Ni, S., Ma, L., and Li, M. (2022b). Porous construction and surface modification of titanium-based materials for osteogenesis: a review. *Front. Bioeng. Biotechnol.* 10, 973297. doi:10.3389/fbioe.2022.973297

Wang, X., Dong, H., Liu, J., Qin, G., Chen, D., and Zhang, E. (2019a). *In vivo* antibacterial property of Ti-Cu sintered alloy implant. *Mater. Sci. Eng. C* 100, 38–47. doi:10.1016/j.msec.2019.02.084

Wang, X., Li, B., and Zhang, C. (2019b). Preparation of BMP-2/chitosan/hydroxyapatite antibacterial bio-composite coatings on titanium surfaces for bone tissue engineering. *Biomed. Microdevices* 21, 89. doi:10.1007/s10544-019-0437-2

Wang, X., Mei, L., Jiang, X., Jin, M., Xu, Y., Li, J., et al. (2021b). Hydroxyapatite-coated titanium by Micro-Arc oxidation and steam-hydrothermal treatment promotes osseointegration. *Front. Bioeng. Biotechnol.* 9, 625877. doi:10.3389/fbioe.2021.625877

Wang, X., Liu, W., Yu, X., Wang, B., Xu, Y., Yan, X., et al. (2022). Advances in surface modification of tantalum and porous tantalum for rapid osseointegration: a thematic review. *Front. Bioeng. Biotechnol.* 10, 983695. doi:10.3389/fbioe.2022.983695

Wang, Y., Yu, H., Chen, C., and Zhao, Z. (2015b). Review of the biocompatibility of micro-arc oxidation coated titanium alloys. *Mater. Des.* 85, 640–652. doi:10.1016/j.matdes.2015.07.086

Wang, Y., Zhao, S., Li, G., Zhang, S., Zhao, R., Dong, A., et al. (2020). Preparation and *in vitro* antibacterial properties of anodic coatings co-doped with Cu, Zn, and P on a Ti–6Al–4V alloy. *Mater. Chem. Phys.* 241, 122360. doi:10.1016/j.matchemphys.2019.122360

Wang, Z., Cheng, Z., Zhang, Y., Shi, X., Rao, M., and Wu, S. (2023). Effect of voltage on the microstructure and high-temperature oxidation resistance of Micro-Arc oxidation coatings on AlTiCrVZr refractory high-entropy alloy. *Coatings* 13, 14. doi:10.3390/coatings13010014

Wennerberg, A., and Albrektsson, T. (2009). Effects of titanium surface topography on bone integration: a systematic review. *Clin. Oral Implants Res.* 20 (4), 172–184. doi:10.1111/j.1600-0501.2009.01775.x

Wu, M., and Jiang, F. (2023). Effect of Na2SiO3 concentration on corrosion resistance and wear resistance of MAO ceramic film on the Al-Mg-Sc alloy. *Int. J. Appl. Ceram. Technol.* 20. doi:10.1111/ijac.14320

Xia, J., Li, Y., He, C., Yong, C., Wang, L., Fu, H., et al. (2023). Synthesis and biological activities of oxazolidinone pleuromutilin derivatives as a potent anti-MRSA agent. *ACS Infect. Dis.* 9, 1711–1729. doi:10.1021/acsinfecdis.3c00162

Xia, Q., Li, X., Yao, Z., and Jiang, Z. (2021). Investigations on the thermal control properties and corrosion resistance of MAO coatings prepared on Mg-5Y-7Gd-1Nd-0.5Zr alloy. *Surf. Coatings Technol.* 409, 126874. doi:10.1016/j.surfcoat.2021.126874

Xiu, P., Jia, Z., Lv, J., Yin, C., Cheng, Y., Zhang, K., et al. (2016). Tailored surface treatment of 3D printed porous Ti6Al4V by microarc oxidation for enhanced osseointegration via optimized bone in-growth patterns and interlocked bone/implant interface. *ACS Appl. Mater Interfaces* 8, 17964–17975. doi:10.1021/acsami.6b05893

Xu, G., and Shen, X. (2019). Fabrication of SiO2 nanoparticles incorporated coating onto titanium substrates by the micro arc oxidation to improve the wear resistance. *Surf. Coatings Technol.* 364, 180–186. doi:10.1016/j.surfcoat.2019.01.069

Xue, T., Attarilar, S., Liu, S., Liu, J., Song, X., Li, L., et al. (2020). Surface modification techniques of titanium and its alloys to functionally optimize their biomedical properties: thematic review. *Front. Bioeng. Biotechnol.* 8, 603072. doi:10.3389/fbioe.2020.603072

Yang, W., Liu, X., Fang, Y., Attarilar, S., Zhu, C., Wang, L., et al. (2023). Osteogenic differentiation of bone marrow stromal stem cells on a novel β titanium alloy-based micro-nano composite. *J. Mater. Res. Technol.* 24, 5864–5875. doi:10.1016/j.jmrt.2023.04.188

Yang, W., Xu, D., Guo, Q., Chen, T., and Chen, J. (2018). Influence of electrolyte composition on microstructure and properties of coatings formed on pure Ti substrate by micro arc oxidation. *Surf. Coatings Technol.* 349, 522–528. doi:10.1016/j.surfcoat.2018.06.024

Yerokhin, A. L., Nie, X., Leyland, A., and Matthews, A. (2000). Characterisation of oxide films produced by plasma electrolytic oxidation of a Ti–6Al–4V alloy. *Surf. Coatings Technol.* 130, 195–206. doi:10.1016/S0257-8972(00)00719-2

Yılmaz, E. (2021). Modification of the micro arc-oxidized Ti surface for implant applications. *J. Bionic Eng.* 18, 1391–1399. doi:10.1007/s42235-021-00101-z

Yong, J., Li, H., Li, Z., Chen, Y., Wang, Y., and Geng, J. (2021). Effect of (NH4)2ZrF6, voltage and treating time on corrosion resistance of Micro-Arc oxidation coatings applied on ZK61M magnesium alloys. *Materials* 14, 7410. doi:10.3390/ma14237410

Yu, S., Guo, D., Han, J., Sun, L., Zhu, H., Yu, Z., et al. (2020). Enhancing antibacterial performance and biocompatibility of pure titanium by a two-step electrochemical surface coating. *ACS Appl. Mater. Interfaces* 12, 44433–44446. doi:10.1021/acsami.0c10032

Yu, S., Zeng, D., Zhu, H., Zhang, W., Wang, L., Yu, Z., et al. (2022). Improvement on biocompatibility and corrosion resistance of a Ti3Zr2Sn3Mo25Nb alloy through surface nanocrystallization and micro-arc oxidation. *J. Mater Sci.* 57, 5298–5314. doi:10.1007/s10853-022-06977-4

Yuan, X., Tan, F., Xu, H., Zhang, S., Qu, F., and Liu, J. (2017). Effects of different electrolytes for micro-arc oxidation on the bond strength between titanium and porcelain. *J. Prosthodont. Res.* 61, 297–304. doi:10.1016/j.jpor.2016.11.001

Zhang, B., Li, B., Gao, S., Li, Y., Cao, R., Cheng, J., et al. (2020a). Y-doped TiO2 coating with superior bioactivity and antibacterial property prepared via plasma electrolytic oxidation. *Mater. Des.* 192, 108758. doi:10.1016/j.matdes.2020.108758

Zhang, B., Li, J., He, L., Huang, H., and Weng, J. (2020b). Bio-surface coated titanium scaffolds with cancellous bone-like biomimetic structure for enhanced bone tissue regeneration. *Acta Biomater.* 114, 431–448. doi:10.1016/j.actbio.2020.07.024

Zhang, L., Guo, J., Yan, T., and Han, Y. (2018). Fibroblast responses and antibacterial activity of Cu and Zn co-doped TiO2 for percutaneous implants. *Appl. Surf. Sci.* 434, 633–642. doi:10.1016/j.apsusc.2017.10.169

Zhang, L., Li, B., Zhang, X., Wang, D., Zhou, L., Li, H., et al. (2020c). Biological and antibacterial properties of TiO2 coatings containing Ca/P/Ag by one-step and two-step methods. *Biomed. Microdevices* 22, 24. doi:10.1007/s10544-020-00482-8

Zhang, R., Xu, N., Liu, X., Yang, X., Yan, H., Ma, J., et al. (2019). Micro/nanostructured TiO2/ZnO coating enhances osteogenic activity of SaOS-2 cells. *Artif. Cells, Nanomedicine, Biotechnol.* 47, 2838–2845. doi:10.1080/21691401.2018.1546187

Zhang, R., Zhong, S., Zeng, L., Li, H., Zhao, R., Zhang, S., et al. (2021a). Novel Mg-incorporated Micro-Arc oxidation coatings for orthopedic implants application. *Mater. (Basel)* 14. doi:10.3390/ma14195710

Zhang, X., Li, J., Wang, X., Wang, Y., Hang, R., Huang, X., et al. (2018c). Effects of copper nanoparticles in porous TiO2 coatings on bacterial resistance and cytocompatibility of osteoblasts and endothelial cells. *Mater. Sci. Eng. C* 82, 110–120. doi:10.1016/j.msec.2017.08.061

Zhang, X., Lu, X., Lv, Y., Yang, L., Zhang, E., and Dong, Z. (2021b). Enhancement of corrosion resistance and biological performances of Cu-incorporated hydroxyapatite/TiO2 coating by adjusting Cu chemical configuration and hydroxyapatite contents. *ACS Appl. Bio Mater.* 4, 903–917. doi:10.1021/acsabm.0c01390

Zhang, X., Lv, Y., Cai, G., Fu, S., Yang, L., Ma, Y., et al. (2021c). Reactive incorporation of Ag into porous TiO2 coating and its influence on its microstructure, *in vitro* antibacterial efficacy and cytocompatibility. *Prog. Nat. Sci. Mater. Int.* 31, 215–229. doi:10.1016/j.pnsc.2021.02.002

Zhang, X., Lv, Y., Shan, F., Wu, Y., Lu, X., Peng, Z., et al. (2020d). Microstructure, corrosion resistance, osteogenic activity and antibacterial capability of Mn-incorporated TiO2 coating. *Appl. Surf. Sci.* 531, 147399. doi:10.1016/j.apsusc.2020.147399

Zhang, X., Peng, Z., Lu, X., Lv, Y., Cai, G., Yang, L., et al. (2020e). Microstructural evolution and biological performance of Cu-incorporated TiO2 coating fabricated

through one-step micro-arc oxidation. *Appl. Surf. Sci.* 508, 144766. doi:10.1016/j.apsusc.2019.144766

Zhang, X., Wang, H., Li, J., He, X., Hang, R., Huang, X., et al. (2016). Corrosion behavior of Zn-incorporated antibacterial TiO2 porous coating on titanium. *Ceram. Int.* 42, 17095–17100. doi:10.1016/j.ceramint.2016.07.220

Zhang, X., Zhang, T., Lv, Y., Zhang, Y., Lu, X., Xiao, J., et al. (2021d). Enhanced uniformity, corrosion resistance and biological performance of Cu-incorporated TiO2 coating produced by ultrasound-auxiliary micro-arc oxidation. *Appl. Surf. Sci.* 569, 150932. doi:10.1016/j.apsusc.2021.150932

Zhang, Y.-Y., Zhu, Y., Lu, D.-Z., Dong, W., Bi, W.-J., Feng, X.-J., et al. (2021e). Evaluation of osteogenic and antibacterial properties of strontium/silver-containing porous TiO2 coatings prepared by micro-arc oxidation. *J. Biomed. Mater. Res. Part B Appl. Biomaterials* 109, 505–516. doi:10.1002/jbm.b.34719

Zhao, B. H., Lee, I. S., Han, I. H., Park, J. C., and Chung, S. M. (2007). Effects of surface morphology on human osteosarcoma cell response. *Curr. Appl. Phys.* 7, e6. doi:10.1016/j.cap.2006.11.004

Zhao, Q., Wu, J., Li, Y., Xu, R., Zhu, X., Jiao, Y., et al. (2022). Promotion of bone formation and antibacterial properties of titanium coated with porous Si/Ag-doped titanium dioxide. *Front. Bioeng. Biotechnol.* 10, 1001514. doi:10.3389/fbioe.2022.1001514

Zhao, Q., Yi, L., Hu, A., Jiang, L., Hong, L., and Dong, J. (2019). Antibacterial and osteogenic activity of a multifunctional microporous coating codoped with Mg, Cu and F on titanium. *J. Mater. Chem. B* 7, 2284–2299. doi:10.1039/C8TB03377C

Zhao, Q.-M., Li, X.-K., Guo, S., Wang, N., Liu, W.-W., Shi, L., et al. (2020). Osteogenic activity of a titanium surface modified with silicon-doped titanium dioxide. *Mater Sci. Eng. C Mater Biol. Appl.* 110, 110682. doi:10.1016/j.msec.2020.110682

Zheng, K., Wu, J., Li, W., Dippold, D., Wan, Y., and Boccaccini, A. (2018). Incorporation of Cu-containing bioactive glass nanoparticles in gelatin-coated scaffolds enhances bioactivity and osteogenic activity. *ACS biomaterials Sci. Eng.* 4. doi:10.1021/acsbiomaterials.8b00051

Zhou, C., Chen, Y. Q., Zhu, Y. H., Lin, G. F., Zhang, L. F., Liu, X. C., et al. (2019a). Antiadipogenesis and osseointegration of strontium-doped implant surfaces. *J. Dent. Res.* 98, 795–802. doi:10.1177/0022034519850574

Zhou, J., Wang, X., and Zhao, L. (2019b). Antibacterial, angiogenic, and osteogenic activities of Ca, P, Co, F, and Sr compound doped titania coatings with different Sr content. *Sci. Rep.* 9, 14203. doi:10.1038/s41598-019-50496-3

Zhou, T., Liu, J., Zhang, X., Shen, B., Yang, J., Hu, W., et al. (2019c). The antibacterial W-containing microarc oxidation coating on Ti6Al4V. *Surf. Coatings Technol.* 374, 242–252. doi:10.1016/j.surfcoat.2019.05.089

Zhou, W., Huang, O., Gan, Y., Li, Q., Zhou, T., and Xi, W. (2019d). Effect of titanium implants with coatings of different pore sizes on adhesion and osteogenic differentiation of BMSCs. *Artif. Cells Nanomed Biotechnol.* 47, 290–299. doi:10.1080/21691401.2018.1553784

Zhu, Y., Shen, Y., Xiang, Y., Fang, K., Xu, K., Ma, P., et al. (2022). Combined application of silica particles and zirconium hydrogen phosphate coating to improve the friction resistance and osteogenic/anti-inflammatory properties of micro-arc oxidation-treated titanium. *Surf. Coatings Technol.* 451, 129037. doi:10.1016/j.surfcoat.2022.129037

Zuo, Y., Li, T., Jiang, X., Wu, M., Zhang, Y., and Chen, F. (2020). Tribocorrosion behavior of Ca–P MAO coatings on Ti6Al4V alloy at various applied voltages. *J. Mater. Res.* 35, 444–453. doi:10.1557/jmr.2019.344

frontiers | Frontiers in Bioengineering and Biotechnology

TYPE Original Research
PUBLISHED 08 January 2024
DOI 10.3389/fbioe.2023.1321197



OPEN ACCESS

EDITED BY
Oommen Podiyan Oommen,
Tampere University, Finland

REVIEWED BY
Vigneshkumar Rangasami,
University of Oregon, United States
Jyothi U. Menon,
University of Rhode Island, United States

*CORRESPONDENCE
Frederik Claeyssens,
f.claeyssens@sheffield.ac.uk

RECEIVED 19 October 2023
ACCEPTED 13 December 2023
PUBLISHED 08 January 2024

CITATION
Jackson CE, Doyle I, Khan H, Williams SF, Aldemir Dikici B, Barajas Ledesma E, Bryant HE, English WR, Green NH and Claeyssens F (2024), Gelatin-containing porous polycaprolactone PolyHIPEs as substrates for 3D breast cancer cell culture and vascular infiltration. *Front. Bioeng. Biotechnol.* 11:1321197. doi: 10.3389/fbioe.2023.1321197



# Gelatin-containing porous polycaprolactone PolyHIPEs as substrates for 3D breast cancer cell culture and vascular infiltration

Caitlin E. Jackson[1,2], Iona Doyle[1], Hamood Khan[1], Samuel F. Williams[3], Betül Aldemir Dikici[4], Edgar Barajas Ledesma[5], Helen E. Bryant[6], William R. English[7], Nicola H. Green[1,2] and Frederik Claeyssens[1,2]*

[1]The Kroto Research Institute, Materials Science and Engineering, University of Sheffield, Sheffield, United Kingdom, [2]Insigneo Institute for in Silico Medicine, The Pam Liversidge Building, University of Sheffield, Sheffield, United Kingdom, [3]Department of Infection, Immunity and Cardiovascular Disease, Royal Hallamshire Hospital, The University of Sheffield, Sheffield, United Kingdom, [4]Department of Bioengineering, Izmir Institute of Technology, Urla, Türkiye, [5]Department of Chemistry, The University of Sheffield, Sheffield, United Kingdom, [6]School of Medicine and Population Health, University of Sheffield, Sheffield, United Kingdom, [7]Norwich Medical School, University of East Anglia, Norwich, United Kingdom

Tumour survival and growth are reliant on angiogenesis, the formation of new blood vessels, to facilitate nutrient and waste exchange and, importantly, provide a route for metastasis from a primary to a secondary site. Whilst current models can ensure the transport and exchange of nutrients and waste via diffusion over distances greater than 200 µm, many lack sufficient vasculature capable of recapitulating the tumour microenvironment and, thus, metastasis. In this study, we utilise gelatin-containing polymerised high internal phase emulsion (polyHIPE) templated polycaprolactone-methacrylate (PCL-M) scaffolds to fabricate a composite material to support the 3D culture of MDA-MB-231 breast cancer cells and vascular ingrowth. Firstly, we investigated the effect of gelatin within the scaffolds on the mechanical and chemical properties using compression testing and FTIR spectroscopy, respectively. Initial *in vitro* assessment of cell metabolic activity and vascular endothelial growth factor expression demonstrated that gelatin-containing PCL-M polyHIPEs are capable of supporting 3D breast cancer cell growth. We then utilised the chick chorioallantoic membrane (CAM) assay to assess the angiogenic potential of cell-seeded gelatin-containing PCL-M polyHIPEs, and vascular ingrowth within cell-seeded, surfactant and gelatin-containing scaffolds was investigated via histological staining. Overall, our study proposes a promising composite material to fabricate a substrate to support the 3D culture of cancer cells and vascular ingrowth.

KEYWORDS

**gelatin, polyHIPE, CAM assay, PCL (polycaprolactone), vascularisation, angiogenesis**

# 1 Introduction

Angiogenesis is the process through which new vasculature is formed from an existing network and is a key process to ensure cell survival and maintenance, facilitating oxygen and nutrient delivery, and waste removal (Adair and Montani, 2010; Rouwkema and Khademhosseini, 2016). Moreover, angiogenesis is critical for tumour survival, maintenance and growth, as well as providing a route for cancer cell metastasis (Nishida et al., 2006; Lugano et al., 2020). However, many current *in vitro* models lack sufficient vasculature to fully recapitulate tumour-driven angiogenesis, tumour growth and metastasis. Therefore, there is a need to design improved *in vitro* culture substrates to support tumour cell culture and growth whilst additionally facilitating tumour-driven angiogenesis and vascular ingrowth.

Substrates for *in vitro* culture are commonly fabricated using polymers, either natural or synthetic (Langer and Tirrell, 2004; Kohane and Langer, 2008; Place et al., 2009). Whilst natural polymers, such as collagen and Matrigel, better recapitulate the architecture of the microenvironment (Habanjar et al., 2021) and lend themselves to optical microscopy analysis techniques better than synthetic polymers, they are often fabricated as hydrogels, and as such, the resultant mechanical properties of the gels can cause challenges in scaffold handling. Synthetic polymers can be fabricated consistently, at low cost, are easier to produce and can often be chemically or mechanically tuned, producing scaffolds which can be easily handled (Rijal et al., 2017; Donnaloja et al., 2020; Reddy et al., 2021). Thus, a substrate fabricated with a combination of natural and synthetic polymers could provide a better solution for improved *in vitro* cell culture, resulting in a substrate which has architecture recognisable by cells whilst still easily handled.

We have previously reported on the use of gelatin to both chemically and mechanically tune porous polymer substrates (Furmidge et al., 2023). Gelatin is a biodegradable and biocompatible polymer with low toxicity that is a molecular derivative of type I collagen, therefore, it has the capability to biologically perform similarly to collagen and is a suitable substitute (Bello et al., 2020). Furthermore, gelatin is readily available, can be extracted from multiple sources and is more cost-effective than extracellular matrix (ECM) proteins such as collagen, laminin and fibronectin (Bello et al., 2020; Lukin et al., 2022).

Due to the amphiphilic properties of gelatin, it has been previously utilised as a surfactant, albeit a weak surfactant and is capable of stabilising emulsions (Aldemir Dikici and Claeyssens, 2020; Zhang et al., 2020; Furmidge et al., 2023) via lowering the interfacial energy of the oil-water interface.

Our previous study demonstrated how the inclusion of gelatin within the internal phase of PCL polyHIPEs led to a significant increase in pore size of the resulting scaffold (Table 1) (Furmidge et al., 2023). Thus, we hypothesised that such increases in the pore size could enable increased vessel ingrowth. Therefore, this study investigates the use of gelatin-containing polyHIPEs as a substrate to support 3D breast cancer cell growth and facilitate angiogenesis. We initially assessed the impact of gelatin within the scaffold on mechanical properties and the cancer cell metabolic activity before using the pre-existing vascular network from an *ex ovo* chick chorioallantoic membrane (CAM) assay to assess the vascular ingrowth of the CAM vessels. Furthermore, we combined 3D cancer cell culture on the substrates as a tumour tissue mimic within the CAM assay, assessing the validity of our approach using a porous polymer substrate to recapitulate angiogenesis surrounding tumour tissue.

# 2 Materials

Photoinitiator (2,4,6-Trimethylbenzoyl Phosphine Oxide/2-Hydroxy-2- Methylpropiophenone blend), Dulbecco's modified Eagle media (DMEM), fetal bovine serum (FBS), pencillin/streptomycin (PS), L-glutamine, trypsin, formaldehyde, resazurin sodium salt, type A gelatine from porcine skin, isopentane and haematoxylin solution were purchased from Sigma Aldrich. Chloroform, toluene, ethanol, acetone and methanol were purchased from Fisher Scientific. The surfactant, Hypermer B246 was received as a sample from Croda (Goole, United Kingdom). The optimal cutting temperature-tissue freezing medium (OCT-TFM) was purchased from CellPath, the VectaMount aqueous mounting medium was purchased from Vector and the eosin solution was purchased from Acros Organics. High molecular weight 4-arm methacrylated polycaprolactone (PCL-M, 20,331 g/mol, 95% methacrylated) was synthesised in the laboratory [a general synthesis method is given in Aldemir Dikici et al. (2019)].

# 3 Methods

## 3.1 PCL-M PolyHIPE fabrication

0.4 g PCL-M and 10 wt% surfactant were heated to melt the surfactant and PCL-M. 0.6 g of 60 wt% chloroform and 40 wt% toluene solvent mixture and 0.03 g photoinitiator were added to the PCL-M-surfactant mixture respectively. The contents were mixed (250 rpm) using a magnetic stirrer (20 mm × 7 mm) for 3 min at 37°C. Once homogeneous, 2 mL of the internal phase (water or 5% gelatin solution prepared with water (wt/v)) was added dropwise and the emulsion was mixed for 5 min. Three compositions were prepared: i) 10 wt% surfactant with water as an internal phase

**TABLE 1 The pore size (Furmidge et al., 2023) and stiffness of PCL-M polyHIPEs fabricated with different combinations of 10% surfactant and 5% gelatin (mean ± SD).**

| PCL-M PolyHIPE | Pore size (μm) (Furmidge et al., 2023) | Stiffness (MPa) |
|---|---|---|
| G0S10 | 53 ± 19 | 0.91 ± 0.23 |
| G5S10 | 39 ± 24 | 2.68 ± 0.60 |
| G5S0 | 80 ± 43 | 1.52 ± 0.20 |

(G0S10), ii) 10 wt% surfactant with 5% gelatin solution as an internal phase (G5S10) and iii) 0 wt% surfactant with 5% gelatin solution as an internal phase (G5S0).

## 3.2 Polymerisation of PCL-M HIPEs

Emulsions were polymerised in a transparent 2 mL syringe. All samples were cured using ultraviolet (UV) light for 5 min on both sides using the OmniCure Series 1,000 system (100 W, Lumen Dynamics, Canada), with 18 W/cm$^2$ reported light density and spectral output from 250–600 nm. The resulting polyHIPEs were removed from the syringe and washed in 100% ethanol for 24 h before washing in 70% ethanol for 48 h, changing the ethanol after each 24 h period. Following this, ethanol was gradually replaced with deionised water for 3 days, changing the water after each 24 h period. All polyHIPE samples were washed and stored in $dH_20$ at room temperature.

## 3.3 Mechanical characterisation

The compressive modulus of the PCL-M polyHIPEs was calculated by compressive mechanical testing (MultiTest 2.5–dv, Mecmesin, Slinford, United Kingdom), using the 250 N load cell at room temperature. Samples were cut into approximately 1 cm cylinders using a scalpel and placed between two compression plates. The compressive tests were performed on each sample at a rate of 1 N/s until the maximum load of 250 N was reached. The stiffness was calculated from the gradient of the initial linear region of the stress-strain curve for each sample.

## 3.4 Chemical characterisation using fourier transform infrared spectroscopy (FTIR)

Measurements were collected using an Agilent 4300 spectrometer fitted with a diamond 3-Bounce-2-Pass attenuated total reflection (ATR) crystal and a mercury cadmium telluride detector (Agilent Technologies, Santa Clara CA, United Kingdom). Data between 4000 cm$^{-1}$ and 1,000 cm$^{-1}$ was obtained by collecting 32 scans at 4 cm$^{-1}$ resolution. All spectra were normalised to the PCL peak (1722 cm$^{-1}$). Spectral processing was conducted using Spectragryph (v1.2.15, 2020).

## 3.5 General cell culture

MDA-MB-231 cells (Aldrich, 2023) were used to evaluate the proliferation of cancer cells within gelatin-containing PCL-M polyHIPEs. The MDA-MB-231 cells were purchased from Merck (ECACC) and transduced to express luciferase2 and mStrawberry by transfection with a transposon and the transposase PiggyBac using methodology developed previously (English et al., 2017). The cells were transduced and selected with puromycin and stocks frozen within 5 passages and then used within 30 passages of receipt from ECACC. The cells were thawed, transferred to media (DMEM supplemented with 10% FBS, 1% PS, 1% L-glutamine) and centrifuged at 95 g for 5 min. The cell pellet was resuspended in fresh media with 1 µg/mL puromycin and cultured until 90% confluence with media changes every 3 days. Puromycin was removed from the media 24 h before each experiment.

## 3.6 MDA-MB-231 cell seeding on PCL-M polyHIPE scaffolds

To initially characterise cell-scaffold interactions, polyHIPE discs (8 mm diameter and 1 mm depth) were used. To sterilise, all scaffolds were washed in ethanol followed by $dH_2O$. Once reaching 90% confluency, cells were detached from the cell culture flask using trypsin. After 4 min the trypsin was neutralised with cell culture media (ratio of 1:2 respectively), followed by centrifugation (95 × g for 5 min) and resuspended in fresh media before counting using the trypan blue exclusion method to assess cell viability. For cell viability and CAM assays, 25 µL of MDA-MB-231 cells at 2 × 10$^6$ cells/mL were transferred onto each scaffold and left for 30 min in the incubator (37°C and 5% $CO_2$) to allow for cell attachment. After 30 min, fresh media was placed in each well and incubated for 7 days with fresh media replaced every 2–3 days.

## 3.7 Cell viability on PCL-M polyHIPE scaffolds

The viability of cells on the scaffold was assessed using the resazurin reduction (RR) assay. 1 mM resazurin stock solution was diluted in cell culture media to form a 10% v/v resazurin working solution. The media was removed and discarded from each well and a further 0.5 mL of the working solution was added to each well. The well plate was protected from light and incubated for 4 h at 37°C. An orbital rocker (30 rpm) was used in the incubator to ensure full penetration of the resazurin working solution. 150 µL was taken, in triplicate, from each scaffold and transferred to a 96 well plate. A fluorescence microplate reader (BioTek FLx800, Agilent BioTek, Santa Clara, CA, United States) was used to read the fluorescence of each well at an excitation wavelength of 540 nm and an emission wavelength of 630 nm. The working solution was removed from the scaffolds, and each scaffold was further washed with PBS three times before adding fresh cell culture media and continuing incubation. The assay was performed at days 1, 3 and 7.

## 3.8 VEGF ELISA

The concentration of VEGF in the supernatant of cell-seeded scaffolds was determined using the Human VEGF ELISA kit, according to the manufacturer's instructions (Abcam, United Kingdom). The optical density was measured on an absorbance microplate reader (BioTek ELx800, Agilent BioTek, Santa Clara, CA, United States) set to 450 nm.

## 3.9 CAM assay

The *ex ovo* CAM assay, as described by Mangir et al. (2019) was used to study the vascularisation of gelatin-containing, cell-seeded

polyHIPEs. Briefly, pathogen-free fertilised eggs (*Gallus domesticus*), obtained from Med Eggs (Fakenham, United Kingdom), were cleaned with 20% v/v industrial methylated spirits (IMS) before incubating in humidified (45%) hatching incubators (Rcom King Suro Max-20, P&T Poultry, Powys, Wales) at 38°C and for 3 days. After 3 days the eggs were cracked into sterile 100 mL weigh boats with 3 mL of PBS + 1% v/v penicillin–streptomycin solution (100 IU/mL–100 mg/mL) (Supplementary Figure S1). The eggs were further incubated at 38°C in a cell culture incubator (Binder, Tuttlingen, Germany). At day 7 of embryonic development, 500 µm polyHIPE discs sectioned using a vibratome (5100 mz, Campden Instruments, Loughborough, United Kingdom), seeded as described in Section 3.6, were implanted within the boundaries of the CAM and incubated for a further 6 days. The scaffolds were placed with the non-seeded surface in contact with the CAM to create a chemotactic gradient through the polyHIPE scaffold from the CAM surface. At day 13 of embryonic development, the CAM was imaged using a digital camera and MicroCapture software (version 2.0). Body lotion (Extracts, Tesco, Welwyn Garden City, UK) was injected into the surrounding area of the sample to provide contrast between blood vessels and the sample (Supplementary Figure S2). Following imaging, all embryos were sacrificed by the end of day 13 of embryonic development. Within each condition, initially 8 scaffolds were placed within the boundary of the CAM of individual eggs. This allowed for compensation when the foetus became unviable or for when the scaffold was not in an optimal position for imaging and analysis following the growth of the foetus. For each condition, the 3 scaffolds which were most optimally positioned were used for image analysis and data collection.

## 3.10 Morphometric quantification of the angiogenesis

Three images from each group were quantified using IKOSA software (CAM Assay, KML Vision GmbH) to assess the total vessel length and area and the number of branching points. Furthermore, a modified version of a well-established method (Barnhill and Ryan, 1983; Eke et al., 2017; Mangir et al., 2019; Dikici et al., 2020; Dikici et al., 2021) was used to assess the number of vessels. Briefly, the following parameters were set to all images in Adobe Photoshop (PS) to improve the ability to discern between the blood vessels; brightness and contrast; −50/10, unsharp; 50/10/0, smart sharpen; 100/5 with Gaussian blur, reduced noise; 5/0/0/50, contrast; 100, and contrast; 20-100. A new layer was created in PS, and all discernible vessels touching the scaffolds were drawn digitally using a Wacom Intuos Pro Medium Tablet with a 2 pixels size-hard round brush. The number of blood vessels was calculated by counting the total count of the vessels touching the border of the scaffolds (Aldemir Dikici et al., 2020).

## 3.11 Haematoxylin and Eosin (H&E) staining

On day 13, following the CAM assay the polyHIPE scaffolds and a surrounding area of tissue were excised from the membrane and were fixed with 3.7% w/v formaldehyde for 30 min at room temperature. The samples were further washed with PBS and stored in 70% ethanol. The excess CAM tissue was trimmed from the edges of the scaffold, and the scaffold was sectioned into 2 semi-circular sections before placing the sections in the cryo-mould with OTC-TFM and freezing in isopentane. The cryo-moulds were placed in liquid nitrogen for 7 min before sectioning on a cryostat (CM 1900, Leica, Germany), 16 µm slices were mounted onto the surface of Thermo SuperFrost® Plus slides. For H&E staining, samples were air dried for 2 h before freezing in a 50% v/v acetone and methanol mixture for 15 min. The slides were washed in PBS for 1 min followed by a wash in $H_2O$ for 3 min. Slides were stained in haematoxylin for 15 s, rinsed for 10 min in $H_2O$ and dehydrated in 70% and 90% ethanol for 1 min each. Slides were further stained in eosin for 8 s before washing in 100%, 95% and 70% ethanol for 1 min each and mounted using aquamount medium.

## 3.12 Statistical analysis

Statistical analysis was carried out using the analysis software GraphPad Prism (Version 9.4.1, CA, United States). All data was analysed using one-way or two-way analysis of variance (ANOVA) followed by Dunnett T3 ($n < 50$) multiple comparisons test. Error bars on graphs indicate standard deviation, and all $n$ values are given in figure captions where relevant. Statistical significance on graphs is represented as $p$-value < 0.033 (*), 0.002 (**) and 0.001 (***).

# 4 Results

## 4.1 Mechanical characterisation

The compression tests were conducted under wet conditions, in which the scaffolds had been washed and pre-soaked in deionised water before the experiment. The inclusion of gelatin within the internal phase of the polyHIPE resulted in a significant increase in stiffness independent of whether the scaffold was fabricated with additional surfactant (Table 1; Figure 1A). The stress-strain curves of the gelatin-containing scaffolds demonstrated a deviation in the curve at ~60% strain, resulting in an S-shaped curve compared to the smooth J-shaped curve observed in the control surfactant-only polyHIPE (G0S10) (Figure 1B).

## 4.2 Biological characterisation

Attenuated total reflection Fourier transform infrared (ATR-FTIR) spectroscopy was used to verify the presence of gelatin in the scaffolds post-processing and before cell seeding. The spectra of all PCL-M polyHIPE samples show characteristic bands for 4 arm PCL, observed at 2,940 $cm^{-1}$ and 2,860 $cm^{-1}$ (Figure 2A), caused by asymmetric and symmetric $CH_2$ stretching, respectively. The fingerprint region also shows strong absorption peaks attributed to PCL at 1722 $cm^{-1}$ (ester carbonyl stretching), 1,290 $cm^{-1}$ (C-O and C-C stretching), 1,240 $cm^{-1}$, (asymmetric C-O-C stretching) and 1,170 $cm^{-1}$ (symmetric C-O-C stretching). Furthermore, the fingerprint region of the spectra of the gelatin-containing polyHIPEs (G5S10 and G5S0) also include peaks at 1,630 $cm^{-1}$ (C=O stretching vibration), corresponding to the amide I band.

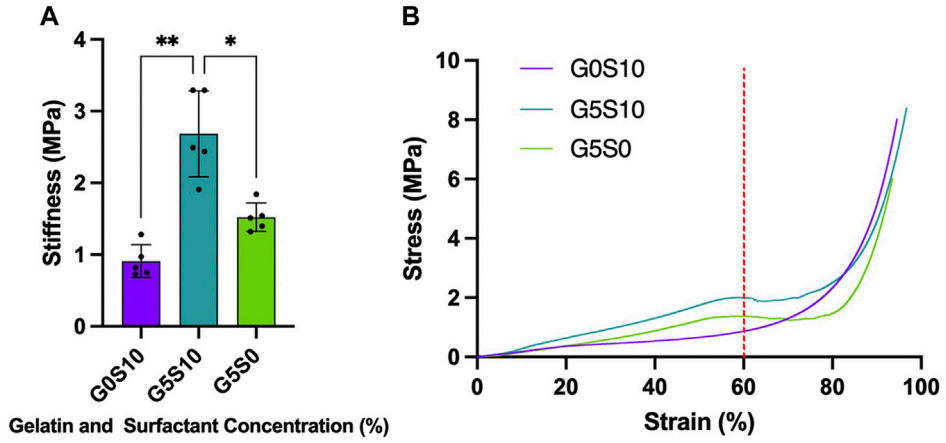


FIGURE 1
Stiffness of PCL-M polyHIPEs fabricated with different combinations of 10% surfactant and 5% gelatin displaying **(A)** the mean stiffness ± SD ($n$ = 5, * $p < 0.033$, ** $p < 0.002$) and **(B)** representative stress-strain curves of each PCL-M polyHIPE condition (red dotted line indicates 60% strain).

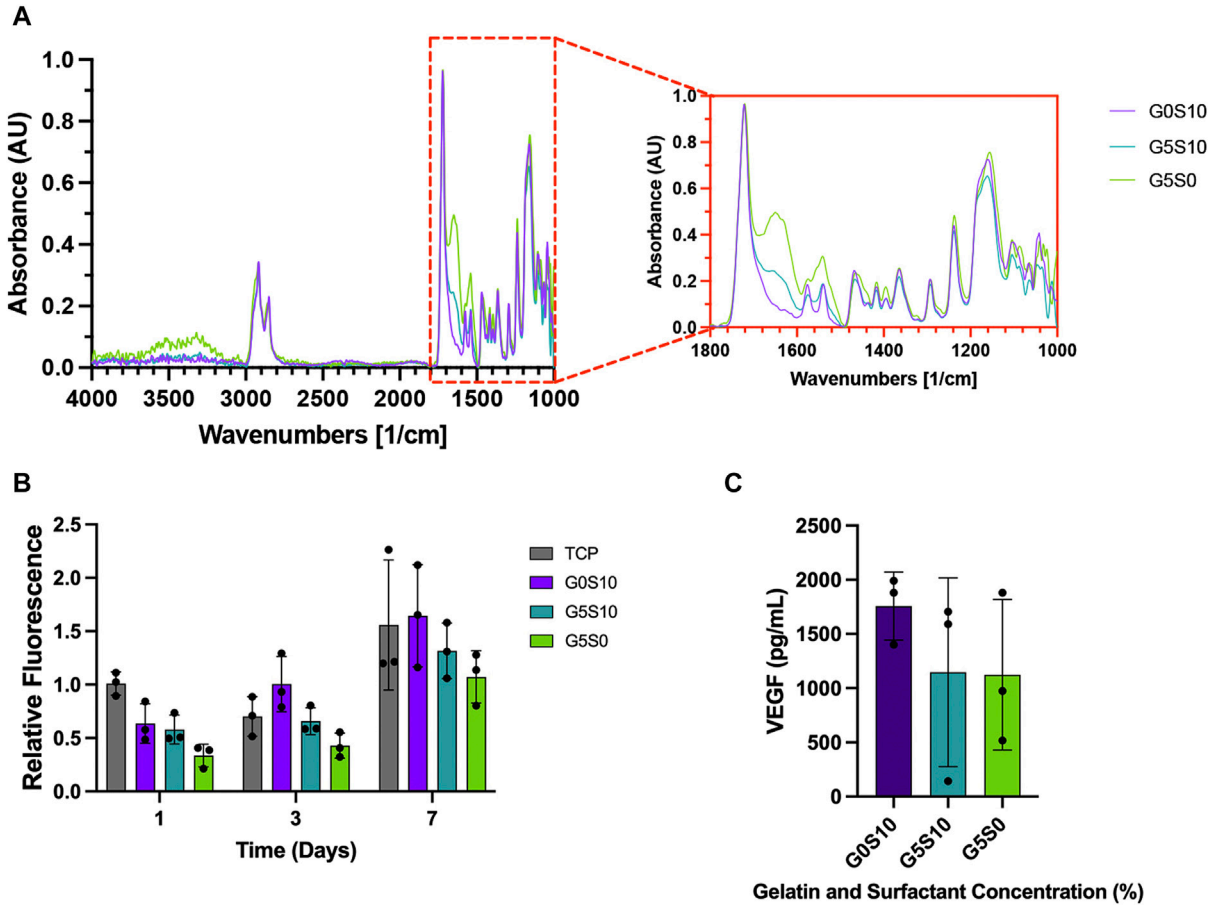


FIGURE 2
Chemical and biological assessment of PCL–M polyHIPEs containing gelatin. **(A)** The mid-infrared spectrum of PCL-M polyHIPEs containing gelatin, the red callout indicates the fingerprint region. **(B)** The metabolic activity of MDA-MB-231 cells via a resazurin reduction assay across 7 days (mean ± SD, $N$ = 3, $n$ = 3). **(C)** The concentration of VEGF expressed by MDA-MB-231 cells following 7 days of culture on PCL-M polyHIPEs containing gelatin (mean ± SD, $N$ = 3, $n$ = 2).

10.3389/fbioe.2023.1321197

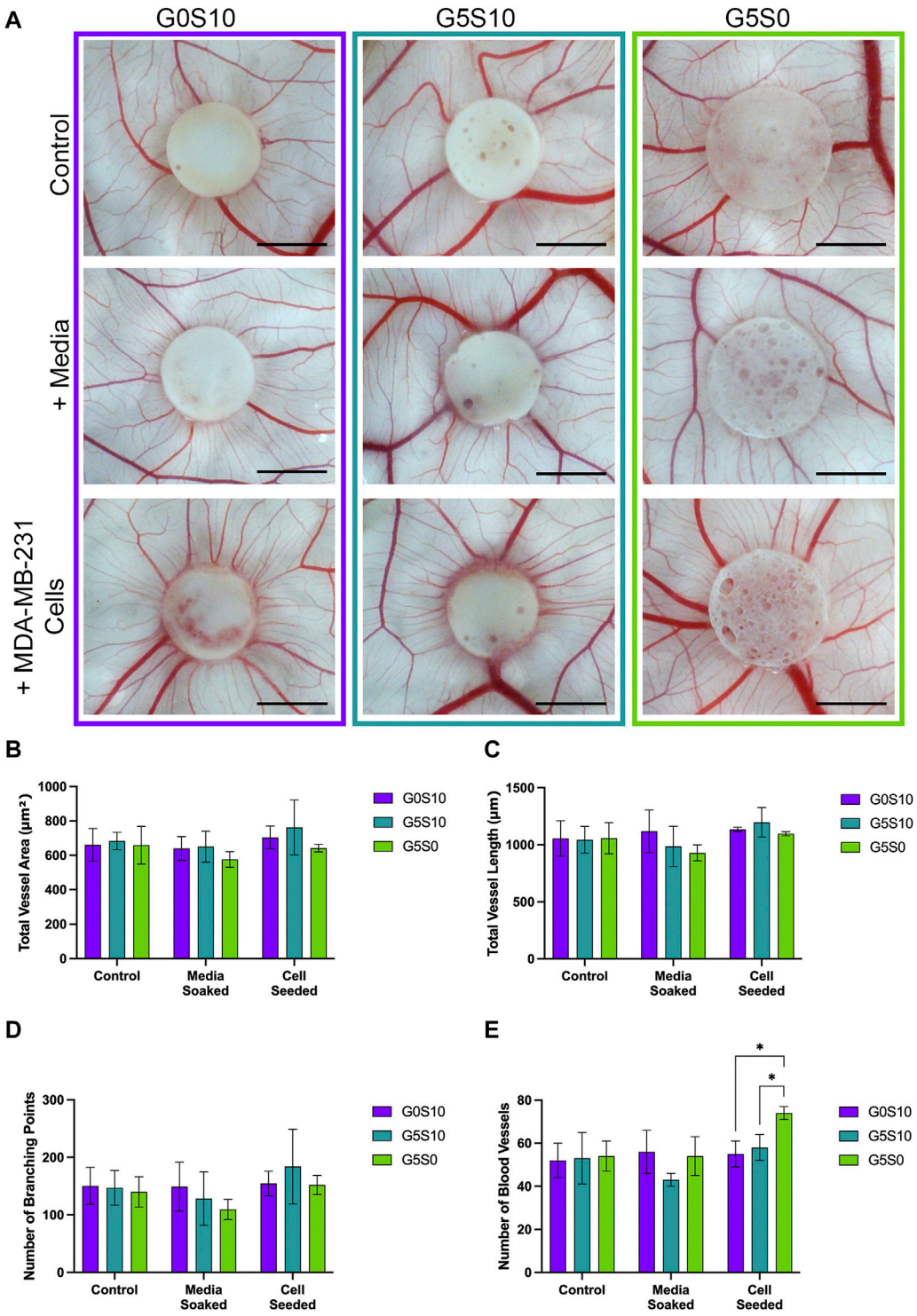


FIGURE 3
Assessment of the angiogenic potential of PCL-M polyHIPEs. **(A)** Digital Images of surfactant-only (G0S10), surfactant and gelatin-containing (G5S10) and gelatin-only (G5S0) PCL-M polyHIPEs prepared in control (PBS soaked), media soaked and cell seeded conditions on chick chorioallantoic membrane (CAM) at day 13 (scalebar represents 5 mm) with quantitative assessment describing **(B)** the total vessel area, **(C)** the total vessel length, **(D)** the number of branching points and **(E)** the number of blood vessels surrounding the PCL-M polyHIPE scaffolds (Mean ±SD, *N* = 3).

The intensity of the amide I bands is higher and more prominent in the spectrum of the gelatin-only PCL-M polyHIPE.

A 7-day resazurin reduction assay was utilised to assess the metabolic activity of MDA-MB-231 cells on PCL-M scaffolds containing gelatin. There was a significant increase in metabolic activity across the 7-day period for all PCL-M polyHIPE scaffolds (Figure 2B). Furthermore, at each time point, there was no significant difference between the PCL-M polyHIPE scaffolds and

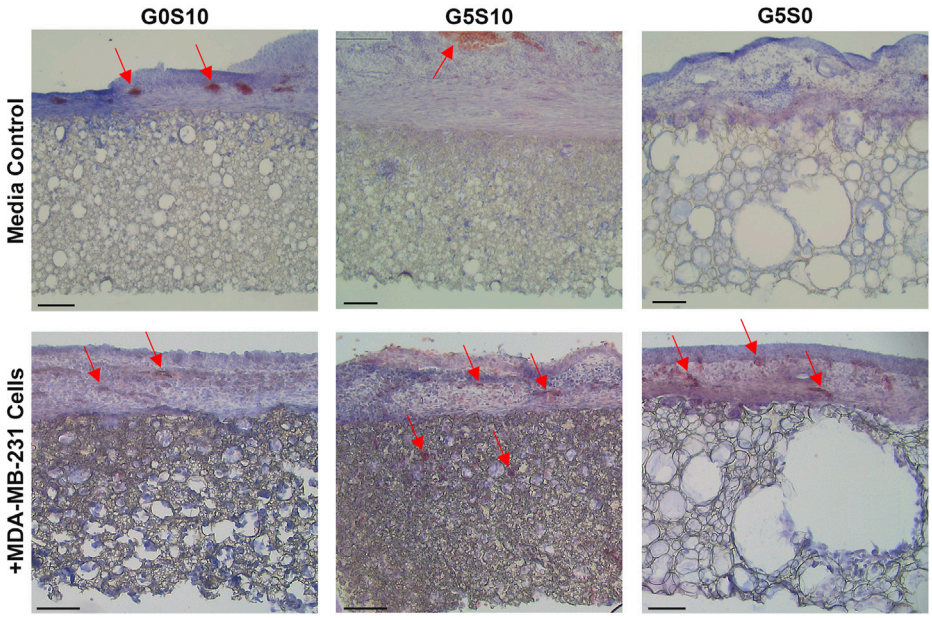


FIGURE 4
Haematoxylin and Eosin staining to analyse the angiogenic potential of surfactant-only (G0S10), surfactant and gelatin-containing (G5S10) and gelatin-only (G5S0) PCL-M polyHIPEs prepared in media soaked and cell-seeded conditions on chick chorioallantoic membrane (CAM) at day 13 (scalebar represents 100 μm, red arrows indicate blood vessels).

the control condition (tissue culture plastic, TCP). A VEGF ELISA was used to quantify the concentration of VEGF expressed by MDA-MB-231 cells following 7 days of culture on PCL-M polyHIPEs. There was no significant difference in the expression of VEGF between the different PCL-M polyHIPEs containing gelatin ± surfactant and standard surfactant-only PCL-M polyHIPEs (Figure 2C).

### 4.3 Ex ovo chorioallantoic membrane assay to assess angiogenic potential

The *ex ovo* CAM assay was utilised to assess the angiogenic potential of PCL-M polyHIPEs seeded with MDA-MB-231 breast cancer cells. Visually, we observed no negative impact of the gelatin-containing scaffolds ± cancer cells on the viability of the chick embryos or vascular network (Figure 3A). We observed increased directionality of the vessels towards the scaffold when seeded with MDA-MB-231 cells. To further investigate this finding, we quantified the vessels, defining the total vessel area and length, number of branching points and the number of vessels surrounding the scaffolds. There was no significant difference in the total vessel area and length or number of branching points between the conditions (Figures 3B–D). There was a significant increase in the number of vessels surrounding the scaffold gelatin-only cell-seeded polyHIPE compared to the surfactant-containing cell-seeded polyHIPEs (Figure 3E).

Haematoxylin and Eosin (H&E) staining was used to further assess the integration of the CAM vasculature within the gelatin-containing PCL-M polyHIPEs (Figure 4). Blood vessels (indicated by red arrows) were observed in the CAM tissue on the polyHIPE scaffolds, with more vessels present in the CAM tissue on the cell-seeded gelatin-containing scaffolds. Moreover, additional blood vessels were observed within the cell-seeded surfactant and gelatin-containing polyHIPE scaffolds.

## 5 Discussion

Within this study, we demonstrate the use of gelatin-containing PCL-M polyHIPEs that can support 3D breast cancer cell culture, whilst maintaining the key functionality of expressing vascular endothelial growth factor (VEGF) to promote angiogenesis. We used an *ex ovo* CAM assay to validate the capability of these gelatin-containing cell-seeded polyHIPEs for vascular ingrowth. Our study presents a potential substrate, with tuneable mechanical properties for use within microphysiological systems (MPS) that can successfully support 3D breast cancer cell culture and vascular ingrowth.

Firstly, we assessed the stiffness of the polyHIPE scaffolds to better understand the mechanical environment around the cells cultured within the substrates. We assessed the stiffness of the polyHIPEs in wet conditions with gelatin remaining in the scaffold to be more physiologically relevant, as has been discussed in previous studies (Aldemir Dikici et al., 2019; Jackson et al., 2023). Interestingly, when compared to our previous study in which PCL-M polyHIPE constructs were compressed in dry conditions with the gelatin removed prior to testing, we observe little difference in the stiffness of the resulting polyHIPEs (Figure 1A). Therefore, this suggests that the fabrication technique, utilising gelatin in the internal phase and the resulting effect it has on the polyHIPE structure is responsible for the change

in stiffness rather than the condition of the scaffolds during testing (wet/dry ± gelatin).

When further analysing the stress-strain curves, all the polyHIPE samples demonstrated typical linear elastic behaviour at low strain with a final region of rapidly increasing stress at high strain, this is likely due to material densifying (Sun et al., 2016). The standard surfactant-only PCL-M polyHIPE displayed standard viscoelastic behaviour, as observed in our previous study (Furmidge et al., 2023). However, the addition of gelatin into the scaffolds alters the response of the polyHIPE to compressive loads, observing a deviation in the curve at 60% strain before increasing to a maximum (Figure 1B). The S-shaped curve observed, indicates elastic instability. Up to 60% strain we observed the stiffness due to the composition of the pores and the gelatin which results in a higher stiffness than the surfactant PCL-M polyHIPE (G0S10). 60%–75% strain is where we observed elastic instability, this is likely due to the gelatin being extruded from scaffold through the collapsed pores. We observed this difference visually, finding that the gelatin-containing polyHIPEs structurally failed following compression, with large sections of gelatin protruding from the broken body of the scaffold compared to surfactant-only polyHIPEs, which remained intact (Supplementary Figure S3). Moreover, gelatin has its own viscoelastic properties which differ from PCL-M, and as such, this may introduce a difference in energy dissipation and the resulting deformation (Guarino et al., 2017; Moučka et al., 2023). At 75% strain onwards the stiffness observed is due to the bulk of the PCL-M in which the gelatin-containing polyHIPE scaffolds demonstrate a similar stiffness to surfactant-only PCL-M polyHIPE scaffolds. In our previous study, compression of gelatin polyHIPE constructs in which the gelatin was removed prior to compression testing did not result in the S-shaped curve observed in this study (Furmidge et al., 2023). This would further suggest it is the gelatin remaining in the scaffold that causes the complex response to the compression rather than any physical changes to the structure of the polyHIPE when using a gelatin solution as the internal phase.

To ensure the presence of gelatin within the scaffolds following the post-processing washing steps and prior to cell seeding we used ATR-FTIR to identify the attributed peaks (Figure 2A). In both samples containing gelatin, amide I peaks were evident and interestingly, sample G5S0 shows the highest absorption in this region, which ties well with the fact that this sample contains gelatin only. Gelatin is widely used in biomaterials due to its cell adhesive properties and capability to provide a more ECM-like environment for cell growth (Bello et al., 2020; Lukin et al., 2022; Asim et al., 2023). Interestingly, the presence of gelatin did not have any significant effect on the metabolic activity of the cells compared to the surfactant-only polyHIPE (Figure 2B), these finding are similar to previous studies in which common coating techniques, such as fibronectin and plasma coating did not yield any significant improvement in 3D cell culture within PCL-M polyHIPEs (Dikici et al., 2019; Jackson et al., 2023). In this study the potential improvement in cell attachment might be mitigated by the lower amount of surface area or the potential for the cells to fall through the pores when being seeded in the larger pore scaffolds. However, this technique, which utilises a cost-effective, biocompatible protein, provides a simple and effective method to alter pore size and stiffness whilst supporting 3D cell culture. Thus, these scaffolds could be used in combination with each other within an MPS cancer model to achieve a diverse range of mechanical cues and environments to influence different stages of the metastatic cascade.

Vascular endothelial growth factor (VEGF) is a factor secreted by tumour cells, including the MDA-MB-231 breast cancer cell line used in this study. Expression of VEGF is a key factor for angiogenesis, promoting the proliferation of vascular endothelial cells. Using a VEGF ELISA kit, we confirmed the expression of VEGF from MDA-MB-231 cells cultured on surfactant-only and gelatin-containing PCL-M polyHIPEs (Figure 2C). There is variation within these results, and it is most likely due to the inefficiency of cell adhesion which arises from using a manual seeding technique. Further improvements in the seeding technique using automation would be beneficial in the future to reduce such variability. The concentration of VEGF expressed is comparable with previous studies which have used similar cell numbers (Matsui et al., 2008; Sohn et al., 2018). This further suggests that PCL-M polyHIPEs (surfactant-only and gelatin-containing) are suitable substrates for 3D cell culture of breast cancer.

It is well documented in the literature that gelatin is a suitable biomaterial to replicate the mechanical properties of breast tissue and has been commonly used to fabricate breast tissue phantoms (McGarry et al., 2020; Cannatà et al., 2021; Amiri et al., 2022). Therefore, whilst the stiffness of the PCL-M scaffolds does not replicate that seen in soft tissue *in vivo,* the gelatin within the structure can provide a more mimetic environment for the breast cancer cells. Furthermore, it has been widely reported that gelatin sponges implanted on CAM assays demonstrate good levels of angiogenesis (Ribatti et al., 1997; Ribatti et al., 2006; Dreesmann et al., 2007). The gelatin sponges used in many previous studies provide a permissive substrate for cell attachment, migration and proliferation resulting in vastly improved rates of angiogenesis compared to commercial collagen sponges. However, it is often difficult to handle and manipulate hydrogels. The combination of gelatin within a PCL-M polyHIPE scaffold provides a synthetic polymer scaffold, which is easily handled and manipulated, and a hydrogel to promote angiogenesis and vascular invasion within the bulk of the scaffold. Similarly, Tan et al. used PCL/gelatin electrospun scaffolds combined with induced pluripotent stem-cell derived endothelial cells (iPSC-ECs) (Tan et al., 2018). When implanted *in vivo* it was observed the iPSC-ECs survived a further 3 days once implanted and there was improved blood perfusion and host-angiogenic responses compared to when the iPSC-ECs were implanted without the composite PCL/gelatin scaffold.

In this study we seeded MDA-MB-231 cells on to gelatin-containing PCL-M polyHIPEs to further support angiogenesis by the expression of VEGF from the triple negative breast cancer cell line. Wang et al. have shown how the addition of VEGF to a PCL/gelatin electrospun scaffold can improve endothelial cell proliferation *in vitro* and enhanced vascularisation *in vivo* (Wang et al., 2015). Sustained release of VEGF was achieved by functionalising the gelatin by heparin immobilisation, creating a binding site for VEGF. Similarly, Del Gaudio et al. functionalised gelatin by crosslinking with genipin, resulting in improved angiogenesis (Del Gaudio et al., 2013). Alternatively, Jiang et al. combined PCL nanofibers with gelatin encapsulated VEGF to enhance angiogenesis of endothelial cells (Jiang et al., 2018). In this study, we simplify the scaffold processing steps, removing the

need for gelatin functionalisation or encapsulation by utilising the innate ability of MDA-MB-231 cells to express VEGF.

To validate the use of gelatin-containing PCL-M polyHIPEs to support vascular invasion and growth, we used the *ex ovo* CAM assay, assessing the effect of cell-seeded PCL-M polyHIPEs on angiogenesis from an established, pre-existing vascular network. The CAM assay has been well documented to study the angiogenic capability of biomaterial scaffolds (Naik et al., 2018; Ribatti et al., 2020). Due to the biological nature of the CAM assay, it is common to see variation within datasets as shown in previous studies which utilise the CAM assay (Aldemir Dikici et al., 2020; Samourides et al., 2020). We report visually increased directionality of the vessels towards the cell-seeded polyHIPE scaffolds (Figure 3). We suggest this observation is due to the expression of VEGF from the breast cancer cells promoting directed vessel growth around the circumference of the scaffolds. This is further supported in literature, in which VEGF is identified as one of the main factors for vascular growth regulation in the CAM (Chen et al., 2021), with many studies observing an increase in scaffold integration and number of blood vessels when the scaffolds were loaded with VEGF (Cidonio et al., 2019a; Cidonio et al., 2019b; He et al., 2019; Marshall et al., 2020). Moreover, similar directional vessel growth has been observed by Guerra et al. in response to varying VEGF concentrations (Guerra et al., 2021). They identified that increased levels of VEGF resulted in vessel growth with increased vessel density towards the VEGF-loaded hydrogel.

There was a statistically significant increase in the number of vessels surrounding the cell-seeded gelatin-only polyHIPE scaffolds (Figure 3E). This was also observed in the H&E staining, we observed there were more vessels present in the CAM tissue on the cell-seeded gelatin-only polyHIPE scaffold compared to the media-soaked gelatin-only polyHIPE scaffold (Figure 4). A study investigating porous poly(glycerol sebacate urethane) scaffolds observed a significant increase in the number of vessels surrounding scaffolds which had larger pores (Samourides et al., 2020). This correlates to the significance observed in this study in which the gelatin-only scaffolds have significantly larger pores than the surfactant-containing polyHIPEs. The average pore sizes have been previously reported, as 80 μm for the gelatin-only scaffold, 39 μm for the gelatin and surfactant scaffold, and 53 μm for the surfactant-only scaffold (Furmidge et al., 2023). On the other hand, whilst we observed a greater number of vessels in the CAM tissue around the gelatin-only scaffolds, we did not observe vessels within the scaffold. The H&E staining of these scaffolds showed the CAM tissue forming a distinct layer on the scaffold with limited integration. This lack of integration was further pronounced when preparing the samples for histological assessment, and the layer of CAM tissue was easily separated from the scaffold, as previously described by Mangir et al. (2019). This lack of integration is likely due to the larger pores in the gelatin-only PCL-M polyHIPEs. Whilst large pores are favourable for vascular invasion and integration, for cell attachment and migration they may need to be significantly smaller. The ingrowing CAM cells are likely fibroblasts, and it is reported that fibroblast ingrowth occurs with scaffold pore sizes of 5–15 μm (Yang et al., 2001). Interestingly, on multiple occasions in the cell-seeded surfactant and gelatin-containing PCL-M polyHIPEs, we observed the CAM membrane starting to grow over and envelop the scaffold (Figure 3. G5S10 +MDA-MB-231; Supplementary Figure S4). This phenomenon has been observed previously as an indicator of tissue/scaffold integration and angiogenesis (Baiguera et al., 2012; Totonelli et al., 2012; Orlando et al., 2013). Interestingly, these studies use ECM-derived matrices to fabricate decellularised scaffolds. Thus, it is likely the gelatin, a heterogenous mixture of peptides which are derived from Collagen, which is one of the most abundant ECM proteins, alongside the expression of VEGF from the MDA-MB-231 cells within the PCL-M polyHIPEs is responsible for stimulating the envelopment of these scaffolds. The H&E staining provided further evidence of vascular integration, where we observed the presence of blood vessels within the surfactant and gelatin-containing scaffold (Figure 4). Whilst these scaffolds have smaller pores [mean = 39 μm (Furmidge et al., 2023)], vascular invasion was observed. Similarly, Paterson et al. demonstrated vascular invasion occurred within emulsion-templated microspheres with small pores (median pore size = 21 μm) however, only in combination with human embryonic stem cell-derived mesenchymal progenitor cells (Paterson et al., 2018). Furthermore, they suggest the expression of VEGF from the cells may be partially responsible for the induction of the angiogenic response. Furthermore, Baker et al. observed vascular ingrowth within porous PCL scaffolds with a similar range of pore sizes as the scaffolds used in this study (Baker et al., 2011). The study also identified that the infiltrating vascular network preferentially aligned along micro-fractures in the structure. Therefore, any similar fractures or weaknesses within the polyHIPE structure could provide additional support for vascular alignment and infiltration and is a possible design feature to investigate in the future to further improve the vascularisation of gelatin-containing PCL polyHIPEs.

## 6 Conclusion

In this study, we demonstrated the use of gelatin-containing PCL-M polyHIPEs to support 3D breast cancer cell culture by assessing the cell metabolic activity and the expression of VEGF. Furthermore, we validated the use of these substrates to support vascular invasion and growth using the CAM assay. Via combining breast cancer cells with the gelatin-containing polyHIPE substrates, we observed a significant increase in the number of blood vessels surrounding the scaffold and improved tissue integration. Thus, we present gelatin-containing PCL-M polyHIPEs as a promising composite material for MPS substrates to support both 3D cancer cell culture and vascular ingrowth.

## Data availability statement

The raw data supporting the conclusions of this article will be made available by the authors, without undue reservation.

## Ethics statement

Ethical approval was not required for the studies on humans in accordance with the local legislation and institutional requirements because only commercially available established cell lines were used. Ethical approval was not required for the study involving animals in accordance with the local legislation and institutional requirements

because the work was completed in *ex ovo* conditions under the 14 days threshold set out by the UK Home Office.

## Author contributions

CJ: Data curation, Formal Analysis, Investigation, Methodology, Writing–original draft, Writing–review and editing. ID: Data curation, Formal Analysis, Investigation, Writing–original draft. HK: Data curation, Investigation, Methodology, Writing–review and editing. SW: Data curation, Formal Analysis, Investigation, Methodology, Writing–original draft, Writing–review and editing. BA: Formal Analysis, Writing–original draft, Writing–review and editing. EB: Supervision, Writing–review and editing. HB: Supervision, Writing–review and editing. WE: Supervision, Writing–review and editing. NG: Supervision, Writing–review and editing. FC: Conceptualization, Supervision, Writing–review and editing.

## Funding

The author(s) declare financial support was received for the research, authorship, and/or publication of this article. This research was funded by EPSRC, grant number: EP/S022201/1 and EP/R513313/1, the Royal Society, grant number: SRF\R1\221053, The Department of Scientific Research Projects of Izmir Institute of Technology (IZTECH-BAP, 2021-IYTE-1-0110 and 2022-IYTE-2-0025), Health Institutes of Turkey (TUSEB-2022B02-22517) and IzTech Integrated Research Centers (IzTech IRC), the Center for Materials Research.

## Acknowledgments

CJ would like to thank the EPSRC, centre for Doctoral Training in Advanced Biomedical Materials for PhD studentship funding (EP/S022201/1). FC also thanks the Royal Society for funding of a Royal Society Leverhulme Trust Senior Research Fellowship 2022 (SRF\R1\221053).

## Conflict of interest

The authors declare that the research was conducted in the absence of any commercial or financial relationships that could be construed as a potential conflict of interest.

## Publisher's note



## Supplementary material

The Supplementary Material for this article can be found online at: https://www.frontiersin.org/articles/10.3389/fbioe.2023.1321197/full#supplementary-material

## References

Adair, T. H., and Montani, J. P. (2010). "Overview of angiogenesis," in *Angiogenesis* (San Rafael (CA): Morgan and Claypool Life Sciences). Available from: https://www.ncbi.nlm.nih.gov/books/NBK53238/.

Aldemir Dikici, B., and Claeyssens, F. (2020). Basic principles of emulsion templating and its use as an emerging manufacturing method of tissue engineering scaffolds. *Front. Bioeng. Biotechnol.* 8, 875. doi:10.3389/fbioe.2020.00875

Aldemir Dikici, B., Reilly, G. C., and Claeyssens, F. (2020). Boosting the osteogenic and angiogenic performance of multiscale porous polycaprolactone scaffolds by *in vitro* generated extracellular matrix decoration. *ACS Appl. Mater Interfaces* 12 (11), 12510–12524. doi:10.1021/acsami.9b23100

Aldemir Dikici, B., Sherborne, C., Reilly, G. C., and Claeyssens, F. (2019). Emulsion templated scaffolds manufactured from photocurable polycaprolactone. *Polym. Guildf.* 175, 243–254. doi:10.1016/j.polymer.2019.05.023

Aldrich, S. (2023). *Authenticated MDA-MB-231 cell line*. Available from: https://www.sigmaaldrich.com/GB/en/product/sigma/cb_92020424.

Amiri, S. A., Berckel, P. V., Lai, M., Dankelman, J., and Hendriks, B. H. W. (2022). Tissue-mimicking phantom materials with tunable optical properties suitable for assessment of diffuse reflectance spectroscopy during electrosurgery. *Biomed. Opt. Express* 13 (5), 2616–2643. doi:10.1364/boe.449637

Asim, S., Tabish, T. A., Liaqat, U., Ozbolat, I. T., and Rizwan, M. (2023). Advances in gelatin bioinks to optimize bioprinted cell functions. *Adv. Healthc. Mater* 12 (17), 2203148. doi:10.1002/adhm.202203148

Baiguera, S., Macchiarini, P., and Ribatti, D. (2012). Chorioallantoic membrane for *in vivo* investigation of tissue-engineered construct biocompatibility. *J. Biomed. Mater Res. B Appl. Biomater.* 100 B (5), 1425–1434. doi:10.1002/jbm.b.32653

Baker, S. C., Rohman, G., Hinley, J., Stahlschmidt, J., Cameron, N. R., and Southgate, J. (2011). Cellular integration and vascularisation promoted by a resorbable, particulate-leached, cross-linked poly(ε-caprolactone) scaffold. *Macromol. Biosci.* 11 (5), 618–627. doi:10.1002/mabi.201000415

Barnhill, R. L., and Ryan, T. J. (1983). Biochemical modulation of angiogenesis in the chorioallantoic membrane of the chick embryo. *J. Investigative Dermatology* 81 (6), 485–488. doi:10.1111/1523-1747.ep12522728

Bello, A. B., Kim, D., Kim, D., Park, H., and Lee, S. H. (2020). Engineering and functionalization of gelatin biomaterials: from cell culture to medical applications. *Tissue Eng. Part B Rev.* 26 (2), 164–180. doi:10.1089/ten.teb.2019.0256

Cannatà, A., Meo, S. Di, Morganti, S., Matrone, G., and Pasian, M. (2021). "Gelatin-Based tissue-mimicking materials for breast phantoms: dielectric and mechanical characterization," in *2021 XXXIVth general assembly and scientific symposium of the international union of radio science* (Rome, Italy: URSI GASS), 1–3.

Chen, L., Wang, S., Feng, Y., Zhang, J., Du, Y., Zhang, J., et al. (2021). Utilisation of chick embryo chorioallantoic membrane as a model platform for imaging-navigated biomedical research. *Cells* 10 (2), 463. doi:10.3390/cells10020463

Cidonio, G., Alcala-Orozco, C. R., Lim, K. S., Glinka, M., Mutreja, I., Kim, Y. H., et al. (2019b). Osteogenic and angiogenic tissue formation in high fidelity nanocomposite Laponite-gelatin bioinks. *Biofabrication* 11 (3), 035027. doi:10.1088/1758-5090/ab19fd

Cidonio, G., Cooke, M., Glinka, M., Dawson, J. I., Grover, L., and Oreffo, R. O. C. (2019a). Printing bone in a gel: using nanocomposite bioink to print functionalised bone scaffolds. *Mater Today Bio* 4, 100028. doi:10.1016/j.mtbio.2019.100028

Del Gaudio, C., Baiguera, S., Boieri, M., Mazzanti, B., Ribatti, D., Bianco, A., et al. (2013). Induction of angiogenesis using VEGF releasing genipin-crosslinked electrospun gelatin mats. *Biomaterials* 34 (31), 7754–7765. doi:10.1016/j.biomaterials.2013.06.040

Dikici, B. A., Dikici, S., Reilly, G. C., MacNeil, S., and Claeyssens, F. (2019). A novel bilayer polycaprolactone membrane for guided bone regeneration: combining electrospinning and emulsion templating. *Materials* 12 (16), 2643. Available from:. doi:10.3390/ma12162643

Dikici, S., Aldemir Dikici, B., Bhaloo, S. I., Balcells, M., Edelman, E. R., MacNeil, S., et al. (2020). Assessment of the angiogenic potential of 2-deoxy-D-ribose using a novel

*in vitro* 3D dynamic model in comparison with established *in vitro* assays. *Front. Bioeng. Biotechnol.* 7, 451. doi:10.3389/fbioe.2019.00451

Dikici, S., Aldemir Dikici, B., Macneil, S., and Claeyssens, F. (2021). Decellularised extracellular matrix decorated PCL PolyHIPE scaffolds for enhanced cellular activity, integration and angiogenesis. *Biomater. Sci.* 9 (21), 7297–7310. doi:10.1039/d1bm01262b

Donnaloja, F., Jacchetti, E., Soncini, M., and Raimondi, M. T. (2020). Natural and synthetic polymers for bone scaffolds optimization. *Polym. (Basel)* 12 (4), 905. doi:10.3390/polym12040905

Dreesmann, L., Ahlers, M., and Schlosshauer, B. (2007). The pro-angiogenic characteristics of a cross-linked gelatin matrix. *Biomaterials* 28 (36), 5536–5543. doi:10.1016/j.biomaterials.2007.08.040

Eke, G., Mangir, N., Hasirci, N., MacNeil, S., and Hasirci, V. (2017). Development of a UV crosslinked biodegradable hydrogel containing adipose derived stem cells to promote vascularization for skin wounds and tissue engineering. *Biomaterials* 129, 188–198. doi:10.1016/j.biomaterials.2017.03.021

English, W. R., Lunt, S. J., Fisher, M., Lefley, D. V., Dhingra, M., Lee, Y. C., et al. (2017). Differential expression of VEGFA isoforms regulates metastasis and response to anti-VEGFA therapy in sarcoma. *Cancer Res.* 77 (10), 2633–2646. doi:10.1158/0008-5472.can-16-0255

Furmidge, R., Jackson, C. E., Velázquez de la Paz, M. F., Workman, V. L., Green, N. H., Reilly, G. C., et al. (2023). Surfactant-free gelatin-stabilised biodegradable polymerised high internal phase emulsions with macroporous structures. *Front. Chem.* 11, 11. doi:10.3389/fchem.2023.1236944

Guarino, V., Gentile, G., Sorrentino, L., and Ambrosio, L. (2017). Polycaprolactone: synthesis, properties, and applications. *Encycl. Polym. Sci. Technol.* 1–36, 1–36. doi:10.1002/0471440264.PST658

Guerra, A., Belinha, J., Mangir, N., MacNeil, S., and Natal Jorge, R. (2021). Simulation of the process of angiogenesis: quantification and assessment of vascular patterning in the chicken chorioallantoic membrane. *Comput. Biol. Med.*, 136, 104647. doi:10.1016/j.compbiomed.2021.104647

Habanjar, O., Diab-Assaf, M., Caldefie-Chezet, F., and Delort, L. (2021). 3D cell culture systems: tumor application, advantages, and disadvantages. *Int. J. Mol. Sci.* 22 (22), 12200. doi:10.3390/ijms222212200

He, D., Zhao, A. S., Su, H., Zhang, Y., Wang, Y. N., Luo, D., et al. (2019). An injectable scaffold based on temperature-responsive hydrogel and factor-loaded nanoparticles for application in vascularization in tissue engineering. *J. Biomed. Mater Res. A* 107 (10), 2123–2134. doi:10.1002/jbm.a.36723

Jackson, C. E., Ramos-Rodriguez, D. H., Farr, N. T. H., English, W. R., Green, N. H., and Claeyssens, F. (2023). Development of PCL PolyHIPE substrates for 3D breast cancer cell culture. *Bioengineering* 10 (5), 522. doi:10.3390/bioengineering10050522

Jiang, Y. C., Wang, X. F., Xu, Y. Y., Qiao, Y. H., Guo, X., Wang, D. F., et al. (2018). Polycaprolactone nanofibers containing vascular endothelial growth factor-encapsulated gelatin particles enhance mesenchymal stem cell differentiation and angiogenesis of endothelial cells. *Biomacromolecules* 19 (9), 3747–3753. doi:10.1021/acs.biomac.8b00870

Kohane, D. S., and Langer, R. (2008). Polymeric biomaterials in tissue engineering. *Pediatr. Res.* 63 (5), 487–491. doi:10.1203/01.pdr.0000305937.26105.e7

Langer, R., and Tirrell, D. A. (2004). Designing materials for biology and medicine. *Nature* 428, 487–492. doi:10.1038/nature02388

Lugano, R., Ramachandran, M., and Dimberg, A. (2020). Tumor angiogenesis: causes, consequences, challenges and opportunities. *Cell. Mol. Life Sci.* 77 (9), 1745–1770. doi:10.1007/s00018-019-03351-7

Lukin, I., Erezuma, I., Maeso, L., Zarate, J., Desimone, M. F., Al-Tel, T. H., et al. (2022). Progress in gelatin as biomaterial for tissue engineering. *Pharmaceutics* 14 (6), 1177. doi:10.3390/pharmaceutics14061177

Mangir, N., Dikici, S., Claeyssens, F., and Macneil, S. (2019). Using ex ovo chick chorioallantoic membrane (CAM) assay to evaluate the biocompatibility and angiogenic response to biomaterials. *ACS Biomater. Sci. Eng.* 5 (7), 3190–3200. doi:10.1021/acsbiomaterials.9b00172

Marshall, K. M., Kanczler, J. M., and Oreffo, R. O. C. (2020). Evolving applications of the egg: chorioallantoic membrane assay and *ex vivo* organotypic culture of materials for bone tissue engineering. *J. Tissue Eng.*, 11. doi:10.1177/2041731420942734

Matsui, J., Funahashi, Y., Uenaka, T., Watanabe, T., Tsuruoka, A., and Asada, M. (2008). Multi-kinase inhibitor E7080 suppresses lymph node and lung metastases of human mammary breast tumor MDA-MB-231 via inhibition of vascular endothelial growth factor-receptor (VEGF-R) 2 and VEGF-R3 kinase. *Clin. Cancer Res.* 14 (17), 5459–5465. doi:10.1158/1078-0432.CCR-07-5270

McGarry, C. K., Grattan, L. J., Ivory, A. M., Leek, F., Liney, G. P., Liu, Y., et al. (2020). Tissue mimicking materials for imaging and therapy phantoms: a review. *Phys. Med. Biol.* 65 (23), 23TR01. doi:10.1088/1361-6560/abbd17

Moučka, R., Sedlačík, M., and Pátíková, Z. (2023). Fractional viscoelastic models of porcine skin and its gelatin-based surrogates. *Mech. Mater.* 177, 104559. doi:10.1016/j.mechmat.2023.104559

Naik, M., Brahma, P., and Dixit, M. (2018). A cost-effective and efficient chick ex-ovo cam assay protocol to assess angiogenesis. *Methods Protoc.* 1 (2), 19–9. doi:10.3390/mps1020019

Nishida, N., Yano, H., Nishida, T., Kamura, T., and Kojiro, M. (2006). Angiogenesis in cancer. *Vasc. Health Risk Manag.* 2 (3), 213–219. doi:10.2147/vhrm.2006.2.3.213

Orlando, G., Booth, C., Wang, Z., Totonelli, G., Ross, C. L., Moran, E., et al. (2013). Discarded human kidneys as a source of ECM scaffold for kidney regeneration technologies. *Biomaterials* 34 (24), 5915–5925. doi:10.1016/j.biomaterials.2013.04.033

Paterson, T. E., Gigliobianco, G., Sherborne, C., Green, N. H., Dugan, J. M., Macneil, S., et al. (2018). Porous microspheres support mesenchymal progenitor cell ingrowth and stimulate angiogenesis. *Apl. Bioeng.* 2 (2), 026103. doi:10.1063/1.5008556

Place, E. S., George, J. H., Williams, C. K., and Stevens, M. M. (2009). Synthetic polymer scaffolds for tissue engineering. *Chem. Soc. Rev.* 38 (4), 1139–1151. doi:10.1039/b811392k

Reddy, M. S. B., Ponnamma, D., Choudhary, R., and Sadasivuni, K. K. (2021). A comparative review of natural and synthetic biopolymer composite scaffolds. *Polym. (Basel)* 13 (7), 1105. doi:10.3390/polym13071105

Ribatti, D., Annese, T., and Tamma, R. (2020). The use of the chick embryo CAM assay in the study of angiogenic activiy of biomaterials. *Microvasc. Res.*, 131, 104026. doi:10.1016/j.mvr.2020.104026

Ribatti, D., Gualandris, A., Bastaki, M., Vacca, A., Iurlaro, M., Roncali, L., et al. (1997). New model for the study of angiogenesis and antiangiogenesis in the chick embryo chorioallantoic membrane: the gelatin sponge/chorioallantoic membrane assay. *J. Vasc. Res.* 34 (6), 455–463. doi:10.1159/000159256

Ribatti, D., Nico, B., Vacca, A., and Presta, M. (2006). The gelatin sponge–chorioallantoic membrane assay. *Nat. Protoc.* 1 (1), 85–91. doi:10.1038/nprot.2006.13

Rijal, G., Bathula, C., and Li, W. (2017). Application of synthetic polymeric scaffolds in breast cancer 3D tissue cultures and animal tumor models. *Int. J. Biomater.* 2017, 1–9. doi:10.1155/2017/8074890

Rouwkema, J., and Khademhosseini, A. (2016). Vascularization and angiogenesis in tissue engineering: beyond creating static networks. *Trends Biotechnol.* 34 (9), 733–745. doi:10.1016/j.tibtech.2016.03.002

Samourides, A., Browning, L., Hearnden, V., and Chen, B. (2020). The effect of porous structure on the cell proliferation, tissue ingrowth and angiogenic properties of poly(glycerol sebacate urethane) scaffolds. *Mater. Sci. Eng. C* 108, 110384. doi:10.1016/j.msec.2019.110384

Sohn, E. J., Jung, D. B., Lee, H. J., Han, I., Lee, J., Lee, H., et al. (2018). CNOT2 promotes proliferation and angiogenesis via VEGF signaling in MDA-MB-231 breast cancer cells. *Cancer Lett.* 412, 88–98. doi:10.1016/j.canlet.2017.09.052

Sun, Y., Amirrasouli, B., Razavi, S. B., Li, Q. M., Lowe, T., and Withers, P. J. (2016). The variation in elastic modulus throughout the compression of foam materials. *Acta Mater* 110, 161–174. doi:10.1016/j.actamat.2016.03.003

Tan, R. P., Chan, A. H. P., Lennartsson, K., Miravet, M. M., Lee, B. S. L., Rnjak-Kovacina, J., et al. (2018). Integration of induced pluripotent stem cell-derived endothelial cells with polycaprolactone/gelatin-based electrospun scaffolds for enhanced therapeutic angiogenesis. *Stem Cell. Res. Ther.* 9 (1), 70. doi:10.1186/s13287-018-0824-2

Totonelli, G., Maghsoudlou, P., Garriboli, M., Riegler, J., Orlando, G., Burns, A. J., et al. (2012). A rat decellularized small bowel scaffold that preserves villus-crypt architecture for intestinal regeneration. *Biomaterials* 33 (12), 3401–3410. doi:10.1016/j.biomaterials.2012.01.012

Wang, K., Chen, X., Pan, Y., Cui, Y., Zhou, X., Kong, D., et al. (2015). Enhanced vascularization in hybrid PCL/gelatin fibrous scaffolds with sustained release of VEGF. *Biomed. Res. Int.* 2015, 1–10. doi:10.1155/2015/865076

Yang, S., Leong, K. F., Du, Z. M. E., and Chua, C. K. (2001). The design of scaffolds for use in tissue engineering. Part I. Traditional factors. *Tissue Eng.* 7 (6), 679–689. doi:10.1089/107632701753337645

Zhang, T., Xu, J., Zhang, Y., Wang, X., Lorenzo, J. M., and Zhong, J. (2020). Gelatins as emulsifiers for oil-in-water emulsions: extraction, chemical composition, molecular structure, and molecular modification. *Trends Food Sci. Technol.* 106, 113–131. doi:10.1016/j.tifs.2020.10.005

frontiers | Frontiers in Bioengineering and Biotechnology

TYPE Review
PUBLISHED 09 January 2024
DOI 10.3389/fbioe.2023.1335211



OPEN ACCESS

EDITED BY
Oommen Podiyan Oommen,
Tampere University, Finland

REVIEWED BY
Jiulong Zhao,
Naval Medical University, China
Kui Xu,
Anhui University of Chinese Medicine, China

*CORRESPONDENCE
Shike Hou,
housk86@163.com
Jie Shi,
jie.shi@tju.edu.cn
Qi Lv,
lvqi@tju.edu.cn

RECEIVED 08 November 2023
ACCEPTED 26 December 2023
PUBLISHED 09 January 2024

CITATION
Wang X, Yang X, Sun Z, Guo X, Teng Y, Hou S, Shi J and Lv Q (2024), Progress in injectable hydrogels for the treatment of incompressible bleeding: an update.
*Front. Bioeng. Biotechnol.* 11:1335211.
doi: 10.3389/fbioe.2023.1335211



# Progress in injectable hydrogels for the treatment of incompressible bleeding: an update

Xiudan Wang[1,2,3], Xinran Yang[1,2,3], Zhiguang Sun[1,2,3], Xiaoqin Guo[1,3], Yanjiao Teng[1,2,3], Shike Hou[1,2,3]*, Jie Shi[1,2,3]* and Qi Lv[1,2,3]*

[1]Institution of Disaster and Emergency Medicine, Tianjin University, Tianjin, China, [2]Wenzhou Safety (Emergency) Institute of Tianjin University, Wenzhou, China, [3]Key Laboratory for Disaster Medicine Technology, Tianjin, China

Uncontrollable haemorrhage from deep, noncompressible wounds remains a persistent and intractable challenge, accounting for a very high proportion of deaths in both war and disaster situations. Recently, injectable hydrogels have been increasingly studied as potential haemostatic materials, highlighting their enormous potential for the management of noncompressible haemorrhages. In this review, we summarize haemostatic mechanisms, commonly used clinical haemostatic methods, and the research progress on injectable haemostatic hydrogels. We emphasize the current status of injectable hydrogels as haemostatic materials, including their physical and chemical properties, design strategy, haemostatic mechanisms, and application in various types of wounds. We discuss the advantages and disadvantages of injectable hydrogels as haemostatic materials, as well as the opportunities and challenges involved. Finally, we propose cutting-edge research avenues to address these challenges and opportunities, including the combination of injectable hydrogels with advanced materials and innovative strategies to increase their biocompatibility and tune their degradation profile. Surface modifications for promoting cell adhesion and proliferation, as well as the delivery of growth factors or other biologics for optimal wound healing, are also suggested. We believe that this paper will inform researchers about the current status of the use of injectable haemostatic hydrogels for noncompressible haemorrhage and spark new ideas for those striving to propel this field forward.

KEYWORDS

**injectable, hydrogel, noncompressible haemostasis, haemostatic material, biomaterial**

## 1 Introduction

Traumatic bleeding remains a significant cause of death, resulting in more than 1.5 million deaths each year (Shi et al., 2021). The type of haemorrhage that accounts for the highest percentage of deaths is noncompressible haemorrhage, which is responsible for up to 90% of deaths in war and 40% of deaths in civilian life (Jamal et al., 2021). Therefore, rapid and effective haemostasis, especially for noncompressible haemorrhage, is crucial for saving lives (Guo et al., 2021; Peng et al., 2021). With gradually increased understanding of the haemostatic process, various haemostatic materials that mimic the

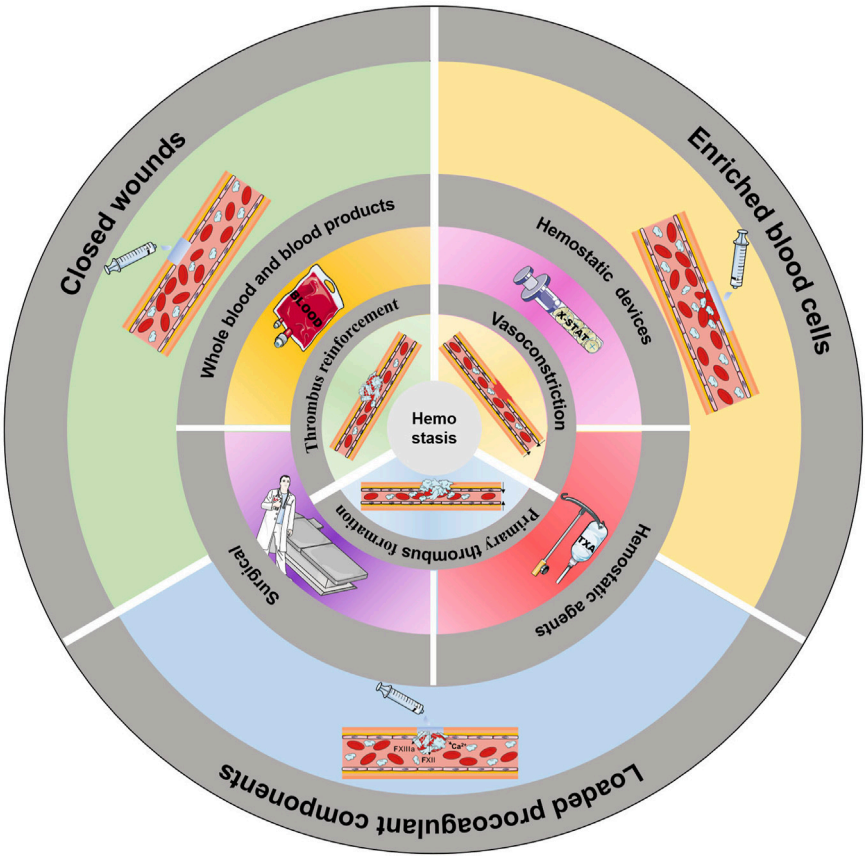


GRAPHICAL ABSTRACT
Common methods of haemostasis. The innermost circle shows the three stages of haemostasis. The middle circle shows the common clinical methods to induce haemostasis. The outermost circle illustrates the use of an injectable hydrogel to induce haemostasis.

human haemostatic mechanism have been developed. Tourniquets, gauze, sponges, and bioadhesives are common types of haemostatic materials, and some marketed haemostatic materials, such as X-STAT, junctional tourniquets and pelvic binders, have shown excellent haemostatic properties in surgical and battlefield emergencies (Zhang et al., 2021). However, there is still a lack of effective treatments for noncompressible bleeding in the chest and abdominal organs.

Hydrogels have a three-dimensional porous structure, exhibit good hydrophilicity, are easily modified, and can be designed to be injectable. Moreover, these materials have great potential to solve the problems of the inability to cover the wound completely, reach the bleeding point, and compress the wound because of their flexible drug delivery, strong tissue adhesion, strong water absorption, blood cell enrichment, and haemostatic component loading (Yu and Ding, 2008; Chin et al., 2019). Through continuous research efforts, the functionality of hydrogels has changed from simple physical coverage or single functionality to multiple properties (Patenaude et al., 2014; Ahmed, 2015; Liu et al., 2015), providing new options for haemostatic treatment. Here, we provide an overview of the coagulation mechanisms and recent applications and research progress of haemostatic materials, especially injectable hydrogels, based on different coagulation mechanisms. We will also discuss the outlook on the challenges and potential in this field.

## 2 Mechanisms of haemostasis and treatment of noncompressible haemorrhage

### 2.1 Mechanisms of haemostasis

Coagulation is a natural physiological process that occurs when the body is traumatized and prevents the continuous flow of blood from broken vessels, mainly through thrombus formation. Haemostasis can be divided into three stages: vasoconstriction, primary thrombosis, and thrombus reinforcement (Figure 1A) (Furie and Furie, 2008).

#### 2.1.1 Vasoconstriction

After vascular injury, a reflexive vascular smooth muscle spasm occurs (Rodrigues et al., 2019), causing rapid vascular contraction after injury, while the damaged vascular endothelium releases endothelin and the damaged cells release prostaglandins, all of which promote vasoconstriction (Godo and Shimokawa, 2017). Vasoconstriction causes a rapid decrease in blood flow and reduces blood loss. However, this stage of haemostasis is transient, and the hypoxic environment of the wound decreases the local pH, causing relaxation of the vascular endothelium, at which blood flow and bleeding resume (Pool, 1977). To achieve prolonged vasomodulation, mediators such as fibrinopeptides, 5-

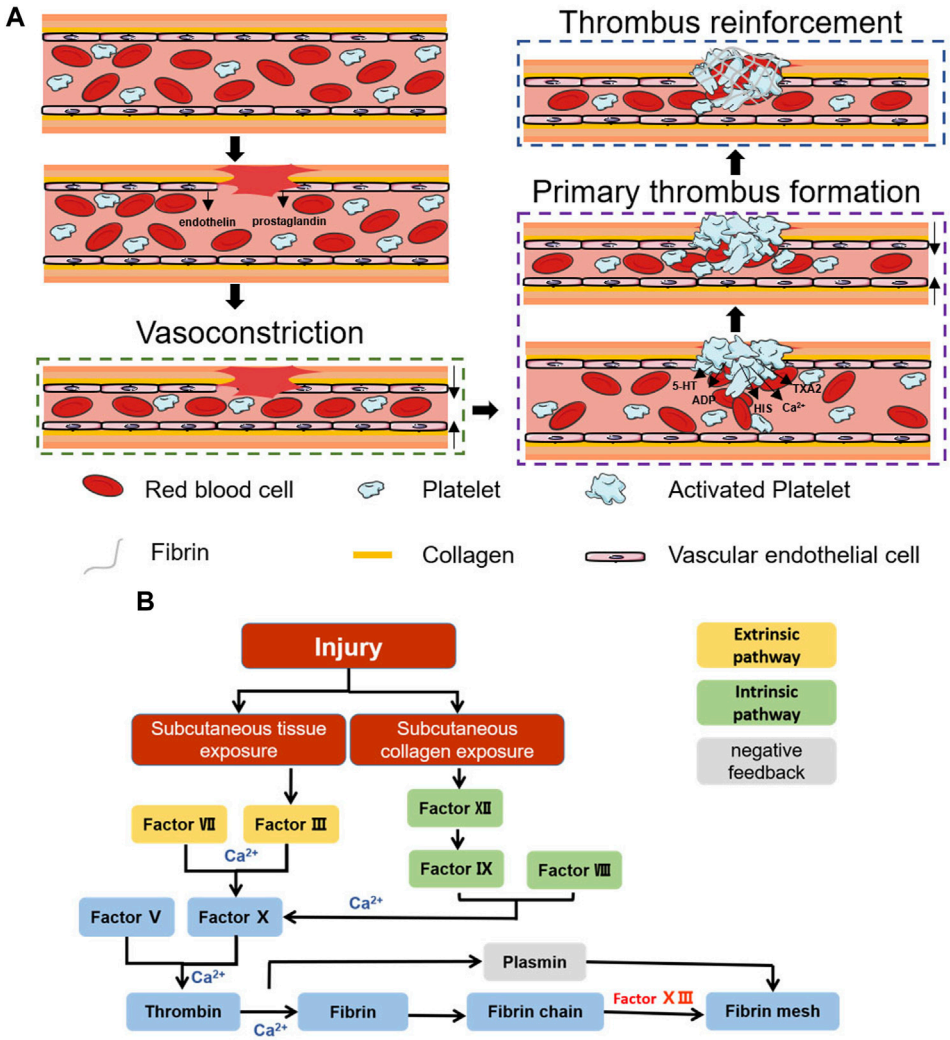


FIGURE 1
Schematic diagram of the haemostatic process. **(A)** Schematic diagram of the coagulation process. **(B)** Schematic diagram of the coagulation cascade reaction.

hydroxy tryptamine (5-HT) and thromboxane A2 (TXA2), which are released after activation of the coagulation cascade, are necessary (Strecker-McGraw et al., 2007; Teller and White, 2009).

### 2.1.2 Primary thrombus formation

This stage is dominated by the formation of platelet thrombi. Platelets were first discovered by Schultze in 1865 as enucleated cells detached from megakaryocytes (Frojmovic and Milton, 1982; Chan Choi et al., 2014). In the presence of intact blood vessels, endothelial cells have antithrombotic properties: they generate nitric oxide (NO), prostacyclin and negatively charged heparin-like glycosaminoglycans, preventing platelet activation, adhesion and aggregation (Golebiewska and Poole, 2015). After vascular injury, collagen exposure can cause platelet adhesion, and integrins on the platelet surface are activated after adhesion occurs. αIIbβ3 is the most abundant integrin on platelets and can promote further platelet aggregation and adhesion by mediating the attachment of fibrinogen, fibronectin, and vascular haemophilia factor (vWF) through RGD sequences (Wagner et al., 1996; Nuyttens et al., 2011). Activated platelets also undergo significant morphological changes, and the filamentous actin content in activated platelets can reach 70%. Moreover, the conformational change in filamentous actin can change platelets from a disk-like structure to an omelette-like structure with multiple pseudopods, which allows platelets to bind tightly to the extracellular matrix (ECM), constrict blood vessels and seal wounds (Sorrentino et al., 2015). Moreover, these activated platelets accelerate platelet activation and aggregation by secreting ADP, 5-HT, calcium ($Ca^{2+}$), histamine (HIS), TXA2, and more than three hundred other active substances (Blair and Flaumenhaft, 2009; Golebiewska and Poole, 2015). Under the combined effect of the above pathways, the initial formation of platelet plugs seals the wound and stops bleeding.

### 2.1.3 Thrombus reinforcement

Primary thrombus formation temporarily closes the wound, stopping the bleeding. However, at this time, the thrombus is not stable, and rebleeding is likely to occur due to external forces. Further reinforcement is necessary, a step we often refer to as the

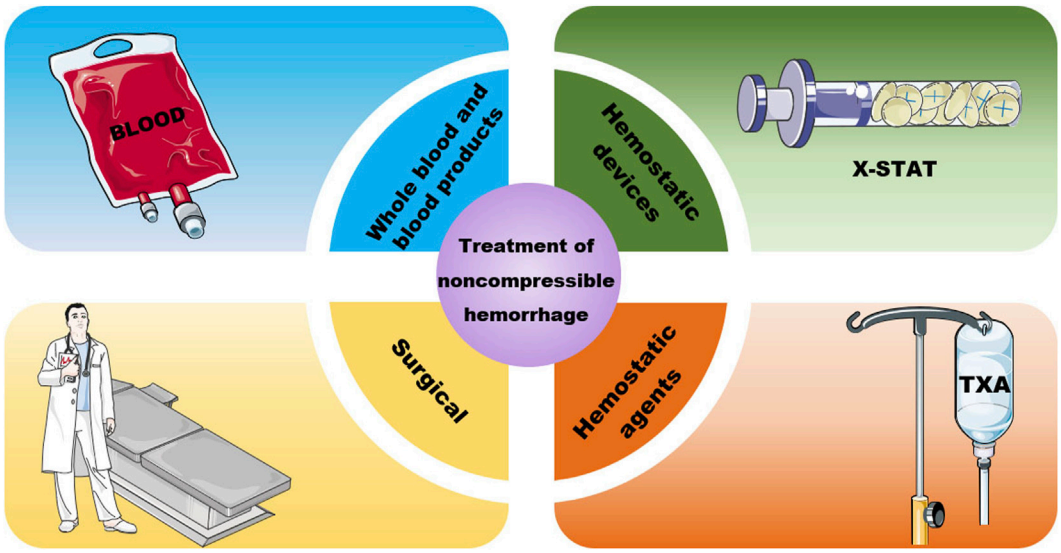


FIGURE 2
Treatment of noncompressible haemorrhage.

coagulation cascade reaction. The coagulation cascade reaction can be divided into two pathways: endogenous and exogenous (Gale, 2011). Both pathways promote the formation of the fibrin network by inducing prothrombogenic fibrin to form thrombin via coagulation factor X (FX) (Versteeg et al., 2013). However, in the exogenous haemostatic pathway, subcutaneous tissues activate FC via factor VII and factor III (prothrombin complex) (Nemerson, 1988; Mackman, 2009; Tormoen et al., 2013). In contrast, in the endogenous haemostatic pathway, subcutaneous collagen activates FX via factor XII, factor VIII, and factor IX (Bhopale and Nanda, 2003; Tormoen et al., 2013) (Figure 1B). The cascading amplification effect of the coagulation cascade reaction and the anionic surface of the platelet peg contribute to the rapid adhesion of blood cells and rapid fibrin network formation, which together complete the thrombus reinforcement process (Morrissey et al., 2012). Correspondingly, the negative feedback regulatory pathway represented by fibrolase maintains the overall dynamic balance and prevents excessive thrombus formation (Hoylaerts et al., 1982; Travis and Salvesen, 1983). The completion of thrombus reinforcement marks the end of the haemostatic process.

## 2.2 Treatment of noncompressible haemorrhage

Currently, there are three clinical treatments for noncompressible trunk haemorrhage: blood transfusion, haemostatic devices and materials, and surgical or endovascular measures (Figure 2). All of these methods have their own advantages and disadvantages and can be chosen on a case-by-case basis.

### 2.2.1 Whole blood and blood products

To date, whole-blood (WB) transfusions remain the most commonly used clinical treatment for noncompressible haemorrhage (Cap et al., 2018). The Committee on Tactical Combat Casualty Care (CoTCCC) gives resuscitation sequence recommendations for treating haemorrhagic shock, as shown in Table 1 (Butler et al., 2014).

TABLE 1 Resuscitation sequence recommendations for treating haemorrhagic shock.

| NO. | Type of resuscitation fluid |
|---|---|
| 1 | Whole blood |
| 2 | 1:1:1 plasma: RBC: platelet |
| 3 | 1:1 plasma: RBC |
| 4 | Plasma or RBC |
| 5 | Hydroxyethyl starch |
| 6 | Ringer's lactate or plasma-lyte A |

However, the storage requirements for WB are very high, and it is difficult to obtain WB in real time on battlefields and at disaster sites; thus, freeze-dried plasma attracted much attention during the Second World War. Freeze-dried plasma is a solid powder of WB obtained after virus inactivation and freeze-drying. The stability and shelf life of blood after freeze-drying are greatly increased, and freeze-dried plasma is widely used in prehospital treatment (Kendrick douglas et al., 1965).

### 2.2.2 Haemostatic devices and agents

Although blood transfusions are effective in the treatment of noncompressible haemorrhage, blood products are available from limited sources and have high storage costs and limited shelf life. To meet clinical needs, various haemostatic devices and agents have been developed. A variety of products have been marketed, each with its own advantages, and have solved some clinical problems; however, there are still limitations that need to be further addressed. Several of these devices and agents are compared in Table 2.

TABLE 2 Haemostatic devices and agents.

| Name | Mechanism | Advantages | Disadvantages | References |
|---|---|---|---|---|
| Abdominal aortic and junctional tourniquet (AAJT) | Pressure on the abdominal aorta or junction after inflation of the balloon | Compression strength can be controlled by inflation volume | Pain, inflammation, liver or intestinal ischaemia | Anonymous (2013), Croushorn et al. (2013), Croushorn (2014), Brännström et al. (2018) |
| Pelvic binder | Reduce the pelvic volume and increase the pressure in the pelvic cavity | Can be used for haemostatic treatment of unspecified bleeding points | Early trauma does not stop bleeding | Ghaemmaghami et al. (2007), Montgomery et al. (2017), Morris et al. (2017) |
| iTClamp | Works like a clamp, closes the wound | Simple to apply and less painful | Can only be applied to superficial wounds | Filips et al. (2013), St John et al. (2015), Onifer et al. (2019), Stuart et al. (2019) |
| XStat | Quickly concentrates blood to promote haemostasis, swells to compress the wound | Can be used for penetrating, rapid haemostasis | Cannot be left in the wound for a long period of time but is difficult to remove from the wound | Sims et al. (2016), Cox and Rall (2017), Rodriguez et al. (2017), Stuart et al. (2019), Warriner et al. (2019), Bonanno et al. (2020) |
| ResQFoam | Foam expands up to 30 times and becomes solid in contact with liquid, allowing compression of the wound | Easy to operate, can be used by nonprofessionals, less traumatic | Poor for arterial haemorrhage, leads to abdominal compartment syndrome, bowel injuries, thermal injuries | Chang et al. (2015) |
| Antifibrinolytic tranexamic acid (TXA) | Antifibrinolytic properties | Administered intravenously, effective for most haemorrhages | Must be used within 3 h of injury | Roberts et al. (2011), Zhang (2018), Picetti et al. (2019), Hanley et al. (2021) |

### 2.2.3 Surgery

Open surgery and endovascular measures become necessary when other treatment methods fail to stop bleeding. Open surgery includes packing, vascular ligation, the removal of solid organs, nonanatomical organ resection and temporary shunting, and it requires not only specialized surgeons but also a fully equipped and sterilized operating room, which is difficult to achieve in a hostile environment. A higher risk of infection and longer recovery time can also occur. As endovascular surgical techniques continue to develop, resuscitative endovascular balloon occlusion of the aorta (REBOA) is being used in a variety of haemostatic scenarios. REBOA can increase vital organ perfusion as well as cardiac afterload and aortic pressure by blocking distal blood flow and balloon bleeding. REBOA significantly improves survival and reduces complications compared to open surgery (Taylor et al., 2017). After insertion and expansion of the sacculus, various imaging methods, such as fluoroscopy, ultrasound, and radiography, can be used to determine whether the designated placement site has been reached. Physicians can also perform blind insertion in emergencies or in prehospital care. Successful placement is determined by changes in systolic blood pressure.

Overall, blood products are still the first choice for clinical haemostasis, but they do not fully meet clinical needs due to factors such as source limitations, preservation, and the risk of viral transmission. Advances in haemostatic devices and agents have increased interest in haemostatic treatment, but these devices can only meet the needs of emergency haemostasis or auxiliary haemostasis and cannot completely replace surgical treatment. Moreover, there are strict requirements for the injury site and the degree of injury. Surgical treatment is the most reliable solution for haemostasis, but it is not suitable for prehospital rescue because of the high requirements for the environment and operators.

# 3 Injectable hydrogels

## 3.1 Advantages of injectable hydrogels

Hydrogel materials have received much attention in recent years; they are three-dimensional polymer networks obtained by crosslinking through chemical bonds or physical interactions that can absorb large amounts of water while maintaining their structural integrity (McKinnon et al., 2014). The three-dimensional network structure resembles the ECM structure and has good biocompatibility while maintaining satisfactory permeability and facilitating the release of loaded components (Schmidt et al., 2008); this structure also endows the hydrogel with good water absorption properties, which are beneficial for haemostasis (Liu et al., 2015). A high degree of hydration facilitates the loading and rapid release of water-soluble components (Hoare and Kohane, 2008; Li and Mooney, 2016), facilitating the incorporation of water-soluble haemostatic components such as tranexamic acid and thrombin (Ker et al., 2012; Morrison et al., 2012; Tripodi, 2016). More importantly, hydrogels can be endowed with additional functions by modifying the polymers that constitute the hydrogel backbone, such as the addition of catechol moieties, to increase the viscosity of hydrogels (Guvendiren et al., 2012). The multiple advantages of hydrogels have made them a topic of intense interest in haemostatic materials (Ahmed, 2015). In recent years, injectable hydrogels have acquired a broader range of applications (Yu and Ding, 2008): injectable hydrogels can be used to solve the problem of deep wound haemostasis facilitating minimally invasive surgery. The fluid precursor of *in situ* gel-forming injectable hydrogels can be used to achieve complete coverage of irregular wounds and precise delivery to the bleeding location with the help of professional delivery devices (Patenaude et al., 2014), addressing deep wounds and noncompressible bleeding.

TABLE 3 Injectable hydrogel design strategy.

| Crosslinking method | Mechanism | Advantages | Disadvantages |
|---|---|---|---|
| Physical | Electrostatic interactions | High biosafety, no crosslinking agent required | Reversible crosslinking, low increase in on mechanical strength |
| | Hydrophobic interactions | | |
| | Host-guest interactions | | |
| | Van der Waals forces | | |
| Chemical | Diel–Alder | High crosslinking efficiency, crosslinking stability, can significantly increase mechanical strength | Some crosslinkers pose biosafety risks and have long degradation cycles *in vivo* |
| | Michael addition | | |
| | Enzyme-mediation | | |
| | Photopolymerization | | |

## 3.2 Injectable hydrogel design strategy

The design of injectable hydrogels involves two main steps: selection of the backbone material and the crosslinking method. The density of hydrophilic groups on the backbone material determines the water absorption capacity, and adequate water absorption is critical for haemostatic materials. Excellent backbone polymers can absorb up to several thousand times their own weight in water (Bhujbal et al., 2020). However, swelling after water absorption will cause rapid disintegration of the material or inability to form gels, so crosslinking is needed to promote the transition from sol to hydrogel or to improve the mechanical properties of the hydrogel. Currently, the commonly used crosslinking methods include physical crosslinking and chemical crosslinking (Lee, 2018; Zhu et al., 2019; Bashir et al., 2020; Zawani and Fauzi, 2021) (Table 3).

In addition, a number of other factors, such as temperature, pH, electric field, magnetic field, light, and enzymes, can also affect the crosslinking and state of injectable hydrogels. These characteristics have been exploited to develop "smart" biomaterials. For example, injectable haemostatic materials that respond to temperature changes have been designed (Ryu et al., 2011).

## 3.3 Design requirements for injectable haemostatic hydrogels

Rapid haemostasis is the most important requirement for a haemostatic material. Injectable hydrogels with adhesive sealing properties are ideal for bleeding sites that cannot be directly compressed (Han et al., 2020). However, such sites present great challenges to material performance. In addition to the moist environment in the case of bleeding, the effects of blood pressure in the arteries also impose high requirements on the adhesive and burst strength of the material (Fan et al., 2020; Kim et al., 2020; Baghdasarian et al., 2022). For materials that achieve haemostasis by enriching blood cells, sites for easy cell loading or strong fluid absorption are key to material design. For materials that activate the coagulation cascade, the appropriate choice of components is critical to successful design.

In addition, to address noncompressible bleeding from in organs and blood vessels in the torso, high biosafety of the material is also essential. In addition to meeting regulatory requirements, the inability to cause excessive thrombosis is a key concern in the development of haemostatic hydrogels.

Finally, timely and rapid intervention with a short therapeutic invasive period is needed for patients with uncontrollable bleeding. Haemostatic hydrogels should be portable, simple to use, and operable not only by medical personnel but also by civilians without a medical background. To be useful in prehospital emergency scenarios, the material should not have strict requirements for storage conditions or allow too short a storage time.

# 4 Injectable hydrogels for the treatment of noncompressible trunk haemorrhages

With increasing understanding of the haemostatic process, a variety of haemostatic materials that mimic the human haemostatic mechanism have been developed (Patenaude et al., 2014). The haemostatic mechanisms used can be divided into three categories: wound closure, blood cell enrichment, and the loading of procoagulant components (Figure 3).

## 4.1 Closed wounds

Closing or minimizing the wound is the most direct and effective way to stop noncompressible bleeding, similar to early vasoconstriction or complete thrombosis in the early stages of bleeding. A well-bonded hydrogel can quickly and effectively stop further blood flow (Zhang et al., 2020). Figure 4 shows the common principles of hydrogel wound closure. Table 4 summarizes the adhesive strength of representative hydrogel adhesives.

### 4.1.1 Mussel protein inspiration

The discovery that mussel proteins exhibit strong adhesion underwater has inspired researchers. 3,4-Dihydroxyphenylalanine (DOPA), which has a catechol structure, is widely considered to be the key to the wet adhesion of mussel proteins (Strausberg and Link, 1990; Lee et al., 2006). This is mainly due to the ease with which the

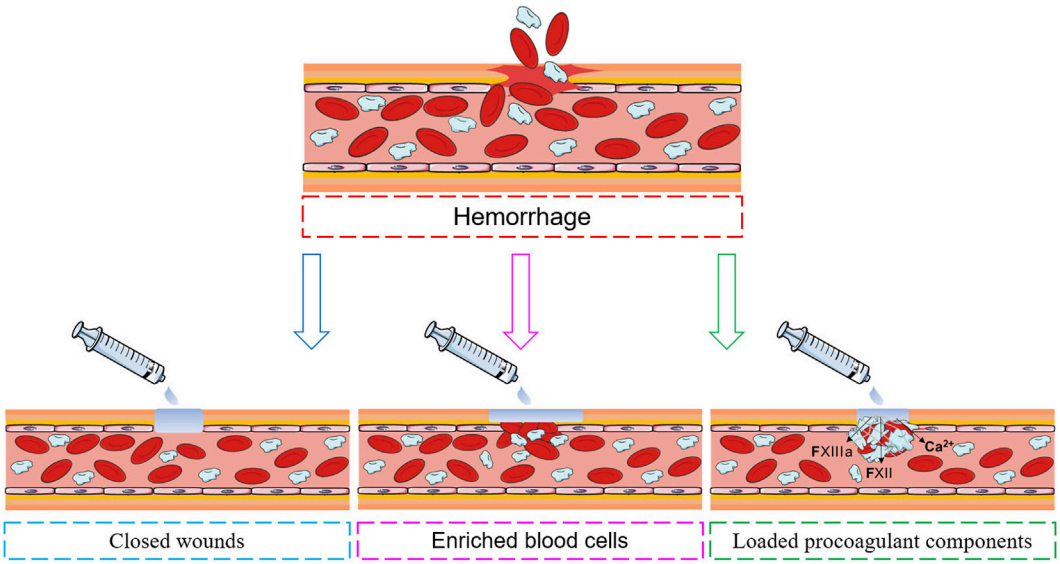


FIGURE 3
Injectable haemostatic hydrogel haemostatic mechanisms.

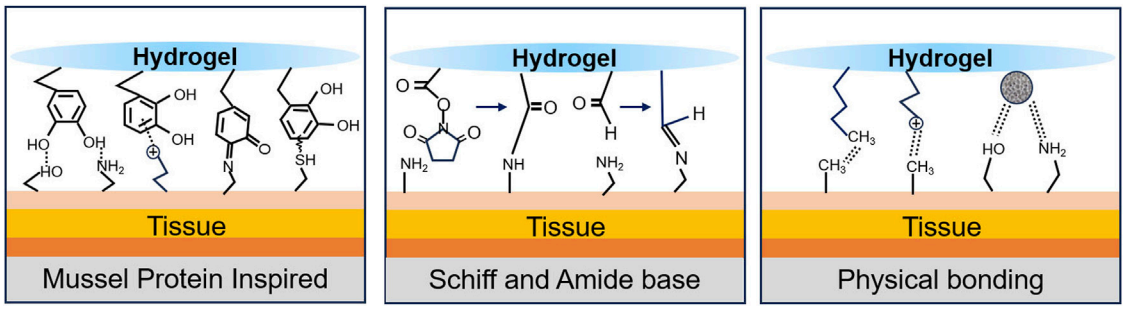


FIGURE 4
Schematic diagram of the bonding principle.

catechol moiety can be oxidized chemically or enzymatically to form reactive quinones. These species can further undergo Michael addition and Schiff base reactions with tissue surface nucleophilic reagents such as amines, thiols and imidazole. These reactions can also synergize with hydrogen bonding, π-π stacking, and cation-π interactions to achieve desirable tissue adhesion through multiple pathways (Strausberg and Link, 1990; Lee et al., 2006; Wang et al., 2017; Chen et al., 2018; Xie et al., 2020).

Adding a catechol structure to the material system can effectively improve the tissue adhesion properties. The most common methods involve the direct incorporation of dopamine or tannic acid (TA) into the material body or functional modification of the backbone structure using dopamine. Mehdizadeh et al. (2012) prepared a hydrogel by mixing PEG, dopamine, citric acid and sodium periodate. Its tissue adhesion strength reached 123 kPa (Mehdizadeh et al., 2012). In the work of Jae Park, TA was introduced into a double network hydrogel consisting of poly (vinyl alcohol) (PVA) and poly (acrylic acid) (PAA) to create tissue adhesives (shear strength of ≈31 kPa) and haemostatic agents (bleeding reduced by more than 80%) (Park et al., 2023). Wei et al. (2023) prepared aldehyde-functionalized hyaluronic acid-catechol-functionalized quaternized chitosan [HA (CHO)-QCS (DOPA)] by grafting the catechol structure onto chitosan. The material offers excellent adhesion strength (Wei et al., 2023). This solution can be further used in combination with other functionalized chitosans to enrich the functionality of the material. For example, preparing CQCS@gel with quaternized chitosan as the main raw material increases the antimicrobial properties of the material (Fang et al., 2023), and HBCS-C prepared using hydroxy butyl chitosan has excellent temperature sensitivity (Shou et al., 2020). In addition to chitosan, hyaluronic acid (HA), sodium alginate (SA), and gelatine can exhibit increased viscosity through dopamine modification (Ryu et al., 2011; Chen et al., 2018; Liang et al., 2019a; Song et al., 2019; Wang et al., 2020; Xia et al., 2022; Yang et al., 2022). The HACN network designed by Xia et al. (2022) is representative. It consists of thiourea-conjugated HA (HA-NCSN) and catechol-conjugated HA (HA-Cat). HACN has been demonstrated to have a good haemostatic effect on the

TABLE 4 Representative research on adhesion strength and adhesion composition/structure.

| Material | System | Maximum adhesion strength (kPa) | Adhesive composition/ structure |
|---|---|---|---|
| HA (CHO)-QCS (DOPA) | Aldehyde-functionalized hyaluroni, acid–catechol-functionalized quaternized chitosan | 140 | Catechol, aldehyde group |
| iCMBAs | PEG, dopamine, citric acid and sodium periodate | 123.0 | Catechol |
| PPD | Poly (lysine) polyethylene glycol backbone, HRP | 147 | Catechol, polylysine |
| SFP | TA, silk protein | 130.0 | Polyphenol, SF |
| RAAS | Methacrylated hyaluronic acid, PF127, AA-NHS | 33.0 | NHS |
| CQCS@gel | CQCS, DB-PEG 2000 | 33.5 | Catechol, aldehyde group |
| GMDA | Dopamine-modified methacrylate gelatine, peroxidase, hydrogen peroxide | 134.3 | Catechol |
| CGD | Chitosan and DHCA, β-glycerophosphate | 32.5 | Catechol |
| PEG-LZM | 4-arm-PEG-NHS, sodium tetraborate, lysozyme | 20 | NHS |
| St-Dopa | Dopamine, carboxylic starch, HRP, hydrogen peroxide | 95.5 | Catechol |
| CMCS-brZnO | CMCS, brZnO | 45.0 | Electrostatic interaction, hydrogen bonding |
| AHES/ACC | AHES, ACC | 42.7 | Aldehyde group, electrostatic |
| PDPC | PVA, DOPA, $Cu^{2+}$ | 26.0 | Catechol |
| DNGel | Catechol-$Fe^{3+}$, NIPAAm-methacryloyl | 3,500.0 | Catechol |
| DGM | Amylopectin from maize, gelatine, MBGN | 107.6 | Hydrogen bonding, electrostatic interaction |
| PBO | PVA, borax, OPC | 29.2 | Catechol, hydroxy |
| CSO | CMCS, SA, ODE | 120.6 | Aldehydes, amino groups, carboxyl groups |
| GTB | Gelatine, TA, borax | 68.0 | Polyphenols, Amino |
| CD | CtNWs, CMCS, DDA | 33.2 | Hydrogen bonding, electrostatic interaction |
| PPBA-PVA | poly (N,N-dimethylethylenediaminephazene), PVA, polymer solution modified with phenylboronic group | 45.0 | Cation–π, π–π, hydrogen bonding |

digestive tract in *in vivo* experiments in pigs (Xia et al., 2022). By modifying collagen and starch chains with the structure of catechols in mussel proteins and the structure of arabinogalactan proteins in creeping plants, the proteins can then be crosslinked by calcium ions to form the hydrogel CoSt. CoSt shows repeatable strong wet tissue adhesiveness (62 ± 4.8 KPa), high sealing performance (153.2 ± 35.1 mmHg), and high haemostatic efficiency compared with fibrin glue (Yang et al., 2023).

Previous studies have confirmed that adhesiveness is determined by the balance and synergy of interfacial adhesion and cohesion qualities inside the sticky matrix (Li et al., 2017; Bu and Pandit, 2022). The introduction of enzymes [e.g., horseradish peroxidase (HRP)] into the material system not only increases the crosslinking strength of the material and thus the cohesion but also aids in the conversion of catechol to catechol aldehyde, which further increases the adhesive properties of the material. Guoqing Wang synthesized highly branched gelatine containing a large number of catechol terminals via synergetic crosslinking of catechol-$Fe^{3+}$ chelation and HRP/$H_2O_2$-triggered covalent bonds, yielding shear strength of 115.0 ± 13.1 kPa and sealing strength of 245.0 ± 33.8 mmHg (Wang GQ. et al., 2022). In the hydrogel prepared by Wang et al. (2017), the catechol structure was grafted onto the poly (lysine) polyethylene glycol (PEG) backbone, catalysed by HRP. The interaction between the catechol structure and lysine resulted in excellent adhesion to dry or wet pigskin, with adhesion strengths up to 147 kPa. The haemostatic effect in a rat liver injury model was also significantly better than that of the fibrin glue group (Wang et al., 2017). Dopamine-coupled starch (St Dopa) macromolecular monomers, which function with the assistance of HRP and hydrogen peroxide to increase the speed of crosslinking and the strength of adhesion, can be injected into the wound surface to quickly form a tough protective barrier to prevent blood loss (Cui et al., 2020). Zhou et al. (2022) utilized GMDA as the main component and introduced photocrosslinking in addition to enzymatic crosslinking to form a dual network structure, which makes the material highly adhesive and able to withstand blood pressures up to 250 mmHg. It has good development prospects in the field of arterial haemostasis (Shin et al., 2015; Bai et al., 2019;

Zhou et al., 2022; He et al., 2022; Kang et al., 2023; Liu et al., 2023). Notably, the complexation of catechol with metals can also effectively increase the crosslinking strength of the material and improve its adhesion properties (Wang et al., 2020; Hou et al., 2022). Hu et al. (2023) prepared PVA-DOPA-Cu (PDPC) by esterification between PVA and DOPA and catechol coordination between $Cu^{2+}$ and the catechol moiety of DOPA. Pig liver, heart, and carotid artery haemorrhage experiments were able to stop bleeding rapidly, significantly improving survival rates.

In addition to increasing the grafting rate of catechol, increasing the exposure of the catechol structure can also result in superior tissue adhesion. Cui et al. (2019) attached the catechol structure to the hydrophobic backbone and subsequently contracted the structure in the liquid environment to expose the catechol structure and achieve high adhesion performance.

### 4.1.2 Schiff and amide bases

Based on the presence of multiple amino structures in tissues, researchers have increased tissue adhesion by preparing materials containing aldehyde structures or NHS for Schiff base or amide reactions with tissues (Xie et al., 2022). Liu et al. (2020) prepared a series of AHES/ACC hydrogels formed from aldehyde hydroxyethyl starch (AHES) and amino carboxymethyl chitosan (ACC). It was also found that varying the ratio of aldehyde to amino groups could tune the properties of the AHES/ACC hydrogels, including gelation time, tissue adhesion strength, swelling rate, degradation and mechanical stretching. Taking advantage of this feature, researchers have prepared Schiff base haemostasis hydrogels with different properties by raw material selection and grafting rate modulation. Cao et al. (2019) constructed a haemostatic hydrogel with carboxymethyl chitosan (CMCS), gelatine and oxidized SA that achieved *in situ* curing within 30 s and reduced bleeding after liver injury in rats by 82.2%. Hao et al. (2022) constructed a haemostatic hydrogel with four-arm-PEG-CHO and polyethyleneimine with a polyamine structure that achieved an *in situ* curing speed of up to 9 s, and the haemostatic speed was comparable to that of Surgiflo®. Li et al. (2022) used glycol chitosan and oxidized HA to construct an injectable haemostatic hydrogel with very strong self-healing properties, prolonging the time the material protects the wound. Xie et al. (2022) reported a multifunctional CSO hydrogel prepared from moist pig skin using CMCS, SA, and oxidized dextran (ODex) with a lap shear strength of up to 120.6 kPa. To further optimize the material properties, researchers have combined various design strategies. The effectiveness of modifying the polyphenol structure on the material backbone (Liu et al., 2022), selecting synthetic raw materials with photocrosslinking properties (Chen et al., 2021), and adding nanosubstances to increase the interactions between the raw materials (Zhu et al., 2017; Pang et al., 2020) have been verified by *in vivo* animal experiments. Notably, Hong et al. (2019) used methacrylate gelatine and butyramide-modified HA to construct a dual crosslinked network hydrogel with UV-induced photocrosslinking and a Schiff base reaction. This material successfully achieved haemostasis of the porcine carotid artery and heart because of its high internal systemic strength and high external tissue adhesion strength (Hong et al., 2019). In addition, the oxidized indole moiety on serotonin can react with amine, thiol, and imidazole residues in ECM proteins and carbohydrates via a Schiff base reaction, which enables the hydrogel to adhere firmly to the wound and seal it, achieving haemostasis. Zhang et al. (2021) designed a CSS hydrogel that reduced bleeding in liver-injured rats by 80%.

In recent years, the application of N-hydroxysuccinimide (NHS) has expanded. Like aldehyde groups, NHS can not only increase the crosslinking strength inside hydrogels and regulate the gelation time of materials but also increase the adhesion strength of materials by binding to amino groups on tissue surfaces (He et al., 2021). Numerous experiments have demonstrated that NHS is not involved in the crosslinking of materials but plays a decisive role in the tissue adhesion of materials (Ye et al., 2022). Owing to their tuneable performance and high biosafety, these materials have a wide range of applications. In addition to effectively controlling rat liver and blood vessel haemorrhage, they also exhibited ideal haemostatic effects on rat cerebral cortex injury, cerebrovascular injury, cardiac injury, and porcine gastric haemorrhage (He et al., 2021; Bian et al., 2022). The addition of borax further increased the gel formation speed. The modulation of the ratio between the components can realize rapid modulation of the wound and enable long-distance delivery in conjunction with minimally invasive surgery (Tan et al., 2021).

### 4.1.3 Physical bonding

In addition to chemical crosslinking, physical bonding affects tissue adhesion. Grafting long-chain alkyl groups on macromolecular backbones has been reported to increase tissue adhesion by interacting with alkyl groups in subcutaneous adipose tissue. Du and Chen used this principle to prepare adhesive hydrogels by mixing long-chain alkyl-modified chitosan with ODex or PEG (Chen et al., 2018; Du et al., 2019a). Positively charged materials (e.g., chitosan and gelatine) can increase adhesion to biological tissues through electrostatic interactions (Hoque et al., 2017). The use of positively charged groups [e.g., ammonium groups, quaternary ammonium groups, and ε-polylysine (ε-PL)] to modify the material backbone has a similar effect (Balan and Verestiuc, 2014; Konieczynska et al., 2016; Zhao et al., 2017; Zou et al., 2022). However, further improvements in adhesion properties are difficult to achieve by relying on these materials alone, as the presence of a hydrated film can strongly interfere with the adhesion of the material. Introducing hydrophobic groups to disrupt the hydration film and allow better contact between the adhesion groups in the material and the tissue surface is an effective solution (Pinnaratip et al., 2019). Inspired by barnacle cement proteins, Ni created a series of dynamic phenyl borate ester-based adhesive hydrogels by coupling cation-structured polyphosphazene with polyvinyl alcohol (PPBA-PVA) (Ni et al., 2022). In a liquid environment, hydrophobic aromatic groups disrupt the hydration film, and the hydrogel achieves an adhesive strength of 45 kPa through cation-π and π-π interactions and hydrogen bonding.

The incorporation of nanocomponents with a porous structure and a high specific surface area can help increase the adhesion properties of materials (Hu et al., 2022). Tian et al. (2022) incorporated mesoporous bioactive glass nanoparticles (MBGNs) into a material system to make DGM and increased the adhesive strength to 107.55 kPa by increasing the cohesion of DGM (Tian et al., 2022). Due to the high temperature sensitivity of these substances, painless removal of the material can be performed by

changing the ambient temperature (e.g., by introducing ice). The diatom biosilica, which contains a large number of surface silanol groups, was incorporated into bletilla striata polysaccharide, a traditional Chinese medicine ingredient with haemostatic effects (Sun et al., 2023). The structural features of the diatom biosilica increased the cohesion of the material and the force applied to the tissue surface to improve the contact efficiency and duration of the material with the wound, reducing the bleeding volume from 452 mg to 250 mg and the bleeding time from 327 s to 186 s. Diatom biosilica was also used to reduce the bleeding time from 327 s to 186 s.

## 4.2 Enrichment of blood cells

Primary thrombus formation is accomplished by the rapid aggregation and activation of red blood cells and platelets. Therefore, the design of many haemostatic materials focuses on the adsorption and concentration enhancement of red blood cells and platelets (Zhu et al., 2018). The longest used strategy is to provide adhesion sites for blood cells as well as to absorb water from the blood. Many substances with this function exist in nature. Chitosan, gelatine and their derivatives are the most common raw materials for haemostatic materials.

Chitosan is a positively charged polysaccharide that can adsorb blood cells and clotting factors through electrostatic interactions to achieve haemostasis (Chou et al., 2003; Okamoto et al., 2003; Lestari et al., 2020). Chitosan has excellent biocompatibility, biodegradability, and low toxicity, undergoes enzyme-controlled degradation, and contains easily modified free amino and hydroxyl groups (Kean and Thanou, 2010). Therefore, it is widely used in various kinds of haemostatic hydrogels. Feng and Wang (2022) mixed chitosan with graphene oxide to further enhance the ability of the material to enrich blood cells through the strong adsorption of graphene oxide. In rat liver injury experiments, the bleeding time was reduced by more than 60% and the bleeding volume by more than 75% compared to that in the control group. However, the water solubility of chitosan is not ideal. Many researchers have chosen to use CMCSs as a raw material for further synthesis. Not only does CMCSs have better water solubility, but the addition of carboxyl groups also increases the material's adsorption of blood cells (Huang et al., 2016). Rao et al. (2022) Combined CMCSs with TA-stabilized silver nanoparticles in a haemostatic gel that can be used for haemostasis in minimally invasive surgery. Poly-gamma-glutamic acid (γ-PGA) can expel water from the wound surface, which can rapidly concentrate blood to increase the concentration of blood cells at the wound site, and combining this property with the adsorption effect of CMCS can achieve a significant reduction in bleeding time (Chen et al., 2023). ε-PL and 1,4-benzenediboronic acid (BDBA) can play a role in regulating the crosslinking strength and gelation rate of hydrogels, and haemostatic gels with different pore structures and gelation times were prepared with different degrees of crosslinking. The most suitable preparation schemes were screened through various application scenarios. The extent of bleeding in mouse livers treated with the hydrogels could be reduced from 240 to 55 mg (77% reduction) (Wang YC. et al., 2020; Geng et al., 2020).

Hydrophobically modified chitosan (hmCS) with hydrophobic aliphatic side chains has excellent erythropoietic capacity (Dowling et al., 2011; Dowling et al., 2015; Duc-Thang and Lee, 2017). Hydrogels prepared from hmCS with ODex using the Schiff base reaction can effectively reduce the clotting time of heparinized WB (Du et al., 2019b). Kong et al. (2021) prepared a series of CuS NP hydrogels using the derivative N-carboxyethyl chitosan (CEC), sodium oxide alginate (OA) with good water absorption, and CuS nanoparticles with high specific surface positivity, which effectively increased the enrichment efficiency of haemocytes. In an *in vivo* study in a rat liver bleeding model, the blood loss was 185.1 ± 18.6 mg in the CEC–OA2.8–CuS0.8 group and 538.6 ± 27.5 mg in the control group (Kong et al., 2021). Choline phosphoryl (CP) is the reverse orientation of phosphatidylcholine (PC, the head group of phospholipids) and can adsorb to adsorbed biofilms by electrostatic interactions. Choline-phosphorylated functionalized chitosan (CS-g-CP) was prepared by grafting CP onto CS and mixing it with OD to obtain self-repairing haemostatic hydrogels (CS-g-CP/ODex). The haemostatic capacity of CS-g-CP/ODex was significantly greater than that of commercially available fibrin sealant in the tail amputation, liver, and spleen of rats (Zhu et al., 2022). Wang prepared with the aid of UV crosslinking CS/4-PA/CAT from dihydrocaffeic acid (CAT), 4-glutamic acid, and chitosan to form a haemostatic hydrogel with a hydrophobic network, which overcame the problem of the material dissolving and extruding the periwound tissue (Wang et al., 2023). Grafting gallic acid (GA) onto CS increased the mechanical strength of the material. Gong et al. (2023) incorporated iron oxide nanoparticle-loaded mica nanosheets with a typical 2D lamellar morphology and negatively charged surface (iron oxide nanoparticles@mica, IM) with a typical 2D sheet-like morphology and negatively charged surface to make a composite magnetic hydrogel, which was able to reduce the bleeding time in a rat model of liver injury by 60% (Yan et al., 2022; Gong et al., 2023).

Gelatine is a hydrolysed product of collagen that retains similar biological functions and has good water absorption and blood cell adhesion properties (Zeugolis et al., 2008; Xu et al., 2013; Yang et al., 2018). However, the mechanical strength of these materials is poor, and they need to be modified or combined with other components. In early research, gelatine and SA were combined to make a precursor gel, which was first used to cover the wound surface and subsequently crosslinked *in situ* using a spraying portion composed of TA and $Ca^{2+}$ chloride to form the low-swelling haemostatic hydrogel $A_GB_S$ (Wang et al., 2022). Hydrogels made from gelatine and hyaluronic acid have also been shown to have haemostatic properties superior to those of fibrin glue. In a rat bleeding model, the fibrin glue group had a blood loss of 109 ± 92 mg, whereas the blood loss in the G/HA hydrogel group was 64 ± 50 mg (Luo et al., 2020). Replacing gelatine with gelatine methacryloyl (GelMA) allows the introduction of a photocrosslinked network into the material system and increases the stability of the hydrogel's three-dimensional network structure. It is often used to construct the base skeleton for loading other haemostatic components (Zhang et al., 2022; Haghniaz et al., 2023). The incorporation of silicate nanosheets (SNs) into GelMA-based composite hydrogels was shown to reduce bleeding in rat liver injury by 50% (Gaharwar et al., 2014).

In addition to gelatine, a number of other peptides or protein derivatives with RGD sequences also have favourable blood cell adhesion effects (Quan et al., 2016). Zhai et al. (2019) designed a haemostatic hydrogel with encouraging haemostatic properties via the coassembly of cell adhesion peptide concatenate (Pept-1) and alginate (ALG) and reduced the amount of bleeding to 18% of the untreated control in a liver puncture mouse model (Zhai et al., 2019). Pept-1/ALG utilizes the RGD fraction present in Pept-1 to bind to the a8b3 receptor on platelets and accelerate haemostasis. Notably, ADP is a platelet-activating factor that readily self-assembles with other peptides. ADP adsorbs platelets and activates platelets, causing the activated platelets to release biologic factors and further enriching platelets to promote coagulation (Lokhande et al., 2018). Zhou et al. (2022) prepared a J-1-ADP hydrogel by self-assembly of the antimicrobial peptide jelloprotein-1 (J-1) and ADP. In a rat liver bleeding model, the blood loss in the J-1-ADP hydrogel treatment group was 41.15 ± 14.43 mg, while the blood loss in the no treatment and PBS treatment groups was 178.08 ± 41.53 and 167.03 ± 23.36 mg, respectively (Zhou et al., 2022).

Some surface-charged materials, such as graphene oxide, limonite nanoclay, and metal nanosheets, can adsorb blood cells through electrostatic interactions to achieve rapid thrombus formation (Gaharwar et al., 2014; Gaharwar et al., 2019; Gu et al., 2023). The addition of such substances not only increases the adsorption of the material to blood cells but also improves the cohesion of the material and increases the mechanical strength. Wang designed a bionic self-assembling peptide (BSAP) hydrogel that is extremely sensitive to $Ca^{2+}$ and coagulation factor XIIIa and can rapidly adsorb and activate platelets and erythrocytes upon contact (Wang et al., 2022).

## 4.3 Activation of the coagulation cascade

Haemostasis must ultimately rely on the activation of the coagulation cascade, which can be effectively achieved by the direct introduction of coagulation factors into the body. $Ca^{2+}$, also known as coagulation factor IV, is an important part of the coagulation cascade. It has become one of the commonly used haemostatic components due to its low cost, easy availability and adjustable mechanical strength. It has been demonstrated that excellent haemostatic effects can be obtained by adding $Ca^{2+}$ directly to the material system without special treatment (Sundaram et al., 2021; Wang et al., 2021). In Weng's study, the $Ca^{2+}$-containing hydrogel NSC-OHA showed blood loss similar to that of a commercial haemostatic agent (Arista™) in an *in vivo* experiment in rats (0.08 ± 0.02 g, 0.10 ± 0.03 g), both of which were significantly lower than that of the control group (0.62 ± 0.08 g), demonstrating the excellent haemostatic effect of NSC-OHA. Pillai found that the addition of Whitlockite nanoparticle nWH, which can release $Ca^{2+}$, to the haemostatic material was able to reduce the blood loss of rat liver perforation by 50% (Pillai et al., 2019).

Thrombin plays an important role in the whole coagulation process and can activate the conversion of fibrinogen to fibrin. Platelet-rich plasma (PRP) activated by thrombin is combined with sodium alginate-$Fe^{3+}$ to prepare a hydrogel with a dual network structure that prevents excessively rapid release of the loaded components and ensures sufficient coagulation components in the patient's body (Wang et al., 2023). Applying the material to the wound surface is equivalent to placing a blood clot at the wound site, fast-tracking the haemostatic process. However, these "artificial thrombi" lack sufficient tissue adhesion properties. Xu et al. (2023) used 6-aminobenzo [c] [1,2] oxaborol-1 (3H)-o (ABO)-conjugated hyaluronic acid (HA-ABO) and DA-grafted alginate (Alg-DA) as the backbone components of the hydrogel (Xu et al., 2023). The excellent adhesion properties and self-healing properties of the materials reduced blood loss from 364.1 ± 52.4 mg to 129.4 ± 23.0 mg. Transglutaminase (factor XIIIa) promotes fibrin network formation and increases thrombus strength. Glutaminase can not only be converted to transglutaminase in the haemorrhagic environment but also be used as a crosslinking agent to prepare hydrogels (Zhou et al., 2019). Sun OPEG-AG-G hydrogels were prepared via double-tube injections (Sun et al., 2022). Tube A contained 10% glutamine and 20% aminated gelatine, and tube B contained 10% oxidized PEG and 1% transglutaminase. OPEG-AG-G achieved haemostasis of porcine arterial rupture without vascular closure.

Activators of distinct coagulation pathways can be coincorporated into the material system to improve haemostasis. Sundaram et al. (2019) found that incorporating nanobio-glass (nBG) containing silica (which activates coagulation factor XII), $Ca^{2+}$ (which activates the endogenous system), and phosphate ions (which initiate the exogenous pathway) into chitosan matrix hydrogels can promote rapid thrombus formation (Sundaram et al., 2019). Loading RG5, which promotes the coagulation cascade reaction, into platelet-activating hydroxyapatite nanotubes (HNTs) to make a haemostatic powder, which is subsequently loaded into an ALG and gelatine hydrogel skeleton, was the goal of Zhang. The prepared HNTs/RG5 possessed haemostatic properties superior to those of commercially available haemostatic products (the haemostasis times of the HNTs/RG5-and Celox®-treated groups were 97.8 ± 8.2 s and 136 ± 22.1 s, respectively) (Zhang TW. et al., 2021). The strategy of using a combination of hydrogel and haemostatic powder results in the superior performance of AGHR hydrogels, which remain injectable even in extremely hot and cold regions and are suitable for many types of first aid and battlefield rescue.

# 5 Summary and outlook

Haemostasis is a key challenge in post-trauma treatment. Although the body's inherent coagulation mechanism can complete the haemostatic repair of small-scale wounds through vasoconstriction, platelet plug formation and coagulation cascade triggering, rapid haemostasis cannot be naturally achieved in large-area trauma bleeding, bleeding from important vessels (such as the common carotid artery and femoral artery), and bleeding from parenchymal organs (such as the liver and heart) solely through the coagulation mechanism alone, and additional injury or even death can ensue. Here, we summarize the main haemostatic methods, including haemostatic compression, which is effective at stimulating vasoconstriction and reducing blood flow but may cause limb necrosis. These methods are currently used only in first aid and require the next step of treatment as soon as possible. Haemostatic

materials with strong water absorption and blood cell adsorption capacity can rapidly increase blood cell concentrations and create a high clotting environment, and gelatine sponges are widely used in intraoperative and postoperative haemostasis. These materials are completely dependent on the patient's coagulation system and are not suitable for patients with coagulation disorders, and some highly absorbent materials may cause local tissue water loss. Thrombinogen and fibrinogen components can effectively promote coagulation cascade reactions and accelerate the formation of blood clots, while the direct addition of coagulation components can help patients with coagulation disorders quickly stop bleeding. However, these materials present problems such as virus transmission, scarce sources, and high cost. Materials with high adhesion properties can bind wounds to achieve haemostatic effects. At present, relatively few haemostatic adhesives, mainly cyanoacrylate and fibrin sealants, are commercially available. Cyanoacrylate adhesives have strong adhesive properties and fast haemostatic efficacy, but they may produce formaldehyde and other harmful degradation products during biodegradation, which need to be considered when using these materials. Fibrin sealants achieve haemostasis through the activation of fibrinogen and thrombin *in vivo*, but they may allow viral transmission and are expensive, limiting their use in clinical practice. Therefore, further research is needed to develop safe, effective, and cost-saving haemostatic adhesives for wound closure.

As mentioned above, a large number of haemostatic products have been used in clinical practice. However, there are still many unresolved issues. One of the most difficult problems is noncompressible haemorrhage, in which direct access to the bleeding site is difficult and bleeding cannot be directly controlled by physical pressure, making this type of injury difficult to address. Clinical treatment is still based on blood transfusion and surgery, but this approach is difficult to implement in emergencies and in war environments. Hydrogels have the advantages of high hydrophilicity, high biosafety, easy modification, easy loading, etc., and are among the most promising materials. Hydrogels with injectable properties are beneficial for haemostasis in incompressible haemorrhage, in narrow and deep wounds, and in minimally invasive surgeries. Researchers have prepared injectable haemostatic hydrogels in a variety of ways. Studies have confirmed that positively charged raw materials or groups, aldehyde structures and catechol structures have positive effects on the adhesion strength of materials and contribute to the rapid closure of wounds. Haemostatic materials that can promote blood cell enrichment can be prepared by selecting materials that have the characteristics of electrostatic adsorption by blood cells and rapid water absorption. Loading coagulation factors, haemostatic peptides and other procoagulant substances can accelerate the progression of the coagulation cascade, which is highly important for patients with coagulation disorders. Notably, the three-dimensional mesh structure of hydrogels easily loads drugs and bioactive factors, which contributes to the expansion of hydrogel functions. Amoxicillin (Liang et al., 2019b; Qu et al., 2019), ampicillin (Refat et al., 2018), tetracycline (Anjum et al., 2016; Rakhshaei and Namazi, 2017; Liu et al., 2018), gentamicin (Singh et al., 2013; Zhang et al., 2015), ciprofloxacin (Radhakumary et al., 2011; Shi et al., 2015; Gao et al., 2019), moxifloxacin (Singh and Dhiman, 2015; Singh et al., 2016), chloramphenicol (Lacin, 2014), sulfadiazine (McMahon et al., 2016), simvastatin (Rezvanian et al., 2017), salicylate (Mi et al., 2011), and other components have been encapsulated in hydrogels to confer antibacterial properties. Some metal ions, such as silver, gold, and zinc, can also have antibacterial effects, and their complexation with the main structure of the hydrogel can also increase the strength of the system (GhavamiNejad et al., 2016; Chen et al., 2019; Liang et al., 2019c; Mahmoud et al., 2019; Shi et al., 2019; Tang et al., 2019). Stem cells can secrete essential factors that facilitate wound repair and stimulate angiogenesis and re-epithelialization. Therefore, many hydrogels promote wound repair by loading stem cells (Oryan et al., 2019; Xu et al., 2019; Yao et al., 2019; Xiong et al., 2022).

Although injectable hydrogels have achieved rapid haemostasis with high adhesion, high water absorption, enrichment of blood cells, and facilitation of the coagulation cascade in past studies, there are still many challenges to overcome. First, the speed and manner of *in situ* hydrogel formation should be further optimized. To better adapt to the wound shape and achieve injectable properties, many hydrogels are prepared by *in situ* gelation: a syringe is used to inject the precursor solution at the wound site and Schiff base crosslinking and photoccrosslinking occur simultaneously to achieve *in situ* gelation at the wound site. Although, after continuous optimization and improvement, many gels can now form within 30 s, there is still a risk that such a gelling speed on the wound surface is insufficient in cases of severe traumatic bleeding or vascular bleeding; the need for UV light and other light sources to achieve gelling also limits the use of gels and increases biosafety risk. Second, exisiting research has mostly used medium- and small-animal models, such as a rat liver injury model, a rat femoral artery injury model, a rat broken tail model, a rabbit ear marginal artery injury model, and a rabbit liver injury model for *in vivo* experimental verification. Although the haemostatic performance of the material can be verified to a certain extent, limited by the animal's size, blood volume, bleeding intensity and other issues, there is still a large gap in understanding the actual clinical bleeding situation. It is recommended that animal models more closely related to the clinical situation should be created in future studies or that large animal models be used for further validation at a more mature stage of material research. Third, implantable biomedical materials will stay in the body for a long time. However, the existing studies mostly focus on short-term haemostatic performance evaluation or simple *in vitro* safety evaluation (such as red blood cell haemolysis tests and *in vitro* safety tests), lacking long-term biocompatibility assessment and posthemostasis prognosis evaluation. These are the key factors determining whether materials can be put into clinical use. In the history of haemostatic material application, there are many examples of excellent haemostatic performance but secondary damage to patients, such as endothelial damage and systemic thrombosis caused by WoundStat® and tissue inflammation and tissue sclerosis caused by the degradation of cyanoacrylate products. Our group also found in previous research that haemostatic hydrogels with strong adhesion properties can cause aggravated tissue adhesion, which is one of the complications that need to be prevented after traumatic bleeding. All these problems can be addressed and further ameliorated through perfect and systematic long-term safety experiments. We hope that researchers can give close attention to long-term safety investigations in future work. Finally, in situations such as car accidents, natural disasters, and war, there are often multiple types of trauma, and there is no visual identification of the bleeding site. Existing injectable hydrogel

haemostatic materials require a clear view of the treatment and direct contact with the wound, and there is a gap in addressing actual clinical needs. In addition to injectable hydrogels, targeted drugs can be developed for intravenous injection in combination with related devices or intelligent equipment developed for rapid diagnosis, accurate positioning, and stable haemostatic integration intelligent haemostatic robots. These new technologies and devices have the potential to address the challenges of multiple and diffuse trauma bleeding events and provide more convenient and efficient treatment options for trauma patients.

The development of perfect haemostatic injectable hydrogels is still a long way off, but we hope that this paper will help researchers interested in understanding the current state of injectable haemostatic hydrogels and has provided some inspiration for the research efforts of those working to advance this field. We encourage further research and innovation in this area to address the remaining challenges and to improve the treatment options available for trauma victims.

## Author contributions

XW: Investigation, Writing–original draft, Writing–review and editing. XY: Investigation, Writing–review and editing. ZS: Investigation, Writing–review and editing. XG: Investigation, Writing–review and editing. YT: Writing–review and editing. SH: Conceptualization, Funding acquisition, Writing–review and editing. JS: Writing–review and editing. QL: Conceptualization, Funding acquisition, Writing–review and editing.

## Funding

The author(s) declare that no financial support was received for the research, authorship, and/or publication of this article.

## Acknowledgments

The authors are very thankful for the financial support from the National Key R&D Program of China (2022YFC3006200) and the Tianjin Research Innovation Project for Postgraduate Students of China (2021YJSB156).

## Conflict of interest

The authors declare that the research was conducted in the absence of any commercial or financial relationships that could be construed as a potential conflict of interest.

## Publisher's note



## References

Ahmed, E. M. (2015). Hydrogel: preparation, characterization, and applications: a review. *J. Of Adv. Res.* 6 (2), 105–121. doi:10.1016/j.jare.2013.07.006

Anjum, S., Arora, A., Alam, M. S., and Gupta, B. (2016). Development of antimicrobial and scar preventive chitosan hydrogel wound dressings. *Int. J. Pharm.* 508 (1-2), 92–101. doi:10.1016/j.ijpharm.2016.05.013

Anonymous, A. (2013). Abdominal aortic tourniquet? Use in Afghanistan. *J. special operations Med. a peer Rev. J. SOF Med. Prof.* 13 (2), 1–2. doi:10.55460/hljc-dmck

Baghdasarian, S., Saleh, B., Baidya, A., Kim, H., Ghovvati, M., Sani, E. S., et al. (2022). Engineering a naturally derived hemostatic sealant for sealing internal organs. *Mater. Today Bio* 13, 100199. doi:10.1016/j.mtbio.2021.100199

Bai, S. M., Zhang, X. L., Cai, P. Q., Huang, X. W., Huang, Y. Q., Liu, R., et al. (2019). A silk-based sealant with tough adhesion for instant hemostasis of bleeding tissues. *Nanoscale Horizons* 4 (6), 1333–1341. doi:10.1039/c9nh00317g

Balan, V., and Verestiuc, L. (2014). Strategies to improve chitosan hemocompatibility: a review. *Eur. Polym. J.* 53, 171–188. doi:10.1016/j.eurpolymj.2014.01.033

Bashir, S., Hina, M., Iqbal, J., Rajpar, A. H., Mujtaba, M. A., Alghamdi, N. A., et al. (2020). Fundamental concepts of hydrogels: synthesis, properties, and their applications. *Polymers* 12 (11), 2702. doi:10.3390/polym12112702

Bhopale, G. M., and Nanda, R. K. (2003). Blood coagulation factor VIII: an overview. *J. Biosci.* 28 (6), 783–789. doi:10.1007/bf02708439

Bhujbal, S. S., Darade, S. B., and Dharmadhikari, S. S. (2020). Biomaterial based injectable hydrogel for controlled drug delivery: a review. *Int. J. Of Pharm. Sci. And Res.* 11 (3), 1007–1021.

Bian, S. Q., Hao, L. Z., Qiu, X., Wu, J., Chang, H., Kuang, G. M., et al. (2022). An injectable rapid-adhesion and anti-swelling adhesive hydrogel for hemostasis and wound sealing. *Adv. Funct. Mater.* 32 (46). doi:10.1002/adfm.202207741

Blair, P., and Flaumenhaft, R. (2009). Platelet α-granules: basic biology and clinical correlates. *Blood Rev.* 23 (4), 177–189. doi:10.1016/j.blre.2009.04.001

Bonanno, A. M., Graham, T. L., Wilson, L. N., and Ross, J. D. (2020). Novel use of XSTAT 30 for mitigation of lethal non-compressible torso hemorrhage in swine. *PloS one* 15 (11), e0241906. doi:10.1371/journal.pone.0241906

Brännström, A., Rocksén, D., Hartman, J., Nyman, N., Gustavsson, J., Arborelius, U. P., et al. (2018). Abdominal Aortic and Junctional Tourniquet release after 240 minutes is survivable and associated with small intestine and liver ischemia after porcine class II hemorrhage. *J. trauma acute care Surg.* 85 (4), 717–724. doi:10.1097/ta.0000000000002013

Bu, Y., and Pandit, A. (2022). Cohesion mechanisms for bioadhesives. *Bioact. Mater.* 13, 105–118. doi:10.1016/j.bioactmat.2021.11.008

Butler, F. K., Jr., Holcomb, J. B., Schreiber, M. A., Kotwal, R. S., Jenkins, D. A., Champion, H. R., et al. (2014). Fluid resuscitation for hemorrhagic shock in tactical Combat casualty Care: TCCC guidelines change 14-01--2 june 2014. *J. special operations Med. a peer Rev. J. SOF Med. Prof.* 14 (3), 13–38. doi:10.55460/dpoc-jwiy

Cao, J. Y., Xiao, L., and Shi, X. W. (2019). Injectable drug-loaded polysaccharide hybrid hydrogels for hemostasis. *Rsc Adv.* 9 (63), 36858–36866. doi:10.1039/c9ra07116d

Cap, A. P., Beckett, A., Benov, A., Borgman, M., Chen, J., Corley, J. B., et al. (2018). Whole blood transfusion. *Mil. Med.* 183 (Suppl. l_2), 44–51. doi:10.1093/milmed/usy120

Chan Choi, Y., Choi, J. S., Jung, Y. J., and Cho, Y. W. (2014). Human gelatin tissue-adhesive hydrogels prepared by enzyme-mediated biosynthesis of DOPA and Fe(3+) ion crosslinking. *J. Mater. Chem. B* 2 (2), 201–209. doi:10.1039/c3tb20696c

Chang, J. C., Holloway, B. C., Zamisch, M., Hepburn, M. J., and Ling, G. S. F. (2015). ResQFoam for the treatment of non-compressible hemorrhage on the front line. *Front. Line. Mil. Med.* 180 (9), 932–933. doi:10.7205/milmed-d-15-00049

Chen, G. P., Yu, Y. R., Wu, X. W., Wang, G. F., Ren, J. N., and Zhao, Y. J. (2018b). Bioinspired multifunctional hybrid hydrogel promotes wound healing. *Adv. Funct. Mater.* 28 (33). doi:10.1002/adfm.201801386

Chen, H., Cheng, R., Zhao, X., Zhang, Y., Tam, A., Yan, Y., et al. (2019). An injectable self-healing coordinative hydrogel with antibacterial and angiogenic properties for diabetic skin wound repair. *Npg Asia Mater.* 11, 3. doi:10.1038/s41427-018-0103-9

Chen, T., Chen, Y. J., Rehman, H. U., Chen, Z., Yang, Z., Wang, M., et al. (2018a). Ultratough, self-healing, and tissue-adhesive hydrogel for wound dressing. *ACS Appl. Mater. interfaces* 10 (39), 33523–33531. doi:10.1021/acsami.8b10064

Chen, Z., Wu, H., Wang, H. B., Zaldivar-Silva, D., Aguero, L., Liu, Y. F., et al. (2021). Notes on the genus messageria bavay amp; dautzenberg, 1904, with descriptions of a new species and a new subspecies (gastropoda: caenogastropoda: cyclophoroidea: alycaeidae). *Mater. Sci. Eng. C-Materials Biol. Appl.* 5067, 129–134. doi:10.11646/zootaxa.5067.1.9

Chen, Z., Yao, J. P., Zhao, J. L., and Wang, S. G. (2023). Injectable wound dressing based on carboxymethyl chitosan triple-network hydrogel for effective wound antibacterial and hemostasis. *Int. J. Biol. Macromol.* 225, 1235–1245. doi:10.1016/j.ijbiomac.2022.11.184

Chin, S. F., Romainor, A. N. B., Pang, S. C., and Lihan, S. (2019). Antimicrobial starch-citrate hydrogel for potential applications as drug delivery carriers. *J. Of Drug Deliv. Sci. And Technol.* 54, 101239. doi:10.1016/j.jddst.2019.101239

Chou, T. C., Fu, E., Wu, C. J., and Yeh, J. H. (2003). Chitosan enhances platelet adhesion and aggregation. *Biochem. biophysical Res. Commun.* 302 (3), 480–483. doi:10.1016/s0006-291x(03)00173-6

Cox, J. M., and Rall, J. M. (2017). Evaluation of XSTAT(r) and QuickClot(r) Combat gauze(r) in a swine model of lethal junctional hemorrhage in coagulopathic swine. *J. special operations Med. a peer Rev. J. SOF Med. Prof.* 17 (3), 64–67. doi:10.55460/rayh-izjp

Croushorn, J. (2014). Abdominal aortic and junctional tourniquet controls hemorrhage from a gunshot wound of the left groin. *J. special operations Med. a peer Rev. J. SOF Med. Prof.* 14 (2), 6–8. doi:10.55460/8iyl-ypcc

Croushorn, J., McLester, J., Thomas, G., and McCord, S. R. (2013). Abdominal aortic tourniquet controls junctional hemorrhage from a gunshot wound of the axilla. *J. special operations Med. a peer Rev. J. SOF Med. Prof.* 13 (3), 1–4. doi:10.55460/61dq-2eiq

Cui, C., Fan, C., Wu, Y., Xiao, M., Wu, T., Zhang, D., et al. (2019). Water-triggered hyperbranched polymer universal adhesives: from strong underwater adhesion to rapid sealing hemostasis. *Adv. Mater* 31 (49), e1905761. doi:10.1002/adma.201905761

Cui, R. H., Chen, F. P., Zhao, Y. J., Huang, W. J., and Liu, C. S. (2020). A novel injectable starch-based tissue adhesive for hemostasis. *J. Of Mater. Chem. B* 8 (36), 8282–8293. doi:10.1039/d0tb01562h

Dowling, M. B., Kumar, R., Keibler, M. A., Hess, J. R., Bochicchio, G. V., and Raghavan, S. R. (2011). A self-assembling hydrophobically modified chitosan capable of reversible hemostatic action. *Biomaterials* 32 (13), 3351–3357. doi:10.1016/j.biomaterials.2010.12.033

Dowling, M. B., MacIntire, I. C., White, J. C., Narayan, M., Duggan, M. J., King, D. R., et al. (2015). Sprayable foams based on an amphiphilic biopolymer for control of hemorrhage without compression. *Acs Biomaterials Sci. Eng.* 1 (6), 440–447. doi:10.1021/acsbiomaterials.5b00067

Du, X. C., Liu, Y. J., Wang, X., Yan, H. Y., Wang, L. N., Qu, L. J., et al. (2019a). Injectable hydrogel composed of hydrophobically modified chitosan/oxidized-dextran for wound healing. *Mater. Sci. Eng. C-Materials Biol. Appl.* 104, 109930. doi:10.1016/j.msec.2019.109930

Du, X. C., Liu, Y. J., Wang, X., Yan, H. Y., Wang, L. N., Qu, L. J., et al. (2019b). Injectable hydrogel composed of hydrophobically modified chitosan/oxidized-dextran for wound healing. *Mater. Sci. And Eng. C-Materials Biol. Appl.* 104, 109930. doi:10.1016/j.msec.2019.109930

Duc-Thang, V., and Lee, C.-K. (2017). Cells capture and antimicrobial effect of hydrophobically modified chitosan coating on *Escherichia coli*. *Carbohydr. Polym.* 164, 109–117. doi:10.1016/j.carbpol.2017.01.093

Fan, X., Wang, S., Fang, Y., Li, P., Zhou, W., Wang, Z., et al. (2020). Tough polyacrylamide-tannic acid-kaolin adhesive hydrogels for quick hemostatic application. *Mater. Sci. And Eng. C-Materials Biol. Appl.* 109, 110649. doi:10.1016/j.msec.2020.110649

Fang, W., Yang, L., Chen, Y. H., and Hu, Q. L. (2023). Bioinspired multifunctional injectable hydrogel for hemostasis and infected wound management. *Acta biomater.* 161, 50–66. doi:10.1016/j.actbio.2023.01.021

Feng, W. J., and Wang, Z. K. (2022). Shear-thinning and self-healing chitosan-graphene oxide hydrogel for hemostasis and wound healing. *Carbohydr. Polym.* 294, 119824. doi:10.1016/j.carbpol.2022.119824

Filips, D., Logsetty, S., Tan, J., Atkinson, I., and Mottet, K. (2013). The itclamp controls junctional bleeding in a lethal swine exsanguination model. *Prehospital Emerg. Care* 17 (4), 526–532. doi:10.3109/10903127.2013.818177

Frojmovic, M. M., and Milton, J. G. (1982). Human platelet size, shape, and related functions in health and disease. *Physiol. Rev.* 62 (1), 185–261. doi:10.1152/physrev.1982.62.1.185

Furie, B., and Furie, B. C. (2008). Mechanisms of thrombus formation. *N. Engl. J. Med.* 359 (9), 938–949. doi:10.1056/nejmra0801082

Gaharwar, A. K., Avery, R. K., Assmann, A., Paul, A., McKinley, G. H., Khademhosseini, A., et al. (2014). Shear-Thinning nanocomposite hydrogels for the treatment of hemorrhage. *ACS Nano* 8 (10), 9833–9842. doi:10.1021/nn503719n

Gaharwar, A. K., Cross, L. M., Peak, C. W., Gold, K., Carrow, J. K., Brokesh, A., et al. (2019). 2D nanoclay for biomedical applications: regenerative medicine, therapeutic delivery, and additive manufacturing. *Adv. Mater.* 31 (23), e1900332. doi:10.1002/adma.201900332

Gale, A. J. (2011). Continuing education course #2: current understanding of hemostasis. *Toxicol. Pathol.* 39 (1), 273–280. doi:10.1177/0192623310389474

Gao, G., Jiang, Y.-W., Jia, H.-R., and Wu, F.-G. (2019). Near-infrared light-controllable on-demand antibiotics release using thermo-sensitive hydrogel-based drug reservoir for combating bacterial infection. *Biomaterials* 188, 83–95. doi:10.1016/j.biomaterials.2018.09.045

Geng, H. M., Dai, Q., Sun, H. F., Zhuang, L. P., Song, A. X., Caruso, F., et al. (2020). Injectable and sprayable polyphenol-based hydrogels for controlling hemostasis. *Acs Appl. Bio Mater.* 3 (2), 1258–1266. doi:10.1021/acsabm.9b01138

Ghaemmaghami, V., Sperry, J., Gunst, M., Friese, R., Starr, A., Frankel, H., et al. (2007). Effects of early use of external pelvic compression on transfusion requirements and mortality in pelvic fractures. *Am. J. Surg.* 194 (6), 720–723. ; discussion 3. doi:10.1016/j.amjsurg.2007.08.040

GhavamiNejad, A., Park, C. H., and Kim, C. S. (2016). *In situ* synthesis of antimicrobial silver nanoparticles within antifouling zwitterionic hydrogels by catecholic redox chemistry for wound healing application. *Biomacromolecules* 17 (3), 1213–1223. doi:10.1021/acs.biomac.6b00039

Godo, S., and Shimokawa, H. (2017). Endothelial functions. *Arteriosclerosis, thrombosis, Vasc. Biol.* 37 (9), e108–e114. doi:10.1161/atvbaha.117.309813

Golebiewska, E. M., and Poole, A. W. (2015). Platelet secretion: from haemostasis to wound healing and beyond. *Blood Rev.* 29 (3), 153–162. doi:10.1016/j.blre.2014.10.003

Gong, J., Hu, J., Yan, X., Xiang, L., Chen, S., Yang, H., et al. (2023). Injectable hydrogels including magnetic nanosheets for multidisciplinary treatment of hepatocellular carcinoma via magnetic hyperthermia. *Small (Weinheim der Bergstrasse, Ger.*, e2300733. doi:10.1002/smll.202300733

Gu, S. Y., Wang, H. C., Wang, Y. B., Wang, X., Liu, X., Wang, Y., et al. (2023). Thermosensitive nanocomposite hydrogel composed of PVPylated poly(D, L-alanine) and laponite as an injectable and bioactive biomaterial. *Chem. Eng. J.* 466. doi:10.1016/j.cej.2023.143128

Guo, B., Dong, R., Liang, Y., and Li, M. (2021). Haemostatic materials for wound healing applications. *Nat. Rev. Chem.* 5, 773–791. doi:10.1038/s41570-021-00323-z

Guvendiren, M., Lu, H. D., and Burdick, J. A. (2012). Shear-thinning hydrogels for biomedical applications. *Soft matter* 8 (2), 260–272. doi:10.1039/c1sm06513k

Haghniaz, R., Montazerian, H., Rabbani, A., Baidya, A., Usui, B., Zhu, Y., et al. (2023). Injectable, antibacterial, and hemostatic tissue sealant hydrogels. *Adv. Healthc. Mater.* 12, e2301551. doi:10.1002/adhm.202301551

Han, W., Zhou, B., Yang, K., Xiong, X., Luan, S., Wang, Y., et al. (2020). Biofilm-inspired adhesive and antibacterial hydrogel with tough tissue integration performance for sealing hemostasis and wound healing. *Bioact. Mater.* 5 (4), 768–778. doi:10.1016/j.bioactmat.2020.05.008

Hanley, C., Callum, J., and Jerath, A. (2021). Tranexamic acid and trauma coagulopathy: where are we now? *Br. J. Of Anaesth.* 126 (1), 12–17. doi:10.1016/j.bja.2020.09.014

Hao, Y., Yuan, C., Deng, J., Zheng, W., Ji, Y., and Zhou, Q. (2022). Injectable self-healing first-aid tissue adhesives with outstanding hemostatic and antibacterial performances for trauma emergency Care. *ACS Appl. Mater. interfaces* 14 (14), 16006–16017. doi:10.1021/acsami.2c00877

He, J. H., Zhang, Z. X., Yang, Y. T., Ren, F. G., Li, J. P., Zhu, S. J., et al. (2021). Injectable self-healing adhesive pH-responsive hydrogels accelerate gastric hemostasis and wound healing. *Nano-Micro Lett.* 13 (1), 80. doi:10.1007/s40820-020-00585-0

He, Y. M., Liu, K. Y., Zhang, C., Guo, S., Chang, R., Guan, F. X., et al. (2022). Facile preparation of PVA hydrogels with adhesive, self-healing, antimicrobial, and on-demand removable capabilities for rapid hemostasis. *Biomaterials Sci.* 10 (19), 5620–5633. doi:10.1039/d2bm00891b

Hoare, T. R., and Kohane, D. S. (2008). Hydrogels in drug delivery: progress and challenges. *Polymer* 49 (8), 1993–2007. doi:10.1016/j.polymer.2008.01.027

Hong, Y., Zhou, F., Hua, Y., Zhang, X., Ni, C., Pan, D., et al. (2019). A strongly adhesive hemostatic hydrogel for the repair of arterial and heart bleeds. *Nat. Commun.* 10 (1), 2060. doi:10.1038/s41467-019-10004-7

Hoque, J., Prakash, R. G., Paramanandham, K., Shome, B. R., and Haldar, J. (2017). Biocompatible injectable hydrogel with potent wound healing and antibacterial properties. *Mol. Pharm.* 14 (4), 1218–1230. doi:10.1021/acs.molpharmaceut.6b01104

Hou, M. D., Wang, X. C., Yue, O. Y., Zheng, M. H., Zhang, H. J., and Liu, X. H. (2022). Development of a multifunctional injectable temperature-sensitive gelatin-based adhesive double-network hydrogel. *Biomater. Adv.* 134, 112556. doi:10.1016/j.msec.2021.112556

Hoylaerts, M., Rijken, D. C., Lijnen, H. R., and Collen, D. (1982). Kinetics of the activation of plasminogen by human tissue plasminogen activator. Role of fibrin. *J. Biol. Chem.* 257 (6), 2912–2919. doi:10.1016/s0021-9258(19)81051-7

Hu, S. S., Yang, Z. X., Zhai, Q. M., Li, D. Z., Zhu, X. Y., He, Q. Q., et al. (2023). An all-in-one "4A hydrogel": through first-aid hemostatic, antibacterial, antioxidant, and angiogenic to promoting infected wound healing. *Small (Weinheim der Bergstrasse, Ger.* 19 (27), e2207437. doi:10.1002/smll.202207437

Hu, T., Wu, G. P., Bu, H. T., Zhang, H. Y., Li, W. X., Song, K., et al. (2022). An injectable, adhesive, and self-healable composite hydrogel wound dressing with excellent antibacterial activity. *Chem. Eng. J.* 450, 138201. doi:10.1016/j.cej.2022.138201

Huang, W., Wang, Y., Chen, Y., Zhao, Y., Zhang, Q., Zheng, X., et al. (2016). Strong and rapidly self-healing hydrogels: potential hemostatic materials. *Adv. Healthc. Mater.* 5 (21), 2813–2822. doi:10.1002/adhm.201600720

Jamal, L., Saini, A., Quencer, K., Altun, I., Albadawi, H., Khurana, A., et al. (2021). Emerging approaches to pre-hospital hemorrhage control: a narrative review. *Ann. Transl. Med.* 9 (14), 1192. doi:10.21037/atm-20-5452

Kang, X. C., Guan, P. F., Xiao, C. R., Liu, C., Guan, Y. J., Lin, Y. Y., et al. (2023). Injectable intrinsic photothermal hydrogel bioadhesive with on-demand removability for wound closure and MRSA-infected wound healing. *Adv. Healthc. Mater.* 12 (13), e2203306. doi:10.1002/adhm.202203306

Kean, T., and Thanou, M. (2010). Biodegradation, biodistribution and toxicity of chitosan. *Adv. drug Deliv. Rev.* 62 (1), 3–11. doi:10.1016/j.addr.2009.09.004

Kendrick Douglas, B., Beckett Ronald, S., and Tovell Ralph, M. (1965). Blood Program in World war II. *Anesthesiology* 26 (4), 584. doi:10.1097/00000542-196507000-00039

Ker, K., Edwards, P., Perel, P., Shakur, H., and Roberts, I. (2012). Effect of tranexamic acid on surgical bleeding: systematic review and cumulative meta-analysis. *Bmj-British Med. J.* 344, e3054. doi:10.1136/bmj.e3054

Kim, S. H., Lee, Y. J., Chao, J. R., Kim, D. Y., Sultan, M. T., Lee, H. J., et al. (2020). Rapidly photocurable silk fibroin sealant for clinical applications. *Npg Asia Mater.* 12 (1), 46. doi:10.1038/s41427-020-0227-6

Kong, Y., Hou, Z. S., Zhou, L. Q., Zhang, P. F., Ouyang, Y. W., Wang, P. W., et al. (2021). Injectable self-healing hydrogels containing CuS nanoparticles with abilities of hemostasis, antibacterial activity, and promoting wound healing. *Acs Biomaterials Sci. Eng.* 7 (1), 335–349. doi:10.1021/acsbiomaterials.0c01473

Konieczynska, M. D., Villa-Camacho, J. C., Ghobril, C., Perez-Viloria, M., Tevis, K. M., Blessing, W. A., et al. (2016). On-Demand dissolution of a dendritic hydrogel-based dressing for second-degree burn wounds through thiol-thioester exchange reaction. *Angew. Chemie-International Ed.* 55 (34), 9984–9987. doi:10.1002/anie.201604827

Lacin, N. T. (2014). Development of biodegradable antibacterial cellulose based hydrogel membranes for wound healing. *Int. J. Biol. Macromol.* 67, 22–27. doi:10.1016/j.ijbiomac.2014.03.003

Lee, H., Scherer, N. F., and Messersmith, P. B. (2006). Single-molecule mechanics of mussel adhesion. *Proc. Natl. Acad. Sci. U. S. A.* 103 (35), 12999–13003. doi:10.1073/pnas.0605552103

Lee, J. H. (2018). Injectable hydrogels delivering therapeutic agents for disease treatment and tissue engineering. *Biomaterials Res.* 22, 27. doi:10.1186/s40824-018-0138-6

Lestari, W., Yusry, WNAW, Haris, M. S., Jaswir, I., and Idrus, E. (2020). A glimpse on the function of chitosan as a dental hemostatic agent. *Jpn. Dent. Sci. Rev.* 56 (1), 147–154. doi:10.1016/j.jdsr.2020.09.001

Li, J., Celiz, A. D., Yang, J., Yang, Q., Wamala, I., Whyte, W., et al. (2017). Tough adhesives for diverse wet surfaces. *Sci. (New York, NY)* 357 (6349), 378–381. doi:10.1126/science.aah6362

Li, J. Y., and Mooney, D. J. (2016). Designing hydrogels for controlled drug delivery. *Nat. Rev. Mater.* 1 (12), 16071. doi:10.1038/natrevmats.2016.71

Li, Z., Zhao, Y., Ouyang, X., Yang, Y., Chen, Y., Luo, Q., et al. (2022). Biomimetic hybrid hydrogel for hemostasis, adhesion prevention and promoting regeneration after partial liver resection. *Bioact. Mater.* 11, 41–51. doi:10.1016/j.bioactmat.2021.10.001

Liang, Y., Wang, M., Zhang, Z., Ren, G., Liu, Y., Wu, S., et al. (2019c). Facile synthesis of ZnO QDs@GO-CS hydrogel for synergetic antibacterial applications and enhanced wound healing. *Chem. Eng. J.* 378, 122043. doi:10.1016/j.cej.2019.122043

Liang, Y., Zhao, X., Hu, T., Chen, B., Yin, Z., Ma, P. X., et al. (2019a). Adhesive hemostatic conducting injectable composite hydrogels with sustained drug release and photothermal antibacterial activity to promote full-thickness skin regeneration during wound healing. *Small (Weinheim der Bergstrasse, Ger.* 15 (12), e1900046. doi:10.1002/smll.201900046

Liang, Y., Zhao, X., Ma, P. X., Guo, B., Du, Y., and Han, X. (2019b). pH-responsive injectable hydrogels with mucosal adhesiveness based on chitosan-grafted-dihydrocaffeic acid and oxidized pullulan for localized drug delivery. *J. Of Colloid And Interface Sci.* 536, 224–234. doi:10.1016/j.jcis.2018.10.056

Liu, C. K., Liu, C., Liu, Z. Y., Shi, Z., Liu, S. H., Wang, X. J., et al. (2023). Injectable thermogelling bioadhesive chitosan-based hydrogels for efficient hemostasis. *Int. J. Biol. Macromol.* 224, 1091–1100. doi:10.1016/j.ijbiomac.2022.10.194

Liu, J., Li, J., Yu, F., Zhao, Y. X., Mo, X. M., and Pan, J. F. (2020). *In situ* forming hydrogel of natural polysaccharides through Schiff base reaction for soft tissue adhesive and hemostasis. *Int. J. Biol. Macromol.* 147, 653–666. doi:10.1016/j.ijbiomac.2020.01.005

Liu, M., Ishida, Y., Ebina, Y., Sasaki, T., Hikima, T., Takata, M., et al. (2015). An anisotropic hydrogel with electrostatic repulsion between cofacially aligned nanosheets. *Nature* 517 (7532), 68–72. doi:10.1038/nature14060

Liu, S. X., Jiang, N., Chi, Y. Q., Peng, Q., Dai, G. R., Qian, L., et al. (2022). Injectable and self-healing hydrogel based on chitosan-tannic acid and oxidized hyaluronic acid for wound healing. *Acs Biomaterials Sci. Eng.* 8 (9), 3754–3764. doi:10.1021/acsbiomaterials.2c00321

Liu, Y., Sui, Y., Liu, C., Liu, C., Wu, M., Li, B., et al. (2018). A physically crosslinked polydopamine/nanocellulose hydrogel as potential versatile vehicles for drug delivery and wound healing. *Carbohydr. Polym.* 188, 27–36. doi:10.1016/j.carbpol.2018.01.093

Lokhande, G., Carrow, J. K., Thakur, T., Xavier, J. R., Parani, M., Bayless, K. J., et al. (2018). Nanoengineered injectable hydrogels for wound healing application. *Acta biomater.* 70, 35–47. doi:10.1016/j.actbio.2018.01.045

Luo, J. W., Liu, C., Wu, J. H., Zhao, D. H., Lin, L. X., Fan, H. M., et al. (2020). *In situ* forming gelatin/hyaluronic acid hydrogel for tissue sealing and hemostasis. *J. Of Biomed. Mater. Res. Part B-Applied Biomaterials* 108 (3), 790–797. doi:10.1002/jbm.b.34433

Mackman, N. (2009). The role of tissue factor and factor VIIa in hemostasis. *Anesth. analgesia* 108 (5), 1447–1452. doi:10.1213/ane.0b013e31819bceb1

Mahmoud, N. N., Hikmat, S., Abu Ghith, D., Hajeer, M., Hamadneh, L., Qattan, D., et al. (2019). Gold nanoparticles loaded into polymeric hydrogel for wound healing in rats: effect of nanoparticles' shape and surface modification. *Int. J. Pharm.* 565, 174–186. doi:10.1016/j.ijpharm.2019.04.079

McKinnon, D. D., Domaille, D. W., Cha, J. N., and Anseth, K. S. (2014). Biophysically defined and cytocompatible covalently adaptable networks as viscoelastic 3D cell culture systems. *Adv. Mater* 26 (6), 865–872. doi:10.1002/adma.201303680

McMahon, S., Kennedy, R., Duffy, P., Vasquez, J. M., Wall, J. G., Tai, H., et al. (2016). Poly(ethylene glycol)-based hyperbranched polymer from RAFT and its application as a silver-sulfadiazine-loaded antibacterial hydrogel in wound Care. *ACS Appl. Mater. interfaces* 8 (40), 26648–26656. doi:10.1021/acsami.6b11371

Mehdizadeh, M., Weng, H., Gyawali, D., Tang, L., and Yang, J. (2012). Injectable citrate-based mussel-inspired tissue bioadhesives with high wet strength for sutureless wound closure. *Biomaterials* 33 (32), 7972–7983. doi:10.1016/j.biomaterials.2012.07.055

Mi, L., Xue, H., Li, Y., and Jiang, S. (2011). A thermoresponsive antimicrobial wound dressing hydrogel based on a cationic betaine ester. *Adv. Funct. Mater.* 21 (21), 4028–4034. doi:10.1002/adfm.201100871

Montgomery, H. R., Butler, F. K., Jr., Kerr, W., Conklin, C. C., Morissette, D. M., Remley, M. A., et al. (2017). TCCC guidelines comprehensive review and update: TCCC guidelines change 16-03. *J. special operations Med. a peer Rev. J. SOF Med. Prof.* 17 (2), 21–38. doi:10.55460/zgaf-inzu

Morris, R., Loftus, A., Friedmann, Y., Parker, P., and Pallister, I. (2017). Intra-pelvic pressure changes after pelvic fracture: a cadaveric study quantifying the effect of a pelvic binder and limb bandaging over a bolster. *Injury* 48 (4), 833–840. doi:10.1016/j.injury.2017.01.046

Morrison, J. J., Dubose, J. J., Rasmussen, T. E., and Midwinter, M. J. (2012). Military application of tranexamic acid in trauma emergency resuscitation (MATTERs) study. *Archives Of Surg.* 147 (2), 113–119. doi:10.1001/archsurg.2011.287

Morrissey, J. H., Choi, S. H., and Smith, S. A. (2012). Polyphosphate: an ancient molecule that links platelets, coagulation, and inflammation. *Blood* 119 (25), 5972–5979. doi:10.1182/blood-2012-03-306605

Nemerson, Y. (1988). Tissue factor and hemostasis [published erratum appears in Blood 1988 Apr;71(4):1178]. *Blood* 71 (1), 1–8. doi:10.1182/blood.v71.1.1.bloodjournal7111

Ni, Z. P., Yu, H. J., Wang, L., Liu, X. W., Shen, D., Chen, X., et al. (2022). Polyphosphazene and non-catechol-based antibacterial injectable hydrogel for adhesion of wet tissues as wound dressing. *Adv. Healthc. Mater.* 11 (1), e2101421. doi:10.1002/adhm.202101421

Nuyttens, B. P., Thijs, T., Deckmyn, H., and Broos, K. (2011). Platelet adhesion to collagen. *Thrombosis Res.* 127 (Suppl. 2), S26–S29. doi:10.1016/s0049-3848(10)70151-1

Okamoto, Y., Yano, R., Miyatake, K., Tomohiro, I., Shigemasa, Y., and Minami, S. (2003). Effects of chitin and chitosan on blood coagulation. *Carbohydr. Polym.* 53 (3), 337–342. doi:10.1016/s0144-8617(03)00076-6

Onifer, D. J., McKee, J. L., Faudree, L. K., Bennett, B. L., Miles, E. A., Jacobsen, T., et al. (2019). Management of hemorrhage from craniomaxillofacial injuries and penetrating neck injury in tactical Combat casualty Care: iTClamp mechanical wound closure device TCCC guidelines proposed change 19-04 06 june 2019. *J. special operations Med. a peer Rev. J. SOF Med. Prof.* 19 (3), 31–44. doi:10.55460/h8bg-8oup

Oryan, A., Alemzadeh, E., Mohammadi, A. A., and Moshiri, A. (2019). Healing potential of injectable Aloe vera hydrogel loaded by adipose-derived stem cell in skin tissue-engineering in a rat burn wound model. *Cell tissue Res.* 377 (2), 215–227. doi:10.1007/s00441-019-03015-9

Pang, J. H., Bi, S. C., Kong, T. T., Luo, X., Zhou, Z. Z., Qiu, K. J., et al. (2020). Mechanically and functionally strengthened tissue adhesive of chitin whisker complexed chitosan/dextran derivatives based hydrogel. *Carbohydr. Polym.* 237, 116138. doi:10.1016/j.carbpol.2020.116138

Park, J., Kim, T. Y., Kim, Y., An, S., Kim, K. S., Kang, M., et al. (2023). A mechanically resilient and tissue-conformable hydrogel with hemostatic and antibacterial capabilities for wound Care. *Adv. Sci. (Weinheim, Baden-Wurttemberg, Ger.* 10 (30), e2303651. doi:10.1002/advs.202303651

Patenaude, M., Smeets, N. M., and Hoare, T. (2014). Designing injectable, covalently cross-linked hydrogels for biomedical applications. *Macromol. rapid Commun.* 35 (6), 598–617. doi:10.1002/marc.201300818

Peng, X., Xu, X., Deng, Y., Xie, X., Xu, L., Xu, X., et al. (2021). Ultrafast self-gelling and wet adhesive powder for acute hemostasis and wound healing. *Adv. Funct. Mater.* 31 (33). doi:10.1002/adfm.202102583

Picetti, R., Shakur-Still, H., Medcalf, R. L., Standing, J. F., and Roberts, I. (2019). What concentration of tranexamic acid is needed to inhibit fibrinolysis? A systematic review of pharmacodynamics studies. *Blood Coagulation Fibrinolysis* 30 (1), 1–10. doi:10.1097/mbc.0000000000000789

Pillai, N. S. M., Eswar, K., Amirthalingam, S., Mony, U., Varma, P. K., and Jayakumar, R. (2019). Injectable nano whitlockite incorporated chitosan hydrogel for effective hemostasis. *Acs Appl. Bio Mater.* 2 (2), 865–873. doi:10.1021/acsabm.8b00710

Pinnaratip, R., Bhuiyan, M. S. A., Meyers, K., Rajachar, R. M., and Lee, B. P. (2019). Multifunctional biomedical adhesives. *Adv. Healthc. Mater.* 8 (11), e1801568. doi:10.1002/adhm.201801568

Pool, J. G. (1977). Normal hemostatic mechanisms: a review. *Am. J. Med. Technol.* 43 (8), 776–780.

Qu, J., Zhao, X., Liang, Y., Xu, Y., Ma, P. X., and Guo, B. (2019). Degradable conductive injectable hydrogels as novel antibacterial, anti-oxidant wound dressings for wound healing. *Chem. Eng. J.* 362, 548–560. doi:10.1016/j.cej.2019.01.028

Quan, K., Li, G., Tao, L., Xie, Q., Yuan, Q., and Wang, X. (2016). Diaminopropionic acid reinforced graphene sponge and its use for hemostasis. *ACS Appl. Mater. interfaces* 8 (12), 7666–7673. doi:10.1021/acsami.5b12715

Radhakumary, C., Antonty, M., and Sreenivasan, K. (2011). Drug loaded thermoresponsive and cytocompatible chitosan based hydrogel as a potential wound dressing. *Carbohydr. Polym.* 83 (2), 705–713. doi:10.1016/j.carbpol.2010.08.042

Rakhshaei, R., and Namazi, H. (2017). A potential bioactive wound dressing based on carboxymethyl cellulose/ZnO impregnated MCM-41 nanocomposite hydrogel. *Mater. Sci. Eng. C-Materials Biol. Appl.* 73, 456–464. doi:10.1016/j.msec.2016.12.097

Rao, K. M., Suneetha, M., Zo, S. M., Won, S. Y., Kim, H. J., and Han, S. S. (2022). Injectable nanocomposite hydrogel as wound dressing agent with tunable multifunctional property. *Mater. Lett.* 307, 131062. doi:10.1016/j.matlet.2021.131062

Refat, M. S., Elsabawy, K. M., Alhadhrami, A., Almalki, A. S. A., El-Sayed, M. Y., and Hassan, R. F. (2018). Development of medical drugs: synthesis and *in vitro* bio-evaluations of nanomedicinal zinc-penicillins polymeric hydrogel membranes for wound skin dressing by new chemical technology. *J. Of Mol. Liq.* 255, 462–470. doi:10.1016/j.molliq.2018.01.187

Rezvanian, M., Ahmad, N., Amin, MCIM, and Ng, S.-F. (2017). Optimization, characterization, and *in vitro* assessment of alginate-pectin ionic cross-linked hydrogel film for wound dressing applications. *Int. J. Biol. Macromol.* 97, 131–140. doi:10.1016/j.ijbiomac.2016.12.079

Roberts, I., Shakur, H., Afolabi, A., Brohi, K., Coats, T., Dewan, Y., et al. (2011). The importance of early treatment with tranexamic acid in bleeding trauma patients: an exploratory analysis of the CRASH-2 randomised controlled trial. *Lancet (London, Engl.* 377 (9771), 1096. doi:10.1016/S0140-6736(11)60278-X

Rodrigues, M., Kosaric, N., Bonham, C. A., and Gurtner, G. C. (2019). Wound healing: a cellular perspective. *Physiol. Rev.* 99 (1), 665–706. doi:10.1152/physrev.00067.2017

Rodriguez, M. I., Jensen, J. T., Gregory, K., Bullard, M., Longo, P., Heidel, J., et al. (2017). A novel tamponade agent for management of post partum hemorrhage: adaptation of the Xstat mini-sponge applicator for obstetric use. *Bmc Pregnancy And Childbirth* 17, 187. doi:10.1186/s12884-017-1373-x

Ryu, J. H., Lee, Y., Kong, W. H., Kim, T. G., Park, T. G., and Lee, H. (2011). Catechol-functionalized chitosan/pluronic hydrogels for tissue adhesives and hemostatic materials. *Biomacromolecules* 12 (7), 2653–2659. doi:10.1021/bm200464x

Schmidt, J. J., Rowley, J., and Kong, H. J. (2008). Hydrogels used for cell-based drug delivery. *J. Of Biomed. Mater. Res. Part A* 87A (4), 1113–1122. doi:10.1002/jbm.a.32287

Shi, C., Li, S., Wang, Z., and Shen, H. (2021). Prehospital aortic blood flow control techniques for non-compressible traumatic hemorrhage. *Injury-International J. Of Care Of Inj.* 52 (7), 1657–1663. doi:10.1016/j.injury.2021.02.070

Shi, G., Chen, W., Zhang, Y., Dai, X., Zhang, X., and Wu, Z. (2019). An antifouling hydrogel containing silver nanoparticles for modulating the therapeutic immune response in chronic wound healing. *Langmuir* 35 (5), 1837–1845. doi:10.1021/acs.langmuir.8b01834

Shi, Y., Truong, V. X., Kulkarni, K., Qu, Y., Simon, G. P., Boy, R. L., et al. (2015). Light-triggered release of ciprofloxacin from an *in situ* forming click hydrogel for antibacterial wound dressings. *J. Of Mater. Chem. B* 3 (45), 8771–8774. doi:10.1039/c5tb01820j

Shin, J., Lee, J. S., Lee, C., Park, H. J., Yang, K., Jin, Y., et al. (2015). Tissue adhesive catechol-modified hyaluronic acid hydrogel for effective, minimally invasive cell therapy. *Adv. Funct. Mater.* 25 (25), 3814–3824. doi:10.1002/adfm.201500006

Shou, Y. F., Zhang, J. H., Yan, S. F., Xia, P. F., Xu, P. L., Li, G. F., et al. (2020). Thermoresponsive chitosan/DOPA-based hydrogel as an injectable therapy approach for tissue-adhesion and hemostasis. *Acs Biomaterials Sci. Eng.* 6 (6), 3619–3629. doi:10.1021/acsbiomaterials.0c00545

Sims, K., Montgomery, H. R., Dituro, P., Kheirabadi, B. S., and Butler, F. K. (2016). Management of external hemorrhage in tactical Combat casualty Care: the adjunctive use of XStat compressed hemostatic sponges: TCCC guidelines change 15-03. *J. special operations Med. a peer Rev. J. SOF Med. Prof.* 16 (1), 19–28. doi:10.55460/6cem-36iy

Singh, B., and Dhiman, A. (2015). Designing bio-mimetic moxifloxacin loaded hydrogel wound dressing to improve antioxidant and pharmacology properties. *Rsc Adv.* 5 (55), 44666–44678. doi:10.1039/c5ra06857f

Singh, B., Sharma, S., and Dhiman, A. (2013). Design of antibiotic containing hydrogel wound dressings: biomedical properties and histological study of wound healing. *Int. J. Pharm.* 457 (1), 82–91. doi:10.1016/j.ijpharm.2013.09.028

Singh, B., Varshney, L., Francis, S., and Rajneesh, A. (2016). Designing tragacanth gum based sterile hydrogel by radiation method for use in drug delivery and wound dressing applications. *Int. J. Biol. Macromol.* 88, 586–602. doi:10.1016/j.ijbiomac.2016.03.051

Song, C. K., Kim, M. K., Lee, J., Davaa, E., Baskaran, R., and Yang, S. G. (2019). Dopa-empowered Schiff base forming alginate hydrogel glue for rapid hemostatic control. *Macromol. Res.* 27 (2), 119–125. doi:10.1007/s13233-019-7026-3

Sorrentino, S., Studt, J. D., Medalia, O., and Tanuj Sapra, K. (2015). Roll, adhere, spread and contract: structural mechanics of platelet function. *Eur. J. Cell Biol.* 94 (3-4), 129–138. doi:10.1016/j.ejcb.2015.01.001

St John, A. E., Wang, X., Lim, E. B., Chien, D., Stern, S. A., and White, N. J. (2015). Effects of rapid wound sealing on survival and blood loss in a swine model of lethal junctional arterial hemorrhage. *J. Of Trauma And Acute Care Surg.* 79 (2), 256–262. doi:10.1097/ta.0000000000000746

Strausberg, R. L., and Link, R. P. (1990). Protein-based medical adhesives. *Trends Biotechnol.* 8 (2), 53–57. doi:10.1016/0167-7799(90)90134-j

Strecker-McGraw, M. K., Jones, T. R., and Baer, D. G. (2007). Soft tissue wounds and principles of healing. *Emerg. Med. Clin. N. Am.* 25 (1), 1–22. doi:10.1016/j.emc.2006.12.002

Stuart, S. M., Zarow, G., Walchak, A., McLean, J., and Roszko, P. (2019). Pilot study of a novel swine model for controlling junctional hemorrhage using the iTClamp in conjunction with hemostatic agents. *Mil. Med.* 184 (3-4), 367–373. doi:10.1093/milmed/usy337

Sun, D., Wang, H., Liu, J., Wang, X. L., Guo, H. B., Xue, L. J., et al. (2022). An enzyme cross-linked hydrogel as a minimally invasive arterial tissue sealing and anti-adhesion barrier. *Nano today* 44, 101467. doi:10.1016/j.nantod.2022.101467

Sun, X., Li, N., Su, C., Mu, Y., Cong, X., Cao, Z., et al. (2023). Diatom-inspired bionic hydrophilic polysaccharide adhesive for rapid sealing hemostasis. *ACS Nano* 17 (19), 19121–19135. doi:10.1021/acsnano.3c05205

Sundaram, M. N., Amirthalingam, S., Mony, U., Varma, P. K., and Jayakumar, R. (2019). Injectable chitosan-nano bioglass composite hemostatic hydrogel for effective bleeding control. *Int. J. Biol. Macromol.* 129, 936–943. doi:10.1016/j.ijbiomac.2019.01.220

Sundaram, M. N., Mony, U., Varma, P. K., and Rangasamy, J. (2021). Vasoconstrictor and coagulation activator entrapped chitosan based composite hydrogel for rapid bleeding control. *Carbohydr. Polym.* 258, 117634. doi:10.1016/j.carbpol.2021.117634

Tan, H. Q., Jin, D. W., Sun, J. J., Song, J. L., Lu, Y., Yin, M., et al. (2021). Enlisting a Traditional Chinese Medicine to tune the gelation kinetics of a bioactive tissue adhesive for fast hemostasis or minimally invasive therapy. *Bioact. Mater.* 6 (3), 905–917. doi:10.1016/j.bioactmat.2020.10.011

Tang, Q., Plank, T. N., Zhu, T., Yu, H., Ge, Z., Li, Q., et al. (2019). Self-assembly of metallo-nucleoside hydrogels for injectable materials that promote wound closure. *ACS Appl. Mater. interfaces* 11 (22), 19743–19750. doi:10.1021/acsami.9b02265

Taylor, J. R., III, Harvin, J. A., Martin, C., Holcomb, J. B., and Moore, L. J. (2017). Vascular complications from resuscitative endovascular balloon occlusion of the aorta: life over limb? *J. Of Trauma And Acute Care Surg.* 83, S120–S123. doi:10.1097/ta.0000000000001514

Teller, P., and White, T. K. (2009). The physiology of wound healing: injury through maturation. *Surg. Clin. N. Am.* 89 (3), 599–610. doi:10.1016/j.suc.2009.03.006

Tian, Y., Guan, P. F., Wen, C. Y., Lu, M. J., Li, T., Fan, L., et al. (2022). Strong biopolymer-based nanocomposite hydrogel adhesives with removability and reusability for damaged tissue closure and healing. *ACS Appl. Mater. interfaces* 14 (49), 54488–54499. doi:10.1021/acsami.2c14103

Tormoen, G. W., Khader, A., Gruber, A., and McCarty, O. J. (2013). Physiological levels of blood coagulation factors IX and X control coagulation kinetics in an *in vitro* model of circulating tissue factor. *Phys. Biol.* 10 (3), 036003. doi:10.1088/1478-3975/10/3/036003

Travis, J., and Salvesen, G. S. (1983). Human plasma proteinase inhibitors. *Annu. Rev. Biochem.* 52, 655–709. doi:10.1146/annurev.bi.52.070183.003255

Tripodi, A. (2016). Thrombin generation assay and its application in the clinical laboratory. *Clin. Chem.* 62 (5), 699–707. doi:10.1373/clinchem.2015.248625

Versteeg, H. H., Heemskerk, J. W., Levi, M., and Reitsma, P. H. (2013). New fundamentals in hemostasis. *Physiol. Rev.* 93 (1), 327–358. doi:10.1152/physrev.00016.2011

Wagner, C. L., Mascelli, M. A., Neblock, D. S., Weisman, H. F., Coller, B. S., and Jordan, R. E. (1996). Analysis of GPIIb/IIIa receptor number by quantification of 7E3 binding to human platelets. *Blood* 88 (3), 907–914. doi:10.1182/blood.v88.3.907.907

Wang, G. Q., Meng, X. Y., Wang, P. Y., Wang, X. P., Liu, G. L., Wang, D. A., et al. (2022a). A catechol bioadhesive for rapid hemostasis and healing of traumatic internal organs and major arteries. *Biomaterials* 291, 121908. doi:10.1016/j.biomaterials.2022.121908

Wang, J. H., Tsai, C. W., Tsai, N. Y., Chiang, C. Y., Lin, R. S., Pereira, R. F., et al. (2021). An injectable, dual crosslinkable hybrid pectin methacrylate (PECMA)/gelatin methacryloyl (GelMA) hydrogel for skin hemostasis applications. *Int. J. Biol. Macromol.* 185, 441–450. doi:10.1016/j.ijbiomac.2021.06.162

Wang, J. Q., Xu, W. X., Zhang, W. X., Da, J., Liu, L. X., Huang, X. W., et al. (2023a). UV cross-linked injectable non-swelling dihydrocaffeic acid grafted chitosan hydrogel for promoting wound healing. *Carbohydr. Polym.* 314, 120926. doi:10.1016/j.carbpol.2023.120926

Wang, L., Zhang, X. H., Yang, K., Fu, Y. V., Xu, T. S., Li, S. L., et al. (2020a). A novel double-crosslinking-double-network design for injectable hydrogels with enhanced tissue adhesion and antibacterial capability for wound treatment. *Adv. Funct. Mater.* 30 (1), 1904156. doi:10.1002/adfm.201904156

Wang, R., Li, J. Z., Chen, W., Xu, T. T., Yun, S. F., Xu, Z., et al. (2017). A biomimetic mussel-inspired epsilon-Poly-L-lysine hydrogel with robust tissue-anchor and anti-infection capacity. *Adv. Funct. Mater.* 27 (8), 1604894. doi:10.1002/adfm.201604894

Wang, T., Yi, W., Zhang, Y., Wu, H., Fan, H., Zhao, J., et al. (2023b). Sodium alginate hydrogel containing platelet-rich plasma for wound healing. *Colloids surfaces B, Biointerfaces.* 222, 113096. doi:10.1016/j.colsurfb.2022.113096

Wang, X. D., Zhang, X., Yang, X. R., Guo, X. Q., Liu, Y. Q., Li, Y. M., et al. (2022b). An antibacterial and antiadhesion *in situ* forming br hydrogel with sol-spray system for noncompressible hemostasis. *ACS Appl. Mater. interfaces* 15 (1), 662–676. doi:10.1021/acsami.2c19662

Wang, Y., Li, X., Yuan, J. Z., Wang, X. D., Tao, K. S., and Yan, J. (2022c). A bionic self-assembly hydrogel constructed by peptides with favorable biosecurity, rapid hemostasis and antibacterial property for wound healing. *Front. Bioeng. And Biotechnol.* 10, 901534. doi:10.3389/fbioe.2022.901534

Wang, Y. C., Cao, H., and Wang, X. Y. (2020b). Synthesis and characterization of an injectable epsilon-polylysine/carboxymethyl chitosan hydrogel used in medical application. *Mater. Chem. And Phys.* 248, 122902. doi:10.1016/j.matchemphys.2020.122902

Warriner, Z., Lam, L., Matsushima, K., Benjamin, E., Strumwasser, A., Demetriades, D., et al. (2019). Initial evaluation of the efficacy and safety of in-hospital expandable hemostatic minisponge use in penetrating trauma. *J. Of Trauma And Acute Care Surg.* 86 (3), 424–430. doi:10.1097/ta.0000000000002091

Wei, C. Y., Shi, W. L., Zhao, C. Q., Yang, S., Zheng, J. J., Zhong, J. P., et al. (2023). Superwetting injectable hydrogel with ultrastrong and fast tissue adhesion for minimally invasive hemostasis. *Adv. Healthc. Mater.* 12 (3), e2201799. doi:10.1002/adhm.202201799

Xia, X. F., Xu, X. Y., Wang, B., Zhou, D., Zhang, W. L., Xie, X., et al. (2022). Adhesive hemostatic hydrogel with ultrafast gelation arrests acute upper gastrointestinal hemorrhage in pigs. *Adv. Funct. Mater.* 32 (16). doi:10.1002/adfm.202109332

Xie, C., Wang, X., He, H., Ding, Y., and Lu, X. (2020). Mussel-inspired hydrogels for self-adhesive bioelectronics. *Adv. Funct. Mater.* 30 (25). doi:10.1002/adfm.201909954

Xie, M. M., Zeng, Y. B., Wu, H., Wang, S. G., and Zhao, J. L. (2022). Multifunctional carboxymethyl chitosan/oxidized dextran/sodium alginate hydrogels as dressing for hemostasis and closure of infected wounds. *Int. J. Biol. Macromol.* 219, 1337–1350. doi:10.1016/j.ijbiomac.2022.08.166

Xiong, Y., Chen, L., Liu, P., Yu, T., Lin, C., Yan, C., et al. (2022). All-in-One: multifunctional hydrogel accelerates oxidative diabetic wound healing through timed-release of exosome and fibroblast growth factor. *Small (Weinheim der Bergstrasse, Ger.* 18 (1), e2104229. doi:10.1002/smll.202104229

Xu, H., Huang, S., Wang, J., Lan, Y., Feng, L., Zhu, M., et al. (2019). Enhanced cutaneous wound healing by functional injectable thermo-sensitive chitosan-based hydrogel encapsulated human umbilical cord-mesenchymal stem cells. *Int. J. Biol. Macromol.* 137, 433–441. doi:10.1016/j.ijbiomac.2019.06.246

Xu, K., Cantu, D. A., Fu, Y., Kim, J., Zheng, X., Hematti, P., et al. (2013). Thiol-ene Michael-type formation of gelatin/poly(ethylene glycol) biomatrices for three-dimensional mesenchymal stromal/stem cell administration to cutaneous wounds. *Acta biomater.* 9 (11), 8802–8814. doi:10.1016/j.actbio.2013.06.021

Xu, K., Deng, S., Zhu, Y., Yang, W., Chen, W., Huang, L., et al. (2023). Platelet rich plasma loaded multifunctional hydrogel accelerates diabetic wound healing via regulating the continuously abnormal microenvironments. *Adv. Healthc. Mater.* 12 (28), e2301370. doi:10.1002/adhm.202301370

Yan, X., Sun, T., Song, Y., Peng, W., Xu, Y., Luo, G., et al. (2022). *In situ* thermal-responsive magnetic hydrogel for multidisciplinary therapy of hepatocellular carcinoma. *Nano Lett.* 22 (6), 2251–2260. doi:10.1021/acs.nanolett.1c04413

Yang, G., Xiao, Z., Long, H., Ma, K., Zhang, J., Ren, X., et al. (2018). Assessment of the characteristics and biocompatibility of gelatin sponge scaffolds prepared by various crosslinking methods. *Sci. Rep.* 8 (1), 1616. doi:10.1038/s41598-018-20006-y

Yang, W., Kang, X., Gao, X., Zhuang, Y., Fan, C., Shen, H., et al. (2023). Biomimetic natural biopolymer-based wet-tissue adhesive for tough adhesion, seamless sealed, emergency/nonpressing hemostasis, and promoted wound healing. *Adv. Funct. Mater.* 33 (6). doi:10.1002/adfm.202211340

Yang, Y., Liang, Y., Chen, J., Duan, X., and Guo, B. (2022). Mussel-inspired adhesive antioxidant antibacterial hemostatic composite hydrogel wound dressing via photo-polymerization for infected skin wound healing. *Bioact. Mater.* 8, 341–354. doi:10.1016/j.bioactmat.2021.06.014

Yao, M., Zhang, J., Gao, F., Chen, Y., Ma, S., Zhang, K., et al. (2019). New BMSC-laden gelatin hydrogel formed *in situ* by dual-enzymatic cross-linking accelerates dermal wound healing. *ACS omega* 4 (5), 8334–8340. doi:10.1021/acsomega.9b00878

Ye, H. J., Xian, Y. W., Li, S. R., Zhang, C., and Wu, D. C. (2022). *In situ* forming injectable gamma-poly(glutamic acid)/PEG adhesive hydrogels for hemorrhage control. *Biomaterials Sci.* 10 (15), 4218–4227. doi:10.1039/d2bm00525e

Yu, L., and Ding, J. (2008). Injectable hydrogels as unique biomedical materials. *Chem. Soc. Rev.* 37 (8), 1473–1481. doi:10.1039/b713009k

Zawani, M., and Fauzi, M. B. (2021). Injectable hydrogels for chronic skin wound management: a concise review. *Biomedicines* 9 (5), 527. doi:10.3390/biomedicines9050527

Zeugolis, D. I., Khew, S. T., Yew, E. S., Ekaputra, A. K., Tong, Y. W., Yung, L. Y., et al. (2008). Electro-spinning of pure collagen nano-fibres - just an expensive way to make gelatin? *Biomaterials* 29 (15), 2293–2305. doi:10.1016/j.biomaterials.2008.02.009

Zhai, Z. R., Xu, K. M., Mei, L. X., Wu, C., Liu, J., Liu, Z. Q., et al. (2019). Co-assembled supramolecular hydrogels of cell adhesive peptide and alginate for rapid hemostasis and efficacious wound healing. *Soft matter* 15 (42), 8603–8610. doi:10.1039/c9sm01296f

Zhang, D., Zhou, W., Wei, B., Wang, X., Tang, R., Nie, J., et al. (2015). Carboxyl-modified poly(vinyl alcohol)-crosslinked chitosan hydrogel films for potential wound dressing. *Carbohydr. Polym.* 125, 189–199. doi:10.1016/j.carbpol.2015.02.034

Zhang, F. (2018). The effect of intra-articular tranexamic acid injection on unicompartmental knee arthroplasty patients' blood loss volume in perioperative period. *Osteoporos. Int.* 29, S208.

Zhang, L., Liu, M., Zhang, Y., and Pei, R. (2020). Recent progress of highly adhesive hydrogels as wound dressings. *Biomacromolecules* 21 (10), 3966–3983. doi:10.1021/acs.biomac.0c01069

Zhang, T. W., Zhao, J., Lv, X. Y., Liu, F., Wang, X. L., Li, K., et al. (2021c). Injectable hydrogel based on short-peptide RG5 combined with halloysite nanotubes for rapid hemostasis. *J. Of Nanoparticle Res.* 23 (11), 240. doi:10.1007/s11051-021-05345-8

Zhang, X. X., Ma, Z. F., Ke, Y., Xia, Y., Xu, X. D., Liu, J. C., et al. (2021b). An injectable serotonin-chondroitin sulfate hydrogel for bio-inspired hemostatic adhesives with high wound healing capability. *Mater. Adv.* 2 (15), 5150–5159. doi:10.1039/d1ma00137j

Zhang, Z. B., Guo, J. D., He, Y. X., Han, J. Z., Chen, M. M., Zheng, Y. Q., et al. (2022). An injectable double network hydrogel with hemostasis and antibacterial activity for promoting multidrug-resistant bacteria infected wound healing. *Biomaterials Sci.* 10 (12), 3268–3281. doi:10.1039/d2bm00347c

Zhang, Z.-Y., Zhang, H.-Y., Talmy, T., Guo, Y., Zhou, S.-R., Zhang, L.-Y., et al. (2021a). Management of non-compressible torso hemorrhage: an update. *Chin. J. Of Traumatology* 24 (3), 125–131. doi:10.1016/j.cjtee.2021.03.005

Zhao, X., Wu, H., Guo, B. L., Dong, R. N., Qiu, Y. S., and Ma, P. X. (2017). Antibacterial anti-oxidant electroactive injectable hydrogel as self-healing wound dressing with hemostasis and adhesiveness for cutaneous wound healing. *Biomaterials* 122, 34–47. doi:10.1016/j.biomaterials.2017.01.011

Zhou, F. F., Yang, Y., Zhang, W. J., Liu, S. Y., Shaikh, A. B., Yang, L., et al. (2022a). Bioinspired, injectable, tissue-adhesive and antibacterial hydrogel for multiple tissue regeneration by minimally invasive therapy. *Appl. Mater. Today* 26, 101290. doi:10.1016/j.apmt.2021.101290

Zhou, J. J., Zhang, H. R., Fareed, M. S., He, Y. H., Lu, Y. Q., Yang, C. Y., et al. (2022b). An injectable peptide hydrogel constructed of natural antimicrobial peptide J-1 and ADP shows anti-infection, hemostasis, and antiadhesion efficacy. *ACS Nano* 16 (5), 7636–7650. doi:10.1021/acsnano.1c11206

Zhou, Y., Gui, Q., Yu, W., Liao, S., He, Y., Tao, X., et al. (2019). Interfacial diffusion printing: an efficient manufacturing technique for artificial tubular grafts. *ACS Biomater. Sci. Eng.* 5 (11), 6311–6318. doi:10.1021/acsbiomaterials.9b01293

Zhu, F., Wang, C., Yang, S., Wang, Q., Liang, F., Liu, C., et al. (2017). Injectable tissue adhesive composite hydrogel with fibroblasts for treating skin defects. *J. Mater. Chem. B* 5 (13), 2416–2424. doi:10.1039/c7tb00384f

Zhu, J., Han, H., Li, F., Wang, X., Yu, J., Qin, X., et al. (2019). Peptide-functionalized amino acid-derived pseudoprotein-based hydrogel with hemorrhage control and antibacterial activity for wound healing. *Chem. Of Mater.* 31 (12), 4436–4450. doi:10.1021/acs.chemmater.9b00850

Zhu, J., Li, F. X., Wang, X. L., Yu, J. Y., and Wu, D. Q. (2018). Hyaluronic acid and polyethylene glycol hybrid hydrogel encapsulating nanogel with hemostasis and sustainable antibacterial property for wound healing. *ACS Appl. Mater. interfaces* 10 (16), 13304–13316. doi:10.1021/acsami.7b18927

Zhu, Z. R., Zhang, K. W., Xian, Y. W., He, G., Pan, Z., Wang, H. F., et al. (2022). A choline phosphoryl-conjugated chitosan/oxidized dextran injectable self-healing hydrogel for improved hemostatic efficacy. *Biomacromolecules* 24, 690–703. doi:10.1021/acs.biomac.2c01143

Zou, F., Wang, Y., Zheng, Y., Xie, Y., Zhang, H., Chen, J., et al. (2022). A novel bioactive polyurethane with controlled degradation and L-Arg release used as strong adhesive tissue patch for hemostasis and promoting wound healing. *Bioact. Mater.* 17, 471–487. doi:10.1016/j.bioactmat.2022.01.009

frontiers | Frontiers in Bioengineering and Biotechnology

TYPE Original Research
PUBLISHED 24 January 2024
DOI 10.3389/fbioe.2024.1331078



OPEN ACCESS

EDITED BY
Hasan Uludag,
University of Alberta, Canada

REVIEWED BY
Seungil Kim,
University of Pittsburgh, United States
Juan C. Cruz,
University of Los Andes, Colombia

*CORRESPONDENCE
Junxi Xiang,
xjx722@163.com
Yi Lv,
luyi169@126.com

RECEIVED 31 October 2023
ACCEPTED 15 January 2024
PUBLISHED 24 January 2024

CITATION
Liu P, Liu X, Yang L, Qian Y, Lu Q, Shi A, Wei S, Zhang X, Lv Y and Xiang J (2024), Enhanced hemocompatibility and rapid magnetic anastomosis of electrospun small-diameter artificial vascular grafts.
*Front. Bioeng. Biotechnol.* 12:1331078.
doi: 10.3389/fbioe.2024.1331078



# Enhanced hemocompatibility and rapid magnetic anastomosis of electrospun small-diameter artificial vascular grafts

Peng Liu[1,2], Xin Liu[3], Lifei Yang[2], Yerong Qian[4], Qiang Lu[5], Aihua Shi[2], Shasha Wei[2], Xufeng Zhang[4], Yi Lv[1,2,4]* and Junxi Xiang[4]*

[1]Center for Regenerative and Reconstructive Medicine, Med-X Institute, The First Affiliated Hospital of Xi'an Jiaotong University, Xi'an, Shaanxi, China, [2]National Local Joint Engineering Research Center for Precision Surgery and Regenerative Medicine, The First Affiliated Hospital of Xi'an Jiaotong University, Xi'an, Shaanxi, China, [3]Department of Graduate School, Xi'an Medical University, Xi'an, Shaanxi, China, [4]Department of Hepatobiliary Surgery, The First Affiliated Hospital of Xi'an Jiaotong University, Xi'an, Shaanxi, China, [5]Department of Geriatric Surgery, The First Affiliated Hospital of Xi'an Jiaotong University, Xi'an, China

**Background:** Small-diameter (<6 mm) artificial vascular grafts (AVGs) are urgently required in vessel reconstructive surgery but constrained by suboptimal hemocompatibility and the complexity of anastomotic procedures. This study introduces coaxial electrospinning and magnetic anastomosis techniques to improve graft performance.

**Methods:** Bilayer poly(lactide-co-caprolactone) (PLCL) grafts were fabricated by coaxial electrospinning to encapsulate heparin in the inner layer for anticoagulation. Magnetic rings were embedded at both ends of the nanofiber conduit to construct a magnetic anastomosis small-diameter AVG. Material properties were characterized by micromorphology, fourier transform infrared (FTIR) spectra, mechanical tests, *in vitro* heparin release and hemocompatibility. *In vivo* performance was evaluated in a rabbit model of inferior vena cava replacement.

**Results:** Coaxial electrospinning produced PLCL/heparin grafts with sustained heparin release, lower platelet adhesion, prolonged clotting times, higher Young's modulus and tensile strength *versus* PLCL grafts. Magnetic anastomosis was significantly faster than suturing (3.65 $\pm$ 0.83 vs. 20.32 $\pm$ 3.45 min, $p < 0.001$) and with higher success rate (100% vs. 80%). Furthermore, magnetic AVG had higher short-term patency (2 days: 100% vs. 60%; 7 days: 40% vs. 0%) but similar long-term occlusion as sutured grafts.

**Conclusion:** Coaxial electrospinning improved hemocompatibility and magnetic anastomosis enhanced implantability of small-diameter AVG. Short-term patency was excellent, but further optimization of anticoagulation is needed for long-term patency. This combinatorial approach holds promise for vascular graft engineering.

KEYWORDS

**coaxial electrospinning, magnetic anastomosis, small-diameter vascular grafts, hemocompatibility, sutureless**

# 1 Introduction

Vascular diseases are major causes of morbidity and mortality globally (Feng et al., 2022). Bypass surgery or vascular reconstruction is the only course of correction in some cases (Seifu et al., 2013; Johnson et al., 2019). Artificial vascular grafts (AVGs) composed of polyethylene terephthalate, polytetrafluoroethylene and polyurethane can effectively replace blood vessels with large diameters (Anderson et al., 2018; Leal et al., 2021; Popa et al., 2022). However, these materials have poor patency and frequent thrombosis when replacing vessels <6 mm (Baguneid et al., 2011; Eilenberg et al., 2020). To address the challenges of small-diameter AVGs, innovations like coaxial electrospinning, decellularization, freeze-drying and 3D printing have been developed (Darie-Niță et al., 2022). Coaxial electrospinning in particular shows promise for nanofibrous vascular grafts (Laktionov et al., 2014; Yin et al., 2017; Liu et al., 2022). This method enables the incorporation of anticoagulant agents (Huang et al., 2013; Kuang et al., 2018), within the core-shell structure of the nanofibers, thus enhancing their antithrombotic properties.

However, electrospun AVGs have limited compliance compared to native vessels (Faturechi et al., 2019a). This makes the anastomosis difficult, increases the leakage risk at the anastomosis site, and impairs patency (Tamimi et al., 2019; Jeong et al., 2020). Magnetic anastomosis enables sutureless magnetic vessel connections, reducing leakage and hemorrhage risks compared to suturing (Kubo et al., 2018; Isozaki et al., 2020). Therefore, we hypothesize this technique can address the compliance mismatch problem in small-diameter AVGs.

In this study, we develop and apply a small-diameter AVG using coaxial electrospinning and magnetic anastomosis. We first fabricated polymer-derived nanofibers with enhanced hemocompatibility by applying coaxial electrospinning. We then developed a small-diameter AVG integrating magnetic anastomosis. Finally, we implanted the AVG in a rabbit model to evaluate its *in vivo* performance (Figure 1).

# 2 Materials and methods

## 2.1 Materials

Poly (l-lactic acid-co-ε-caprolactone) (PLCL, LLA/CL = 1/1, 15 kDa, Jinan Daigang Biomaterial Co., Ltd., China) was dissolved in 1,1,1,3,3,3-hexafluoro-2-propanol (HFIP, Aladdin, United States) at 200 mg/mL. Heparin sodium (13 kDa, Runjie Medicine Chemical, China) was dissolved in saline at a concentration of 100 mg/mL. NdFeB magnetic rings were procured from Jiujiu High-Tech Magnetic Materials Ltd. in China, featuring an inner diameter of 3.3 mm, an outer diameter of 4.9 mm, and a thickness of 1.5 mm.

## 2.2 Artificial vascular grafts preparation

AVGs were prepared as previously described (Liu et al., 2022) with modifications. As shown in Figure 2, a 3D printer (Xiao Fang

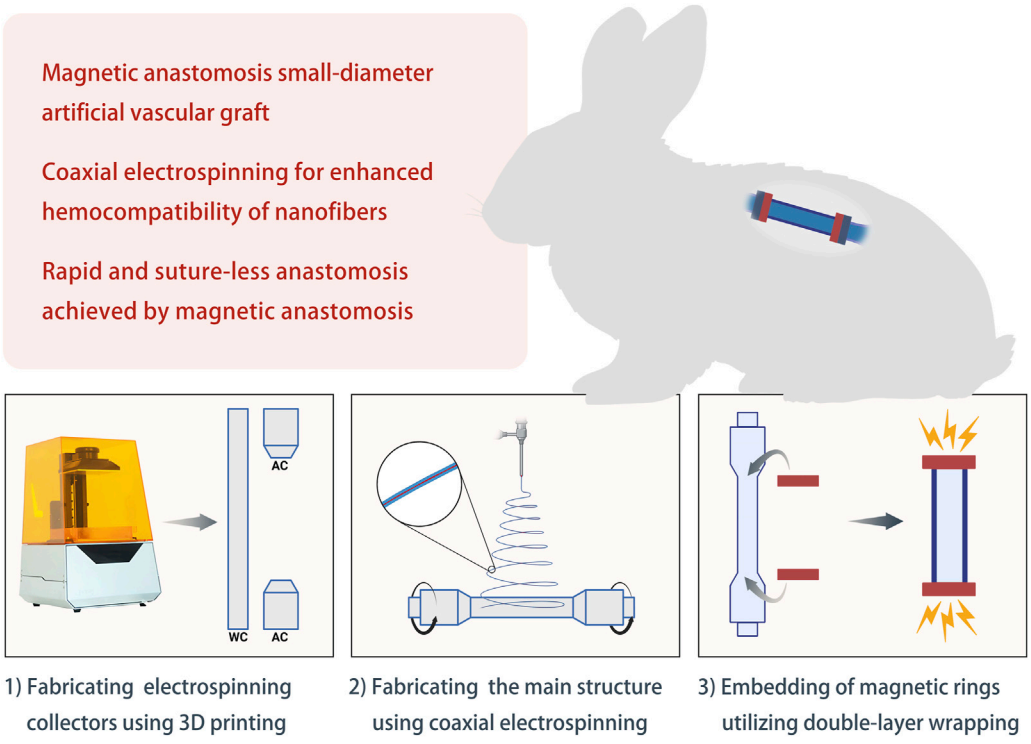


FIGURE 1
Schematic diagram of the study design Abbreviations: WC, working collector; AC, auxiliary collector.

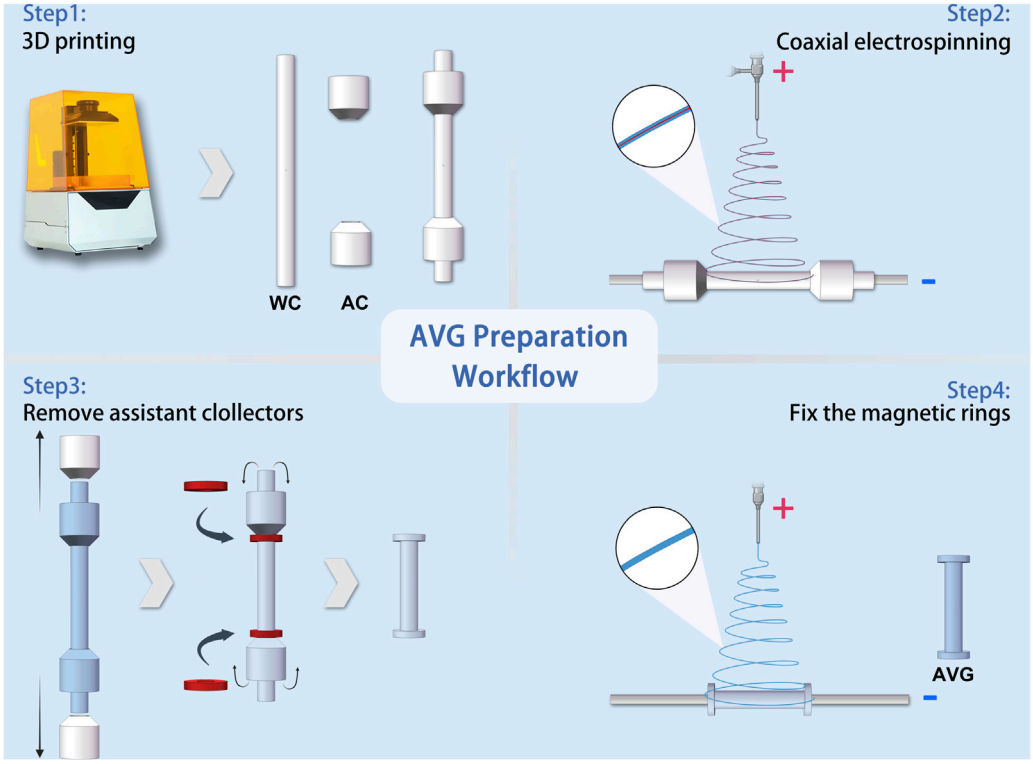


FIGURE 2
Schematic workflow of artificial vascular graft preparation Abbreviations: WC, working collector; AC, auxiliary collector.

ONE, Exquisitely 3D, China) was used to fabricate electrospun collectors. The collectors were classified into two distinct types based on their functions: the working collector (WC) and the auxiliary collector (AC).

An electrospinning machine (ET-2535H, Beijing Yongkang Leye Technology Development Co., Ltd.) was used to create the electrospun fibers. The machine had two syringe pumps to deliver solutions to a coaxial needle (22G+17G, Hefei Sipin Technology Co., Ltd.). The outer needle dispensed the outer solution at 2 mL/h, while the inner needle dispensed the inner solution at 0.2 mL/h. A high-voltage power supply generated 18 kV positive voltage with a 15 cm distance between the spinneret and collector. The coaxial needle had an inner diameter of 22G and outer diameter of 17G. For comparison, single-spinneret electrospinning was done under the same conditions, except with a 9 kV voltage and a 22G single-channel needle.

The magnetic anastomosis AVG (mag-AVG) was fabricated using a double layer wrapping method. Figure 2 illustrates the workflow of the process, which involved coaxial electrospinning on one working collector (WC) and two auxiliary collectors (ACs) at a speed of 75 rpm, forming an inner layer with a bell-mouth structure. Afterward, the ACs were removed, and the magnetic rings were inserted. Subsequently, the magnetic rings were wrapped with the bell-mouth structure. Finally, a second layer of electrospinning was performed on the WC at a speed of 50 rpm for 15 min. In contrast, the suture anastomosis AVG (suture-AVG) was fabricated using a similar method, except that no magnetic rings were embed.

## 2.3 Micromorphology

The surface/cross-section morphologies were measured via a scanning electron microscope (SEM, TM-1000, Japan). The core-shell structures were confirmed by electrospinning fibers onto a carbon-coated copper mesh and examining them with transmission electron microscopy (TEM, H-7650, Japan) at 80 kV.

## 2.4 Fourier transform infrared spectroscopy

IR spectra (PLCL fibers, PLCL/heparin fibers, and heparin) were acquired using a Thermo Nicolet iS50 FTIR infrared spectrometer. Each spectrum was obtained by averaging 64 scans, and the wavenumber range spanned from 400 to 4,000 $cm^{-1}$.

## 2.5 Mechanical properties

To assess the mechanical properties of the AVGs, we conducted tensile testing utilizing a universal testing machine (CMT8502, New Sans Test Technical Company, China). The specimens were loaded at a constant strain rate of 10 mm/min until rupture.

The burst pressure of the artificial blood vessels was determined by a vascular anastomosis experimental system (YZ-08, Xi'an Magnat Medical Technical Company, China).

Following ANSI 7198, compliance measurements were made on ~6 cm AVG segments by a vascular anastomosis experimental system, as described in 2.5. The external diameter was measured from digital images recorded. Compliance was calculated and reported as % per 100 mmHg as follows (Konig et al., 2009):

$$C = \frac{(R_1 - R_0)/R_0}{P_{outlet} - P_{inlet}} \times 10^4$$

where C is compliance (%), $R_0$ is the original graft diameter, $R_1$ is the changed graft diameter, $P_{inlet}$ is the inlet pressure and $P_{outlet}$ is the outlet pressure.

## 2.6 *In vitro* release of heparin

To assess heparin release, 300 mg samples were immersed in 10 mL PBS (pH 7.4) at 37°C. At specific time intervals, 1 mL of the solution was extracted and replaced with fresh PBS to measure heparin concentration. Heparin test kits (G-CLONE Biotechnology Co., Ltd.) evaluated the initial heparin loading and release, with all measurements done in triplicate.

## 2.7 Hemocompatibility analysis

To investigate platelet adhesion, fresh anticoagulated rabbit blood was centrifuged to obtain platelet-rich plasma (PRP) (Liu et al., 2022). A 1.0 × 1.0 $cm^2$ sample was immersed in PRP and incubated at 37°C for 1 h. The morphology and number of platelets adhered to the electrospun membrane were observed and quantified using SEM.

The hemolysis test began by collecting freshly anticoagulated rabbit blood and diluting it with saline. A 1 cm × 1 cm electrospun membrane was washed and incubated in saline at 37°C for 30 min. The diluted blood was applied to the membrane, gently mixed, and incubated at 37°C for 1 hour. Hemolysis degree was quantified by measuring the absorbance of the supernatant at 540 nm after centrifugation.

PT and APTT assays were done using a 2 cm × 3 cm electrospun membrane incubated with platelet-poor plasma (PPP) at 37°C for 15 min. The coagulation analyzer automatically measured PT and APTT to assess clotting functionality.

In the partial thromboplastin time (PRT) assay, a 2 × 3 cm electrospun membrane was incubated with PPP at 37°C for 10 min. Subsequently, calcium chloride was added, and the time required for clot formation was recorded.

## 2.8 *In vivo* implantation

Animal procedures were approved by the Animal Welfare Act and Institutional Animal Care and Use Committee at Xi'an Jiaotong University. All rabbits were individually housed in separate cages and provided with *ad libitum* access to diets and water. Ten healthy male New Zealand rabbits, each weighing 2.5 ± 0.5 kg and aged 3 months, were randomly assigned to two groups ($n$ = 5 each): mag-AVG, implanted using magnetic anastomosis, and suture-AVG, implanted using conventional manual suturing.

Before surgery, rabbits fasted 12 h and lacked water 6 h. Anesthesia was administered by intravenous injection of 3% pentobarbital sodium at a dosage of 1 mL/kg through the auricular vein. The abdomen was prepared, sterilized and draped. The inferior vena cava was exposed via midline incision. The vena cava was clamped at both ends then excised between clamps.

The procedure for mag-AVG implantation was as follows. First, the magnetic rings were affixed to the vascular clamps separately. Then, the vena cava wall was flipped and wrapped around the rings. Next, one end of the mag-AVG was affixed to the magnetic ring. Heparin saline was injected into the lumen. The other end of the mag-AVG was affixed with the other magnetic ring to complete the anastomosis. Clamps were removed to restore blood flow. For suture-AVG, the vena cava was clamped, transected between clamps, and anastomosed end-to-end with two continuous 8–0 polypropylene sutures. After the operation, both groups of rabbits received analgesia and antibiotics, with no further additional treatments administered.

The status of AVGs was assessed using noninvasive vascular ultrasound (Xuzhou Paier Electronics Co., Ltd.) by vascular medicine specialists on the 2nd and 7th postoperative days. Angiography of the inferior vena cava through the femoral vein was performed on the rabbits at 2 weeks postoperatively.

## 2.9 Statistical methods

Data were analyzed using SPSS 22.0 software (IBM, Armonk, NY). Quantitative data were expressed as mean ± standard deviation ($\bar{x}\pm$ s). $T$ -tests were used for comparisons between two groups, and one-way ANOVA was used for comparisons between multiple groups. The $\chi 2$ test was used to compare categorical data. Differences were considered statistically significant at $p < 0.05$.

# 3 Results

## 3.1 Morphological characteristics of electrospun nanofibers

The average diameters of the PLCL/heparin and PLCL nanofibers (Figure 3A) were measured to be 1.10 ± 0.22 μm and 2.99 ± 0.56 μm, respectively. It is evident that the PLCL nanofibers displayed a wider range of diameter distribution compared to the PLCL/heparin nanofibers (Figure 3B).

Figure 3C showed a clear contrast between the dark core and the bright shell of PLCL/heparin nanofibers, and the diameter of the core layer constitutes approximately 26.45% of the entire fiber diameter. As shown in Figure 3D, the FTIR spectrum of PLCL nanofibers displayed a strong absorption peak at 1746 $cm^{-1}$ corresponds to the stretching of the C=O bond. Heparin exhibits vibrations at 1,606 $cm^{-1}$ (indicating COO− antisymmetric stretching) and at 1,225 $cm^{-1}$ and 1,049 $cm^{-1}$ (indicating $SO_2$-asymmetric stretching). The PLCL/heparin nanofibers revealed a

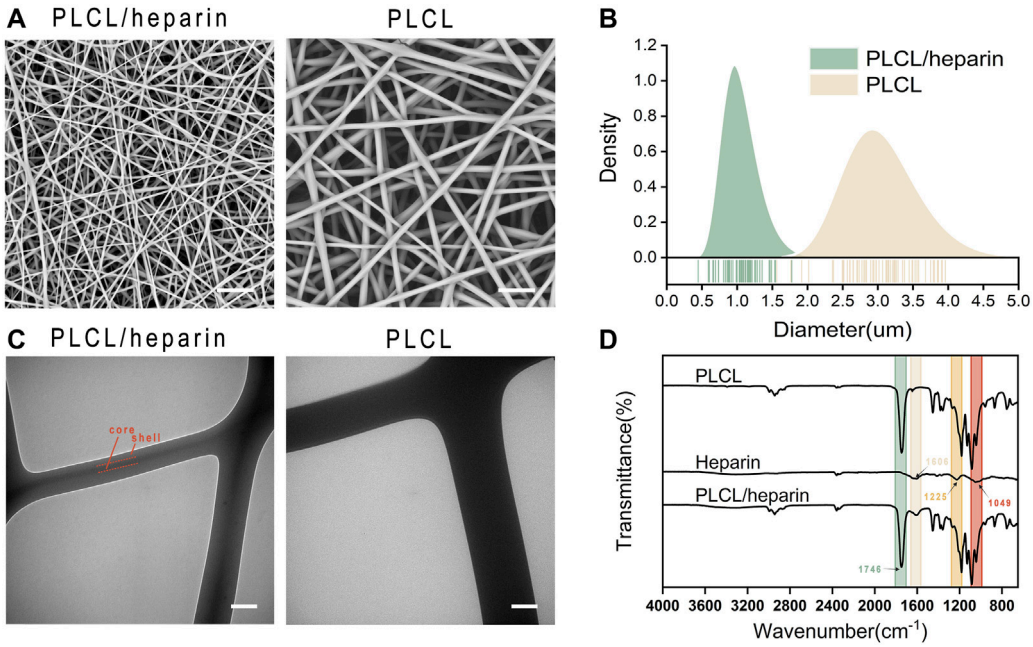


FIGURE 3
Characterization of electrospun nanofibers. **(A)** SEM images (scale bar = 20 μm); **(B)** Diameter distribution; **(C)** TEM (scale bar = 500 nm); **(D)** FTIR spectra.

discernible band at 1746 $cm^{-1}$, originating from the -C=O functional group of PLCL, along with peaks at 1,606 $cm^{-1}$, attributable to the -COO− moiety present in heparin. These findings conclusively demonstrate the successful encapsulation of heparin within the PLCL/heparin coaxial structure.

## 3.2 Hemocompatibility assay

A distinct two-stage release pattern was observed, characterized by an initial burst release within the first day, followed by a sustained release phase (Figure 4A) (Liu et al., 2022). Specifically, within the initial 24 h, a significant proportion of heparin, amounting to 40.5%, was released. Subsequently, over a span of 14 days, the cumulative amount of released heparin reached approximately 76%.

The SEM images in Figure 4B show that the PLCL nanofibers had a much higher number of adherent platelets than the PLCL/heparin nanofiber group (18.0 ± 6.24 vs. 2.6 ± 0.84 $\times 10^5$/$cm^2$, $p < 0.01$).

The hemolysis rate of both the heparin/PLCL fibers and the PLCL fibers met the international standard ASTM-F756-17, which classifies a hemolytic index of less than 2% as "no hemolysis" (Figure 4C). No significant difference was found in the prothrombin time (PT) between these two groups (20.24 ± 2.15s vs. 21.4 ± 3.21 s, $p = 0.57$) (Figure 4D). However, the activated partial thromboplastin time (APTT) (152 ± 30.0 s vs. 43.2 ± 11.15 s, $p < 0.01$) (Figure 4E) and the partial thromboplastin time (PRT) (116.23 ± 14.21 s vs. 90.01 ± 12.34 s, $p < 0.01$) (Figure 4F) were significantly prolonged in the PLCL/heparin nanofiber group compared to the PLCL nanofiber group.

## 3.3 Mechanical properties of AVGs

The mechanical properties of the AVGs were depicted in Figure 5. The compliance of the AVGs appears to be relatively poor, as observed in Figure 5B (1.22% ± 0.41% vs. 1.88% ± 0.32% vs. 1.48% ± 0.68%/100 mmHg). The compliance of all AVGs was lower than that of the native blood vessels (4.4%/100 mmHg for vein and 11.5%/100 mmHg for artery) (Camasão and Mantovani, 2021). The AVGs constructed using PLCL/heparin nanofibers exhibited significantly higher Young's modulus (6.22 ± 0.38 vs. 2.58 ± 0.25 MPa, $p < 0.001$), and tensile strength (14.64 ± 2.3 vs. 8.08 ± 3.25 MPa, $p < 0.01$) compared to those made of PLCL nanofibers. Furthermore, the incorporation of a double-layer structure further enhanced the Young's modulus (8.43 ± 0.81 MPa, $p < 0.001$), while the tensile strength remained largely unaltered (17.52 ± 2.62 MPa, $p = 0.82$). Furthermore, as depicted in Figure 5E, the burst pressure of the PLCL/heparin AVGs exceeded that of the PLCL AVGs but fell short of the double-layer conduits (704.3 ± 31.2 vs. 195.79.07 ± 34.2 vs. 868.21 ± 41.32 mmHg, $p < 0.001$).

## 3.4 *In vivo* implantation of AVGs

The AVGs are cylindrical with a 3 mm inner diameter and 20 mm length (Figure 6A). Magnetic rings are embedded at both ends (Figure 6A). The total AVG thickness is ~0.2 mm with two layers (Figure 6B). The inner PLCL/heparin fiber layer is ~160 μm thick. The outer PLCL fiber layer is ~80 μm thick.

To mitigate the challenge of mismatched artificial blood vessels, we selected rabbits with inferior vena cava diameters closely aligned

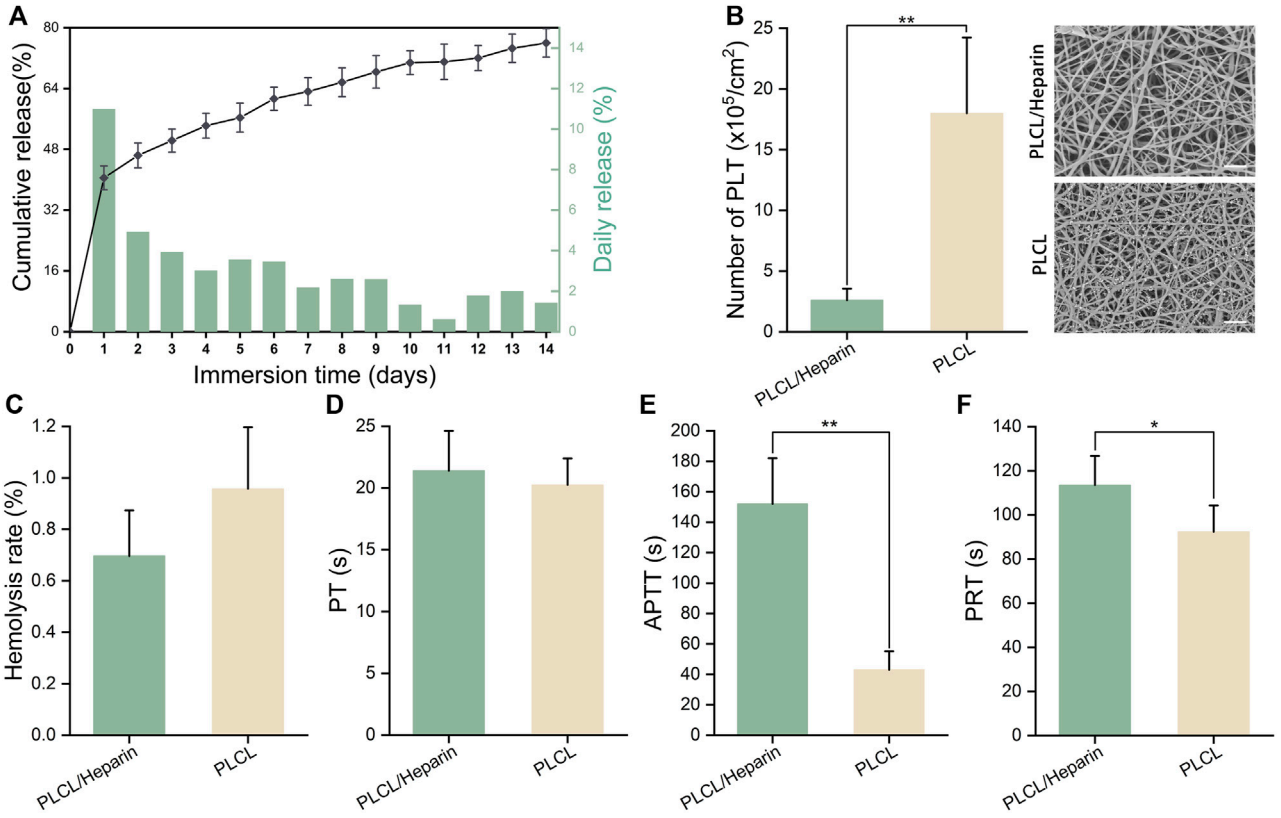


FIGURE 4
Hemocompatibility of electrospun nanofibers. **(A)** *In vitro* heparin release; **(B)** The number of adherent platelets (scale bar = 20 μm); **(C–F)** Hemolysis rate, prothrombin time (PT), activated partial thromboplastin time (APTT), partial thromboplastin time (PRT).

with those of the artificial blood vessels. In cases of slight disparity, we employed techniques such as warm saline or water bag application to dilate the blood vessels. Additionally, we utilized specific methods during manual suturing, such as angulated trimming of the blood vessels, to ensure diameter matching. Procedures of mag-AVG and suture-AVG implantation are illustrated in Figures 6D, E. Magnetic anastomosis was faster, averaging 3.65 ± 0.83 min, compared to suturing, which averaged 20.32 ± 3.45 min ($p < 0.001$, Figure 6C).

All 5 mag-AVG rabbits had successful surgery without complications like infection or bleeding. However, 1 suture-AVG rabbit died during surgery from excessive bleeding at the anastomosis site. For vascular patency, all 5 mag-AVGs were patent on day 2 post-op, 2 remained patent on day 7 (Figure 6F, G), and all were occluded by day 14. In contrast, 2 suture-AVGs showed early occlusion by day 2, and all were occluded by day 7. In summary, the mag-AVGs reduced surgical difficulty and risk and improved early patency, but further optimization of material properties is needed to enhance long-term anticoagulation and patency.

## 4 Discussion

Coaxial electrospinning is a novel technique for producing core-shell nanofibers that provide a robust structure and deliver bioactive agents (Yin et al., 2017; Liu et al., 2020). It has been applied to various fields, such as antibacterial materials (Dong et al., 2023), tissue engineering scaffolds (Iliou et al., 2022; Nagiah et al., 2022), catalysts (Choi et al., 2016), and others. Especially, this technique has unique advantages for creating anticoagulant materials (Huang et al., 2013; Kuang et al., 2018; Strobel et al., 2018). Using a bilayer or multilayer coaxial structure, structural polymers form the outer layer, while natural anticoagulants like heparin are incorporated in the inner layer. This design enables sustained anticoagulant release while maintaining mechanical properties. Compared to physical encapsulation or chemical conjugation, the coaxial structure better preserves anticoagulant bioactivity and provides more controllable release kinetics (Figure 4). Coaxial electrospinning has great potential for small-diameter vascular tissue engineering applications.

However, coaxial electrospinning of AVGs has some limitations. The low elasticity and compliance of electrospun materials impairs suturability and increases the risk of anastomotic complications like leakage and thrombosis (Li et al., 2008a; Rahmati et al., 2020). In this study, for example, the compliance of the AVG was only one-third of natural blood vessels (vein: 4.4%/100 mmHg; artery: 11.5%/100 mmHg) (Camasão and Mantovani, 2021). After suturing, incomplete sealing and enlargement of the anastomosis due to suture cutting led to a high leakage risk. Approaches like cross-linking, coating, blending, and reinforcement have been proposed to improve the compliance (Faturechi et al., 2019b; Furdella et al.,

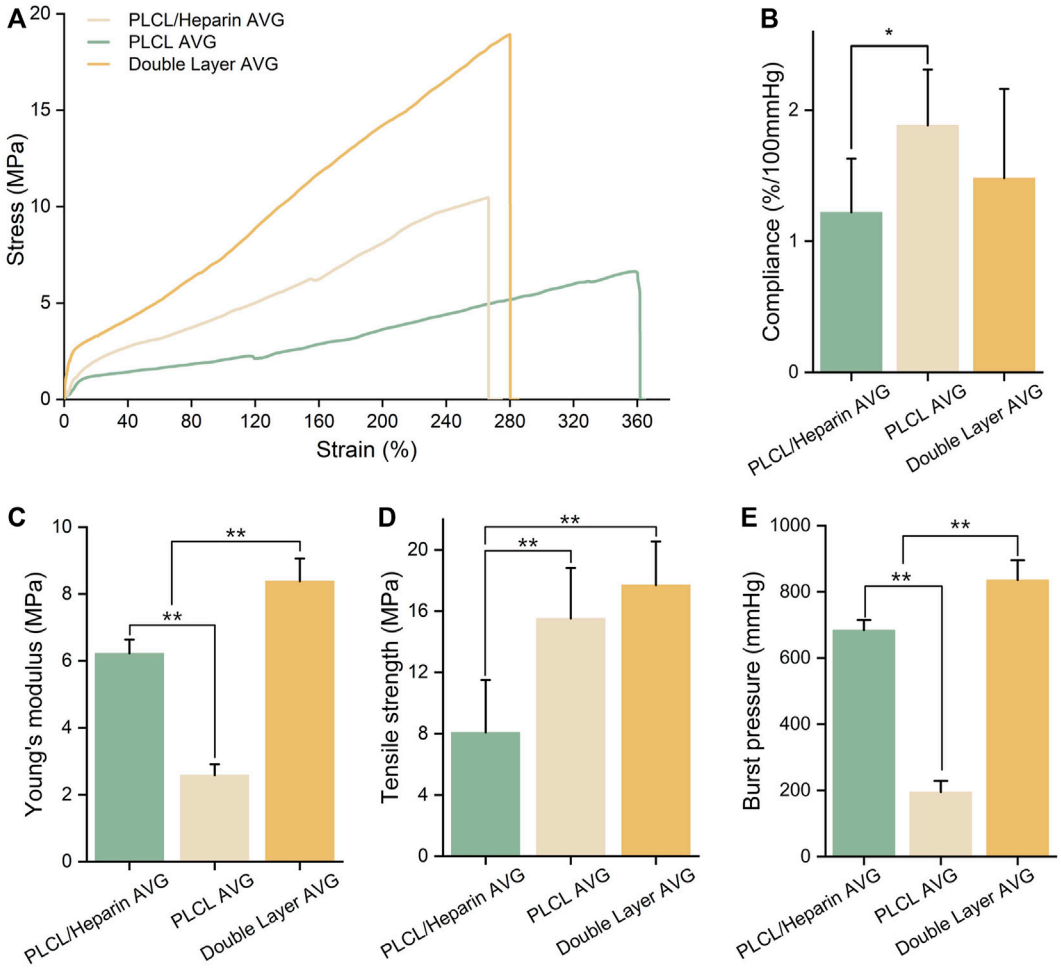


FIGURE 5
Characterization of AVG. **(A)** Uniaxial tensile stress-strain curves; **(B–E)** Compliance, Young's modulus, tensile strength and burst pressure of AVG.

2021), but may also affect hemocompatibility, requiring optimization. Given these limitations, we propose magnetic anastomosis to address the inadequate compliance of electrospun AVGs.

The main finding of this study was that the mag-AVG group had lower surgical complication rates (0% vs. 20%) and higher patency than the suture-AVG group (2 days: 100% vs. 60%; 7 days: 40% vs. 0%). This demonstrates the advantages of magnetic anastomosis compared to sutured anastomosis. First, magnetic anastomosis seals with magnetic fields instead of sutures, resulting in a more effective closure and eliminating leakage risk, as shown in prior intestinal(Chen et al., 2020; Zhang. et al., 2023a), biliary(Jang et al., 2011), vascular(Yang et al., 2018; Zhang et al., 2023b), and biliary-enteric (Li et al., 2008b) anastomoses. Second, magnetic anastomosis leaves no intraluminal sutures and creates a smoother anastomotic stoma, reducing turbulence and platelet adhesion.

Beyond addressing compliance, magnetic anastomosis is easy and quick to perform, with a short learning curve. Brief training enables novice students to outperform experienced surgeons in quality and time (3.65 ± 0.83 vs. 20.32 ± 3.45 min, $p < 0.001$). Magnetic anastomosis also ensures safety and reversibility - unsatisfactory anastomoses can be detached without damage and repeated until favorable.

In comparison to existing AVGs in the market and those documented in the literature, our mag-AVG design offers significant improvements. Traditional AVGs, such as those made from expanded polytetrafluoroethylene (ePTFE) and Dacron, have been associated with high rates of thrombosis and stenosis due to their intrinsic material properties and the technical challenges associated with their implantation (Halbert et al., 2020; Ratner, 2023). These grafts often require precise suturing techniques and can lead to neointimal hyperplasia at the venous anastomosis site. In contrast, our mag-AVG facilitates a rapid and secure connection between vessels with its innovative magnetic mechanism, which not only reduces operative time but also minimizes the inflammatory response typically triggered by suture materials (Deng et al., 2021).

However, our AVGs exhibited lower patency in the long term compared to other studies. For instance, (Wang et al., 2013) attained a 37.5% patency rate over 24 weeks using electrospun coaxial fibers composed of a heparin core and PLCL shell. The low patency rate

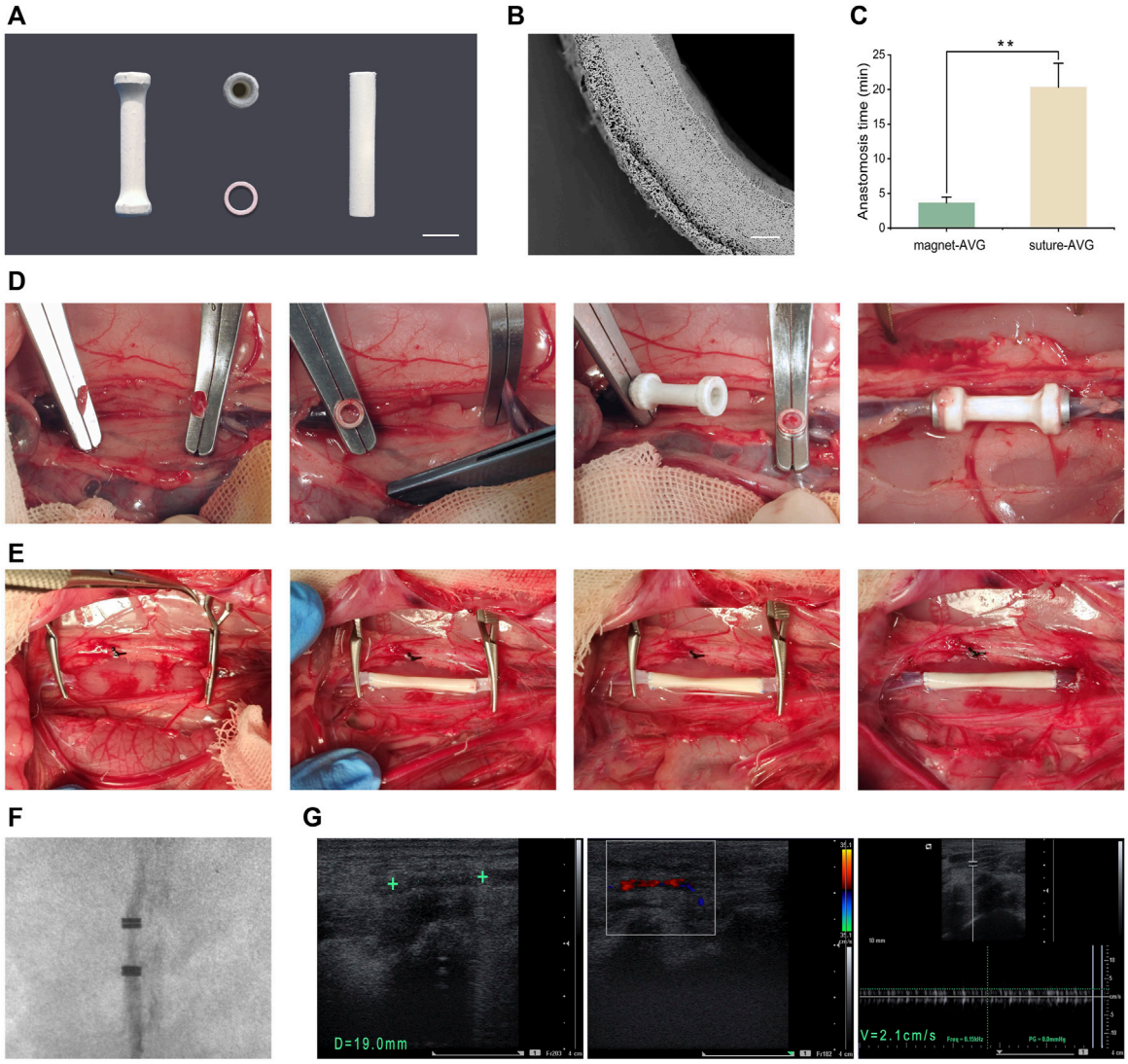


FIGURE 6
*In vivo* implantation. **(A)** Images of mag-AVG, magnetic rings and suture-AVG; **(B)** The cross-sectional SEM image of AVG; **(C)** Comparison of the anastomosis time between mag-AVG and suture-AVG. **(D)** Images of mag-AVG implantation; **(E)** Images of suture-AVG implantation. **(F)** X-ray image of the implanted mag-AVG; **(G)** Ultrasound images of the implanted mag-AVG on the 2nd day post-implantation; Measurement of AVG length (19 mm) and diameter (3 mm), "+" symbol representing the magnetic rings; Doppler ultrasound reveals blood flow signals within the AVG; The blood flow velocity within the AVG is recorded at 2.1 cm/s.

could be due to several factors. First, unlike other studies, we employed AVGs to replace veins rather than arteries. Veins have lower blood flow velocity and pressure than arteries, increasing thrombus formation risk. Creating artificial veins is challenging and requires outstanding anticoagulation. Second, we abstained from using any anticoagulants in our experiment to assess the optimal effectiveness of our AVGs. Nevertheless, we also recognize the potential benefits of anticoagulant therapy for our AVGs. It is well known that the early stages post-implantation are particularly prone to thrombosis. The administration of anticoagulant medications such as aspirin or heparin during this critical period may potentially enhance the long-term patency of our AVGs. Nonetheless, this hypothesis requires further experimental validation. Third, *in vitro* tests showed ~76% of heparin released within 2 weeks, impairing long-term anticoagulation. Moreover, long-term patency necessitates fully developed endothelialization, which artificial veins typically lack.

The biocompatibility of the implant is crucial. Our novel graft comprises the biodegradable PLCL and non-degradable magnetic rings, the latter posing dual risks regarding biocompatibility and potential magnetic field effects on tissues. However, several factors in this study mitigate biocompatibility concerns over the short term: Firstly, the electrospun PLCL fibers fully encapsulate the magnetic rings, avoiding any direct exposure. Secondly, we have surface-treated the rings with nickel electroplating, a coating known to enhance biocompatibility by isolating the poorly biotolerated magnetic NdFeB core. Our previous work demonstrates the biocompatibility of this coating (Yang et al., 2018; Wang et al.,

2019; Lu et al., 2020). Notably, titanium nitride deposition would be ideal for prolonged implantation according to our expertise, given its widespread application in modifying implantable devices (Iacovacci et al., 2021). Finally, the relatively brief implantation period limits any coating or PLCL degradation, consequently evidencing no tangible biocompatibility issues presently. Nonetheless, regarding potential effects of the magnetic fields, our previous studies found no deleterious effects on surrounding tissue vasculature (Wang et al., 2019; Lu et al., 2020; Xu et al., 2022). Some research even suggests magnetic fields may beneficially promote tissue healing, regeneration and microcirculation (Marycz et al., 2018). Nonetheless, future iterations will ideally incorporate fully degradable magnetic rings composed of nanomaterials that completely degrade within months. This would eliminate any risks of long-term biocompatibility or exposure concerns.

Despite reduced long-term patency, our AVGs have promising applications. Excellent short-term anticoagulation was achieved, with 100% patency by postoperative day 2. Therefore, these AVGs are suitable temporary blood diversion cases. In a separate study, we utilized these AVGs for veno-venous bypass (VVB) during rat liver transplantation (Liu et al., 2022). This enabled rapid bypass without systemic anticoagulation, improving survival and biochemistry. This progress could enhance patient outcomes following complex liver surgeries. Additionally, these vessels may have utility in extracorporeal circulation, ECMO quick connectors, and other scenarios needing swift anastomosis and thrombosis prevention.

However, there exist some limitations in our study. The magnetic ring design requires optimization, as the current thickness is relatively large. Consequently, this method is only suitable for venous reconstruction and cannot yet be utilized for arterial. In future research, we will aim to refine the magnetic ring and AVG design to enable arterial reconstruction applications.

## 5 Conclusion

This study demonstrates the fabrication of small-diameter AVGs using the innovative techniques of coaxial electrospinning and magnetic anastomosis. Coaxial electrospinning enables the incorporation of heparin within the grafts, thereby enhancing their hemocompatibility. Magnetic anastomosis provides a rapid, simple, and safe means of graft implantation while overcoming the compliance mismatch encountered with electrospun grafts. Our findings reveal that grafts implanted by magnetic anastomosis have significantly higher short-term patency and lower surgical risks compared to conventional sutured grafts. However, long-term patency remains a challenge due to the lack of sustained anticoagulation. Further research should optimize the material design and anticoagulation strategies to improve long-term graft performance. Overall, this combinatorial approach of advanced materials and magnetic anastomosis provides a promising platform for small-diameter artificial vascular graft engineering with tremendous clinical potential.

## Data availability statement

The raw data supporting the conclusion of this article will be made available by the authors, without undue reservation.

## Ethics statement

The animal study was approved by the Animal Welfare Act and Institutional Animal Care and Use Committee at Xi'an Jiaotong University. The study was conducted in accordance with the local legislation and institutional requirements.

## Author contributions

PL: Conceptualization, Investigation, Methodology, Writing–original draft. XL: Investigation, Writing–review and editing. LY: Investigation, Methodology, Writing–review and editing. YQ: Investigation, Writing–review and editing. QL: Methodology, Writing–review and editing. AS: Investigation, Writing–review and editing. SW: Funding acquisition, Writing–review and editing. XZ: Investigation, Writing–review and editing. YL: Conceptualization, Funding acquisition, Supervision, Writing–review and editing. JX: Conceptualization, Funding acquisition, Supervision, Writing–review and editing.

## Funding

The author(s) declare financial support was received for the research, authorship, and/or publication of this article. This work was supported by the National Natural Science Foundation of China (82000624), Natural Science Basic Research Program of Shaanxi (2022JQ-899 and 2021JM-268), Shaanxi Province Innovation Capability Support Program (2023KJXX-030), Shaanxi Province Key R&D Plan University Joint Project-Key Project (2021GXLH-Z-047).

## Conflict of interest

The authors declare that the research was conducted in the absence of any commercial or financial relationships that could be construed as a potential conflict of interest.

## Publisher's note

# References


Anderson, D., Pohan, G., Raman, J., Konecny, F., Yim, E., and Hinds, M. T. (2018). Improving surgical methods for studying vascular grafts in animal models. *Tissue Eng. Part C Methods* 24, 457–464. doi:10.1089/ten.TEC.2018.0099

Baguneid, M., de Mel, A., Yildirimer, L., Fuller, B. J., Hamilton, G., and Seifalian, A. M. (2011). *In vivo* study of a model tissue-engineered small-diameter vascular bypass graft. *Biotechnol. Appl. Biochem.* 58, 14–24. doi:10.1002/bab.8

Camasão, D. B., and Mantovani, D. (2021). The mechanical characterization of blood vessels and their substitutes in the continuous quest for physiological-relevant performances. A critical review. *Mater Today Bio* 10, 100106. doi:10.1016/j.mtbio.2021.100106

Chen, H., Ma, T., Wang, Y., Zhu, H. Y., Feng, Z., Wu, R. Q., et al. (2020). Fedora-type magnetic compression anastomosis device for intestinal anastomosis. *World J. Gastroenterol.* 26, 6614–6625. doi:10.3748/wjg.v26.i42.6614

Choi, S. J., Chattopadhyay, S., Kim, J. J., Kim, S. J., Tuller, H. L., Rutledge, G. C., et al. (2016). Coaxial electrospinning of wo3 nanotubes functionalized with bio-inspired pd catalysts and their superior hydrogen sensing performance. *Nanoscale* 8, 9159–9166. doi:10.1039/c5nr06611e

Darie-Niță, R. N., Râpă, M., and Frąckowiak, S. (2022). Special features of polyester-based materials for medical applications. *Polym. (Basel)* 14, 951. doi:10.3390/polym14050951

Deng, X., Qasim, M., and Ali, A. (2021). Engineering and polymeric composition of drug-eluting suture: a review. *J. Biomed. Mater Res. A* 109, 2065–2081. doi:10.1002/jbm.a.37194

Dong, Y., Yao, L., Cai, L., Jin, M., Forouzanfar, T., Wu, L., et al. (2023). Antimicrobial and pro-osteogenic coaxially electrospun magnesium oxide nanoparticles-polycaprolactone/parathyroid hormone-polycaprolactone composite barrier membrane for guided bone regeneration. *Int. J. Nanomedicine* 18, 369–383. doi:10.2147/IJN.S395026

Eilenberg, M., Enayati, M., Ehebruster, D., Grasl, C., Walter, I., Messner, B., et al. (2020). Long term evaluation of nanofibrous, bioabsorbable polycarbonate urethane grafts for small diameter vessel replacement in rodents. *Eur. J. Vasc. Endovasc. Surg.* 59, 643–652. doi:10.1016/j.ejvs.2019.11.004

Faturechi, R., Hashemi, A., Abolfathi, N., Solouk, A., and Seifalian, A. (2019a). Fabrications of small diameter compliance bypass conduit using electrospinning of clinical grade polyurethane. *Vascular* 27, 636–647. doi:10.1177/1708538119850994

Faturechi, R., Hashemi, A., Abolfathi, N., Solouk, A., and Seifalian, A. (2019b). Fabrications of small diameter compliance bypass conduit using electrospinning of clinical grade polyurethane. *Vascular* 27, 636–647. doi:10.1177/1708538119850994

Feng, L., Feng, L., Shi, J., Guo, J., and Wang, S. (2022). Recent strategies for improving hemocompatibility and endothelialization of cardiovascular devices and inhibition of intimal hyperplasia. *J. Mater Chem. B* 10, 3781–3792. doi:10.1039/D2TB00478J

Furdella, K. J., Higuchi, S., Behrangzade, A., Kim, K., Wagner, W. R., and Vande, G. J. (2021). *In-vivo* assessment of a tissue engineered vascular graft computationally optimized for target vessel compliance. *Acta Biomater.* 123, 298–311. doi:10.1016/j.actbio.2020.12.058

Halbert, R. J., Nicholson, G., Nordyke, R. J., Pilgrim, A., and Niklason, L. (2020). Patency of eptfe arteriovenous graft placements in hemodialysis patients: systematic literature review and meta-analysis. *Kidney360* 1, 1437–1446. doi:10.34067/KID.0003502020

Huang, C., Wang, S., Qiu, L., Ke, Q., Zhai, W., and Mo, X. (2013). Heparin loading and pre-endothelialization in enhancing the patency rate of electrospun small-diameter vascular grafts in a canine model. *Acs Appl. Mater Interfaces* 5, 2220–2226. doi:10.1021/am400099p

Iacovacci, V., Naselli, I., Salgarella, A. R., Clemente, F., Ricotti, L., and Cipriani, C. (2021). Stability and *in vivo* safety of gold, titanium nitride and parylene c coatings on ndfeb magnets implanted in muscles towards a new generation of myokinetic prosthetic limbs. *Rsc Adv.* 11, 6766–6775. doi:10.1039/D0RA07989H

Iliou, K., Kikionis, S., Ioannou, E., and Roussis, V. (2022). Marine biopolymers as bioactive functional ingredients of electrospun nanofibrous scaffolds for biomedical applications. *Mar. Drugs* 20, 314. doi:10.3390/md20050314

Isozaki, T., Murakami, K., Yamanouchi, E., Uesato, M., Toyozumi, T., Koide, Y., et al. (2020). Magnetic compression anastomosis is effective in treating stenosis after esophageal cancer surgery: a case report. *Surg. Case Rep.* 6, 213. doi:10.1186/s40792-020-00974-y

Jang, S. I., Kim, J. H., Won, J. Y., Lee, K. H., Kim, H. W., You, J. W., et al. (2011). Magnetic compression anastomosis is useful in biliary anastomotic strictures after living donor liver transplantation. *Gastrointest. Endosc.* 74, 1040–1048. doi:10.1016/j.gie.2011.06.026

Jeong, Y., Yao, Y., and Yim, E. (2020). Current understanding of intimal hyperplasia and effect of compliance in synthetic small diameter vascular grafts. *Biomater. Sci.* 8, 4383–4395. doi:10.1039/d0bm00226g

Johnson, R., Ding, Y., Nagiah, N., Monnet, E., and Tan, W. (2019). Coaxially-structured fibres with tailored material properties for vascular graft implant. *Mater Sci. Eng. C Mater Biol. Appl.* 97, 1–11. doi:10.1016/j.msec.2018.11.036

Konig, G., McAllister, T. N., Dusserre, N., Garrido, S. A., Iyican, C., Marini, A., et al. (2009). Mechanical properties of completely autologous human tissue engineered blood vessels compared to human saphenous vein and mammary artery. *Biomaterials* 30, 1542–1550. doi:10.1016/j.biomaterials.2008.11.011

Kuang, H., Wang, Y., Hu, J., Wang, C., Lu, S., and Mo, X. (2018). A method for preparation of an internal layer of artificial vascular graft co-modified with salvianolic acid b and heparin. *Acs Appl. Mater Interfaces* 10, 19365–19372. doi:10.1021/acsami.8b02602

Kubo, M., Wada, H., Eguchi, H., Gotoh, K., Iwagami, Y., Yamada, D., et al. (2018). Magnetic compression anastomosis for the complete dehiscence of hepaticojejunostomy in a patient after living-donor liver transplantation. *Surg. Case Rep.* 4, 95. doi:10.1186/s40792-018-0504-6

Laktionov, P. P., Lebedeva, A. O., Korobeinikov, M. V., Yunoshev, A. S., Karpenko, A. A., Popova, I. V., et al. (2014). Electrospun produced small diameter vascular grafts: modification of physical properties and assessment of biocompatibility. *Eur. J. Vasc. Endovasc. Surg.* 47, 692. doi:10.1016/j.ejvs.2014.03.025

Leal, B. B. J., Wakabayashi, N., Oyama, K., Kamiya, H., Braghirolli, D. I., and Pranke, P. (2021). Vascular tissue engineering: polymers and methodologies for small caliber vascular grafts. *Front. Cardiovasc Med.* 7, 592361. doi:10.3389/fcvm.2020.592361

Li, J., Lü, Y., Qu, B., Zhang, Z., Liu, C., Shi, Y., et al. (2008a). Application of a new type of sutureless magnetic biliary-enteric anastomosis stent for one-stage reconstruction of the biliary-enteric continuity after acute bile duct injury: an experimental study. *J. Surg. Res.* 148, 136–142. doi:10.1016/j.jss.2007.09.014

Li, L., Terry, C. M., Shiu, Y. T., and Cheung, A. K. (2008b). Neointimal hyperplasia associated with synthetic hemodialysis grafts. *Kidney Int.* 74, 1247–1261. doi:10.1038/ki.2008.318

Liu, P., Yang, L., Shi, A., Qian, Y., Liu, X., Dong, D., et al. (2022). Regional anticoagulation magnetic artificial blood vessels constructed by heparin-plcl core-shell nanofibers for rapid deployment of veno-venous bypass. *Biomater. Sci.* 10, 3559–3568. doi:10.1039/d2bm00205a

Liu, Z., Ramakrishna, S., and Liu, X. (2020). Electrospinning and emerging healthcare and medicine possibilities. *Apl. Bioeng.* 4, 030901. doi:10.1063/5.0012309

Lu, Q., Liu, K., Zhang, W., Li, T., Shi, A. H., Ding, H. F., et al. (2020). End-to-end vascular anastomosis using a novel magnetic compression device in rabbits: a preliminary study. *Sci. Rep.* 10, 5981. doi:10.1038/s41598-020-62936-6

Marycz, K., Kornicka, K., and Röcken, M. (2018). Static magnetic field (smf) as a regulator of stem cell fate – new perspectives in regenerative medicine arising from an underestimated tool. *Stem Cell Rev. Rep.* 14, 785–792. doi:10.1007/s12015-018-9847-4

Nagiah, N., El, K. R., Othman, M. H., Akimoto, J., Ito, Y., Roberson, D. A., et al. (2022). Development and characterization of furfuryl-gelatin electrospun scaffolds for cardiac tissue engineering. *Acs Omega* 7, 13894–13905. doi:10.1021/acsomega.2c00271

Popa, L., Ghica, M. V., Tudoroiu, E. E., Ionescu, D. G., and Dinu-Pirvu, C. E. (2022). Bacterial cellulose-a remarkable polymer as a source for biomaterials tailoring. *Mater. (Basel)* 15, 1054. doi:10.3390/ma15031054

Rahmati, N. M., Yousefzadeh, M., and Solouk, A. (2020). Electrospun pet/pcl small diameter nanofibrous conduit for biomedical application. *Mater Sci. Eng. C Mater Biol. Appl.* 110, 110692. doi:10.1016/j.msec.2020.110692

Ratner, B. (2023). Vascular grafts: technology success/technology failure. *Bme Front.* 4, 0003. doi:10.34133/bmef.0003

Seifu, D. G., Purnama, A., Mequanint, K., and Mantovani, D. (2013). Small-diameter vascular tissue engineering. *Nat. Rev. Cardiol.* 10, 410–421. doi:10.1038/nrcardio.2013.77

Strobel, H. A., Qendro, E. I., Alsberg, E., and Rolle, M. W. (2018). Targeted delivery of bioactive molecules for vascular intervention and tissue engineering. *Front. Pharmacol.* 9, 1329. doi:10.3389/fphar.2018.01329

Tamimi, E. A., Ardila, D. C., Ensley, B. D., Kellar, R. S., and Vande, G. J. (2019). Computationally optimizing the compliance of multilayered biomimetic tissue engineered vascular grafts. *J. Biomech. Eng.* 141. doi:10.1115/1.4042902

Wang, H. H., Ma, J., Wang, S. P., Ma, F., Lu, J. W., Xu, X. H., et al. (2019). Magnetic anastomosis rings to create portacaval shunt in a canine model of portal hypertension. *J. Gastrointest. Surg.* 23, 2184–2192. doi:10.1007/s11605-018-3888-5

Wang, S., Mo, X. M., Jiang, B. J., Gao, C. J., Wang, H. S., Zhuang, Y. G., et al. (2013). Fabrication of small-diameter vascular scaffolds by heparin-bonded p(lla-cl) composite nanofibers to improve graft patency. *Int. J. Nanomedicine* 8, 2131–2139. doi:10.2147/IJN.S44956

Xu, X. H., Lv, Y., Liu, S. Q., Cui, X. H., and Suo, R. Y. (2022). Esophageal magnetic compression anastomosis in dogs. *World J. Gastroenterol.* 28, 5313–5323. doi:10.3748/wjg.v28.i36.5313

Yang, L., Lu, J., Wang, Y., Zhang, M., Shi, Y., Wei, S., et al. (2018). A rat model of orthotopic liver transplantation using a novel magnetic anastomosis technique for suprahepatic vena cava reconstruction. *J. Vis. Exp.*, 56933. doi:10.3791/56933

Yin, A., Luo, R., Li, J., Mo, X., Wang, Y., and Zhang, X. (2017). Coaxial electrospinning multicomponent functional controlled-release vascular graft: optimization of graft properties. *Colloids Surf. B Biointerfaces* 152, 432–439. doi:10.1016/j.colsurfb.2017.01.045

Zhang, M., Ma, J., Gai, J., Zhang, Z., Wang, H., Zhang, Y., et al. (2023a). Magnetic anchor technique assisted laparoscopic cholecystectomy in swine. *Sci. Rep.* 13, 4864. doi:10.1038/s41598-023-32157-8

Zhang, M. M., Li, C. G., Xu, S. Q., Mao, J. Q., Zhang, Y. H., Shi, A. H., et al. (2023b). Magnetic compression anastomosis for reconstruction of digestive tract after total gastrectomy in beagle model. *World J. Gastrointest. Surg.* 15, 1294–1303. doi:10.4240/wjgs.v15.i7.1294

frontiers | Frontiers in Bioengineering and Biotechnology

TYPE Review
PUBLISHED 14 February 2024
DOI 10.3389/fbioe.2024.1358246



OPEN ACCESS

EDITED BY
Wenliang Wang,
The University of Texas at Austin, United States

REVIEWED BY
Seungil Kim,
University of Pittsburgh, United States
Dana Akilbekova,
Nazarbayev University, Kazakhstan

*CORRESPONDENCE
Lili Cao,
caoll215@163.com

RECEIVED 19 December 2023
ACCEPTED 31 January 2024
PUBLISHED 14 February 2024

CITATION
Cao L, Zhang Z, Yuan D, Yu M and Min J (2024), Tissue engineering applications of recombinant human collagen: a review of recent progress. *Front. Bioeng. Biotechnol.* 12:1358246. doi: 10.3389/fbioe.2024.1358246



# Tissue engineering applications of recombinant human collagen: a review of recent progress

Lili Cao[1]*, Zhongfeng Zhang[1], Dan Yuan[1], Meiping Yu[1] and Jie Min[2]

[1]Department of Plastic Surgery, Zhejiang Rongjun Hospital, Jiaxing, Zhejiang, China, [2]General Surgery Department, Jiaxing No.1 Hospital, Jiaxing, Zhejiang, China

With the rapid development of synthetic biology, recombinant human collagen has emerged as a cutting-edge biological material globally. Its innovative applications in the fields of material science and medicine have opened new horizons in biomedical research. Recombinant human collagen stands out as a highly promising biomaterial, playing a pivotal role in crucial areas such as wound healing, stroma regeneration, and orthopedics. However, realizing its full potential by efficiently delivering it for optimal therapeutic outcomes remains a formidable challenge. This review provides a comprehensive overview of the applications of recombinant human collagen in biomedical systems, focusing on resolving this crucial issue. Additionally, it encompasses the exploration of 3D printing technologies incorporating recombinant collagen to address some urgent clinical challenges in regenerative repair in the future. The primary aim of this review also is to spotlight the advancements in the realm of biomaterials utilizing recombinant collagen, with the intention of fostering additional innovation and making significant contributions to the enhancement of regenerative biomaterials, therapeutic methodologies, and overall patient outcomes.

KEYWORDS

**tissue engineering, regenerative, biomaterials, recombinant human collagen, biomedicine**

## 1 Introduction

Collagen, the most abundant protein in the extracellular matrix of animal cells, plays a pivotal role in providing structural support and regulating cellular behavior (Avila Rodríguez et al., 2018; Coppola et al., 2020). To date, 29 types of collagens have been identified, with types I, II, and III constituting over 90% of the total collagen in the human body (Meyer, 2019; Naomi et al., 2021). Collagen provides tensile strength and is the primary component of skin, bones, cartilage, and connective tissues (Law et al., 2017; Jafari et al., 2020). Due to its biocompatibility, biodegradability, and low immunogenicity, collagen has been extensively investigated and employed as a biomaterial in the field of tissue engineering and regenerative medicine (Irawan et al., 2018; Copes et al., 2019; Lin et al., 2019).

However, the majority of collagen used for biomedical applications is still derived from animal sources, such as the skin, tendons, and bones of bovines, pigs, and avian species (Avila Rodríguez et al., 2018; Felician et al., 2018). Animal-sourced collagen has inherent drawbacks. It exhibits batch-to-batch variability in quantity and quality, can potentially

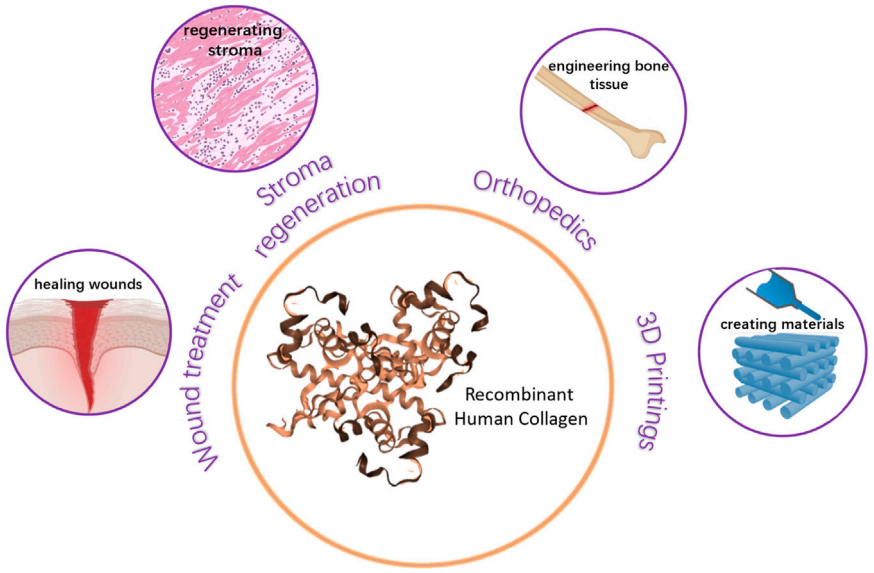


GRAPHICAL ABSTRACT
Recombinant human collagen applications in biomedical systems.

trigger immunogenic responses, and carries the risk of transmitting animal viruses and prions (Gauza-Włodarczyk et al., 2017a; Coppola et al., 2020). Despite the success of animal-derived collagen products like Zyderm, the pursuit of recombinant collagen aims to refine the safety and efficacy of collagen-based treatment (Shekhter et al., 2019). Produced through intricate *in vitro* techniques, recombinant collagens are designed to emulate the post-translational modifications seen in natural collagens, such as hydroxylation and glycosylation, thereby achieving a high degree of similarity to human collagen (Kim et al., 2017). Recombinant human collagen produced via biotechnological methods can overcome these limitations associated with xenogeneic or allogeneic collagen (Wang et al., 2022). Over the past few decades, research on recombinant collagen has made significant strides in genetic recombination, protein expression, and material preparation (Ma et al., 2022). This article provides a comprehensive review of the latest advancements in recombinant human collagen and its applications as biomaterials in tissue engineering and regenerative medicine.

Collagen possesses a characteristic triple-helical structure, composed of three polypeptide chains known as α-chains (Mi et al., 2018; Rappu et al., 2019). *In vitro* studies have recombinantly produced different types of collagens from isolated genes, including types I, II, III, and V collagen (Woodley et al., 2017; Doan et al., 2019; Shuai et al., 2023). Compared to natural collagen, recombinantly produced collagen achieves proper post-translational modifications, including hydroxylation and glycosylation (Shekhter et al., 2019; Deng et al., 2021). Based on the composition of α-chains, recombinant collagen can be categorized into homotrimeric (I, II, III), heterotrimeric (XI), and hybrid forms (IX) (Ferraro et al., 2017; Chen et al., 2020). Type I collagen is the most abundant type in many tissues, while type III collagen is relatively less abundant but plays a crucial role in maintaining tissue integrity and regulating scar formation (Kuivaniemi and Tromp, 2019; Di Martino et al., 2022; Harris et al., 2022). Extensive research has also been focused on type III collagen due to its therapeutic potential in promoting wound healing and tissue regeneration (Zhang Wei et al., 2018a; Xia et al., 2018; Davison-Kotler et al., 2019).

To produce recombinant collagen, expression systems including mammalian, insect, yeast, and bacterial cells have been explored (Capella-Monsonís et al., 2018; Davison-Kotler et al., 2019). Mammalian cells like CHO and HEK293 have translation mechanisms most similar to human cells and can therefore produce collagen with correct modifications (Gauza-Włodarczyk et al., 2017b; Lim et al., 2019). However, their relatively low yield and high cost hinder industrial-scale production (Felician et al., 2018; Song et al., 2018; Meng et al., 2019). Bacterial and yeast expression systems are more cost-effective but do not achieve proper post-translational processing (Amyoony et al., 2023). Therefore, strategies have been developed to enhance the quality of recombinantly produced collagen by genetically modifying host cells or supplementing post-translational enzymes. Recent research has made significant strides in optimizing expression systems and purifying large quantities of structurally native collagen (Knüppel et al., 2017; Rittié, 2017).

Following purification, recombinant collagen is fabricated into various biomaterials for biomedical applications (Zhang et al., 2019; Ghomi et al., 2021). Collagen hydrogels prepared by differential mechanisms have been extensively studied as scaffolds and drug delivery carriers (Li et al., 2020). By adjusting the hydrogel density, degree of cross-linking, and the incorporation of other biomolecules, its degradation, mechanical strength, and biological activity can be customized. The inclusion of growth factors and cells further enhances the regenerative potential of collagen hydrogels (Arakawa et al., 2017; Sarrigiannidis et al., 2021). Lyophilized collagen materials processed through freeze-drying present another format as wound dressings (Magro et al., 2017). Scaffold formats of collagen have been expanded further by various techniques including 3D printing, electrospinning, and particle sintering (Rashedi et al., 2017; Zhang et al., 2018b; Abbas et al.,

TABLE 1 Tissue engineering applications of recombinant human collagen.

| Applications | Advantages | Challenges | Reference |
|---|---|---|---|
| Wound treatment | 1. Promotes accelerated wound healing | 1. Potential for immune response | Han and Roger, (2017); Koehler et al. (2018); Sun et al. (2018); Las Heras et al. (2020); Mathew-Steiner et al. (2021) Thapa et al. (2020) Muhonen et al. (2017); Kathawala et al. (2019); Su et al. (2021); Xu et al. (2022) |
| | 2. Provides excellent biocompatibility and cell adhesion | 2. Cost of production and purification can be high | |
| | 3. Can be fabricated into various forms (e.g., dressings, hydrogels) | | |
| Stroma regeneration | 1. Supports cell proliferation and differentiation | 1. Possible immunogenicity | Addi et al. (2017); Parmar et al. (2017); Quinlan et al. (2017); Sheehy et al. (2018); McPhail et al. (2020); Yang et al. (2021a); Yang et al. (2021b); Kong et al. (2022) Haagdorens et al. (2019); Wang, (2021) Jeon et al. (2017); He et al. (2018); Huang et al. (2018) |
| | 2. Can be used to construct diverse tissue scaffolds | 2. Control over mechanical properties can be challenging | |
| | 3. Promotes skin regeneration | | |
| Orthopedics | 1. Can be used for bone tissue engineering | 1. Mechanical strength may be less than some synthetic materials | Chan et al. (2017); Ramírez-Rodríguez et al. (2017); Andrews et al. (2019); Bien et al. (2020); Fushimi et al. (2020) |
| | 2. Offers good biocompatibility and bioresorbability | 2. Potential for immune response | |
| | 3. Can potentially stimulate bone growth | | |
| 3D printing | 1. Enables the creation of complex and patient-specific structures | 1. Requires specialized 3D printing technology | Włodarczyk-Biegun and Del Campo, (2017); Hong et al. (2018); Lee et al. (2019); Osidak et al. (2020); Tytgat et al. (2020); Muthusamy et al. (2021) Gungor-Ozkerim et al, (2018); Isaacson et al. (2018); Gudapati et al. (2020); Cui et al. (2017); Zhang et al. (2017); Curtin et al. (2018); Nocera et al. (2018); Matai et al. (2020); Dai et al. (2021); Elalouf, (2021); Tang et al. (2021) |
| | 2. Can be combined with other materials for enhanced properties | 2. Control over mechanical properties and print resolution can be challenging | |
| | 3. Potential for creating personalized implants | | |

2020). Functionalizing recombinant collagen biomaterials with nanoparticles, peptides, and stem cells has emerged as a promising strategy for precisely guiding tissue regeneration.

In tissue engineering applications, recombinant collagen biomaterials have been widely studied for skin regeneration due to the natural abundance of collagen in the dermis (Koons et al., 2020). Collagen hydrogels promote wound healing by stimulating cell proliferation, migration, angiogenesis, and collagen deposition (Nguyen et al., 2019; Roshanbinfar et al., 2023). When used as covers for skin grafts or wound dressings, they accelerate re-epithelialization. For load-bearing tissues, collagen scaffolds combined with stem cells hold potential in bone and cartilage regeneration. Upon implantation of collagen/stem cell constructs, substantial new bone and cartilage formation was observed in animal models (Wang et al., 2020). In vascular engineering, cell-seeded collagen tubular scaffolds have demonstrated the ability to remodel into vascular grafts (Copes et al., 2019; Minor and Kareen, 2020). New evidence has also validated the feasibility of using collagen implants to repair damaged myocardium and cornea. Looking forward, the development of optimized recombinant collagen production, functional biomaterial design, and translational research will further expand its regenerative applications (Carrabba and Madeddu, 2018; Minor and Kareen, 2020). The future of recombinant human collagen lies in overcoming the limitations of animal-sourced collagen and propelling the development in the fields of tissue engineering and regenerative medicine. Establishing stable high-yield expression systems and purification processes for industrial-scale production remains a major challenge.

This review summarizes the research on recombinant human collagen's applications in biomedical systems, including its effects in wound treatment, stroma regeneration, and orthopedics. We explore studies on recombinant collagen-based hydrogels, scaffolds, microspheres, and dressings for healing wounds, regenerating skin, and engineering bone tissue. The review also encapsulates research on 3D printings containing recombinant collagen (Table 1). Our goal is to shed light on the advancements and inspire further innovations in recombinant collagen's biomaterial and clinical uses, with the hope that ongoing development will improve biomaterials, therapies, and patient outcomes.

## 2 Hydrogel delivery of recombinant collagen for chronic wounds healing

Chronic wounds, including diabetic foot ulcers, are characterized by impaired healing and persistent inflammation (Mathew-Steiner et al., 2021). The wounds become trapped in a prolonged inflammatory stage and are unable to progress through the normal phases of healing (Las Heras et al., 2020). This results in significantly delayed closure compared to acute wounds. Chronic wounds also frequently become colonized with bacteria, leading to infection. The sustained inflammatory environment causes continuous tissue breakdown and inhibits cell proliferation and angiogenesis (Han and Roger, 2017).

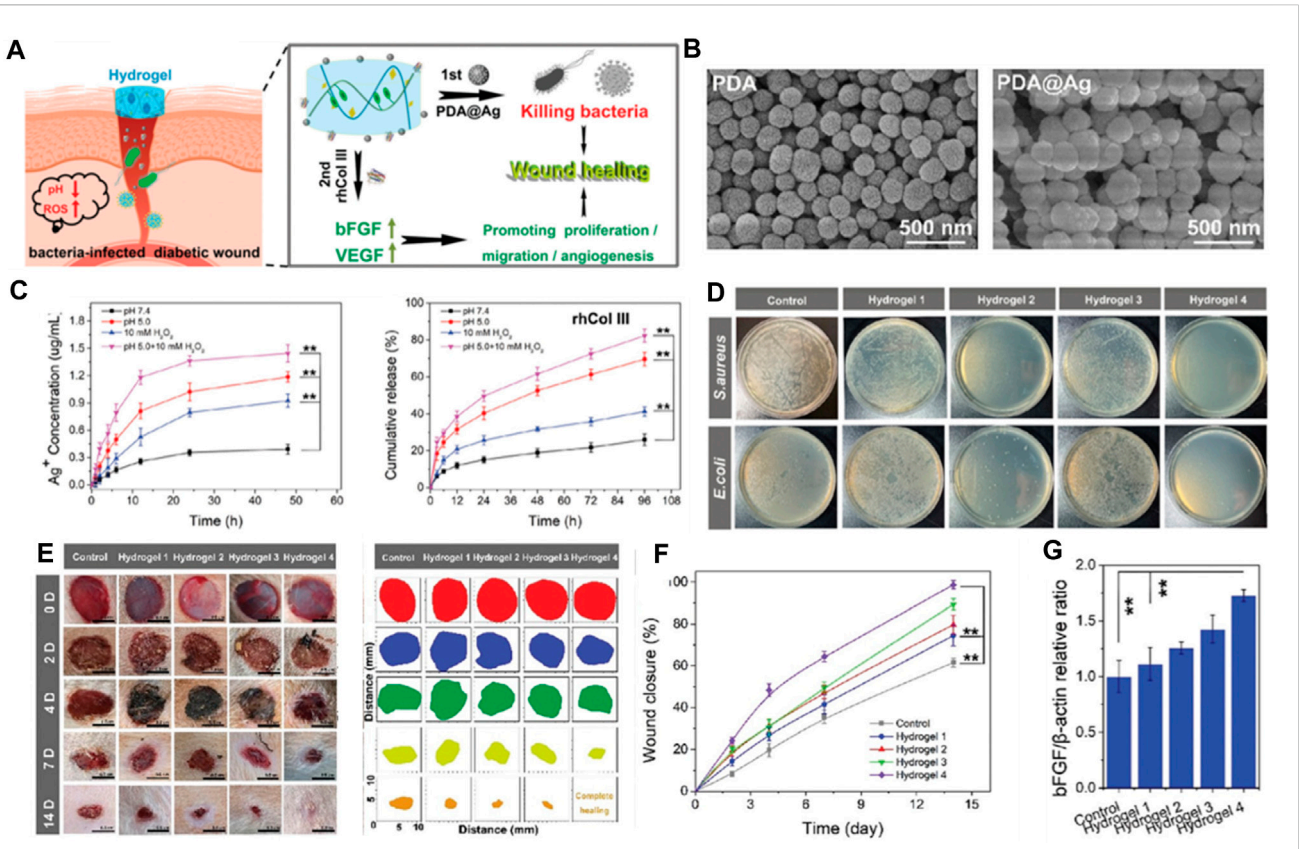


FIGURE 1
**(A)** The microenvironment-responsive hydrogel and its therapeutic mechanism contributing to the promotion of chronic wound healing. **(B)** The SEM images of for PDA and PDA@Ag NPs. **(C)** The release profiles of payloads from hydrogel. **(D)** Representative images of *S. aureus* and *E. coli* following a 12-h treatment with various hydrogel formulations. **(E)** Illustrative examples of the progression of wound closure on days 0, 2, 4, 7, and 14 (right) after being subjected to different treatments at predetermined time points (left, $n = 8$). **(F)** Over the course of 14 days, the rate of wound contraction was also tracked and quantified. **(G)** The proportional protein expression ratio of bFGF to b-actin. Note the following hydrogel types: (1) Hydrogel 1: Control hydrogel. (2) Hydrogel 2: Hydrogel encapsulating PDA@Ag nanoparticles. (3) Hydrogel 3: Hydrogel encapsulating rhCol III. (4) Hydrogel 4: Hydrogel encapsulating both PDA@Ag and rhCol III. Reproduced with permission from ref Hu et al. (2021).

Recombinant collagen scaffolds offer several advantages for chronic wound treatment (Sun et al., 2018). As the major structural component of the extracellular matrix, collagen provides an ideal environment to facilitate cell migration and enable wound closure (Koehler et al., 2018; Sun et al., 2018). Recombinant collagen allows precise control over scaffold properties like porosity and bioactivity (Catanzano et al., 2021). Despite these benefits, challenges remain in optimizing delivery of recombinant collagen to improve healing. Fast degradation rates make it difficult to achieve sustained collagen presence within dynamic wound environments. Enhancing collagen scaffold stability through chemical or physical crosslinking may help prolong bioactivity but can also negatively impact integration with native tissue (Thapa et al., 2020). Therefore, effective chronic wound therapies will likely require recombinant collagen delivery platforms that balance scaffold remodeling with regeneration of functional tissue (Ahmad et al., 2021). Further research is needed to translate the promise of recombinant collagen into effective wound treatments that overcome the barriers to healing in chronic wounds.

RhCol III, the primary collagen type in early granulation tissue, shows potential for accelerating wound closure. Hydrogels composed of rhCoI lII have been developed. These hydrogels feature porous microstructure, near-physiological swelling ratios, and significant cell adhesion. *In vivo* testing in diabetic mice demonstrated expedited wound closure with rhCol III treatment compared to controls. The hydrogels provide a moist environment conducive to healing and act as an *in situ* forming scaffold for cell migration.

In a study, Wang et al. developed a specialized recombinant human type III collagen (rhCol III) and constructed a multifunctional, microenvironment-responsive hydrogel system integrating this custom rhCol III and multifunctional antimicrobial nanoparticles (PDA@Ag NPs) (Hu et al., 2021). This advanced hydrogel showcases accelerated degradation in the setting of chronic diabetic wounds, orchestrating the regulated and demand-driven release of various therapeutic agents. Initially, the hydrogel releases PDA@Ag NPs which possess potent antimicrobial activity against *Staphylococcus aureus* and *Escherichia coli*, thereby facilitating rapid bacterial eradication. Concurrently, these nanoparticles exhibit antioxidant and anti-inflammatory properties within the wound environment. Subsequently, the release of rhCol III stimulates the proliferation and migration of murine fibroblasts and endothelial cells during the proliferative and

10.3389/fbioe.2024.1358246

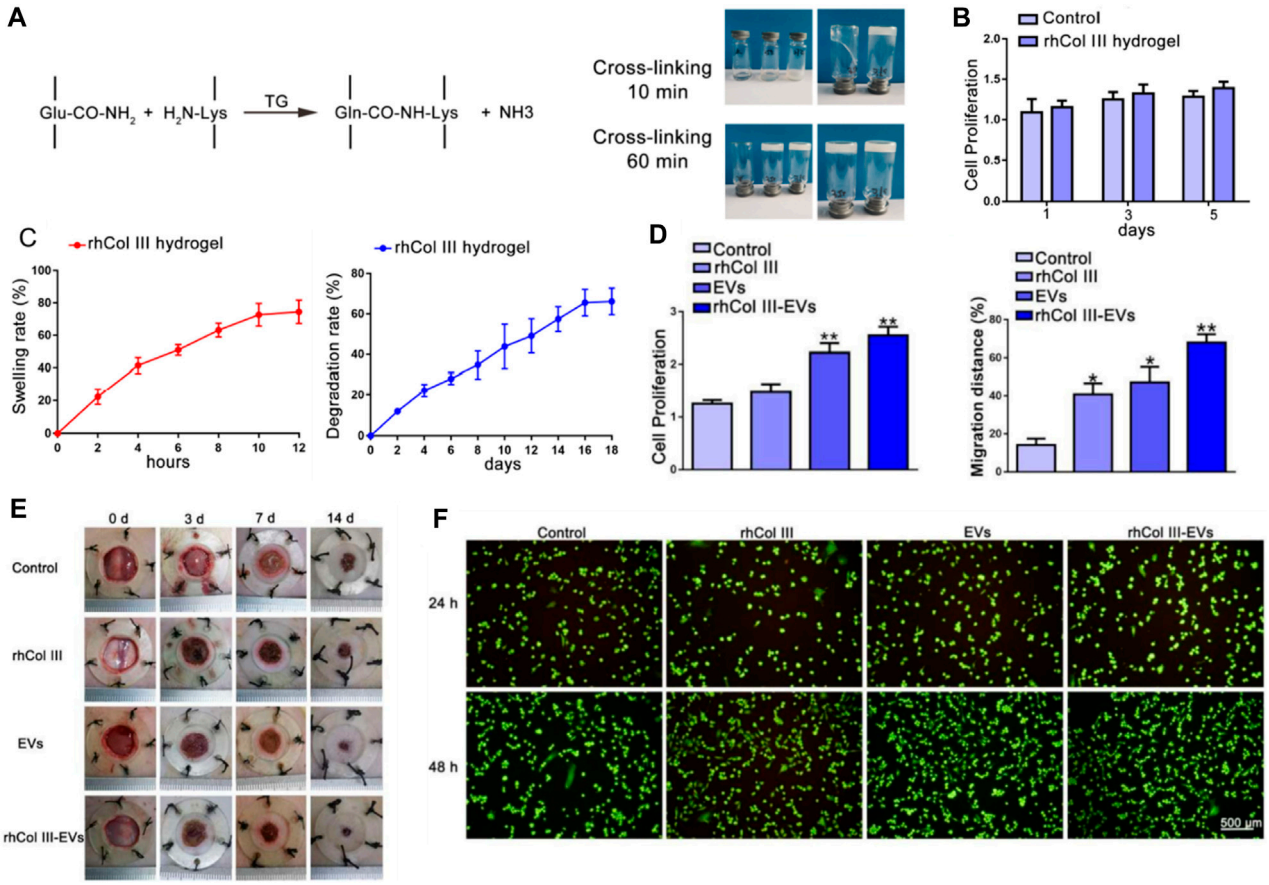


FIGURE 2
**(A)** Illustrative representation of the procedure for preparing the recombinant human collagen III (rhCol III) hydrogel. **(B)** Impact of the rhCol III hydrogel extract on cellular proliferation. **(C)** Swelling ratio observed in the rhCol III hydrogel and the rate of degradation identified in the rhCol III hydrogel. **(D)** Proliferations and migration distance of L292 cells in rhCol III hydrogel. **(E)** images of wounds from each group, taken at baseline (0 days) and subsequent timepoints (3, 7, and 14 days). **(F)** Comparison of angiogenesis in human umbilical vein endothelial cells (HUVECs) in various groups. Reproduced with permission from ref Xu et al. (2022).

remodeling phases of wound healing. Upon exposure to a diabetic wound site with bacterial infection, the hydrogel encounters an environment rich in reactive oxygen species and characterized by low pH, indicative of inflammation. This specific environment triggers a rapid dissolution of the boronic ester bonds within the hydrogel structure, causing it to collapse and enabling the staged release of PDA@Ag NPs and rhCol III.

As a result, the hydrogel framework collapses, facilitating the staged discharge of PDA@Ag NPs and rhCol III (Figure 1A). The Scanning Electron Microscopy (SEM) findings depicted in Figure 1B illustrate the spherical form of both PDA and PDA@Ag NPs. The payloads encapsulated within the hydrogel demonstrate a pH-sensitive release dynamic, where the rate of release notably escalates under the more acidic conditions of pH 5 (Figure 1C). The agar plate counting experiment demonstrated that the hydrogel@Ag&rhCol III group exhibited the most substantial antibacterial efficiency, as indicated by the fewest bacterial colonies (Figure 1D). The efficacy of the hydrogel in facilitating chronic wound healing was evaluated using a rat wound model infected with *E. coli*. Among all groups, the hydrogel@Ag&rhCol III group exhibited the most rapid wound healing, achieving a 64% wound healing rate by day 7 (Figures 1E, F). As presented in Figure 1G, the hydrogel@Ag&rhCol III group exhibited notably elevated levels of bFGF expression compared to other groups. This observation implies that the hydrogel@Ag&rhCol III has the potential to amplify the expression of bFGF, thereby fostering enhanced cell proliferation and angiogenesis.

To summarize, the hydrogel responsive to microenvironmental changes has shown exceptional capabilities in combating bacteria and promoting cell growth and movement, successfully speeding up the healing process of chronic diabetic wounds in both laboratory and real-world scenarios. This research confirms the significant potential of newly designed rhCol III for use in mending and regenerating long-term wounds. As the authers look ahead, they foresee the creation and implementation of further bespoke products based on recombinant human collagen, contributing to advancements in human health and wellbeing.

Wang et al. centers on a pivotal study that delves into the application of recombinant human collagen III protein hydrogels and extracellular vesicles (EVs) in skin wound healing (Figure 2A) (Xu et al., 2022). The research team conducted a series of experiments to assess the efficacy of these hydrogels and EVs in promoting wound healing. The findings suggest that the hydrogels capably released the EVs, thereby stimulating cell proliferation,

migration, and angiogenesis (Figures 2B–D). Initially, the study underscores the crucial role of skin as a protective barrier for the human body and tackles the challenges associated with the wound healing process, such as diabetes, vascular insufficiency, and local pressure alterations. The authors elucidate that collagen III, a vital component of the extracellular matrix, plays a significant role in wound healing (Figures 2E, F). They delineate the preparation process of recombinant human collagen III protein hydrogels and discuss the role of EVs in sustained therapeutic agent release for wound healing promotion.

The researchers conducted several experiments to determine the efficacy of these hydrogels and EVs in wound healing. The hydrogels successfully released the EVs, enhancing cell proliferation, migration, and angiogenesis. They also suppressed the inflammatory response and promoted wound healing in a diabetic rat skin injury model. The study concludes that these hydrogels and EVs hold significant potential in skin wound healing, presenting a novel approach for chronic wound treatment. In summary, the authors offer an intricate discourse on the employment of hydrogels as a delivery system for recombinant collagen, and the utilization of EVs for sustained therapeutic agent release. They effectively illustrate that the hydrogels proficiently discharge the EVs, thereby facilitating wound healing in a diabetic rat skin injury model. This insight contributes a novel and promising stratagem to the therapeutic repertoire for chronic wound management.

Presently, hydrogels stand as an encouraging scaffold material for tissue engineering and regenerative strategies, largely due to their high-water content, tissue-like mechanical properties, and adjustable physical features (Kathawala et al., 2019; Su et al., 2021). Collagen-based hydrogels, in particular, are appealing for their ability to mimic the extracellular matrix of connective tissues. Recombinant collagen boasts several advantages over tissue-extracted collagen, such as enhanced standardization and tunability, and it circumvents issues of immunogenicity or pathogen transmission (Muhonen et al., 2017). Nevertheless, striking the right balance between factors like swelling, degradation, pore size, and mechanics remains a challenge in optimizing hydrogel design and collagen incorporation. Moreover, the production of most recombinant collagen relies on mammalian cell culture systems, adding a considerable cost (Chen et al., 2020). There is a call for further research to boost recombinant collagen yields and devise efficient purification strategies to curtail expenses (Chen et al., 2022). In summary, while recombinant collagen-loaded hydrogels offer a promising path in tissue repair, further optimization and cost-cutting measures are essential to usher these technologies from the laboratory to clinical practice. Future research should focus on scalable recombinant collagen production, the incorporation of cell instructive signals, and *in vivo* assessment of performance and host response.

## 3 The broad application potential of recombinant collagen in corneal stroma regeneration

Recombinant collagen has emerged as a promising biomaterial for various regenerative medicine applications owing to its versatility, biocompatibility, and improved safety compared to animal-derived collagens (Strauss and Chmielewski, 2017). As the most abundant protein in the human body and a major component of connective tissue, collagen plays a critical role in supporting cell growth, adhesion, and organization during tissue regeneration (Sheehy et al., 2018). Recombinant collagen can be biosynthesized using genetic engineering approaches, allowing precise control over collagen type, structure, degradation kinetics, and functionalization with biological signals (Felician et al., 2018). This advanced engineering of molecular and material properties makes recombinant collagen highly adaptable for developing scaffolds, hydrogel, coatings, and delivery systems tailored to promote regeneration across diverse tissues including skin, bone, cartilage, vasculature, and others (Addi et al., 2017; Quinlan et al., 2017; Yang et al., 2021a). The modular and customizable nature of recombinant collagen, along with its inherent bioactivity and biodegradability, enables the design of therapeutic platforms that synergize with endogenous regenerative processes (McPhail et al., 2020). Further research and clinical translation of recombinant collagen-based therapies holds promise for enabling more effective and safer regenerative medicine solutions. In 2021, Sun et al. developed recombinant human collagen hydrogels with hierarchically ordered microstructures to regenerate corneal stroma (Kong et al., 2022). The RHC are modified with methacrylate anhydride (MA) to mimic native corneal properties. The collagen hydrogels have aligned microgrooves and inverse opal nanopores (MI-RHCMA). *In vitro* experiments show MI-RHCMA hydrogels guided organized growth and differentiation of limbal stromal stem cells into keratocytes compared to random collagen gels. *In vivo* rat studies demonstrated MI-RHCMA implants integrate with host tissue and regenerate damaged corneal stroma better than controls.

In their research, RHCMA was engineered by integrating MA onto the collagen macromolecular chain via a condensation reaction between amino and carboxyl groups, as depicted in Figure 3A. This method effectively maintained the inherent superior biocompatibility of collagen hydrogel. The distinctive structure of the MI-RHCMA hydrogel patch is clearly illustrated in Figure 3B. The cross-sectional view showcases the convexity and indentation of the microgrooves, which further reveal the existence of inverse opal pores within the microgroove. Figures 3C, D provide a graphical representation of the compressive strain-stress relationship, along with the maximum compressive stress experienced by the RHCMA hydrogel when submerged in PBS. When it comes to cell behavior, LSSCs displayed a tendency to form an organized and elongated structure on MI-RHCMA hydrogel patches, contrasting with their random distribution on unpatterned RHCMA hydrogel surfaces, as shown in Figure 3E. The surgical and post-surgical observations are depicted in Figure 3F. MI-RHCMA hydrogel patches were grafted onto the left eyes of rats, with the right eyes serving as controls. These assessments were performed immediately post-surgery and at 1, 2, and 4 weeks following the operation. Figure 3G presents the results of a histological analysis for measuring corneal stromal and epithelial thickness. Interestingly, no significant statistical variation was observed in the thickness of the corneal epithelium across the allograft, MI-RHCMA, RHCMA, and native corneas.

To summarize, researchers fabricated a novel recombinant human collagen hydrogel designed for corneal tissue restoration.

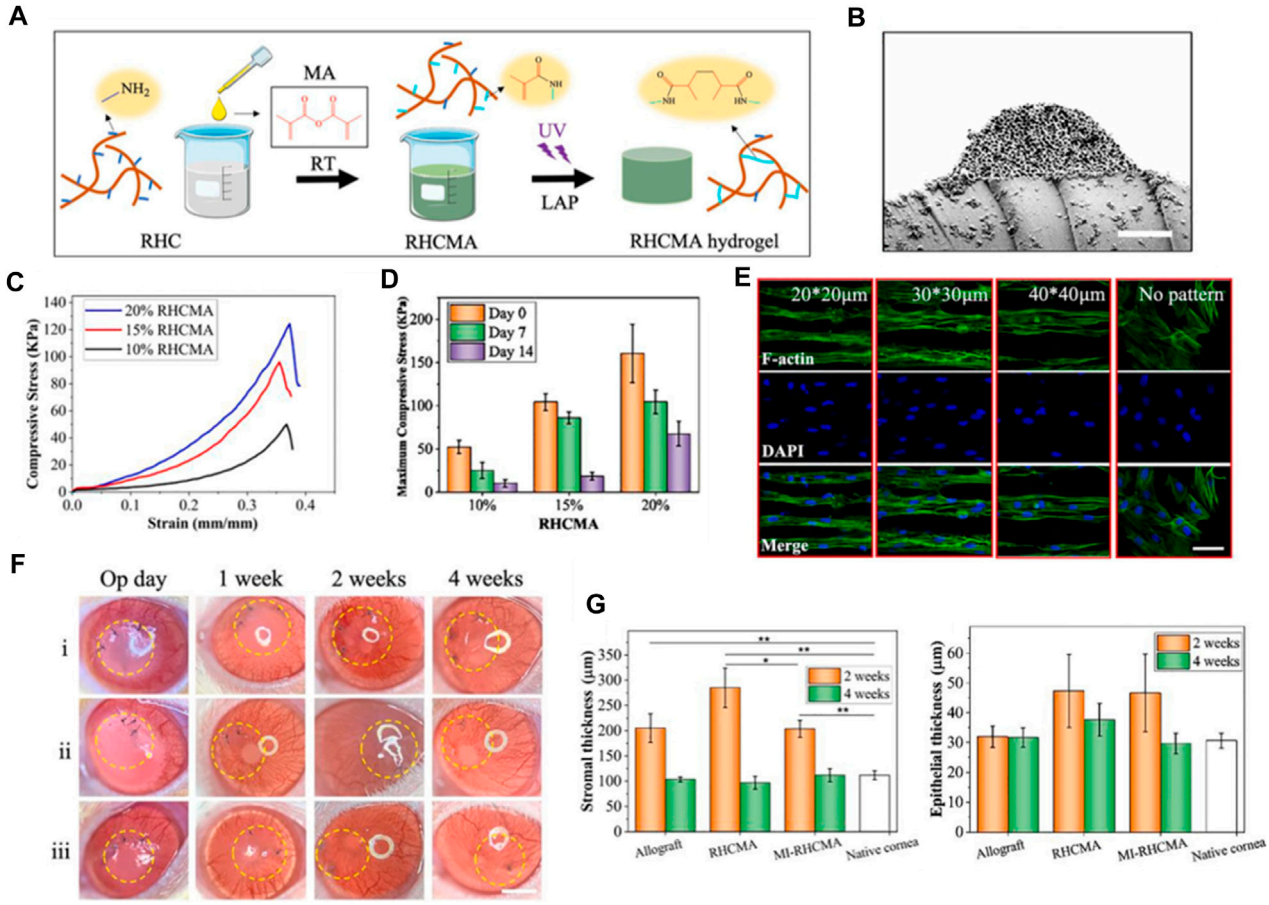


FIGURE 3
**(A)** Graphic representation of rhcma hydrogel synthesis process. **(B)** Cross-sectional SEM visuals of the mi-RHCMA hydrogel patch. Scale bar, 5 μm. **(C)** Compressive strain-stress relationships of various RHCMA hydrogels post 60-min PBS soak. **(D)** Histograms displaying the peak compressive stress for different RHCMA hydrogels following immersed in PBS. **(E)** Diagram exhibiting the cytoskeletal and nuclear staining in LSSCs hosted on constructs. Scale bar, 5 μm. **(F)** Representative photographs illustrating the post-surgical ocular conditions of corneas that treated with i) allograft, ii) RHCMA, and iii) MI-RHCMA hydrogel patches, captured immediately. Scale bar, 1.5 mm. **(G)** Measurements of the thickness of the stroma **(B)** and the epithelium **(C)** were taken at day 14 and day 28 post-operation for corneas that had undergone transplantation with allograft, RHCMA, and MI-RHCMA hydrogel patches. Reproduced with permission from ref Kong et al. (2022).

The final product was a hierarchically structured hydrogel, crafted through the amalgamation of RHCMA hydrogel, lithography, and photonic crystal techniques. This material, featuring inverse opal nanopores and aligned microgrooves, alongside ordered topological indications, promoted the aligned growth and differentiation of LSSCs into keratocytes *in vitro*. Moreover, RHCMA hydrogels with these organized microstructures were found to boost tissue repair processes and foster the regeneration of damaged stromal tissue *in vivo*. These attributes underscore their promising potential in the domains of tissue repair and stroma regeneration.

Recombinant human collagen (RHC) polypeptide holds a significant edge over natural collagen sources in the realm of tissue engineering applications (Yang et al., 2021b). This is particularly advantageous when compared to animal-derived collagens, as it considerably reduces the risk of immune rejection upon implantation (Parmar et al., 2017). One of the key advantages of RHC is its capacity for precise and customizable biosynthesis. This allows for the engineering of specific peptide sequences, integrin binding sites, growth factors, and cross-linking into the polypeptide chain (Haagdorens et al., 2019; Wang, 2021). Such level of control paves the way for tuning the properties of RHC to achieve optimal performance in specific applications. In addition, the production of RHC yields a highly consistent and reproducible biomaterial, thereby ensuring uniformity in its quality (Wang, 2021). This process also eradicates risks associated with pathogen transmission from animal sources and negates the need for reliance on animal harvesting, thus providing an abundant, sustainable supply of human collagen (Rico-Llanos et al., 2021). The degradation rate of RHC is tunable, and it boasts processing versatility, and overall customizability, which further enhances its suitability as a biomaterial. These properties make RHC an ideal biomaterial for the development of engineered tissues and scaffolds for various applications. These include, but are not limited to, skin grafts, tendon/ligament repair, wound healing, and other regenerative medicine applications.

The potential for employing scaffolds as vehicles for recombinant collagen in the fields of tissue engineering and regenerative medicine is considerable. These scaffolds deliver a

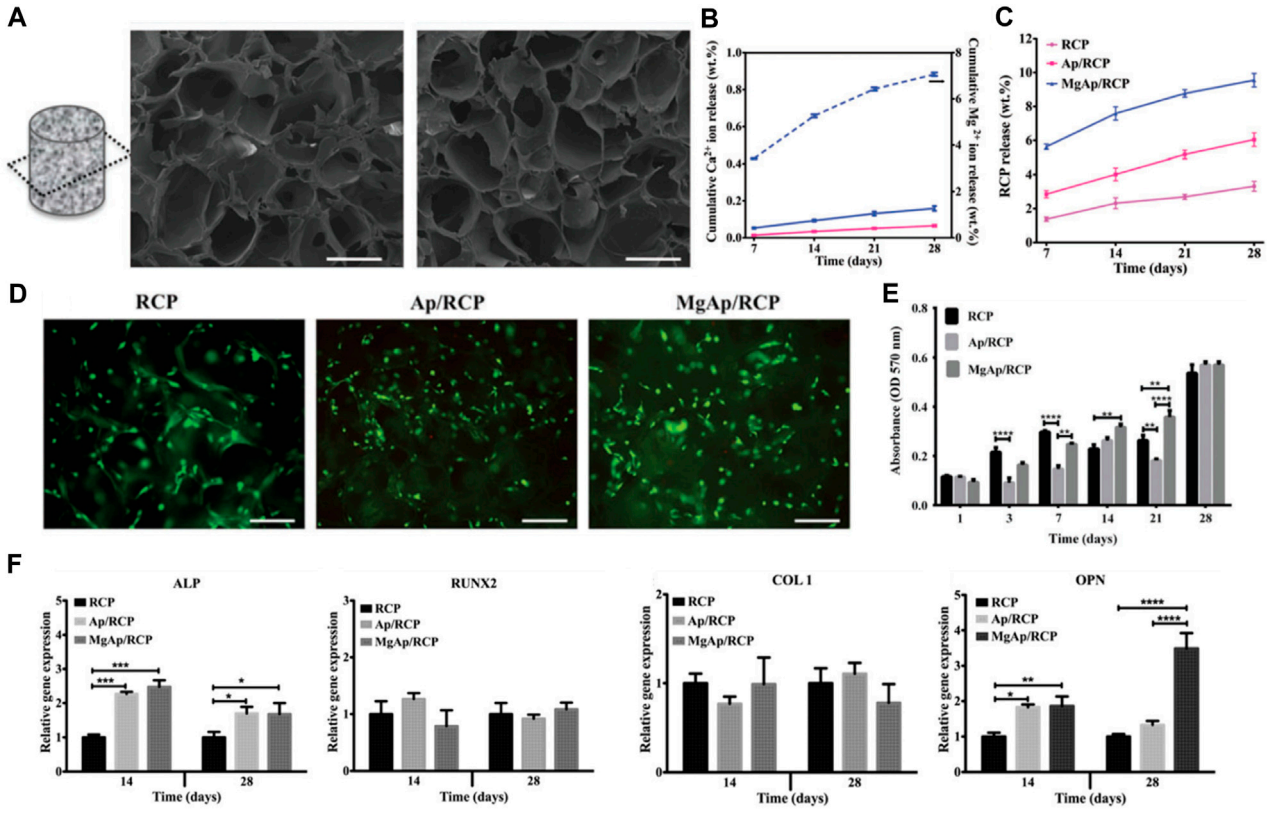


FIGURE 4
**(A)** SEM analysis of MgAp/RCP scaffolds. Scale bar, 250 mm. Release profiles of **(B)** $Ca^{2+}$ and **(C)** RCP from MgAp/RCP scaffolds. **(D)** Staining of live and dead cells was performed for the investigation of cytocompatibility. **(E)** The MTT assay was employed to evaluate cell viability at multiple time points: after 1, 3, 7, 14, 21, and 28 days. **(F)** mRNA expression investigation of alkaline phosphatase (ALP), collagen I (COL1), osteopontin (OPN) and runtrelated transcription factor 2 (RUNX2). Reproduced with permission from ref Ramírez-Rodríguez et al. (2017).

three-dimensional construct reminiscent of the natural extracellular matrix, fostering cellular attachment, proliferation, and differentiation. Scaffolds comprising recombinant collagen present numerous benefits compared to conventional scaffolds manufactured from animal-derived collagen. The former can be produced on a large scale, with meticulous regulation of composition and purity (He et al., 2018). Additionally, recombinant collagen scaffolds can be functionalized with elements such as cell-binding motifs, growth factors, and other biologically active molecules to enhance their efficacy.

Nevertheless, significant obstacles remain. Emulating the intricate architecture and diverse protein composition of native ECM continues to be a challenging task. Matching the degradation rate of scaffolds with the pace of cell/tissue growth persistently proves difficult (Jeon et al., 2017). Engineering tissues over 1 mm in thickness necessitates innovative strategies for vascularization. Moreover, understanding how the physicochemical properties of scaffolds impact cell behavior is still lacking. Current research pursuits are focused on deepening our understanding of cell-matrix interactions, designing innovative biomaterials and processing methodologies, and augmenting the functional characteristics of engineered tissues (Huang et al., 2018). In conclusion, while recombinant collagen scaffolds represent a promising avenue for regenerative medicine, additional research is required to enhance scaffold bioactivity, degradation, and integration within host tissues.

## 4 Utilization of recombinant human collagen in bone tissue repair

Recombinant human collagen has emerged as a significant asset in the field of bone regenerative engineering (Andrews et al., 2019; Fushimi et al., 2020). RhCOL retains the biological attributes of natural collagen while circumventing the issues associated with immunogenicity and pathogen transmission. RhCOL scaffolds facilitate the adhesion, proliferation, and differentiation of osteoblasts *in vitro*. *In vivo* studies illustrate enhanced bone regeneration when rhCOL is used in conjunction with bone marrow-derived mesenchymal stem cells (BMSCs) and/or osteogenic growth factors (Chan et al., 2017).

The composition and structure of rhCOL scaffolds can be precisely tailored to mimic the native bone extracellular matrix. This is achieved through manipulation of collagen crosslinking, mineral content, and the incorporation of bioactive motifs, enabling a controlled degradation rate that synchronizes with new bone deposition (Bien et al., 2020). Moreover, rhCOL scaffolds surpass the limitations of traditional bone graft materials by supporting cellular growth and providing precise control over structural and

10.3389/fbioe.2024.1358246

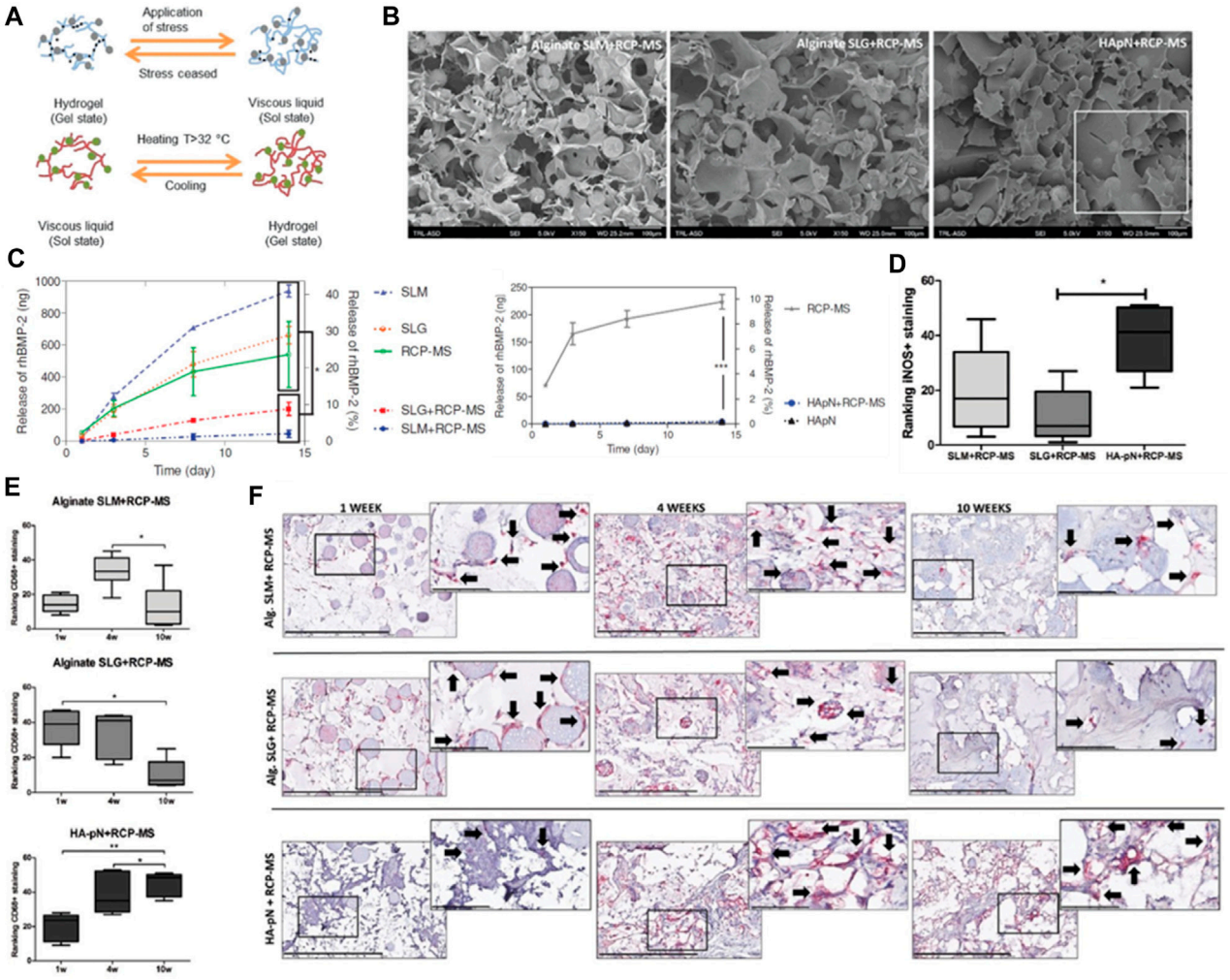


FIGURE 5
**(A)** The diagram depicts the structural network of a hydrogel infused with microspheres. **(B)** SEM visuals of the SLM+RCP-MS, SLG+RCP-MS, and HApN+RCP-MS formulations are presented. Scale bar, 100 μm. **(C)** The dispersion of BMP-2 is contrasted among various precursors. **(D)** Positive iNOS staining observed in the formulations after a period of 10 weeks. **(E)** Two impartial reviewers classified the implants based on the occurrence of CD68 positive staining observed in the formulations at the intervals of 1, 4, and 10 weeks. **(F)** Representative sample from each implant formulation at 1 and 10 weeks, with a scale bar indicating 400 μm. Reproduced with permission from ref Fahmy-Garcia et al. (2018).

functional properties (Muhonen et al., 2017; Bien et al., 2020). Ongoing research endeavors aim to optimize integration and healing outcomes as rhCOL transitions from laboratory research to clinical implementation for bone engineering applications.

Sandri et al. delves into the creation of a synthetic bone substitute that emulates the biochemical and biophysical cues intrinsic to the native bone extracellular matrix (Ramírez-Rodríguez et al., 2017). The investigative team employed a recombinant collagen-based scaffold, which was enriched with the tri-amino acid sequence arginine-glycine-aspartate (RGD), aiming to bolster the interaction and differentiation of mesenchymal stem cells. The study witnessed promising progress in the generation of superior quality bone grafts, a feat achieved through biomimetic mineralization of synthetic engineering peptides under the influence of magnesium ions. The novelty of this study hinges on the application of a synthetic bone substitute that, across all scales from macro to nano, replicates the biochemical and biophysical cues of the bone extracellular matrix.

Three distinct scaffold compositions were characterized by SEM analysis, non-mineralized (RCP), mineralized (Ap/RCP), and mineralized alongside magnesium (MgAp/RCP) possess a highly porous structure with interconnected pores. The mineralized scaffolds exhibit a more compact structure compared to their non-mineralized counterpart, and the incorporation of magnesium leads to a more uniform and homogeneous structure (Figure 4A). Encapsulated $Ca^{2+}$ and Rcp display a consistent and prolonged release pattern (Figures 4B, C). The scaffold demonstrates superior cytocompatibility, exhibiting no adverse or toxic effects on cells (Figure 4D). Detailed examination revealed that the MgAp/RCP scaffolds exhibited the most pronounced MSC proliferation within 28 days (Figure 4E). Through the use of qPCR, they analyzed the messenger RNA (mRNA) levels of ALP, RUNX2, OPN, and COL1, aiming to discern the influence that the three types of scaffolds exerted on the expression of osteogenic markers. Scaffolds exert a significant influence on the expression levels of these mRNAs (Figure 4F).

In 2018, Farrell et al. presented a research investigation focused on developing a novel *in situ* gelling hydrogel, embedded with recombinant collagen peptide microspheres (Fahmy-Garcia et al., 2018). This unique slow-release system is designed to stimulate ectopic bone formation. The study's objective was to introduce a promising solution for extensive bone defect repair, employing natural biomaterials which are biodegradable, biocompatible, and can actively interact with the extracellular matrix and cells. The injectable formulation simplifies application and can potentially expedite patient recovery time.

The research process comprised the production of the hydrogel and microspheres, succeeded by *in vitro* and *in vivo* examinations to assess their properties and effectiveness. The hydrogel was synthesized using a blend of gelatin, hyaluronic acid, and β-glycerophosphate (Figure 5A), while the microspheres were fashioned using recombinant collagen peptide and poly (lactic-co-glycolic acid) (PLGA). Various techniques, including scanning electron microscopy (Figure 5B), Fourier-transform infrared spectroscopy, and rheological analysis, were employed to characterize the hydrogel and microspheres. Alginate hydrogels containing RCP-MS demonstrated a slower release rate, indicating the synergistic effect of microspheres and hydrogels in controlling the release. During the *in vitro* experiments, the hydrogel and microspheres' biocompatibility and osteogenic potential were evaluated. The findings indicated that the hydrogel and microspheres promoted cells proliferation and differentiation into osteoblasts, suggesting their potential for bone tissue engineering applications. *In vivo* experiments evaluated the hydrogel and microspheres' efficacy in stimulating ectopic bone formation in a rat model. The results revealed significant enhancement in bone formation in comparison to the control group, as substantiated by micro-computed tomography and histological analysis. The hydrogel and microspheres also facilitated the infiltration of immune cells, including macrophages and M2-like macrophages, which play an essential role in bone regeneration.

In summary, the research demonstrated the potential of the novel *in situ* gelling hydrogel loaded with recombinant collagen peptide microspheres as a slow-release system to induce ectopic bone formation. Both the hydrogel and microspheres displayed excellent biocompatibility and osteogenic potential *in vitro* and significantly augmented bone formation *in vivo*. The findings indicate that this injectable formulation could serve as a promising solution for extensive bone defect repair by leveraging natural, biodegradable, and biocompatible biomaterials that interact with the extracellular matrix and cells.

## 5 Application of recombinant human collagen in 3D bioprinting

Recombinant human collagen has attracted growing interest in 3D bioprinting due to its biocompatibility, low immunogenicity, and customizable biochemical and mechanical properties (Lee et al., 2019; Osidak et al., 2020; Muthusamy et al., 2021). Studies have engineered recombinant human collagen with tailored supramolecular assemblies, crosslinking densities, and matrix stiffnesses to resemble native extracellular matrices (Włodarczyk-Biegun and Del Campo, 2017; Hong et al., 2018). This permits precise control over microenvironments for directing cell fate processes (Tytgat et al., 2020). Moreover, recombinant collagen allows incorporation of cell-adhesive peptides, growth factors, and cytokines to modulate cell behaviors. Currently, recombinant human collagen-based bioinks have been utilized to bioprint tissue constructs such as skin, cartilage, bone, blood vessels, and liver (Zhang et al., 2021). Looking ahead, recombinant human collagen bioinks hold great promise for fabricating complex heterogeneous tissues with biomimetic architectures, compositions, and functions (Gungor-Ozkerim et al., 2018; Isaacson et al., 2018; Gudapati et al., 2020). However, challenges remain in scalable recombinant collagen production and developing universal crosslinking strategies to enhance print fidelity (Martyniak et al., 2022). Further interdisciplinary research on optimizing recombinant human collagen designs, crosslinking mechanisms, and printing processes is critical to enable wide clinical translations of 3D bioprinted tissues and organs (Stepanovska et al., 2021).

In 2022, Jin et al. presents the formulation of photo-responsive bioinks based on chitosan and recombinant human collagen for 3D bioprinting (Yang et al., 2022a). The authors delve into the merits of employing these materials, including their biocompatibility, biodegradability, and their proficiency to foster cell proliferation and differentiation. They underscore the cruciality of managing shear stress during the printing operation to preserve the integrity of stem cells (Figure 6).

Type-III recombinant human collagen methacryloyl/acidified chitosan (CS-RHCMA) bioinks were synthesized by incorporating acidified chitosan into a RHCMA solution. The RHCMA was derived by altering recombinant human collagen with methacrylic anhydride. The CS-RHCMA composites were created by amalgamating the acidified chitosan with the RHCMA solution in varying proportions, facilitating the adjustment of the bioinks' mechanical resilience and internal pore dimensions. The integration of chitosan into RHCMA enhanced the printability of the bioinks, yielding well-structured 3D constructs via extrusion-based 3D printing (Figure 6A). Figure 6B shows different structures created by 3D printed constructs using the CS-RHCMA bioinks. The authors demonstrate the versatility of the bioinks by creating various structures, including a honeycomb structure, a spiral structure, and a grid structure. The printed HUVECs are well sustained within the lattices prepared from the CS-RHCMA samples, with nearly 80% of the cells being alive after the extrusion-based printing. This suggests that the CS-RHCMA bioinks are suitable for 3D bioprinting and can support the growth and viability of HUVECs. SEM images present the internal structure of freeze-dried RHCMA and CS-RHCMA samples. Both samples show a uniformly distributed, interconnected pore structure (Figure 6C). Introducing chitosan to RHCMA increased pore size: average pore size in CS-RHCMA 1: 3 is 128 μm, larger than 66 μm in 10% RHCMA. Further CS content increases lead to smaller pores and denser pore walls, with CS-RHCMA 3:3 having the smallest size of 58 μm. These findings indicate that adding chitosan to RHCMA allows control over the bioinks' internal structure, influencing the mechanical properties and cell behavior in printed constructs. Figure 6D depict the degradation of RHCMA and CS-RHCMA in PBS (pH 7.2) and lysozyme solution (pH 6.5), measured by weight loss over time. Lysozyme-incubated samples degraded completely in 4 days, while

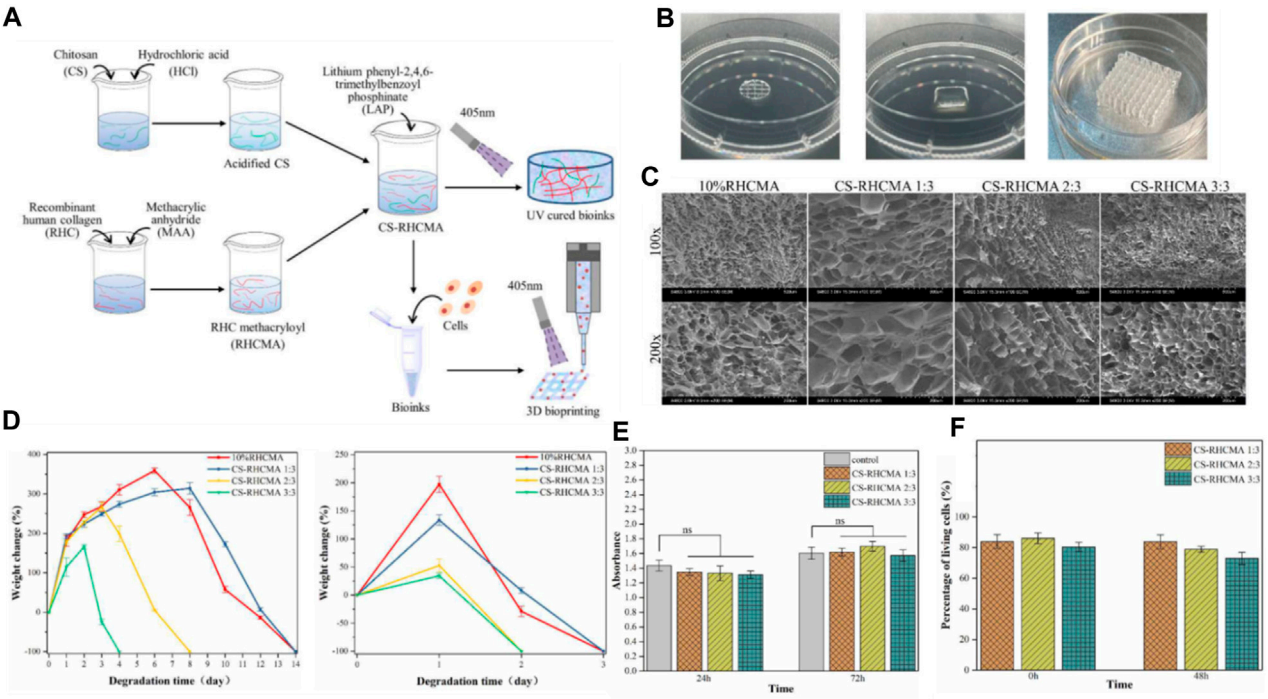


FIGURE 6
**(A)** Diagrammatic representation of the CS-RHCMA bioinks preparation process. **(B)** Different structures created by 3D printed constructs. **(C)** SEM images of the internal morphology of freeze-dried RHCMA and CS-RHCMA samples. Scale bar, 200 μm. **(D)** Degradation of RHCMA and CS-RHCMA samples when incubated in PBS solution (pH 7.2) and lysozyme solution (pH 6.5), respectively. **(E)** Assessment of HUVECs viability cultured in sample extracts at timeframes of 24 and 72 h. None significant (ns) indicates $p > 0.05$. **(F)** Evaluation of *in vitro* biocompatibility for HUVECs-laden CS-RHCMA bioinks post-printing. Reproduced with permission from ref Yang et al. (2022a).

those in PBS took 14 days. RHC and CS-RHCMA 1:3 degraded slower but increasing CS ratio sped up degradation. This is likely due to changes in mechanical properties from added acidified CS disrupting gelation networks. Thus, higher strength UV-cured bioinks resist fast breakdown, and degradation rate can be adjusted by varying bioink composition, influencing the stability and longevity of printed constructs. Figure 6E demonstrates that all the UV-cured CS-RHCMA bioinks were cytocompatible and suitable for 3D bioprinting *in vitro*.

The findings affirm the cytocompatibility of UV-cured CS-RHCMA bioinks, rendering them suitable for *in vitro* 3D bioprinting. The viability of cells within the bioprinted lattice approximated 80%, underscoring the bioinks' ability to foster HUVECs growth and survival (Figure 6F). These insights are pivotal in advancing bioinks for 3D bioprinted vascularized tissues and organ constructs.

The novelty of this research rests on the generation of a photo-responsive bioink capable of fabricating intricate 3D constructs with superior resolution and cell viability. The authors illustrate the promise of this bioink for tissue engineering applications, encompassing the production of skin and cartilage tissues.

Nonetheless, this work is not without its challenges. These include the necessity for further refinement of the printing protocol and the imperative to scale up manufacturing for clinical use. Moreover, the authors acknowledge that additional research is requisite to fully comprehend the enduring impacts of employing these materials in a living organism.

Recombinant human collagen has garnered interest in 3D bioprinting due to its biocompatibility, low immunogenicity, and adaptable biochemical and mechanical traits (Elalouf, 2021). Research has tailored RHC to mimic native extracellular matrices with custom supramolecular assemblies, crosslinking densities, and matrix firmness, allowing precise control over cellular microenvironments for directing cell fate (Cui et al., 2017). Furthermore, RHC allows the integration of cell-adhesive peptides, growth factors, and cytokines to influence cell behaviors (Dai et al., 2021). At present, RHC-based bioinks are used to bioprint various tissue constructs, including skin, cartilage, bone, blood vessels, and liver (Tang et al., 2021). Moving forward, RHC bioinks possess significant potential for crafting complex, heterogeneous tissues with biomimetic structures, compositions, and functionalities (Zhang et al., 2017; Matai et al., 2020). Nevertheless, hurdles persist in scalable RHC production and devising universal crosslinking strategies for improved print fidelity. Continued interdisciplinary research on refining RHC designs, crosslinking mechanisms, and printing methodologies is crucial for broad clinical translation of 3D bioprinted tissues and organs.

## 6 Conclusion and discussion

The production of recombinant human collagen (RHC) is a complex biotechnological process that encompasses the utilization

of specific host cells modified to express human collagen genes. The process begins with the isolation of the relevant human genes encoding collagen, which are then cloned into vectors–DNA molecules capable of carrying foreign DNA into a host cell. These vectors are subsequently introduced into host cells such as *Escherichia coli*, yeast, or mammalian cells, which have been chosen based on their ability to produce collagen in a form that retains its native structure and function (He et al., 2018; Sheehy et al., 2018).

Following transformation, the host cells are cultured in a controlled environment that is optimized for the expression of the collagen gene. The production involves the scaling up of cell cultures in bioreactors, where conditions such as temperature, pH, and nutrient supply are meticulously managed to maximize yield and product quality (Włodarczyk-Biegun and Del Campo, 2017; Lee et al., 2019). Post-translational modifications crucial for collagen stability and function, such as hydroxylation and glycosylation, are carefully orchestrated within the production system.

The benefits of using RHC instead of animal-derived collagen are multifaceted (Radke et al., 2018; Lagali, 2020; Elalouf, 2021): (1) safety: RHC reduces the potential for zoonotic disease transmission and immunogenic reactions as it is produced in a controlled environment without sourcing from animal tissues; (2) Consistency: the production of RHC can be tightly regulated to ensure batch-to-batch consistency, which is a significant challenge with animal-derived collagen due to natural biological variability; (3) Customization: RHC can be modified at the genetic level to include specific amino acid sequences or to introduce particular post-translational modifications, which is not feasible with animal-derived collagen. This allows for the creation of collagen with precise characteristics required for specific applications. (4) Ethical Considerations: RHC production avoids the ethical concerns associated with the use of animal products.

It is important to highlight that customizing animal-derived collagen is inherently challenging. The extraction process from animal tissues can lead to batch variability, and the complexity of the native collagen structure makes it difficult to modify post-translationally. This results in a product that may not be consistently reliable for precise biomedical applications, where uniformity in structure and function is paramount (Osidak et al., 2020).

RHC has emerged as a biomaterial with extraordinary versatility and promise in the realms of tissue engineering and regenerative medicine, presenting a multitude of benefits over traditional animal-derived collagens. Its uniform composition, markedly reduced immunogenicity, and the amenability to molecular engineering for bespoke applications highlight its broad potential in diverse biomedical applications (Nocera et al., 2018). Research has underscored the adaptability of RHC in various formulations such as hydrogels, scaffolds, and lyophilized substances, which have been successfully applied in healing wounds, regenerating skin, and reconstructing osseous and cartilaginous tissues.

The ability to enhance these RHC-based materials with growth factors, cellular elements, or nanoparticles opens up avenues for precision customization, aligning material properties with the nuanced demands of specific therapeutic contexts. The efficacy of RHC is evident in its application to skin grafts, weight-bearing tissue repair, and the engineering of vascular grafts—areas where there is substantial documentation of its success, particularly in preclinical animal studies (Curtin et al., 2018; Elalouf, 2021; Yang et al., 2022a).

To expand upon this, the future of RHC research is poised to delve into next-level innovations that may redefine therapeutic approaches. For instance, the integration of RHC with cutting-edge bio-fabrication technologies, such as 3D bioprinting, has the potential to construct tissues and organs with unprecedented complexity and functionality (Liverani et al., 2017; Rico-Llanos et al., 2021). This would not only revolutionize how we approach complex tissue reconstruction but also hold implications for personalized medicine, where RHC-based tissues are tailored to individual patient's biological profiles.

Moreover, there exists a burgeoning interest in exploring the synergistic combinations of RHC with synthetic polymers, which may yield composite materials with enhanced mechanical properties and biological functionalities. Such composites could offer new solutions for the regeneration of tissues that require a high degree of biomechanical resilience, such as in the case of intervertebral disc repair or the reconstruction of load-bearing joints (He et al., 2018; Rico-Llanos et al., 2021; Binlateh et al., 2022).

Another prospective area of RHC application lies in the realm of controlled drug delivery systems (Lagali, 2020; Yang et al., 2022b). By embedding therapeutic agents within RHC matrices, it may be possible to achieve localized, sustained release of drugs at injury sites, thereby enhancing the healing process while minimizing systemic side effects.

The ongoing research and future explorations are expected to not only address the current limitations surrounding RHC production and application but also to unlock novel therapeutic paradigms. As we stand on the cusp of these scientific advancements, RHC research is truly at an inflection point, with the anticipation that future studies will bring forth groundbreaking applications that will cement RHC's status as an invaluable asset in biomedical engineering and beyond. (Liverani et al., 2017).

RHC is an area of intense research interest due to its potential applications in biomedicine, particularly in tissue engineering and regenerative medicine (Parmar et al., 2017; Yang et al., 2021b; Gajbhiye and Wairkar, 2022). The future direction of RHC-related research is shaped by the need for safer, more effective, and customizable biomaterials. Here are several promising avenues for future research:

## 6.1 Enhanced biomimicry

Future research will likely focus on improving the biochemical and biomechanical properties of RHC to more closely mimic the native characteristics of human collagen. This includes fine-tuning the amino acid composition, crosslinking patterns, and molecular alignment to replicate the mechanical strength and biological signaling present in the human body.

## 6.2 Genetic engineering advances

Advancements in genetic engineering techniques can be applied to modify the genes used to produce RHC, leading to collagens with specific properties or functions that are difficult to obtain from

natural collagens. This can enable the custom design of collagen molecules for specific medical applications.

### 6.3 3D Bioprinting integration

The integration of RHC with advanced 3D bioprinting techniques is an exciting frontier. Research will likely explore the development of specialized bioinks that can be used to print complex, multicellular tissues and organs with high precision.

### 6.4 Smart biomaterials

The development of "smart" RHC-based materials that can respond to physiological stimuli, such as changes in pH or temperature, could revolutionize drug delivery systems and dynamic tissue scaffolds that adapt to the healing process.

### 6.5 Personalized medicine applications

With the advent of personalized medicine, RHC could be tailored to individual patients based on their genetic makeup, potentially improving the outcomes of treatments and reducing the risk of adverse reactions.

By addressing these future directions, RHC research can contribute to creating more effective therapeutic strategies and innovative solutions for complex medical challenges.

However, challenges persist. To fully realize the potential of RHC, high-yield, cost-effective production systems need to be established (Fu et al., 2019; Groetsch et al., 2019). Systems based on mammalian cells are often associated with low yields and high costs, while bacterial and yeast systems, although more cost-effective, may not achieve the necessary post-translational modifications. Innovations in genetic manipulation and enzyme supplementation may offer potential solutions to these problems (Radke et al., 2018). The use of RHC in 3D bioprinting also invites further exploration. As technologies evolve, RHC's potential to be used in the fabrication of complex, heterogeneous tissues with biomimetic architectures, compositions, and functionalities could be transformative.

In summary, the research summarized in this review underscores the significant potential of RHC in tissue engineering and regenerative medicine. Despite remaining challenges, the progress made so far in the development and application of RHC is encouraging, and the future of RHC looks promising. As the field continues to advance, RHC is likely to play an increasingly important role in the development of improved biomaterials, therapies, and patient outcomes.

## Author contributions

LC: Conceptualization, Supervision, Writing–original draft, Writing–review and editing. ZZ: Writing–review and editing. DY: Writing–review and editing. MY: Writing–review and editing. JM: Writing–review and editing.

## Funding

The author(s) declare that no financial support was received for the research, authorship, and/or publication of this article.

## Conflict of interest

The authors declare that the research was conducted in the absence of any commercial or financial relationships that could be construed as a potential conflict of interest.

## Publisher's note



## References

Abbas, Y., Brunel, L. G., Hollinshead, M. S., Fernando, R. C., Gardner, L., Duncan, I., et al. (2020). Generation of a three-dimensional collagen scaffold-based model of the human endometrium. *Interface Focus* 10 (2), 20190079. doi:10.1098/rsfs.2019.0079

Addi, C., Murschel, F., and De Crescenzo, G. (2017). Design and use of chimeric proteins containing a collagen-binding domain for wound healing and bone regeneration. *Tissue Eng Part B Rev.* 23, no. 2 : 163–182. doi:10.1089/ten.teb.2016.0280

Ahmad, T., McGrath, S., Sirafim, C., Amaral, R. J. F. C. do, Soong, S.-L., Sitram, R., et al. (2021). Development of wound healing scaffolds with precisely-triggered sequential release of therapeutic nanoparticles. *Biomater. Sci.* 9 (12), 4278–4288. doi:10.1039/d0bm01277g

Amyoony, J., Gorman, M., Dabas, T., Moss, R., and McSweeney, M. B. (2023). Consumer perception of collagen from different sources: an investigation using hedonic scale and check all that apply.

Andrews, S., Cheng, A., Stevens, H., Logun, M. T., Webb, R., Jordan, E., et al. (2019). Chondroitin sulfate glycosaminoglycan scaffolds for cell and recombinant protein-based bone regeneration. *Stem Cells Transl. Med.* 8 (6), 575–585. doi:10.1002/sctm.18-0141

Arakawa, C., Ng, R., Tan, S., Kim, S., Wu, B., and Lee, M. (2017). Photopolymerizable chitosan-collagen hydrogels for bone tissue engineering: photopolymerizable chitosan-collagen hydrogels. *Photopolymerizable Chitosan–Collagen Hydrogels Bone Tissue Eng.* 11 (1), 164–174. doi:10.1002/term.1896

Avila Rodríguez, M. I., Rodríguez Barroso, L. G., and Sánchez, M. L. (2018). Collagen: a review on its sources and potential cosmetic applications. *J. Cosmet. Dermatol* 17 (1), 20–26. doi:10.1111/jocd.12450

Bien, N. D., Miura, K.-ichiro, Sumita, Y., Nakatani, Y., Shido, R., Kajii, F., et al. (2020). Bone regeneration by low-dose recombinant human bone morphogenetic protein-2 carried on octacalcium phosphate collagen composite. *J. Hard Tissue Biol.* 29 (2), 123–130. doi:10.2485/jhtb.29.123

Binlateh, T., Thammanichanon, P., Rittipakorn, P., Thinsathid, N., and Jitprasertwong, P. (2022). Collagen-based biomaterials in periodontal regeneration: current applications and future perspectives of plant-based collagen. *Biomimetics* 7 (2), 34. doi:10.3390/biomimetics7020034

Capella-Monsonís, H., Coentro, J. Q., Graceffa, V., Wu, Z., and Dimitrios, I. (2018). An experimental toolbox for characterization of mammalian collagen type I in biological specimens. *Nat. Protoc.* 13 (3), 507–529. doi:10.1038/nprot.2017.117

Carrabba, M., and Madeddu, P. (2018). Current strategies for the manufacture of small size tissue engineering vascular grafts. *Front. Bioeng. Biotechnol.* 6, 41. doi:10.3389/fbioe.2018.00041

Catanzano, O., Quaglia, F., and Joshua, S. (2021). Wound dressings as growth factor delivery platforms for chronic wound healing. *Expert Opin. Drug Deliv. Boateng* 18 (6), 737–759. doi:10.1080/17425247.2021.1867096

Chan, Su J., Love, C., Spector, M., Cool, S. M., Nurcombe, V., and Lo, E. H. (2017). Endogenous regeneration: engineering growth factors for stroke. *Neurochem. Int.* 107, 57–65. doi:10.1016/j.neuint.2017.03.024

Chen, Lu, Guttieres, D., Koenigsberg, A., Barone, P. W., Sinskey, A. J., and Stacy, L. (2022). Large-scale cultured meat production: trends, challenges and promising biomanufacturing technologies. *Biomaterials* 280, 121274. doi:10.1016/j.biomaterials.2021.121274

Chen, Z., Fan, D., and Shang, L. (2020). Exploring the potential of the recombinant human collagens for biomedical and clinical applications: a short review. *Biomed. Mater.* 16 (1), 012001. doi:10.1088/1748-605x/aba6fa

Copes, F., Pien, N., Van Vlierberghe, S., Boccafoschi, F., and Mantovani, D. (2019). Collagen-based tissue engineering strategies for vascular medicine. *Front. Bioeng. Biotechnol.* 7, 166. doi:10.3389/fbioe.2019.00166

Coppola, D., Oliviero, M., Andrea Vitale, G., Lauritano, C., D'Ambra, I., Iannace, S., et al. (2020). Marine collagen from alternative and sustainable sources: extraction, processing and applications. *Mar. Drugs* 18 (4), 214. doi:10.3390/md18040214

Cui, H., Nowicki, M., Fisher, J. P., and Grace Zhang, L. (2017). 3d bioprinting for organ regeneration. *Adv. Healthc. Mater.* 6 (1), 1601118. doi:10.1002/adhm.201601118

Curtin, C., Nolan, J. C., Conlon, R., Deneweth, L., Gallagher, C., Tan, Y. J., et al. (2018). A physiologically relevant 3d collagen-based scaffold–neuroblastoma cell system exhibits chemosensitivity similar to orthotopic xenograft models. *Acta biomater.* 70, 84–97. doi:10.1016/j.actbio.2018.02.004

Dai, M., Belaïdi, J.-P., Fleury, G., Garanger, E., Rielland, M., Schultze, X., et al. (2021). Elastin-like polypeptide-based bioink: a promising alternative for 3d bioprinting. *Biomacromolecules* 22 (12), 4956–4966. doi:10.1021/acs.biomac.1c00861

Davison-Kotler, E., Marshall, W. S., García-Gareta, E., and García-Gareta, E. (2019). Sources of collagen for biomaterials in skin wound healing. *Bioengineering* 6 (3), 56. doi:10.3390/bioengineering6030056

Deng, A., Yang, Y., Du, S., Yang, X., Pang, S., Wang, X., et al. (2021). Preparation of a recombinant collagen-peptide (Rhc)-Conjugated chitosan thermosensitive hydrogel for wound healing. *Mater Sci Eng C Mater Biol Appl.* 119, 111555, doi:10.1016/j.msec.2020.111555

Di Martino, J. S., Nobre, A. R, Mondal, C., Taha, I., Farias, E. F., Fertig, E. J., et al. (2022). A tumor-derived type iii collagen-rich ecm niche regulates tumor cell dormancy. *Nat. cancer* 3 (1), 90–107. doi:10.1038/s43018-021-00291-9

Doan, N.-D., DiChiara, A. S., M Del Rosario, A., and Schiavoni, R. P. (2019) Matthew D collagen: methods shoulders, and protocols mass spectrometry-based proteomics to define intracellular collagen interactomes. *Methods Mol. Biol.* 95–114. doi:10.1007/978-1-4939-9095-5_7

Elalouf, A. (2021). Immune response against the biomaterials used in 3D bioprinting of organs. *Transpl. Immunol.* 69, 101446. doi:10.1016/j.trim.2021.101446

Felician, F. F., Xia, C., Qi, W., and Xu, H. (2018). Collagen from marine biological sources and medical applications. *Chem Biodivers* 15, 5, e1700557, doi:10.1002/cbdv.201700557

Ferraro, V., Gaillard-Martinie, B., Sayd, T., Chambon, C., Anton, M., and Santé-Lhoutellier, V. (2017). Collagen type I from bovine bone. Effect of animal age, bone anatomy and drying methodology on extraction yield, self-assembly, thermal behaviour and electrokinetic potential. *Int. J. Biol. Macromol.* 97, 55–66. doi:10.1016/j.ijbiomac.2016.12.068

Fu, Yu, Therkildsen, M., Aluko, R. E., and Lametsch, R. (2019). Exploration of collagen recovered from animal by-products as a precursor of bioactive peptides: successes and challenges. *Crit. Rev. Food Sci. Nutr.* 59 (13), 2011–2027. doi:10.1080/10408398.2018.1436038

Fushimi, H., Hiratsuka, T., Ai, O., Ono, Y., Ogura, I., and Nishimura, I. (2020). Recombinant collagen polypeptide as a versatile bone graft biomaterial. *Commun. Mat.* 1 (1), 87. doi:10.1038/s43246-020-00089-9

Gajbhiye, S., and Wairkar, S. (2022). Collagen fabricated delivery systems for wound healing: a new roadmap. *Biomater. Adv.* 142, 213152. doi:10.1016/j.bioadv.2022.213152

Gauza-Włodarczyk, M., Kubisz, L., and Dariusz, W. (2017a), Amino acid composition in determination of collagen origin and assessment of physical factors effects. *Int J Biol Macromol* 104, 987–991. doi:10.1016/j.ijbiomac.2017.07.013

Gauza-Włodarczyk, M., Kubisz, L., Mielcarek, S., and Włodarczyk, D. (2017b). Comparison of thermal properties of fish collagen and bovine collagen in the temperature range 298–670 K. *Mater Sci Eng C Mater Biol Appl.* 80, 468–471. doi:10.1016/j.msec.2017.06.012

Ghomi, E. R., Nourbakhsh, N., and Kenari, M. A. (2021). Mina zare, and seeram journal of biomedical materials research Part B: applied biomaterials ramakrishna. *Collagen-Based Biomaterials Biomed. Appl.* 109 (12), 1986–1999. doi:10.1002/jbm.b.34881

Groetsch, A., Gourrier, A., Schwiedrzik, J., Sztucki, M., Beck, R. J., Shephard, J. D., et al. (2019). Compressive behaviour of uniaxially aligned individual mineralised collagen fibres at the micro-and nanoscale. *Acta biomater.* 89, 313–329. doi:10.1016/j.actbio.2019.02.053

Gudapati, H., Parisi, D., Colby, R. H., and Matter Ozbolat, I. T. S. (2020). Rheological investigation of collagen, fibrinogen, and thrombin solutions for drop-on-demand 3d bioprinting. *Soft Matter* 16 (46), 10506–10517. doi:10.1039/d0sm01455a

Gungor-Ozkerim, P. S., Inci, I., Zhang, Yu S., Ali, K., and Remzi, M. (2018). Bioinks for 3D bioprinting: an overview. *Biomater. Sci.* 6 (5), 915–946. doi:10.1039/c7bm00765e

Haagdorens, M., Cėpla, V., Melsbach, E., Koivusalo, L., Skottman, H., Griffith, M., et al. (2019). Vitro cultivation of limbal epithelial stem cells on surface-modified crosslinked collagen scaffolds. *Stem Cells Int.* 2019, 7867613. doi:10.1155/2019/7867613

Han, G., and Roger, C. (2017). Chronic wound healing: a review of current management and treatments. *Adv. Ther.* 34, 599–610. doi:10.1007/s12325-017-0478-y

Harris, R. B., Fonseca, F. L. A., Sharp, M. H., and Charlie, R. (2022). Functional characterization of undenatured type ii collagen supplements: are they interchangeable? *J. Diet. Suppl. Ottinger* 19 (6), 717–732. doi:10.1080/19390211.2021.1931621

He, B., Zhao, J., Ou, Y., and Jiang, D. (2018). Biofunctionalized peptide nanofiber-based composite scaffolds for bone regeneration. *Mater Sci Eng C Mater Biol.* 90, 728–738. doi:10.1016/j.msec.2018.04.063

Hong, N., Yang, G.-H., Lee, J., and Kim, G. (2018). 3d bioprinting and its *in vivo* applications. *J. Biomed. Mat. Res.* 106 (1), 444–459. doi:10.1002/jbm.b.33826

Hu, C., Liu, W., Long, L., Wang, Z., Yuan, Y., Zhang, W., et al. (2021). Microenvironment-responsive multifunctional hydrogels with spatiotemporal sequential release of tailored recombinant human collagen type iii for the rapid repair of infected chronic diabetic wounds. *J. Mater. Chem. B Lu* 9 (47), 9684–9699. doi:10.1039/d1tb02170b

Huang, B., Wu, Z., Ding, S., Yuan, Y., and Changsheng, L. (2018). Localization and promotion of recombinant human bone morphogenetic protein-2 bioactivity on extracellular matrix mimetic chondroitin sulfate-functionalized calcium phosphate cement scaffolds. *Acta Biomater.* 71, 184–199. doi:10.1016/j.actbio.2018.01.004

Irawan, V., Sung, T.-C., Higuchi, A., and Ikoma, T. (2018). Collagen scaffolds in cartilage tissue engineering and relevant approaches for future development. *Tissue Eng. Regen. Med.* 15, 673–697. doi:10.1007/s13770-018-0135-9

Isaacson, A., Stephen, S., and Che, J. (2018). 3D bioprinting of a corneal stroma equivalent. *Exp. Eye Res.* 173, 188–193. doi:10.1016/j.exer.2018.05.010

Jafari, H., Lista, A., Mafosso Siekapen, M., Ghaffari-Bohlouli, P., Nie, L., Alimoradi, H., et al. (2020). Fish collagen: extraction, characterization, and applications for biomaterials engineering. *Polym. (Basel).* 12 (10), 2230. doi:10.3390/polym12102230

Jeon, E. Y., Choi, B. H., Jung, D., Hwang, B. H., and Cha, H. J. (2017), Natural healing-inspired collagen-targeting surgical protein glue for accelerated scarless skin regeneration, *Biomaterials* 134, 154–165. doi:10.1016/j.biomaterials.2017.04.041

Kathawala, M. H., Ng, W. L., Liu, D., Naing, M. W., Yeong, W. Y., Spiller, K. L., et al. (2019). Healing of chronic wounds: an update of recent developments and future possibilities. *Tissue Eng Part B Rev.* 25, 5, 429–444. doi:10.1089/ten.teb.2019.0019

Kim, C.-H., Ju, M.-Ha, and Kim, B. J. (2017). Comparison of recombinant human bone morphogenetic protein-2-infused absorbable collagen sponge, recombinant human bone morphogenetic protein-2-coated tricalcium phosphate, and platelet-rich fibrin-mixed tricalcium phosphate for sinus augmentation in rabbits. *J. Dent. Sci.* 12 (3), 205–212. doi:10.1016/j.jds.2017.01.003

Knüppel, L., Ishikawa, Y., Aichler, M., Heinzelmann, K., Hatz, R., Behr, J., et al. (2017). A novel antifibrotic mechanism of nintedanib and pirfenidone. Inhibition of collagen fibril assembly. *Am. J. Respir. Cell Mol. Biol.* 57 (1), 77–90. doi:10.1165/rcmb.2016-0217oc

Koehler, J., Brandl, F. P., and Goepferich, A. M. (2018). Hydrogel wound dressings for bioactive treatment of acute and chronic wounds. *Eur. Polym. J.* 100, 1–11. doi:10.1016/j.eurpolymj.2017.12.046

Kong, B., Sun, L., Liu, R., Chen, Y., Shang, Y., Tan, H., et al. (2022). Recombinant human collagen hydrogels with hierarchically ordered microstructures for corneal stroma regeneration. *Chem. Eng. J.* 428, 131012. doi:10.1016/j.cej.2021.131012

Koons, G. L., Diba, M., and Antonios, G. (2020). Materials design for bone-tissue engineering. *Nat. Rev. Mater. Mikos* 5 (8), 584–603. doi:10.1038/s41578-020-0204-2

Kuivaniemi, H., and Tromp, G. (2019). Type iii collagen (Col3a1): gene and protein structure, tissue distribution, and associated diseases. *Gene* 707, 151–171. doi:10.1016/j.gene.2019.05.003

Lagali, N. (2020). Corneal stromal regeneration: current status and future therapeutic potential. *Curr. Eye Res.* 45 (3), 278–290. doi:10.1080/02713683.2019.1663874

Las Heras, K., Igartua, M., Santos-Vizcaino, E., and Hernandez, R. M. (2020). Chronic wounds: current status, available strategies and emerging therapeutic solutions. *J. Control. Release* 328, 532–550. doi:10.1016/j.jconrel.2020.09.039

Law, J. X., Liau, L. L., Saim, A., Yang, Y., and Idrus, R. (2017). Electrospun collagen nanofibers and their applications in skin tissue engineering. *Electrospun Collagen Nanofibers Their Appl. Skin Tissue Eng.* 14, 699–718. doi:10.1007/s13770-017-0075-9

Lee, ARHA, Hudson, A. R., Shiwarski, D. J., Tashman, J. W., Hinton, T. J., Yerneni, S., et al. (2019). 3d bioprinting of collagen to rebuild components of the human heart. *Science* 365, 6452, 482–487. doi:10.1126/science.aav9051

Li, J., Zhang, Y.-J., Lv, Z.-Y., Liu, K., Meng, C.-X., Zou, Bo, et al. (2020). The observed difference of macrophage phenotype on different surface roughness of mineralized collagen. *Regen. Biomater.* 7 (2), 203–211. doi:10.1093/rb/rbz053

Lim, Y.-S., Ye-Jin, Ok, Hwang, S.-Y., Kwak, J.-Y., and Yoon, S. (2019). Marine collagen as a promising biomaterial for biomedical applications. *Mar. drugs* 17 (8), 467. doi:10.3390/md17080467

Lin, K., Zhang, D., Helena Macedo, M., Cui, W., Bruno, S., and Guofang, S. (2019). Advanced collagen-based biomaterials for regenerative biomedicine. *Adv. Funct. Mater.* 29 (3), 1804943. doi:10.1002/adfm.201804943

Liverani, C., Mercatali, L., Cristofolini, L., Giordano, E., Minardi, S., Della Porta, G., et al. (2017). Investigating the mechanobiology of cancer cell–ECM interaction through collagen-based 3D scaffolds. *Cell. Mol. Bioeng.* 10, 223–234. doi:10.1007/s12195-017-0483-x

Ma, L., Liang, X., Yu, S., and Zhou, J. (2022). Expression, characterization, and application potentiality evaluation of recombinant human-like collagen in pichia pastoris. *Bioresour. Bioprocess.* 9 (1), 119–215. doi:10.1186/s40643-022-00606-3

Magro, M. G., Carlos Kuga, M., Adad Ricci, W., Cristina Keine, K., Rodrigues Tonetto, M., Linares Lima, S., et al. (2017). Endodontic management of open apex teeth using lyophilized collagen sponge and mta cement: report of Two cases. *Iran. Endod. J.* 12 (2), 248–252. doi:10.22037/iej.2017.48

Martyniak, K., Lokshina, A., Cruz, M. A., Karimzadeh, M., Kemp, R., and Thomas, J. (2022). Biomaterial composition and stiffness as decisive properties of 3D bioprinted constructs for type II collagen stimulation. *Acta Biomater.* 152, 221–234. doi:10.1016/j.actbio.2022.08.058

Matai, I., Kaur, G., Amir, S., McClinton, A., and Laurencin, C. T. B. (2020). Progress in 3d bioprinting technology for tissue/organ regenerative engineering. *Biomaterials* 226: 119536. doi:10.1016/j.biomaterials.2019.119536

Mathew-Steiner, S. S., Roy, S., and Chandan, K. S. (2021). Collagen in wound healing. *Bioeng. (Basel).* 8 (5), 63. doi:10.3390/bioengineering8050063

McPhail, M. J., Janus, J. R., and Lott, D. G. (2020). Advances in regenerative medicine for otolaryngology/head and neck surgery. *BMJ* 29, 369. doi:10.1136/bmj.m718

Meng, D., Tanaka, H., Kobayashi, T., Hatayama, H., Zhang, Xi, Ura, K., et al. (2019). The effect of alkaline pretreatment on the biochemical characteristics and fibril-forming abilities of types I and II collagen extracted from bester sturgeon by-products. *Int. J. Biol. Macromol.* 131, 572–580. doi:10.1016/j.ijbiomac.2019.03.091

Meyer, M. (2019), Processing of collagen based biomaterials and the resulting materials properties. *Biomed Eng Online* 18, 1: 1–74. doi:10.1186/s12938-019-0647-0

Mi, Yu, Gao, Y., Fan, D., Duan, Z., Fu, R., Liang, L., et al. (2018). Stability improvement of human collagen α1(I) chain using insulin as a fusion partner. *Chin. J. Chem. Eng.* 26 (12), 2607–2614. doi:10.1016/j.cjche.2018.04.008

Minor, A. J., and Kareen, L. K. (2020). Engineering a collagen matrix for cell-instructive regenerative angiogenesis. *J. Biomed. Mater Res. B Appl. Biomater.* 108 (6), 2407–2416. doi:10.1002/jbm.b.34573

Muhonen, V., Narcisi, R., Nystedt, J., Korhonen, M., van Osch, G. J. V. M., and Kiviranta, I. (2017). Recombinant human type ii collagen hydrogel provides a xeno-free 3d micro-environment for chondrogenesis of human bone marrow-derived mesenchymal stromal cells. *J. Tissue Eng. Regen. Med.* 11 (3), 843–854. doi:10.1002/term.1983

Muthusamy, S., Kannan, S., Lee, M., Sanjairaj, V., Lu, W. F., Fuh, J. Y. H., et al. (2021). 3D bioprinting and microscale organization of vascularized tissue constructs using collagen-based bioink. *Biotechnol. Bioeng.* 118 (8), 3150–3163. doi:10.1002/bit.27838

Naomi, R., Ridzuan, P. M., and Polymers Bahari, H. (2021). Current insights into collagen type I. *Polym. (Basel).* 13 (16), 2642. doi:10.3390/polym13162642

Nguyen, T.-U., Watkins, K. E., and Kishore, V. (2019). Photochemically crosslinked cell-laden methacrylated collagen hydrogels with high cell viability and functionality. *J. Biomed. Mat. Res. A* 107 (7), 1541–1550. doi:10.1002/jbm.a.36668

Nocera, A. D., Comín, R., Salvatierra, N. A., and Paula Cid, M. (2018). Development of 3d printed fibrillar collagen scaffold for tissue engineering. *Biomed. Microdevices* 20, 26–13. doi:10.1007/s10544-018-0270-z

Osidak, E. O., Vadim Igorevich, K., Mariya Sergeevna, O., and Sergey Petrovich, D. (2020). Collagen as bioink for bioprinting: a comprehensive review. *Int. J. Bioprint.* 6 (3), 270. doi:10.18063/ijb.v6i3.270

Parmar, P. A., Jean-Philippe St-Pierre, L. W. C., Spicer, C. D., Stoichevska, V., Peng, Y. Y., Werkmeister, J. A., et al. (2017). Enhanced articular cartilage by human mesenchymal stem cells in enzymatically mediated transiently RGDS-functionalized collagen-mimetic hydrogels. *Acta Biomater.* 51, 75–88. doi:10.1016/j.actbio.2017.01.028

Quinlan, E., López-Noriega, A., Thompson, E. M., Hibbitts, A., Cryan, S. A., and O'Brien, F. J. (2017). Controlled release of vascular endothelial growth factor from spray-dried alginate microparticles in collagen-hydroxyapatite scaffolds for promoting vascularization and bone repair: functionalized CHA scaffolds for controlled release of VEGF to enhance bone repair. *J. Tissue Eng. Regen. Med.* 11 (4), 1097–1109. doi:10.1002/term.2013

Radke, D., Jia, W., Sharma, D., Fena, K., Wang, G., Goldman, J., et al. (2018). Tissue engineering at the blood-contacting surface: a review of challenges and strategies in vascular graft development. *Adv. Healthc. Mater.* 7 (15), 1701461. doi:10.1002/adhm.201701461

Ramírez-Rodríguez, G. B., Montesi, M., Panseri, S., Sprio, S., and Sandri, M. (2017). Biomineralized recombinant collagen-based scaffold mimicking native bone enhances mesenchymal stem cell interaction and differentiation. *Tissue Eng. Part A* 23 (23-24), 1423–1435. doi:10.1089/ten.tea.2017.0028

Rappu, P., M Salo, A., Myllyharju, J., and Heino, J. (2019). Role of prolyl hydroxylation in the molecular interactions of collagens. *Essays Biochem.* 63 (3), 325–335. doi:10.1042/ebc20180053

Rashedi, I., Talele, N., Wang, X.-H., Hinz, B., Radisic, M., and Keating, A. (2017). Collagen scaffold enhances the regenerative properties of mesenchymal stromal cells. *PLoS ONE* 12 (10), e0187348. doi:10.1371/journal.pone.0187348

Rico-Llanos, G. A., Borrego-González, S., Moncayo-Donoso, M., Becerra, J., and Visser, R. (2021). Collagen type I biomaterials as scaffolds for bone tissue engineering. *Polym. (Basel).* 13 (4), 599. doi:10.3390/polym13040599

Rittié, L. (2017), Type I collagen purification from rat tail tendons. *Methods Mol Biol* 1627, 287–308. doi:10.1007/978-1-4939-7113-8_19

Roshanbinfar, K., Kolesnik-Gray, M., Angeloni, M., Schruefer, S., Fiedler, M., Schubert, D. W., et al. (2023). Collagen hydrogel containing polyethylenimine-gold nanoparticles for drug release and enhanced beating properties of engineered cardiac tissues. *Adv. Healthc. Mater.* 12, 2202408. doi:10.1002/adhm.202202408

Sarrigiannidis, S. O., Rey, J. M., Dobre, O., González-García, C., J Dalby, M., and Salmeron-Sanchez, M. (2021). A tough act to follow: collagen hydrogel modifications to improve mechanical and growth factor loading capabilities. *Mat. Today Bio* 10, 100098. doi:10.1016/j.mtbio.2021.100098

Sheehy, E. J., Cunniffe, G. M., and O'Brien, F. J. (2018). "Collagen-based biomaterials for tissue regeneration and repair," in *Peptides and proteins as biomaterials for tissue regeneration and repair* (Elsevier), 127-50.

Shekhter, A. B., Fayzullin, A. L., Vukolova, M. N., Rudenko, T. G., Osipycheva, V. D., and Litvitsky, P. F. (2019). Medical applications of collagen and collagen-based materials. *Curr. Med. Chem.* 26 (3), 506–516. doi:10.2174/0929867325666171205170339

Shuai, X., Kang, N., Li, Y., Bai, M., Zhou, X., Zhang, Y., et al. (2023). Recombination humanized type iii collagen promotes oral ulcer healing. *Oral Dis.* doi:10.1111/odi.14540

Song, K.-Mo, Jung, S. K., Kim, Y.Ho, Kim, Y. E., and Hyouck Lee, N., (2018). Development of industrial ultrasound system for mass production of collagen and biochemical characteristics of extracted collagen. *Food Bioprod. Process.*, 110, 96–103. doi:10.1016/j.fbp.2018.04.001

Stepanovska, J., Supova, M., Hanzalek, K., Broz, A., and Matejka, R. (2021). Collagen bioinks for bioprinting: a systematic review of hydrogel properties, bioprinting parameters, protocols, and bioprinted structure characteristics. *Biomedicines* 9 (9), 1137. doi:10.3390/biomedicines9091137

Strauss, K., and Chmielewski, J. (2017). Advances in the design and higher-order assembly of collagen mimetic peptides for regenerative medicine. *Curr. Opin. Biotechnol.* 46, 34–41. doi:10.1016/j.copbio.2016.10.013

Su, J., Li, J., Liang, J., Zhang, K., and Li, J. (2021). Hydrogel preparation methods and biomaterials for wound dressing. *Life* 11 (10), 1016. doi:10.3390/life11101016

Sun, L., Gao, W., Fu, X., Shi, M., Xie, W., Zhang, W., et al. (2018). Enhanced wound healing in diabetic rats by nanofibrous scaffolds mimicking the basketweave pattern of collagen fibrils in native skin. *Biomater. Sci.* 6 (2), 340–349. doi:10.1039/c7bm00545h

Tang, M., Rich, J. N., and Chen, S. (2021). Biomaterials and 3d bioprinting strategies to model glioblastoma and the blood–brain barrier. *Adv. Mater.* 33 (5), 2004776. doi:10.1002/adma.202004776

Thapa, R. K., Margolis, D. J., Kiick, K. L., and Millicent, O. (2020). Enhanced wound healing via collagen-turnover-driven transfer of PDGF-BB gene in a murine wound model. *ACS Appl. Bio Mat.* 3 (6), 3500–3517. doi:10.1021/acsabm.9b01147

Tytgat, L., Agnes Dobos, A, Markovic, M., Lana Van Damme, Van Hoorick, J., Bray, F., et al. (2020). High-resolution 3d bioprinting of photo-cross-linkable recombinant collagen to serve tissue engineering applications. *Biomacromolecules* 21 (10), 3997–4007. doi:10.1021/acs.biomac.0c00386

Wang, C., Brisson, B. K., Terajima, M., Li, Q., Hoxha, K., Han, B., et al. (2020). Type III collagen is a key regulator of the collagen fibrillar structure and biomechanics of

articular cartilage and meniscus. *Matrix Biol.* 85, 47–67. doi:10.1016/j.matbio.2019.10.001

Wang, H. (2021). A review of the effects of collagen treatment in clinical studies. *Polym. (Basel).* 13 (22), 3868. doi:10.3390/polym13223868

Wang, J., Hu, H., Wang, J., He, Q., Gao, Y., Xu, Y., et al. (2022). Characterization of recombinant humanized collagen type iii and its influence on cell behavior and phenotype. *John J. Leather Sci. Ramshaw, Eng.* 4 (1), 33. doi:10.1186/s42825-022-00103-5

Włodarczyk-Biegun, M. K., and Del Campo, A. (2017). 3D bioprinting of structural proteins. *Biomaterials* 134, 180–201. doi:10.1016/j.biomaterials.2017.04.019

Woodley, D. T., Cogan, J., Hou, Y., Lyu, C., Marinkovich, M. P., Keene, D., et al. (2017). Gentamicin induces functional type VII collagen in recessive dystrophic epidermolysis bullosa patients. *J. Clin. Invest.* 127 (8), 3028–3038. doi:10.1172/jci92707

Xia, H., Li, X., Gao, W., Fu, X., Fang, R. H., Zhang, L., and Zhang, K. (2018). Tissue repair and regeneration with endogenous stem cells. *Nat. Rev. Mat.* 3 (7), 174–193. doi:10.1038/s41578-018-0027-6

Xu, L., Liu, Y., Tang, L., Xiao, H., Yang, Z., and Wang, S. (2022). Preparation of recombinant human collagen iii protein hydrogels with sustained release of extracellular vesicles for skin wound healing. *Int. J. Mol. Sci.* 23 (11), 6289. doi:10.3390/ijms23116289

Yang, Li, Wu, H., Lu, Lu, He, Q., Xi, B., Yu, H., et al. (2021b). A tailored extracellular matrix (Ecm)-Mimetic coating for cardiovascular stents by stepwise assembly of hyaluronic acid and recombinant human type iii collagen, *Biomaterials* 276, 121055. doi:10.1016/j.biomaterials.2021.121055

Yang, Y., and Ritchie, A. C. (2021a). Recombinant human collagen/chitosan-based soft hydrogels as biomaterials for soft tissue engineering. *Mater Sci Eng C Mater Biol Appl.* 121, 111846. doi:10.1016/j.msec.2020.111846

Yang, Y., Wang, Z., Xu, Y., Xia, J., Xu, Z., Zhu, S., et al. (2022a). Preparation of chitosan/recombinant human collagen-based photo-responsive bioinks for 3d bioprinting. *Gels* 8 (5), 314. doi:10.3390/gels8050314

Yang, Y., Xu, R., Wang, C., Guo, Y., Sun, W., and Ouyang, L. (2022b). Recombinant human collagen-based bioinks for the 3D bioprinting of full-thickness human skin equivalent. *Int. J. Bioprinting* 4, 18.

Zhang, D., Wu, X., Chen, J., and Lin, K. (2018b). The development of collagen based composite scaffolds for bone regeneration. *Bioact. Mat.* 3 (1), 129–138. doi:10.1016/j.bioactmat.2017.08.004

Zhang, N., Cheng, Y., Hu, X., and Yeo, J. (2019). Toward rational algorithmic design of collagen-based biomaterials through multiscale computational modeling. *Curr. Opin. Chem. Eng.* 24, 79–87. doi:10.1016/j.coche.2019.02.011

Zhang, W., Bai, X., Zhao, B., Li, Y., Zhang, Y., Li, Z., et al. (2018a). Cell-free therapy based on adipose tissue stem cell-derived exosomes promotes wound healing via the PI3K/Akt signaling pathway. *Exp. Cell Res.* 370 (2), 333–342. doi:10.1016/j.yexcr.2018.06.035

Zhang, Yi, Kumar, P., Lv, S., Xiong, Di, Zhao, H., Cai, Z., et al. (2021). Recent advances in 3D bioprinting of vascularized tissues. *Recent Adv. 3d Bioprinting Vasc. Tissues* 199, 109398. doi:10.1016/j.matdes.2020.109398

Zhang, Yu S., Kan, Y., Aleman, J., Mollazadeh-Moghaddam, K., Mahwish Bakht, S., Yang, J., et al. (2017). 3d bioprinting for tissue and organ fabrication. *Ann. Biomed. Eng.* 45, 148–163. doi:10.1007/s10439-016-1612-8

frontiers | Frontiers in Bioengineering and Biotechnology

TYPE Original Research
PUBLISHED 21 March 2024
DOI 10.3389/fbioe.2024.1357056



OPEN ACCESS

EDITED BY
Oommen Podiyan Oommen,
Tampere University, Finland

REVIEWED BY
Stephane Avril,
Institut Mines-Télécom, France
Yonghui Qiao,
Northwestern Polytechnical University, China

*CORRESPONDENCE
Jianbo Li,
100390@cqmu.edu.cn

RECEIVED 17 December 2023
ACCEPTED 07 March 2024
PUBLISHED 21 March 2024

CITATION
Chen H, Zhao M, Li Y, Wang Q, Xing Y, Bian C and Li J (2024), A study on the ultimate mechanical properties of middle-aged and elderly human aorta based on uniaxial tensile test.
*Front. Bioeng. Biotechnol.* 12:1357056.
doi: 10.3389/fbioe.2024.1357056



# A study on the ultimate mechanical properties of middle-aged and elderly human aorta based on uniaxial tensile test

Hongbing Chen[1,2,3], Minzhu Zhao[1,2,3], Yongguo Li[1,2,3], Qi Wang[1,2,3], Yu Xing[1,2,3], Cunhao Bian[1,2,3] and Jianbo Li[1,2,3]*

[1]Department of Forensic Medicine, College of Basic Medicine, Chongqing Medical University, Chongqing, China, [2]Chongqing Engineering Research Center for Criminal Investigation Technology, Chongqing, China, [3]Chongqing Key Laboratory of Forensic Medicine, Chongqing, China

**Background:** The mechanical properties of the aorta are particularly important in clinical medicine and forensic science, serving as basic data for further exploration of aortic disease or injury mechanisms.

**Objective:** To study the influence of various factors (age, gender, test direction, anatomical location, and pathological characteristics) on the mechanical properties and thickness of the aorta.

**Methods:** In this study, a total of 24 aortas (age range: 54–88 years old) were collected, one hundred and seventy-four dog-bone-shaped samples were made, and then the uniaxial tensile test was run, finally, pathological grouping was performed through histological staining.

**Results:** Atherosclerotic plaques were mainly distributed near the openings of blood vessel branches. The distribution was most severe in the abdominal aorta, followed by the aortic arch. Aortic atherosclerosis was a more severe trend in the male group. In the comparison of thickness, there were no significant differences in age (over 50 years) and test direction, the average thickness of the aorta was greater in the male group than the female group and decreased progressively from the ascending aorta to the abdominal aorta. Comparing the mechanical parameters, various parameters are mainly negatively correlated with age, especially in the circumferential ascending aorta ($\varepsilon_p$ "$Y = -0.01402*X + 1.762$, $R^2 = 0.6882$", $\varepsilon_t$ "$Y = -0.01062*X + 1.250$, $R^2 = 0.6772$"); the parameters of males in the healthy group were larger, while the parameters of females were larger in atherosclerosis group; the aorta has anisotropy, the parameters in the circumferential direction were greater than those in the axial direction; the parameters of the ascending aorta were the largest in the circumferential direction, the ultimate stress [$\sigma_p$ "1.69 (1.08,2.32)"] and ultimate elastic modulus [$E_2$"8.28 (6.67,10.25)"] of the abdominal aorta were significantly larger in the axial direction; In the circumferential direction, the stress [$\sigma_p$ "2.2 (1.31,3.98)", $\sigma_t$ "0.13 (0.09,0.31)"] and ultimate elastic modulus ($E_2$ "14.10 $\pm$ 7.21") of adaptive intimal thickening were greater than those of other groups, the strain ($\varepsilon_p$ "0.82 $\pm$ 0.17", $\varepsilon_t$ "0.53 $\pm$ 0.14") of pathological intimal thickening was the largest in the pathological group.

**Conclusion:** The present study systematically analyzed the influence of age, sex, test direction, anatomical site, and pathological characteristics on the biomechanical properties of the aorta, described the distribution of aortic

atherosclerosis, and illustrated the characteristics of aortic thickness changes. At the same time, new insights into the grouping of pathological features were presented.

KEYWORDS

**human aorta, uniaxial tensile test, material properties, pathology, atherosclerosis**

# 1 Introduction

The aorta, the largest blood vessel in the human body, is rich in multiple layers of elastic membranes and many elastic fibers (Sokolis, 2007). The anatomy of the aorta influences how well it functions. Atherosclerosis (AS) is the result of the aorta's constant growth, aging, blood flow, or other diseases. These factors alter the aorta's structure, particularly the breakdown or damage of elastic fibers and the proliferation of collagen fibers, which narrows the lumen and hardens the wall of the artery, and increases the risk of other cardiovascular diseases (aneurysm, arterial dissection, intramural hematoma, etc (Mussa et al., 2016; Herrington et al., 2018)). The death rate in forensic cases involving aortic rupture can reach 80%–94% (Ye et al., 2022). In particular, the co-occurrence of external violence and pathological tissue changes complicates cases of death from aortic rupture following traffic accidents or medical mishaps.

The biomechanical properties of the aorta are indispensable data for establishing a finite element model of the aorta (Garcia–Herrera et al., 2016) and performing computational hemodynamics based on fluid-structure interaction (Qiao et al., 2023). In addition, it provides important basic data in clinical surgical treatment and biomaterial development (Sherifova and Holzapfel, 2019). The current research is based on *in vitro* mechanical testing (for example, uniaxial tension (Franchini et al., 2021), biaxial tension (Pukaluk et al., 2022), peeling test (Myneni et al., 2020), bulge inflation tests (Romo et al., 2014), etc.) to evaluate the mechanical properties of the aorta. Uniaxial tensile testing is one of the most commonly used methods. Its advantages include loose test conditions, many types of test samples (for example,: brain tissue (Zwirner et al., 2020), lungs (Bel-Brunon et al., 2014), trachea (Teng et al., 2012), liver (Estermann et al., 2021), etc.), and relatively simple operation (Li et al., 2023). Some researchers prepared the aorta as a long strip for tensile testing (Kobielarz et al., 2020; Franchini et al., 2021), but Yi-Jiu Chen et al. confirmed that dog bone-shaped samples are better suited for tensile testing (Pei et al., 2021). Numerous academics have examined the aorta's mechanical properties from a variety of perspectives, including age (Haskett et al., 2010), gender (Sokolis et al., 2017), pathological features (Bai et al., 2018), different segments (Peña et al., 2019), and test directions (axial and circumferential) (Franchini et al., 2021; Polzer et al., 2021), and so forth.

Some studies summarised the variability in previous test results (Walsh et al., 2014; Sherifova and Holzapfel, 2019), and a lack of systematic research due to the absence of uniform test standards in earlier studies (such as the geometric shape of the sample, etc.). In addition, Fewer studies have provided a more detailed description of the mechanical properties of the aorta in middle-aged and elderly people. At the same time, we provide new insights into the pathological grouping of the aorta, which may provide some reference value for subsequent studies.

Based on the above issues. The current study used a fresh aorta removed during autopsy. Basic data, such as age and sex, was then gathered. The aorta was first observed grossly morphologically. Next, samples of the aorta were taken in two directions (circumferential and axial) from four anatomical regions: the ascending aorta, aortic arch, thoracic aorta, and abdominal aorta. Then, a thickness measurement was taken on a dog bone-type sample, and a uniaxial tensile test was conducted. Histological staining was used to classify the aorta into four groups: Normal, Adaptive intimal thickening, Pathological Intimal thickening, and Fibrous atherosclerosis group. Finally, statistical analysis was carried out.

# 2 Materials and methods

## 2.1 Specimen collection

This study was approved by the Ethics Committee of Chongqing Medical University and informed consent was given by the deceased's next of kin.

The aorta (death within 24 h, no aortic disease, and intact aortic structure) and pertinent information were obtained from the autopsy of the Forensic Medicine Department of Chongqing Medical University (Chongqing Forensic Injury Examination Institute). The entire aorta was collected and transferred to the laboratory in a crisper box with phosphate buffer at an internal temperature of 4°C–5°C.

## 2.2 Uniaxial tensile test

### 2.2.1 Tensile test configuration

The tensile test was carried out using an electronic universal material testing machine that was controlled by a microcomputer (Figure 1). A buffer strip with a frosted paper strip was adhered to the inside of the clamp to lessen the force the clamp applied to the sample and its tendency to slip. In operation, the upper clamp stretches until the sample breaks at a quasi-static speed of 4 mm/min after going through three preconditioning cycles (about 5% stretching at a speed of 4 mm/min) to get rid of the hysteresis effect.

Before the test, the adventitia's surrounding connective tissue was cut away, and aortic branch vessel openings were avoided, 174 dog-bone-shaped samples (where "N" denotes the number of samples) were created using a stamping die. Use a vernier caliper (accurate to 0.01 mm) to measure the original thickness (measure three times, taking the average value), the clamp clamped both ends of the sample and started running. The fracture near the middle of the sample was judged as a valid sample (Figure 2C) (Loree et al.,

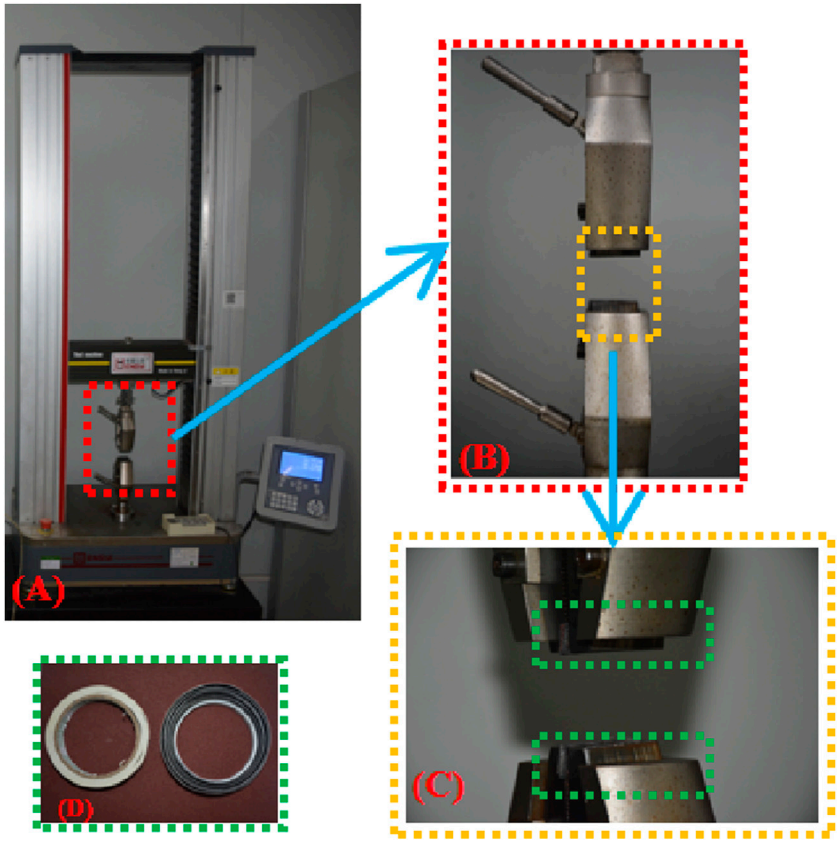


FIGURE 1
**(A)** Axial tensile test platform; **(B)** Clamp; **(C)** Buffer strip added inside the clamp; **(D)** Buffer strip material.

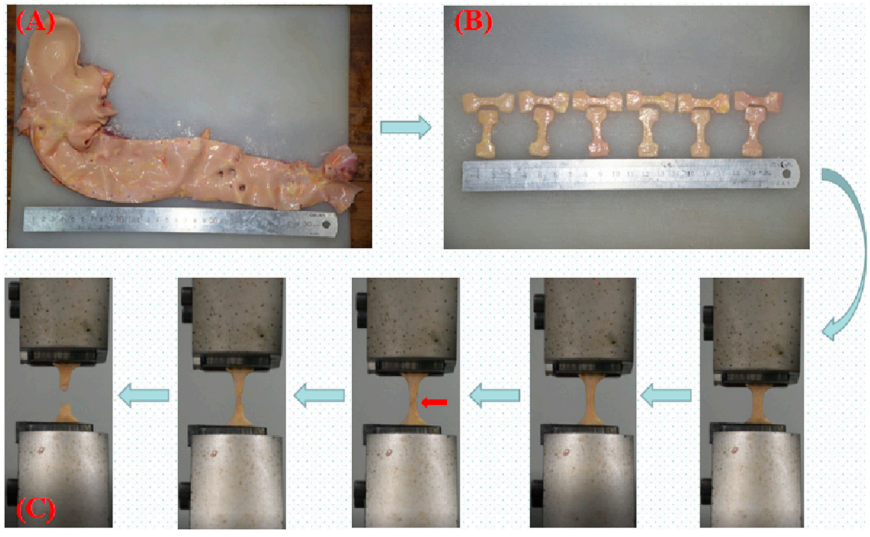


FIGURE 2
**(A)** Complete aorta; **(B)** Dog bone-shaped aorta sample; **(C)** Uniaxial tensile test process; the red arrow indicates the beginning of intimal rupture.

1994; Pei et al., 2021), there were 156 valid samples (accounting for 89.66%). The number of samples in each group is shown in Table 1. The test was completed within 48 h (Walsh et al., 2014).

### 2.2.2 Test data processing

We depict the real stress-strain because it more accurately captures the dynamic mechanical properties of the sample in real time. The

TABLE 1 Number of samples in each group.

| Factor | Group | N |
|---|---|---|
| Age | Range (54-88 years) | 156 |
| Gender | Male | 98 |
| | Female | 58 |
| Anatomic Location | Ascending Aorta | 21 |
| | Aortic Arch | 40 |
| | Thoracic Aorta | 54 |
| | Abdominal Aorta | 41 |
| Direction | Circumferential | 80 |
| | Longitudinal | 76 |
| Anatomic Location | Normal | 32 |
| | Adaptive Intimal Thickening | 16 |
| | Pathological Intimal Thickening | 68 |
| | Fibrous Atherosclerosis | 40 |

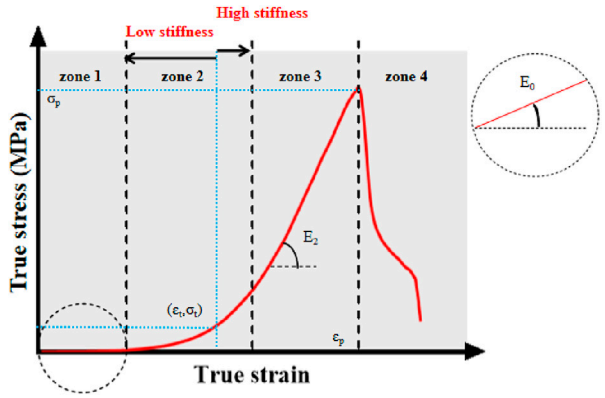


FIGURE 3
True stress-strain curve. Note: $\sigma_p$-ultimate stress; $\varepsilon_p$-ultimate strain; $E_2$-ultimate modulus of elasticity; $\sigma_t$-middle stress point; $\varepsilon_t$-middle strain point; $E_0$-starting modulus of elasticity. Zone 1, 2, 3, and four denote the starting, transition, strengthening, and failure phases of the aortic tensile test, respectively.

stress, strain, and elastic modulus at each stage can be obtained using a curve graph (Figure 3). We depict the real stress-strain because it more accurately captures the dynamic mechanical properties of the sample.

The raw data (load $F$, displacement $L1$) are processed to obtain the true stress and strain.

The specific processing is as follows:

Assuming that the aortic tissue is incompressible (Chuong and Fung, 1983; Wang et al., 2023), the sample initial thickness $T0$, width $W0$, length $L0$, the sample thickness $T$, width $W$, length $L$ during stretching, then:

$$L = L0 + L1 \tag{1}$$

$$W0 \cdot T0 \cdot L0 = W \cdot T \cdot L \tag{2}$$

The initial cross-sectional area $A0$ and the current cross-sectional area $A$, then:

$$A0 \cdot L0 = A \cdot L \tag{3}$$

$$A0 = W0 \cdot T0 \tag{4}$$

$$A = \frac{A0 \cdot L0}{L} \tag{5}$$

The true stress is the ratio of the current load to the current cross-sectional area and is mathematically formulated as:

$$\sigma T = \frac{F}{A} = \frac{FL}{A0 \cdot L0} \tag{6}$$

The true strain is the natural logarithm of the ratio of the current length to the initial length, and its mathematical formula is:

$$\varepsilon T = ln\left(\frac{L}{L0}\right) \tag{7}$$

The modulus of elasticity is the stress required for the elastic deformation of a material produced by an external force. It is an indicator of the material's ability to resist elastic deformation, usually expressed as $E$. The modulus of elasticity is a measure of the material's ability to resist elastic deformation. The bigger the value, the more rigid the material is and the more stress it experiences during a certain elastic deformation. Defined as the ratio of stress to strain in the elastic deformation stage of a material:

$$E = \frac{d\sigma T}{d\varepsilon T} \tag{8}$$

The graph has four stages. In the first, alterations in elastic fibers predominate when subjected to physiological stresses. During the transition stage, the slope gradually increases as collagen fibers engage in the activity, indicating hyperelasticity (Li et al., 2023; Wang et al., 2023); during the reinforcing stage, the slope reaches its maximum and the collagen fibers provide their greatest effect; during the failure stage, the sample completely shreds as the ultimate load is met (Utrera et al., 2022).

The middle variables ($\sigma_t$, $\varepsilon_t$) are obtained based on the first order derivatives of the ture stress-strain curves ($d\sigma T/d\varepsilon T$). In this curve, the midpoint of the transition zone is defined in this study as the middle variable (García-Herrera et al., 2012).

## 2.3 Histological staining and classification

After testing, the samples were put in an embedding box and fixed for 24 h with 10% formalin added. After paraffin slices (4 μm in thickness) were made, they were stained with HE (hematoxylin and epoxy resin), which showed red coloration of the cytoplasm as well as the extracellular matrix, and bluish-purple coloration of the chromatin in the nucleus and nucleic acids in the cytoplasm as well as the calcium deposit under a light microscope.

Previous studies have taken tissue from neighboring samples for histological staining (Kobielarz et al., 2020; Pukaluk et al., 2022), whereas there may be different pathological features between the sample and the neighboring area or in different areas of the same sample (Figure 4). Therefore, we observed the pathological features of the samples by taking the broken end of the sample as the weakest point and then grouped them according to the development of atherosclerosis (normal group, adaptive intimal thickening group,

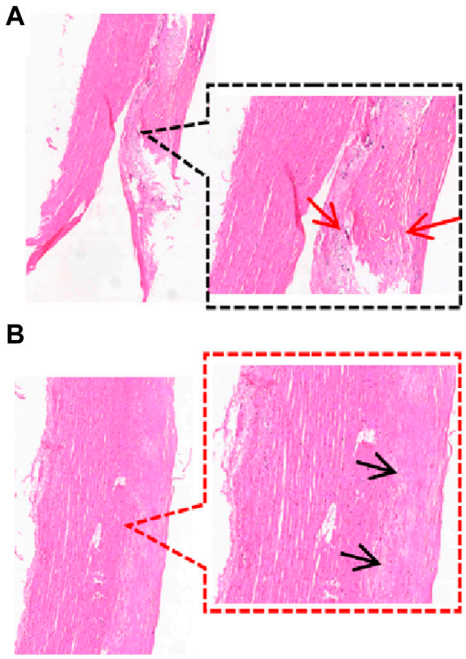


FIGURE 4
Different regions of a sample. **(A)** The sample's broken end exhibits thickening of the intimal collagen fibers, calcium salt deposits, cholesterol crystals under the fibrous cap (HE staining reveals needle cracks), and foam cell formation within the necrotic core (red arrows), defined as fibrillary atherosclerosis; **(B)** The sample's mid-section exhibits thickening of the intima of, with the presence of acellular lipid pools in the intima, and near the media where lipid deposition and proteoglycans are abundant but SMCs are absent (black arrows), defined as pathological intimal thickening. (HE staining, 40×, 80×).

pathological intimal thickening group, fibrous atherosclerosis group) (Otsuka et al., 2014; Jing et al., 2022) (Figure 5).

# 3 Statistical analysis

SPSS 24.0 software was used for statistical analysis and Graphpad Prim9 for plotting. Mean ± standard deviation (Mean ± SD) was used for normally distributed measures, and median (interquartile range) [M(P25, P75)] was used for non-normally distributed measures; t-test or Mann-Whitney U-test was used for comparisons between two groups; one-way ANOVA or Kruskal-Wallis test was used for comparisons between three or more groups; Indicators with significant differences were tested by LSD multiple comparisons or Kruskal-Wallis pairwise comparison test; regression analysis was carried out by linear regression method; when a *p*-value was less than 0.05, it was assumed to be significant, and was denoted by "*", "**" indicates $p \leq 0.01$, and "***" indicates $p \leq 0.001$.

# 4 Results

## 4.1 Gross morphological observations

The pathological alterations in the aortic intima are shown in Figure 6. We found that the distribution of the segments was most severe in the abdominal aorta, followed by the aortic arch, and least severe in the ascending aorta. Atherosclerotic plaques were mostly seen in the openings of the vascular branches, particularly at the left subclavian artery opening and at the branches of the common iliac artery. When comparing the two genders, males had a more severe tendency of aortic atherosclerosis (Figure 7).

## 4.2 Comparison of thickness

Between age and thickness, there is no discernible linear connection. Comparisons of thicknesses between anatomical locations, test orientations, and genders are shown in Figure 8. The axial and circumferential directions do not significantly differ from one another. Males' average thickness was noticeably higher than females' when it came to gender. The abdominal aorta is substantially thinner than the aortas in other anatomical regions, and the aorta thickness gradually declines from the proximal to the distal end.

## 4.3 The relationship between age and parameters

There is a negative correlation between age and several parameters in different anatomical regions. The most significant one is strain ($\varepsilon_p$, $\varepsilon_t$), which means that as age increases, strain gradually decreases (Figure 9), especially in the circumferential ascending aorta ($\varepsilon_p$ "$Y = -0.01402*X + 1.762$, $R^2 = 0.6882$", $\varepsilon_t$ "$Y = -0.01062*X + 1.250$, $R^2 = 0.6772$"). In the axial direction of the ascending aorta, age is related to stress ($\sigma_p$ "$Y = -0.02607*X + 3.018$, $R^2 = 0.3557$", $\sigma_t$ "$Y = -0.005977*X + 0.8938$, $R^2 = 0.5066$") and elastic modulus ($E_2$ "$Y = -0.1346*X + 14.82$, $R^2 = 0.5125$", $E_0$ "$Y = -0.001010*X + 0.1091$, $R^2 = 0.4545$").

## 4.4 Comparison of parameters for different genders

The influence of gender on mechanical characteristics in various orientations at various anatomical regions is shown in Figure 10. In general, females exhibit more dominance, as evidenced by statistically significant differences in stress ($\sigma_p$, $\sigma_t$) and ultimate modulus of elasticity ($E_2$). The gender differences were more significant in the circumferential direction of the ascending aorta ($\sigma_p$ "3.25 ± 0.59", $\sigma_t$ "0.23 ± 0.11", $E_2$ "20.28 ± 3.74"), and in the axial direction of the aortic arch [$\sigma_p$ "1.28 ± 0.33", $\sigma_t$ "0.07 (0.06,0.12)", $E_2$ "7.09 ± 1.87"]. In addition, we separated into normal and atherosclerotic groups to compare the parameters between genders (Table 2). In the normal group, the parameters were greater in males, ultimate stress [$\sigma_p$ "1.20 (1.00,1.85)"] and ultimate strain ($\varepsilon_p$ "0.76 ± 0.13") were the most significant differences, while in the atherosclerotic group, the parameters were greater in females, and all parameters have significant differences [except initial modulus of elasticity ($E_0$) and ultimate strain ($\varepsilon_p$)].

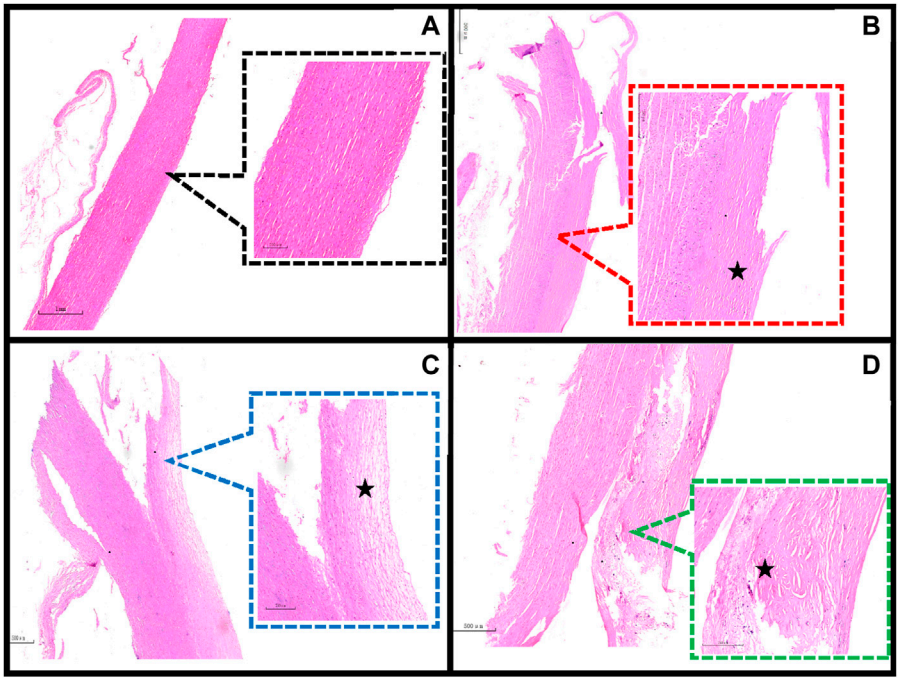


FIGURE 5
Classification of the main pathological features in the region of the sample dissection. **(A)** Normal aorta (20×, 80×); **(B)** Adaptive intimal thickening is characterized by intimal thickening begins with an increase in smooth muscle cells (SMCs) and proteoglycan-collagen matrix with little or no infiltration of inflammatory cells (40×, 80×); **(C)** Pathological intimal thickening is characterized by the intima has many fusiform, foamy cells clustered beneath the arterial endothelium, and in some areas of the intima there are numerous proteoglycan and lipid deposition of lipid pools (80×, 200×); **(D)** Fibrillary atherosclerotic is characterized by calcium salt deposits and cholesterol crystals under the fibrous cap (HE staining shows needle cracks), foam cell formation and infiltration of inflammatory cells are seen within the necrotic core (40×, 80×). ★ indicates the main lesion area. Additional note: Figure 4 and Figure 5D are taken from the same sample.

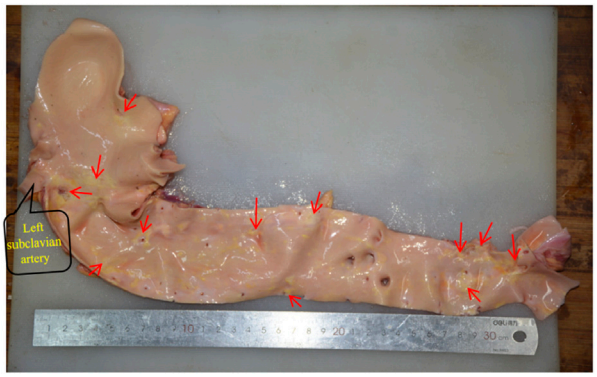


FIGURE 6
The distribution of aortic atherosclerosis. The concentrated region of hardened plaques is indicated by the red arrow.

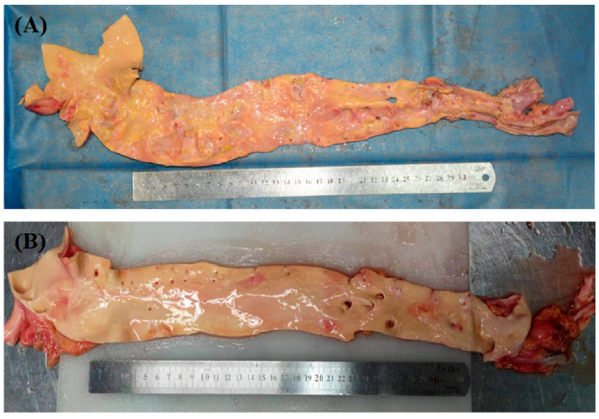


FIGURE 7
**(A)** Male, 58 years old; **(B)** Female, 58 years old.

## 4.5 Comparison of parameters in different test directions

In general, the mechanical characteristics exhibit higher values in the circumferential direction as compared to the axial direction (Figure 11). Except for the abdominal aorta group, there were significant differences in stress ($\sigma_p$, $\sigma_t$) and ultimate modulus of elasticity ($E_2$), whereas the initial modulus of elasticity ($E_0$) showed significant differences only in the aortic arch.

## 4.6 Comparison of parameters at different anatomical parts

The mechanical parameters of the ascending aorta were greater in the circumferential direction, with the most significant higher ultimate stress ($\sigma_p$ "2.09 ± 0.89") and ultimate modulus of elasticity ($E_2$ "12.93 ± 5.29"). On the other hand, the abdominal aorta had significantly greater

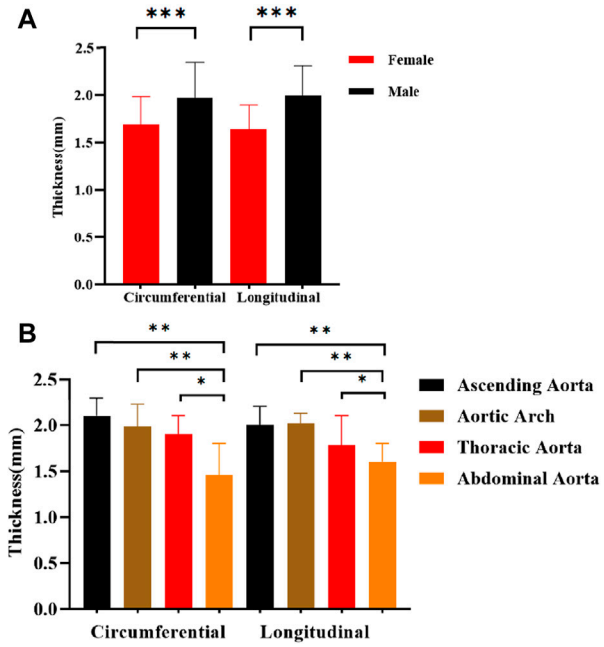


FIGURE 8
Comparison of thickness in different directions of stretching. **(A)** Different genders; **(B)** Different anatomical parts.

ultimate stress [$\sigma_p$ "1.69 (1.08,2.32)"] and ultimate modulus of elasticity [$E_2$ "8.28 (6.67,10.25)"] than the rest of the part in the axial direction (Figure 12). In the initial and transitional phases, the differences were not significant, but the ascending aorta still had a strong advantage.

## 4.7 Comparison of parameters for different pathological features

In general, the mechanical parameters tended to increase and then decrease with the development of atherosclerosis. In the circumferential direction, the stresses [$\sigma_p$ "2.2 (1.31,3.98)", $\sigma_t$ "0.13 (0.09,0.31)"] and ultimate modulus of elasticity ($E_2$ "14.10 ± 7.21") of the adaptive Intimal thickening group were significantly greater than the other groups, whereas the strain ($\varepsilon_p$ "0.82 ± 0.17", $\varepsilon_t$ "0.53 ± 0.14") was greater in the pathological Intimal thickening group. There was no statistically significant difference in the parameters of the axial direction (Figure 13).

# 5 Discussion

This study systematically analyzed the mechanical parameters of the aorta under the influence of age, gender, test direction, anatomical location, and pathological characteristics. In addition, we elaborated on the distribution of aortic atherosclerosis through gross morphological observation. The characteristics of aortic thickness changes were analyzed. At present, there is no relatively comprehensive study.

## 5.1 Comparison of thickness and atherosclerosis distribution

There are certain differences in aortic thickness with age, gender, and anatomical location (Albu et al., 2022), which is attributed to its composition on the one hand and atherosclerosis and intimal thickening on the other hand (Li et al., 2004). In the present study, there is no discernible trend in aortic thickness at 50 years of age and above. When comparing genders, the Male group had greater thickness (Li et al., 2004) and higher prevalence and extent of atherosclerosis than the female group (Mathur et al., 2015), the reasons could be increased endothelial fibroblast proliferation and accumulation of collagen fibers, and muscle sympathetic nerve activity (MSNA) was greater in males, stimulating smooth muscle hypertrophy, which was not present in females (Holwerda et al., 2019). In terms of anatomical parts, the thickness of the aorta decreases progressively from proximal to distal, which is mainly related to the structural composition of the aorta, where elastin, collagen, and smooth muscle form the laminar units, which are the structural and functional units of the aorta (O Connell et al., 2008). Arteries in the proximal part of the aorta have denser laminar units.

Among the segments, the abdominal aorta has the most severe atherosclerosis, followed by the aortic arch, and the ascending aorta is the least severe. The abdominal aorta has fewer laminar units, poor elasticity, and is itself a high-incidence part of endothelial injury (Czamara et al., 2020). In addition, the abdominal aorta has more macrovascular branches (abdominal celiac trunk arteries and common iliac arteries, among others), which makes it more susceptible to vortex phenomena (Qin et al., 2021). The unique geometric features of the aortic arch make it subject to higher shear forces, especially at the opening of the left subclavian artery.

## 5.2 The effect of age on parameters

Despite the age limitation of the present study, the results show parameters gradually decrease with age, which is consistent with previous studies (Huh et al., 2019). The most significant difference of these was strain ($\varepsilon_p$, $\varepsilon_t$). It could be due to weaker or reduced fiber cross-linking caused by structural elastin and collagen degeneration (Astrand et al., 2011), decreased density of elastin and smooth muscle (Jadidi et al., 2021), thicker intima-media collagen fibers, but no major change in overall collagen content. These factors remodel the aortic structure (Morrison et al., 2009; Albu et al., 2022), and have an impact on the aorta's mechanical properties.

## 5.3 The effect of gender on parameters

In the healthy group, the mechanical parameters of males were greater (Ninomiya et al., 2015; Li et al., 2023), whereas, in the atherosclerotic group, the mechanical parameters of females were higher, especially in the proximal part of the aorta (ascending aorta and aortic arch) (Figure 8). The samples were taken from postmenopausal females. Estrogen mainly acts on endothelial cells and smooth muscle cells in premenopausal females, promoting the release of vasoactive mediators and mediating the functional balance of vascular inflammation, lipid metabolism, and

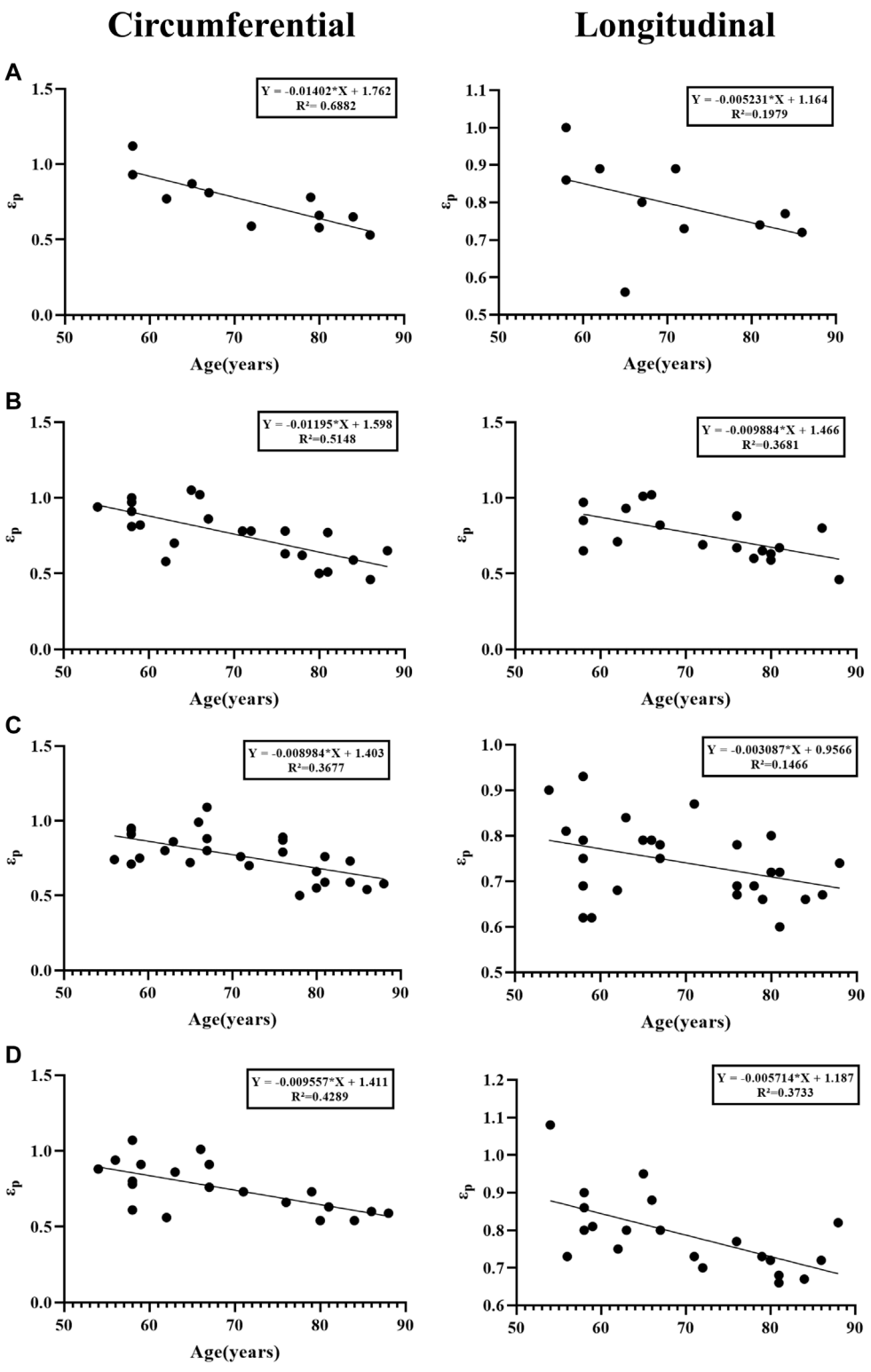


FIGURE 9
Linear regression analysis between age and strain. **(A)** Ascending aorta; **(B)** Aortic arch; **(C)** Thoracic aorta; **(D)** Abdominal aorta.

oxidative stress (Zahreddine et al., 2021). For premenopausal females, the prevalence of atherosclerosis is lower than that of males (Man et al., 2020). After menopause, females' ovarian function decreases, dyslipidemia increases (Peters et al., 1999), vascular smooth muscle cells migrate or proliferate, and oxidative stress and inflammatory reactions aggravate. Generally speaking, the prevalence of atherosclerosis increases in postmenopausal females, and the stiffness of the female vasculature increases (Zhang et al., 2022). Findings also suggest that the effects of estrogen may be concentrated in the proximal aortic region (Waddell et al., 2001).

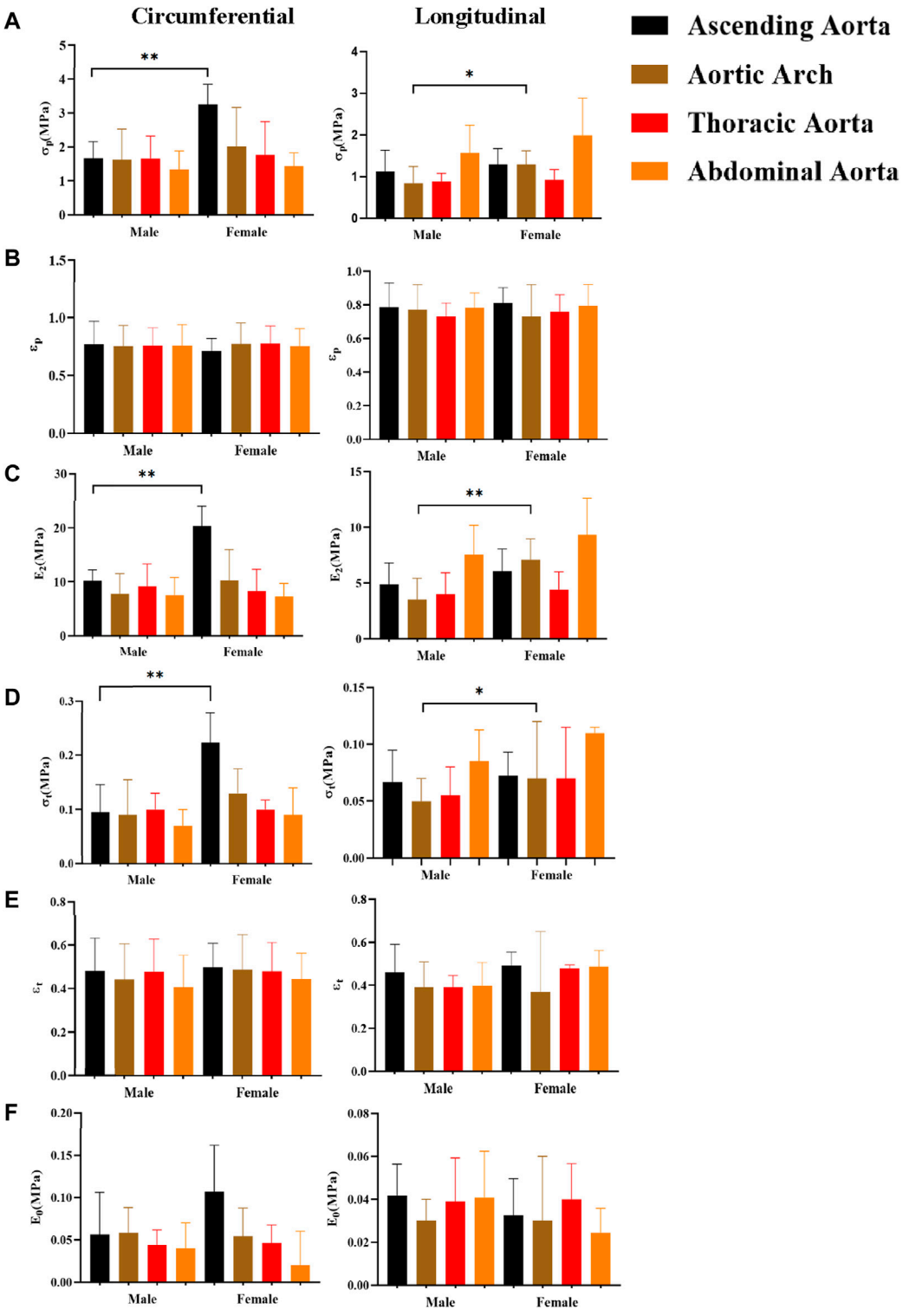


FIGURE 10
Comparing the effect of gender on mechanical parameters. **(A)**, **(B)**, **(C)**, **(D)**, **(E)**, and **(F)** denote the ultimate stress ($\sigma_p$), ultimate strain ($\varepsilon_p$), ultimate modulus of elasticity ($E_2$), middle stress point ($\sigma_t$), middle strain point ($\varepsilon_t$), and initial modulus of elasticity ($E_0$), respectively.

## 5.4 The effect of different test directions on parameters

The circumferential direction is the primary orientation of the aortic laminar unit (O Connell et al., 2008; Holzapfel and Ogden, 2018), and the mechanical characteristics of the aorta exhibit anisotropy (Sigaeva et al., 2019; Pukaluk et al., 2022). The result showed that the parameters of the circumferential direction were greater than the axial direction group, in line with previous studies (Gaur et al., 2020), but there were no significant differences in the

TABLE 2 Comparison of parameters between genders in normal aorta and atherosclerotic groups.

| Sex | Pathology | $\sigma_p$ | $\varepsilon_p$ | $E_2$ | $\sigma_t$ | $\varepsilon_t$ | $E_0$ | N |
|---|---|---|---|---|---|---|---|---|
| Male | Normal | 1.20 (1.00,1.85)* | 0.76 ± 0.13* | 7.45 ± 3.39 | 0.07 (0.05,0.11) | 0.43 ± 0.10 | 0.05 (0.03,0.07) | 19 |
| | Atherosclerosis | 1.24 (0.78,1.75)** | 0.76 ± 0.15 | 6.88 (3.76,9.16)** | 0.07 (0.05,0.10)*** | 0.42 (0.32,0.49)** | 0.06 (0.04,0.07) | 79 |
| Female | Normal | 0.95 (0.71,1.34)** | 0.66 ± 0.11* | 6.27 ± 2.78 | 0.06 (0.05,0.09) | 0.37 ± 0.08 | 0.03 (0.02,0.05) | 12 |
| | Atherosclerosis | 1.58 (1.21,2.23)* | 0.79 ± 0.13 | 7.77 (5.67,11.14)** | 0.10 (0.07,0.14)*** | 0.48 (0.40,0.57)** | 0.04 (0.02,0.06) | 46 |

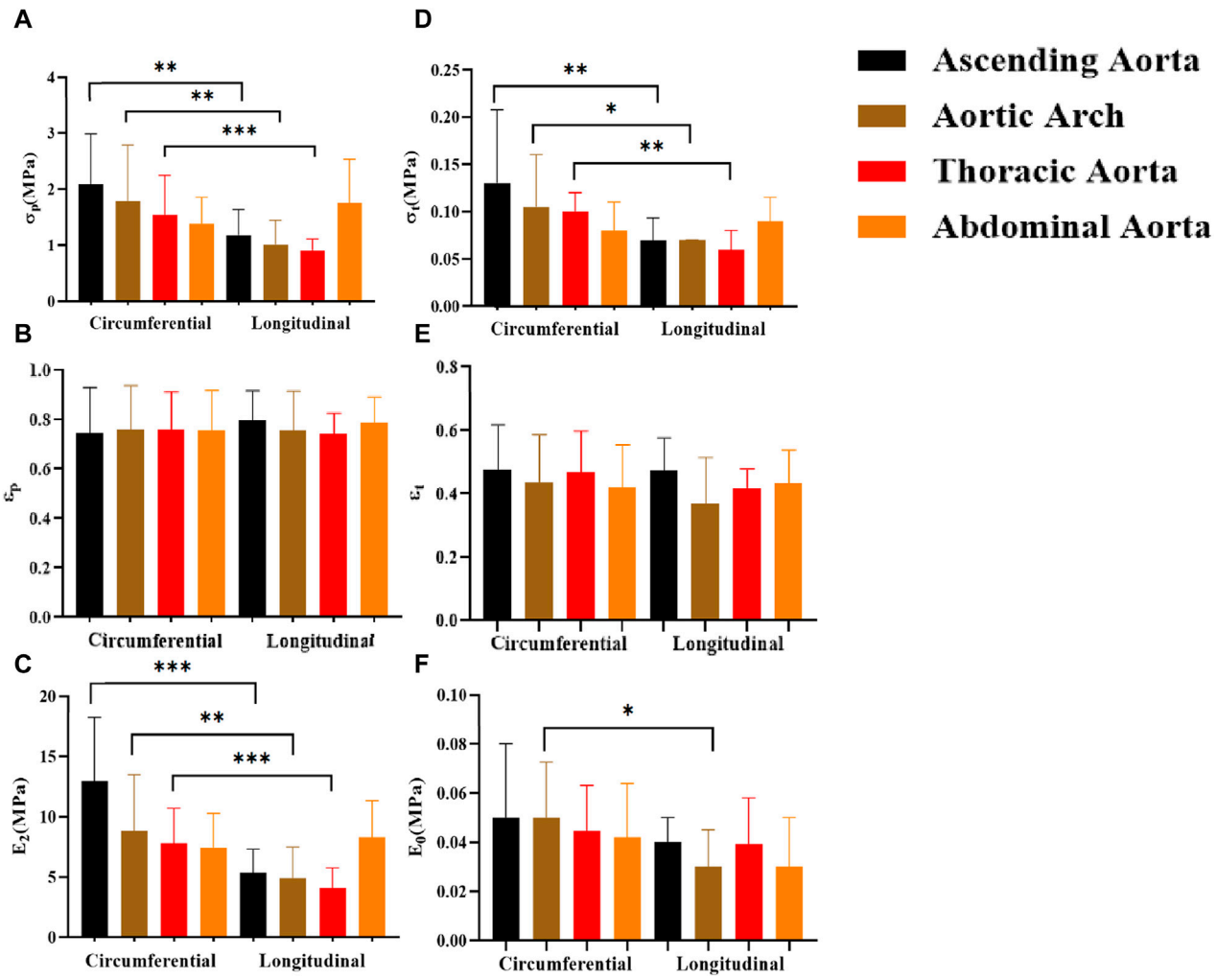


FIGURE 11
Comparison of the effects of different test orientations on mechanical parameters. **(A–F)** denote the ultimate stress ($\sigma_p$), ultimate strain ($\varepsilon_p$), ultimate elastic modulus ($E_2$), middle stress point ($\sigma_t$), middle strain point ($\varepsilon_t$), and initial elastic modulus ($E_0$), respectively.

abdominal aorta. It may be due to an increased gradually proportion of collagen fibers from proximal to distal, which are predominantly aligned in a longitudinal direction (Assoul et al., 2008). Meanwhile, the ascending aorta is subjected to the greatest blood pressure and wall shear, whereas the descending aorta is subjected to less blood pressure and wall shear based on the results of computational hemodynamic analysis (Malvindi et al., 2017). This may explain the decreasing prevalence of aortic dissection from the ascending aorta to the distal end of the abdominal aorta, and the fact that the tear direction of dissection tends to be transverse (Sherk et al., 2021). The structural and hemodynamic characteristics of the abdominal aorta may be made intima less prone to tear, and then form isolated abdominal aortic dissection (Sen et al., 2021), but it more prone to abdominal aorta aneurysms (Song et al., 2023).

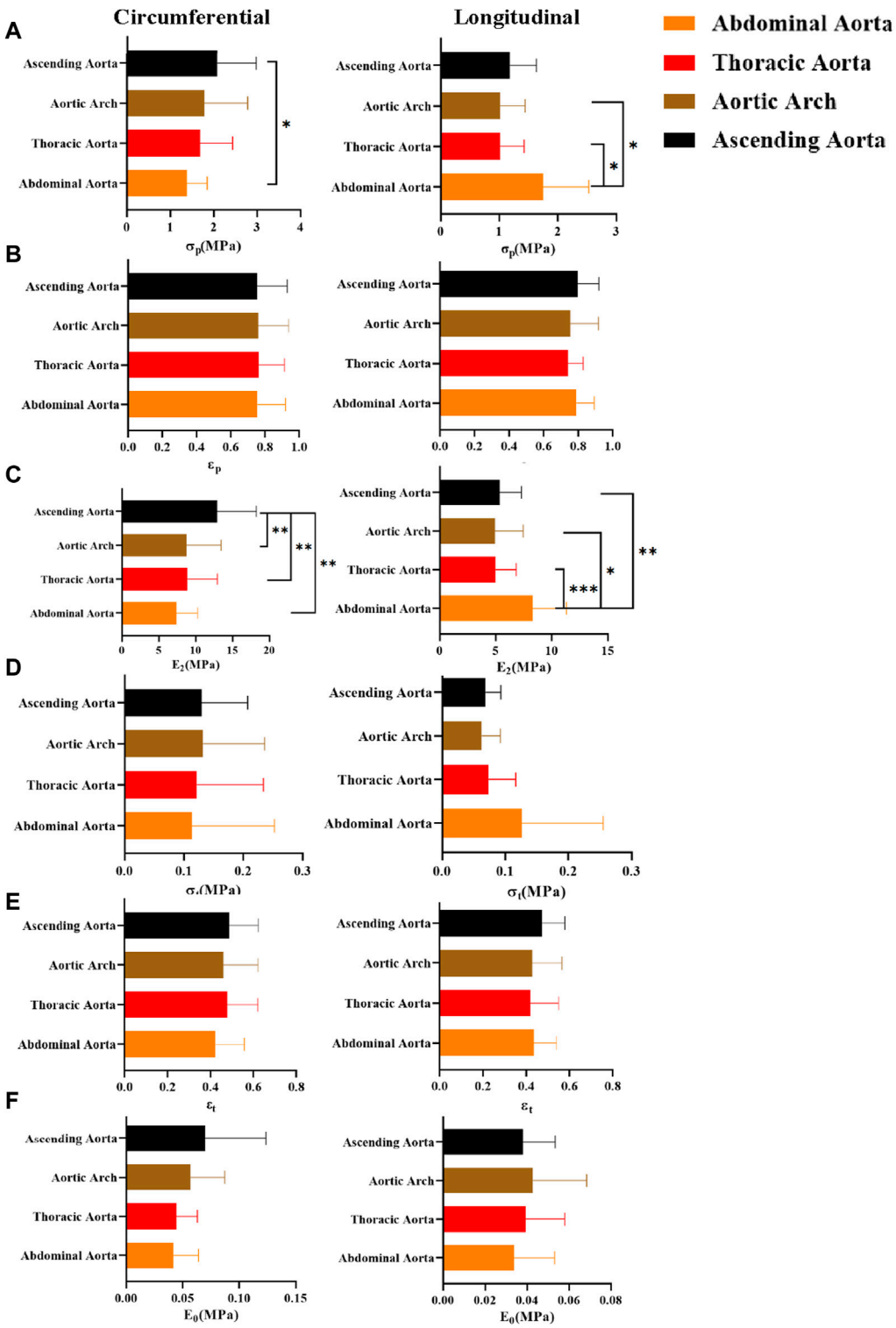


FIGURE 12
Comparison of mechanical parameters at different anatomical parts. **(A–F)** denote the ultimate stress ($\sigma_p$), ultimate strain ($\varepsilon_p$), ultimate modulus of elasticity ($E_2$), middle stress point ($\sigma t$), middle strain point ($\varepsilon_t$), and initial modulus of elasticity ($E_0$), respectively.

## 5.5 The effect of different anatomical parts on parameters

Currently, there are no studies of uniaxial stretching tests on four anatomical parts together. In the previous study, Ninomiya et al. found that the strength and elasticity of the thoracic aorta were higher than that of the abdominal aorta in circumferential stretching (Ninomiya et al., 2015). Our study showed that the ascending aorta had the greatest parameters in circumferential stretching, with the most significant differences in ultimate stress ($\sigma_p$) and ultimate modulus of elasticity

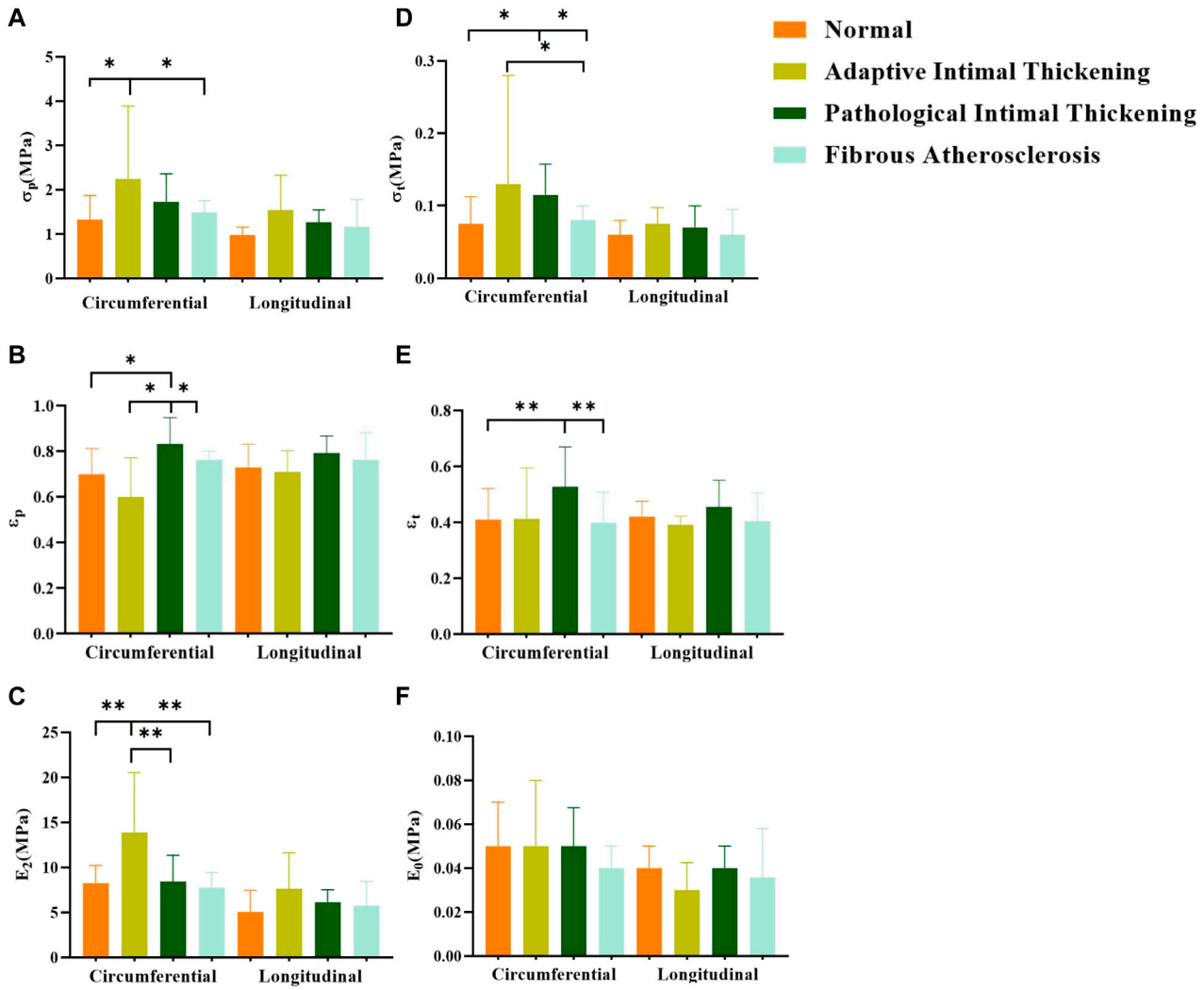


FIGURE 13
Comparison of parameters for different pathological features. **(A–F)** denote the ultimate stress ($\sigma_p$), ultimate strain ($\varepsilon_p$), ultimate modulus of elasticity ($E_2$), middle stress point ($\sigma_t$), middle strain point ($\varepsilon_t$), and initial modulus of elasticity ($E_0$), respectively.

($E_2$). the ascending aorta has more laminar units, greater total fibronectin content and density, and a more complete structure (Emmott et al., 2016). In axial tension, the abdominal aorta had the greatest ultimate stress ($\sigma_p$) and ultimate modulus of elasticity ($E_2$) (Figure 10). As mentioned earlier, collagen fibers grow longitudinally and the abdominal aorta has a higher collagen fiber content, collagen fibers are stretched during the strengthening phase and elevate the abdominal aorta's tensile strength.

## 5.6 The effect of different pathological features on parameters

With the development of aortic atherosclerosis, the mechanical parameters showed a tendency to increase and then decrease (Koniari et al., 2011). The adaptive intimal thickening group exhibited the highest stress ($\sigma_p$, $\sigma_t$) and ultimate modulus of elasticity ($E_2$). This may be explained by the increased collagen fiber content and density in the intima, as well as the absence of pathological alterations including aberrant fiber structural organization and fibrin denaturation (Glagov et al., 1993; Herity et al., 1999). The strain ($\varepsilon_p$, $\varepsilon_t$) was significantly higher in the pathological intimal thickening group (multilayered foam cells or lipid pools with loose intima) than that of other groups, which suggested that the aorta stretches longer. The abnormal proliferation and migration of smooth muscle cells or macrophage infiltration gradually forms layers of lipid cells and foam cells (Bennett et al., 2016), resulting in the relaxation of the connective action between fibrous tissues. Compared with the fibrous atherosclerosis group, the normal group did not show significant differences in any of the parameters, but the modulus of elasticity ($E_2$, $E_0$) was slightly higher than that of the fibrous atherosclerosis group. Fibrous atherosclerosis is mainly due to the formation of lipid cores, atherosclerotic substances, or calcium salt deposits under the intima, resulting in a severe effect on the structure of the tunica intima and media tunica (Jing et al., 2022). To some extent, thickening of the intimal collagen fibers improves the aortic stiffness, but the internal structural integrity is damaged, and

some of the elastic and collagen fibers are structurally and functionally impaired (Tsamis et al., 2013). A balance between damage and repair is achieved (Uimonen, 2021) to keep the original mechanical properties.

### 5.7 Outlook

Only human aorta samples older than 50 years old were collected for this research. In addition, the aorta is anisotropy, and multi-axial tensile testing may better simulate physiological conditions. Bulge inflation tests are a more demanding test condition method for multiaxial testing to determine ultimate properties (Duprey et al., 2016). The present study focuses on how different variables affect the aorta's mechanical characteristics at different phases. In previous studies, some scholars have used optical extensometers to solve the strain problem, and our study uses the crosshead displacement to derive the strains, which may hinder the comparison with the results of previous studies but does not influence the study of the changing pattern of the mechanical properties of the aorta. In further research, we will make efforts to further illustrate the mechanical properties of the aorta by collecting samples (normal aorta, aortic dissection, aneurysm, etc.) in a targeted manner and selecting the optimal test method according to the required parameters.

## 6 Conclusion

This study concluded that the abdominal aorta is most susceptible to atherosclerosis. With the development of atherosclerosis, mechanical parameters decrease, and the risk of injury increases. The average thickness of the aorta was greater in males than that of females and decreased progressively from the ascending aorta to the abdominal aorta. Mechanical parameters were smaller in the axial direction, which may explain the greater risk of injury to blood vessels in axial stretching. For the grouping of pathological features, we proposed the pathological features of the sample's broken end as the condition for grouping. In addition, we consider that stiffness may be greater in middle-aged and elderly females after the occurrence of atherosclerosis.

## Data availability statement

The original contributions presented in the study are included in the article/Supplementary material, further inquiries can be directed to the corresponding author.

## Ethics statement

This study was approved by the Ethics Committee of Chongqing Medical University and informed consent was given by the next of kin of the deceased.

## Author contributions

HC: Conceptualization, Methodology, Project administration, Writing–original draft, Writing–review and editing. MZ: Writing–review and editing. YL: Writing–review and editing, Methodology. QW: Methodology, Writing–review and editing. YX: Methodology, Writing–review and editing. CB: Methodology, Writing–review and editing. JL: Conceptualization, Methodology, Supervision, Writing–review and editing.

## Funding

The author(s) declare that no financial support was received for the research, authorship, and/or publication of this article.

## Acknowledgments

The authors are particularly grateful to the editors and reviewers for their valuable comments on this study.

## Conflict of interest

The authors declare that the research was conducted in the absence of any commercial or financial relationships that could be construed as a potential conflict of interest.

## Publisher's note

All claims expressed in this article are solely those of the authors and do not necessarily represent those of their affiliated organizations, or those of the publisher, the editors and the reviewers. Any product that may be evaluated in this article, or claim that may be made by its manufacturer, is not guaranteed or endorsed by the publisher.

## References

Albu, M., Şeicaru, D. A., Pleşea, R. M., Mirea, O. C., Gherghiceanu, F., Grigorean, V. T., et al. (2022). Remodeling of the aortic wall layers with ageing. *Rom. J. Morphol. Embryol.* 63 (1), 71–82. doi:10.47162/rjme.63.1.07

Assoul, N., Flaud, P., Chaouat, M., Letourneur, D., and Bataille, I. (2008). Mechanical properties of rat thoracic and abdominal aortas. *J. Biomech.* 41 (10), 2227–2236. doi:10.1016/j.jbiomech.2008.04.017

Astrand, H., Stalhand, J., Karlsson, J., Karlsson, M., Sonesson, B., and Länne, T. (2011). *In vivo* estimation of the contribution of elastin and collagen to the mechanical properties in the human abdominal aorta: effect of age and sex. *J. Appl. physiology* 110 (1), 176–187. doi:10.1152/japplphysiol.00579.2010

Bai, Z., Gu, J., Shi, Y., and Meng, W. (2018). Effect of inflammation on the biomechanical strength of involved aorta in type A aortic dissection and ascending thoracic aortic aneurysm: an initial research. *Anatol. J. Cardiol.* 20 (2), 85–92. doi:10.14744/AnatolJCardiol.2018.49344

Bel-Brunon, A., Kehl, S., Martin, C., Uhlig, S., and Wall, W. A. (2014). Numerical identification method for the non-linear viscoelastic compressible behavior of soft tissue using uniaxial tensile tests and image registration - application to rat lung parenchyma. *J. Mech. Behav. Biomed. Mater* 29, 360–374. doi:10.1016/j.jmbbm.2013.09.018

Bennett, M. R., Sinha, S., and Owens, G. K. (2016). Vascular smooth muscle cells in atherosclerosis. *Circulation Res.* 118 (4), 692–702. doi:10.1161/circresaha.115.306361

Chuong, C. J., and Fung, Y. C. (1983). Three-Dimensional stress distribution in arteries. *J. biomechanical Eng.* 105 (3), 268–274. doi:10.1115/1.3138417

Czamara, K., Majka, Z., Sternak, M., Koziol, M., Kostogrys, R. B., Chlopicki, S., et al. (2020). Distinct chemical changes in abdominal but not in thoracic aorta upon atherosclerosis studied using fiber optic Raman spectroscopy. *Int. J. Mol. Sci.* 21 (14), 4838. doi:10.3390/ijms21144838

Duprey, A., Trabelsi, O., Vola, M., Favre, J. P., and Avril, S. (2016). Biaxial rupture properties of ascending thoracic aortic aneurysms. *Acta Biomater.* 42, 273–285. doi:10.1016/j.actbio.2016.06.028

Emmott, A., Garcia, J., Chung, J., Lachapelle, K., El-Hamamsy, I., Mongrain, R., et al. (2016). Biomechanics of the ascending thoracic aorta: a clinical perspective on engineering data. *Can. J. Cardiol.* 32 (1), 35–47. doi:10.1016/j.cjca.2015.10.015

Estermann, S. J., Forster-Streffleur, S., Hirtler, L., Streicher, J., Pahr, D. H., and Reisinger, A. (2021). Comparison of Thiel preserved, fresh human, and animal liver tissue in terms of mechanical properties. *Ann. Anat.* 236, 151717. doi:10.1016/j.aanat.2021.151717

Franchini, G., Breslavsky, I. D., Holzapfel, G. A., and Amabili, M. (2021). Viscoelastic characterization of human descending thoracic aortas under cyclic load. *Acta Biomater.* 130, 291–307. doi:10.1016/j.actbio.2021.05.025

García-Herrera, C. M., Atienza, J. M., Rojo, F. J., Claes, E., Guinea, G. V., Celentano, D. J., et al. (2012). Mechanical behaviour and rupture of normal and pathological human ascending aortic wall. *Med. Biol. Eng. Comput.* 50 (6), 559–566. doi:10.1007/s11517-012-0876-x

Garcia–Herrera, C. M., Celentano, D. J., and Herrera, E. A. (2016). Modelling and numerical simulation of the *in vivo* mechanical response of the ascending aortic aneurysm in Marfan syndrome. *Med. Biol. Eng. Comput.* 55 (3), 419–428. doi:10.1007/s11517-016-1524-7

Gaur, P., Sharma, S., Kumar, D., Chawla, A., Mukherjee, S., Jain, M., et al. (2020). Inverse material characterisation of human aortic tissue for traumatic injury in motor vehicle crashes. *Int. J. Crashworthiness* 27 (2), 347–366. doi:10.1080/13588265.2020.1807678

Glagov, S., Zarins, C. K., Masawa, N., Xu, C. P., Bassiouny, H., and Giddens, D. P. (1993). Mechanical functional role of non-atherosclerotic intimal thickening. *Front. Med. Biol. Eng. Int. J. Jpn. Soc. Med. Electron. Biol. Eng.* 5 (1), 37–43.

Haskett, D., Johnson, G., Zhou, A., Utzinger, U., and Vande Geest, J. (2010). Microstructural and biomechanical alterations of the human aorta as a function of age and location. *Biomech. Model Mechanobiol.* 9 (6), 725–736. doi:10.1007/s10237-010-0209-7

Herity, N. A., Ward, M. R., Lo, S., and Yeung, A. C. (1999). Review: clinical aspects of vascular remodeling. *J. Cardiovasc. Electrophysiol.* 10 (7), 1016–1024. doi:10.1111/j.1540-8167.1999.tb01273.x

Herrington, D. M., Mao, C., Parker, S. J., Fu, Z., Yu, G., Chen, L., et al. (2018). Proteomic architecture of human coronary and aortic atherosclerosis. *Circulation* 137 (25), 2741–2756. doi:10.1161/circulationaha.118.034365

Holwerda, S. W., Luehrs, R. E., DuBose, L. E., Majee, R., and Pierce, G. L. (2019). Sex and age differences in the association between sympathetic outflow and central elastic artery wall thickness in humans. *Am. J. physiology Heart circulatory physiology* 317 (3), H552–H560. doi:10.1152/ajpheart.00275.2019

Holzapfel, G. A., and Ogden, R. W. (2018). Biomechanical relevance of the microstructure in artery walls with a focus on passive and active components. *Am. J. physiology Heart circulatory physiology* 315 (3), H540–H549. doi:10.1152/ajpheart.00117.2018

Huh, U., Lee, C.-W., You, J.-H., Song, C.-H., Lee, C.-S., and Ryu, D.-M. (2019). Determination of the material parameters in the holzapfel-gasser-ogden constitutive model for simulation of age-dependent material nonlinear behavior for aortic wall tissue under uniaxial tension. *Appl. Sci.* 9 (14), 2851. doi:10.3390/app9142851

Jadidi, M., Razian, S. A., Habibnezhad, M., Anttila, E., and Kamenskiy, A. (2021). Mechanical, structural, and physiologic differences in human elastic and muscular arteries of different ages: comparison of the descending thoracic aorta to the superficial femoral artery. *Acta Biomater.* 119, 268–283. doi:10.1016/j.actbio.2020.10.035

Jing, L., Shu-Xu, D., and Yong-Xin, R. (2022). A review: pathological and molecular biological study on atherosclerosis. *Int. J. Clin. Chem.* 531, 217–222. doi:10.1016/j.cca.2022.04.012

Kobielarz, M., Kozun, M., Gasior-Glogowska, M., and Chwilkowska, A. (2020). Mechanical and structural properties of different types of human aortic atherosclerotic plaques. *J. Mech. Behav. Biomed. Mater* 109, 103837. doi:10.1016/j.jmbbm.2020.103837

Koniari, I., Mavrilas, D., Papadaki, H., Karanikolas, M., Mandellou, M., Papalois, A., et al. (2011). Structural and biomechanical alterations in rabbit thoracic aortas are associated with the progression of atherosclerosis. *Lipids health Dis.* 10, 125. doi:10.1186/1476-511x-10-125

Li, A. E., Kamel, I., Rando, F., Anderson, M., Kumbasar, B., Lima, J. A., et al. (2004). Using MRI to assess aortic wall thickness in the multiethnic study of atherosclerosis: distribution by race, sex, and age. *AJR Am. J. Roentgenol.* 182 (3), 593–597. doi:10.2214/ajr.182.3.1820593

Li, Z., Pei, M., Zhang, J., Liu, N., Wang, J., and Zou, D. (2023). A study to characterize the mechanical properties and material constitution of adult descending thoracic aorta based on uniaxial tensile test and digital image correlation. *Front. Bioeng. Biotechnol.* 11, 1178199. doi:10.3389/fbioe.2023.1178199

Loree, H. M., Grodzinsky, A. J., Park, S. Y., Gibson, L. J., and Lee, R. T. (1994). Static circumferential tangential modulus of human atherosclerotic tissue. *J. Biomech.* 27 (2), 195–204. doi:10.1016/0021-9290(94)90209-7

Malvindi, P. G., Pasta, S., Raffa, G. M., and Livesey, S. (2017). Computational fluid dynamics of the ascending aorta before the onset of type A aortic dissection. *Eur. J. Cardiothorac. Surg.* 51 (3), 597–599. doi:10.1093/ejcts/ezw306

Man, J. J., Beckman, J. A., and Jaffe, I. Z. (2020). Sex as a biological variable in atherosclerosis. *Circulation Res.* 126 (9), 1297–1319. doi:10.1161/circresaha.120.315930

Mathur, P., Ostadal, B., Romeo, F., and Mehta, J. L. (2015). Gender-related differences in atherosclerosis. *Cardiovasc. drugs Ther.* 29 (4), 319–327. doi:10.1007/s10557-015-6596-3

Morrison, T. M., Choi, G., Zarins, C. K., and Taylor, C. A. (2009). Circumferential and longitudinal cyclic strain of the human thoracic aorta: age-related changes. *J. Vasc. Surg.* 49 (4), 1029–1036. doi:10.1016/j.jvs.2008.11.056

Mussa, F. F., Horton, J. D., Moridzadeh, R., Nicholson, J., Trimarchi, S., and Eagle, K. A. (2016). Acute aortic dissection and intramural hematoma: a systematic review. *JAMA* 316 (7), 754–763. doi:10.1001/jama.2016.10026

Myneni, M., Rao, A., Jiang, M., Moreno, M. R., Rajagopal, K. R., and Benjamin, C. C. (2020). Segmental variations in the peel characteristics of the porcine thoracic aorta. *Ann. Biomed. Eng.* 48 (6), 1751–1767. doi:10.1007/s10439-020-02489-x

Ninomiya, O. H., Tavares Monteiro, J. A., Higuchi Mde, L., Puech-Leão, P., de Luccia, N., Raghavan, M. L., et al. (2015). Biomechanical properties and microstructural analysis of the human nonaneurysmal aorta as a function of age, gender and location: an autopsy study. *J. Vasc. Res.* 52 (4), 257–264. doi:10.1159/000442979

O Connell, M. K., Murthy, S., Phan, S., Xu, C., Buchanan, J., Spilker, R., et al. (2008). The three-dimensional micro- and nanostructure of the aortic medial lamellar unit measured using 3D confocal and electron microscopy imaging. *Matrix Biol.* 27 (3), 171–181. doi:10.1016/j.matbio.2007.10.008

Otsuka, F., Sakakura, K., Yahagi, K., Joner, M., and Virmani, R. (2014). Has our understanding of calcification in human coronary atherosclerosis progressed? *Arteriosclerosis, thrombosis, Vasc. Biol.* 34 (4), 724–736. doi:10.1161/atvbaha.113.302642

Pei, M., Zou, D., Gao, Y., Zhang, J., Huang, P., Wang, J., et al. (2021). The influence of sample geometry and size on porcine aortic material properties from uniaxial tensile tests using custom-designed tissue cutters, clamps and molds. *PLoS One* 16 (2), e0244390. doi:10.1371/journal.pone.0244390

Peña, J. A., Martínez, M. A., and Peña, E. (2019). Failure damage mechanical properties of thoracic and abdominal porcine aorta layers and related constitutive modeling: phenomenological and microstructural approach. *Biomechanics Model. Mechanobiol.* 18 (6), 1709–1730. doi:10.1007/s10237-019-01170-0

Peters, H. W., Westendorp, I. C., Hak, A. E., Grobbee, D. E., Stehouwer, C. D., Hofman, A., et al. (1999). Menopausal status and risk factors for cardiovascular disease. *J. Intern. Med.* 246 (6), 521–528. doi:10.1046/j.1365-2796.1999.00547.x

Polzer, S., Man, V., Vlachovsky, R., Kubicek, L., Kracik, J., Staffa, R., et al. (2021). Failure properties of abdominal aortic aneurysm tissue are orientation dependent. *J. Mech. Behav. Biomed. Mater* 114, 104181. doi:10.1016/j.jmbbm.2020.104181

Pukaluk, A., Wolinski, H., Viertler, C., Regitnig, P., Holzapfel, G. A., and Sommer, G. (2022). Changes in the microstructure of the human aortic medial layer under biaxial loading investigated by multi-photon microscopy. *Acta Biomater.* 151, 396–413. doi:10.1016/j.actbio.2022.08.017

Qiao, Y. H., Fan, J. R., and Luo, K. (2023). Mechanism of blood flow energy loss in real healthy aorta using computational fluid-structure interaction framework. *Int. J. Eng. Sci.* 192, 103939. doi:10.1016/j.ijengsci.2023.103939

Qin, S., Chen, R., Wu, B., Shiu, W. S., and Cai, X. C. (2021). Numerical simulation of blood flows in patient-specific abdominal aorta with primary organs. *Biomechanics Model. Mechanobiol.* 20 (3), 909–924. doi:10.1007/s10237-021-01419-7

Romo, A., Badel, P., Duprey, A., Favre, J. P., and Avril, S. (2014). *In vitro* analysis of localized aneurysm rupture. *J. Biomech.* 47 (3), 607–616. doi:10.1016/j.jbiomech.2013.12.012

Sen, I., D'Oria, M., Weiss, S., Bower, T. C., Oderich, G. S., Kalra, M., et al. (2021). Incidence and natural history of isolated abdominal aortic dissection: a population-based assessment from 1995 to 2015. *J. Vasc. Surg.* 73 (4), 1198–1204.e1. doi:10.1016/j.jvs.2020.07.090

Sherifova, S., and Holzapfel, G. A. (2019). Biomechanics of aortic wall failure with a focus on dissection and aneurysm: a review. *Acta Biomater.* 99, 1–17. doi:10.1016/j.actbio.2019.08.017

Sherk, W. M., Khaja, M. S., and Williams, D. M. (2021). Anatomy, pathology, and classification of aortic dissection. *Tech. Vasc. Interv. Radiol.* 24 (2), 100746. doi:10.1016/j.tvir.2021.100746

Sigaeva, T., Sommer, G., Holzapfel, G. A., and Di Martino, E. S. (2019). Anisotropic residual stresses in arteries. *J. R. Soc. Interface* 16 (151), 20190029. doi:10.1098/rsif.2019.0029

Sokolis, D. P. (2007). Passive mechanical properties and structure of the aorta: segmental analysis. *Acta Physiol. (Oxf)* 190 (4), 277–289. doi:10.1111/j.1748-1716.2006.01661.x

Sokolis, D. P., Savva, G. D., Papadodima, S. A., and Kourkoulis, S. K. (2017). Regional distribution of circumferential residual strains in the human aorta according to age and gender. *J. Mech. Behav. Biomed. Mater* 67, 87–100. doi:10.1016/j.jmbbm.2016.12.003

Song, P., He, Y., Adeloye, D., Zhu, Y., Ye, X., Yi, Q., et al. (2023). The global and regional prevalence of abdominal aortic aneurysms: a systematic review and modeling analysis. *Ann. Surg.* 277 (6), 912–919. doi:10.1097/sla.0000000000005716

Teng, Z., Trabelsi, O., Ochoa, I., He, J., Gillard, J. H., and Doblare, M. (2012). Anisotropic material behaviours of soft tissues in human trachea: an experimental study. *J. Biomech.* 45 (9), 1717–1723. doi:10.1016/j.jbiomech.2012.04.002

Tsamis, A., Krawiec, J. T., and Vorp, D. A. (2013). Elastin and collagen fibre microstructure of the human aorta in ageing and disease: a review. *J. R. Soc. Interface* 10 (83), 20121004. doi:10.1098/rsif.2012.1004

Uimonen, M. (2021). Synthesis of multidimensional pathophysiological process leading to type A aortic dissection: a narrative review. *J. Thorac. Dis.* 13 (10), 6026–6036. doi:10.21037/jtd-21-829

Utrera, A., Navarrete, Á., González-Candia, A., García-Herrera, C., and Herrera, E. A. (2022). Biomechanical and structural responses of the aorta to intermittent hypobaric hypoxia in a rat model. *Sci. Rep.* 12 (1), 3790. doi:10.1038/s41598-022-07616-3

Waddell, T. K., Dart, A. M., Gatzka, C. D., Cameron, J. D., and Kingwell, B. A. (2001). Women exhibit a greater age-related increase in proximal aortic stiffness than men. *J. Hypertens.* 19 (12), 2205–2212. doi:10.1097/00004872-200112000-00014

Walsh, M. T., Cunnane, E. M., Mulvihill, J. J., Akyildiz, A. C., Gijsen, F. J., and Holzapfel, G. A. (2014). Uniaxial tensile testing approaches for characterisation of atherosclerotic plaques. *J. Biomech.* 47 (4), 793–804. doi:10.1016/j.jbiomech.2014.01.017

Wang, X., Carpenter, H. J., Ghayesh, M. H., Kotousov, A., Zander, A. C., Amabili, M., et al. (2023). A review on the biomechanical behaviour of the aorta. *J. Mech. Behav. Biomed. Mater* 144, 105922. doi:10.1016/j.jmbbm.2023.105922

Ye, W. Q., He, J., Wu, Z. B., and Cai, L. X. (2022). Analysis of thoracic aorta injury in 27 road traffic accident deaths. *Fa Yi Xue Za Zhi* 38 (4), 486–489. doi:10.12116/j.issn.1004-5619.2020.410502

Zahreddine, R., Davezac, M., Buscato, M., Smirnova, N., Laffargue, M., Henrion, D., et al. (2021). A historical view of estrogen effect on arterial endothelial healing: from animal models to medical implication. *Atherosclerosis* 338, 30–38. doi:10.1016/j.atherosclerosis.2021.10.013

Zhang, S., Zhou, J., Li, L., Pan, X., Lin, J., Li, C., et al. (2022). Effect of dehydroepiandrosterone on atherosclerosis in postmenopausal women. *Biosci. trends* 15 (6), 353–364. doi:10.5582/bst.2021.01320

Zwirner, J., Ondruschka, B., Scholze, M., Schulze-Tanzil, G., and Hammer, N. (2020). Load-deformation characteristics of acellular human scalp: assessing tissue grafts from a material testing perspective. *Sci. Rep.* 10 (1), 19243. doi:10.1038/s41598-020-75875-z

frontiers | Frontiers in Bioengineering and Biotechnology

TYPE Original Research
PUBLISHED 26 April 2024
DOI 10.3389/fbioe.2024.1346404



OPEN ACCESS

EDITED BY
Hasan Uludag,
University of Alberta, Canada

REVIEWED BY
Kui Xu,
Anhui University of Chinese Medicine, China
Ruiqiang Hang,
Taiyuan University of Technology, China

*CORRESPONDENCE
Xiaojun Sun,
xis1972sun@163.com
Bin Zhang,
zhangbin2009@sxicc.ac.cn
Xing Wang,
kqwx100@163.com

†These authors have contributed equally to this work

RECEIVED 29 November 2023
ACCEPTED 11 April 2024
PUBLISHED 26 April 2024

CITATION
Zhao X, Zhang X, Zhou Z, Meng F, Liu R, Zhang M, Hao Y, Xie Q, Sun X, Zhang B and Wang X (2024), Atomic layer deposited $TiO_2$ nanofilm on titanium implant for reduced the release of particles.
*Front. Bioeng. Biotechnol.* 12:1346404.
doi: 10.3389/fbioe.2024.1346404



# Atomic layer deposited $TiO_2$ nanofilm on titanium implant for reduced the release of particles

Xiangyu Zhao[1†], Xiaoxuan Zhang[1†], Zilan Zhou[1], Fanchun Meng[2], Ruilin Liu[2], Mengyuan Zhang[1], Yujia Hao[1], Qingpeng Xie[1], Xiaojun Sun[3]*, Bin Zhang[2]* and Xing Wang[1]*

[1]Shanxi Medical University School and Hospital of Stomatology, Taiyuan, China, [2]State Key Laboratory of Coal Conversion, Institute of Coal Chemistry, Chinese Academy of Sciences, Taiyuan, China, [3]Department of Stomatology, The First Hospital of Shanxi Medical University, Taiyuan, China

**Objective:** Titanium implants are widely used in surgeries for their biocompatibility and mechanical properties. However, excessive titanium particle release can cause implant failure. This study explores Atomic Layer Deposition (ALD) to coat commercially pure titanium (Cp-Ti) with $TiO_2$, aiming to improve its frictional and corrosion resistance while reducing particle release. By comparing $TiO_2$ films with varying ALD cycle numbers, we assess surface properties, particle release, friction, and corrosion performance, providing insights into mitigating particle release from implants.

**Methods:** Cp-Ti surfaces were prepared and coated with $TiO_2$ films of 100, 300, and 500 ALD cycles. Surface characterization involved SEM, EDX, and XRD. Friction was tested using SEM, nanoindentation, and ICP-MS. Corrosion resistance was evaluated through immersion tests and electrochemical analysis. Cytotoxicity was assessed using BMSCs.

**Results:** Surface characterization revealed smoother surfaces with increased ALD cycles, confirming successful $TiO_2$ deposition. Friction testing showed reduced friction coefficients with higher ALD cycles, supported by nanoindentation results. Corrosion resistance improved with increasing ALD cycles, as evidenced by electrochemical tests and reduced titanium release. Cytotoxicity studies showed no significant cytotoxic effects.

**Conclusion:** ALD-coated $TiO_2$ films significantly enhance frictional and corrosion resistance of titanium implants while reducing particle release. The study underscores the importance of ALD cycle numbers in optimizing film performance, offering insights for designing implants with improved properties.

KEYWORDS

**atomic layer deposition, titanium dioxide, titanium implant, particles release, friction and corrosion**

## 1 Introduction

Commercially pure titanium (Cp-Ti) has been acknowledged as a premier implant material with bio-safety and nearly 1,000 tons of titanium is used annually in clinical applications in diverse applications, such as artificial joints, dental implants and heart valves (Xu et al., 2020). However, despite the excellent performance, many cases of implant Ti failure still exist. The failure rate of dental implants has been reported to be about 1%–20% (Alves et al., 2017), and

more than 35% for orthopedic implants (Tobin, 2017). In 75% of these cases, implant failure was due to aseptic loosening and impaired implant fixation (Awad et al., 2022). It has been shown that titanium implants in bone can continuously release titanium species (He et al., 2016), and the release of titanium ions and titanium particles can contribute to peri-implantitis and aseptic implant loosening (Eger et al., 2017). The released Ti species are not confined to the periphery of the implant, and even migrate with the blood and progressively accumulate in distal organs (Heringa et al., 2018), which leads to systemic hypersensitivity and allergic reactions. Released Ti particles are not limited to the periphery of the implant; they can migrate with the bloodstream and gradually accumulate in distant organs. In most studies, Ti nanoparticles have been found to cause oxidative stress, tissue pathology changes, carcinogenesis, genetic toxicity, and immune disruption (Shakeel et al., 2016). Worryingly despite the reported importance of excessive titanium species release on implant success and systemic health, the problem is routinely ignored by clinicians, patients and implant manufacturers, lacking sufficient attention and preventive measures.

Mechanical friction and corrosion are the main reasons for the physical degradation of titanium implants (Mombelli et al., 2018). Mechanical friction and corrosion are the primary factors leading to the degradation of titanium implants. Even within the bone-encased portions of the implant, frictional corrosion still occurs. This phenomenon arises from minute relative vibrations between two surfaces (implant surface and bone surface) under mechanical loads (friction), leading to irreversible corrosion degradation of the implant through electrochemical interactions with the surrounding environment (Berbel et al., 2019; Prestat and Thierry, 2021). Generally, increasing the strength of Ti and Ti alloys against friction and corrosion suppresses the mechanical friction to titanium particles. On the other hand, corrosion originates from the surface chemical reaction of metallic Ti in acidic environments. Although $TiO_2$ films formed spontaneously on Ti surfaces in contact with oxygen are resistant to corrosion when in contact with acids and reactive substances (Peron et al., 2021). However, the growth of the oxide layer is a dynamic equilibrium process involving oxidation and reduction reactions. Under certain conditions, the growth rate of the $TiO_2$ layer may be slow or non-uniform, resulting in an unstable layer quality that is easily damaged by external factors (Lara Rodriguez et al., 2014).

Surface overcoating has attracted extensive interest from researchers in recent years due to its ability to maintain the surface morphology of the implant and to be matched to the mechanical properties. There are various coating techniques available for implant modification. Such as anodic oxidation (Fazel et al., 2018), pulsed laser deposition (PLD) (Gnanavel et al., 2018), and physical vapor deposition (PVD) (Esmaeili et al., 2017), have been implemented to improve corrosion resistance. Forming anodic oxide coatings requires precise control of multiple process parameters such as electrolyte composition, temperature, and current density (Leinenbach and Eifler, 2009) and, therefore, requires complex process control and operation techniques with poor reliability and stability. The PLD technique is subject to effects such as phase explosion, which causes large particle sputtering, thus reducing the film quality and generating localized high-temperature effects on the titanium surface, which may lead to lattice structure alterations and thermal stresses in the titanium material, which may impact the properties and structure of the material (Deng et al., 2021). In addition, the coating thickness of PVD deposition is inhomogeneous on the surface of complex-shaped implants (Mohseni et al., 2014). This could lead to delamination of the substrate with the thinner coating, and the local oxide film will break if a critical strain is reached. It is still necessary to develop implant modification technique that can achieve uniform deposition at low temperatures and is easy to handle.

Atomic layer deposition (ALD) has unique advantages in sub-nanometer film thickness and uniformity control with increasing applications in biomedical advanced materials (Yang, 2020). Atomic Layer Deposition (ALD) is a precise thin-film deposition technique that enables highly accurate control over film thickness and composition by depositing films atom by atom on the material surface. During the reaction process, precursor molecules adhere to the substrate surface in a "self-limiting" manner, forming a single-molecule layer. Once the substrate surface is fully covered, excess precursor molecules no longer adsorb, resulting in the automatic termination of the deposition process. This means that regardless of the quantity of precursor molecules provided, only enough molecules can adsorb and participate in the reaction. This ensures the uniformity and consistency of the film. Compared to PCD, ALD is based on surface self-limiting and self-saturating adsorption reactions (Kim et al., 2023), which enables precise deposition at the atomic level on the complex surface of implants (Blendinger et al., 2021), and one study reported that the thickness of the film deposited per cycle on the implant surface is only 0.097 nm (Yang et al., 2017). The uniformity and consistency of ALD film avoid problems such as surface inhomogeneity and thickness variation. Compared with PLD, which usually operates at 500°C–800°C, ALD can even be conducted at a low temperature of 100°C (Wree et al., 2023), avoiding heat damage and shape changes to the implant material and maintaining the integrity and structural stability of the implant. The homogeneous films deposited by ALD are stable in properties; consequently, ALD-deposited TiO2 films have the potential to be used for implant surface coatings (Hashemi Astaneh et al., 2021).

Herein, we have used ALD technology to overcoat the titanium surface with stable $TiO_2$ film to enhance its frictional corrosion resistance and reduce the release of titanium particles (Figure 1). To our knowledge, this is the first study of the utilization of ALD $TiO_2$ films to solve the problem of titanium particle release from implants. The simplicity of the ALD technique, the lower working temperature, and the uniformity and stability of the films compared to other deposition techniques make it a viable solution. In addition, to further evaluate the friction and corrosion resistance of the films with different cycles and the particle release after friction and corrosion, we deposited 100, 300, and 500 cycles of $TiO_2$ films on Cp-Ti using the ALD technique. Through this study, we intended to provide a feasible solution to the problem of implant particle release, demonstrating that the ALD modification technique has tremendous potential in implant research to enhance the performance and long-term success of titanium implants, providing a new direction and opportunity for research to reduce titanium particle release from implants.

## 2 Materials and methods

### 2.1 Sample preparation and thin film deposition

A commercial pure Ti (CP-Ti) plate was utilized as a surrogate for titanium implants in this study. CP-Ti (10 mm × 10 mm × 5 mm) was

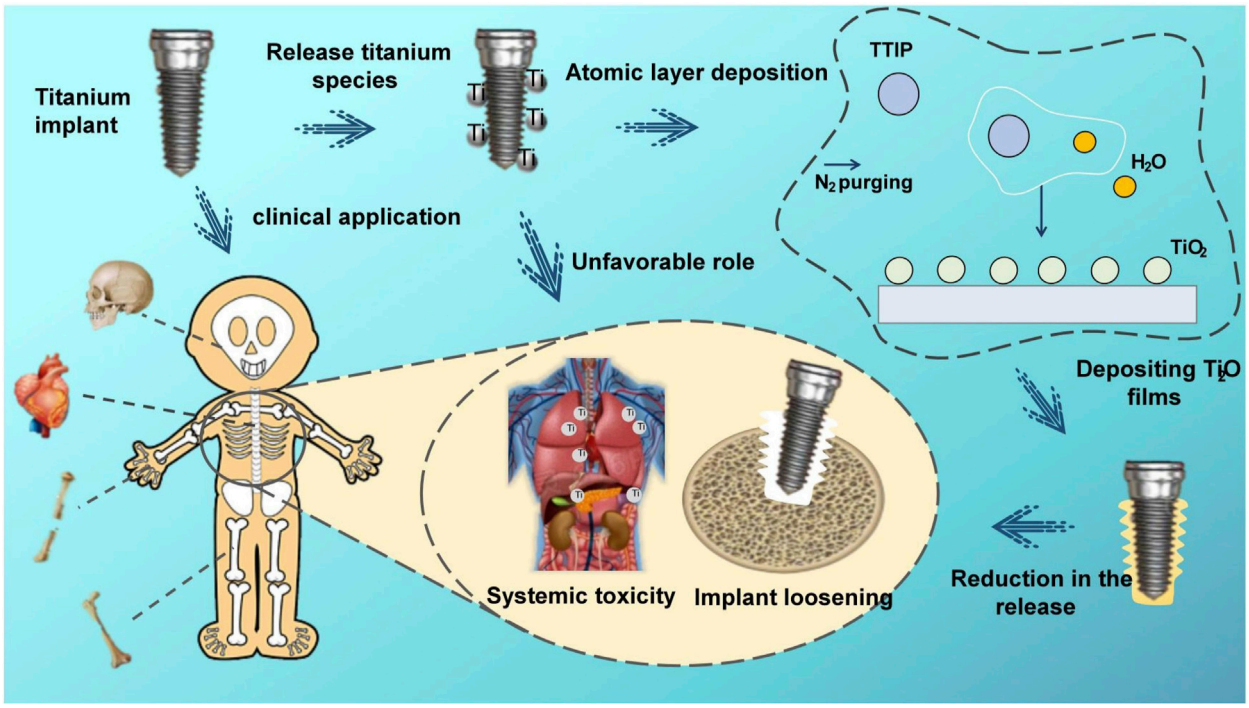


FIGURE 1
Schematic illustration of the research of $TiO_2$ films deposited through ALD on CP-Ti.

ground sequentially with silicon carbide sandpaper of different particle sizes (600, 800 and 1200), and then cleaned sequentially with acetone and ethanol by ultrasonication for 15 min. The ALD process was carried out in a homemade closed-chamber type ALD reactor. High-purity $N_2$ (99.999%) was utilized as a carrier gas.

The selection of Titanium tetraisopropoxide (TTIP) and ultrapure water as precursors offers advantages such as usability, affordability, chemical stability, availability, low maintenance, safety, and a lower deposition temperature range (150°C–300°C) (Niemelä et al., 2017). Deposition at 160°C prevents thermal damage to the substrate material at high temperatures, which holds significant importance for the structure and applications of titanium implants. TTIP and water were kept at 80°C and 25°C, respectively. The pulse, exposure, and purge times for titanium tetraisopropoxide were 1, 8, and 20 s, and those for $H_2O$ were 0.1, 8, and 25 s, respectively. To explore the role of different number of cycles on particle release, we deposited 100, 300, and 500 cycles of ALD layers.

## 2.2 Surface characterization

Scanning Electron Microscopy (SEM) using the JSM-7900F was employed to meticulously observe the surface morphology of thin films, providing crucial insights into the microstructure and surface features of different cyclically deposited films. Additionally, Focused Ion Beam (FIB) was used to cut samples for Transmission Electron Microscopy (TEM), enabling the measurement of nanofilm thickness and cross-sectional elemental distribution.

Energy-Dispersive X-ray Spectroscopy (EDX) was utilized to quantitatively analyze the elemental composition of the films, helping determine whether variations in titanium-to-oxygen ratios exist across different cycles. The combination of SEM, FIB-TEM, and EDX provides a comprehensive understanding of the morphology and elemental distribution of $TiO_2$ coatings.

Research findings indicate that rutile-type $TiO_2$ nanoparticles cause more significant damage to murine bone tissue compared to anatase-type $TiO_2$ nanoparticles (Cheng et al., 2021). By comparing measured XRD patterns with standard reference cards in databases, the phase structure can be accurately determined. Therefore, we employed a PANalytical X'Pert Pro X-ray Diffractometer (XRD) to examine the film's structure within an angular range of 20°–60°.

## 2.3 Friction tests

In the oral environment, dental implants are exposed to various components present in saliva, including organic substances, dissolved oxygen, inorganic anions (such as $Cl^-$, $HPO_4^{2-}$, $HCO^{3-}$), and cations (such as $Na^+$, $K^+$, $Ca^{2+}$, $Mg^{2+}$), as well as amino acids and proteins. These constituents may contribute to the degradation of the $TiO_2$ layer (Ossowska and Zieliński, 2020). To study oral implants, we conducted friction-corrosion tests simulating the oral microenvironment, also known as bio-tribocorrosion. In these experiments, we selected artificial saliva as the medium to better understand the performance and durability of titanium-based implants and prostheses in the oral environment.

According to ASTM G119-93 (ASTM, 1993), a material surface property tester (MFT-4000, Huahui, China) was used to perform the friction corrosion test under artificial saliva immersion. In this study, GCr15 steel balls were used as the friction counterpart

because the hardness of GCr15 bearing steel can reach HRC 58–63 after heat treatment, which is much higher than that of titanium alloy (HRC 28–33) which would not cause plastic deformation of the friction counterpart leading to wear and thus affect the experimental results during the tribocorrosion experiments (Zhou et al., 2019). A normal force of 5 N was applied to the counterpart, using the Hertzian contact stress model, corresponding to a maximum contact pressure of about 950 MPa, while the radius of the wear track was set to 5 mm, the speed of the sample table was set to 200 mm/min, and the test time was 10 min.

Two different methods were employed to assess the frictional performance. Scratch experiments were conducted using an ultra-nanoindenter with a diamond probe featuring a radius of 1 μm and an angle of 60°. The experiments were performed under a constant load of 500 μN, with a scratch distance of 10 μm and a duration of 1 min.

The surfaces of the four sample groups after friction were examined for surface scratches and particle detachment using SEM. In the presence of titanium nanoparticles in the sample, the distribution of elements no longer exhibits uniformity but appears as discrete atomic clusters. This non-uniformity hinders accurate quantitative analysis. Addressing this challenge, we employed the high-sensitivity ICP-MS (Inductively Coupled Plasma Mass Spectrometry) technique, specifically designed for elemental analysis in samples (Laborda et al., 2014). In this experiment, we collected titanium nanoparticles from artificial saliva dissolved in nitric acid and utilized ICP-MS for precise quantitative and statistical analysis of titanium content in the solution. To gain a more detailed insight into the morphology and size of titanium particles, we further employed SEM.

## 2.4 Corrosion tests

### 2.4.1 Corrosion resistance test

Infection, medication, dietary factors, periodontal disease, smoking, and systemic illnesses can potentially decrease the pH of normal saliva from 6.3–7.0 to <6.0 (Licausi et al., 2013). Under acidic conditions, the oxide layer on implant surfaces may be compromised, resulting in surface erosion and eventual release of titanium particles in the absence of wear. Commonly used oral medications, such as citric acid, tetracycline, and sodium fluoride, can lower the solution's pH to <3 (Wheelis et al., 2016), causing rapid breakdown of the implant surface oxide layer and release of Ti particles. Therefore, this experiment simulated different acidic environments in the oral cavity using artificial saliva with pH values of 2.5, 5.5, and 7.0.

Each set of samples was immersed in 2 mL artificial saliva with different pH values, at 37°C for 7 days. SEM was utilized to compare the corrosion status of the samples before and after immersion, and EDX was employed to detect elemental changes on the corroded surface. To assess titanium release in highly acidic conditions, artificial saliva with a pH of 2.5 was collected, and the titanium content was quantified using ICP-MS, followed by statistical analysis. TEM was employed to investigate the morphology and size of particles that might exist in the solution.

### 2.4.2 Electrochemical tests

The electrochemical workstation (CHI6600E, Chinstruments, China) was used to perform the electrochemical tests on four sets of samples, respectively. A three-electrode setup was used, with the sample as the working electrode, the saturated glyceryl electrode as the reference electrode, and the platinum plate electrode as the counter electrode. Artificial saliva at pH 6.5°C and 37°C was used as the electrolyte. All tests were performed in a simulated oral environment at 37°C ± 1°C. Electrochemical tests were performed according to ASTM-G61 standard. The first step was system stabilization, and after 3600s of open circuit potential (OCP) monitoring, dynamic potential polarization tests and electrochemical impedance spectroscopy (EIS) tests were performed at a stable OCP. EIS tests were performed in the frequency range of 100 kHz-0.005 Hz, and Nyquist plots were plotted using EIS data. The dynamic potential polarization test was performed at a scan rate of 0.5 mV/s, and the corrosion potential (Ecorr) and the corresponding current density (Icorr) were estimated using Tafel curves. The measurements were repeated three times for each condition.

## 2.5 Cytotoxic studies

### 2.5.1 Cell cultures

Biocompatibility tests were performed according to ISO 7405–2018 (ISO, 2018). The cells used in this test were bone marrow mesenchymal stem cells (BMSCs)Cultivate under conditions of 37°C, 5% $CO_2$, and saturated humidity until cells reach 70%–80% growth. Perform passage using 0.25% trypsin. Cells cultivated up until passage 3 (P3) then ready for experimental use. The titanium samples were placed in complete medium and in a 37°C for 72 h to obtain the extracts for the cell experiments.

### 2.5.2 Fluorescent staining

Cells at a density of $1\times10^5$ cells/mL were incubated in confocal dishes for 24 h. Cells were seen to adhere to the wall under an inverted microscope, the original culture medium was discarded, an immersion fluid exchange was performed, and the plates were incubated in an incubator for 24 h. And then rinsed three times with PBS. Add 150 μL of staining working solution A, incubate for 30 min at 37°C protected from light, rinse three times with PBS, add 150 μL of staining working solution B, and incubate for 20 min at 37°C protected from light. Observe the cell morphology at 488 nm under a laser confocal microscope (FV3000, Olympus, Japan).

### 2.5.3 LDH tests

The cytotoxicity of the samples was assessed by quantifying the release of lactate dehydrogenase (LDH) from BMSCs. Following cultivation, cells were seeded into a 96-well plate and treated with different material extracts. After 12 h of incubation, LDH release reagent was added, and the cells were incubated for an additional hour. The cell culture plate was then centrifuged at 400g for 5 min using a multi-well plate centrifuge. Supernatant (120 μL) from each well was transferred to a new 96-well plate, and absorbance was measured at 490 nm.

## 2.6 Statistical analysis

OriginPro 8.5 and Graphpad Prism9 software have been used for all graphical and statistical analyses. All experiments were conducted

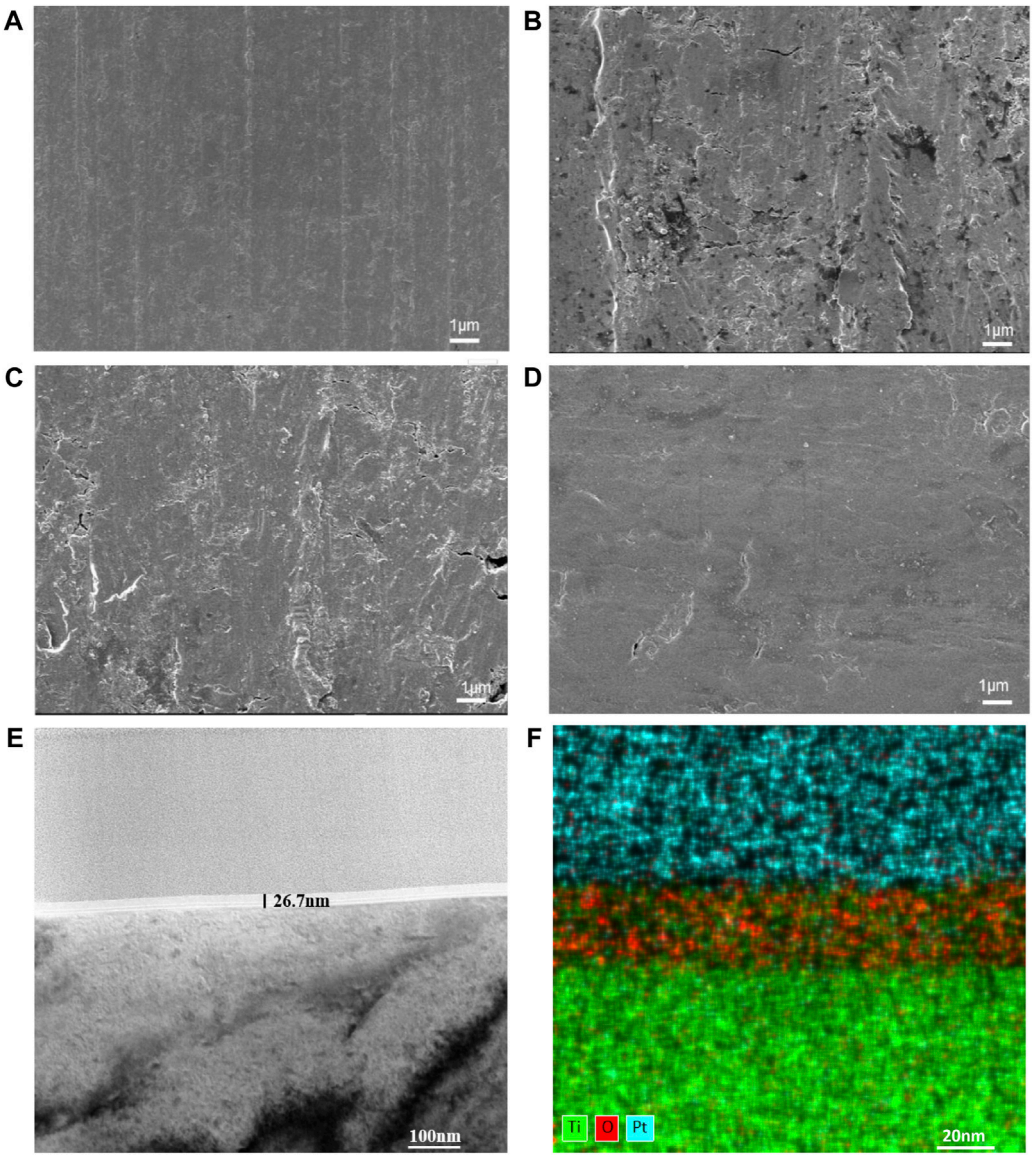


FIGURE 2
Surface morphologies of CP-Ti with different ALD cycles. **(A)** CP-Ti, **(B)** 100ALD-Ti, **(C)** 300ALD-Ti and **(D)** 500ALD-Ti of SEM. **(E)** TEM and **(F)** mapping for 300ALD-Ti.

three times, except for the LDH assay, which was performed four times. All repeated measurements were expressed as standard deviation (SD). The statistical significance of the data was estimated using a one-way analysis of variance (ANOVA). $p < 0.05$ was considered statistically significant for significance levels, * for $p < 0.05$ and ** for $p < 0.01$.

# 3 Results

## 3.1 Surface characterization

The surface morphologies of the modified samples are shown in Figure 2. The SEM results (Figures 2A–D) showed that the surface of the $TiO_2$ films generated by ALD was significantly smoother as the number of cycles increased. Since the thinness of $TiO_2$ nanofilm increases with the ALD cycle number, a thick enough $TiO_2$ film improves the surface smoothness. TEM was employed to examine the 300-cycle group, and the results are depicted in Figures 2E, F. The nanofilm exhibited a thickness of 26.7 nm, with an average $TiO_2$ film thickness of 0.089 nm per cycle. Figure 2F illustrates the even distribution of titanium and oxygen elements across the cross-section of the film. The upper layer, containing platinum for detection purposes, is clearly distinguished from the lower layer, representing the pure titanium substrate without additional elements.

The EDX spectra (Figures 3A–D) show the elemental distribution of titanium and oxygen on the surfaces of each group. Table 1 and Figure 3E indicates the titanium and oxygen content of the sample surface. The increase of oxygen

10.3389/fbioe.2024.1346404

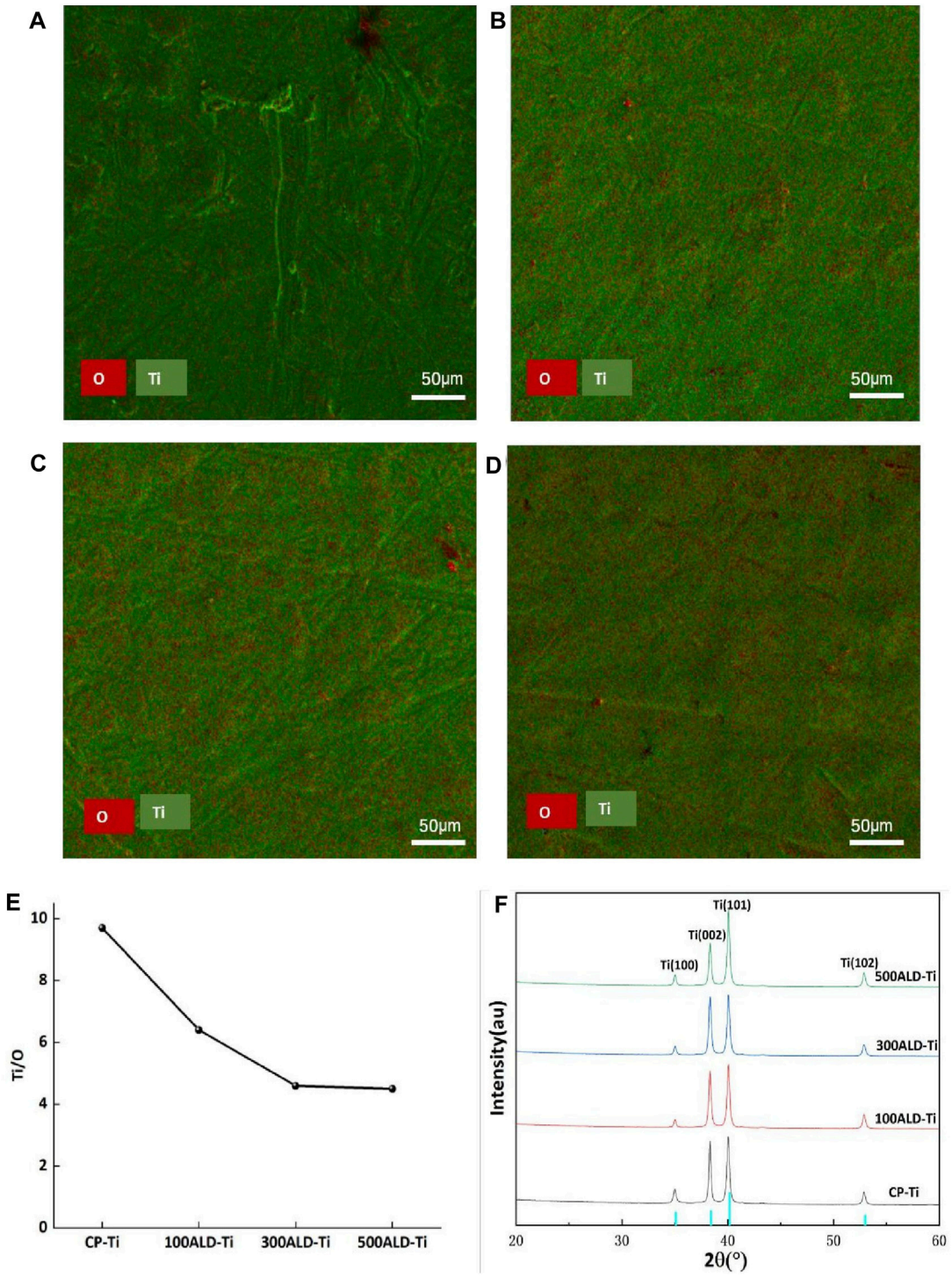


FIGURE 3
Phase composition and elemental distribution. **(A)** CP-Ti, **(B)** 100ALD-Ti, **(C)** 300ALD-Ti and **(D)** 500ALD-Ti is the mapping diagram after EDX, with O in red and Ti in green. **(E)** Titanium oxygen ratio by EDX spectra. **(F)** XRD patterns. The blue color of the horizontal axis indicates Amorphous $TiO_2$ type.

ratio on the surface suggests the covering of $TiO_2$ on the Ti surface. Since the oxygen content is not changed after 300 cycles of $TiO_2$, a uniform overcoating is realized. The XRD spectra of the samples are in Figure 3F. All diffraction peaks are in good agreement with the standard JCPDS data. The anatase $TiO_2$ films had strong diffraction peaks at $2\theta = 25.4^{\circ}$ and $48.0^{\circ}$, while none of the three groups of ALD-Ti saw this diffraction peak, indicating that the increase in the number of cycles at the deposition temperature of 160°C did not change the crystalline shape of $TiO_2$.

TABLE 1 Surface analysis of the elemental composition of $TiO_2$ films deposited by EDX.

| | CP-Ti | 100ALD-Ti | 300ALD-Ti | 500ALD-Ti |
|---|---|---|---|---|
| Ti (%) | 90.7 | 86.6 | 82.3 | 82.0 |
| O (%) | 9.3 | 13.4 | 17.7 | 18.0 |
| Ti/O | 9.7 | 6.4 | 4.6 | 4.5 |

## 3.2 Friction tests

The surface morphology of the sample after friction is shown in Figures 4A–D. It is evident that all four groups showed friction marks on the surface after friction. However, as the number of cycles increased, the friction marks became shallower, with the 500 ALD-Ti exhibiting the shallowest marks among the four groups.

To facilitate the observation of trends in friction resistance, the friction tests data were smoothed and then plotted, and the relationship between the number of cycles and the coefficient of friction (COF) is illustrated in Figure 4E. Evidently, both the experimental and control groups displayed a progressive increase in friction coefficient followed by a tendency to stabilize. This pattern arises from initial challenges like surface roughness and uneven contact, resulting in a COF increase. As the friction surface adapts and readjusts, the COF gradually stabilizes. And COF is inversely proportional to the friction resistance (Matijošius et al., 2020), from the smooth segment in the graph. As the cycle increases, COF becomes smaller, indicating that the friction resistance increases. The nanoscratch results, as shown in Figure 4F, indicate that the titanium dioxide nanofilm enhances the friction performance, with an improvement observed as the number of cycles increases.

To quantify the titanium species shed from the sample surface into the solution, the solution was acid dissolved and subjected to ICP-MS. The test results are summarized in Figure 4G. Analysis of the data showed that the release of titanium particles was significantly reduced in each experimental group compared to the control group ($p < 0.001$), indicating that the ALD-deposited $TiO_2$ coating was able to substantially reduce the release of titanium particles from the implant surface. The reduction in titanium particle release with increasing number of cycles was also observed between the experimental groups ($p < 0.05$), which suggests that the improvement of titanium particle release by the coating is closely related to the number of ALD cycles. SEM (Figure 4H) was employed to determine the size of residual particles in the immersion liquid. A total of 20 particles were identified and measured in the liquid. The particle sizes were predominantly in the micrometer range, exhibiting diverse shapes and forms.

## 3.3 Corrosion tests

### 3.3.1 Corrosion resistance test

Figures 5A–D show the SEM comparisons before and after corrosion. As can be seen from the figures, there is no change in the four groups of samples before and after corrosion at a PH of 7.0 and 5.5. 100ALD-Ti corrosion traces are more obvious at a PH of 2.5, followed by the 300ALD-Ti. While the 500ALD-Ti and CP-Ti groups had almost no corrosion. This indicates that the corrosion resistance increases with the increase in the number of ALD cycles. The basically unchanged morphology of the CP-Ti before and after corrosion is due to the uniform distribution of the CP-Ti surface and the consistent corrosion resistance, which results in no significant change in the overall surface structure before and after corrosion.

Further EDX analysis of the corroded samples shows that the darker areas in Figure 5C image have a low titanium-to-oxygen ratio (Figure 5E), which corresponds to the $TiO_2$ coating. While the brighter region has a high titanium-to-oxygen ratio (Figure 5F), which corresponds to a pure titanium substrate. This suggests that when the titanium implant comes into contact with an acidic environment, the $TiO_2$ coating is the first to be corroded, providing protection for the underlying titanium. In addition, as the number of ALD cycles increases, the coatings become thicker, exhibit better corrosion resistance, and provide stronger protection for the titanium. The TEM results (Figure 5G) revealed the presence of nanoscale titanium particles in the solution, exhibiting diverse morphologies and shapes.

To determine the titanium ions released from the sample surface into the solution, artificial saliva at a pH of 2.5 was collected and subjected to ICP-MS testing. The results, shown in Figure 6A, revealed that compared to the control group, all experimental groups exhibited a decrease in titanium content ($p < 0.05$). However, in comparison to the other two sample groups, the 500ALD-Ti exhibited a significant reduction in titanium ion release ($p < 0.001$). This finding is consistent with the SEM images, indicating that the decrease in titanium content in the experimental groups may be attributed to the protective effect of the $TiO_2$ coating on the underlying titanium substrate. The 500ALD-Ti, which had the thickest deposited $TiO_2$ coating, demonstrated the strongest protective effect on the substrate, resulting in the least amount of titanium ion release.

### 3.3.2 Electrochemical tests

Figure 6B depicts the typical electrochemical reactions that may occur during the corrosion process of uncoated titanium implants without protective coatings. In this process, water molecules play a role in providing hydroxide ions ($OH^-$) while oxygen acts as the oxidizing agent. In such a corrosive environment, titanium metal is oxidized into various oxidation states, releasing electrons. It is essential to note that this is just a simplified electrochemical reaction equation representing one possible aspect of the complex process of biocorrosion. The actual scenario is influenced by various factors such as the composition of oral fluids, temperature, pH levels, among others. Therefore, this simplified reaction equation only represents a potential aspect of the corrosion process.

Figure 6C reports the dynamic potential polarization curves of the experimental and control groups. The corrosion potentials of the samples in the experimental group were all shifted to the left compared to the control group. This may indicate a positive effect of the coating on the corrosion resistance of CP-Ti. According to the Tafel equation, the average values of corrosion potential (Ecorr) and corrosion current density

10.3389/fbioe.2024.1346404

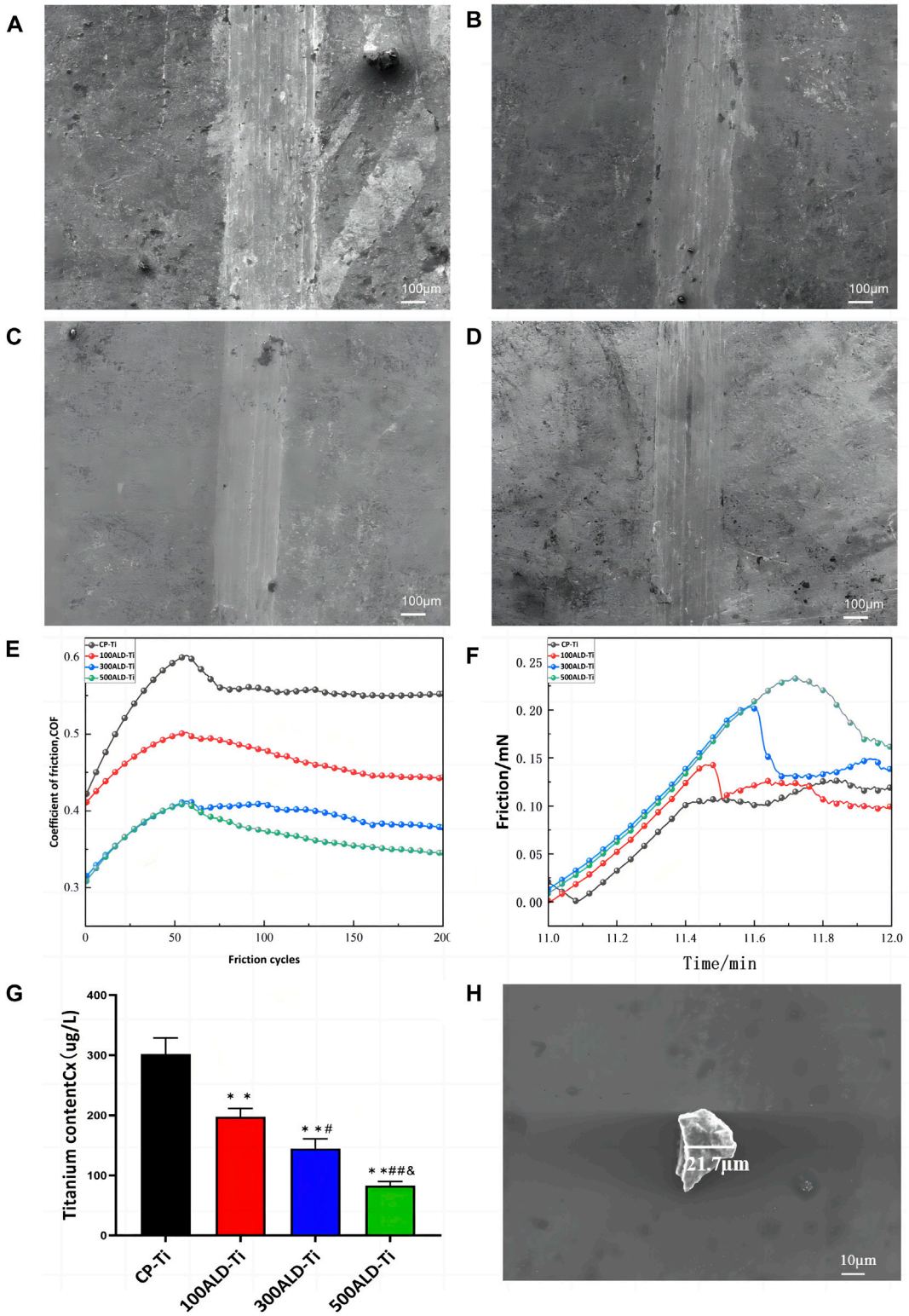


FIGURE 4
Friction performance. SEM images of **(A)** CP-Ti, **(B)** 100ALD-Ti, **(C)** 300ALD-Ti and **(D)** 500ALD-Ti. **(E)** Influence of different deposition cycles on coefficient of friction. **(F)** Friction analysis of nano scratch testing. **(G)** ICP-MS of post-friction solutions. The results represent the average of three experiments. (n = 3, $*p < 0.05$, $**p < 0.001$ compared with the CP-Ti group; $\#p < 0.05$, $\#\#p < 0.001$ compared with the 100ALD-Ti group; and $p < 0.001$ compared with the 300ALD-Ti group). **(H)** SEM of particles in solution.

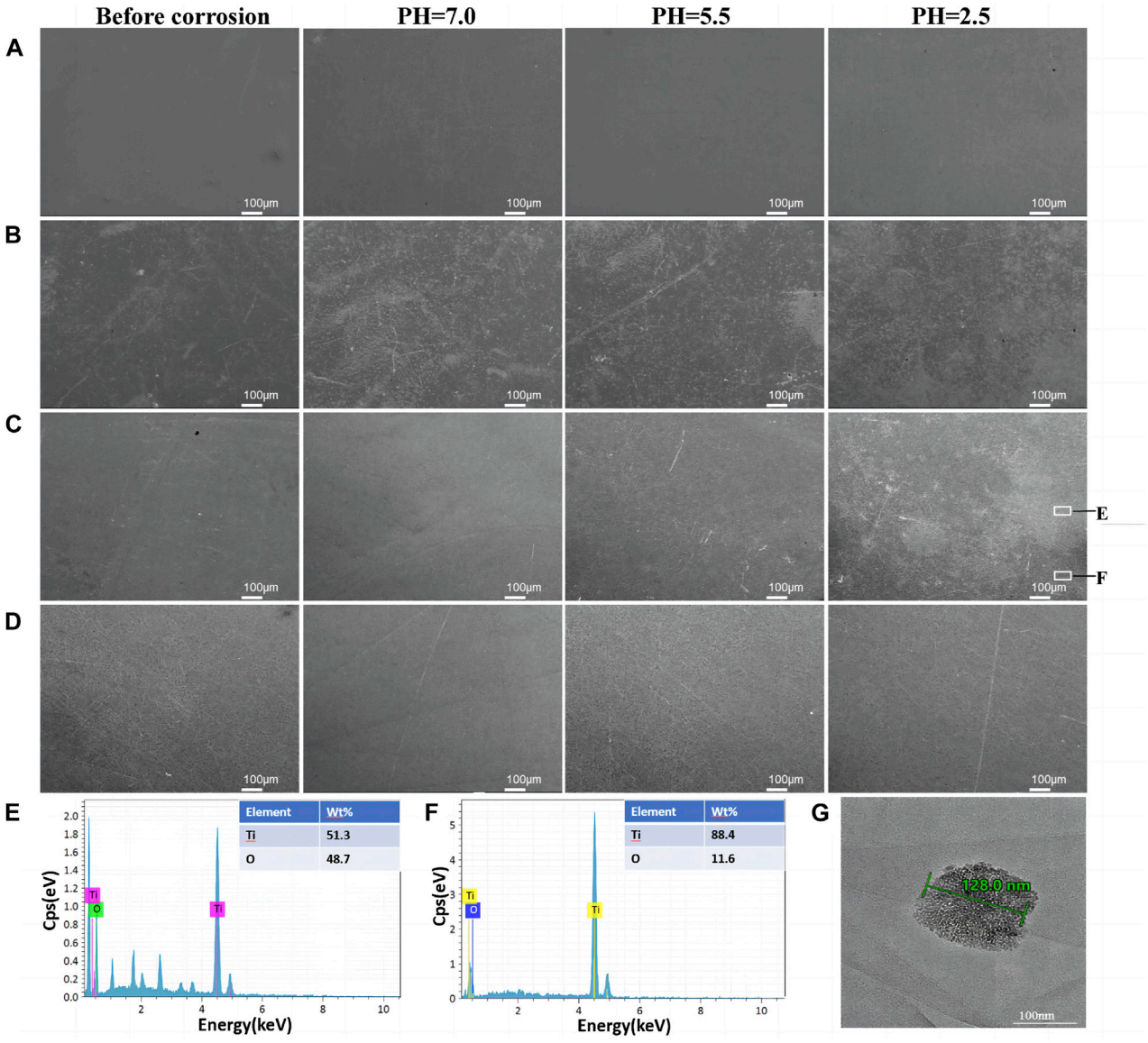


FIGURE 5
Surface morphology after corrosion. SEM images of **(A)**CP-Ti, **(B)** 100ALD-Ti, **(C)** 300ALD-Ti and **(D)** 500ALD-Ti. **(E,F)** correspond to the EDX spectra of the white boxed region in the last image **(C)**. **(G)** TEM image of Ti particles.

(Icorr) are shown in Table 2. The lower the corrosion current density, the lower the corrosion rate. The higher the corrosion potential in the case of similar currents, the lower the corrosion tendency, it can be observed that the corrosion current of experimental group are lower than the control group, indicating that the presence of $TiO_2$ coating increases the corrosion resistance of the material. And the number of cycles increased corrosion resistance also increased, 500ALD-Ti shows the best ability of corrosion resistance.

Figure 6D reveals the Nyquist (real vs. imaginary impedance) plots used to study the EIS data. The Nyquist plot reveals a significant increase in capacitance loop for the experimental group compared to the control group. A larger capacitance loop diameter correlates with higher corrosion resistance. This indicates that the 500ALD-Ti coating has the highest corrosion resistance and is considerably higher than the control group. 100ALD-Ti has the smallest semicircular ring and therefore has the lowest corrosion resistance in the experimental group. However, 100ALD-Ti still has corrosion resistance compared to the control group.

## 3.4 Cytotoxic studies

Because BMSCs are sensitive to external environmental changes and materials, and can reflect the effect of implant modification materials on cell activity and function, BMSCs are involved in the bone tissue regeneration and repair process *in vivo*, which is

10.3389/fbioe.2024.1346404

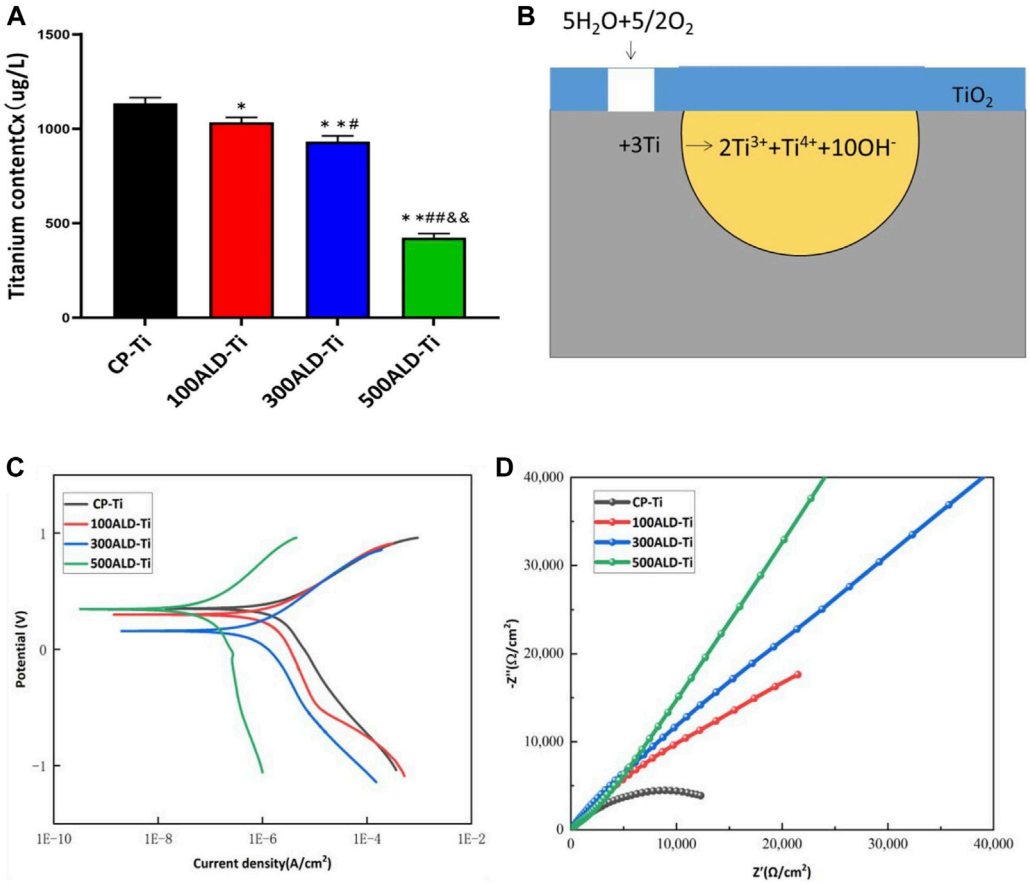


FIGURE 6
Corrosion performance. **(A)** ICP-MS of post-corrosion solution. The results represent the average of three experiments. (n = 3, *$p < 0.05$, **$p < 0.001$ compared with the CP-Ti group; #$p < 0.05$, ##$p < 0.001$ compared with the 100ALD-Ti group; and&$p < 0.001$ compared with the 300ALD-Ti group). **(B)** The reaction route for titanium corrosion. **(C)** Potentiodynamic polarization (Tafel) plots and **(D)** Nyquist plots for electrochemical corrosion.

**TABLE 2** Means and standard deviations of Icorr and Ecorr for each group, n = 3.

| | CP-Ti | 100ALD-Ti | 300ALD-Ti | 500ALD-Ti |
|---|---|---|---|---|
| Icorr ($A/cm^2$) | (3.44 ± 2.29) | (1.41 ± 0.62) | (7.17 ± 2.25) | (1.46 ± 1.59) |
| | E−6 | E−6 | E−7 | E−7 |
| Ecorr(V) | 0.14 ± 0.04 | 0.21 ± 0.12 | 0.22 ± 0.08 | 0.24 ± 0.07 |

important for implant compatibility and bioactivity, BMSCs were selected for this test. To analyze the cytotoxicity, confocal microscopy experiments were performed using both xanthophyll-AM and propidium iodide (PI) solutions, which were used to stain live and dead cells, respectively, and the results are displayed in Figures 7A–D. There were fewer dead cells in both the control and experimental groups.

In LDH test on BMSCs indicated that both pure titanium and ALD-deposited $TiO_2$ films were not cytotoxic and were not correlated with the number of cycles. The results of the cytotoxicity test are shown in Figure 7E. Compared to the CP-Ti group, the cell death rates in all other groups did not show a statistically significant increase.

## 4 Discussion

Implant surface degradation in the human body is caused by both friction (resulting in mechanical particle breakdown) and corrosion (leading to chemical degradation of soluble metal ions) (Delgado-Ruiz and Romanos, 2018). Titanium implants with $TiO_2$ coatings exhibit strong resistance to friction and corrosion (Matijošius et al., 2020). To address the issue of particle release due to friction and corrosion of these implants, this study deposited thin $TiO_2$ films using the ALD technique to create protective layers. ALD's step-by-step deposition process allows precise control at the atomic level, ensuring uniformity and accurate thickness control of the film (Kim et al., 2021).

10.3389/fbioe.2024.1346404

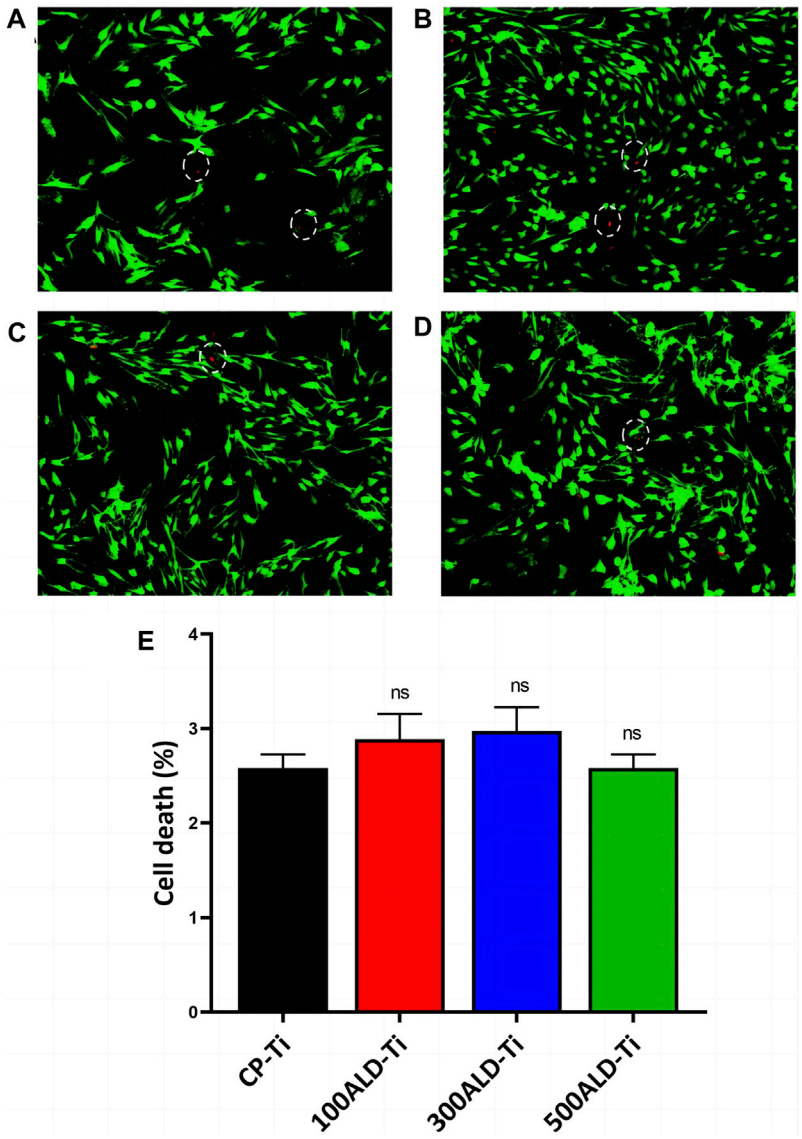


FIGURE 7
Cytotoxic assays. Fluorescence images after live/dead staining of bone marrow mesenchymal stem cells (BMSC) after culturing for 48 h **(A)** CP-Ti **(B)** 100ALD-Ti **(C)** 300ALD-Ti and **(D)** 500ALD-Ti. **(E)** LDH assay of BMSC. The results represent the average of three experiments. (n = 4, ns mean $p > 0.05$).

The crystalline shape of $TiO_2$ deposited by ALD is related to the deposition temperature (Jolivet et al., 2023). The XRD results show that $TiO_2$ is an amorphous structure when the temperature is 160°C, consistent with literature reports (Liu et al., 2017). Moreover, the $TiO_2$ of different cycles did not show anatase titanium dioxide, which indicates that the crystalline form is not related to the number of cycles but to the working temperature. Anatase $TiO_2$ may be toxic to osteoblasts (Bernier et al., 2012). So the amorphous $TiO_2$ films in this study can avoid the toxicity problem. Furthermore, different cycle counts of ALD have been reported in the literature to have an effect on the corrosion resistance of zirconia films (Yang et al., 2017), but there is little literature comparing the friction and corrosion resistance of $TiO_2$ deposited on the surface of titanium implants with different ALD cycles. This study was therefore conducted with three gradients of cycle numbers to investigate the relationship between cycle numbers and friction and corrosion resistance.

In this study, we assessed how different ALD cycles affect titanium implant performance, specifically focusing on species release and friction corrosion resistance. We simulated intraoral conditions with artificial saliva at 37°C. We found that the $TiO_2$ coating initially experienced wear and corrosion, but it effectively protected the underlying titanium substrate. Thicker $TiO_2$ coatings showed greater resistance to both wear and corrosion, providing better protection for the titanium implant.

ICP analysis of the immersion solution confirmed reduced ion levels, with the 500ALD-Ti group having significantly lower titanium ion concentrations compared to other groups. This aligns with our friction and corrosion results, confirming that the titanium dioxide film effectively limits the release of titanium species from the implant's surface. Overall, increasing the number of ALD cycles enhances friction corrosion resistance and reduces titanium species release.

Despite the small thickness of $TiO_2$ overcoating layers, they significantly contributed to the corrosion behavior of CP-Ti. The smaller corrosion current (Icorr) values of the coated samples obtained by fitting the dynamic potential polarization curves using Tafel curves indicate that the coatings effectively reduced the corrosion rate of Ti and protected its surface from electrochemical reactions. And the 500-cycle $TiO_2$ films showed the smallest Icorr compared to the other two sets of coatings, a trend consistent with that reported in the literature (Kania et al., 2021). Moreover, Nyquist plots of impedance spectra showed that the experimental group had a larger semicircle diameter than the control group, while the 500-cycle group had the largest, which suggested that the films improved the insulating properties of the surface. In other words, the ALD films are better capacitors with a higher protection level than pure titanium. This may be due to the fact that the standard electrode potential of $TiO_2$ is the same as that of titanium, which slows down the oxidation rate. This paper used three different methods to evaluate the corrosion resistance: dynamic polarization curves, EIS spectroscopy and immersion experiments. The results of the three methods are basically consistent. By increasing the number of ALD cycles of the $TiO_2$ film, the corrosion resistance of the titanium surface can be significantly improved, the corrosion rate reduced, the corrosion area minimized, and the ions release reduced, providing an effective method for the corrosion protection of titanium materials in various applications.

It is worth mentioning that although the cell activity of the experimental group in the *in vitro* cell test was higher than that of the control group and increased with cycling, the cell activity of all four groups of samples was smaller than that of the blank group, and there was no statistical difference between the groups. Therefore, the experimental results can only show that $TiO_2$ is not cytotoxic, but cannot prove that the coating can increase cellular activity. This is inconsistent with the report of Liu et al. on the ability of $TiO_2$ to increase cytocompatibility (Liu et al., 2017), which may be due to the fact that the number of cycles in the literature is 2500, while the number of cycles in this experiment is less, and the uncoated pure titanium can also show high biocompatibility and stimulate cell differentiation in the osteogenic direction, so the difference between the experimental group and the control group is smaller.

While Atomic Layer Deposition (ALD) technology demonstrates significant advantages in surface modification, it still encounters challenges in large-scale manufacturing. The layer-by-layer deposition process of ALD results in a relatively slow preparation speed, as each layer needs to go through a complete cycle. This limitation hampers the technology compared to other surface modification techniques. To address this issue, optimizing the reaction conditions of ALD to enhance the efficiency of each cycle and consequently increase the preparation speed could be considered. Another significant challenge is reducing the cost associated with ALD in manufacturing. The ALD process requires substantial energy for heating and vacuum, making optimization in throughput crucial (Zhuiykov et al., 2017). Adjusting the reactor to maximize precursor utilization and reducing precursor costs is a potential solution. Additionally, exploring more economical and readily available precursor materials can effectively alleviate cost pressures.

From the comprehensive experimental results, it is worth affirming that the ALD-deposited $TiO_2$ coating can both enhance the frictional corrosion resistance of pure titanium and reduce the release of titanium species. In this experiment, three sets of gradient cycle times were set, so it is presumed that the increase of ALD cycle numbers has positively affects the reduction of species release. However, no conclusion has been reached on the optimal number of cycles for the friction resistance and corrosion performance; therefore, the optimal number of cycles for the friction resistance and corrosion performance will be further investigated. Furthermore, the relationship between the biocompatibility of ALD-$TiO_2$ films and their resistance to frictional corrosion remains uncertain. To address this uncertainty, we plan to conduct additional biocompatibility experiments in subsequent studies, examining the biological performance of $TiO_2$ films under different frictional corrosion conditions. Through these experiments, we aim to determine the optimal number of $TiO_2$ film cycles to achieve the best performance in various aspects.

## 5 Conclusion

In this study, $TiO_2$ films were prepared on the titanium surface by the ALD technique, which significantly improved the friction corrosion resistance of the material and thus reduced the release of titanium species. Three different cycle designs demonstrated that the increase in the number of ALD cycles significantly impacted the morphology and properties of the $TiO_2$ films, significantly improving the friction corrosion resistance of the $TiO_2$ films and reducing release of titanium species. This provides important guidance for designing and preparing titanium implants with more resistance to friction and corrosion. Future studies can further explore optimizing ALD parameters and selecting coating materials to achieve better friction corrosion resistance and biocompatibility.

## Data availability statement

The original contributions presented in the study are included in the article/Supplementary material, further inquiries can be directed to the corresponding authors.

## Ethics statement

The animal study was approved by the Ethics Committee of The School of Stomatology of Shanxi Medical University. The study was conducted in accordance with the local legislation and institutional requirements.

## Author contributions

XZo: Conceptualization, Methodology, Writing–original draft. XZg: Conceptualization, Methodology, Writing–original draft. ZZ: Formal Analysis, Methodology, Writing–review and editing. FM:

Formal Analysis, Writing–review and editing. RL: Formal Analysis, Investigation, Writing–review and editing. MZ: Formal Analysis, Investigation, Writing–review and editing. YH: Formal Analysis, Investigation, Writing–review and editing. QX: Formal Analysis, Investigation, Writing–review and editing. XS: Supervision, Writing–review and editing. BZ: Supervision, Writing–review and editing. XW: Conceptualization, Supervision, Validation, Writing–review and editing.

## Funding

The author(s) declare financial support was received for the research, authorship, and/or publication of this article. This work was supported by National Natural Science Foundation of China (82071155, 82271023), the Project of Shanxi Province Key Laboratory of Oral Diseases Prevention and New Materials [grant number RC2021-02 and RC202301], the Shanxi Applied Basic Research Program Outstanding Youth Cultivation Project Fund [grant numbers 202203021223006], Graduate Education Innovation Project of Shanxi Province (2021Y432, 2023SJ170), and R&D Program of Beijing Municipal Education Commission (KM202010025013).

## Conflict of interest

The authors declare that the research was conducted in the absence of any commercial or financial relationships that could be construed as a potential conflict of interest.

## Publisher's note



## References

Alves, S. A., Patel, S. B., Sukotjo, C., Mathew, M. T., Filho, P. N., Celis, J.-P., et al. (2017). Synthesis of calcium-phosphorous doped TiO2 nanotubes by anodization and reverse polarization: a promising strategy for an efficient biofunctional implant surface. *Appl. Surf. Sci.* 399, 682–701. doi:10.1016/j.apsusc.2016.12.105

ASTM (1993). *Standard guide for determining synergism between wear and corrosion*.

Awad, K., Young, S., Aswath, P., and Varanasi, V. (2022). Interfacial adhesion and surface bioactivity of anodized titanium modified with SiON and SiONP surface coatings. *Surf. Interfaces* 28, 101645. doi:10.1016/j.surfin.2021.101645

Berbel, L. O., Banczek, E. D. P., Karoussis, I. K., Kotsakis, G. A., and Costa, I. (2019). Determinants of corrosion resistance of Ti-6Al-4V alloy dental implants in an *in vitro* model of peri-implant inflammation. *PLoS One* 14, e0210530. doi:10.1371/journal.pone.0210530

Bernier, M. C., El Kirat, K., Besse, M., Morandat, S., and Vayssade, M. (2012). Preosteoblasts and fibroblasts respond differently to anatase titanium dioxide nanoparticles: a cytotoxicity and inflammation study. *Colloids Surf. B Biointerfaces* 90, 68–74. doi:10.1016/j.colsurfb.2011.09.044

Blendinger, F., Seitz, D., Ottenschlager, A., Fleischer, M., and Bucher, V. (2021). Atomic layer deposition of bioactive TiO2 thin films on polyetheretherketone for orthopedic implants. *ACS Appl. Mater Interfaces* 13, 3536–3546. doi:10.1021/acsami.0c17990

Cheng, W., Xu, X., Lang, Y., Cheng, Z., Rizwan, M., Tang, X., et al. (2021). Anatase and rutile TiO2 nanoparticles lead effective bone damage in young rat model via the igf-1 signaling pathway. *Int. J. Nanomedicine* 16, 7233–7247. doi:10.2147/ijn.s333632

Delgado-Ruiz, R., and Romanos, G. (2018). Potential causes of titanium particle and ion release in implant dentistry: a systematic review. *Int. J. Mol. Sci.* 19, 3585. doi:10.3390/ijms19113585

Deng, Z., Jia, Q., Feng, B., and Liu, L. J. J. C. L. (2021). Research progress on fabrication and applications of high-performance films by pulsed laser deposition. *J. Nanomater.* 8, 0802010. doi:10.3788/cjl202148.0802010

Eger, M., Sterer, N., Liron, T., Kohavi, D., and Gabet, Y. (2017). Scaling of titanium implants entrains inflammation-induced osteolysis. *Sci. Rep.* 7, 39612. doi:10.1038/srep39612

Esmaeili, M. M., Mahmoodi, M., and Imani, R. J. I. (2017). Tantalum carbide coating on Ti-6Al-4V by electron beam physical vapor deposition method: study of corrosion and biocompatibility behavior. *Int. J. Appl. Ceram. Technol.* 14, 374–382. doi:10.1111/ijac.12658

Fazel, M., Salimijazi, H. R., and Shamanian, M. (2018). Improvement of corrosion and tribocorrosion behavior of pure titanium by subzero anodic spark oxidation. *ACS Appl. Mater Interfaces* 10, 15281–15287. doi:10.1021/acsami.8b02331

Gnanavel, S., Ponnusamy, S., Mohan, L., and Muthamizhchelvan, C. J. J. (2018). *In vitro* corrosion behaviour of Ti–6Al–4V and 316L stainless steel alloys for biomedical implant applications. *J. Bio- Tribo-Corrosion* 4, 1–8. doi:10.1007/s40735-017-0118-8

Hashemi Astaneh, S., Faverani, L. P., Sukotjo, C., and Takoudis, C. G. (2021). Atomic layer deposition on dental materials: processing conditions and surface functionalization to improve physical, chemical, and clinical properties - a review. *Acta Biomater.* 121, 103–118. doi:10.1016/j.actbio.2020.11.024

He, X., Reichl, F. X., Wang, Y., Michalke, B., Milz, S., Yang, Y., et al. (2016). Analysis of titanium and other metals in human jawbones with dental implants - a case series study. *Dent. Mater* 32, 1042–1051. doi:10.1016/j.dental.2016.05.012

Heringa, M. B., Peters, R. J. B., Bleys, R., van der Lee, M. K., Tromp, P. C., van Kesteren, P. C. E., et al. (2018). Detection of titanium particles in human liver and spleen and possible health implications. *Part Fibre Toxicol.* 15, 15. doi:10.1186/s12989-018-0251-7

ISO (2018). *Dentistry - evaluation of biocompatibility of medical devices used in dentistry*.

Jolivet, A., Labbé, C., Frilay, C., Debieu, O., Marie, P., Horcholle, B., et al. (2023). Structural, optical, and electrical properties of TiO2 thin films deposited by ALD: impact of the substrate, the deposited thickness and the deposition temperature. *Appl. Surf. Sci.* 608, 155214. doi:10.1016/j.apsusc.2022.155214

Kania, A., Szindler, M. M., and Szindler, M. J. C. (2021). Structure and corrosion behavior of TiO2 thin films deposited by ALD on a biomedical magnesium alloy. *Coatings* 11, 70. doi:10.3390/coatings11010070

Kim, H.-M., Kim, D.-G., Kim, Y.-S., Kim, M., and Park, J. (2023). Atomic layer deposition for nanoscale oxide semiconductor thin film transistors: review and outlook. *Int. J. Extreme Manuf.* 5, 012006. doi:10.1088/2631-7990/acb46d

Kim, Y., Woo, W. J., Kim, D., Lee, S., Chung, S. M., Park, J., et al. (2021). Atomic-layer-deposition-based 2D transition metal chalcogenides: synthesis, modulation, and applications. *Adv. Mater* 33, e2005907. doi:10.1002/adma.202005907

Laborda, F., Bolea, E., and Jimenez-Lamana, J. (2014). Single particle inductively coupled plasma mass spectrometry: a powerful tool for nanoanalysis. *ACS Publications* 86 (5), 2270-2278. doi:10.1021/ac402980q

Lara Rodriguez, L., Sundaram, P. A., Rosim-Fachini, E., Padovani, A. M., and Diffoot-Carlo, N. (2014). Plasma electrolytic oxidation coatings on γTiAl alloy for potential biomedical applications. *J. Biomed. Mater Res. B Appl. Biomater.* 102, 988–1001. doi:10.1002/jbm.b.33079

Leinenbach, C., and Eifler, D. (2009). Influence of oxidation treatment on fatigue and fatigue-induced damage of commercially pure titanium. *Acta Biomater.* 5, 2810–2819. doi:10.1016/j.actbio.2009.03.029

Licausi, M.-P., Muñoz, A. I., and Borrás, V. (2013). Influence of the fabrication process and fluoride content on the tribocorrosion behaviour of Ti6Al4V biomedical alloy in artificial saliva. *J. Mech. Behav. Biomed. Mater* 20, 137–148. doi:10.1016/j.jmbbm.2013.01.019

Liu, L., Bhatia, R., and Webster, T. J. (2017). Atomic layer deposition of nano-TiO(2) thin films with enhanced biocompatibility and antimicrobial activity for orthopedic implants. *Int. J. Nanomedicine* 12, 8711–8723. doi:10.2147/IJN.S148065

Matijošius, T., Pivoriūnas, A., Čebatariūnienė, A., Tunaitis, V., Staišiūnas, L., Stalnionis, G., et al. (2020). Friction reduction using Nanothin Titanium layers on

anodized aluminum as potential bioceramic material. *Ceram. Int.* 46, 15581–15593. doi:10.1016/j.ceramint.2020.03.105

Mohseni, E., Zalnezhad, E., and Bushroa, A. R. (2014). Comparative investigation on the adhesion of hydroxyapatite coating on Ti–6Al–4V implant: a review paper. *Int. J. Adhesion Adhesives* 48, 238–257. doi:10.1016/j.ijadhadh.2013.09.030

Mombelli, A., Hashim, D., and Cionca, N. (2018). What is the impact of titanium particles and biocorrosion on implant survival and complications? A critical review. *Clin. Oral Implants Res.* 29 (18), 37–53. doi:10.1111/clr.13305

Niemelä, J.-P., Marin, G., and Karppinen, M. J. S. (2017). Titanium dioxide thin films by atomic layer deposition: a review. *A Rev.* 32, 093005. doi:10.1088/1361-6641/aa78ce

Ossowska, A., and Zieliński, A. J. C. (2020). The mechanisms of degradation of titanium dental implants. *Coatings* 10, 836. doi:10.3390/coatings10090836

Peron, M., Cogo, S., Bjelland, M., Bin Afif, A., Dadlani, A., Greggio, E., et al. (2021). On the evaluation of ALD TiO2, ZrO2 and HfO2 coatings on corrosion and cytotoxicity performances. *J. Magnesium Alloys* 9, 1806–1819. doi:10.1016/j.jma.2021.03.010

Prestat, M., and Thierry, D. (2021). Corrosion of titanium under simulated inflammation conditions: clinical context and *in vitro* investigations. *Acta Biomater.* 136, 72–87. doi:10.1016/j.actbio.2021.10.002

Shakeel, M., Jabeen, F., Shabbir, S., Asghar, M. S., Khan, M. S., and Chaudhry, A. S. (2016). Toxicity of nano-titanium dioxide (TiO2-NP) through various routes of exposure: a review. *a Rev.* 172, 1–36. doi:10.1007/s12011-015-0550-x

Tobin, E. J. (2017). Recent coating developments for combination devices in orthopedic and dental applications: a literature review. *Adv. Drug Deliv. Rev.* 112, 88–100. doi:10.1016/j.addr.2017.01.007

Wheelis, S. E., Gindri, I. M., Valderrama, P., Wilson Jr, T. G., Huang, J., and Rodrigues, D. C. J. (2016). Effects of decontamination solutions on the surface of titanium: investigation of surface morphology, composition, and roughness. *Clin. Oral Implants Res.* 27, 329–340. doi:10.1111/clr.12545

Wree, J. L., Rogalla, D., Ostendorf, A., Schierbaum, K. D., and Devi, A. (2023). Plasma-Enhanced atomic layer deposition of molybdenum oxide thin films at low temperatures for hydrogen gas sensing. *ACS Appl. Mater Interfaces*. doi:10.1021/acsami.2c19827

Xu, J., Aoki, H., Kasugai, S., and Otsuka, M. (2020). Enhancement of mineralization on porous titanium surface by filling with nano-hydroxyapatite particles fabricated with a vacuum spray method. *Mater Sci. Eng. C Mater Biol. Appl.* 111, 110772. doi:10.1016/j.msec.2020.110772

Yang, B. (2020). Applications of titania atomic layer deposition in the biomedical field and recent updates. *Am. J. Biomed. Sci. Res.* 8, 465–468. doi:10.34297/ajbsr.2020.08.001321

Yang, Q., Yuan, W., Liu, X., Zheng, Y., Cui, Z., Yang, X., et al. (2017). Atomic layer deposited ZrO(2) nanofilm on Mg-Sr alloy for enhanced corrosion resistance and biocompatibility. *Acta Biomater.* 58, 515–526. doi:10.1016/j.actbio.2017.06.015

Zhou, J., Sun, Y., Shu, H., Jie, S., Jing, L., Emmanuel, A. B. J. O., et al. (2019). Effect of laser peening on friction and wear behavior of medical Ti6Al4V alloy. *Opt. Laser Technol.* 109, 263–269. doi:10.1016/j.optlastec.2018.08.005

Zhuiykov, S., Kawaguchi, T., Hai, Z., Akbari, M. K., and Heynderickx, P. (2017). Interfacial engineering of two-dimensional nano-structured materials by atomic layer deposition. *Appl. Surf. Sci.* 392, 231–243. doi:10.1016/j.apsusc.2016.09.040

# Frontiers in
# Bioengineering and Biotechnology

**Accelerates the development of therapies, devices, and technologies to improve our lives**

A multidisciplinary journal that accelerates the development of biological therapies, devices, processes and technologies to improve our lives by bridging the gap between discoveries and their application.

---

## Discover the latest Research Topics

See more →

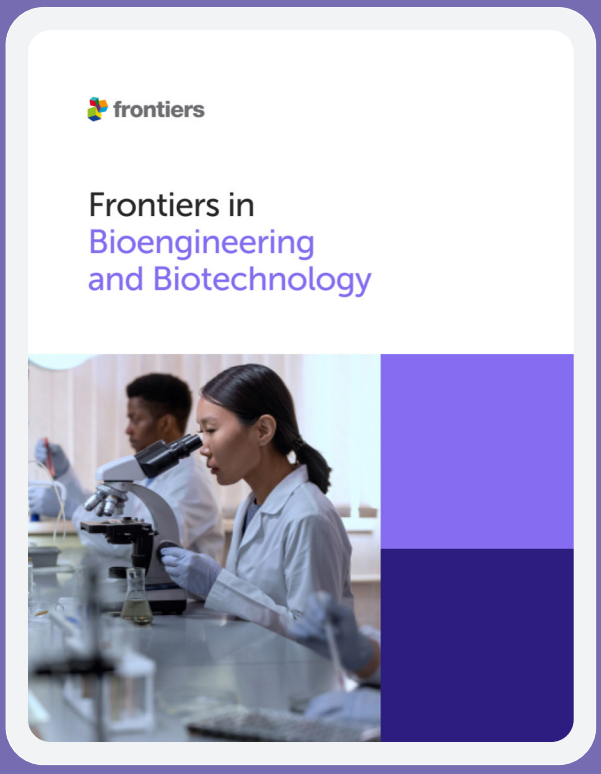


**Frontiers**

Avenue du Tribunal-Fédéral 34
1005 Lausanne, Switzerland
frontiersin.org

**Contact us**

+41 (0)21 510 17 00
frontiersin.org/about/contact